Optimizing The Installation Of Steel, Open-Ended Piles Through Impact Hammering For Offshore Applications

A Parametric, Experimental Study in The Geocentrifuge

T.O. Quinten

Thesis committee

Dr. Sc. A. Askarinejad	TU Delft
Prof. dr. K. Gavin	TU Delft
Dr. F. Pisano	TU Delft
Dr. ir. M. Alvarez Grima	IHC MTI
Dr. ir. C. van 't Hof	IHC MTI

IHC

TU Delft

Optimizing The Installation Of Steel, Open-Ended Piles Through Impact Hammering For Offshore Applications

A Parametric, Experimental Study In The Geocentrifuge

By

T.O.Quinten

in partial fulfilment of the requirements for the degree of

Master of Science
in Civil Engineering

at the Delft University of Technology,

to be defended publicly on Friday August 23, 2019 at 14:00 PM.

Supervisor:	Dr. Sc. A. Askarinejad	TU Delft
Thesis committee:	Prof. dr. K. Gavin	TU Delft
	Dr. F. Pisano	TU Delft
	Dr. ir. M. Alvarez Grima	IHC MTI
	Dr. ir. C. van ’t Hof	IHC MTI

Preface

Although it is generally believed that writing a thesis is a soloistic venture, I am happy to state that this report is the result of a large, well-orchestrated team effort which was maintained over the past 16 months. Back then, after an unsuccessful search for a topic of my liking at various companies, I decided try my luck at university and inquire about available dissertation topics with a selection of staff member, whom I knew well from my time as a teaching assistant. Shortly after, I was sitting in the office of Amin Askarinejad to discuss the possible continuation of the work of Joris van Zeben. Due to numerous discussions I had with him in the TA room, I had become quite enthusiastic about his research. Consequently, it did not take me long to decide that this was the topic I wanted to explore in my final time as a student. After the some final formalities at the IHC MTI office, which is conveniently located on the university's campus, and a warm welcome on behalf of IHC by Mario Alvarez Grima and Cornelis van 't Hof, the journey began.

After about 3 months an ambitious plan had been formulated to improve the existing actuator and conduct a total of 28 experiments at 50g. Looking back, I realize how ambitious the scope of the research really was. However, following a souring kick-off presentation, my own enthusiasm had infected the entire committee. Hence, everyone settled for itinerary I had ferociously presented over the course on 30 minutes. Later, I would come to realize that every minute I presented would effectively equate to >0.5 month of work. Consequently, there were times where the scope of the work felt a bit overwhelming. Fortunately, Amin, Cornelis and Mario, were very supportive and always willing to share knowledge, contacts and recourses for the sake of the project. Consequently, the number of people which were involved in the work gradually increased. This added a challenging but also rewarding aspect to the project; as it gave me the opportunity to closely work together with numerous experts in various fields but also meant that time management and planning were becoming a top priority. However, I believe I eventually found the right balance between the social and formal aspects of teamwork, which I found highly rewarding.

As we were approaching the end of 2018, I was practically became full member of the DEMO team in Stevin lab II. Together with Kees van Beek and Ronald van Leeuwen, numerous challenges in the area of mechanical and electrical design were tackled, and the first iteration of the improved set-up rapidly took shape. I am very grateful for the time I could spend in their presence, as it taught me some invaluable lessons about the multidisciplinary nature of research and the importance occasionally zoom out to critically review and discuss your work in a broad context. Only when you also explore the edges of your research domain, you appreciate how blurry these are. Implying that you will occasionally need to explore new territories and make new (social and theoretical) connections to get everything in focus.

Unfortunately, the new year was not festively ushered in as the actuator to proved incapable of executing its job in the under the effects enhanced gravity of the centrifuge. In the days leading up and following the new year, the silence that descends over the CEG faculty during the Christmas holidays was abruptly disturbed by the sound of hammers, drills and saws. In about 4 days, the set-up was entirely resigned and ready for deployment in the centrifuge. In this respect I owe a huge thank you to Kees, who conceitedly spend part of the holidays envisioning and constructing the second iteration of the actuator and thus spared me from the dreadful prospect of multiple weeks delay. Then, after about 10 months, it was finally time to put the actuator to the test with the execution of the first tests from the test matrix.

From here on, everything evolved rapidly. The preparation of samples and viscous fluid was

streamlined while the actuator was tweaked to enable the execution of the high frequency experiments. After some adjustments to the test matrix to account for the operational limitations of the actuator, the final tests were executed without major issues. At this time, my decision seek a job prior to finalizing my thesis, was putting heavy strain on the progress of the project. It is during these weeks that I truly learned what 'hard work' actually means. In this sens I truly experienced the Ng environment of the centrifuge. I will always be able to recall they Joy I relieve and feeling of achievement I felt on the 16th of June at about 9:00 PM, when the last test from the test matrix was finalized under the gaze of an equally happy Amin.

Finally, I want to express my gratitude for the opportunity to conduct advanced experimental research as a master student and the allocation of time, people and rescources by both Delft University of Technology and Royal IHC, which enabled me to make it all the way. Also, thank you Amin, for the your willingness to assist me with the centrifuge even when it is 9:00 PM on Saturday. Thank you Kees, Ron and Han, for endless support in terms of development, trouble shooting and amelioration of the actuator and the surrounding ecosystem. Jens and Marc, I appreciate your assistance when others were not available and your airiness when my mood was wighted down by the enhanced gravity. Cornelis and Mario, thank your for your honest feedback and dedication to help me realize the aims of the research. I am thankful to Erik Slis and Harry Bos for their expertize and help in the field of sensory equipment. A work of thanks is most certainly due to my roommate, Stijn Mouroulis, for celebrating the highs and mirroring the lows. As well as my family and girlfriend, for their unconditional support during all my endeavors, both a professionally and personally. Finally, a thank you to DEME N.V., for their comprehension and patience.

Tristan Quinten
August 2019

Contents

1

Abstract

As a result of population growth and economical prosperity, energy consumption has been on the rise for decades. Present-day projections predict the continuation of this trend with the rapid industrialization of former second world countries. Together with the rise of energy demand, incentives fo the scientific community to quantify the environmental impact of the ever increasing need for energy have gained momentum. It now is clear that continued use of carbon-based energy sources will have a catastrophic, irreversible impact on the global climate. The urgency of this message, which is supported by nearly the entire scientific community, was finally heard in 2012 when the Paris Agreement was drafted. Nearly collectively, the world's countries are committing themselves to start the transition to durable sources of energy.

One of the most promising sources of energy to facilitate the aforementioned transition, is the wind. Europe specifically is home to large patches of sea, which are ideally suited for the construction of offshore wind farms. Due to high construction costs, these endeavors out at sea were, until recently, heavily dependent of governmental support. However, due to advances in technology, wind frams have become profitable enough to be realized without governmental grands. Of the current offshore wind farms, the majority of the budget is allocated to the foundation design, construction and ultimately installation. Monopiles are convincingly the most common foundation type found. Although alternatives under development, it is unlikely for the popularity of this simplistic foundation will diminish in the near future. Especially, as the hollow, large diameter, hollow, steel profiles are finding their way into other foundations types, in example tripods.

The installation of the monopiles offshore is mostly done through costly operations involving large hydraulic hammers. Prior to installation, drivability analyses are commissioned which determine the required hammer capacity. The rather simplistic software (in terms of soil representation) used to conduct these calculations, offers limited room for the optimization of the installation process. On the other hand, several full scale experiments have demonstrated that clever manipulation of driving parameters, specifically: (I) hammer weight; (II) driving frequency; (III) falling height/impact velocity; can significantly benefit installation times. This leaves a huge potential for cost savings (several millions EUR) per farm and forms a prime opportunity to stimulate the transition of offshore wind energy towards the mainstream.

However, no consensus has been reached on the dynamic processes which positively contribute to the drivability of monopiles, let alone how these processes can be consciously induced in the subsoil. This research sets out to, by means of a parametric experimental study in the centrifuge, evaluate the effects of changes in driving parameters on driving time. Three hypothesis has have been drafted in an attempt to explain the higher efficiency piling operations employing HiLO (high frequency, low falling height) techniques instead of conventional driving, namely: (I) aggravated friction fatigue along the shaft due to an increased number of load cycles as a result of frequency

increase; (II) Less dynamic soil resistance following from lower impact velocities, yielding the more efficient usage of available piling energy; (III) accumulation of excess pore water pressures, which reduce the effective stress regime surrounding the pile and thereby benefit piling rates. Through 24 centrifuge experiments, the aforementioned hypotheses are evaluated. During the experiments the effect of changes in driving parameters in monitored. Moreover, water pressure sensors mounted both on the pile shaft and inside the surrounding soil body record the soil response during driving.

Results indicate that the dynamic installation of open-ended tubular piles in sandy soil, characterized by a high R_d (≈80%), is associated with the development of excess pore water pressures at larger radial distances from the pile due propagation of seismic waves. However, unlike similar experiments of samples with a lower R_d, the generated excess pore fluid pressures are limited in their magnitude as the soil exhibits no contraction to aid further generation. Moreover, closer to the pile, a transition towards a dilative soil regime is observed, where the increase of driving frequency is arguably related to the accumulation of tensile pore fluid pressures along the shaft, which negatively affects pile drivability. Results indicate the aforementioned adverse effect is partially compensated through the use of a heavy hammer due to subtle difference in soil-structure interaction related to the different geometry of the hammer. Consequently, it seems that HiLo driving is not a technique which guarantees better drivability under all circumstances. Hence, in the quest for optimum drivability, the prevailing soil conditions should play a decisive role in the selection of the best suited pile-hammer combination and driving technique.

2

Offshore wind energy

2.1. A call for renewable energy

Over the half a century, the world's energy consumption has soared. This observation can mainly be contributed to unprecedented population growth and progressive worldwide economic development. To put this claim into perspective, the world's total primary energy supply increased from 5500 Million Tons Oil Equivalent (*MTOE*) in 1971 to 13700 *MTOE* in 2015 [35]. Current projections suggest that this upward trend is expected to continue into 2040, where the world energy consumption will have risen by 28% [35]. At this moment, >75% of the world's energy demand is generated by the combustion of fossil fuels, i.e. natural gas, oil and coal. Apart from the finite nature of fossil fuels, the scientific community has generally acknowledged the environmental threats associated with its use as the globe's primary source of energy. With the Paris Agreement, the world, nearly collectively, showed its commitment to combat the adverse effects of greenhouse gas (GHG) emissions i.e. global warming, and lead the way towards a sustainable future.

In the light of the aforementioned events, the European Commission (EC) has the ambition to by 2030 have reduced GHG emissions by 40%. This would safeguard Europe's position to meet the 80-95% reduction of GHG emissions (with respect to 1995 levels) by 2050, as is required in order to meet the internationally agreed targets mentioned in the Paris Agreement [36]. To accomplish its goals, the EU strives to accelerate the adaptation of renewable energy sources. It aims at 27% renewable energy consumption by the year 2030, which could thereby also realize the EU's bold ambition to acquire the leading position in the field of renewable energy [38]. Contrastingly, future projections based on the current policies of the EU's member states indicate that the share of renewable energy, as a percentage of the total production within the EU, is likely to increase to 24.3% by 2030 respectively. Thereby underlining the need for the EU to update its political framework with regard to renewable energy [37]. Therefore, there is reason to expect new policy to stimulate the investment effort needed for the continued development and use of renewable energy sources.

One of the most promising means through which the EU but also the rest of the world can reach their goals regarding reduction of GHG emissions is wind energy generation. European statistics from 2005-2016 indicate that the share of wind energy was raised from 6%, 41 *GW*, in 2005 to 16.7%, 154 *GW*, in 2016, see Figure 2.1, thereby overtaking coal and becoming the second largest power capacity in the EU [120]. Although less pronounced, similar trends were seen all over the world. In 2015, 50% of the increase in global electricity generation was provided by wind energy [101]. This is a trend that is expected to continue over the coming decades. The latter is supported by the Global Wind Energy Council (GWEC). In one of its recent publications, it is mentioned that by 2030 the share of wind energy in the global energy generation capacity can amount to 14% [101]. GWEC also foresees a sustained increase over the successive decades after 2030. When focusing on the European continent, this upward trend is highlighted even further. Provided that the EU is successful at

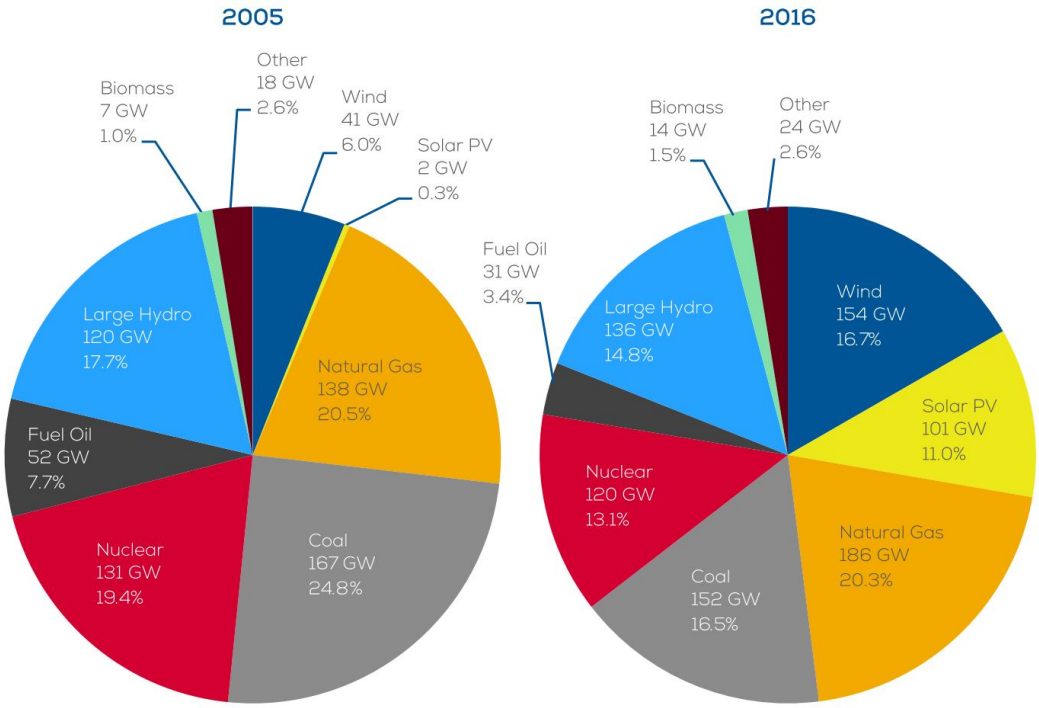

Figure 2.1: Share per source in EU's total installed generation capacity for 2005 and 2016 [120]

implementing and enforcing a new policy with regard to renewable sources of energy, WindEurope (formerly the European Wind Energy Association or EWEA) foresees that the cumulative generation capacity in the EU will amount to 323 *GW* (253 *GW* onshore, 70 *GW* offshore) by the year 2030. This would be equivalent to 29.6% of the EU's total electricity demand [39], thereby roughly doubling the currently installed capacity. Particularly in Europe, offshore wind energy shows great potential. Up to 11% of the EU's electricity demand could be generated by offshore wind farms by 2030 according simulations made by WindEurope [122] . Interestingly, even the advocated 'best case scenario' would barely touch upon the potential of offshore wind energy in Europe. Thereby clearly underlining the presence of pristine market for development by both governments and private firms through policy adaptations, entrepreneurship and technological advancement.

2.2. Europe's offshore wind potential

Historical data on the evolution of Europe's offshore wind capacity, clearly shows the potential of this market, as can also be observed in Figure 2.2. Even at this moment, Europe has, by far, the largest offshore wind market in the world, accounting for 89.1% of the total capacity [101]. In 2017 alone, 560 new turbines were installed across 17 offshore wind farms. Their combined net capacity yielding 3148 *MW*, a new installation record. Thereby bringing the total offshore wind capacity to 15780 *MW*. Moreover, 6 new projects, representing a 2.5 *GW* grid expansion worth €7.5bn, reached the Final Investment Decision (FID) [121]. Although the latter is a 60% decrease when compared to 2016 investment levels, it clearly shows the will of investors to allocate substantial resources to offshore wind energy projects.

In its current form, offshore wind is still reliant on subsidies granted by governments. Additionally, one of the main concerns regarding offshore wind energy is its ability to compete with its onshore counterpart [107]. This is because the cost of energy is often calculated as the Leveraged Cost of Energy (LCOE):

$$LCOE = \frac{\text{Total costs over lifetime}}{\text{Electricity produced over liftime}} \tag{2.1}$$

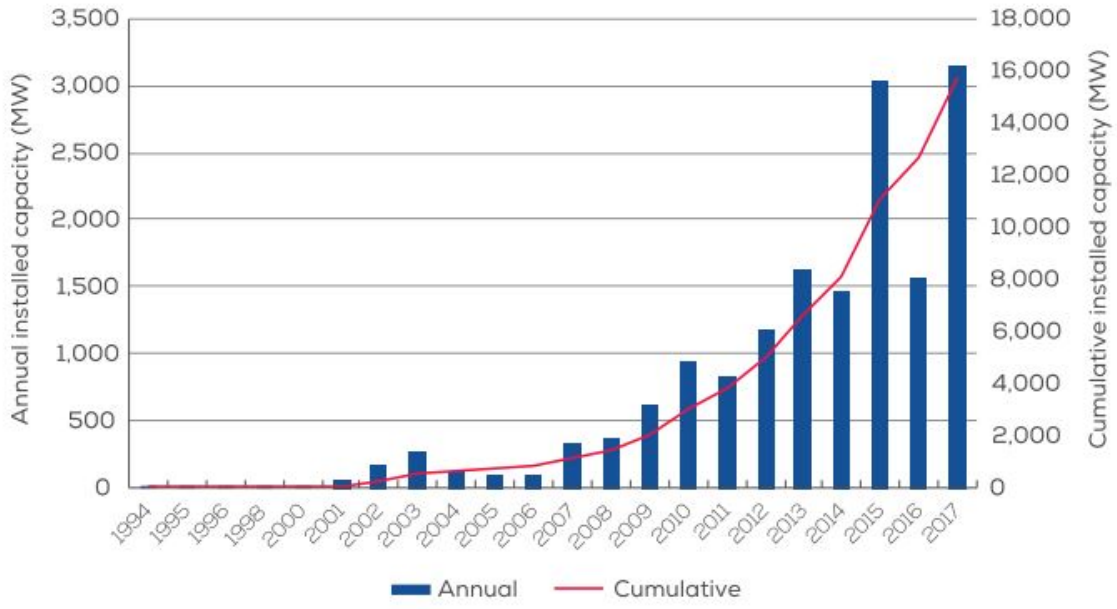

Figure 2.2: Installation of offshore wind energy from 1994 to 2017 [121]

However, by using Society's Costs of Electricity (SCOE), as advocated in a publication of Siemens [103], offshore wind can compete with its onshore counterpart by 2025. Especially when considering the emergence of wind as a main stream energy source, continued cost reductions and efficiency increases [101], offshore wind is well on track to become a viable alternative for fossil fuel by that time. Another factor that will likely simulate the widespread use of offshore wind, is the abundance of suitable ocean surface. Following the conclusions drawn in a recent publication by WindEurope, offshore wind has the potential to produce between 2600 and 6000 *TWh* a year at an economically viable price [122]. Therefore, it would be possible to provide between 80% and 180% of the EU's total electricity demand by solely by offshore wind energy.

Several other factors which contribute to the likelihood of Europe exploiting a substantial part of its offshore potential are listed below:

1. Better and more consistent wind conditions genuinely prevail offshore;
2. Installation of onshore wind turbines in hampered by spacial and nuisance restrictions;
3. Marine equipment is much larger that its onshore counterpart, making it possible to construct wind turbines at a larger scale;
4. The North, Baltic and Irish sea are particularly well suited for the offshore wind projects due to the relatively shallow water depths (30-40 *m*) which allow for the use of (economically advantageous) rigid foundations;
5. Possibilities to realize energy farms which combine wind, solar and wave energy to offer renewable engery at a competitive price [44].

2.3. Construction

In this section general information regarding the construction of offshore wind turbines is presented. Firstly, in 2.3.1, the state-of-the-art regarding placement, dimensions and turbine capacity is discussed. Secondly, in 2.3.2, existing types of substructures are identified and elaborated upon. The installation procedure of the substructure and superstructure is addressed in 2.3.3. Following the installation procedure, general information on offshore pile drivers is presented in 2.3.4. Subsequently, best practices regarding the assessment of soil variability and its importance to the success

of the project are discussed in 2.3.5. Finally, in 2.3.6, the importance of pile drivability analyses is elaborated upon.

2.3.1. Placement, dimensions and capacity

In 2017, on average, the water depth in which offshore wind farms were constructed, was 27.5 *m*. The average distance to shore of amounted to 41 *km*. Moreover, the mean size of installed turbines was 5.9 *MW*, an 23% increase over 2016 . Dimensions of similarly sized turbines can be seen in Figure 2.3. State-of-the-art wind turbines are generally placed 90 to 100 *m* above the waterline. Furthermore, rotor diameters vary between 100 and 154 *m*. The embedment depth of the foundation, in the majority of cases a monopile, lays between 20 and 30 *m*. The diameter of these monopile foundations generally ranges between 4 and 6 *m*. However, with the emergence of an 8 *MW* turbine class, monopiles with diameters larger than 8 *m* now make it onto the market.

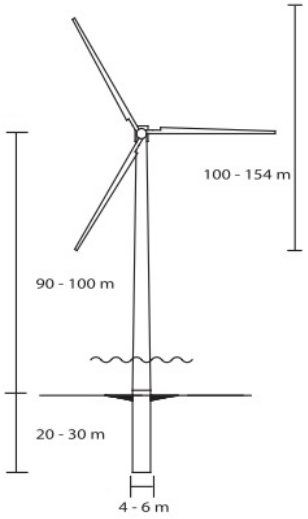

Figure 2.3: Schematic with indicative dimensions of an 5 *MW* offshore wind mill, adapted from [15]

2.3.2. foundation types

Offshore foundations for wind turbines can be allocated to three different categories, namely [25]:

1. Rigid structures;
2. Flexible structures;
3. Floating structures.

A summary of the substructure types that fall into the three aforementioned catagories can be found in Table 2.1. The design of an offshore wind turbine usually commences by specifying the desired turbine class. This process is highly standardized as a result of wind turbines being mass-produced in four predefined classes based on wind velocity [75]. The selection procedure for a suitable type of substructure is more extensive and involves the consideration of the dynamic environment and boundary conditions, specifically: (I) water depth; (II) soil conditions; (III) dynamic loads. By adequately accounting for these influencing factors, the most economical design foundation design is achieved.

In Europe, the previously discussed design approach has resulted in monopiles becoming the most commonly used type of substructure. Based on a recent publication of WindEurope, they represent 81.7% of all installed substructures [121]. In Figure 2.4, the cumulative market share of each type of substructure in Europe for 2017 is presented. From Figure 2.4 it can be concluded

Rigid structures	Flexible structures	Floating structures
Jackets	Articulated towers	Semi-submersibles
Jack-ups	Guyed towers	Floating Barge
Gravity base	Tension leg platform	Floating Spar Buoy
Bucket foundations		
Tripods		
Tripiles		
Monopiles		

Table 2.1: Possible foundation types per category, adapted from [15]

that monopiles, together with jackets, tripod and tripile foundations, all of which require piling works for their respective realization, represent ≥90% of installed substructures. Additionally, only a handful of today's substructures fall into the flexible and floating foundation category. The latter is due to the fact that flexible and floating foundations are not yet suitable for industrial use. Gavin *et al.* (2011) predict that future, deeper water (30 - 70 m), wind farms shall likely be supported by jacket structures. Generally, jacket structures consist of tripedal or quadrilateral space frame where each extremity is supported by a driven open-ended steel pile. Provided the aforementioned observations, the scope of this work is delimited to piled offshore foundations, specifically those composed of one (monopile) or multiple driven steel open-ended piles.

Several reasons can be appointed to clarify the success of driven open-ended foundation piles, particularly monopiles, as the preferred substructure for off-shore wind projects in Europe. The first considers the typical cost profile of an offshore wind energy project. Contrary to the typical cost profiles seen in the offshore oil and gas industry, up to 35% of the entire quotation may be attributed to the foundation of a wind turbine [**?**]. Similarly, in a 2015 publication of the National Renewable Energy Laboratory (NREL), foundation and installation costs account for 34% of the total expenditure [81]. It is apparent that the foundation itself and the commissioning of installation equipment (including potential hold-up of due to disadvantageous weather circumstances) weigh heavy on the budget. This empathizes the need for a substructure which allows for a smooth installation. Momentarily, monopiles are the best option to meet this criterion due to the relative simplicity with which they are fabricated and installed. Secondly, monopiles are a proven and convenient option for relatively shallow waters, i.e. water depths up to 30-40 m [119]. Finally, although somewhat compensated by the fact that monopiles require piling works for installation, their reduced footprint keeps the environmental impact reduces to a minimum.

2.3.3. Installation of monopiles

Ongoing development of the offshore wind market continuously pushes the limits of wind turbine engineering. Dimensions, outputs and efficiencies have all grown substantially since the conception of commercial wind energy. This trend will likely continue well into the future. Progressions have also led to an increase in the dimensions of both monopiles and installation equipment. Figure 2.2 presents an outline of the market's development up to 2020. As can be observed, steel monopiles are currently fabricated up to lengths of 80 m and 8 m in diameter. Wall thicknesses range up to 150 mm.

Monopiles, like lots of other offshore structures, start their life in a prefabrication plant somewhere onshore. They are fabricated to specification, following requirements which are derived based on: (I) the size of the turbine (static loading conditions); (II) the geology at the project location; (III) the water depth on site; (IV) dynamic loading conditions. Once the prefabrication process has been terminated, a Heavy Lifting Vessel (HLV) or Jack-up Vessel is commissioned to transport the monopile to the project site. This type of vessel is required as the self weight of a monopile to

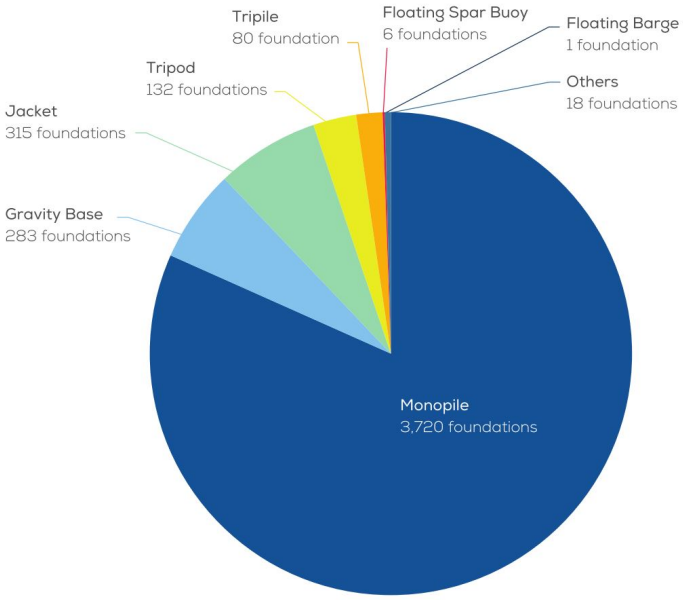

Figure 2.4: Cumulative market share (units) of type of substructures used for grid-connected turbines in 2017 [121]

Wind turbuine particulars					
		2015	2017	2020	
Turbine capacity	P_T	4	8	12	MW
Rotor diameter	D_R	130	165	200	m
Water depth	d	32	40	50	m
Monopile dimensions					
Length	L_{MP}	65	80	90	m
Diameter	D_{MP}	7	8	10	m
Mass	M_{MP}	800	1300	2200	ton

Table 2.2: Development of turbine particulars and monopile dimensions, adapted from [21]

support a typical 5 MW turbine (<1300 t) is too large to be handled by an ordinary crane. The pile driving operation requires a support which exhibits little or ideally no motion during pile driving operation [100]. Hence, there is a preference for bottom supported (jack-up) vessels. A fixed installation platform does however come at a price. The time required for the jack-up procedure increases deployment time, thereby causing additional strain on the budget and promoting the use of a HLV.

Installing the monopile to the desired depth, two techniques are available, namely: (I) vibration; (II) (impact) hammering techniques. For onshore applications, due to vibration and noise restrictions, the former is usually preferred in densely populated areas. Moreover, nowadays offshore companies are forced (by means of legislation) to take measures to combat the adverse effects induced by installation and operation of offshore wind turbines. Employing vibratory techniques for monopile installation, could make noise mitigation measures (e.g. anti-sound and bubble screens), which are often obligatory during hammering operations, superfluous. Other advantages of vibratory techniques are: (I) reduced risk of pile running; (II) A smaller chance of inducing fatique into the pile; (III) The possibility to extract the pile after installation, e.g. for repositioning or recycling purposes.

However, granted are a few successful case histories (Hong Kong-Zhuhai-Macau Bridge (China) and Riffgat Wind Farm Project [30]), vibro-installation methods are yet to prove themselves in terms

Hammer type	Hammer efficiency η_h
Vibratory hammer	1.00
Free-fall hammer	0.90 - 0.95
Hydraulic drop hammer (self-monitored)	0.85 - 0.95
Hydraulic drop hammer (other types)	0.55 - 0.85
Single-acting air/steam hammer	0.55 - 0.70
Double and differential acting air/steam hammer	0.35 - 0.50
Diesel hammer	0.30 - 0.40

Table 2.3: Hammer efficiencies for various types of hammers specifically suited for the installation of steel piles. After [96].

of widespread commercial use. Additionally, impact hammering has an edge over vibratory installation methods in following ways: (I) impact hammering is able to penetrate hard and stiff soil types, i.e. (over-consolidated) stiff clays; (II) there is extensive offshore experience with the impact hammering techniques and equipment; (III) driving data and performance logs are abundantly available. Therefore, it is unlikely that the impact hammering will be overtaken or squished by vibro-installation methods in the foreseeable future. Instead, following the line of though by presented by De Neef *et al.* (2011) ([30]), both techniques are likely coexist and complement one another. Thereby establishing the need for continued research in both fields. In need of delimiting the scope, this research solely focuses on optimizing pile installation through impact hammering.

2.3.4. Hammers

Presently, a large variety of hammers exist to enable the offshore installation of open-ended steel piles. The types of hammers which are currently on the market can be categorized in three types, namely:

- Vibarotry hammers. This type of hammer utilizes the centrifugal force of a set of large eccentric weights. A heavy hydraulic engine is used to drive the weights, thereby introducing vibrations which allow the pile to penetrate the soil;
- Single acting hammer. This type of hammer relies on hydraulics, combustion, steam or air pressure to lift the ram mass. Subsequently, the ram mass is released. The latter enables the conversion of potential engery into kinetic energy which is ultimately used to propel the pile into the ground;
- Double and differential acting hammer. Like single acting hammers, hydraulics, combustion, steam or air pressure are used to lift the ram mass. Contrastingly, double or differential hammers, actively accelerate the ram mass to increase the impulse delivered to the pile.

Each type of hammer has its own efficiency η_h. Hammer efficiency is calculated by division of the kinetic energy of the ram mass just prior to impact with the helmet cushion or anvil, by the potential energy based on initial hammer position [78]. Driver efficiency is an important input parameter for dynamic formulae and wave equation analysis, as respectively addressed in 3.2 and 3.3. Table 2.3 shows recommend efficiencies for various hammer types.

As can be observed from Table 2.3, vibratory hammers attain the optimal efficiently level. The latter is likely due to the rigid mounting between the vibratory driving system and the pile. Presently, hydraulic hammers are the most heavily used type in the field. Chief reasons for their extensive use include: (I) the ability to operate underwater if required; II) full control over impact energy; (III) high operating efficiencies; (IV) a proven track record in terms of system reliability. Hence, this work solely addresses pile installation by hydraulic hammers.

In terms of functionality, hammers that are used to install open-end steel piles (monopiles) offshore, do not differ significantly from their onshore counterparts. The most notable difference being

size. Nowadays, the largest hydraulic hammer available on the market, the IHC IQIP S-4000, stands over 20 *m* tall, weights 430 *t* and is equipped with a 200 *t* ram mass. This latest evolution of the Hydrohammer® has variable blow energy between 397 and 4000 *kJ* at a blowrate of 36 *blows/min*. Using state-of-the-art equipment, nominal monopile installation times are in the order of 4 hours [21].

After the monopile has successfully been installed through impact hammering, vertical alignment is verified. As wind turbines are highly sensitive to even the slightest rotation of the substructure, this is a necessity. To comply with the current serviceability limit requirement, rotations must be <0.5°. Of this figure only a mere 0.25° can be due to installation, the remaining 0.25° is a redundancy further rotation due to loading during the operation lifetime [113]. The turbine tower cannot be placed directly on top of the monopiles. To overcome this, a transitional piece is used. This transition piece is placed on top op the monopile. Subsequently, the connection is grouted. Thereby finishing the substructure and making it possible to install the turbine tower. The latter is also presented in Figure 2.5. These finalizing steps bring the total installation time of a monopile to 19 hours [21].

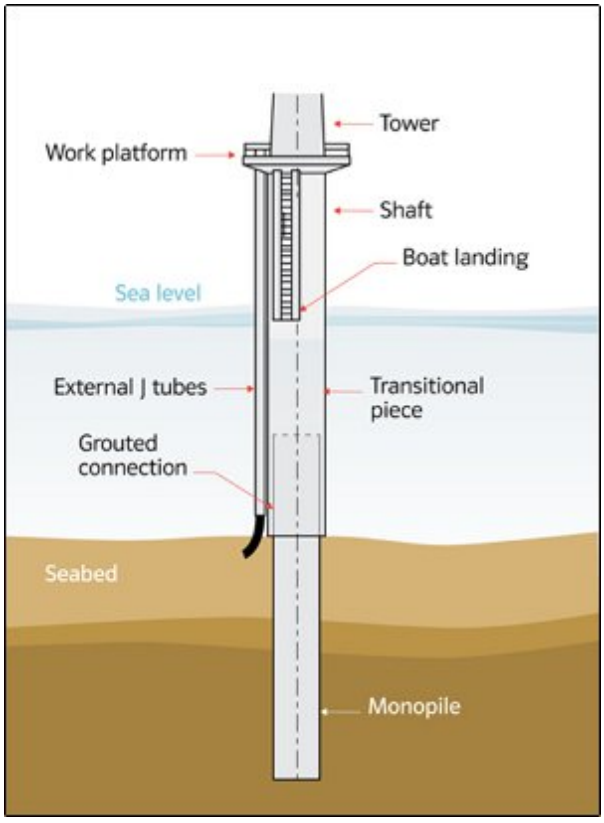

Figure 2.5: monopile foundation with transitional piece installed [1]

2.3.5. Soil variability assessment

Unlike man-made materials, soil has a natural origin and can therefore exhibit large variations in design properties. This heterogeneity is well recognized in practice and referred to as *soil variability*. Soil variability has important implications on the design of any geotechnical project, especially in terms of reliability and thus the management of geotechnical risks. Additionally, establishing a proper understanding of soil's heterogeneity can aid the process of reducing design redundancies and therefore lead to an economical design. It is therefore safe to state that the quantification of the degree of variability is vitally important to the project's success. Hence, best practices dictate the

commissioning of a thorough geotechnical site investigation to acquire high-quality soil data. For the construction of wind farms in particular, the site investigation is generally configured as follows [123]:

1. **Desk study**. The chief purposes of a desk study are: (I) to gather and consolidate existing geotechnical information; (II) to establish a clear understanding of critical design parameters; (III) to identify potential geotechnical risks; (IV) to conceptualize possible foundation structures, given the project's design requirements.
2. **Geophysical survey**. Following the desk study a site wide geophysical survey is commissioned. Key objectives include: (I) identification of undocumented geological traits; (II) outlining the scope of the subsequent geotechnical investigation.
3. **Preliminary geotechnical investigation**. This often consists of a series of CPT tests, boreholes and possibly advanced laboratory tests. Here, the main objectives include: (I) Verification of desk study and geophysical survey; (II) Acquisition of the data required of the development of the geological site model; (III) Deepen and broaden the understanding of geotechnical risks.
4. **Ground model build-up**. Whilst using the information gathered in the three aforementioned stages of the site investigation, the site's ground model is developed. The resulting model serves an important role in the preliminary design process.
5. **Extended geotechnical investigation**. Either from interpretation of the ground model itself or upon request of a stakeholder, it can be decided to extend the geotechnical survey to further reduce design uncertainties and the related risks. An extension of the investigation usually involves more CPT testing, borehole sampling and advanced lab testing.

Considering the scale of an average wind farm easily exceeds dozens of square kilometers and high level of spatial variability commonly encountered in soil, obtaining an accurate account of fundamental soil properties for an offshore wind project is by all means challenging. Consequently, the site investigation process is littered with trade-offs between cost, accuracy and redundancy of the acquired data. In this respect, the use of site investigation techniques that allow for continuous data acquisition, i.e. CPT tests, is preferred. Due to the fact that CPT data, e.g. cone resistance q_c, sleeve friction f_s and pore water pressure u are abundantly available, it is preferred to obtain soil parameters by means of correlations. Whist the use of correlations allows for the preservation of redundancy, their respective empirical nature complicates development of a highly accurate soil model. Additionally, many parameters required to run advanced soil models cannot be obtained from CPT data [51]. Although it is possible to relatively reliably fill this knowledge gap by means of laboratory tests, it is not possible to properly account for variability without drastically increasing expenditure. Hence, the use of advanced constitutive models and finite element algorithms is omitted by the industry. Instead, simplified, computationally inexpensive soil models are employed, which can be calibrated on a limited amount of parameters. However, as the soil model often also serves as a tool assess the drivability of the monopiles, which is a highly disruptive process characterized by complex soil-structure interactions, drastic simplifications are arguably undesired.

2.3.6. Pile drivability analyses

The ground model developed on the data gathered form the site investigation serves two purposes: (I) to facilitate the design process; (II) to conduct pile drivability studies. The former has been discussed in 2.3.5. Hence, the latter is considered here. Assessing the drivability of monopiles is of the essence for several reasons, most critically:

1. The logistic operation required for the offshore installation of monopiles in extensive and costly. Due to the use of highly specialized construction equipment, e.g. jack-up vessel or HLV, which is often reserved for deployment within a specific time frame, time is of the essence.

Hold-up needs to be avoided wherever possible. In practice this roughly translates to the following demands: (I) optimize drive time; (II) prevent (fatigue) damage to pile and/or driving hammer; (III) commission an appropriate hammer to prevent pile refusal.

2. During the installation of the monopile, shaft friction degrades for an increasing number of imposed load cycles [117]. My maintaining the driving process for longer periods of time, the aforementioned effect, often denoted as *friction fatigue*, causes that frictional resistance to increases in a less-than-linear fashion [52]. Hence, the amount of time and energy required to reach the desired penetration depth is reduced. Intermittent pauses and/or break-downs should therefore be avoided as these give rise to *set-up effects*. Set-up increases the soil's resisting capacity over time, through the process of relaxation and consolidation, thereby placing additional strain on the project's schedule.

Based on the summation above, it can be deduced that a drivability study serves the purpose of selecting an appropriate driver system and substantiating an optimum driving plan to guarantee the desired penetration depth is reached in the least amount of time, whist maintaining induced stresses below the plastic threshold value and restricting the manifestation of fatigue effects.

3

Drivability of displacement piles

3.1. Introduction

As discussed in 2.3.6, pile drivability studies are indispensable tools to enable economical installation of the wind farm's substructures whilst safeguarding the project's desired longevity. Over the years, several tools have been developed predict pile drivability, namely: (I) Dynamic analysis; (II) One dimensional wave equation analysis; (III) Two- or three-dimensional finite element analysis. These methods are, respectively, discussed in 3.2, 3.3 and 3.4. In 3.5 a critical note on the use of drivability studies is presented.

3.2. Dynamic analysis

In the early 1900s, engineers attempted to evaluate the capacity of driven piles by using dynamic formulas. These formulas, which originate form the energy balance of the driving process, were a first attempt to calculate pile capacity is a representative, yet easy fashion. Generally, dynamic formulas relate the energy delivered by the hammer to the work done in the surrounding soil mass, whilst accounting for possible losses. Given this definition, dynamic formulas are commonly denoted as follows:

$$\eta_{ds} \cdot a \cdot m_H \cdot h = R_u \cdot s_b + E_{\text{pile}} + E_{\text{soil}} \tag{3.1}$$

Where a is ram-mass acceleration, m_H is the mass of the ram, h is the hammer's stroke; R_u is the total pile resistance, s_b is the pile displacement (per blow), E_{pile} and E_{soil} are energy dissipation terms for the pile and soil respectively. Continuing, η_{ds} is the efficiency of the driving system. Depending on the used type of hammer, the driving system is, besides the hammer itself, composed of hammer and/or pile cushions (for steam hammers) and the anvil. The efficiency of the total driving system is therefore the product of the efficiencies of its respective elements. Theoretically, it is possible to calculate the pile set (per blow) s_b from Equation 3.1, given that all other variables are known. This technically makes it possible to assess drivability with formulas originally intended to determine pile capacity.

However, in reality it is proven difficult to employ the dynamic formulae with the aforementioned goal in mind. The latter is due to difficulties encountered whith the approximation of E_{pile} and E_{soil}, as these fundamental parameters influencing these dissipation terms cannot be measured directly. Solving Equation 3.1 therefore requires extensive simplification of the underlying energy dissipation processes, thereby undermining the usability of dynamic formulas for the evaluation monopile drivability.

Nonetheless, over the years, different authors developed various versions of Equation 3.1, by altering underlying simplifications at their own discretion. Yet, few of these formulas are actively used in practice. For a few frequently used variations see in example Gates (1957) ([43]), Olson & Flaate

(1967) ([84]) or Allen (2005) ([2]). For the most commonly used variations, critical simplifications are presented in the summation below, after [88] and [50]:

- The value for efficiency of the driving system, η_{ds}, used in the calculations is often merely a crude assumption. The efficiency of the combined driving system is expected to fluctuate alongside the driving process parameters, i.e. driving frequency and ram stroke. Assuming a constant value may therefore not adequately represent the variability of field conditions.
- Soil resistance resulting from driving is constant and thereby independent of the imposed load and rate-of-loading. The choice to not differentiate between static and dynamic soil resistance is inherently wrong. Both load and rate-of-loading are known to be profoundly important to stress-strain behavior exhibited by the soil, as they alter the observed stiffness, e.g. the modulus of elasticity E and the shear modulus G, as well as the damping ratio D and generation of excess PFP. Additionally, shear stress reduction, effectively due to *friction fatigue* (also a dynamic process) is not considered.
- The pile is modeled as a completely rigid mass. Moreover, its length is not taken into account in the calculations. In reality, compression waves propagate through he pile, which is in fact an elastic medium, thereby driving it into the soil. In the latter case, pile length cannot be overlooked when appointing the pile's capability to penetrate the soil. Moreover, the reflection of compression waves at the pile's extremities is not considered, leading to an overestimation of pile set s.

The use of these simplifications consequently makes the reliability of the developed dynamic formulas highly volatile. Moreover, dynamic formulas cannot be used to assess stress levels in the pile during driving. Therefore, it is impossible to track manifestation of fatigue and/or plastic strain in the pile. The unity of simplifications and shortcomings makes the risk associated with employment of dynamic analysis for drivability studies for monopiles intolerable. Mostly as an improper installation procedure has severe implications on the construction schedule and budget (also see 2.3.6).

3.3. One dimensional wave equation analysis

3.3.1. Introduction

To overcome the apparent shortcoming of dynamic analyses, as discussed in 3.2, Smith (1960) ([105]) envisioned an integral approach to the problem of modeling the drivability of piles. Smith (1960) presented a physical model of the pile and driving system and a corresponding finite difference algorithm to calculate stresses and motions induced during driving [50]. The potential of the aforementioned methodology was quickly recognized by the scientific community. Hence, it was swiftly incorporated into several computational software packages, e.g. Texas Transportation Institute (TTI) program [54] and WEAP [45]. Continued development of the WEAP program, including the implementation of a more refined finite difference solution scheme, eventually saw the establishment of GRLWEAP [48]. Through thorough calibration, the latter has developed into a proven commercial software package, which is widely used by the industry. The program's relative simplicity, few calibration parameters and short computation time can be appointed as the main drivers behind its industry wide use [50].

3.3.2. Wave propagation through piles

The physical process underlying the installation of piles through impact hammering can be divided into five phases, namely: (I) impact of ram mass, compressing the upper extremity of the pile, thereby exerting an force pulse into the pile; (II) propagation of force pulse through free-standing pile segment in the form of a compression wave, which travels at constant phase velocity; (III) interaction of the compression wave with the surrounding medium, thereby reducing its respective amplitude; (IV) reflection of incident compression wave at the pile's tip, causing a (tensile) force

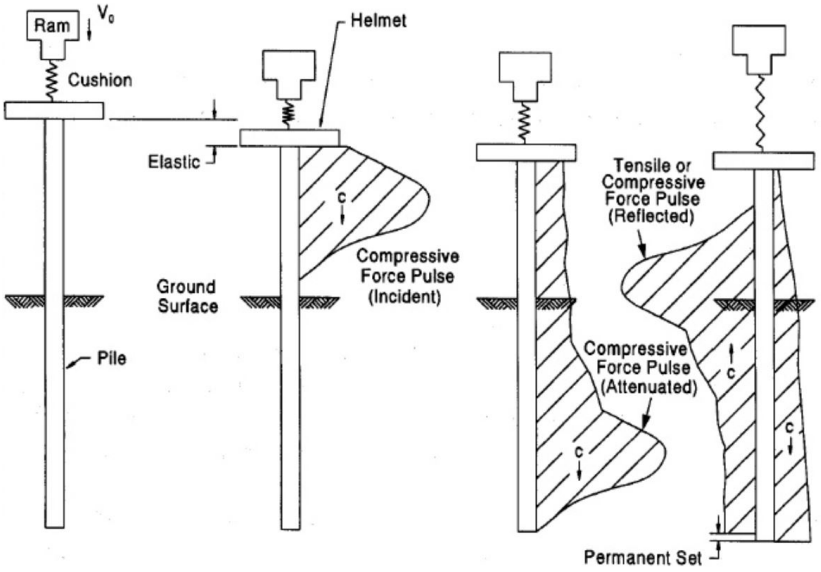

Figure 3.1: Wave propagation in a pile due to impact hammering, modified from [50]

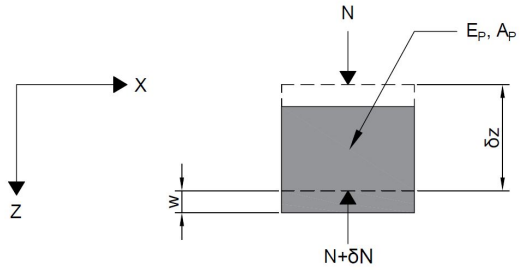

Figure 3.2: Free body diagram of a pile segment with modulus of elasticity E_P and cross-sectional area A_P subjected to displacement w

pulse to travel in opposite direction towards the upper extremity; (V) development permanent displacement at the pile's due to the whole of incident and reflected force pulses propagating through the pile, given that their summed energy exceeds the static and dynamic soil resistance. The entire process is illustrated in Figure 3.1.

3.3.3. One dimensional wave equation

Following the physical background of wave propagation through piles, which was outlined in 3.3.2, a mathematical wave propagation model is derived. For the sake of simplicity, in the initial derivation, all soil-pile interactions are disregarded. Now, consider an infinitesimal pile segment, with height δz, made up of linearly elastic material with modulus of elasticity E_P. It is assumed that the cross-sectional area of the element, A_P, is constant over the entire length. The element is subjected to an arbitrary displacement w in the positive z-direction. Additionally, the normal forces acting at the top and bottom of the element (in z-direction), are respectively given as N and $N+\delta N$. An overview of the segment's geometry, displacements and forces can be found in Figure 3.2. For the previously described case, the equation of motion for the pile element is given by:

$$\frac{dN}{dz} = \rho_P A_P \cdot \frac{d^2 w}{dt^2} \tag{3.2}$$

In Equation 3.2 ρ_P is the density of the pile's material. Now, relating the normal force, N, to stress:

$$N = \sigma \cdot A_P \tag{3.3}$$

Recalling the pile is made of a linearly elastic material, Hooke's law is employed to relate stress to the E and the observed strain:

$$\sigma = E_P \cdot \epsilon \tag{3.4}$$

Subsequently, by relating strain to the arbitrary displacement of the pile element w, the following is obtained for the normal force:

$$N = E_P A_P \cdot \frac{dw}{dz} \tag{3.5}$$

Finally, by combining expression 3.2 and 3.5, the following differential equation is obtained:

$$E_P A_P \cdot \frac{d^2 w}{dz^2} = \rho A_P \cdot \frac{d^2 w}{dt^2} \tag{3.6}$$

Equation 3.6 is also known as the *wave equation*. Now, by considering shear stresses alongside the pile's shaft as a result of the arbitrary displacement w, an additional term appears in Equation 3.6:

$$E_P A_P \cdot \frac{d^2 w}{dz^2} - \frac{\pi {D_P}^2}{4} \cdot \tau = \rho_P A_P \cdot \frac{d^2 w}{dt^2} \tag{3.7}$$

Where D_P is the outer diameter of the pile and τ is the shaft friction (per unit area). Dividing all terms by $E_P A_P$ yields:

$$\frac{d^2 w}{dz^2} - \frac{\pi {D_P}^2}{4 E_P A_P} \cdot \tau = \frac{1}{{c_P}^2} \cdot \frac{d^2 w}{dt^2} \tag{3.8}$$

Where c_P is the elastic wave velocity, which is the speed at which stress waves propagate through the pile medium with modulus of elasticity E_P and density ρ_P. The phase speed is formally defined as:

$$c = \sqrt{\frac{E}{\rho}} \tag{3.9}$$

For a steel pile (ρ = 7800 kg/m^3 and E = 210 GPa), the phase velocity of stress waves is approximately 5200 m/s. Recalling from 2.3.1 that the nominal size of a monopile is in the order of 50-60 m, stress waves take 9-12 ms to travel the entire length of the pile. Naturally, a full cycle is completed in twice this amount.

3.3.4. Smith model (1960)

Several ways exist to obtain a solution to Equation 3.8, a few examples: (I) Laplace transformation; (II) separation of variables; (III) numerical solution methods. Numerical solutions are especially useful when considering more intricate problems that involve i.e. heterogeneous soil or a variable pile cross-section [114]. The latter is often true for real-life engineering challenges. Smith (1960) ([105]) suggested a lumped mass-spring model together with a finite difference scheme in order to obtain a solution to wave equation. Although the numerical algorithm was later refined by others, the model's representation of the pile and driving system remained largely unchanged. This mass-spring model and its driving equations are described in 3.3.4. The numerical solution algorithm is elaborated upon in 3.3.4.

Physical model and governing equations An illustration of the mass-spring model, as first proposed by Smith (1960), is shown in Figure 3.3. As can be observed in Figure 3.3 the hammer, anvil and pile are modeled as a chain of concentrated masses with weightless interconnecting elasto-plastic springs and (linearly) viscous dash-pots. The combination of springs and dash-pots ensures that the system is dominated by *Static Resistance to Driving* (SRD) for slowly moving piles, whist accounting for dynamic soil resistance in case of rapid movements. Please observe that both a hammer cushion and pile cushion, as present in conventional hydro hammers, are incorporated into

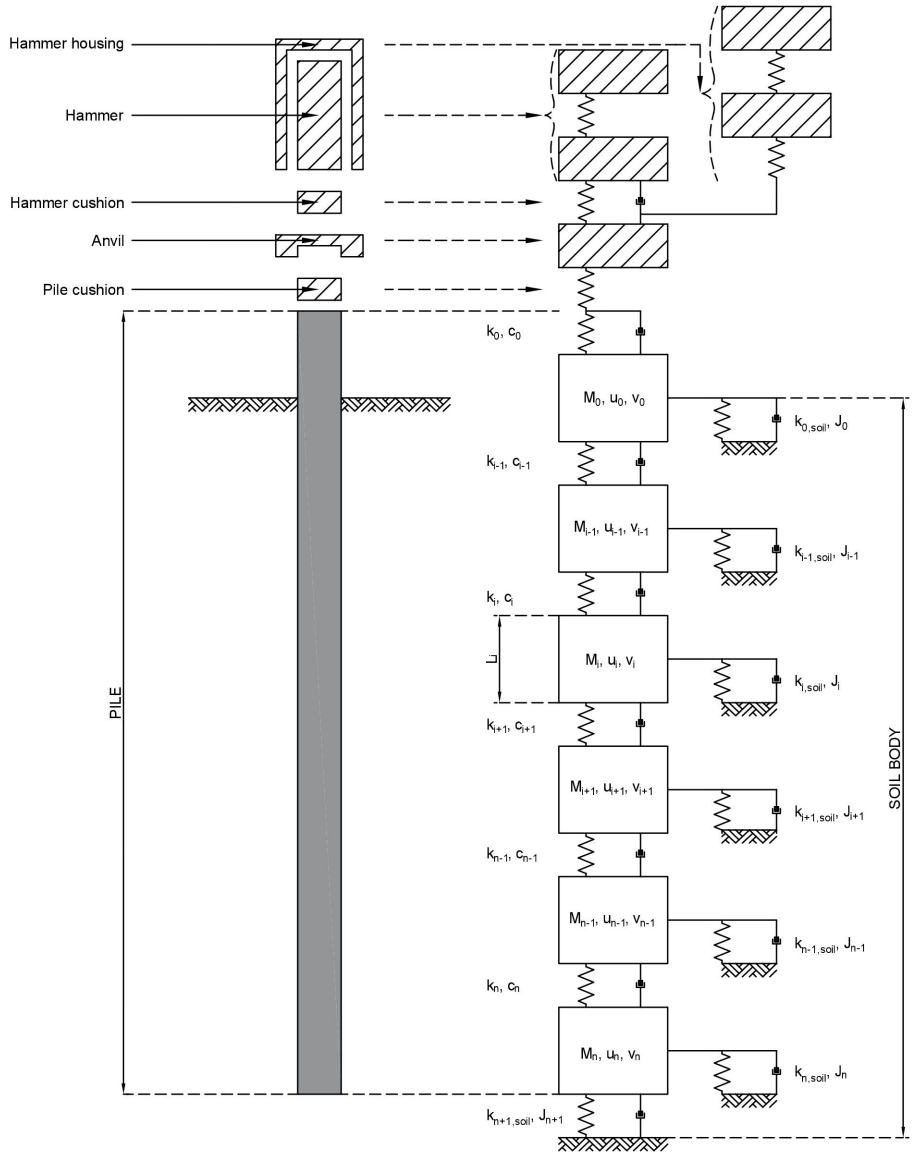

Figure 3.3: Lumped mass-spring model to replicate hammer-pile-soil interaction during driving with a *conventional* hydraulic hammer and numerically solve Equation 3.8, inspired by [50]. Please recall that k_{soil} is calculated from R_u in accordance with Equation 3.11

the model shown in Figure 3.3 as additional springs. For the latter case, the stiffnesses of the springs are calculated from: (I) cushion surface area A; (II) cushion's modulus of elasticity E; (III) cushion thickness d. Hydrohammer®, as developed by Royal IHC, allows for steel to steel contact between the ram and anvil, thus eliminating the need for cushions and allowing for further simplification of the model. Each mass depicted in Figure 3.3 represents approximately 1 m of hammer or pile respectively. The length of the segments should naturally be such that soil layering and the variation of governing soil parameters are demonstrable accounted for, especially if a high resolution (CPT-based) SRD model is used. However, model accuracy should not excessively increase model runtime.

In the model, total soil resistance encountered by the pile during driving is given by the following expression:

$$R_t = R_s + R_d \tag{3.10}$$

Where R_t, R_s and R_d indicate the total, static and dynamic resistance respectively. Both R_s and R_d are related to the ultimate static resistance, R_u, which is a calibration parameter of Smith's model. R_u is obtained through employment of a SRD model. SRD models are discussed in more detail in section 3.3.5.

Next to R_u, users are ought to specify *quake*, which formally designates the elastic-plastic displacement threshold for soil behavior and is used to infer the soil spring constant, k_{soil}:

$$k_{\text{soil}} = \frac{R_u}{q} \tag{3.11}$$

Now, the following relationship for the static resistance R_s from Equation 3.10 it is obtained:

$$R_s = \begin{cases} k \cdot w, & \text{for } w < q \\ R_u, & \text{for } w \geq q \end{cases} \tag{3.12}$$

In Equation 3.12, w indicates the actual pile displacement. The dynamic soil resistance R_d is dependent on the static driving resistance R_s, Smith's dampening coefficient J, rate of displacement v and dampening exponent n:

$$R_d = R_s \cdot J \cdot v^n \tag{3.13}$$

Please note that the dampening coefficient in Equation 3.13 has SI dimension *[T/M]* (for n=1). Subsequently, by substitution of Equation 3.13 into Equation 3.10, it is found:

$$R_t = (1 + J \cdot v^n) \cdot R_u \tag{3.14}$$

Some discussion remains on the use of the non-linear relationship for R_d by use of the dampening exponent n (see Equation 3.13). Use of this parameter was first advocated by Coyle & Gibson (1970) ([26]), who preferred R_d to vary exponentially with v instead of linearly. Later, other authors, e.g. [18] and [97], proposed other variations of the non-linear relationship. Due to weak dependency of J on soil type, use of these non-linear relationships has been encouraged by i.e. [98]. However, due to use of a dampening exponent, the dimension of Smith's dampening coefficient changes to $[T/M]^{1/n}$. The latter complicates the transition to a non-linear model for dynamic soil behavior. Instead, use of *n=1* and a carefully chosen value of J is mostly used in today's practice. Proven commercial software like GRLWEAP do however offer the possibility to choose between different dampening models.

Numerical solution algorithm To run the analysis, several variables need to be assigned to every pile segment. In the following, such variables are recognizable through the use of subscript i, which respectively refers to the pile segment's index. Required input variables are as follows:

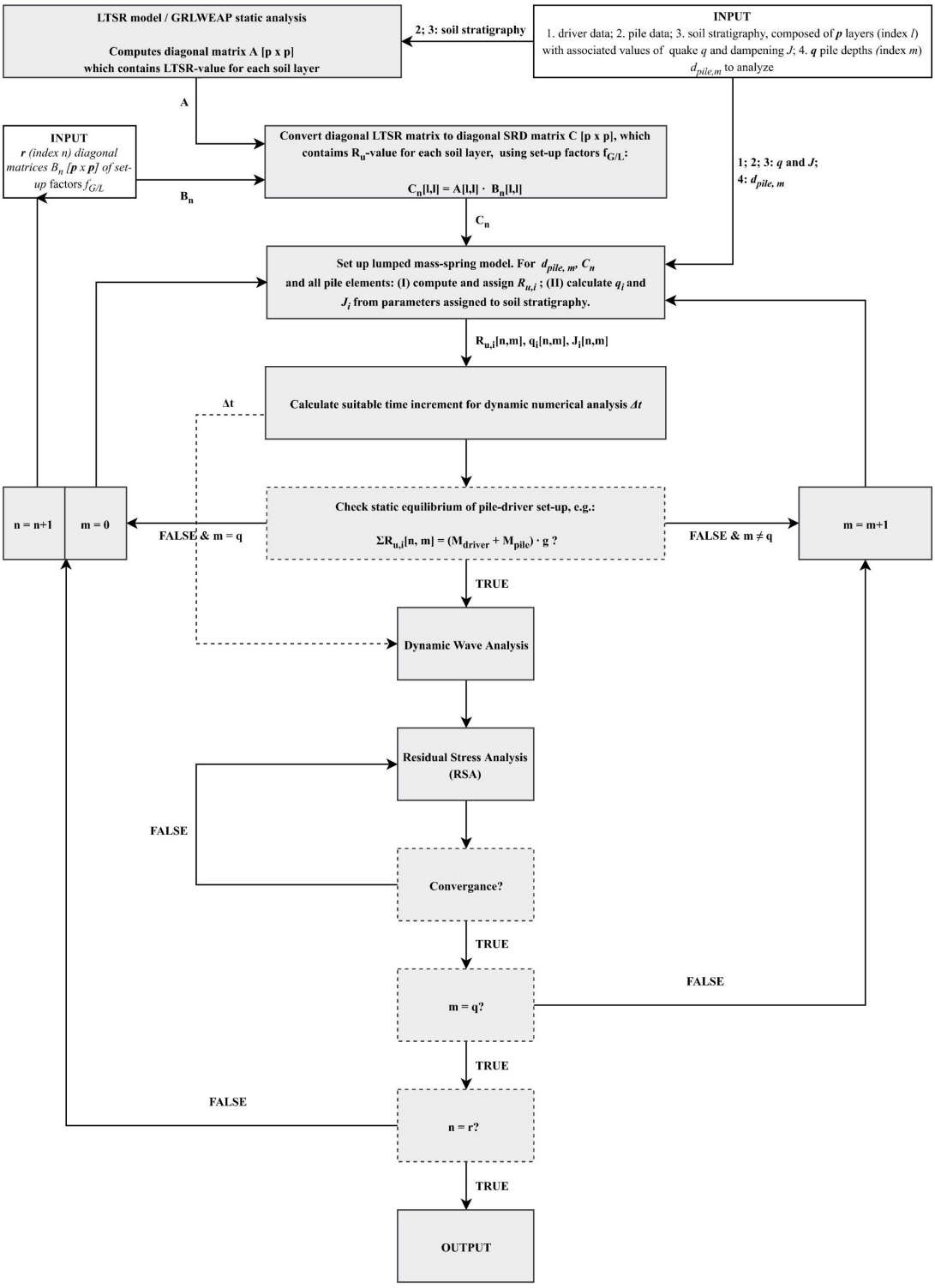

Figure 3.4: Flow diagram for drivability analysis as conducted by GRLWEAP, provided an LTSR model for static soil resistance calculation

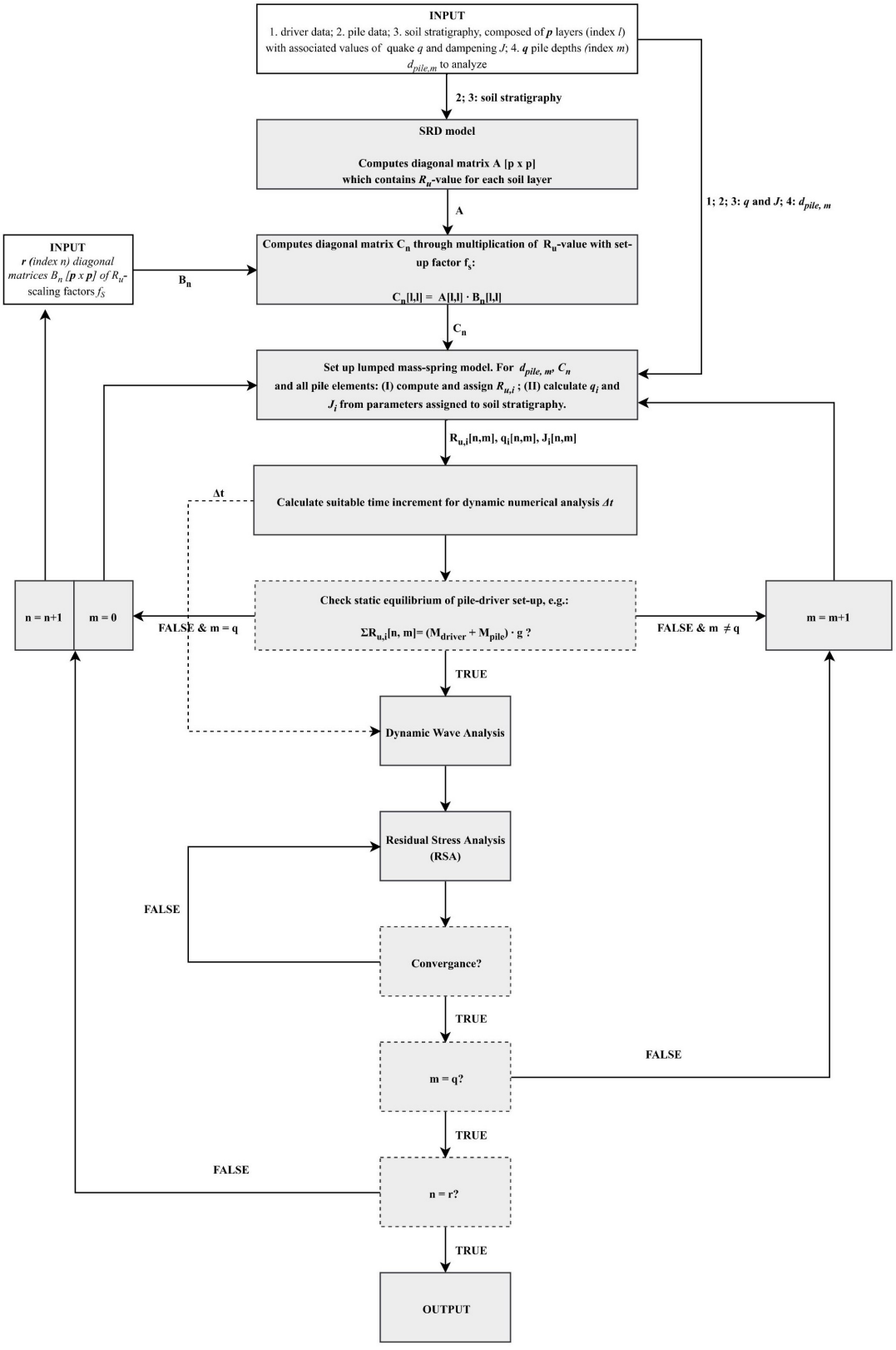

Figure 3.5: Flow diagram for drivability analysis as conducted by GRLWEAP, provided an SRD model for static soil resistance calculation

1. Pile geometry and material properties (specifically pile-stiffness coefficient k_i and pile-dampening coefficient c_i);
2. Driver type (see Table 2.3) and its respective specifications (in example ram weight, maximum stroke, efficiency etc.);
3. Soil stratigraphy, which consists of $\boldsymbol{p}$ layers (index l). For each identified layer quake and damping coefficients, respectively denoted as q_l and J_l, are ought to be specified;
4. $\boldsymbol{q}$ pile depths d_{pile} (index m) for which drivability should be determined by the program;
5. Depending on the choice for an long-term static resistance model (*LTSR*) or SRD model , respectively $\boldsymbol{r}$ set-up factors $f_{G/L}$ (index n) per layer or $\boldsymbol{r}$ R_u-scaling factors f_s per layer. All coefficients should be provided in ascending level of conservativeness.

As can be inferred from 5, ultimate static resistance values R_u can be determined both indirectly and directly through respectively: (I) use of an (software integrated) long-term static resistance (*LTSR*) model; (II) use of a SRD model. Initialization of both models happens on the basis of the same information, specifically that provided under 1 and 3. The former of the two options, the use of an (integrated) LTSR model, provides users with long-term pile resistance. Hence, output modification is required. Generally, a set-up factor $f_{G/L}$ is used to covert LTSR to SRD. $f_{G/L}$ is a function of soil type, soil characteristics, stress history and governing stress level and is provided through user input. Figure 3.4 shows the flow diagram for GRLWEAP drivability analysis using an LTSR model. A flowchart associated with the latter option, determination of R_u through a SRD model, is shown as Figure 3.5. The need to specify multiple values of $f_{G/L}$ or f_s originates from the low reliability of a single drivability simulation. Several factors contribute to the low reliability of a single analysis, chiefly: (I) limited sample-density of field investigation, which complicates the assessment of spacial variability; (II) measurement induced disturbance of in-situ soil conditions; (III) limitations to equipment sensitivity; (III) post-processing software simplifications.

The specification of $\boldsymbol{q}$ pile depths d_{pile} and $\boldsymbol{r}$ scaling factors $f_{G/L}$ or f_s (depending on the static resistance model) emanate $\boldsymbol{q}$ x $\boldsymbol{r}$ scenarios for which drivability is analyzed. As can be observed in both Figure 3.4 and 3.5, each of these analyses requires a static equilibrium check to verify that the pile is not moving under its own weight. Provided the latter has been established, a dynamic wave analysis is initiated. The Smith model ([105]) inherently assumes a stress-free state for both pile and soil at the start of driving, as well as full rebound development. However, cases where the aforementioned simplifications are incompatible with reality, exist. Hence, residual stress analysis (*RSA*) is expedient. Conceptually, RSA performs a sequence of dynamic and static analyses aimed at obtaining displacement convergence. The exact steps undertaken by the program to achieve the latter are fully explained by Pile Dynamics ([90]) and thus not further explained. Following successful RSA analysis, the succeeding scenario is analyzed or output is presented. Model output is further elaborated in 3.3.4.

From list of variables given above, it can be inferred that quake q and damping coefficients J are soil layer properties. Pile Dynamics (2010) ([90]) does not provide insight into how the conversion of the aforementioned variables into model properties q_i and J_i is handled by GRLWEAP. However, it is likely that for each pile segment q and J of adjacent soil layers are weighted by their respective contribution to $R_{u,i}$, the total static resistance acting on the segment, and subsequently averaged to obtain q_i and J_i. Where $R_{u,i}$ follows from summation of individual R_u values over the length of a pile segment. It should be noted that the previously described method can only produce accurate results if the thickness of soil layers is approximately one order smaller than the height of a pile segment. The latter is required to limit the difference in radial stress over a single layer such that the use of a single R_u per layer can be justified.

Following the assembly lumped mass-spring model, the predictor-corrector solution scheme is initiated. A complete model discretization is depicted as Figure 3.3. First a predictor establishes intimal displacement u_i and velocity v_i (mandatory for the calculation of spring and dash-pot force

components) of each pile segment. Corresponding equations are shown as Equation 3.15 and 3.16 respectively, where the superscript indicates the time step in which corresponding values were obtained.

$$u_i^t = u_i^{t-1} + \Delta t \cdot v_i^{t-1} \tag{3.15}$$

$$v_i^t = v_i^{t-1} + \Delta t \cdot a_i^{t-1} \tag{3.16}$$

To initiate the predictor step, users are ought to specify two initial conditions (respectively for *i=0*), specifically: (I) v_0^{ini} ; (II) a_0^{ini}. The former is directly user-specified and is also used to determine the required hammer stroke h, provided the hammer type and its respective efficiency η_h (see 2.3.4). The latter is often equated to the acceleration of the ram. For hammers with an active driving mechanism, like IHC Hydrohammer®, ram mass acceleration can exceed gravitational acceleration g.

Subsequently, the internal spring forces F_i (respectively at the top and bottom of each segment) are calculated using the predictor displacement u_i and velocity v_i:

$$F_i^t = k_i \cdot (u_i^t - u_{i-1}^t) + c_i \cdot (v_i^t - v_{i-1}^t) \tag{3.17}$$

Where k_i designates the pile-stiffness factor (for a homogeneous pile with constant cross-section $k_i = EA/L_i$) and c_i is a pile-dampening coefficient.

Now, for the current time step, acceleration a_i of each segment is computed from a force balance equation as follows:

$$a_i^t = (F_i^t - F_{i+1}^t + M_i \cdot g - R_{\text{tot},i}^{t-1}) \cdot \frac{1}{M_i} \tag{3.18}$$

Where M_i is the mass of considered pile segment and $R_{tot,i}$ is defined as the sum of static and dynamic soil resistance components:

$$R_{\text{tot},i}^{t-1} = R_{s,i}^{t-1} + R_{d,i}^{t-1} \tag{3.19}$$

Assuming linear acceleration, corrector integration is preformed to iteratively recalculate displacements u_i and velocities v_i:

$$u_i^t = u_i^{t-1} + (a_i^{t-1} + a_i^t) \cdot \frac{\Delta t}{2} \tag{3.20}$$

$$v_i^t = u_i^{t-1} + (2a_i^{t-1} + a_i^t) \cdot \frac{\Delta t^2}{6} \tag{3.21}$$

Results are used to update internal spring forces F_i until a velocity v_i convergence criterion is satisfied or allowable number of iterations is exceeded. The quotient of force over cross-sectional area of each segment yields the internal stresses. The latter serve an important role in evaluating the occurrence of plastic deformation and fatigue effects .

The numerical scheme now proceeds with the recalculation of both static and dynamic soil resistance, respectively through the use of Equations 3.12 and 3.13. Resulting expressions are shown as Equation 3.22 and 3.23.

$$R_{s,i}^t = \begin{cases} k_{\text{soil},i} \cdot (u_i^t - u_{i-1}^t) = k_{\text{soil},i} \cdot w_i^t, & \text{for } w_i^t < q_i \\ R_{u,i}, & \text{for } w_i^t \geq q_i \end{cases} \tag{3.22}$$

$$R_{d,i}^t = R_{s,i}^t \cdot J_i \cdot (v_i^t - v_{i-1}^t) \tag{3.23}$$

It is unclear why resistive forces $R_{s,i}$ and $R_{d,i}$ in post-analysis, thus after the iterative re-evaluation of u_i and v_i. Following the determination of individual soil resistance components, summation yields the total soil resistance for the current time step:

$$R_{\text{tot},i}^t = R_{s,i}^t + R_{d,i}^t \tag{3.24}$$

Once final values for pile displacement, pile velocity, pile forces and resistive forces are obtained, pile set s is calculated by subtracting the weighted average quake from the maximum tip displacement, hence:

$$s^t = u^t_{\text{toe,max}} - q^t_{\text{avg}} = u^t_{\text{toe,max}} - \frac{\Sigma(R^t_{u,i} \cdot q^t_i)}{\Sigma R^t_{u,i}} \tag{3.25}$$

Upon reevaluation of the pile's position, the next time step is initiated. This process is repeated until the desired depth is reached or pile refusal sets in.

Numerical results As highlighted in 3.3.4, drivability is determined for $\boldsymbol{q}$ x $\boldsymbol{r}$ scenarios. Where respectively $\boldsymbol{q}$ denotes the number pile depths d_{pile} and $\boldsymbol{r}$ the number of ultimate static capacities analyzed. The ensemble of analyses for one particular ultimate static capacity and all pile depths d_{pile}, produces a single graph for SRD and blow count versus depth, see Figure 3.6a. Repetition of the aforementioned analysis for the same ultimate static resistance regime R_u but various driving energies (modeled through adjustment of impact velocity v_0^{ini}), a bearing graph is obtained. As only a finite number of combinations depths and capacities are analyzed, interpolation is frequently used to artificially widen the range of test scenarios, as can be seen in Figure 3.6b. The resulting bearing graphs are indispensable for post-driving analysis. In practice, Signal Matching Analysis (*SMA*) (executed contemporaneously with installation) is carried out to determine ultimate resistance during driving R_t. Through use of bearing graph data, it is possible to back-calculate R_t during the driving process, provided blow count and driving energy. The back-calculated ultimate capacity data is subsequently utilized to rerun GRLWEAP drivability analysis and iteratively fine-tune user-specified quake q_l and dampening J_l coefficients per layer. Arguably, the aforementioned procedure to back-analyze driving records, allows for the continuous refinement of model calibration. Thus ultimately improving result fidelity.

In addition, stresses and/or transferred energy versus depth plots are obtained form drivability analysis. The latter are used to infer the effect of fatigue manifestation, which is often a critical parameter for pile driving studies. If driving damage is critical, it can be beneficial to optimize the driving sequence to limit fatigue inducement. To this end, Ozsu *et al.* (2013) ([86]) conducted drivability analysis for a single soil stratigraphy while varying driving energy (which is dependent on impact velocity) as well as hammer type, in an effort to seek an optimum driving plan regarding fatigue manifestation. They report that varying driving energy in operation is a promising tool to keep fatigue damage below the critical threshold as a 30% reduction in peak damage can be realized. Additionally, Ozsu *et al.* (2013) ([86]) indicate that the use of large hammers at low efficiencies can further reduce driving stresses in comparison to small hammers at high efficiencies, whist maintaining similar energy transmission levels. A broad driving energy spectrum further promotes the use of larger hammers in practice.

3.3.5. SRD models

As mentioned in 3.3.4, the ultimate static resistance R_u is an important calibration parameter for Smith's model and obtained through a *Static Resistance to Driving* (SRD) model. Research has produced multiple variations of SRD models over the years. SRD models can be divided into two categories: (I) fundamental models, e.g. Toolan and Fox Method (1977) ([111]) and Stevens *et al.* Method (1982) ([108]); (II) models based on CPT data, q_c, f_s and u, e.g. Alm and Hamre Method (1998) ([4] and [5]) or more recently UWA-05 and ICP-05. All the previously mentioned methods are fully- or semi-emperical and used in present day practice. The latter demonstrates that no consensus on the use of a particular SRD model has been reached. To this end, it has been decided to discuss the general concept of SRD models, instead of addressing the theoretical background of a limited number of variations

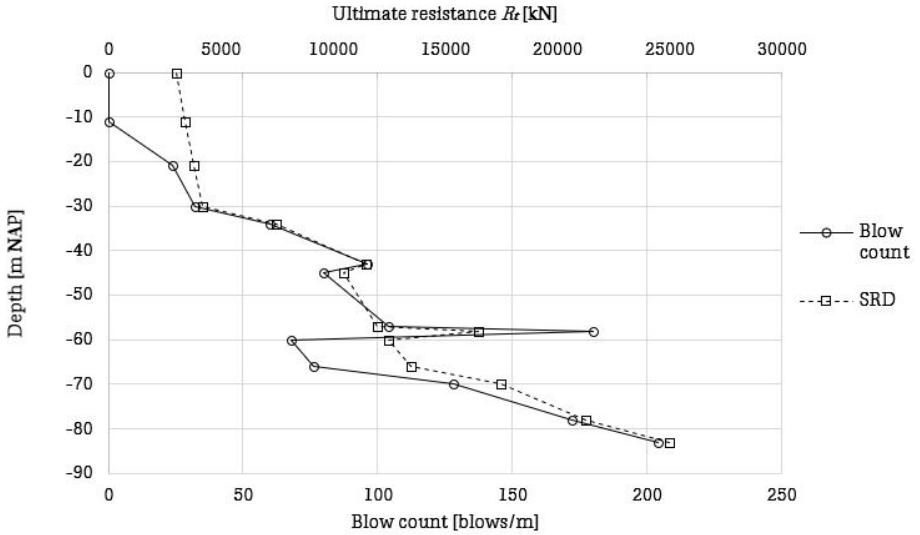

(a) Drivability chart for a single ultimate static capacity (index n) and $\boldsymbol{q}$ depths (see Figures 3.4 and 3.5 for index demarcation)

.

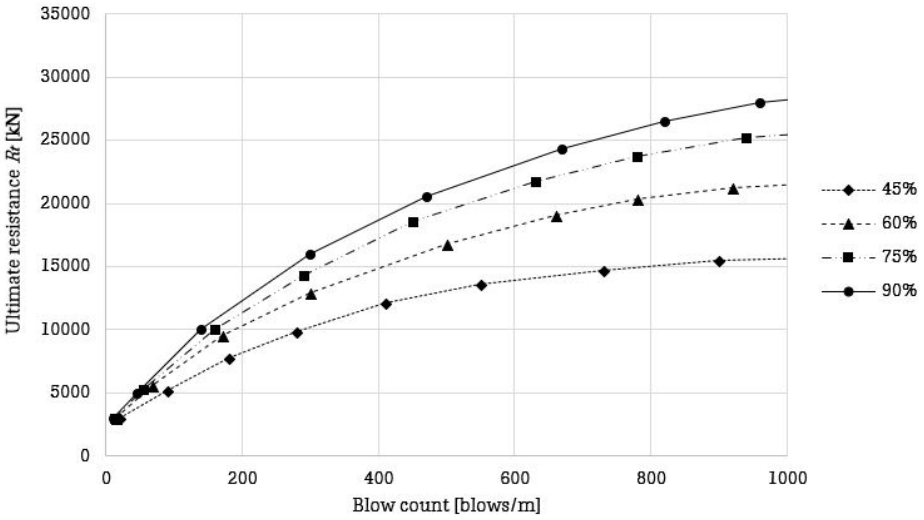

(b) Bearing graph for a single ultimate static resistance regime, each dot represents one analysis carried out for a single depth d_{pile} at a particular driving energy (denoted as a percentage of the ultimate driving energy), connecting lines follow from interpolation

Theoretically, the total resistance encounter by the pile during driving results from the following general relationship:

$$R_u = \pi \cdot D_o \int_0^d f_{s,o} dz + \pi \cdot D_i \int_0^d f_{s,i} dz + q_{\text{tip}} \cdot A_{\text{tip}} \tag{3.26}$$

Where, respectively, D_o and D_i are the outer and inner pile diameter, $f_{s,o}$ and $f_{s,i}$ are the outer and inner shaft shear stress, q_{tip} is the bearing stress and A_{tip} is the tip's surface area. However, various relations are employed by different SRD models to quantity the variables related to shaft and bottom friction of Equation **??**, thereby subtlety deviating from the general expression. The theoretical background regarding the determination of the aforementioned variables is discussed in 3.3.5 and 3.3.5 respectively. It should be noted that this analysis exclusively considers sandy soils and assumes fully coring behavior, i.e. no plugging.

Side friction For large diameter open-ended steel tubular piles, monopiles, a significant part of the total resistance during driving results from skin friction and therefore requires careful consideration. Generally, SRD models calculate skin friction from the Mohr-Coulomb criterion:

$$f_s = \sigma_h^{'} \tan(\delta_f) = K\sigma_{v0}^{'} \tan(\delta_f) \tag{3.27}$$

Where $\sigma_h^{'}$ is the effective horizontal stress and δ_f is the operational interface friction angle. For sands, δ_f is equal to the constant volume friction angle δ_{cv}, a residual value measured when interface layer has seized contracting or dilating. Determination of $\sigma_h^{'}$ is done through correlation with CPT data to avoid bias in the determination of the horizontal earth pressure coefficient *K*. Moreover, SRD models do not strictly use δ_{cv} for the determination of f_s, 45° or empirical relationships involving the friction angle ϕ are common substitutes. For most SRD model, the general relationship for determination of f_s can therefore be reduced to the following form [51]:

$$f_s(z) = C_{\text{method}} \cdot f_0 \cdot F_{\text{ff}} \cdot \tan(\phi_{\text{method}};\ \delta_{\text{method}}; 45°) \tag{3.28}$$

Where, C_{method} denotes the corrected pile circumference to correctly account for internal and external friction, f_0 is a base-value for side friction which is a function of q_c, $\sigma_{v0}^{'}$, R_o and R_i. Continuing, F_{ff} is a coefficient accounting for the effect of shear stress degradation or *friction fatigue*. The latter is a function of position relative to the pile's tip h, q_c, $\sigma_{v0}^{'}$, R_o and R_i. Integration of Equation 3.28 over depth gives the external total shaft capacity. More importantly, friction fatigue is not explicitly considered in all SRD models. For a linear cone resistance profile, the side friction calculated by a variety of SRD relationships is shown in Figure 3.7. Inclusion or exclusion of *friction fatigue* effects is clearly visible in Figure 3.7. However, even when exclusively comparing output from models which respectively do and do not consider *fiction fatigue*, significant variation remains. The latter can partially be explained by the data from which models have been derived. Underlying design particulars, geometrical characteristics and geological boundary conditions, yield an optimum performance range.

Gavin *et al.* (2011) ([44]) conducted a reliability study of solely for CPT methods, specifically: NGI-05, ICP-05, UWA-05, Fugro-05 and DNV-07. Gavin's consistent of two parts, namely: (I) assessment of the reliability of the aforementioned design methodologies based on a well-documented case studies of open-ended pile installation; (II) an investigation focused on the performance of the different models for a hypothetical but representative case study, which considered the installation of a 5 *MW* turbine in the North Sea. With regard to the former point, the investigation focused on the sensitivity of the models to slenderness ration *L/D* and relative density D_r. Concluding that, on average, results were not entirely unsatisfying but that the (un)conservatism, variability of results and potential bias of the models remains demands careful consideration. Considering the second part of Gavin's research, the case study, the following assumption were made:

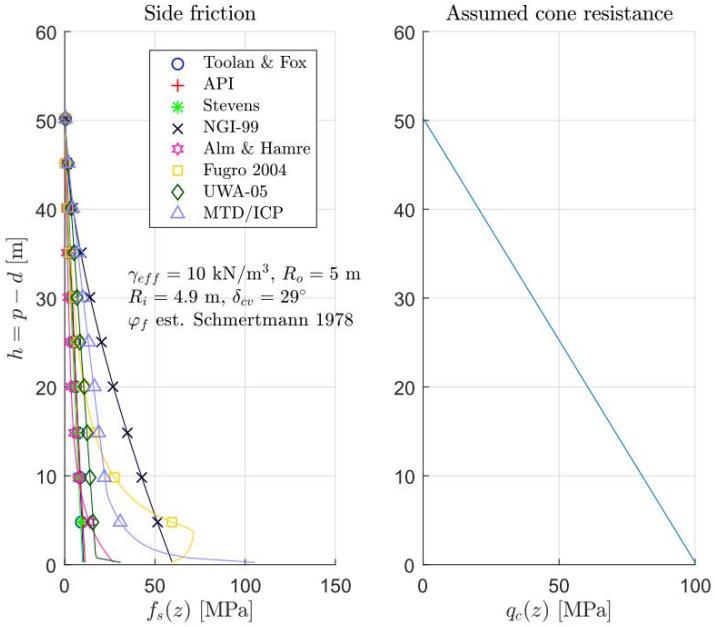

Figure 3.7: Side friction as a function of depth, provided a linear cone resistance profile, for various SRD models. For additional background please see [51]

.

- The effective soil weight is 10 kN/m^3;
- The interface friction angle is 27°.

For two different pile diameters, namely 1.5 and 2.5 m the results are illustrated in Figure 3.8a and 3.8b respectively. The work of Gavin *et al.* (2011) ([44]) shows a wide range of predicted pile lengths, mostly due to differences in the consideration of friction fatigue effects (and their influence of the lateral stress distribution). Judging by the work of Harpoth (2017) ([51]), it is probable that a similar range of pile capacities would have been obtained. Further analyses by Gavin *et al.* (2011) ([44]) into the behavior of arguably the most reliable CPT methods, UWA-05 and ICP-05, demonstrated that both methods yielded largely similar results for the ultimate capacity of closed-ended piles. The latter is not entirely surprising considering both methods were derived based on installation records of closed-ended piles. However, estimations of the ultimate capacity of an open-ended pile caused a severe output deviation. Hence, stretching models beyond the geometries and loading conditions accounted for in their formulation, can be cumbersome and should therefore be approached with caution. Generally, Gavin *et al.* (2011) ([44] noted at tenancy to conservatism with regard to the ultimate bearing capacity in operation, particularly in dense sand. For future wind farms in the North Sea the latter offers a promising perspective, as it demonstrates room for design optimization.

Tip resistance According to Jardine *et al.* (2005) ([60]) for fully unplugged piles the base capacity is solely due to soil resistance underneath the tip's respective area. Generally it is preferred to calculate base resistance from CPT measurements as shallow bearing capacity theories, i.e. Terzaghi, do not adequately capture field behavior [60]. The latter can also be seen as the reason why almost all SRD models infer base capacity directly from CPT test, which allow for the direct measurement of in-situ soil resistance under conditions similar to those prevailing at the pile tip. Hence, the general form for evaluation of the base resistance by SRD models is given as [51]:

$$q_{tip} = a \cdot q_c^b \cdot F_{A_{\text{end}}} \cdot F_{\sigma_v'} \cdot F_{\overline{q_c}} \tag{3.29}$$

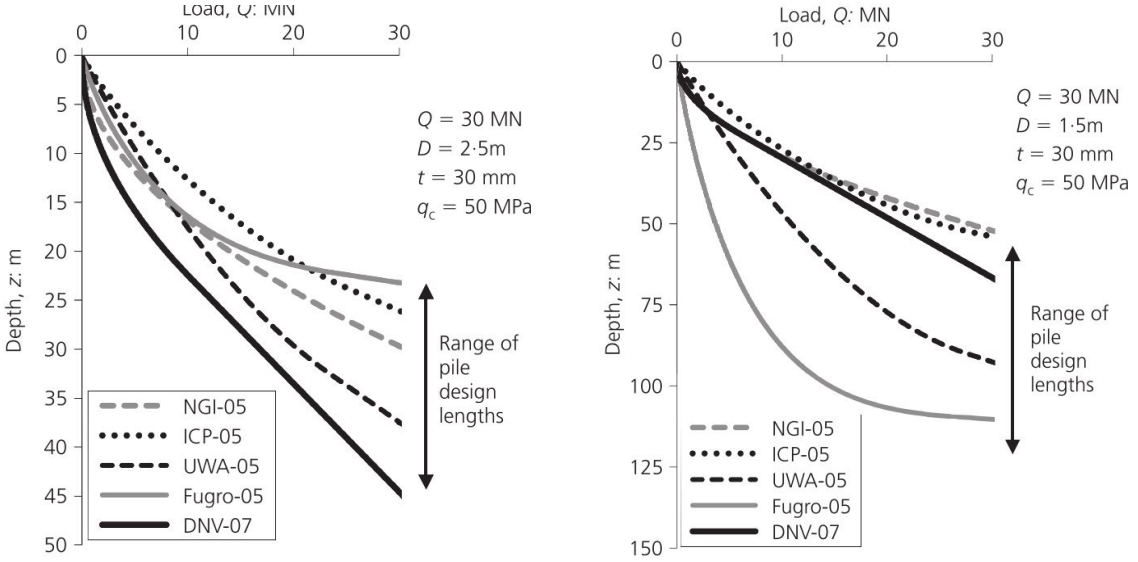

(a) D = 1.5 m (b) D = 2.5 m

Figure 3.8: Required pile length to the support of an 5 MW turbine in the North Sea according to different CPT models. After [44]

Where, a and b are fitting constants; $F_{A_{end}}$, $F_{\sigma'_{v0}}$ and $F_{\overline{q_c}}$ are normalization factors for area, overburden pressure and cone resistance averaging respectively. For a variety of SRD relationships, tip resistance q_{tip} is plotted as a function of σ'_{v0}, q_c and $\overline{q_c}$ in Figure 3.9. As can be observed in Figure 3.9 model output differs quite significantly, highlighting the non-ambiguity that exists between the empirical quantification methods for tip resistance. Given that there is no general framework to differentiate between shaft and tip resistance, most models employ a unique differentiation relationship, thereby partially explaining the significant scatter.

3.4. Two- or three-dimensional finite element analysis

Due to the rapid digitization which has taken place since the 1980s, vast amounts of computation power are now to the public. This revolution made it possible to use numerical tools, such as wave equation analysis, routinely as computation times drastically reduced [50]. Similarly, research in the field of numerical methods intensified significantly. The latter has lead to the development of several other numerical algorithms to conduct drivability studies. Particularity, the work of Smith & Chow (1982) ([106]) and Deeks (1992) ([33]), who devised a three-dimensional and axisymmetric FEM model respectively, is well-known. Currently, commercially available software packages i.e. PLAXIS and Abaqus, are popular tools to simulate pile driving in a finite element environment [51]. Such models allow for a three-dimensional description of structure and surrounding soil [80]. Within the discredited domain, advanced constitutive material models can be used to adequately capture intricate soil behavior and the propagation of P-, S- and R-waves, making FEM a very potent tool. However, these models are computationally expensive and calibration procedures are extensive and require well-founded calibration parameters, which can be hard to obtain. Hence, FEM models have not yet managed to replace their wave equation based competitor [80].

3.5. Discussion

Dynamic, wave equation and finite element analysis are methods to quantify the pile drivability. Due to extensive assumptions and simplifications, dynamic formulas are not well-suited for sophisticated drivability analyses. On the other hand, extensive calibration procedures and long compu-

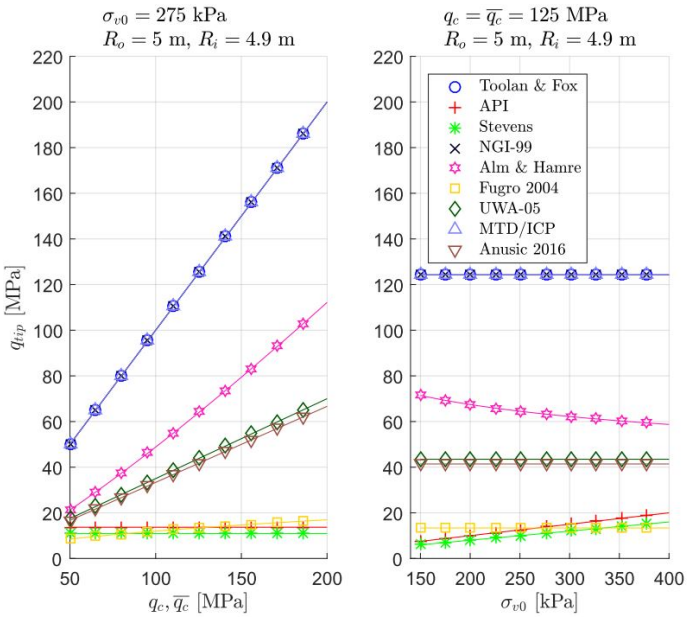

Figure 3.9: Tip resistance as a function of (average) cone resitance and overburden pressure, for various SRD models. For additional background please see [51]

tation times are hampering the adaptation of advanced FEM by the industry. Additionally, inherent soil variability often compensates for gains in computational accuracy, further discouraging their use. Hence, software programs such as GRLWEAP, which are based on one dimensional wave equation analysis, remain the most intensively used tool for drivability studies. Although the former model possesses several inherent shortcomings, thorough calibration of underlying SRD models enabled the attainment of reasonably accurate results.

Software packages such as GRLWEAP, model the pile and driver set-up as a series of lumped massed with interconnecting springs and dash-pots, which quite accurately capture the behavior of its physical counterpart. The behavior of the surrounding soil mass during driving is also modelled using elasto-plastic springs and linearly viscous dash-pots. This combination enables the simulation of both static and dynamic soil behavior, a distinction which cannot be made by dynamic models. To determine the static soil resistance, either a LTSR or SRD model is used. Personal preference dictates which model is used and affects the analysis' initiation procedure. Lately, SRD models have risen in popularity due to the emergence of empirical relations between SRD and CPT data, which is often abundantly available for piling projects. Ultimately, the total static driving resistance R_u is obtained, which is the sum of base and shaft resistance components. A wide range range of relationships exist to quantify the two aforementioned components. As a result, mutual comparison of the output of different models, shows significant variation and is by all means ambiguous. For tubular piles in particular, the largest shortcomings are associated with the distinction of inner and outer shaft friction, as well as the determination of base resistance. Consequently, both soil intrusion into the inner pile cavity and pile-soil interaction in the vicinity of the pile's base are a live topic of research.

Apart from the initiation procedure, the dynamic analysis in itself has several shortcomings. GRLWEAP in particular, couples static and dynamic soil behavior by relating them to the SRD, even though scientific evidence backing this dependency is non-existent. Additionally, parameters governing the dynamic soil behavior, e.g. quake q and dampening coefficient J_s, are user defined and therefore not related to fundamental soil properties. To prevent the choice of dynamic parameters solely based on experience, they are often inferred from pile driving back-analysis. SMA is the accustomed way to conduct the aforementioned analysis and is formally comprised of two steps,

namely [86]:(I) determination of ultimate resistance to driving R_t from the driving log (driving energy vs. blow count) and bearing graph (obtained through the preliminary drivability study); (II) iterative determination of dynamic driving parameters, specifically q and J_s, by rerunning dynamic analysis until output coincides with the driving log. However, the differences between the driving log and the results of the preliminary analysis can also originate from inconsistencies in static resistance model (LTSR or SRD), a possibility which is overlooked in the described procedure. The resulting set of calibration parameters are highly case specific and only applicable to new projects if they are compatible in terms of geology, geometry and driving set-up. Moreover, R_u should be obtained using the same LTSR or SRD model as for the reference case. Partial unification of case characteristics may yield debatable results.

As previously highlighted, choosing an appropriate static soil resistance model is of the essence. However, the latter can be a cumbersome process. Research by both Gavin *et al.* (2011) and Harpoth (2017) has demonstrated that SRD models yield a wide range of predicted pile capacities. The most predominant reason for the aforementioned observation is the use of a particular model on a soil stratigraphy which deviates from the test conditions of the experimental research underlying each model. A common way to overcome this problem is by introducing empirical parameters to accommodate for different geological conditions, geometries and design particularities. However, the latter methodology causes well-founded design methodologies to produce conflicting results [44]. Hence, it is important to theoretically substantiate the choice for a particular static resistance model instead inconsiderately using empirical fitting constants. In addition to opting for an soil model compatible with local soil conditions, the understanding of radial stress degradation during installation as well as stress remobilization due to aging and interface dilation (upon static loading) should be deepened. Disunity on formulation of relationships to account for these effects in (CPT-based) SRD models is apparent from ultimate capacity calculations with different models. Conservatism in pile design methodologies would undoubtedly be reduced if consensus is reached with regard to the former point.

Additionally, due to the coupling between static and dynamic soil resistance, model output can be traced back to the underlying static resistance model. These (LTSR or SRD) models estimate static pile capacity post-installation. Hence, it is inherently assumed that pore fluid pressure is hydrostatically distributed. However, several researchers, e.g. [56] and [112] presented evidence that (dynamic) pile installation impose different loading conditions on portions of the surrounding soil mass. The latter, in turn, can cause pore fluid pressure to locally deviate form hydrostatic conditions. Hence, the effective stress regime surrounding the pile in altered, which should theoretically affect soil resistance during pile installation. Research on the latter subject is however limited making it difficult to quantify the extend to which pile drivability is influenced by PFP fluctuations.

Finally, discussion remains on several other aspects of Smith's model. Predominant discussion points concern: (I) the use of a (non)linear relationship for the dynamic soil resistance; (II) the definition of the initial condition, which is currently the impact velocity of the ram mass. Regarding the former point, it can be argued that the use of a linear relationship does not take into account the strain-rate dependency of soil behavior, as advocated by [98]. Current practice however often dictates the use of n equal to 1, thus resulting in a linear relationship. However, most software packages offer users the possibility to change the dampening model although their implementation is cumbersome and requires measurement matching. Considering the latter point, defining the initial condition by a force-time series (impulse) is arguably more representative of the pile driving physics as it omits the simplification of the driver set-up to a series masses of adjoined by springs and dash-pots. Deeks and Randoph (1993) ([34]) proposed an analytical model to simulate hammer impact in the aforementioned way, though its respective use remains limited.

4

Displacement pile installation through impact hammering: phenomena to consider

4.1. Introduction

The installation of displacement piles is generally associated with large deformations of the adjacent soil. In literature, deformations associated with the installment of displacement piles are also denoted as *installation effects*. In general, installation effects alter the steady state of the surrounding soil within the so-called *zone of influence*, the soil body directly affected by the insertion process. When considering impact pile driving, observations can commonly be assigned to one, or a combination of the following processes: (I) shock wave generation and propagation due to the hammering process; (II) soil compression at the tip due to pile penetration; (III) cyclic soil shearing alongside the pile shaft; (IV) excess Pore Fluid Pressure (PFP) development; (V) dissipation of excess PFP and soil relaxation, also denoted as *set-up effects*.

4.2. Stress wave propagation due to pile driving

Over the last decades, research carried out in the field of vibrations induced by man has drastically increased. The latter is not entirely surprising given the fact that consideration of (disadvantageous) environmental effects in the design cycle has become a common practice. Moreover, construction is more than ever carried out in heavily urbanized areas. Through the development of high quality measurement equipment and an improved conceptional understanding of the physical processes that underlie the generation an propagation of man-made vibrations, significant progress has been made in this field of research [**?**]. Vibrations are formally defined as oscillations around an equilibrium state. The magnitude of ground vibrations is generally described in terms particle velocity. The latter is convenient as strains in the propagation medium are directly proportional to particle velocity. In the following, a differentiation is made between wave generation and propagation due to: (I) pile-driver interaction, which is respectively discussed in 4.2.1; (II) pile-soil interaction, which is respectively discussed in 4.2.2.

4.2.1. Pile-driver interaction

When the driver ram mass impacts the top of the pile, a stress wave is introduced into the pile. The wave, which is in fact a collection of different frequencies and amplitudes, propagates down the pile. When the wave front reaches the top of the soil mass, wave reflections are introduced into the system. Reflections are also generated at the pile tip in the form of either a compression or tension

wave. The latter respectively dependents on whether the pile tip is free or restricted in its movement [114]. Reflection can again take place at the upper extremity of the pile. Hence, depending on the boundary conditions, a collection of tension and compression waves propagate and interact after the pile is struck by the hammer. As a result of pile and soil attenuation, all energy is dissipated after several propagation cycles.

The analysis of dynamic waves through man made media, in example piles, has seen significant progression over the past decades. See in example Globe *et al.* (1968 & 1980) ([46] & [47]). The most common way to gain insight in dynamic wave propagation is by installing strain gages and accelerometers to the pile prior to installation. The combination of strain and acceleration measurement allows for the capture of two key parameters, namely: (I) force, by employment of fundamental stress-strain theory; (II) particle velocity, or pile velocity, through time integration of acceleration measurements. In the following, subscripts H and P indicate whether a parameter relates to the hammer or pile properties respectively.

Pile impedance: derived following a simplified physical approach Particle velocity and the force can be related through impedance. In the words of Massarsch and Fellenius (2008) ([78]): "*The impedance of the pile and of the soil are the single most important parameters for calculating ground vibrations as these govern the transfer and propagation of vibrations in the pile, along the pile-soil interface, and in the surrounding soil*". An expression for pile impedance is derived by considering the deformation of the pile directly after impact of the ram, as is also illustrated in Figure 4.1. Please observe that for simplicity, velocities, stresses, strains and forces are assumed constant in time. At time $t_0 + \Delta t$, the ram mass exerts force F on top of the pile. As a result, the tip is the pile displaced by Δu. The portion of the pile in compression is equal to the total length of the stress wave L_W, which can be expressed as:

$$L_W = c_P \cdot \Delta t \tag{4.1}$$

Where, c_P is the phase velocity of the stress wave in the pile (see Equation 3.9) and Δt is the duration of the force pulse. Given total pile displacement and pulse duration, the particle velocity v_p of the pile can be computed:

$$v_p = \frac{\Delta u}{\Delta t} \tag{4.2}$$

As the part of the pile with can deform due to impact is delimited by the length of the stress wave L_w, the strain ϵ is expressed as:

$$\epsilon = \frac{\Delta u}{L_W} \tag{4.3}$$

Hence, after rearranging of the terms in Equation 4.3, it is found for Δu:

$$\Delta u = \epsilon \cdot L_W \tag{4.4}$$

As stress waves can propagate in two directions, in the following subscripts d and u respectively indicate the propagation direction, *down* or *up*. Now, by combining Equations 4.2 and 4.4, it is found for a downward wave:

$$v_{d,P} = \epsilon_{d,P} \cdot c_P \implies \epsilon_{d,P} = \frac{v_{d,P}}{c_P} \tag{4.5}$$

Where $v_{d,P}$ denotes the particle velocity of the downward stress wave. For upward stress waves, particle velocity is negative (following the sign convention used in Figure 4.1). However, as the end of the pile is constricted, the reflected wave is also compressive [114]. Hence, associated stresses, strains and forces are also compressive and thus should be positive. Therefore, to compensate for an unintended sign change, a minus is introduced such that for the upward wave, it holds:

$$-v_{u,P} = \epsilon_{u,P} \cdot c_P \implies \epsilon_{u,P} = \frac{-v_{u,P}}{c_P} \tag{4.6}$$

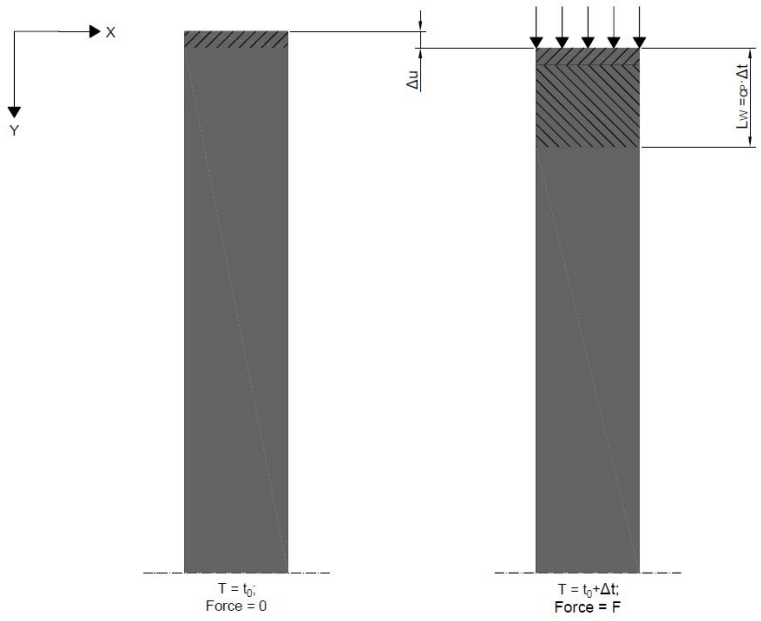

Figure 4.1: Pile deformation the first instant after impact by the ram mass

Where $v_{u,P}$ denotes the particle velocity of the upward stress wave. Subsequently, by combining Hooke's law and Equation 4.5, expression 4.7 is obtained for the stress in the pile as a result of the downward wave:

$$\sigma_{d,P} = \frac{v_{d,P} \cdot E_P}{c_P} \tag{4.7}$$

Now merging Equation 4.6 with Hooke's law, a similar expression is found for the stress as a result of the upward wave:

$$\sigma_{u,P} = \frac{-v_{u,P} \cdot E_P}{c_P} \tag{4.8}$$

For both Equation 4.5 and 4.6, E_P is the modulus of elasticity of the medium. Given the expression for stress as indicated by Equation 4.7. The upward internal force can be expressed as:

$$F_{d,P} = v_{d,P} \cdot (\frac{E_P \cdot A_P}{c_P}) = v_{d,P} \cdot Z_P \tag{4.9}$$

Similarly, the downward internal force, following from 4.8, is expressed as:

$$F_{u,P} = -v_{u,P} \cdot (\frac{E_P \cdot A_P}{c_P}) = -v_{u,P} \cdot Z_P \tag{4.10}$$

As can be observed from Equation 4.9 and 4.10, pile impedance Z_P, is a scalar which can be written as:

$$Z_P = \frac{E_P \cdot A_P}{c_P} = c_P \cdot \rho_P \cdot A_P \tag{4.11}$$

Where, ρ_P is the density of the pile material. Hence, for a general case, the relationship between force F, particle velocity v_P and impedance Z_P is:

$$F = v_P \cdot Z \tag{4.12}$$

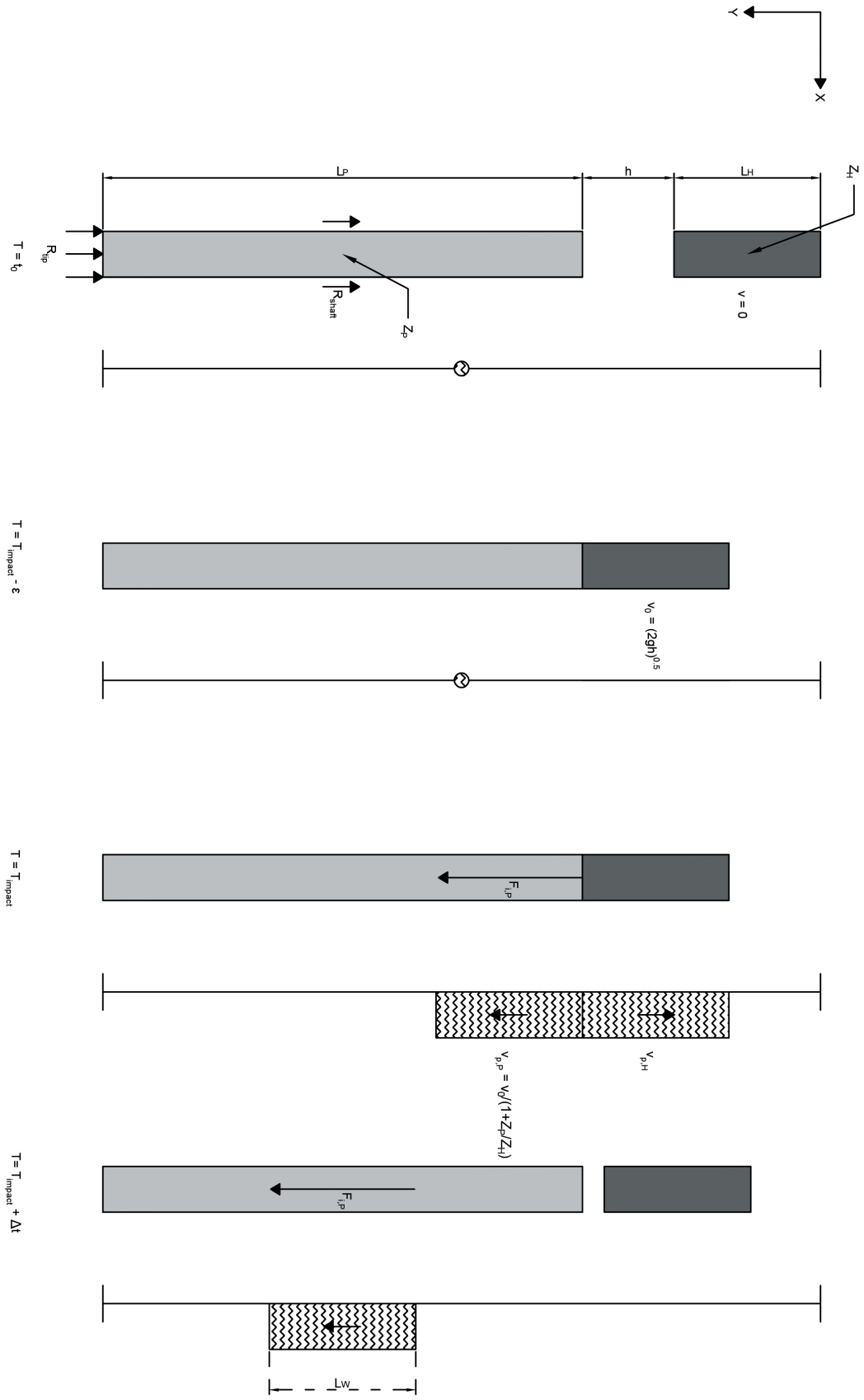

Figure 4.2: Definition of parameters governing dynamic pile behavior, inspired by [78]

Particle velocity, internal force and impact time: an idealized theoretical approach Now, having addressed the physical meaning and derivation of impedance, the analysis of dynamic pile behavior is further elaborated upon. One dimensional stress wave theory is often used to conduct similar analyses, see in example Smith (1960) ([105]). Following the approach advocated by the latter methodology, requires knowledge of the impedance of both hammer and pile, Z_H and Z_P respectively. Initially, the ram mass at rest in a suspended position, where the distance between the top of the pile and bottom of the ram mass is denoted as h. Vertical equilibrium of the pile is maintained through shear along the shaft and bearing pressure at the tip. The latter situation is shown in Figure 4.2 for $T = t_0$. By means of energy conservation (i.e. no friction), it is established that the particle velocity of the ram mass v_0, at an infinitesimal instant before impact, is expressed as:

$$v_0 = \sqrt{2 \cdot g \cdot h} \tag{4.13}$$

The aforementioned situation is illustrated in Figure 4.2 for $T = T_{\text{impact}} - \epsilon$. Upon impact (see Figure 4.2 for $T = T_{\text{impact}}$), two (compression) stress waves are simultaneously generated. Consequently, a wave with particle velocity $v_{p,H}$ is generated which propagates up the ram mass. Please recall that this wave has a negative velocity. Additionally, a downward directed stress wave, with **initial** particle velocity $v_{p,P}$, is generated in the pile. Combining force equilibrium at the interface with Equation 4.12 yields:

$$F_H = F_P \implies Z_H \cdot -v_{p,H} = Z_P \cdot v_{p,P} \implies Z_H \cdot |v_{p,H}| = Z_P \cdot v_{p,P} \tag{4.14}$$

Additionally, at the first instant of pile-driver contact, the top of the pile assumes the same particle velocity as the ram mass. Hence:

$$v_0 - |v_{p,H}| = v_{p,P} \tag{4.15}$$

Now, by combining Equations 4.14 and 4.15, an the following expression for $v_{p,P}$ is obtained:

$$v_{p,P} = \frac{Z_H \cdot v_0}{Z_P + Z_H} \implies v_{p,P} = \frac{v_0}{1 + \frac{Z_P}{Z_H}} \tag{4.16}$$

Hence, given the impedance of the hammer and the pile, respectively Z_H and Z_P, the particle velocity in the pile can be estimated. Consequently, the internal force in the pile (at the first instant of contact) can be computed through Equation 4.17:

$$F_{i,P} = Z_P \cdot v_{p,P} \implies F_{i,P} = Z_P \cdot \frac{v_0}{1 + \frac{Z_P}{Z_H}} \tag{4.17}$$

As can be observed for Equation 4.17, internal pile force is independent of the mass of the ram M_H. However, the hammer's mass does play an important role in the degradation of the pile top force over time. Any increase in ram mass, will reduce the degradation coefficient. Hence, the pile top force remains at elevated levels for longer stretches of time. The latter is qualitatively illustrated in Figure 4.3. As similar degradation curves are almost exclusively derived form field measurements, the derivation of an analytical expression is omitted. The time interval between impact and separation of the ram mass and pile head is known as *impact time*. The stress wave which is create upon impact, travels up the hammer and in reflected at its respective top as a tension wave. The latter is due to the fact that the hammer is not constrained at the top and thus has a free end. The latter implies that the force should be zero at all times [78]. Hence, a tension wave in created upon reflection at the upper extremity. The propagation velocity of both waves is equal, and defined as c_H. As the connection between the hammer and pile is broken when the tension wave arrived at the interface, impact time can be expressed as:

$$\Delta t = \frac{2 \cdot L_H}{c_H} \tag{4.18}$$

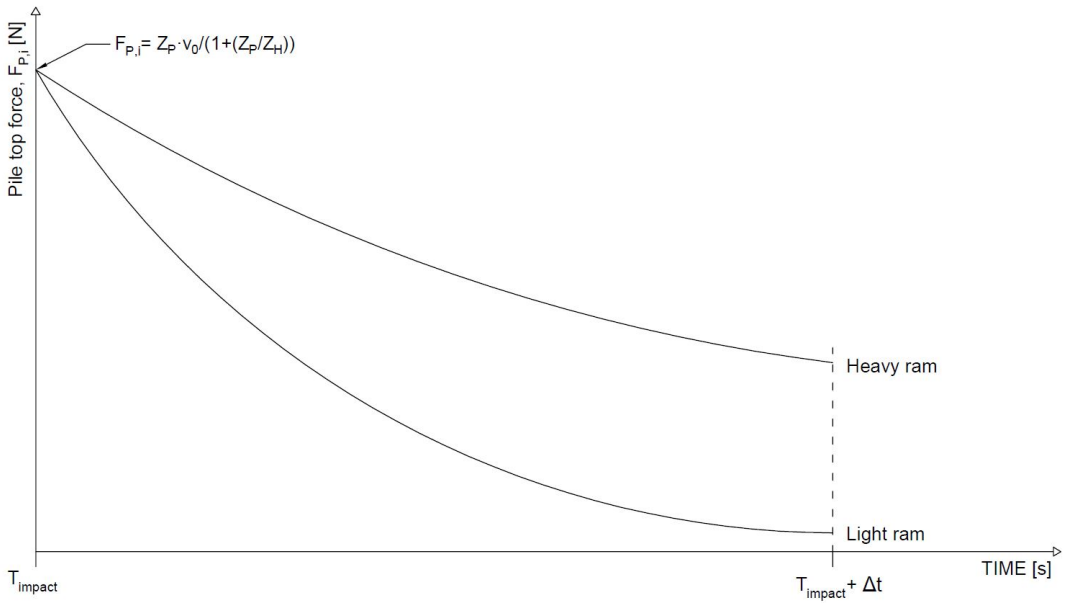

Figure 4.3: Degradation of pile top force with time for a light and heavy ram mass respectively. Please observe that both masses have the same impact velocity v_0 (same stroke h), impedance Z_H and height h_H (as impact time Δt is the same.

Where L_H is the length of the hammer. Separation of the hammer and pile is illustrated in Figure 4.2 for $T = T_{\text{impact}} + \Delta t$. Given the impact time Δt, the length of the wave front L_W in the pile can be calculated with Equation 4.1:

$$L_W = c_P \cdot \Delta t$$

Where c_P is the phase velocity of the stress wave in the pile, which can be computed using Equation 3.9.

Wave analysis: the theoretical framework put to practice The relationship between force F and velocity v through impedance Z is most extensively used for dynamic wave analysis. The method relies on the use of strain gages and an accelerometer just below the upper pile extremity. This combination respectively allows internal pile force $F_{P,m}$ and particle velocity $v_{P,m}$ to be recorded during driving. Knowing pile impedance Z_P, internal pile force can be back-calculated from the particle velocity measurements. By plotting the measured force measured ($F_{P,m}$) and back-calculated force ($v_{P,m} \cdot Z_P$) against time, so-called force traces are obtained. For a hypothetical resistance free scenario, it can be demonstrated that the trace for measured force coincides with the back-calculated force trace ($v_P \cdot Z_P$). However, during pile installation, stress waves cannot propagate freely due to resistance which is mobilized at the shaft and tip of the pile. The latter causes a portion of the incident (downward) stress wave to be reflected. As a result of the partially reflected stress wave, strain is superimposed at the top of the pile:

$$\epsilon_{P,m} = \epsilon_{d,P} + \epsilon_{u,P} \implies F_{P,m} = F_{d,P} + F_{u,P} \tag{4.19}$$

Where $\epsilon_{P,m}$ is the strain measured at the upper pile extremity. Hence, as a consequence of the superposition of strain, the measured force trace increases. The latter is observable in Figure 4.4. Substitution of expression 4.9 and 4.10 into Equation 4.19 yields:

$$F_{P,m} = v_{d,P} \cdot Z_P - v_{u,P} \cdot Z_P \implies F_{P,m} = v_{d,P} \cdot Z_P + |v_{u,P}| \cdot Z_P \tag{4.20}$$

Simultaneously, particle velocities at the top of the pile are also superimposed and recorded:

$$v_{P,m} = v_{d,P} + v_{u,P} \implies v_P = v_{d,P} - |v_{u,P}| \tag{4.21}$$

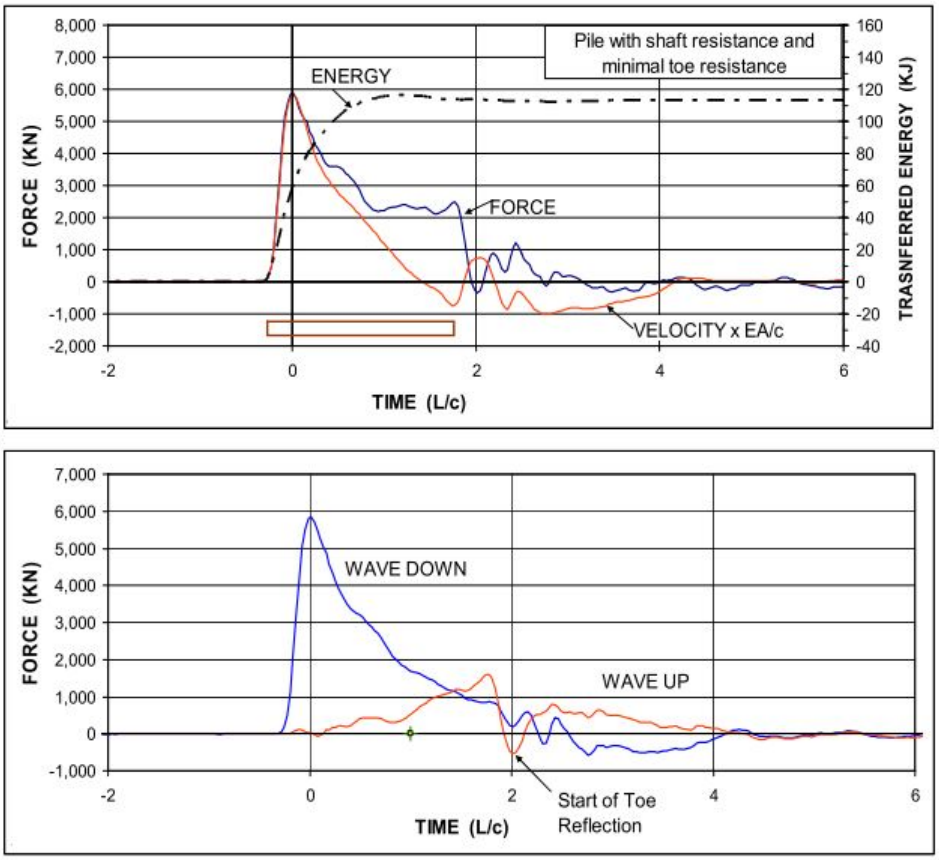

Figure 4.4: Above: dynamic force and velocity recordings for a pile encountering mostly shaft resistance. Below: calculated wave up and wave down traces. Adapted from [78]

Multiplication of Equation 4.21 by Z_P yields:

$$v_{P,m} \cdot Z_P = v_{d,P} \cdot Z_P - |v_{u,P}| \cdot Z_P \tag{4.22}$$

Hence, the recording of particle velocity multiplied by impedance decreases, as is also visible in Figure 4.4. Consequently, the measured force and back-calculated force trace diverge. The extend of separation forms a measurement of the total soil resistance, which is the summation of static and dynamic resistance contributions, encountered during driving.

Form the information presented in the upper graph of Figure 4.4, it is possible to approximate the respective downward and upward stress wave trace. An expression for the downward wave is obtained by adding Equation 4.22 to 4.20 and rearrange terms to obtain an expression for $F_{d,P}$:

$$F_{P,m} + v_{P,m} \cdot Z_P = v_{d,P} \cdot Z_P + |v_{u,P}| \cdot Z_P + (v_{d,P} \cdot Z_P - |v_{u,P}| \cdot Z_P) \implies v_{d,P} \cdot Z_P = F_{d,P} = \frac{F_{P,m} + v_{P,m} \cdot Z_P}{2} \tag{4.23}$$

Similarly, an expression for the upward wave is found by subtracting Equation 4.22 from 4.20 and rearrange terms to obtain an expression for $F_{u,P}$:

$$F_{P,m} - v_{P,m} \cdot Z_P = v_{d,P} \cdot Z_P + |v_{u,P}| \cdot Z_P - (v_{d,P} \cdot Z_P - |v_{u,P}| \cdot Z_P) \implies v_{u,P} \cdot Z_P = F_{u,P} = \frac{F_{P,m} - v_{P,m} \cdot Z_P}{2} \tag{4.24}$$

The result of the operations expressed by Equation 4.23 and 4.24 is graphically illustrated in the bottom graph of Figure 4.4. Besides reconstruction of the upward and downward wave traces, the

force and velocity measurements (both of which are a function of time) are also used to calculated the energy transmitted to the pile E_T:

$$E_T = \int_{T_{\text{impact}}}^{T_{\text{impact}}+\Delta t} F_{P,m} \cdot v_{P,m} \, \text{dt} \tag{4.25}$$

Knowing the energy transferred to the pile, it is possible ot calculate the driver system efficiency η_{ds} as follows:

$$\eta_{ds} = \frac{E_T}{E_H} \tag{4.26}$$

Where E_H is the kinetic energy of the hammer at an infinitesimal instant before impact with the helmet cushion or anvil:

$$E_H = (m_H \cdot a \cdot h) \cdot \eta_h \tag{4.27}$$

Where m_H is the mass of the hammer, a is the acceleration, h is the drop height and η_h is the hammer efficiency as defined in Table 2.3. Please not that Equation 4.27 only holds for 1g conductions. Due to the presence of a gravity curve in the centrifuge, acceleration is averaged over the stroke h (for derivation please consult Equation E.3 to E.8. Hence, it is obtained:

$$E_{H,\text{centrifuge}} = (m_H \cdot \overline{a} \cdot h) \cdot \eta_h \tag{4.28}$$

4.2.2. Pile-soil interaction

The installation of displacement piles is known to cause vibrations in the surrounding soil body. Vibrations are formally defined as oscillations around an equilibrium state. The magnitude of ground vibrations is generally described in terms of particle velocity. The latter is convenient as strains in the propagation medium are directly proportional to particle velocity. Due to pile-soil interaction, different types of waves or vibrations are introduced into the surrounding soil mass. Firstly, shear or S-waves, which are emitted cylindrically, are generated due to interactions along the pile shaft. Secondly, further progression of the stress wave down the pile gives rise the effects of interaction at the pile tip. Thereby introducing a spherical wave front comprised of compression or P-waves. The third wave type, Rayleigh or R-waves, which are also referred to as *surface waves*, originate from wave refraction at the surface [78]. Refraction along the ground surface can only take place for a critical angle of incidence. Hence, surface waves can only be observed at some distance away from the pile. The latter is often denoted as *critical distance* [78]. The concept of critical distance, d_{crit}, and critical angle of incidence, θ_{crit}, is further illustrated in Figure 4.5. Additionally Figure 4.5 depicts the three wave types and their respective source of origin. The intensity of the vibrations generated at the pile-soil interface is coupled to the dynamic soil resistance. Dynamic soil resistance, unlike static soil resistance, is a velocity dependent component of the total soil resistance encountered which is inherent to dynamic installation methods, in example driving. Upon impact of the ram mass with the pile head, a stress wave is induced in the pile. Consequently, pile particles are accelerated and temporarily assume a velocity which is commonly referred to as *particle velocity*. Due to interaction mechanisms at the pile shaft and toe, momentum is exchanged with the surrounding soil mass. The resulting movement of adjacent soil particles gives rise to dynamic soil resistance and simultaneously induces vibrations in the surrounding soil. Due to energy dissipation associated with plastic deformation and remoulding (an effect which is particularly relevant at the shaft) only part of the energy transferred to the soil gives rise to dynamic resistance and soil vibrations. In order to quantify the dynamic soil resistance, one should consider the dynamic soil parameters. Chiefly, soil impedance Z_S and soil dampening J_s. The importance of the previously mentioned dynamic parameters is discussed in the following. The total dynamic resistance R_d can be split into its two respective components: (I) dynamic shaft resistance $R_{d,s}$; (II) dynamic toe resistance $R_{d,t}$. In the following (for convenience), a differentiation is made between the two components of dynamic

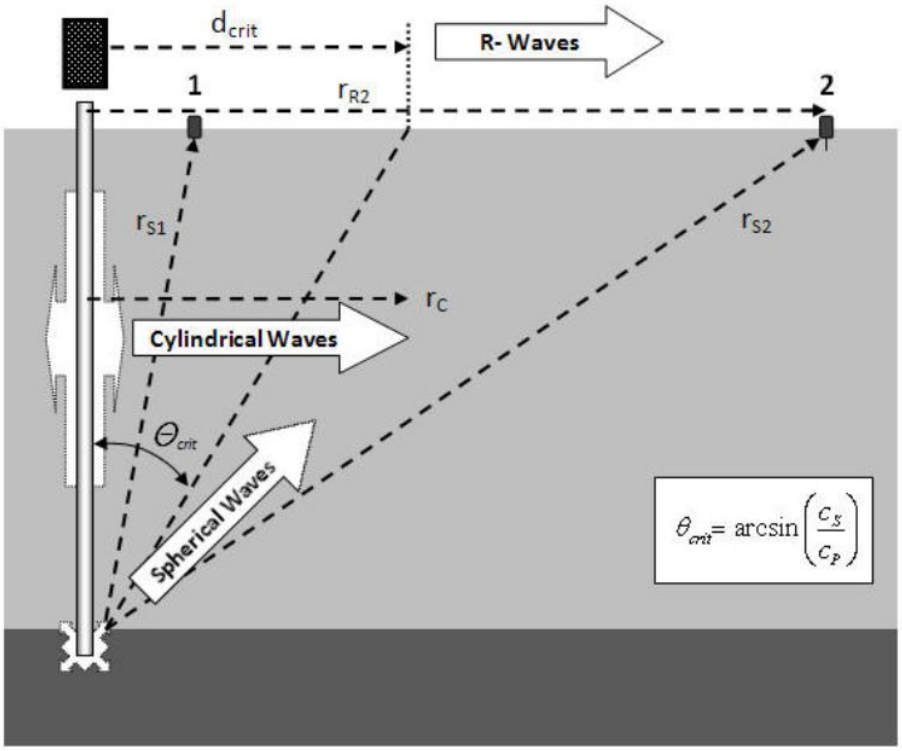

Figure 4.5: Terminology regarding the generation of vibrations as a result of dynamic pile installation, after [78]

soil resistance. Hence, the estimation of dynamic shaft resistance is addressed in 4.2.2 and dynamic toe resistance in 4.2.2.

Dynamic shaft resistance Dynamic soil resistance along the shaft, which is the source of the cylindrically emitted S-waves, can be estimate by use of Equation 4.29:

$$R_{d,\text{shaft}} = z_{s,\text{S-wave}} \cdot v_P \cdot A_P \tag{4.29}$$

Where $R_{d,shaft}$ is the dynamic shaft resistance, $z_{s,S\text{-}wave}$ is the **specific** soil impedance for shear waves, v_P is the particle velocity of the pile and A_P is the contact area between the shaft and soil. $z_{s,S\text{-}wave}$ is determined from Equation 4.30:

$$z_{s,\text{S-wave}} = c_s \cdot \rho_s \tag{4.30}$$

Where c_s is the (small strain) shear wave velocity of the interface layer and ρ_s is the soil density. Please observe that the latter makes $z_{s,S\text{-}wave}$ a soil parameter as it is geometry-independent. As indicated by Massarsch and Fellenius (2008) ([78]), direct use of small strain shear wave velocity, would lead to over-conservative estimates of pile penetration. Generally, due to the effects of strain softening and remoulding, the shear wave velocity is decreased at the interface. Hence, Massarsch and Fellenius (2008) ([78]) advocate the use of two reduction factors, R_C and R_R respectively, to account for the aforementioned effects in calculations. Hence, Equation 4.29 can be rewritten as follows:

$$R_{d,\text{shaft}} = (R_C \cdot R_R \cdot c_s \cdot \rho_s) \cdot v_P \cdot (D_P \cdot \pi \cdot L_{\text{embedment}}) \tag{4.31}$$

Where D_P is the pile diameter and $L_{embedment}$ is the length of the pile which is embedded in the soil. Massarsch (2005) ([77]) established that the strain-softening reduction factor R_C is a function of the soil's plasticity index PI and penetration resistance, see [77] for further information.

Dynamic toe resistance The dynamic toe resistance $R_{d,toe}$, which is the origin of P-waves that are emitted spherically from the toe, can be estimated form Equation 4.32:

$$R_{d,\text{toe}} = J_c \cdot Z_P \cdot v_P \tag{4.32}$$

Where J_c is a **dimensionless** dampening coefficient (not to be confused with the Smith dampening coefficient J_s), Z_P is the pile's impedance and v_P is the particle velocity of the pile. An analytical expression for J_c was established by Iwanowski (1988) ([59]):

$$J_c = 2 \cdot \frac{Z_{s,\text{P-wave}}}{Z_P} \tag{4.33}$$

Where $Z_{s,P\text{-}wave}$ is the soil impedance for P-waves and Z_P is pile impedance. In order to derive expression 4.33 Iwanowski ([59]) employed a model of spherical vibrating plate in infinite elastic medium, to simulate the interplay between the pile tip and the underlying soil. The soil impedance for P-waves is, similar to the pile impedance (see Equation 4.11), defined as:

$$Z_{s,\text{P-wave}} = A_P \cdot c_{s,\text{P-wave}} \cdot \rho_S \tag{4.34}$$

Where, A_P is the surface area of the pile tip and $c_{s,P\text{-}wave}$ is the phase velocity of P-waves (in the soil). Combination of Equation 4.32 and 4.33 yields the final expression for $R_{d,toe}$:

$$R_{d,\text{toe}} = 2 \cdot Z_{s,\text{P-wave}} \cdot v_P \tag{4.35}$$

4.3. Stress states during pile driving

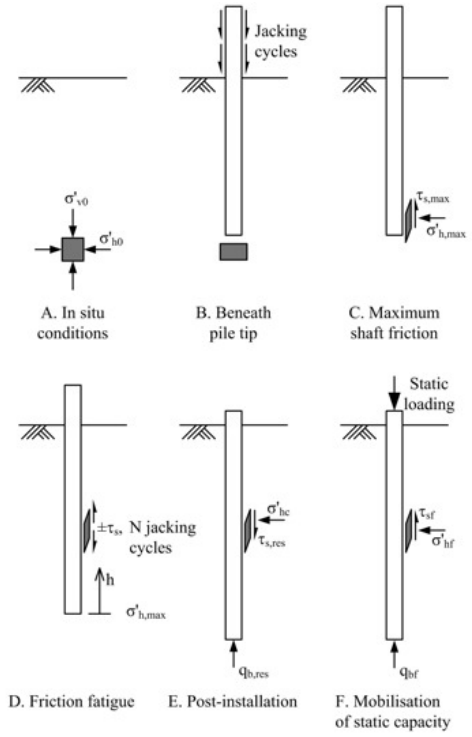

Figure 4.6: Stress states observed during pile driving

During installation of a displacement pile, the soil is exposed to a number of different stress states, as described by [55] & [115]. These stress states (A. to F.) can be observed in Figure 4.6. Both

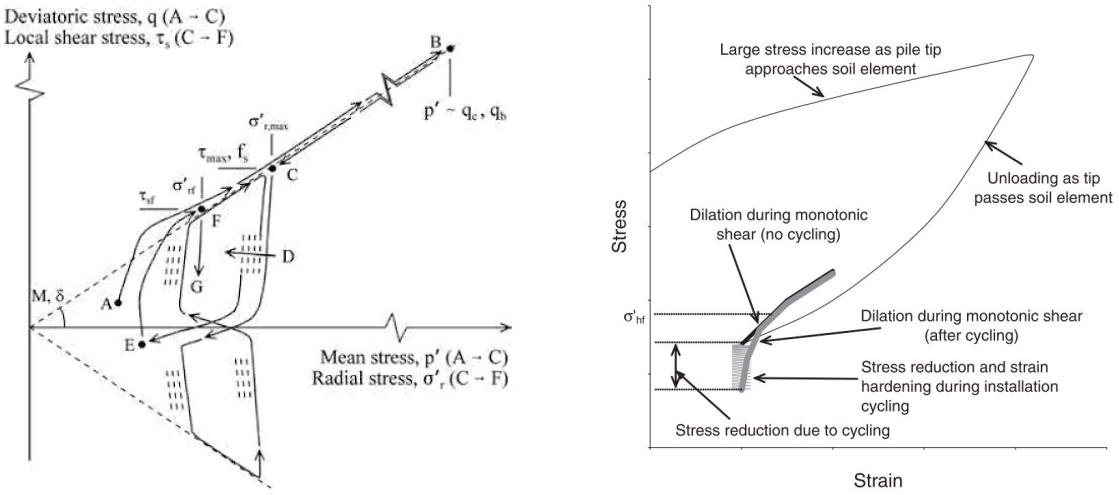

(a) Stress paths associated with installation stages for a reference soil body in the vicinity of a displacement pile during installation [115]

(b) Postulated stress-strain paths for a reference soil body in the vicinity of a displacement pile during installation [69]

Figure 4.7: Stress states (a) and associated stress paths (b) observed during pile installation

the associated stress and stress-strain paths are conceptualized in Figure 4.7a and Figure 4.7b, respectively. It should be noted that both of the aforementioned figures, neither consider the development of Poisson strains nor excess pore water pressures. In Figure 4.6, stage A. describes the soil conditions that prevail prior to installation, which are also referred to as the in-situ stress conditions. In-situ stress conditions can easily be derived from common site investigation techniques and are, as a result, generally well-understood. However, interactions between the pile and the surrounding soil alter the in-situ stress conditions. Hence, the suitability of in-situ soil parameters for design calculations is restricted. Arguably the most critical stress alteration during pile installation concerns the radial effective stress. Knowledge on the development of the radial effective stress from the in situ stress state, is by all means limited. In order to close the aformentioned knowledge gap and improve design and installation methods, White (2005) argues that the total stress history of a soil element during pile installation should be considered [115]. Although this study formally is strictly limited to the installation of displacement piles, installation procedure can have important implications for the loading phase. Therefore, in the following, all installation stages (A. through F.) are considered.

4.3.1. Stage A. and B.

Upon the start of installation, the in situ stress conditions, depicted in terms of σ'_{v0} and σ'_{h0} (stage A. in Figure 4.6) are altered. This is due to progression of the pile towards the reference soil body (stage B. in Figure 4.6). This process, which formally causes the first alteration to the in situ stresses, is characterized by large soil deformation and effective stress fluctuations due to vertical compression underneath the pile tip. As the pile tip approaches, the local mean effective stress rises from the in situ stress value. For impact hammering, the highest stress mobilized during each hammer blow is related to the base resistance, q_b, at that depth. The value of q_b is usually two orders of magnitude greater than the in situ mean stress [115]. The loading conditions for stage A. and B. are described in terms of a mean and deviatoric stress, p' and q respectively. The corresponding stress path is depicted in 4.7a, there p' and q are defined as:

$$p' = \frac{\sigma_1' + \sigma_2' + \sigma_3'}{3} \tag{4.36}$$

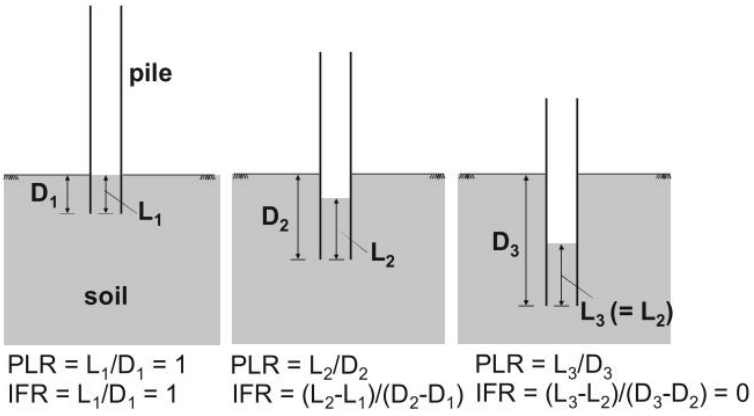

Figure 4.8: Definition of soil plugging mode in terms of IFR and PLR [49]

$$q = \sqrt{\frac{(\sigma_1{}' - \sigma_2{}')^2 + (\sigma_1{}' - \sigma_2{}')^2 + (\sigma_1{}' - \sigma_2{}')^2}{2}} \tag{4.37}$$

The stress-strain path for the first part of installation is shown in Figure 4.7b.

Soil plugging As monopiles are fabricated as open-ended steel tubular piles, a column of soil penetrates the pile cavity upon installation. Due to the development of frictional resistance, continued soil mass influx may be hampered. The latter phenomena is referred to as pile plugging. In this case, an open-ended pile assumes the penetration characteristics of a closed-ended pile [89]. The formation of a soil (partial) soil plug has severe implications on soil-structure interaction, both during and following installation.

The degree to which plugging effects play a role during installation is governed by hammer characteristics [44], soil properties and the pile's interface friction angle [19]. Of all soil properties, relative density plays the most predominant role in the plugging process. The latter is due to strong correlation between the soil's bearing resistance (which is a function of relative density) underneath the pile tip and the internal stresses in the soil plug. Moreover, high relative density soils tend to dilate upon shearing, thereby further affecting the internal stress regime and leading to larger plugging tendency [32].

Soil plugging is the result of arching in the intruding soil column. For this arching to occur, the soil must be able to drain. Drainage, in turn, allows for an increase in effective stresses, thereby raising the internal shear force exerted onto the pile [93]. The capacity of soil plug has been showed to increase exponentially with plug length [95]. Two methods exist of evaluate the capacity of a soil plug: (I) evaluation by means of the Incremental Filling Ratio (IFR) [19]; (II) evaluation by employing the Plug Length Ratio (PLR) [87]. IFR and PLR are defined in Equation 4.38 and 4.39 respectively. To further clarify these definitions, they are illustrated in Figure 4.8.

$$IFR = \frac{\Delta L}{\Delta D} \tag{4.38}$$

$$PLR = \frac{L}{D} \tag{4.39}$$

In Equation 4.38 and 4.39 L is defined as the height of the plug, D describes the embedment depth of the pile. Based on the IFR value, three plugging scenarios can be defined, namely: (I) IFR = 1, meaning that the top of the plug is stationary and does not penetrate the soil with continued progression of the pile, this situation is also referred to as full coring mode [49]. Effectively meaning that there is no plugging. The latter is the case for undrained conditions. As any axial load increment

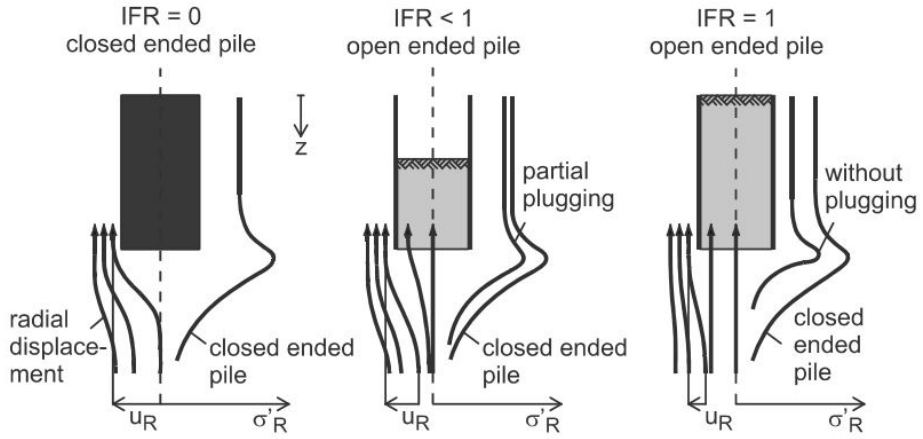

Figure 4.9: Schematic showing radial displacement and associated radial stress around pile tip for different IFR values [74] (adapted from [115])

is entirely compensated for by a raise in pore fluid pressure. This prevents an increase in effective stress and thereby counteracts plug formation; (II) IFR = 0, in this case the pile is fully plugged and essentially behaves as a close-ended pile; (III) 0 < IFR < 1, this intermediate state describes a partially plugged pile, where the plug length is variable and dependent of pile embedment. Lower IFR values result in larger radial displacements around the pile tip and thereby in higher radial stresses, the latter can also be observed in Figure 4.9.

The formation of a soil plug causes additional resistance while driving the pile to the desired depth. Occasionally, the additional resistance is insurmountable by the driving hammer, thereby completely holding the driving procedure, this also called pile refusal. The latter can be the case in very dense sands. For offshore applications, pile refusal is usually overcome by removing the plug through drilling or jetting [58]. Although this is the most economically advantageous solution, the high operating costs of offshore equipment still make it a costly procedure. Practice therefore dictates that prevention of pile plugging during installations is always preferred. Although research is limited, it is believed that soil arching, which is required for plug formation, is less effective for larger pile diameters [19], [60]. As illustrated in Figure 4.10, an increasing relaive desity can provoke plugging for pile diameters ≤1.5 m.

4.3.2. Stage C.

At a given moment, the pile tip surpasses the reference soil element, this proces causes the most significant change in loading condition during installation. The soil element, which was primarily vertically compressed in stage B., is now in a state of horizontal compression and vertical extension as it flows around the pile tip. This change formally causes a °90 rotation of the principle stress directions, as described by e.g. [62], [73], [65]. As the soil element passes the pile, a short spike in radial stress is observed and the soil element exerts the maximum unit shaft resistance onto the lower part of the pile shaft [115]. Thereafter, as the soil element progresses further along the soil-pile interface, the radial stress level reduces. Consequently, the shear stress exerted onto the pile shaft decreases, this process is schematically illustrated in Figure 4.9. The soil relaxiation which occurs right after passing of the pile front is also clearly visible in Figure 4.7b. In contrast to stage A. and B., the prevailing stress conditions at the interface can be characterized by means of a normal stress, $\sigma_r^{'}$ and a shear stress, τ_s [115]. The associated stress path can be observed in 4.7a. In order to quantify the resulting strains and stresses during stage C. of installation, cavity expansion theory can be employed as has been done by i.e. [124].

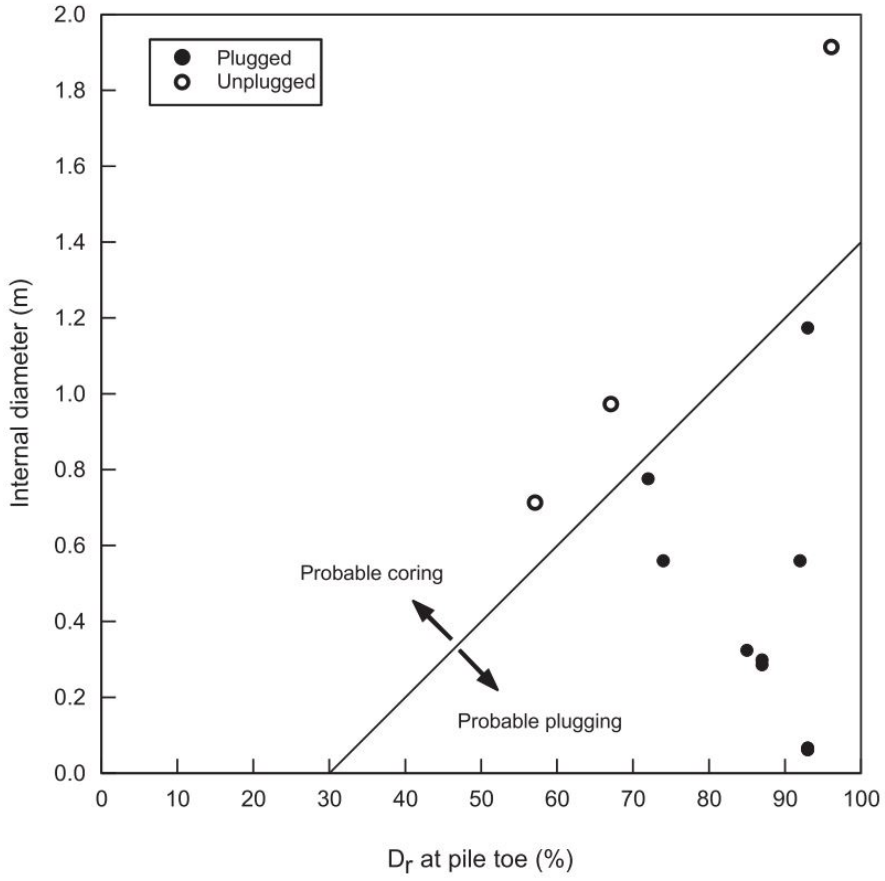

Figure 4.10: Plugging criterion for tubular piles in sand based on field experience [60]

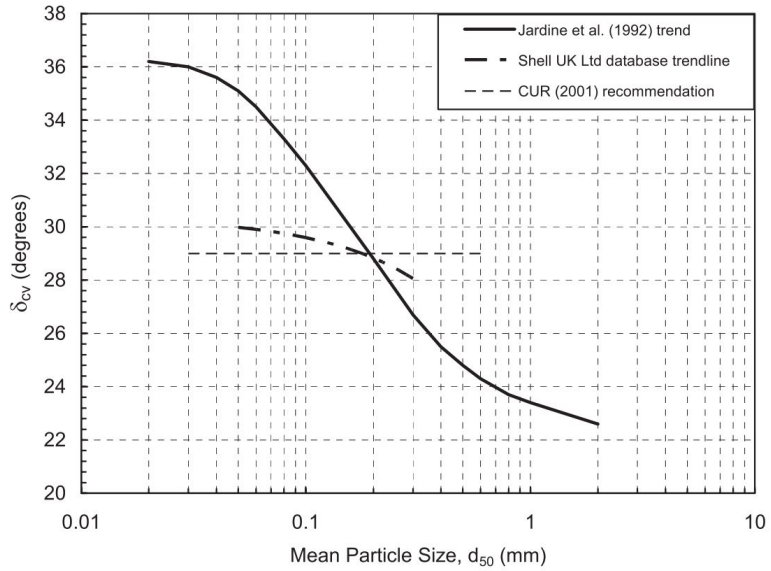

Figure 4.11: Steel-sand interface friction angle δ_{cv} obtained from direct shear tests carried out by Jardine (1993) ([63]) and Shell UK Ltd. CUR (2001) ([27]) recommendation is also included. Retrieved from [60].

Pore water pressure development To be added later.

4.3.3. Stage D.

Stage D. of installation is initiated when the pile tip has reached a greater depth than the considered soil element, shown as stage D. in Figure 4.6. Upon reaching the soil-pile interface, the reference soil element is cyclically sheared. The interface layer can be thought of as the shear zone that exists in the direct vicinity of the loaded pile shaft and, in contrast to the far field soil, exhibits significant deformation. The observed behavior of the interface layer is strongly affected by the loading conditions that prevailed during stage A. through C. of installation. Similar to stage C., stress conditions in stage D. are characterized by means of a normal stress, and a shear stress.

Friction fatigue For successful pile installation, hammer induced forces must exceed the interim bearing capacity of the pile. When solely focusing on the pile shaft capacity at failure, the latter entails that the interface shaft resistance must be overcome. The ultimate shear stress at the interface is expressed by the Coulomb criterion:

$$\tau_f = \sigma'_{\mathrm{rf}} \cdot \tan\delta_{\mathrm{cv}} \tag{4.40}$$

In Equation 4.40, τ_f, is the shear stress; σ'_{rf} is the radial effective stress (along the pile shaft); δ_{cv} is the constant volume friction angle.

Literature provides several approaches to estimate the interface friction angle δ_{cv} between steel and sand, e.g. [63], [27]. Jardine *et al.* (2005) ([60]) argues that δ_{cv} is dependent on: (I) mean grain size d_{50}; (II) particle shape; (III) hardness; (IV) roughness of the pile"s shaft. Arguably, the effective radial stress is also influential. Figure 4.11 summarizes design recommendations with respect to δ^{cv} as argued by Jardine (1993) ([63]), CUR 2001 ([27]) and Shell UK Ltd. According to Jardine *et al.* (2005) ([60]), ring interface shear tests executed at Imperial College on sand samples similar to those employed by Jardine *et al.* (1993) ([63]) indicate that, for high stress regimes, dependency of δ_{cv} on d_{50} is reduced, yielding δ_{cv} between °26 and °30. Hence, it is recommended to obtain representative design values of δ_{cv} through ring interface shear tests, as had priorly been advocated by Lehane *et al.* (1993) ([73]).

Contrastingly, it is proven more cumbersome formally quantify the radial effective stress σ'_{rf}, as this value is known to reduce under the cyclic loading conditions which prevail during pile installation. Heerema (1980) was the first to thoroughly investigate the aforementioned phenomenon and its influence on pile drivability, naming the phenomenon *friction fatigue*. Lateral stress reduction for a given sand horizon, and how one should account for this effect in pile design, has been heavily researched. These efforts debouched into three distinct formulations for the evaluation of *friction fatigue* effects, namely:

- Design methods which relate the degree of *friction fatigue* in terms of distance between a soil horizon and pile tip, e.g. [52], [110], [94], [5];
- Design methods which relate the degree of *friction fatigue* in terms of distance between a soil horizon and pile tip, normalized by pile diameter, e.g. [61], [60];
- Design methods which relate the degree of *friction fatique* in terms of the number of load cycles experienced by the surrounding soil, e.g. [118], [69].

Randolph *et al.* (1994) ([94]) sought to define*friction fatigue* in terms of an exponentially degrading lateral earth pressure coefficient K (and hence diminishing shear stress):

$$K(h) = K_{min} + (K_{max} - K_{min})e^{-(\mu h/D)} \tag{4.41}$$

Where K_{min} and K_{max} respectively indicate the minimum and maximum lateral earth pressure coefficient, the decay rate is represented by μ, h the distance above the pile tip and D the pile diameter. Numerous researchers, e.g. [31] and [20], have deduced the μ form lab and field test. However, these efforts failed to produce matching results. White and Bolton (2002) ([116]) sought to identify the cause of the widespread results. Ultimately concluding that the decay rate μ is neither a function of absolute shearing distance, nor of absolute shear distance normalized by pile diameter D or mean grain size D_{50}. Thus indicating a fundamental flaw is the formulation originally proposed by [94]. Moreover, Gavin *et al.* (2011) ([44]) emphasize the that estimation of the lateral earth pressure coefficient K (see Equation 4.41) is cumbersome. Hence, methods which correlate in situ data to shaft resistance are preferred.

As a result of efforts to bypass design methodologies which rely on averaged shaft resistances, numerous new design techniques have been developed. Jardine *et al.* (2005) ([60]) introduced a well-known equation for effective lateral stress, which has a dependency on cone resistance q_c. Moreover, Jardine *et al.* (2005) sought to attribute friction degradation to the "*h/R* effect" by means of an inverse power law:

$$\sigma'_{\mathrm{rf}} = \frac{q_c}{34}(\sigma'_{\mathrm{v0}}/P_{atm})^{0.13}(h/R)^{-0.38} \tag{4.42}$$

Where, q_c is the cone resistance, σ'_{v0}/P_{atm} is the effective overburden pressure normalized by the atmospheric pressure (=100 *kPa*) and h/R is the relative distance to the pile's tip h normalized by the radius R. The latter is limited to minimum value of 8. The value -0.38 is an emperical degradation parameter, derived from arguably the most insightful research on *friction fatigue* conducted by Lehane (1992) [70] and Chow (1996) ([23]. Aforementioned research was carried out with the Imperial College pile (ICP) on respectively medium-dense dune sand at Labenne and on dense sand at Dunkirk, two locations in France [44]. Results from Lehane's (1992) ([70]) are depicted in Figure 4.12. Figure 4.12 clearly illustrates the effect of *friction fatigue*, as the local shear stress evidently reduces as the (normalized) distance to the pile's tip rises.

Research carried out by Kelly (2001) ([64]) arguably disputes the connection between *friction factigue* and the "*h/R effect*" as promoted by Jardine *et al.* (2005) ([60]). Kelly conducted large displacement ring shear tests on Sydney sand with high R_d. Initially, Kelly (2001) ([64]) monotonically sheared under constant normal stress, causing dilation. Subsequently, 10 two-way cyclic displacement cycles were carried out, each with a varying cycling amplitude, leading to volume contraction.

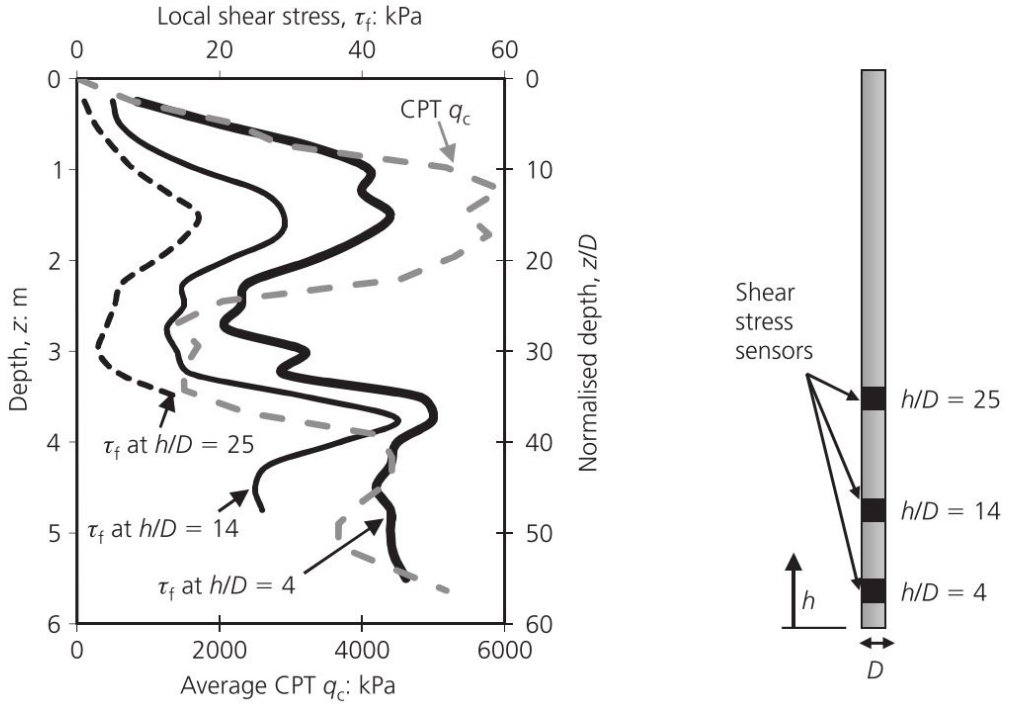

Figure 4.12: Data obtained from ICP tests conducted by Lehane (1992) ([70]) at Labenne in France, illustrating an augmenting degree of friction degradation for higher *h/D*. Retrieved from [44]

.

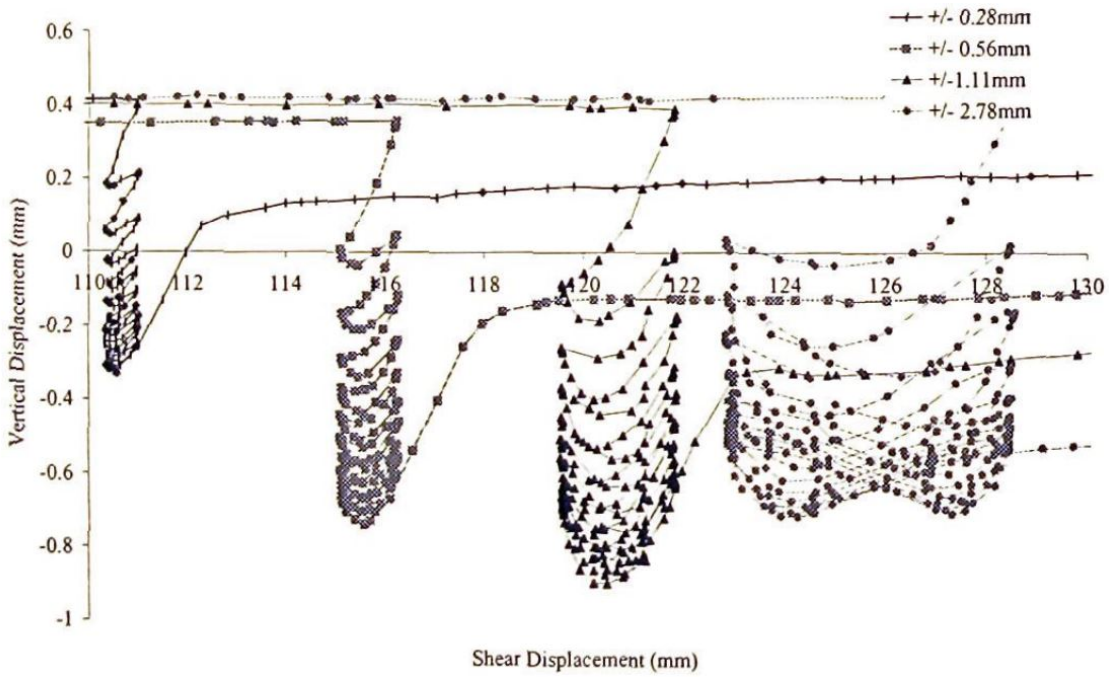

Figure 4.13: Observed vertical displacements for two-way cyclic tests with varying cycling amplitudes for silica sand: σ'_n; D_r = 81% (according to [115]); $h_{initial} \approx 10\ mm$ [64].

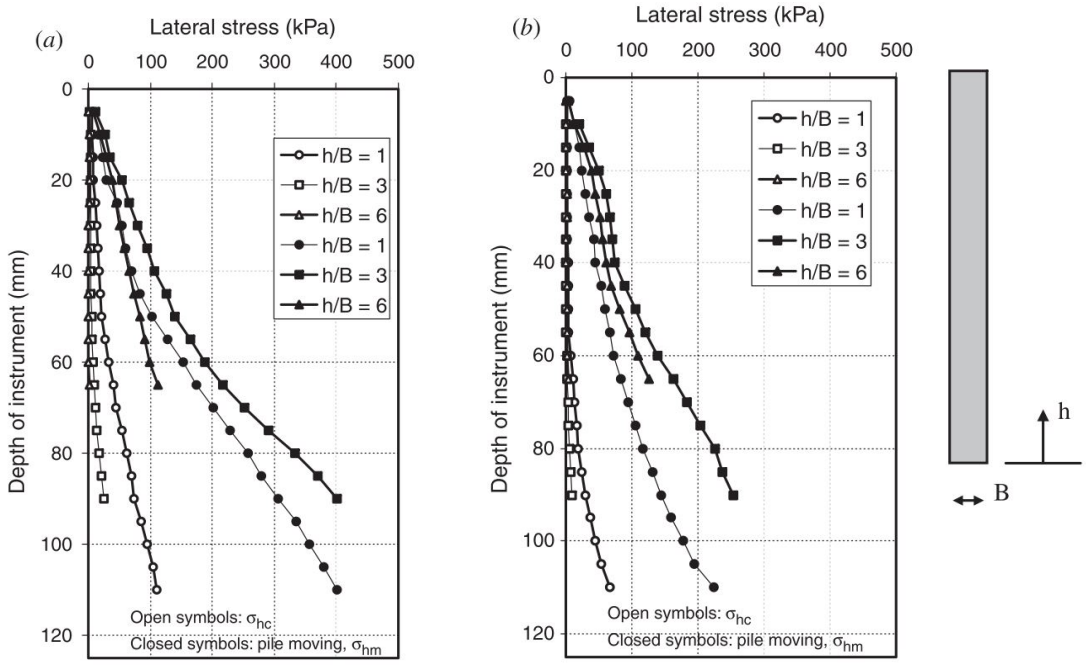

(a) Pile jacking (b) Impact hammering

Figure 4.14: Recorded lateral stress levels from drum centrifuge tests conducted by Lehane and White (2005) different installation methods (values are test series averages). Retrieved from [69]

Finally, the sample was again monotonically sheared. Results are shown in Figure 4.13. Figure 4.13 demonstrates that permanent volume contraction is greater for larger cycling amplitudes and the residual state is approached faster [64]. Moreover, Figure 4.13 presents evidence that contraction of interface layer, which induces friction fatigue, is better described in terms of the number induced load cycles N, instead shear amplitude and thus absolute shear displacement as advocated by [61] and [94]. Although the latter was not formally recognized by Kelly (2001) ([64]), it was later hypothesized in the work of White and Lehane (2004) ([118]).

Lehane and White (2005) ([69]) present further evidence in favor of the aforementioned hypothesis, stating that under dry conditions, the stationary lateral stress $\sigma^{'}_{hc}$ significantly decreases with the number of imposed load cycles. Figures 4.14a and 4.14b show lateral stress profiles with depth for jacked (one-way load cylce) and pseudo-dynamic installation (two-way load cycle) respectively, obtained through the installation of a pile fitted with multiple earth pressure sensors (located at different h/D) in a drum centrifuge. As can be observed in Figure 4.14a and 4.14b the stationary lateral stress σ_{hc} (denoted by open symbols respectively), pressure sensors placed at a larger distance from the pile tip (increasing h/D) record increasingly smaller stationary lateral stresses at a given soil horizon. Additionally, from Figures 4.14a and 4.14b it is apparent that impact hammering (pseudo-dynamic installation) reinforces degradation effects with respect to jacking. The latter is due to different loading conditions, respectively one-way cyclic loading for jacking and two-way cyclic loading for impact hammering. The connection between the induced load cycle and the rate of volume reduction is also mentioned by White and Lehane (2004) ([118]).

Impact hammering, a dynamic installation method, is best characterized by a two-way loading cycle, i.e. a load cycle comprised of both a compressive and tensile part. Tensile loading makes it possible to mimic the effects of pile rebound and shaft friction reversal, both of which are known to occur during the installation of displacement piles through impact hammering. Typical stress paths for a two-way cyclic loading of the interface are shown in $\tau_s - \sigma^{'}_n$-space in Figure 4.15a and 4.15b. A more in depth look at the cyclic and small-strain loading characteristics is given by Figure 4.7b.

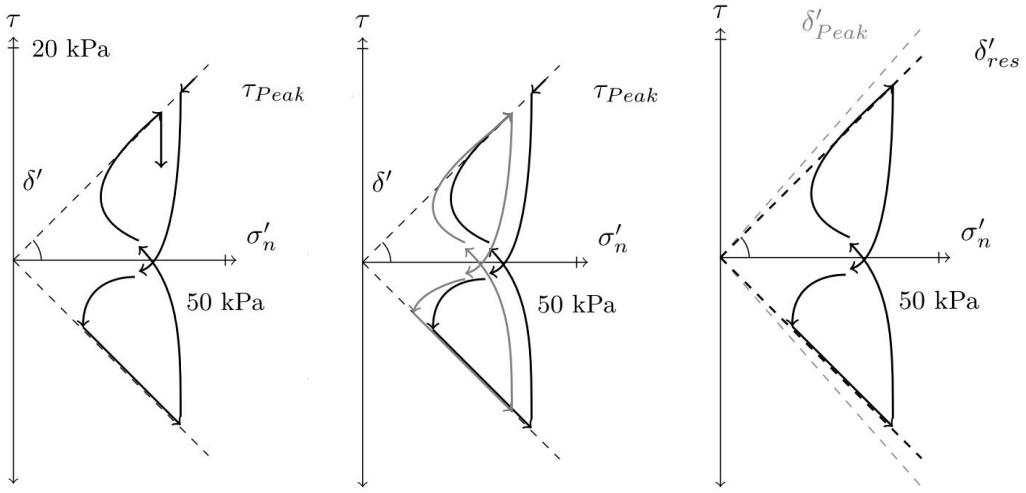

(a) Load cycle for two-way (cyclic) interface loading

(b) Shear and normal stress reduction

(c) Degradation of δ_{cv} due to surface abrasion

Figure 4.15: Stress paths and failure envelope development for two-way cyclic shear in pile-soil, modified from [13]

As can be observed in both Figure 4.7b and 4.15b cyclic shearing causes degradation of the normal stresses acting on the pile and hence shear resistance. Continued contraction of the interface layer due to prevailing cyclic loading conditions provides the best explanation for the aforementioned observation, as in illustrated in Figure 4.16. This effect is even observed in dense sands, as mentioned by [28], [82] and [115]. Interface contraction is further aided by the migration of fine particles away from the soil-pile interface into the far field's undisturbed soil matrix [116]. Moreover, degradation of the interface friction angle $\delta^{'}$ due to abrasion of the pile's surface also contributes to friction fatigue effects observed along the pile-soil interface [55]. The latter is demonstrated in Figure 4.15c.

4.3.4. Stage E.

Following the complete pile installation cycle, consolidation and relaxation effects come into play. The combined effect of both of these phenomena on the bearing capacity of the pile, is also known as *set-up*. Under the influence of *set-up effects* both shaft friction and tip resistance have been shown to increase over time, e.g. [24], [22], [29]. Especially for sands, typical consolidation time scales are shorter than those for soil relaxation due to high permeability coefficients. Hence, long-term set-up effects are almost exclusively attributed to relaxation related effects, namely [29]: (I) relaxation induced creep effects in the soil arch surrounding the pile, which elevates radial stress levels; (II) a relaxation induced augmentation of the soil's stiffness and dilatancy, thereby causing higher lateral effective stress levels. Skov and Denver (1988) ([104]) were the first to propose a method to approximate the evolution of (post-installation) pile capacity with time:

$$Q_t = Q_0 \cdot (1 + A \cdot \log(\frac{t}{t_0})) \tag{4.43}$$

In Equation 4.43, t_0 is a post-installation reference time, t is the time for which the bearing capacity should be approximated, Q_0 represents the pile capacity at time t_0, Q_t is the pile capacity at time t, finally A is a dimensionless empirical parameter. For cohesion-less soils (i.e. sand) it is recommended to use A = 0.2. However, other values of A have been reported in literature, i.e. Axelsson (1998) ([11]) reported values for A between 0.2 and 0.8.

From equation 4.43, it can be inferred that relaxation effects come into play directly after the end of driving. Therefore, to a certain degree, relaxation effects are relevant for quantification of short

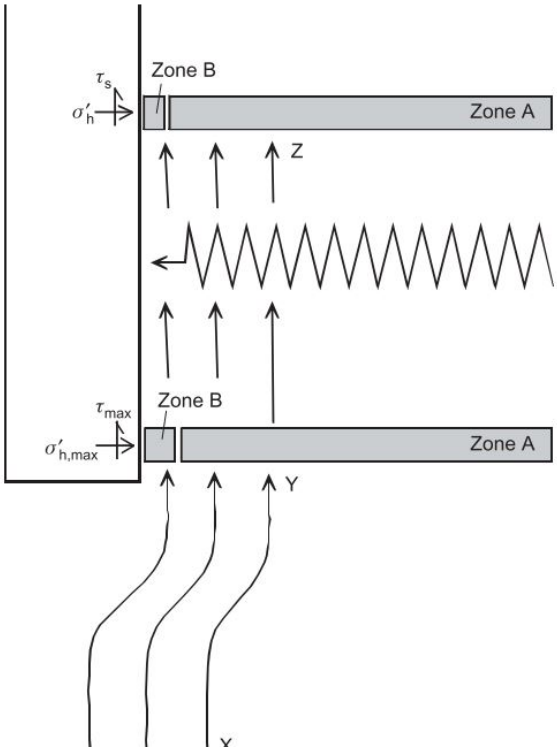

Figure 4.16: Contraction of interface layer (*zone B*) due to cyclic loading conditions prevailing along the shaft of the pile, leading to relaxation of the far field soil (*zone A*) and hence a reduction of effective horizontal stress. After [117].

term set-up effects. Therefore, it can be argued that the aforementeioned effects are ought to be considered alongside the dissipation of excess pore water pressure [11]. The latter can be appointed as the main cause of set-up observed directly after driving, particularly in sandy soils. Thus underlining the importance of prevention of *pile refusal* through adequate pile driving analysis, choice of equipment and proper planning. All in an effort to prevent situations which inhibit uninterrupted pile installation.

4.3.5. Stage F.

Shortly after the installation of the steel open-ended foundation pile(s), the work load is incrementally increased due to the phased build-up of the turbine tower. The application of the working load alters the stress soil state due to dilation effects observed under monotonic shear, hence influencing the ultimate pile capacity. Research by Lehane and White (2004) ([118]) produced results which clearly highlight the aforementioned effect. These results are shown in Figure 4.17. From Figure 4.17 it can be derived that even after 100 load cycles (i.e. N>100) dilation due to shear-induced deformation can increase normal stresses at the interface beyond 100 kPa under monotonic conditions [118]. The observed strain hardening is a direct result of the dense soil configuration at the along the pile-soil interface, which originates from compaction and grain crushing during stage B. and C. of installation [117]. The latter is also illustrated in Figure 4.14a and 4.14b. The aforementioned figures indicate that dynamic lateral stresses σ_{hm} are as much as 10 times greater that stationary stresses σ_{hc}. Hence, dilation effects, observed upon reloading, can (under the right circumstances) compensate the loss of normal stress due to cyclic loading during pile installation [71].

However, Lehane and White (2004) ([118]), note that the loss of normal stress cannot be fully recovered. Thus, reductions in radial effective stress during installation permanently influence the ultimate pile capacity τ_f. In more recent work, Lehane and White (2005) ([69]) indicate that the absolute magnitude of the observed recovery is larger for a higher number of load cycles *N*. How-

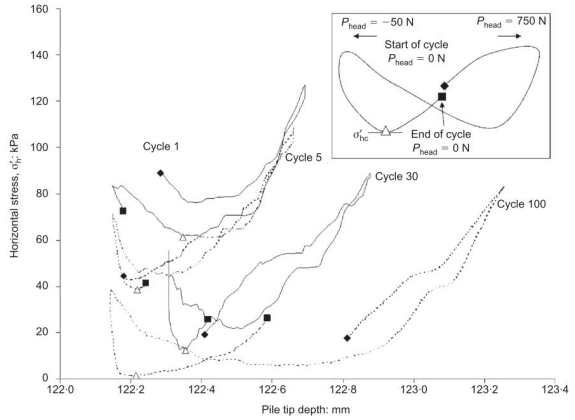

Figure 4.17: Horizontal stress degradation for a two-way cyclic load test after [118]

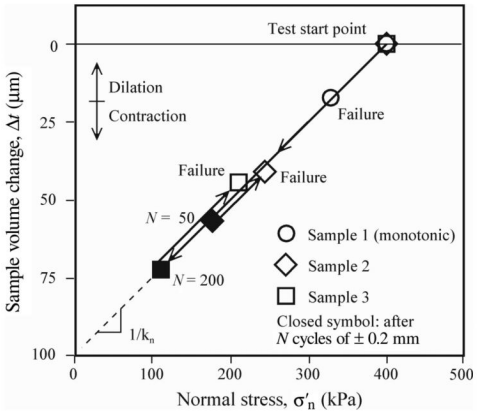

Figure 4.18: Effective normal stress vs. sample volume change during CNS tests on sand. After [69]

ever, relative to a sample which was exposed to fewer load cycles and thus experienced a smaller reduction of normal effective stress, the radial stress level at failure is inferior. Additionally, larger displacements are required to attain the maximum shear stress levels for heavily cycled samples. The previously mentioned conclusions can also be inferred from Figure 4.18. As the installation procedure has a profound effect on the soil behavior observed during loading, it should be part of the integral design approach.

Cavity expansion theory Elastic cavity expansion theory is a widely used tool to qualify stress changes at the pile-soil interface during loading. For convenience, the total radial effective stress σ'_{rf} (see Equation 4.40) is approximated as the sum of neutral radial stress (i.e. when no load is present), σ'_{rc} and deviatoric horizontal stress (resulting from deformation of the interface layer) $\Delta\sigma'_{rd}$:

$$\sigma'_{\mathrm{rf}} = \sigma'_{\mathrm{rc}} + \Delta\sigma'_{\mathrm{rd}} \tag{4.44}$$

The deviatoric horizontal stress component ($\Delta\sigma'_{rd}$ in Equation 4.44), which is induced dilation of the shear band Δt, around a cylindrical pile with diameter D, can be written as follows [17]:

$$\Delta\sigma'_{\mathrm{rd}} = \frac{4G}{D} \cdot \Delta t \tag{4.45}$$

In 4.45 Δt is the change in shear band thickness, G is the soil shear modulus and D is the pile diameter. Other forms of Equation 4.45 exist, i.e. where the thickness of the interface layer is added to the pile diameter. However, as the soil-pile interface is generally several orders of magnitude smaller than the average monopile diameter, this effect is negligible and thus use of an alternative formulation is omitted. Boulon and Faray (1986) were the first to demonstrate that the lateral stress changes observed during cyclic loading of the pile-soil interface are similar to the observed soil behavior in Constant Normal Stiffness (CNS) tests, thereby making is possible to rewrite Equation **??** as follows:

$$\Delta\sigma'_{\mathrm{h}} = k_n \cdot \Delta t. \tag{4.46}$$

In Equation 4.46, k_n is the stiffness of the spring used in the CNS test. The analogy between the CNS test and interface soil behavior is illustrated in Figure 4.19. Continued research into interface dilation by Bolton *et al.* (1988) lead identification of several influencing factors, namely: (I) relative density; (II) mean grain size D_{50}; (III) pile roughness; (IV) governing stress level. Lehane and Jardine (1994) ([72]) were the first to verify the validity of Equations 4.45 and 4.46 by comparing their respective output with actual records or estimates of σ'_h. The inversely proportional dependency

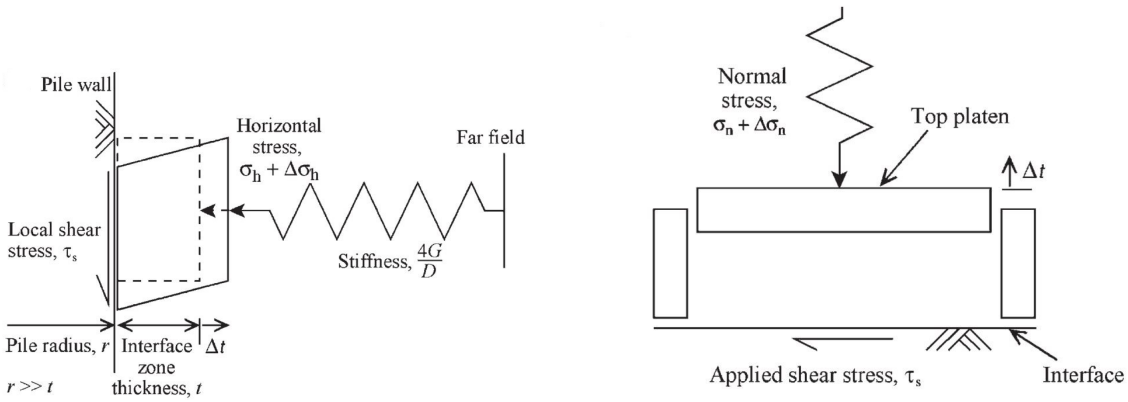

(a) Schematized pile-soil behavior at interface (b) Schematic overview of CNS test

Figure 4.19: Anology between CNS test and soil behavior at the interface [69]

on pile diameter of Formula 4.45 was also acknowledged by the work of Lehane and Jardine (1994) ([72]). Lehane and White (2005) ([69]), arrived at the same conclusion by comparing the results of displacement pile installation tests in the drum centrifuge of University of Western Australia (UWA) to well-documented case studies. The conclusions drawn by [72] and [69], imply that dilation effects during loading could therefore be negligible for large diameter open-ended displacement piles, in example monopiles. Hence, radial stress recovery due to dilation would be less pronounced.

The formulation presented as Equation 4.45 solely accounts for dilative interface behavior as a result of static loading. However, two other phenomena can arguably also influence the radial stress regime around the pile, namely [60]: (I) the transfer of vertical shear stress into the surrounding soil mass; (II) lateral expansion of the pile shaft under the working load, also referred to as the *Poisson effect.*

4.4. Conclusion

To model driver-pile interaction, pile-soil interaction and the associated vibrations inducted in the surrounding soil mass, a relatively comprehensive (idealized) theoretical framework exists. Alongside impact velocity v_0, driver and pile impedance, respectively denoted as Z_H and Z_P, are the single most important parameters to describe the force exchange between the driver system and the pile. Remarkably, the ram's mass does not directly influence the pile force. However, the mass of the ram does govern the degradation of the pile force as force degradation coefficients are inversely proportional to the hammer's mass. Pile-driver interaction is accompanied by energy dissipation. The net efficiency of the aforementioned dynamic process cannot be inferred from analytical formulas. Hence, field measurements of pile particle velocity $v_{p,P}$ and pile force $F_{i,P}$ are indispensable. Previously mentioned key parameters are respectively measured by an accelerometer and strain gages. Subsequently, by integrating the product of particle velocity and pile force over the impact time, the total energy transmitted to the pile is computed.

In part, the transmitted energy causes a permanent displacement of the pile tip, which is also known as the pile set. The remainder of the energy is employed to overcome the soil resistance along the shaft and at the tip. The total soil resistance is the summation of static and (velocity dependent) dynamic soil resistance. The dynamic soil resistance also gives rise to vibrations with are emitted from the pile into the surrounding soil mass. These vibrations can be attributed to three categories, namely: (I) P-waves, are stress waves which are emitted spherically from the pile toe; (II) S-waves, are shear waves which are cylindrically emitted from the pile shaft; (III) R-waves, are surface waves which are formed through refraction of P-waves at the ground surface. The latter process can only take place for a critical angle of incidence. Hence, R-waves are only observed at a some (critical)

distance away from installation site [78].

Diving further into the loading conditions associated with the installation and operation of open-ended steel displacement piles, six soil loading stages can be identified. Each stage loads the surrounding soil mass in a profoundly different way. Hence, the associated soil behavior differs significantly. Initially, the soil underlying the pile's tip is increasingly compressed under the influence of continued penetration. Consequently, local mean effective stress levels far exceed the initial soil stress state. Often, the soil-specific stress threshold is exceeded, causing particle crushing underneath the pile tip.

Subsequently, a soil mixture, consisting of intact particles and fragments, is forced passed the lower extremity of the pile. At this instant the soil exerts its respective maximum shear onto the passing pile. Additionally, a part of the reference soil mass penetrates the pile's inner cavity, and the remainder ends up in the outer pile-soil interface layer. The degree to which the penetration of a soil column into the pile's inner cavity is inhibited, determines the degree of plugging. Pile plugging is a phenomena relevant to consider at to specific instances, namely: (I) during installation, where plugging can result in *pile refusal*, which temporarily paralyzes the driving operation; (II) during static loading, where plugging behavior can add to the ultimate pile capacity. Brucy *et al.* (1991) ([19]) and Paik *et al.* (1993) ([87]) envisioned two methods to evaluate the capacity of a soil plug, respectively: (I) evaluation by means of the Incremental Filling Ratio (IFR); (II) evaluation by employing the Plug Length Ratio (PLR) [87]. Jardine *et al.* (2005) ([60]) argues that plugging effects are only relevant for pile diameters $\leq$1.5 *m*. Therefore, the odds of encountering plugging behavior during installation of large open-ended steel piles is virtually nonexistent. However, for centrifuge experiments there is a chance that soil plugging is in fact observed at model scale whist, in reality (at prototype scale), plugging effects are entirely absent. The latter therefore requires careful consideration during set-up design and ultimately practical verification.

Soil particles which reach the soil-pile interface are cyclically sheared upon further penetration of the pile. The cyclic loading at the interface gives rise to one of the most critical effects observed during pile installation, namely *friction fatigue*. *Friction fatigue* was first reported by Heerema (1980) ([52]), who described the degradation of lateral effective stress acting on the pile's shaft for a given sand horizon. Heerema (1980) ([52]) linked the degree of degradation to relative distance between the soil layer and the pile tip. In later years, many other researches sought to capture the phenomena in a theoretical framework. Based on the results of two well-documented studies carried out with the ICP, Jardine *et al.* (2005) ([60]) proposed a relationship which relates *friction factigue* to "h/R effect". White (2005) ([115]) found that neither relative distance between the pile's tip and an arbitrary soil horizon *h*, nor the distance normalized by pile radius *h/R*, adequately captured friction degradation. Therefore, White (2005) advocates an approach in which friction degradation is related to the number of load cycles *N*. In contrast to e.g. Heerema (1980) ([52]) and Jardine *et al.* (2005) ([60]), White (2005) ([115]) did not present any formulation in which his findings have been consolidated. The latter, combined with the fact that the number of load cycles experienced by the soil is hard to quantify in practice, makes that *SRD models* nearly exclusively relate *friction fatigue* to (normalized) distance to the pile's tip.

In an attempt to deepen the understanding of *friction fatigue*, researchers have sought out ways to mimic interface behavior in the laboratory. Many fruitful attempts involved the use of a constant normal stiffness (CNS) apparatus. By use of CNS tests, White and Lehane (2004) ([118]), among others, found a dependency between *friction fatigue* and the type of cycling, i.e. one-way or two-way. Additionally, they underlined the influence of cycling amplitude on the manifestation of *friction fatigue*. Looking specifically at dynamic installation methods, which are characterized by both compressive and tensile cyclic loading (two-way load cylce), friction degradation is expected to have a more profound effect on pile drivability. Lehane *et al.* (2005) ([69]) acknowledge the potential of CNS test but underline the importance of: (I) using representative values for the shear modulus *G* to

compute lateral soil stiffness; (II) caring for sufficient resemblance between the cyclic displacement history in the laboratory and the field.

Upon termination of the driving procedure, *set-up effects* resurface quickly. Especially in sandy soils, piles can exhibit a significant capacity increase in a short time frame. The latter is due to high permeability and hence swift dissipation of excess pore fluid pressures (PFP). Parallel to the dissipation of excess PFP, soil relaxation affects the evolution pile capacity with time. The latter stresses the importance of preventing delay during the driving procedure, as *set-up effects* can significantly increase time and labor associated with reaching the desired depth. Naturally, the manifestation of *set-up effects* following successful pile installation is beneficial to the ultimate bearing capacity and allows for smaller design redundancy. Remarkably, the effects of *friction fatigue* which can essentially be exploited to streamline the installation process, restrict the capacity increase associated with dilation of the interface layer upon application of the working load. In other words: the reduction of lateral effective stress as a result of *friction fatigue* is not fully recovered upon shearing to failure [118]. Furthermore, Lehane and White (2005) ([69]) indicate that for larger values of N, larger displacements are required to mobilize maximum shear stress levels. The latter can therefore weaken efforts to economically optimize the design of open-ended steel piles. However, as also implied by Lehane and Jardine (1994) [72] and Lehane and White (2005) [69], the relevance of interface dilation decreases with pile diameter. It is therefore possible that large diameter piles, i.e. monopiles, do not benefit from the aforementioned effect. Contrastingly, Gavin *et al.* (2011) ([44]) remains optimistic, stating that the combined effect of dilation and aging effects can lead notable recovery of the shaft resistance.

5

Centrifuge modelling

Generally speaking, there a three distinctly different ways to conduct experimental research, namely: (I) 1g-model tests; (II) centrifuge model tests; (III) full scale (1g) tests. Each of the three test types has well-defined advantages and disadvantages when is comes down to conducting geotechnical experimental research. The easiest and most economical way to model geotechnical problems is by using 1g-model tests. For this type of test, the physical dimensions of the body of interest are scaled down by a certain factor. However, the non-linear nature of geotechnical mechanical properties often causes the soil behavior observed in 1g-model tests to deviate from reality at full scale. The non-linear soil properties are a direct result of their respective dependency on stress history and prevailing effective stress levels. For this reason, one might argue to use full scale model tests. Although full scale tests guarantee proper modeling of soil parameters and hence soil behavior, the physical scale and preparation time associated with this type of test, make it extremely costly. Centrifuge tests combine the small scale aspect of 1g-model tests with almost true-to-nature soil behavior free of scaling effects, commonly only reserved to full scale tests. In centrifuge tests, centrifugal acceleration is used to create an artificial "gravitational" field to which the small scale model is subjected. By doing so, it is possible to adequately capture the non-linear stress-strain relationship of soils. However, it should be noted that not all model parameters are equally scaled in a centrifuge. Therefore, it is possible to introduce significant discrepancies into the model if these effects are not properly accounted for. Fortunately, extensive research has been carried out on the scaling laws for centrifuge modeling. Granier *et al.* (2007) conveniently consolidated this work into a "scaling law catalogue" [42]. In this chapter, section 5.1 addresses how scaling laws have been properly incorporated into the used centrifuge model. Secondly, the relevance of the installed sensory equipment with respect to the research's scope is elaborated upon in section 5.2. Model properties are adressed in section 5.3. Finally, the sample preparation method is discussed in section 5.4.

5.1. Scaling laws and effects

5.1.1. Scaling laws

Due to the non-linear stress-strain relationships commonly found in geotechnical materials, 1g-model tests often cannot capture true-to-nature soil behavior. This is the foremost disadvantage of this type of test, as is also argued by [9]. Enhancing the gravitational field by means of a centrifuge is a common way the overcome the aforementioned problem and create stress-conditions similar to those observed in full scale models, while maintaining a stress-free upper boundary. In addition, centrifuge modeling is a cost-effective method, that can yield results with high repeatability. Mimicking full scale stress states involves subjecting the centrifuge model to an enhanced gravitation field. The amplification factor with respect to Earth's gravitational constant is commonly denoted

Term [SI dimension]	Prototype	Model
Acceleration [L/T^2]	1	N
Velocity [L/T]	1	1
Linear dimension (macroscopic) [L]	1	1/N
Area [L^2]	1	1/N^2
Volume [L^3]	1	1/N^3
Density [M/L^3]	1	1
Unit weight [M^2/T^2 L^3]	1	N
Mass [M]	1	1/N^3
Force [ML/T^2]	1	1/N^2
Stress [L/MT^2]	1	1
Strain [-]	1	1
Dynamic time [T]	1	1/N
Seepage time [T]	1	1/N^2
Frequency [1/T]	1	N
Energy [ML^2/T^2]	1	1/N^3
Impulse[ML/T]	1	1/N^3

Table 5.1: Relevant scaling laws for dry and saturated centrifuge testing, adapted from [42]

as *N*. It should be noted that replication of prototype stress conditions in model and thus mechanical behavior is only possible when the same soil in used [109]. Soil heterogeneity and non-linearity prevent a truely straightforward way of scaling down problems from prototype to model scale. Instead a large variety of scaling laws has been developed to ensure a proper match between prototye and model behavior. Therefore, when conducting centrifuge experiments, it is of the utmost importance that these scaling laws and their respective implication on the model's behavior are fully appreciated. For this particular research, the installation of a steel open-ended tubular pile through impact hammering (under both dry and fully saturated conditions), important (scaling) parameters are shown in Table 5.1 (after [102], [109] and [42]).

As can be observed in Table 5.1, amplification of the gravity constant impacts each physical quantity differently. Additionally, two particularities become apparent when looking at Table 5.1, namely: (I) Grain size, which could be perceived as a variation on linear dimension, is not directly scaled; (II) By scaling prototype properties to model size, a important discrepancy is introduced between dynamic time and seepage time. The two aforementioned scale effects demand careful consideration and are therefore further elaborated upon in 5.1.3 and 5.1.4 respectively.

5.1.2. Stress distribution

The g-level acting on a model in the centrifuge can by expressed by means of the following equation:

$$a = N \cdot g = r \cdot \omega^2 \tag{5.1}$$

Where N is the gravitational scaling factor, r is the distance from the axis of rotation and ω is the angular velocity. By multiplying the acceleration with density of the soil used in the model (ρ) and subsequently integrating the expression from the stress-free top boundary (located at r_t from the rotation axis, see Figure 5.1b); to an arbitrary point in the soil body (at distance r from axis of rotation, see Figure 5.1b), the following stress relationship is obtained:

$$\sigma_{v,model}(r_e) = \int_{r_t}^{r} \rho \cdot r \cdot \omega^2 dr = \frac{\rho \cdot \omega^2}{2} \cdot (r^2 - r_t^2) \text{ where } r_t \leq r \leq (r_t + h_m) \tag{5.2}$$

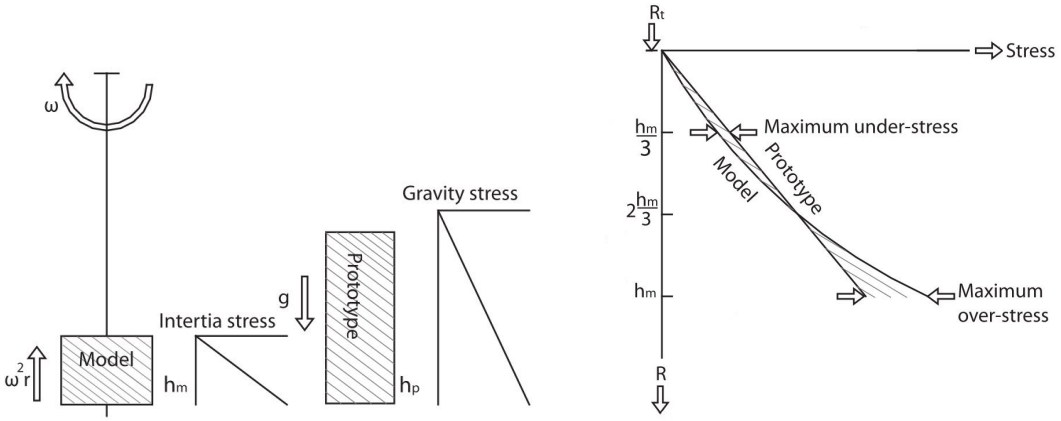

(a) Development of inertia stress over model height and corresponding development of gravitational stress over prototype height, [15] (adapted from [109])

(b) Stress variation with depth for centrifuge model and its corresponding prototype, adapted from [15] and [109]

Figure 5.1: Comparison of stress relationship for centrifuge model and prototype

In Equation 5.2 h_m is the model's height, as can be seen in Figure 5.1a. In reality, i.e. at prototype scale, the stress relationship (as a function of depth) is expressed by the following equation:

$$\sigma_{v,prototype}(z) = \rho \cdot g \cdot z \tag{5.3}$$

By comparing Equation 5.2 and 5.3 it is concluded that; (I) at prototype scale, the stress level is linearly dependent on depth z; (II) at model scale, stresses vary quadratically with axial distance (r). Hence, the stress relationship in the model deviates from reality (or prototype). From Equation 5.2, it also follows that it is beneficial if the ratio h_m/r_t is high, as this would reduce the gravity gradient in the model and hence the magnitude of the aforementioned stress deviation. In the presence of a large gravity gradient, it is particularly important to pick a suitable depth for which the inertia and gravity stress curve coincide, as only at this depth true-to-nature soil behavior can be observed.

5.1.3. Time discrepancy effects

During the dynamic installation of the monopiles under fully saturated conditions, the effective soil stress state is continuously altered due to the generation and dissipation of (excess) PFP. The build-up of (excess) PFP is a dynamic process, whereas the dissipation is governed by diffusion. At prototype scale, both of these processes take place on similar timescales. However, for centrifuge modeling this statement is no longer valid as the generation and decay of (excess) PFP have distinctly different timescales. The latter can also be demonstrated by recalling that the decay of (excess) PFP is coupled to soil deformation by the consolidation process. The degree of consolidation is commonly denoted as T_v which is a function of time (t), drainage length (D) and the consolidation coefficient (c_v):

$$T_v = \frac{c_v \cdot t}{D^2} \tag{5.4}$$

For the same degree of consolidation in both the model and prototype, the following should hold:

$$T_{v,model} = T_{v,prototype} \implies \frac{c_{v,model} \cdot t_{model}}{D^2_{model}} = \frac{c_{v,prototype} \cdot t_{prototype}}{D^2_{prototype}} \tag{5.5}$$

If the same soil is used in the model as is present in the prototype, it can reasonably be said that $c_{v,model} = c_{v,prototype}$. Recalling the scaling law for linear dimension:

$$d_{model} = \frac{1}{N} \cdot d_{prototype} \tag{5.6}$$

Where d_{model} and $d_{prototype}$ represent a linear dimension at model and prototype scale respectively. Combining Equation 5.5 and 5.6 yields:

$$\frac{c_v \cdot t_{model}}{1/N^2 \cdot D^2_{prototype}} = \frac{c_v \cdot t_{prototype}}{D^2_{prototype}} \implies t_{model} = \frac{1}{N^2} \cdot t_{prototype} \tag{5.7}$$

Similarly, the scaling law for dynamic time can be derived by recalling the scaling law for acceleration:

$$a_{model} = N \cdot a_{prototype} \tag{5.8}$$

Where, a_{model} and $a_{prototype}$ represent acceleration levels in model and prototype respectively. In agreement with the recommendation of the SI-standard with respect to the denotation of dimensions, acceleration can be expressed as L/T^2. Combining the latter notion with Equation 5.8, yields:

$$\frac{L_{model}}{T^2_{model}} = N \cdot \frac{L_{prototype}}{T^2_{prototype}} \tag{5.9}$$

Lastly, by incorporating the scaling law for linear dimension (Equation 5.6) into Equation 5.9, it is obtained:

$$\frac{1/N \cdot L_{prototype}}{T^2_{model}} = N \cdot \frac{L_{prototype}}{T^2_{prototype}} \implies T_{model} = \frac{1}{N} \cdot T_{prototype} \tag{5.10}$$

Form the derivation above, it can be inferred that by using the centrifuge, a discrepancy between dynamic and seepage time is introduced as (at model scale) the former physical quantity is scaled by 1/N, against $1/N^2$ for the latter, respectively. This implies that *pore fluid pressure* (PFP) dissipation and the associated consolidation happens N times faster in the model than in the prototype.

The aforementioned discrepancy can be solved by increasing the coefficient of consolidation c_v. Formally, c_v is defined as:

$$c_v = \frac{k}{m_v \cdot \rho_f \cdot g} \tag{5.11}$$

Where m_v, k and ρ_f respectively denote soil compressibility, soil permeability and fluid density. In term of practicality, scaling down k N times is most manageable. Soil permeability is calculated from the following expression:

$$k = \frac{\kappa_s \cdot \rho_f \cdot g}{\mu_f} = \frac{\kappa_s \cdot g}{\nu_f} \tag{5.12}$$

Where κ_s, μ_f and ν_f respectively express intrinsic soil permeability, dynamic viscosity and kinematic viscosity. Substituting Equation 5.12 into Equation 5.11, it is found:

$$c_v = \frac{\kappa_s}{m_v \cdot \rho_f \cdot \nu_f} \tag{5.13}$$

Form Equation 5.13 it follows that two ways exist to ensure proper coupling between dynamic time and seepage time (by scaling c_v by factor N) [68]:

1. Decreasing the intrinsic impermeability k_s of the medium N times, in example by using smaller grain sizes. See in example Kutter & Bruce (1992) ([67]);
2. Increasing the dynamic viscosity ν_f in the saturated medium N times while maintaining a similar the fluid density ρ_f. An approach analogous to that advocated by in example Askarinejad *et al.* (2013) ([8]).

The process of decreasing the k_s can be tedious as changing the particle size, affects the density, stiffness and strength, thus altering the soil's constitutive behavior. Hence, it is generally preferred to use viscous fluid to decrease soil permeability. However, it should be noted that any increase of $\rho_{f,\,model}$ with respect to $\rho_{f,\,prototype}$ is detrimental based on Equation 5.13. Moreover, the use of a fluid with a higher density than water would alter the effective stress profile in the soil body.

5.1.4. Grain size effects

Intuitively, one would argue that grain size is another parameter which should be scaled directly if one were to carry out centrifuge experiments. However, many mechanical soil properties are a function of grain size. Scaling grain size, can therefore lead to inappropriate stress-strain volume change characteristics, mainly with respect to grain crushing and dilatancy [16], [8]. Instead, proper stress-strain volume change relationships can obtained if predefined a ratio between particle size and model dimensions are attained, given that the same type of soil is used in both model and prototype. Oveson (1979) was the first to demonstrate the existence of such a relationship for round shallow foundations. Research on the importance of particle scaling was subsequently extended by many others for a large variety of geotechincal applications, e.g. [32], [41]. Recalling that the installation of steel open-ended tubular pile through impact hammering is simulated in the centrifuge, two relevant geometrical ratios between model and soil dimensions were identified.

Firstly, the mean particle size should maximally equal 1/15 of key model dimensions [85]. For this research the following should therefore be established:

$$t/D_{50} \geq 15 \tag{5.14}$$

In Equation 5.14, t represents the pile thickness, D_{50} is the mean particle size. Other values for the minimum ratio of average particle size over wall thickness have been mention in literature, i.e. $t/D_{50} \geq 10$ [83].

Secondly, volumetric strain development in the direct vicinity of the pile shaft, particularly at the pile-soil interface, should be properly scaled in the model. As a direct result of pursuing similar mechanical soil properties for both model and prototype, the same soil is generally used [16]. Consequently, the thickness of the shear band developed in the model could become unrealistic when compared to the prototype [69]. Typically, the shear band thickness at the soil-pile interface is in the order of 10 times the average grain size D_{50} [41]. The development of the shear band is governed by several parameters which are mention in 4.3.5. For values of D_{50} less than 0.75 mm, the shear band thickness (for fully developed conditions) is independent of D_{50} and roughly 2 mm thick [40]. To limit the extend to which scale effects influence the development of shear band at the soil-pile interface, the following inequality should be satisfied by the model [41]:

$$D_{outer}/D_{50} \geq 100 \tag{5.15}$$

In Equation 5.15, D_{outer} represents the outer pile diameter, and D_{50} is the mean particle size.

5.1.5. Soil plugging effects

As discussed in 4.3.1, to installation of open-ended tubular piles, is associated with the progression of a soil column into the pile's inner cavity. Under certain circumstances, the progression of the soil into the inner cavity can stagnate, thereby "plugging" the pile. Although plug formation is beneficial for the final bearing capacity of the pile, it can severely hamper installation as the plug drastically increases the tip resistance. The normative parameter to assess the degree of plugging is the Incremental Filling Ratio (IFR), see 4.3.1. Based on IFR, it is possible to distinguish three plugging scenarios:

1. IFR = 0: Fully plugged pile, observed behavior similar to a full displacement pile;
2. 0 ≤ IFR ≤ 1: Partially plugged behavior, in this case the plug length is variable and dependent of pile embedment;
3. IFR = 1: No plugging behavior, the top of the plug is stationary and not dependent on pile penetration (also defined as full coring mode).

However, it is difficult to measure the degree of plugging, i.e. by means of IFR, for even routine piling works [49]. For this reason Lehane *et al.* (2005) sought to determine the average degree of plugging

by means of an empirical formula. This research yielded a formula that allows for an estimation of $IFR_{average}$, which is the mean IFR value over 20 pile diameters of penetration, based on the pile's internal diameter (in m):

$$IFR_{average} = min[1, (D_i/1.5)^{0.2}] \tag{5.16}$$

From Equation 5.16 it can be deduced that plugging effects only occur up pile diameters of 1.5 m. The latter can be explained by considering that for an increasing pile diameter, the increase in plug volume is an order of magnitude larger than the increase of surface area for shear resistance mobilization. Hence, larger pile diameters are less likely to experience plugging upon installation. In light of the foregoing, it can be states that the monopiles which serve as the prototype for this research are unlikely to plug upon installation. Therefore, it should be demonstrated that plugging effects do not play a role during installation of the model pile in the centrifuge. To this end, half pile tests are carried out in the centrifuge.

5.1.6. Strongbox boundary effects

Boundary conditions from an important consideration when conducting physical experiments. As the experiments are carried out in the centrifuge, soft boundaries are impracticable those would deform under the influence of high g-forces. Therefore, hard boundaries are used instead. However, this choice means that soil deformation and P- and S-wave propagation are completely obstructed when a boundary is reached, which could have implications for the obtained test results. For this particular research, hard boundaries can affect measurements in three distinct ways, namely: (I) by reflection (P- and S-) waves of the strongbox boundaries, thereby reintroducing energy into the system which would have been lost in an infinite medium; (II) by inhibition of lateral soil movement, thereby artificially increasing lateral soil stresses and potentially hampering shear band formation at the pile-soil interface; (III) inhibition of axial soil movement, thereby leading to an increased base resistance and hence impeding further pile penetration, as also observed by White *et al.* (2004) during the installation of flat ended piles in a calibration chamber. De Nicola *et al.* (1996) ([31]) argues that, for the installation of open-ended piles, the lateral boundaries should be at least 6 pile diameters away from the pile. For a round strongbox where the pile is placed exactly in the center, the aforementioned recommendation respectively translates to the following formula:

$$R_{\text{strongbox}}/R_{\text{pile}} \geq 13 \tag{5.17}$$

Where $R_{strongbox}$ is the radius of the strongbox and R_{pile} is the radius of the (model) pile. Now, considering the minimum distance from the pile's tip to the strongbox's base, Prakasha et al. (2005) ([91]) advocates a spacing of two pile diameters. Hence, the following equation should be satisfied:

$$d_{\text{soil, min}}/R_{\text{pile}} \geq 4 \tag{5.18}$$

Where $d_{soil,\ min}$ is the minimum thickness of the soil underneath the pile top, e.g. when the pile has reached its maximum penetration depth.

5.1.7. Conclusion

To be added later.

5.2. Description of set-up

5.2.1. TU Delft centrifuge

The g-level for any test sequence in the centrifuge is generally determined based the test specifications and the available test facility. For this research, the centrifuge at Delft University of Technology is used. It is located in the Geo-Engineering lab of the Civil Engineering and Geosciences Faculty.

The centrifuge was originally designed by Allersma in 1990, and was thoroughly refurbished by Dijkstra in 2009. The key features of the centrifuge are summarized in Table 5.2, the facility has been described in detail by [3].

Key feature [dimension]	**Number**
Maximum payload [N]	≈300
Maximum acceleration [g]	300
Carriage dimensions (L x W x H) [m]	0.4 x 0.4 x 0.5
Nominal radius [m]	1.3
Max. rotation velocity [RPM]	450

Table 5.2: Summary of key features of centrifuge at Delft University of Technology, adapted from [3]

5.2.2. Mechanical aspects

For a detailed explanation of the inner workings of the test set-up employed for this work, the reader is referred to the work of Van Zeben (2017) ([112]), specifically section 3.2, which is titled: "*Centrifuge setup*".

5.2.3. Sensors

The actuator is fitted with a large variety of sensors to monitor various processes in the pile and soil and simultaneously quantify and regulate different driving parameters. Important information with regard to certain aspects of the sensors, as well as their respective inner workings are discussed in this section.

Potentiometer Both pile penetration and motor displacement are measured by a draw wire potentiometers. Respectively, the measurement range of the sensors amounts to 150 and 250 *mm*. It would be preferred to have to potentiometers of the same type as it would facilitate the calibration. However, provided the latter is adequately done, the combined system can be used without major issues. An M4 bolt which extrudes from the pile shaft is fitted with a ring to which a piece of cable is attached with a small hook at the end. The cable which runs down from the potentiometer, which is fixated on the upper plate of the centrifuge carriage, has a loop a the end. The combination of the hook and the ring creates a reliable connection between the two elements. Especially as an internal spring in the potentiometer ensures that the connection remains under tension at all times. Additionally, the system is easy to dismount, for example when the the sample needs to be changed. The second potentiometer is bolted to the frame at the back of the actuator. The cable if fitted with a small ring through which a bolt is inserted, which is subsequently fixated to the back of the motor housing. Together, the two potentiometers run a the servo-system, which is responsible the displacement of the motor housing to maintain the stroke of the hammer during driving. Before the test, the reference position of the servo-system is specified. During the driving operation, the servo-system constantly checks whether the current situation is different from the reference. If the latter is true, the servo corrects the difference by displacing the motor housing until the reference condition is reinstated. End switches are used to ensure that the servo-system operates between physical applicable range limitations.

Frequency controller To provided a basic form of frequency control, which is especially relevant for the multi-blow tests, a frequency controller is installed on the motor housing. The working principle relies on a light lock used in combination with a perforated wheel. The wheel is connected to the end axle which drives the flywheel. Consequently, it directly measures the number or revolutions per unit of time of the flywheel, which equals the blow frequency. The number of pulses

Distance ID	Hall Sensors	Light Sensors
B - 1 [mm]	8	5.5
1 - 2 [mm]	13	15.5
2 - T [mm]	4	4

Table 5.3: Relevant distances for the hall and light sensors used to infer impact velocity. Annotations in the left column respectively denote: (I) *B - 1* The distance between the bottom of the anvil and sensor 1 (bottom sensor); (II) *1 - 2* the distance between the sensor 1 (bottom sensor) and sensor 2 (upper sensor); (III) *2 - T* the distance between sensor 2 (upper sensor) and the top of the anvil.

per second (1 full rotation generates 8 pulses) is used to infer the blow frequency. Subsequently, the flow of power to the engine is regulated to compensate for any deviations with respect to the desired driving frequency.

Hall and light sensors To measure the velocity at which the hammer makes conctact with the anvil, two different velocity measurement systems are usesd namely: (I) Hall sensors, which register changes in the polarity of a magnetic field; (II) Light sensors, which registers the interruption of a light beam associated with the downward motion of the ram mass. Both systems are comprised of two sensors are rely on the inference of velocity from the time difference between both triggers in the output signal. Hence, it is important to know how far the sensors are apart from each other. To this end, Table 5.3 was drafted; which indicate the critical distances for both the hall and light sensors.

Strain gauges To measure the quantify the piling energy and corresponding driver system efficiency η_{ds}, the pile strain is recorded alongside the particle acceleration. As the material properties, specifically the modulus of elasticity *E*, are known; the strain readings can be converted into a force signal. The strains are measured with a full Wheatstone bridge, consisting of four unidirectional strain gauges, type FLA-6. The strain gauges are places axially on the outside of the pile, evenly spaced at 90°intervals. To ensure that the signal maintains its natural characteristics, the length of the strain gauges should be negligible with respect to the expected stress wavelengths. To quantify the measurement error the minimum length of the stress wave in the pile is determined. The latter requires specification of the following variables: (I) the dimensions of the ram mass; (II) the modulus of elasticity E and density ρ of the ram mass; (III) the modulus of elasticity E and density ρ of the pile. A model calumniation is presented. With regard to the aforementioned items, the following assumptions are made:

1. In reality, the ram mass consists of both an aluminum and steel section; held together by four M3 bolds. Although E and ρ of aluminum and steel differ significantly, the phase velocity of stress waves is comparable. For the definition of the phase velocity, consult Equation 3.9. Consequently, it is assumed that the entire ram mass is made of a solid block steel, for which the phase velocity amounts to 5200 *m/s*;
2. As the contact time between the ram mass and pile is determined by the length of the ram mass; the shortest ram mass used in normative in the determination of the shortest wave length in the pile. As only ram mass II and III where employed in this research, ram mass II is governing for the following calculation. Its respective length is ≈52 *mm*.

Given the aforementioned assumptions and the following pile properties: ρ = 7800 kg/m^3; E = 210 *GPa*; the dwell time for ram mass II Δt_{II} is computed:

$$\Delta t_{II} = \frac{2 \cdot 0.0520}{5200} = 20.0 \mu s \tag{5.19}$$

Sensor ID	dv [mm]	dr [mm]
SPFPS1	60	34
SPFPS2	80	24
SPFPS3	100	14

Table 5.4: Vertical (*dv*) and radial (*dr*) position of SPFPS in [*mm*].

Where the dwell time is defined in accordance with Equation 4.18, as the time is takes a stress wave to fully cycle through the ram mass. Provided Δt, the length of the stress wave in the pile can be estimated as follows:

$$L_W = 5200 \cdot 20.0/1.00e6 = 0.104m \tag{5.20}$$

Following from the determination of L_W, it is established that the length of the strain gages is ≈6 % of the wave length L_W. To quantify the measurement error (due to signal averaging over the length of the strain gauges), it is assumed that the excitation of the sensor can be modeled a sinusoidal signal, where the wave length L_W is proportional to a full period, 2π. Consequently, the length of the strain gauges is proportional to $3\pi/26$. The measurement error is maximized when the proportional length of the strain gauges encapsulates the peak of the sinusoid. For the latter scenario, the stress at the extremities of strain gauges is ≈98% of the peak signal. However, as the peak signal gets averaged over the length of the strain gauges, the mean (measured) stress peak is ≈99% of the theoretical maximum. Consequently, the maximum error is in the order of 1%, which lies within the margin of tolerance.

Accelerometer In order to be able to infer how much energy is admitted to the pile, PDA systems are used in practice. The PDA system consists of a combination of an accelerometer and a load cell. Respectively, the sensors are used to measure pile velocity and force. E fully elaborates how energy is inferred from the combination of both measurements. The accelerometer which is used for this research consists of an Endevco 7270A-60K, which was borrowed from the pyro lab of TNO, which is located in Delft. The sensor has an capacity of 60000 g, which is at least one order of magnitude larger than expected accelerations. The high capacity was a conscious decision in order to protect the sensor from overload during testing. In order to measure accelerations, the sensor is placed perpendicular to the direction of measurement. As this research is interested in the axial acceleration of the pile, the means that the accelerometer should be installed horizontally. Consequently, two extrusions were fabricated from aluminum. Subsequently, these were both glued and bolted to the shaft of the pile. Finally, the accelerometer was installed on top of the extruded block. However, it should be noted that this system posesses some mechanical disadvantages. These relate mainly to the added mass of the extrusion (which is also mirrored on the opposite side of the pile for symmetry) and the indirect measurement of acceleration as the mounting block itself will influence the signals which pass through the pile (even if the connection with the pile is rigid).

Static pore fluid pressure sensors (SPFPS) To capture the development of pore fluid pressures (PFP) during the driving operation, static pore fluid pressure sensors (SPFPS) are installed in the samples. For each experiments three of these senors are used. In order to capture the evolution of PFP with both depth and radial distance, the position of the three sensors in varied in both dimensions. Respectively, the positions for the three sensors, henceforth denoted as SPFPS1, SPFPS2 and SPFPS3 are provided by table 5.4. Please consider that the vertical distance is measured with respect to the upper extremity of the strongbox and not the soil surface level. For convenience both the radial and vertical position are denoted as *dr* and *dv*.

Type of Fluid	Density [kg/m^3]	Kinematic viscosity* [cSt]	Reference
79% v/v glycerine-water solution	1205.3	50.231	[10]
Deltares (water-based) viscous fluid	1006.0	52.3	[112] & [10]
HPMC (Methocel® F4M) fluid	1002.3	49.9	[92]

* at 20 °C

Table 5.5: Summary of relevant properties of viscous fluids suitable for use is centrifuge

Optical pore fluid pressure sensors In order to monitor and quantitatively assess the evolution of pore fluid pressure at the interface layer OPFPS are used. OPFPS are optical sensors pressure sensors which are inserted into capillary tubes, which in turn are partially embedded in the pile shaft. By filling the capillaries with silicon oil, and subsequently closing them off at the top with a water-resistant silicon adhesive, a closed chamber is obtained in which pressure fluctuations along the shaft can be monitored. At the bottom of the capillary, a small slit (behind which a filter is installed), allows for the transmittance of pressure from the pore fluid at the interface to the sensor. In this case, the incompressibility of the silicon oil is leveraged to achieve an ideal pressure transfer. As the sensors are directly installed on the pile shaft, the interface is not disrupted attempts to record the prevailing PFP from a more distant location in the soil body. Another advantage of the OPFPS is that they follow the movement of the pile, contrastingly to the SPFPS, which remain stationary in the soil body. In total three OPFPS are used, which are installed at different distances with respect to the tip of the pile. For OPFPS1, OPFPS2 an OPFPS3, these distances respectively amount to: (I) 10 mm ($\approx \Phi_p/4$); (II) 30 mm ($\approx 3 \cdot \Phi_p/4$); (III) 60 mm ($\approx 6 \cdot \Phi_p/4$). Where Φ_p is the pile diameter, which is equal to 42 mm.

5.3. Model properties

5.3.1. Viscous pore fluid

As was mentioned in 5.1.3, the improper coupling between the dynamic generation and diffusive dissipation of excess PFP, is compensated by the use of a viscous pore fluid. The required increase in dynamic viscosity is equal to the amplification factor of the gravity field N, which is present during centrifuge testing. Another possibility is to increase the dynamic viscosity ν_f by N, provided that the density of the fluid in the prototype $\rho_{f,\,prototype}$ is maintained. As tests are conducted at 50g and ≈ 20°C, the following equation should hold:

$$\mu_{\text{model}} = N \cdot \mu_{\text{prototype}} \leftrightarrow \begin{cases} \nu_{\text{f, model}} = N \cdot \nu_{\text{f, prototype}} \\ \rho_{\text{f, model}} = \rho_{\text{f, prototype}} \end{cases} \tag{5.21}$$

Three potential fluids for use in the centrifuge were identified, namely: (I) An biodegradable variant of the viscous fluid developed by Allard & Schenkeveld (1994) developed by Deltares in 1999; (II) A solution of 79% v/v glycerine to water ratio as used by Askarinejad *et al.* (2017) ([10]); (III) Hydroxypropyl Methylcellulose (HPMC) fluid using water as solvent, which is produced by Dow™ as type F4M. Relevant properties of candidate fluids are summarized in Table 5.5.

Solely based of kinematic viscosity ν, the glycerine-water solution is the best match to water in terms of the desired kinematic viscoisty for centrifuge experiments. However, this solution fails to comply to the density criterion as stated by Equation 5.21. Conclusions of Askarinejad *et al.* (2017), regarding the use of a glycerine-water solution for centrifuge experiments also indicate the disadvantageous effects of fluids where the ρ_f cannot be unified between model and prototype. Consequenctly, Askarinejad *et al.* (2017) states that density deviations directly affect the generation of PFP and hence the soil's stress state, thereby distinctly altering the mechanical response of the system. Hence, the effect of the pore fluid density on the evolution of excess PFP should demands

careful consideration as is also implied by 5.21. Consequently, the option to use the glycerine-water solution is abandoned. Of the remaining two contestants, the Dow^{trademark} HPMC F4M (using water as the dissolution agent) was selected based on economical advantages.

5.3.2. Soil properties

To avoid particle scaling effects, it is preferred to use the same sand in the model as is present in the prototype. Hence, the mechanical soil parameters of the model's sand should match those encountered by Royal IHC on (potential) off-shore project sites throughout Europe. Based on data provided by Royal IHC, it was determined that GEBA sand reasonably matched prototype soil characteristics. GEBA is a well-graded, high silica sand (99% v/v SiO_2) and therefore has a narrow, uniform grain size distribution. Due to its frequent use in research activities at Delft University of Technology, its respective mechanical parameters have been extensively studied (in example by [66]) and are therefore well-defined. A summary of relevant properties of GEBA sand is provided by Table 5.6.

Table 5.6: Summary of GEBA soil parameters after [66]

Soil property	**Symbol**		**SI Unit**
Shape	-	Rounded / sub-angular	-
Color	-	Grey / white / off-white	-
Specific gravity	γ_s	2.65	t/m^3
Average grain size	D_{50}	0.103	mm
10% finer grain size	D_{10}	0.090	mm
60% finer grain size	D_{60}	0.110	mm
Maximum void ratio	e_{max}	0.934	-
Minimum void ratio	e_{min}	0.596	-
Critical state friction angle	ϕ_{cs}	30 ± 1*	°
Coefficient of curvature	C_c	1.47	-
Coefficient of uniformity	C_u	1.22	-

* Masin (2017) reported a critical state friction angle of °34 for GEBA sand [76]

5.3.3. Boundary conditions

As discussed in 5.1.4, 5.1.5 and 5.1.6, grain size effects, soil plugging and strongbox boundaries can potentially influence the results obtained from centrifuge experiments. To limit the influence of the previously addressed phenomena and physical boundaries, literature provides dimensional recommendations. Respectively, recommendations with regard to: (I) grain size effects; (II) soil plugging; (III) strongbox dimensions, are summarized in 5.1.4, 5.1.5 and 5.1.6. In the following, the dimensional guidelines derived from literature are verified using set-up dimensions and soil sample characteristics. Grain size effects are addressed first in 5.3.3. Secondly, soil plugging is discussed in 5.3.3. Finally, strongbox dimensions are checked in 5.3.3.

Verification of grain size effects Firstly, a sufficient amount of grains should be present below the pile tip. As the experiments employ an open-ended pile, the criterion considers the thickness of the pile t as is expressed by Equation 5.14. Pile thickness t (model scale) is equal 2 mm. The average grain size of GEBA sand, D_{50} amounts to 0.103 mm. Hence, it is found:

$$t/D_{50} \geq 15 \rightarrow 20/0.103 \approx 19 \implies \textit{Sufficent}$$

To ensure that the thickness ($\approx 10 \cdot D_{50}$) of the interface layer is not disproportionate to the model pile dimensions, Equation 5.15 should be appreciated. The outer diamter of the (model) pile equals

40.2 *mm*. Thus the following is established:

$$D_{outer}/D_{50} \geq 100 \rightarrow 40.2/0.103 \approx 390 \implies \textit{Sufficent} \tag{5.22}$$

Verification of soil plugging Unfortunately, literature does not provide any recommendation regard to plugging effects for scaled tests carried out in centrifuge. Van Zeben (2017) ([112]), whom conducted experiments with the same centrifuge set-up on a pile of highly comparable dimensions under both dry and saturated conditions, did not report plugging for any test. Nonetheless, the author appreciates the need for visual verification of the aforementioned claim during the execution of experiments for this work.

Verification of strongbox boundary effects Following the recommendations of De Nicola *et al.* (1996) ([31]) and Prakasha et al. (2005) ([91]), respectively with regard to lateral and axial boundary tolerance, it is established that the criteria presented earlier as Equations 5.17 and 5.18 should be satisfied. Provided the pile and strongbox have a diameter of 40.2 *mm* and 315 *mm* respectively, the former criterion equates to:

$$R_{\text{strongbox}}/R_{\text{pile}} \geq 13 \rightarrow 157.5/20.1 \approx 8 \implies \textit{Insufficient}$$

Hence, the lateral space in the strongbox is insufficient to reach optimal test conditions and the influence boundary effects on the collected data should be appreciated. According to Van Zeben (2017) ([112]) numerical simulations by Azua-Gonzalez (2017) ([12]) have produced results that agree with the latter statement. Simulations demonstrated that dense, saturated samples expressed the highest susceptibility to boundary influences. Loose, fully drained samples showed the lowest influenceability. Quantitatively, results indicated a discrepancy in pile penetration and excess PFP development of less than 10%. Hence, the influence of boundary effects on the test results is appreciable but inadequate to require redesign of the strongbox.

Now, considering the axial space requirement and provided the minimum distance between the pile tip and the bottom of the strongbox $d_{soil,\,min}$ is 57.5 *mm*, it is found:

$$d_{\text{soil, min}}/R_{\text{pile}} \geq 4 \rightarrow 57.5/20.1 \approx 3 \implies \textit{Insufficient}$$

Hence, according to theory, axial strongbox dimensions form are likely to influence soil behavior. It should however be noted that due to the strong gravity curve (as the centrifuge's radius is small centrifuge with respect to set-up dimensions), the minimum soil cover is effectively increased at prototype scale. Hence, there is a possibility that axial boundary effects are reduced. For the sake of completeness, it has been determined that the distance between the pile's tip and bottom of the strongbox should be ≥ 80.4 *mm* is achieve ideal driving conditions according to Equation 5.18.

5.4. Sample preparation

For this research both dry and saturated dense ($D_r \approx 80$) soil samples are used. The employed methods of preparation for both types of samples, differ significantly and are consequently separately discussed in this section. The dry sample preparation method is elaborated upon in 5.4.1. The formation of saturated samples is described in 5.4.2.

5.4.1. Dry sample preparation

The preparation of dry samples relies on a combination of the dry pluviation technique and vibratory compaction. Using a dry pluviation device, sand is rained into the sample container (with predetermined mass) from a height of 45 *cm*. The nominal diameter of the apertures in the pluviation device is 5 *mm*. As the soil storage capacity of the device is limited to a few kilos, it is not possible

to deposit the required amount of sand in the soil container at once. Consequently, the sample is gradually built up in layers of several centimeters thick. Using dry pulviation alone, practice has demonstrated that samples reach a medium-dense state of compactness; where the relative density of the deposited layers falls in the 35-40% range consistently. Although not all permutations were explored, the outcome of efforts to increase the state of compactness by alteration of the falling height and aperture diameter were marginal. The effect of variation of aperture spacing, which would also allow to control the rate of deposition to a higher extend, was not considered when optimizing the pluviation device. It is acknowledged that full consideration of the three aforementioned variables, would likely yield a better pluviation set-up. The latter could potentially make sample densification through other means (to attain an R_d of 80%) superfluous. However, as the combination of sand pluviation and vibratory compaction (by means of a ASTM vibrating table) yielded homogeneous samples with a high degree reproducibility, the optimization effort was sized.

The total mass of sand to be deposited is calculated before hand. Input variables for the calculation include:

- The geometry of the sample container, specifically:
  - The (3-point mean) diameter of the sample container;
  - The (3-point mean) internal height of the sample container;
- The desired soil surface level, referenced to the upper extremity of the sample container;
- The desired relative density, expressed as a quotient between 0 and 1.
- Specific weight of the GEBA sand γ_s, 2650 kg/m^3

From the nominal diameter and internal height of the container, the total volume of the strongbox is calculated. Subsequently, the volume of the void between delimited by: (I) the desired surface level; (II) top of the sample container; is subtracted. As no sensors are present in the soil for dry samples, no further volume corrections are needed. From the desired relative density, the required porosity of the sample is determined as follows:

$$n = \frac{e_{\max} - D_r \cdot (e_{\max} - e_{\min})}{1 + e_{\max} - D_r \cdot (e_{\max} - e_{\min})} \tag{5.23}$$

From porosity n and the specific gravity of the GEBA sand γ_s, the required dry mass of soil $M_{s,\,dry}$ is calculated from the known volume of the strongbox V_{tot}:

$$M_{\text{s, dry}} = (V_{tot} \cdot (1 - n)) \cdot \gamma_s \tag{5.24}$$

My placing the strongbox on a scale during the filling process, the amount of sand added is precisely controlled. When the designated mass is reached, the filling process is terminated and the entire sample is placed on the ASTM vibrating table. The vibration amplitude is set to a value of 1.5 throughout the entire densification process. As the sample container has a large footprint, some concerns were raised with respect to the uniformity of the densification process due to undesired wave interaction inside the strongbox. To compensate, the sample is gradually rotated while is sits on the vibrating table. In order to ensure that the desired relative density is obtained, the location of the soil surface with respect to the edge of the container is monitored continuously. When it is observed that the aforementioned distance approximates the desired value, the shaking process is terminated. To account for the possibility that the soil surface is not entirely level, three readings are taken, which are subsequently averaged to obtain a single value representative for the entire sample. Finalization of the dry sample preparation entails the determination of the final weight of the container and its contents. Hereafter, the final weight, together with the mean distance from soil surface to the edge of the container, are used to calculate the obtained relative density. Samples for which the aforementioned calculation demonstrates that the criterion $78 \leq R_d \leq 82$ is satisfied, are approved for centrifuge testing.

5.4.2. Saturated sample preparation

Saturated sample preparation is done according to the drizzle method (as envisioned by Rietdijk *et al.* (2010) ([99])) and consists of the following steps:

1. Creation of a sand sample saturated with de-aired water and RD≈0;
2. Shock-wave compaction until the desired D_r is achieved;
3. Substitution of the de-aired pore water by viscous fluid with predetermined viscosity.

In order to realize a saturated sand sample with $D_r \approx 0$, two containers are used, namely: (I) A first container (composed of the actual strongbox and an extension piece) is exclusively filled with de-aired water, the ensemble of the two parts is referred to as C1 in the following; (II) A second container (hereunder denoted as C2) contains a (de-aired) water-sand slurry, which is constantly agitated to prevent the settlement of particles. A peristaltic pump, installed in container C2, transports the sand-water mixture to container C1, where a fully submerged shower head creates a fine mist of particles under water. Provided that the height of container C1 is sufficient, the extruded particles settle evenly resulting in a homogeneous soil sample with RD≈0. The water displaced by the settling particles, flows back into the storage container (C2) through a spillway. A set of valves is used to control the return flow through the spillway and maintain a constant water level in container C1. Figure 5.2 provides a schematic overview of the sample preparation device, its real counterpart is shown in Figure 5.3. A weight threshold is used to pinpoint the time of termination of the drizzling process. Therefore, a steady water level inside the model cell is essential to accurately track the amount of deposited sand. The desired relative density D_r serves as the basis for calculation of the final mass. First, the required porosity is calculated in accordance with Equation 5.23. Subsequently, similar to the determination of the required mass of sand for dry samples (as described by Equation 5.24 in 5.4.1), the required dry soil weight is calculated from the effective volume of the strong box V_{tot} using n_{req}. To compute V_{tot} complementary input variables are needed, specifically: (I) container geometry (diameter and internal height); (II) the desired surface level (with respect to the upper extremity of the container); (III) soil specific weight γ_s. The resulting volume is finally corrected to account for the presence of (three) static pore water pressure sensors in the soil body. As for every volume of sand which is transported from C2 to C1, the same volume of water flows through the spillway, the mass increment of container C1 is proportional to the product of the deposited volume and buoyant unit weight of the soil, the latter is henceforth denoted as ΔM_{tot}. To compute ΔM_{tot} from the known dry soil mass $M_{s,\,dry}$ (see Equation 5.24), the upcoming formula is used [99]:

$$\Delta M_{\text{tot}} = \frac{\gamma_s - \rho_w}{\gamma_s} M_{\text{s, dry}} \tag{5.25}$$

Here, ΔM_{tot}, γ_s and ρ_w respectively represent the total weight increment of of container C1, the specific weight of the soil and the bulk density of water accordingly. The stop criterion for the drizzling process can be formulated as follows:

$$M_{\text{tot}} \approx M_{\text{ini}} + \Delta M_{\text{tot}} \tag{5.26}$$

Where, M_{ini} is the total mass of container C1 (strongbox and extension piece), including (three) static pore water pressure sensors installed and (de-aired) water up to an internal demarcation line.

Once the criterion, as described by Equation 5.26, is satisfied; the soil sample is densified in order to attain the required D_r. Prior to densification, the majority of the water on top of the sample is drained and the extension piece is removed. Next, the sample is densified using shock-wave compaction. The latter entails lifting the strongbox several centimeters and subsequently dropping it on a flat surface. The impact generates a shock-wave which axially propagates through the sample. The three aforementioned steps are schematically shown in the top three frames of Figure 5.5. In order to achieve the same level of densification near the top of the sample, weight is added on top. Figure 5.4

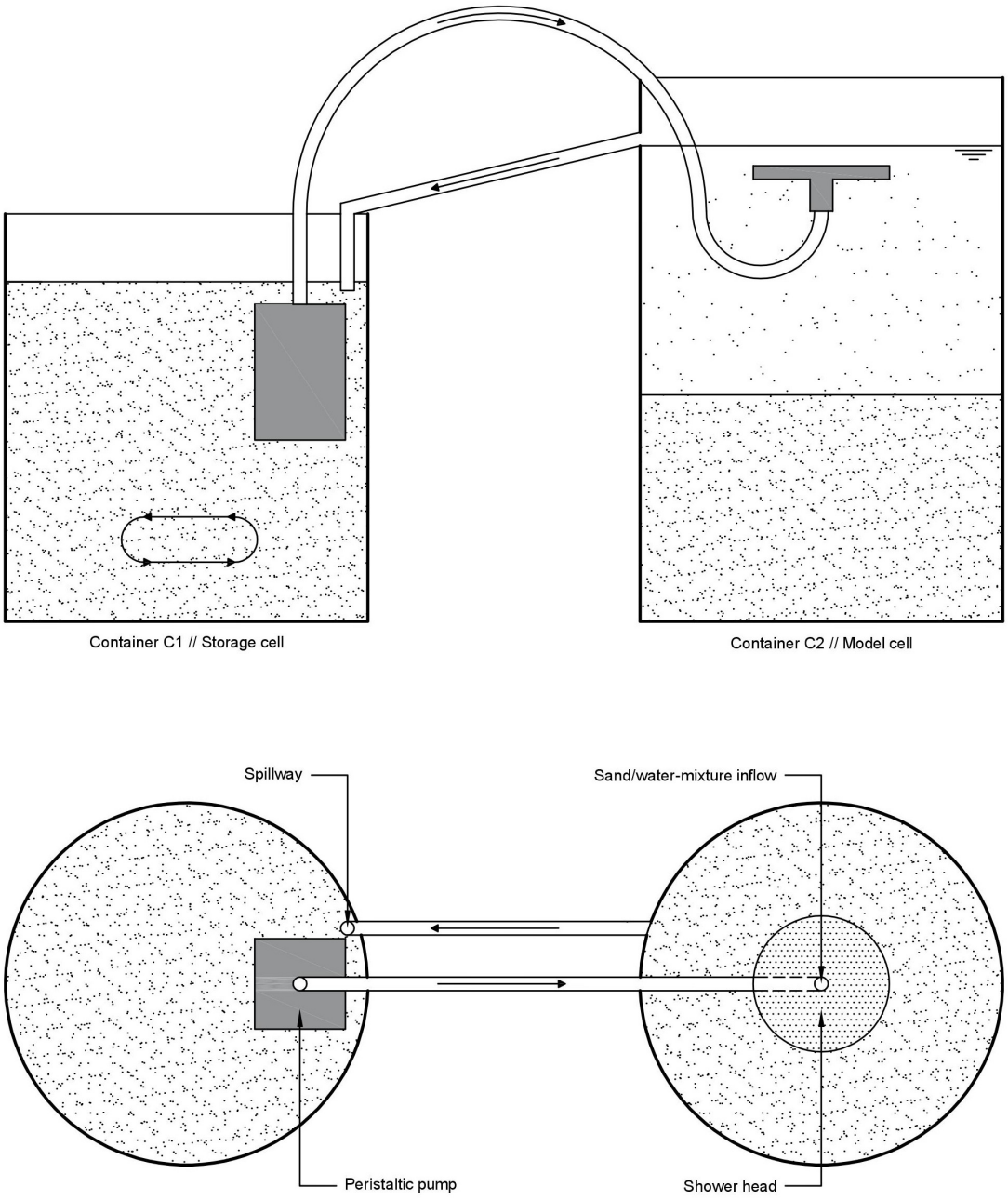

Figure 5.2: Schematic overview of sample preparation set-up according to the drizzle method. Adapted from [99].

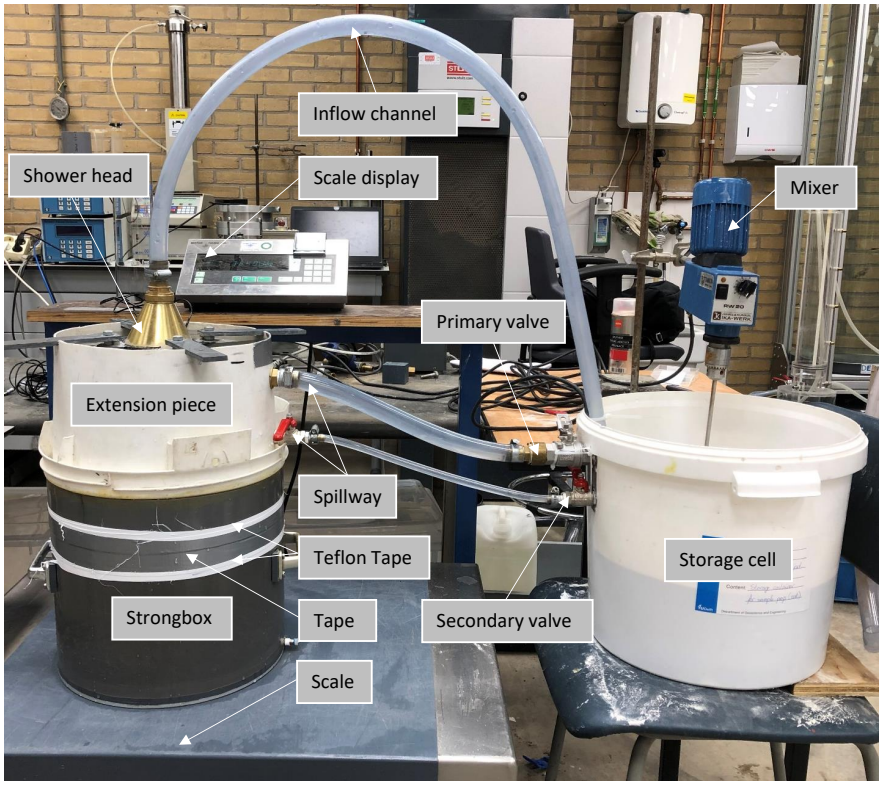

Figure 5.3: Saturated sample preparation device with designated parts

shows D_r as a function of volumetric strain ϵ_{vol} for GEBA sand and used to aid the sample preparation process. Please consider that Figure 5.4 is derived under the assumption that volumetric strain depends solely on pore volume change. Hence, it is assumed that the soil particles are effectively incompressible, which is a valid idealization for the aforementioned densification method. Similar to the dry sample preparation, the end of compaction is marked when the (three-point mean) distance from the soil surface to the rim of the strongbox approximates the desired (input) value. Hereafter, the dry mass of the drizzled sand, together with the mean distance from soil surface to the edge of the container, are used to calculate the obtained relative density. Samples for which the aforementioned calculation demonstrates that the criterion $78 \leq R_d \leq 82$ is satisfied, are approved for viscous fluid saturation.

The final step in the preparation process is saturation of the soil sample with viscous fluid. The associated proceedings are graphically displayed by frames four to ten (starting on the left-hand side of the second row) of Figure 5.5. As can be observed, the associated process first requires the remainder of the stagnant water column on top of the sample to be drained and replaced by thin layer of viscous fluid. To prevent particles from being washed out by the flow of viscous fluid, a geotextile is placed on top through which helps to spread the viscous fluid gradually over the sample surface. By creating a head difference at the free end of the drainage tube (attached to the bottom of the sample container C1), water is removed while the viscous fluid slowly penetrates the soil matrix form the top. To match the inflow of viscous fluid to the outflow of water, a set of valves is used (one to control the influx of viscous fluid, another to adjust the drainage rate). By placing the sample on a scale, it is possible to precisely regulate the volume balance of the system. The latter ensures that the sample remains fully saturated throughout the entire process. To provide further insight into the balancing of flow in practice, Figure 5.6 explicates the aforementioned process and additionally denominates key features of the preparation set-up.

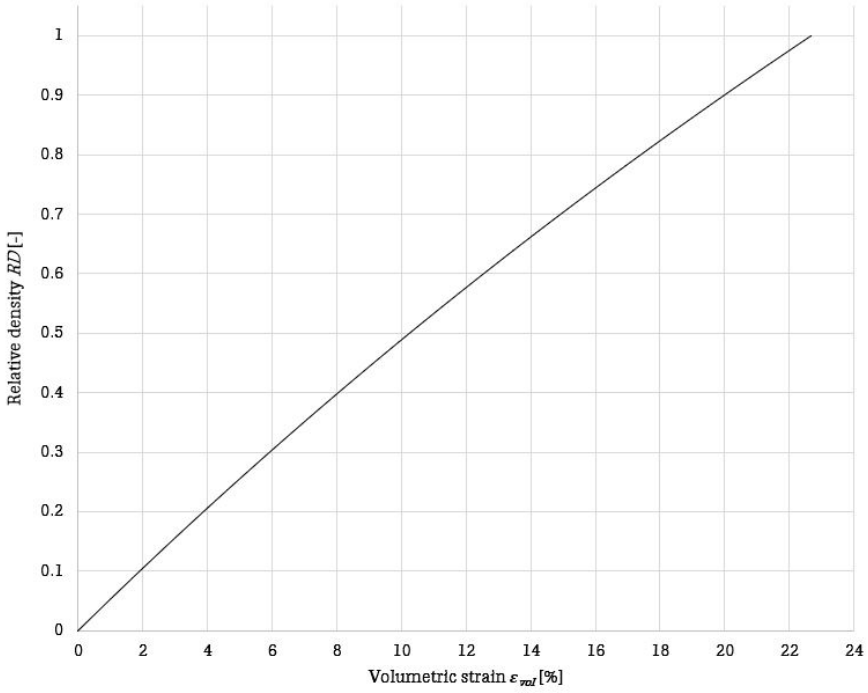

Figure 5.4: Relative density (RD) as a function of volumetric strain ϵ_{vol} for GEBA sand

To verify that the saturation is complete, the mass of the water efflux is measured. As the relative density and the volume of the sand body are know, the final mass of expelled water can be precisely calculated beforehand. Thereby establishing a clear termination criterion. The latter, together with an manual inspection of the viscosity of the drained fluid, ensures that all water is drained from the sample. Practice demonstrated that the advocated method preformed consistently well, as comparison of the actual mass of exorcised water to the theoretical estimate yielded a matching percentage of 98-100%. Where the remaining discrepancy can be explained by a minor water over-drainage prior to the realization of a layer of viscous fluid on top of the sample. Due to contact between water and viscous fluid inside the soil body, dilution of the viscous fluid can occur. As this has disadvantageous consequences for the overall viscosity, it is advisable to drain slightly more fluid than strictly required. Besides ensuring the complete removal of water, the latter also guarantees the viscous properties of the fluid inside the sample. Van Zeben (2017) ([112]) highlights the importance of restricting the flow rate between the sample and the drainage reservoir to avoid the creation of a preferential flow path for the viscous fluid prior to the removal of all water. Due to the large differences in fluid viscosity and the associated reduction of soil permeability, the probability of occurrence of the aforementioned phenomena is limited to very extreme cases. For this research, practice demonstrated that a drainage rate of ± 3 L/h could safely be maintained during sample preparation.

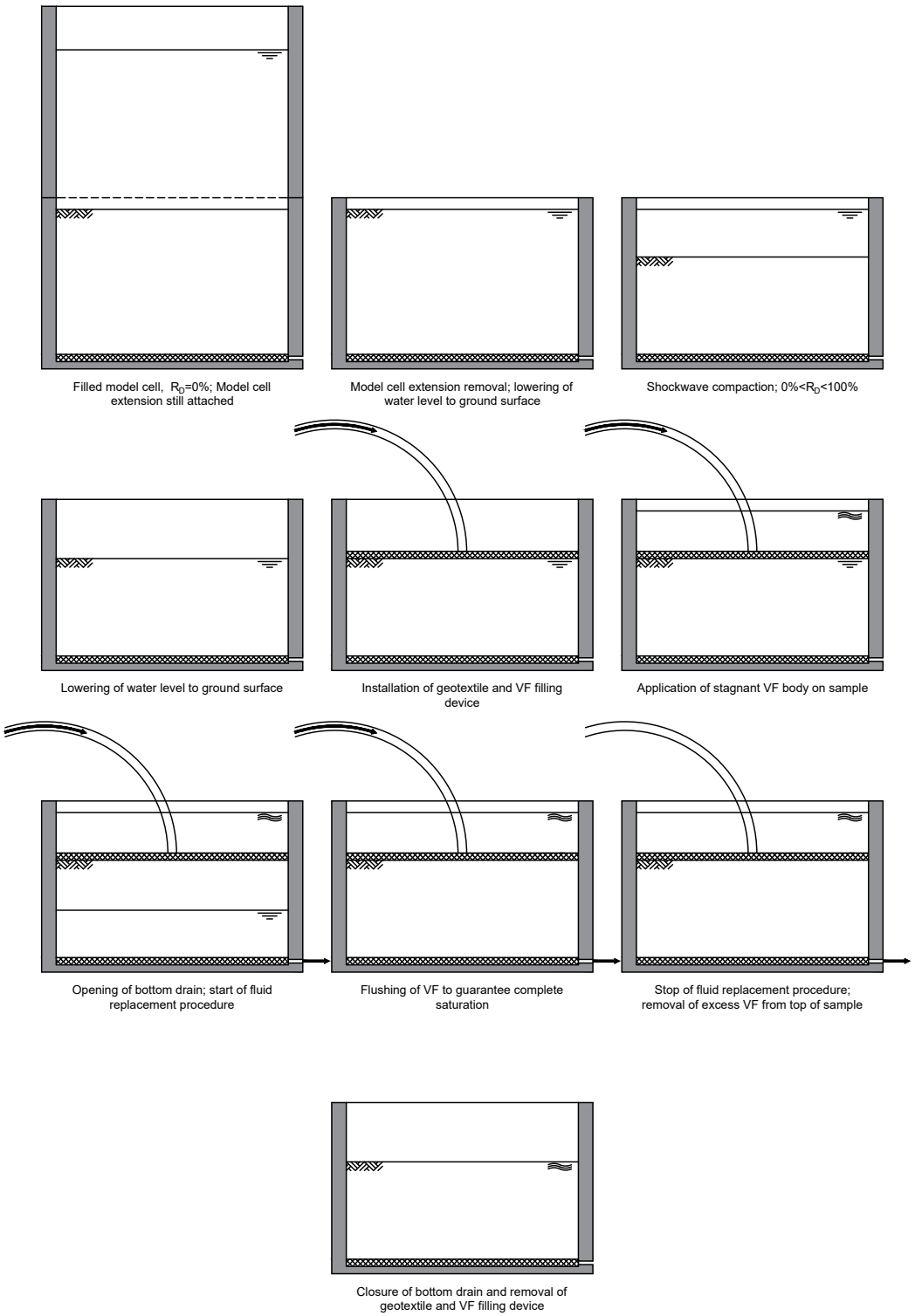

Figure 5.5: Schematic visualization of the preparation steps after the drizzling process is completed to obtain a fully (viscously) saturated sample at the right D_r

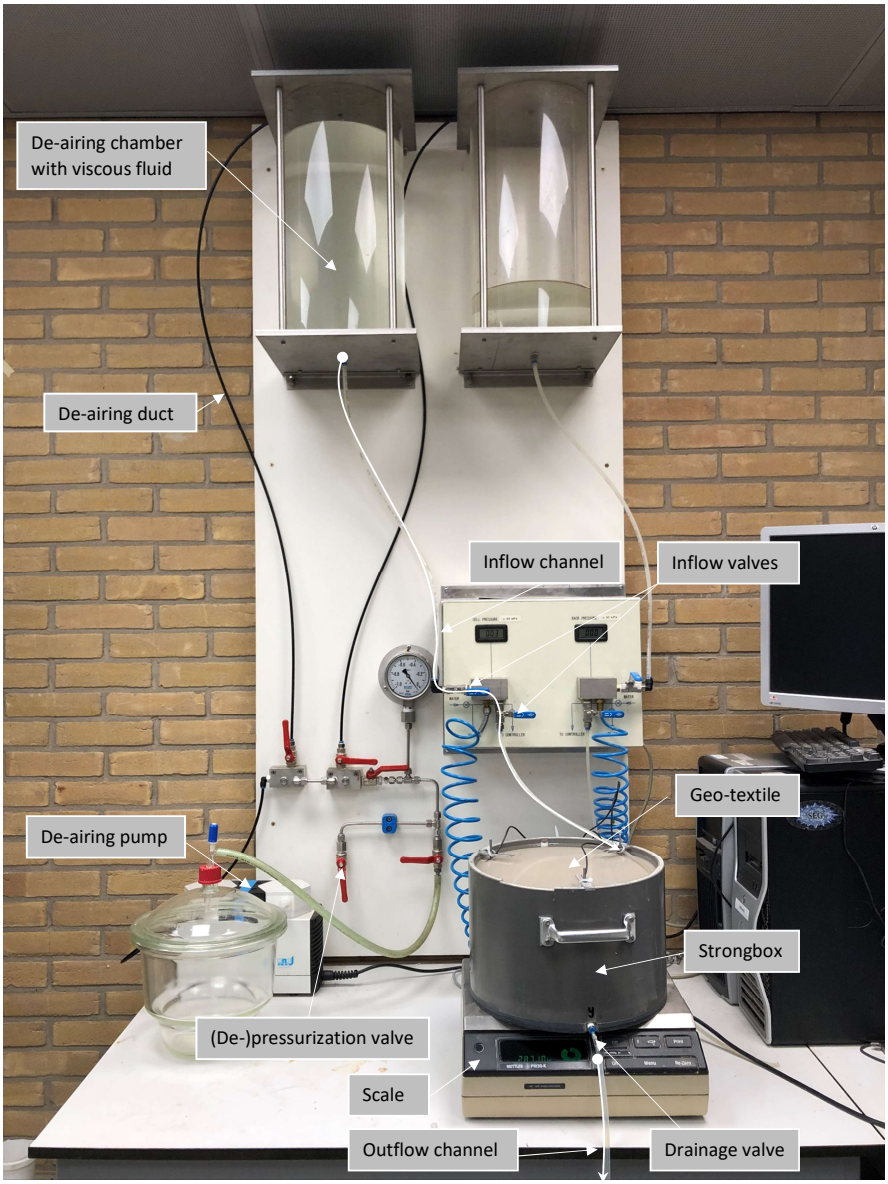

Figure 5.6: Viscous fluid saturation device in operation with designated parts

6

Thesis statement

6.1. Problem description

Over the last decades, the world's energy consumption has risen dramatically. Population growth and economical property can be appointed as the main drivers behind the aforementioned observation. Future outlooks with regard to energy consumption foresee a further rise for the coming 20 years [35]. Given that the gross of world's energy demand is generated from fossil fuels, which weights down on the global climate. For some time, staying the current course is regarded as a potential ecological catastrophe by the scientific community. Hence, the call for a switch towards sustainable sources of energy has steadily loudened over the past years. In the Paris Agreement, the world's governments, nearly collectively, anchored their ambitions to combat the adverse effects of greenhouse gas (GHG) emissions (specifically global warming), and lead the way towards a sustainable future.

In the light of the aforementioned events, the European Commission (EC) has the ambition to by 2030 have reduced GHG emissions by 40%. To accomplish its goals, the EC strives to accelerate the adaptation of renewable energy sources. By 2030, 27% of the respective energy consumption should be generated from renewable sources, which could thereby also realize the EU's bold ambition to acquire the leading position in the field of sustainable energy [38].

One of the most promising means through which global ambitions regarding the reduction of GHG can be materialized is wind energy generation. The Global Wind Energy Council (GWEC), expects the share of wind energy in the global energy consumption to augment to 14% [101] by 2030. Additionally, GWEC also foresees a sustained increase over the successive decades after 2030. For Europe in particular, offshore wind energy shows great potential. WindEurope ([122]) states that, in theory, it would be possible to generate 80% to 180% of the EU's total electricity demand solely by offshore wind energy.

Exploiting the Europe's full offshore energy potential is however not an easy task. In its current form, offshore wind is still reliant on subsidies granted by governments. The latter is mainly due to high costs associated with the substructure, costly installation and expensive design provisions to withstand harsh off-shore conditions. Byrne and Houlsby (2003) ([**?**]) as well as Mone *et al.* (2015) ([81]) indicate that cost related to the substructure account for 35% the constriction costs. Gavin *et al.* (2011) ([44]) even mentions a share of up to 50%. Unsurprisingly, the previously mentioned expenditure suppresses efforts to materialize the advantages related to off-shore generation of wind energy; which can be summarized as follows:

1. Better and more consistent wind conditions genuinely prevail offshore;
2. Installation of onshore wind turbines in hampered by spacial and nuisance restrictions, whereas its offshore counterpart is not;

3. Marine equipment is much larger that its onshore counterpart, making it possible to construct wind turbines at a larger scale;
4. Possibilities to realize energy farms which combine wind, solar and wave energy to offer renewable energy at a competitive price [44].

6.2. Motivation

Despite the large costs associated with offshore wind energy, Vattenfall was recently awarded the tender for the first unsubsidized offshore wind farm, which is to be constructed off the coast of Holland's Zuid-Holland province [53]. Hence, unsubsidized offshore wind energy is not an unattainable utopia. However, indisputably, bold effort through continued innovation and entrepreneurship is required for the prospect of offshore wind to materialize in the near future.

Transforming off-shore wind energy into an economically viable alternative for fossil fuels is an ongoing process and can be approached from many angles. However, it makes sense to seek optimizations in the area which account for the most predominant part of costs related to offshore wind projects: substructure design and installation.

Of existing offshore wind turbines, the vast majority (≥95%) of substructures require the installation of one (monopile) or multiple open-ended steel piles. Research into design and installation optimization of this structure is ongoing as it will likely be implemented in most future offshore wind endeavors. The latter is supported by Gavin *et al.* (2011) ([44]) who state that as turbines move into water of increasingly larger depth (30 - 70 m), the use of jacket structures, which are anchored by driven open-ended steel piles, as foundation becomes more probable.

Currently, drivability studies serve the purpose of selecting an appropriate driver system and substantiating an optimum driving plan to guarantee the desired penetration depth is reached in the least amount of time, whist maintaining induced stresses below the plastic threshold value and restricting the manifestation of fatigue effects. Hence, they are indispensable to preparation and planning of installation. Essentially, three different techniques exist to conduct drivability studies, namely: (I) Dynamic analysis; (II) One dimensional wave equation analysis; (III) Two- or three-dimensional finite element analysis. However, in practice, one dimensional wave equation analysis is the most extensively employed methodology. Despite several inherent shortcomings, through extensive calibration it produces reasonably satisfactory results in terms of designing a pile-driver system capable of reaching the desired depth whist limiting excessive strain and fatigue. However, driving time optimizations are not carried out while they arguably present a pronounced opportunity for optimization.

The latter statement originates from an unexpected source. As impact hammering of piles is characterized by a high noise impact, which is possible harmful to marine life, a new approach to pile installation has been introduced named *HiLo driving*. The method delivers similar amounts of energy as conventional hammering techniques (≈30-40 bl/min), but distinguishes itself by using a higher blow rate (≈60-70 bl/min) while decreasing the energy per blow [7]. Although based on a single case study, back-analysis of driving records of the installation of monopiles for a windfarm within the North Sea, as done by Anusic *et al.* (2017) ([7]) indicate that HiLo driving results in similar driving times while reducing noise emissions and fatigue effects. Remarkably, the total energy for *HiLo driving* mode was 10% lower than normal driving mode. This observation gives reason to believe that there is a temporary reduction is mobilized soil resistance during *HiLo driving*. Furthermore, one dimensional wave equation analysis failed to reproduce the installation behavior observed during use of the HiLo technique.

6.3. Hypotheses

Three hypotheses, which possibly explain the observations by Anusic *et al.* (2017), as described in 6.2, were formulated and are separately discussed below.

6.3.1. Hypothesis one - excess PFP generation

Given that attempts to replicate the HiLo driving log by wave equation analysis were unsuccessful, there is a possibility that phenomena underlying the observations are unaccounted for in the methodology's formulation. An *SRD model* lies at the heart of the employed back-calculation method. *SRD models* are formally used to determine the ultimate bearing capacity for foundation piles in the post installation phase. Consequently, a hydrostatic distribution of PFP is assumed. It could be argued that the latter is not necessarily true for pile during installation. In example, the centrifuge tests by Van Zeben (2017) ([112]) indicate, despite high soil permeability, the accumulation of excess PFP during impact hammering in saturated sand. Although the influence of the elevated water pressure in vicinity of the pile on drivability remains a current research topic, the assumption of hydrostatically distributed PFP is refutable. Moreover, following a line of reasoning which relies on the fundamental *effective stress principle*, any increase in PFP should provoke a similar decrease in effective stress under constant loading conditions. Hence, a possibility remains that the generation of excess PFP results provokes a reduction of the effective stresses surrounding the pile and consequently of the friction exerted along the shaft. However, the influence of soil packing on its ability to generate excess PFP should not be overlooked. Constrained dilation, which is a phenomenon likely to occur for densely packed, poorly permeable soil under sufficient shear, could give rise to tensile PFP thus further increasing the soil resistance. For the installation of open-ended steel piles, the most predominant shear zones are located along the shaft and at the shear planes of the failure mechanism below the tip. To assess the susceptibility of soil zones to constrained dilative behavior, the influence of large overburden pressure or normal stress σ'_n should be considered. For high values of σ'_n dilative behavior is entirely suppressed and the net volumetric strain is negative (contractive behavior). Consequently, it is likely that the constrained dilation could exclusively lead to a temporal strength increase in low permeable soil under low to moderate overbunden pressure. As the majority of energy is transmitted into the soil at the tip, local shear zones are the best candidate for the aforementioned behavior. At the pile-soil interface, the effects of *friction fatigue* on the crushed and remoulded soil induce a zone of net contraction along the shaft, which makes it unlikely that constrained dilative soil behavior is observed, even at low overburden pressure. The predominantly sandy soil present on project sites combined with the limited thickness of the shear band (short associated drainage times), further decrease the likelihood of strength increase at the interface.

6.3.2. Hypothesis two - enhanced radial stress degradation

A second possibility concerns the cyclic loading of the soil along the interface. In their respective formulation, most modern (CPT based) *SRD models* account for the effects of *friction fatigue* by consideration of the "*h/R effect*". The latter notion relates the decrease in radial stress along the shaft, which is due to cyclic loading at the pile-soil interface, to the distance between a soil layer and the pile tip h normalized by the pile radius R. Hence, the driving frequency, which is characteristic for *HiLo driving*, does not influence the degree of friction degradation. However, following the conclusions presented by White and Lehane (2004) ([118]), the decreases in radial stress varies systematically with the number of load cycles N. The latter gives rise to the possibility that the effects of *friction fatigue* are enhanced for *HiLo driving*. Thus leading to less (shaft) resistance during driving.

6.3.3. Hypothesis three - reduced dynamic soil resistance

The final hypothesis recognizes the reduction in operational energy level per blow as a result of the high driving frequency used for *HiLo driving*. Increasing the driving frequency while decreasing the energy per blow is achieved by lowering the fall height of the ram mass. Consequently, impact speed is reduced and acceleration at the top of the pile tip is decreased. Integration of acceleration over time, yields the particle velocity of the pile. By recalling the aforementioned differences between

HiLo driving and conventional driving, it is argued that the latter velocity is lower for a HiLo driving mode. This is an important conclusion as the velocity-dependent or dynamic soil resistance is in this case reduced. Hence, the total soil resistance, which is composed of a static and dynamic part, is reduced. However, contrasting to the other two hypotheses, the rate-of-strain dependency of dynamic soil resistance is accounted for in most commercial software packages which preform wave equation analysis. Hence, the discrepancy between model and reality can only be caused by improper formulation of the aforementioned phenomenon or improper use of the modeling software. It is true that way in which dynamic soil resistance is calculated by most commercial software packages remains under debate. Particularly, the linear dependency of dynamic soil resistance on particle velocity has been criticized by in example Briaud and Gerland (1984) ([18]) and Rausche *et al.* (1992) ([97]). This criticism has so far produced some tangible results as modeling software like GRLWEAP offer the possibility to use non-linear dampening expressions. Yet, successful implementation can only be achieved by carefully matching field measurements to model output, which can be a cumbersome process and is consequently reserved to experienced users. Hence, by default, dynamic resistance remains linearly dependent on particle velocity in programs such as GRLWEAP [90], although the former adds to output conservativeness. A thought experiment suffices to establish that in the majority of cases, a monotonically increasing, non-linear relationship would, for the same reduction of particle velocity, yield a larger decrease in dynamic soil resistance than a linear relationship. Hence, this research sets out to establish whether the use of a linear dampening model can be justified.

6.3.4. Ambition

The previously discussed hypotheses, indicate highly interesting research opportunities with regard to optimization of pile installation. Hence, this work, by means of experimental research, sets out to:

Identify the processes underlying the observed reduction of driving resistance for a high frequency impact hammering technique, with purpose of economizing the installation of open-ended steel piles for offshore applications.

6.4. Research questions

Research question have been divided into two parts, relating to: (I) literature review; (II) the experimental investigation. Both sets of questions are, respectively, presented in 6.4.1 and 6.4.2.

6.4.1. Aims of literature study

- *How are drivability studies executed in practice?*
  - What is the underlying theoretical framework?
  - Which soil behavioral effects are accounted for?
- *What are the soil stress states that are present during impact hammering of open-ended steel piles and to which soil behavioral phenomena do these give rise?*
  - What are the underlying processes causing the observation of these phenomena?
  - What are the limiting factors to the observation of these processes?
- *How are excess pore water pressures generated and dissipated during the driving process?*
  - Under which circumstances can the soil exhibit liquefaction?
  - What are associated time scales?
- *How does the failure mechanism develop underneath the pile tip?*
  - How does the failure mechanism effect the stress state around the pile tip?
  - What are limiting factors?

6.4.2. Aims of experimental investigation

- *How is the energy input by the driver system into the pile best characterized?*
  - How are nominal time scales affected by changes in impact velocity?
  - How are nominal time scales affected by changes in impact energy?
- *Under dry conditions, how is pile set affected by variation is hammering frequency if energy input is maintained?*
- *Under saturated conditions, how does blow rate affect the generation of excess PFP in the surrounding soil mass?*
  - How does this process affect pile drivability?
- *How does the failure mechanism below the pile tip develop during driving?*
  - For a constant energy input, how is the observed failure mechanism dependent on driving frequency?
  - For a constant driving frequency, how is the observed failure mechanism dependent on energy input?
  - What are the differences between failure mechanisms caused by conventional driving and HiLo driving?

6.5. Economical prospect

To substantiate potential savings which can be obtained though optimization of the installation procedure of open-ended steel piles through impact driving, a simplified calculation for a fictive case study has been made. In the following, several statistics relating to offshore wind generation are employed, namely:

- A megawatt of turbine capacity roughly costs 1.5€ million [**?**];
- A nominal offshore wind turbine produces 5.9 *MW* [121];
- The turbine accounts for 31.8% of the total project expenditure [81];
- Of the total costs, 35% are related to the substructure [**?**] & [81];
- Installation and design optimizations can yield a 10% cost reduction [14].

Now, considering that a mere 5% of total savings potential can be attributed to enhanced monopile installation procedures, € 48700 could be saved on every turbine installed. Extrapolating the latter figure to the scale of a nominal offshore wind farm, comprised of 50-150 turbines, the saving potential amounts to € 2.5 million to € 7.5 million.

6.6. Testplan

The test matrix is presented in Table 6.1. **Please consider that the test table has been revised over the course of the thesis due to operational challenges relating to the actuator. Appendix A contains the original test matrix and explains the reasoning behind the changes which resulted in Table 6.1.**

The horizontal dashed lines used in Table 6.1 delimit test subsets. As can be observed, for tests in the same subset, the three symbols of test label match. Hence, in the following, tests subsets are indicated by their corresponding three symbol sequence. The matrix has been designed based on the ambition to research the effect of hammering frequency on the drivability of open-ended steel piles. Two types of tests can be distinguished, namely: (I) repeated single blow; (II) multi blow. Repeated single blow test serve the purpose of establishing a baseline for the multi blow tests in terms of pile set, wave propagation time and PFP generation and dissipation. To accommodate for a potential depth trend in soil properties, which might lead to different soil behavior at different depths,

Test [-]	Acceleration [g]	Type [SINGLE /MULTI]	Ram mass [-]	Frequency [Hz]	Energy/blow* [J] (Capacity [%])	Energy flux [J/s]	Relative packing [LOOSE/DENSE]	Saturation [%]
S2DXL	50	SINGLE	II; 140 g	n.a.	1.87 (67%)	n.a.	DENSE	0
S2DXH	50	SINGLE	II; 140 g	n.a.	2.80 (100%)	n.a.	DENSE	0
S2SXL	50	SINGLE	II; 140 g	n.a.	1.87 (67%)	n.a.	DENSE	100
S2SXH	50	SINGLE	II; 140 g	n.a.	2.80 (100%)	n.a.	DENSE	100
S3DXL	50	SINGLE	III; 220 g	n.a.	1.87 (42%)	n.a.	DENSE	0
S3DXH	50	SINGLE	III; 220 g	n.a.	2.80 (67%)	n.a.	DENSE	0
S3SXL	50	SINGLE	III; 220 g	n.a.	1.87 (42%)	n.a.	DENSE	100
S3SXH	50	SINGLE	III; 220 g	n.a.	2.80 (67%)	n.a.	DENSE	100
M2DLL	50	MULTI	II; 140 g	10	1.87 (67%)	17	DENSE	0
M2DLH	50	MULTI	II; 140 g	10	2.80 (100%)	28	DENSE	0
M2DHL	50	MULTI	II; 140 g	15	1.87 (67%)	28	DENSE	0
M2DHH	50	MULTI	II; 140 g	15	2.80 (100%)	42	DENSE	0
M2SLL	50	MULTI	II; 140 g	10	1.87 (67%)	17	DENSE	100
M2SLH	50	MULTI	II; 140 g	10	2.80 (100%)	28	DENSE	100
M2SHL	50	MULTI	II; 140 g	15	1.87 (67%)	28	DENSE	100
M2SHH	50	MULTI	II; 140 g	15	2.80 (100%)	42	DENSE	100
M3DLL	50	MULTI	III; 220 g	10	1.87 (42%)	17	DENSE	0
M3DLH	50	MULTI	III; 220 g	10	2.80 (67%)	28	DENSE	0
M3DHL	50	MULTI	III; 220 g	15	1.87 (42%)	28	DENSE	0
M3DHH	50	MULTI	III; 220 g	15	2.80 (67%)	42	DENSE	0
M3SLL	50	MULTI	III; 220 g	10	1.87 (42%)	17	DENSE	100
M3SLH	50	MULTI	III; 220 g	10	2.80 (67%)	28	DENSE	100
M3SHL	50	MULTI	III; 220 g	15	1.87 (42%)	28	DENSE	100
M3SHH	50	MULTI	III; 220 g	15	2.80 (67%)	42	DENSE	100

* Please note that this is the kinetic energy carried by the ram mass at an infinitesimal instant before impact (assuming no friction during fall). Hence, it is not equal to the net energy administered to the pile E_T. Theoretically, if driver system efficiency η_{ds} and the friction regime during the drop is the same, values for E_T should coincide. Experiments should establish whether the latter statement holds or if hammer stroke should be reevaluated. For more information, consult Appendix E

Table 6.1: Updated test matrix

single blows are applied sequentially. The time interval between subsequent blows is chosen such that there is minimal interaction between physical phenomena in pile and soil. Multi blow tests serve two purposes: firstly, to separately determine the effect of driving frequency and fall height (which governs impact energy) on pile drivability; secondly, to assess the combined effect of an increase in driving frequency and decrease in fall height, as is true for HiLo driving. Finally, both (repeated) single blow and multi blow tests are carried out under dry and fully saturated conditions to establish the influence of pore fluid and the associated change of certain soil parameters, on the observations.

S2D and S2S are repeated single blow tests carried out using the intermediate ram mass II, which has a respective weight of 140 *g*. Tests from S2D are carried out on a dry soil sample. Tests from subset S2S use a fully saturated sample. Within subset S2D and S2S, the fall height is changed between tests. Following the theory presented in 4.2.1, an increase fall height and thus impact speed v_0, yields a higher particle velocity and thus impact force. Recalling that impact time is dependent on the height of the hammer and the same hammer is used, impact time between the tests in subset S2D and S2S is constant. By combining the two previous observations, it follows that the total transferred energy, which the product of impact force and particle velocity integrated over impact time (Equation 4.25), is increased due to the larger fall height. Hence, SD1 and SS1 should demonstrate the influence of changes in impact energy (per blow) on: (I) pile penetration (for both dry and saturated conditions); (II) wave propagation through the pile (for both dry and saturated conditions); (III) excess PFP generation and dissipation (only for saturated conditions). For S2D, the next blow is initiated when stress wave reflections in the pile are damped out. The latter is also true for S2S, with the added prerequisite that excess PFP are entirely dissipated. As discussed in 4.2.2, dynamic soil resistance is governed by the particle velocity of the pile. Hence, by mutual comparison of results from the tests in subset S2D and S2S respectively, the influence of dynamic soil resistance on pile penetration can be studied. Hence, the first steps towards the verification of Hypothesis III are taken. Moreover, by mutual comparison of dry and saturated effectuations (for the same energy per blow), the influence of pore fluid on the results is studied, thus yielding information to aid the verification of hypothesis I.

Subset S3D and S3S, similar to subset S2D and S2S, are repeated single blow tests. Tests from subset S3D, are carried out on and dry soil samples. Tests from subset S3S, use fully saturated soil. Initiation criteria for subsequent blows do not differ from those used for S2D and S2S. However, for this second set of repeated single blow tests ram mass III is used, which has a respective weight of 220 *g*. Further adjustments to the fall height ensure that the impact energy (per blow) of S2D and S2S is matched. Hence, S3D and S3S can improve insight into the effect of ram mass on: (I) pile penetration (for both dry and saturated conditions); (II) wave propagation (for both dry and saturated conditions); (III) excess PFP generation/dissipation (for saturated conditions only). Compared to S2D and S2S, impact velocity, particle velocity and internal pile force are reduced for S3D and S3S. Moreover, compared to ram mass II, ram mass III is slightly longer, thus impact time is slightly increased with respect to S2D and S2S. Additionally, due to the increased hammer mass, the force at the top of the pile will degrade slower with time for S3D and S3S. Despite the aforementioned differences in impact velocity, impact time and force degradation rate, it is expected that the total energy transferred to the pile for S3D and S3S is in the same order as S2D and S2S. However, this statement should be verified through dynamic wave analysis (see 4.2.1) by the use of strain gages and an accelerometer, both of which are attached to the pile. If this approach is proven successful, by mutual comparison of S2D and S3D, respectively S2S and S3S, Hypothesis III can be further researched. This comparison would also yield particularly interesting results into the difference between the use of a small hammers at high capacity or a large hammer at low capacity, as has also been researched by Ozsu *et al.* (2013) ([86]). Finally, mutual comparison of S3D and S3S can yield further insight into the effect of pore fluid and thus aid the (dis)prove of Hypothesis I.

M2D and M2S are the first two sets of multi blow tests which are executed with ram mass II and respectively use dry (M2D) and fully saturated (M2S) soil samples. Unlike the repeated single blow tests, physical phenomena in the pile and soil are free to interact. Tests are executed at two model frequencies, namely: (I) 10 *Hz*; (II) 15 *Hz*. At prototype scale these frequencies translate to 12 *blow/min* and 18 *blow/min*. This is lower than conventional hammering frequencies for offshore projects ($\approx 40 blow/min$). Due to technical limitations, a further increase of the hammering frequency beyond 15 *Hz* is inhibited without extensive revisions to the test matrix. Apart from frequency, energy per blow is also varied, respectively between 1.87 *J/blow* and 2.80 *J/blow*. For both M2D and M2S, the frequency and blow rate variations yield 4 possible test configurations. Hence, it is possible to individually assess the influence of hammering frequency and energy per blow. Furthermore, as two out of the four test configurations match in terms of energy flux *[J/s]*, it is possible to compare high energy driving at low frequencies to low energy driving at high frequencies (similar to *HiLo driving*). This comparison could provide insights valuable to the answering of Hypothesis II. Mutual comparison of M2D to M2S will further demonstrate the influence of pore fluid on the driving process.

M3D and M3S form the second two sets of multi blow tests and are executed with ram mass III, respectively on dry (M3D) and fully saturated (M3S) soil samples. Tests are carried out at the same frequencies as M2D and M2S (10 *Hz* and 15 *Hz*). Similar to the repeated single blow tests carried out with ram mass III, the fall height for the multi blow tests carried out with ram mass III is reduced with respect to M2D and M2S to match the respective levels of energy per blow. Hence, for both M3D and M3S, four test configurations have been included in Table 6.1. Like M2D and M2S, the latter allows the effect of hammering frequency and energy per blow to be studied separately. As two out of the four test configurations match in terms of energy flux *[J/s]*, it is possible to compare high energy driving at low frequencies to low energy driving at high frequencies (similar to *HiLo driving*). This comparison could provide further insights valuable to the answering of Hypothesis II. By comparison of results from M2D and M3D, respectively M2D and M3S, Hypothesis III can be further researched. Finally, mutual comparison of M3D to M3S will further demonstrate the influence of pore fluid on the driving process.

Complementary to the test matrix presented in Table 6.1, another four saturated single test are part of the test plan. The prime objective of these tests is to deepen the insight into the processes which influence the generation of either excess or tensile PFP inside the soil. Additionally, the timescales associated with both the generation and dissipation of the aforementioned hydrostatic pressure deviations are of interest. Table 6.2 provides an overview of the employed test configuration during execution of the saturated single blow tests. Unlike the tests detailed in Table 6.1, aforementioned complementary single blow tests are not repeated to obtain a full depth profile; they consist of one single blow administered to the pile at a known embedment level. The latter also explains the dedicatory identification labels (starting with *T* instead of *S*).

Important remarks regarding Table A.1

- For statistical relevance, it is preferred (see PREF in Table A.1) to repeat the tests presented in Table A.1 several times. However, at this point it is not clear whether this is possible in the given time frame.
- The energy per blow has been determined based on a calculation which assumes no resistance during the free fall of the ram mass. Hence, the conversion fo potential to kinetic energy is 100% efficient. It is acknowledged that this assumption may not adequately reflect reality thus, in the worst case, demanding a revision of the calculations and test parameters;
- The use of loosely packed sand has been omitted due to practical difficulties. Placement on the set-up in the centrifuge as the start-up procedure have both demonstrated to influence soil packing. Moreover, a dense soil configuration is more representative of that commonly

Test [-]	**Acceleration** [g]	**Type** [SINGLE /MULTI]	**Ram mass** [-]	**Frequency** [Hz]	**Energy/blow*** [J] (**Capacity** [%])	**Energy flux** [J/s]	**Relative packing** [LOOSE/DENSE]	**Saturation** [%]
T2SXL	50	SINGLE	II; 140 g	n.a.	2.80 (100%)	n.a.	DENSE	100
T3SXL.I	50	SINGLE	III; 220 g	n.a.	1.87 (42%)	n.a.	DENSE	100
T3SXL.II	50	SINGLE	III; 220 g	n.a.	2.80 (67%)	n.a.	DENSE	100
T3SXH	50	SINGLE	III; 220 g	n.a.	1.87 (42%)	n.a.	DENSE	100

* Please note that this is the kinetic energy carried by the ram mass at an infinitesimal instant before impact (assuming no friction during fall). Hence, it is not equal to the net energy administered to the pile E_T. Theoretically, if driver system efficiency η_{ds} and the friction regime during the drop is the same, values for E_T should coincide. Experiments should establish whether the latter statement holds or if hammer stroke should be reevaluated.

Table 6.2: Test matrix extension

found in the field. The influence of soil packing on drivability is thereby not considered. As a consequence of the dense soil configuration both tip and shaft resistance are expected to increase. Furthermore, the development of compressive pore water pressures is likely less pronounced, which could thereby counteract the development of a liquefied zone in the soil body. In the worst case, due to prevented dilation, tensile PFP are developed which effectively increase soil strength and thus further impede the driving process. If present, this effect is likely most pronounced near the tip. Due to cyclic shearing along the shaft, the interface layer (heavily remoulded soil matrix, largely composed of fragments) is likely to compact. The limited thickness of the interface layer shortens drainage time, which further reduces the likelihood of constrained dilation. Regardless, tensile PFP development is arguably exclusively observed in the upper part of the soil column, where overburden pressure is not a limiting factor to dilative behavior.

- The possibility to execute tests at $30g$ to better approach HiLo frequencies at prototype scale has been considered. Due to the increased influence of the boundaries at lower g-levels and reduced prototype dimensions, which would augment the likelihood of pile plugging significantly, the decision was made to execute the tests a $50g$.
- Due to limitations of the set-up it is not possible to increase the hammering frequency above 15 *Hz* (model scale). At prototype scale, the latter translates to roughly 18 *blow/min*. New HiLo driving methods reach prototype frequencies of 60-70 *blow/min*, which would require a model blow rate of $\approx 50-59Hz$. The possibility to extrapolate results to from frequencies has been considered. However, data procurement at a sufficient number of frequencies is an extensive process. Moreover, the extrapolation process in itself is cumbersome and often does not produce ideal results. Especially seen the large difference between the attained driving frequency and the frequency required to genuinely speak of HiLo driving. Consequently, the latter option is abandoned beforehand.

7

Results

7.1. Introduction

In this chapter, the results that were obtained during execution tests mentioned in the test matrix (shown earlier as Table A.1) are presented. However, due to new insight with respect to the capabilities of the centrifuge actuator, the aforementioned matrix is subject to several revisions. Therefore, prior to discussing the results of the centrifuge experiments, the reason underlying the aforementioned alterations and the justification of the adopted method of revision are discussed in **??**. The aforementioned section also includes a note on the incorporation of another four, saturated, single blow tests in the tests matrix, alongside the respective configuration of these tests. Hereafter, the experimental results are addressed. Here, two district parts can be distinguished, namely: (I) (repeated) single blow tests, 7.3; (II) the ensemble of tests from the test matrix, multi-blow tests, **??**. The former category is further subdivided into two sections: (I) Dry, repeated single blow tests; (II) Saturated, (repeated) single blow tests. Forgoing sections are respectively labeled as 7.3.1 and 7.3.2. For further information regarding the employed sensors, consult 5.2.3.

7.2. Important remarks with respect to the data acquisition and processing

Due to the large number of tests and elaborate comparison of results, a clear baseline with regard to which data portions permit the most representative comparison to be made. Generally speaking, the latter entails homogenizing both sample preparation and sample installation. The most important remarks with regard to the three aforementioned proceedings are summarized below in appropriate sections, respectively in 7.2.1 and 7.2.2.

7.2.1. Homogenization of sample preparation

To limit variation in the samples used during for the centrifuge experiments, the preparation of both dry and saturated samples is conducted in agreement with a well-defined routines. Both routines can be found entirely in 5.4.1 and 5.4.2, respectively. As all tests are ideally carried out on specimens with $D_r \approx 80\%$, an acceptance criterion with regard to the target relative density was formulated. Samples, which (by means of calculation) demonstrate to fulfill $78 \leq D_r \leq 82$, are approved for centrifuge testing.

7.2.2. Homogenization of sample installation

Due to the presence of an acceleration curve in the centrifuge, consistent installation of the pile at a predetermined distance from the centrifuge center is essential. Any deviation from this target position has implications on: (I) initial soil resistance, variation of the pile position, provokes a change

in the initial soil resistance; (II) impact velocity, the hammer uses the centrifugal forcefield to built momentum following its release; a different initial position has an effect of the average acceleration of the ram following and consequently also on impact velocity. Consequently the pile installation procedure is standardized. Key aspects of the installation procedure include:

- Raising the motor housing to the highest position prior to installing the pile;
- Insertion of the pile into the soil only when it is standing up straight. The latter prevents disturbance of the soil surface due to tilting of the pile (which could giev rise to the formation of wedges near the top of the sample);
- Embedment of the pile up to the desired level through a series of gentle pushes. While the motor housing remains in top position, the embedment process continues until the (bottom of the) ram mass' notch sits at the 50 mm demarcation line on the motor housing. For the repeated single blow tests, the aforementioned value marks the intimal penetration level, where the pile tip is radially located at 1.029 m from the centrifuge center. For the multi-blow tests, initial embedment in increased by another 20 mm, up to a distance of 1.049 m from the centrifuge center. If the initial penetration level is unintentionally exceeded during pile installation, the deviation (overshoot) is recorded and considered when post-processing the experimental results.

7.3. (Repeated) single blow tests

This section addresses the experimental results from the (repeated) single blow tests on both dry and saturated samples of $D_r \approx 80\%$. As previously mentioned, four saturated single blow tests were added to the research' scope; predominately to improve the understanding of generation and dissipation of deviatoric PFP and quantify the associated timescales. Specifics relating to the test configuration employed for the aforementioned tests are listed in Table 6.2. The remaining experiments are classified as repeated single blow experiments, which are purposefully executed at driving frequencies well below those commonly used in practice, specifically at a blow frequency of 0.33 Hz (model scale) which equates to a blow rate of 3.6 $blow/min$ at prototype scale. The drastic decrease in driving frequency with respect to conventional driving rates, allows for the elimination of interaction between dynamic phenomena in both the pile and the soil, chiefly: (I) interaction of stress (and associated strain) waves in the anvil and pile; (II) interaction of vibrations in the soil body, specifically in the form of S-, P- and R-waves; (III) Accumulation compressive or tensile pore fluid pressure fluctuations (exclusively for saturated tests), and their influence on the prevailing effective stress regime. To verify the aforementioned claim and thus assess the extend to which the decrease in blow frequency successfully inhibited the occurrence of the three aforementioned phenomena, sensory data from the load cell, accelerometer and static pore fluid pressure sensors (SPFPS) is examined in this section. As the precise sensory configuration slightly differs between tests, Table 7.1 provides an overview of the installed sensors equipment per test. To improve clarity and comprehensiveness, the data of the repeated single blow tests split into two categories, namely: (I) Dry, repeated single blow tests; (II) Saturated, (repeated) single blow tests. Respectively, test types are addressed in a separate section, specifically 7.3.1 and 7.3.2.

7.3.1. Dry, repeated, single blow tests

To determine whether the decrease in blow frequency to 0.33 Hz is adequate to allow the system to return to a steady state prior to re-excitation by the subsequent blow, load cell and accelerometer signals are presented for the four repeated single blows tests on dry specimens. Respectively, the sensory signals for the 10th blow of the sequence are presented in Figure 7.1 and 7.2. Please observe that the leading part of the sensory signal was trimmed up to the point of excitation. The latter explains why there is an apparent difference in the length of the signals for different tests. Due to the way in which the data was recorded, a signals consists of 800 samples at most. As is inferred

Test ID	LC [-]	LC Type [-]	ACC [-]	ACC Type [-]	SPFPs [-]	# SPFPs [-]	SPFPs depth [mm]
S2DXL	V	DRY	V	60K	X	n.a.	n.a.
S2DXH	V	DRY	V	60K	X	n.a.	n.a.
S3DXL	V	DRY	V	60K	X	n.a.	n.a.
S3DXH	V	DRY	V	60K	X	n.a.	n.a.
S2SXL	V	DRY	V	60K	V	3	60; 80; 90
S2SXH	V	DRY	V	60K	-	3 (0)	(60); (80); (100)
S3SXL	V	DRY	V	60K	V	3 (2)	60; (80); 100
S3SXH	V	SAT	V	60K	-	3 (0)	(60); (80); (100)
T2SXL	V	SAT	X	n.a.	V	3	60; 80; 100
T3SXL.I	V	SAT	X	n.a.	V	3	60; 80; 100
T3SXL.II	V	SAT	X	n.a.	V	3	60; 80; 100
T3SXH	V	SAT	X	n.a.	V	3	60; 80; 100

Table 7.1: Overview of sensory instruments installed for (repeated) single blow tests; X = not installed; - = installed but (partially) faulty; V = installed, operational. Please not that the depth of the SPFPs (as listed in the last column) is with respect to the upper extremity of the strongbox.

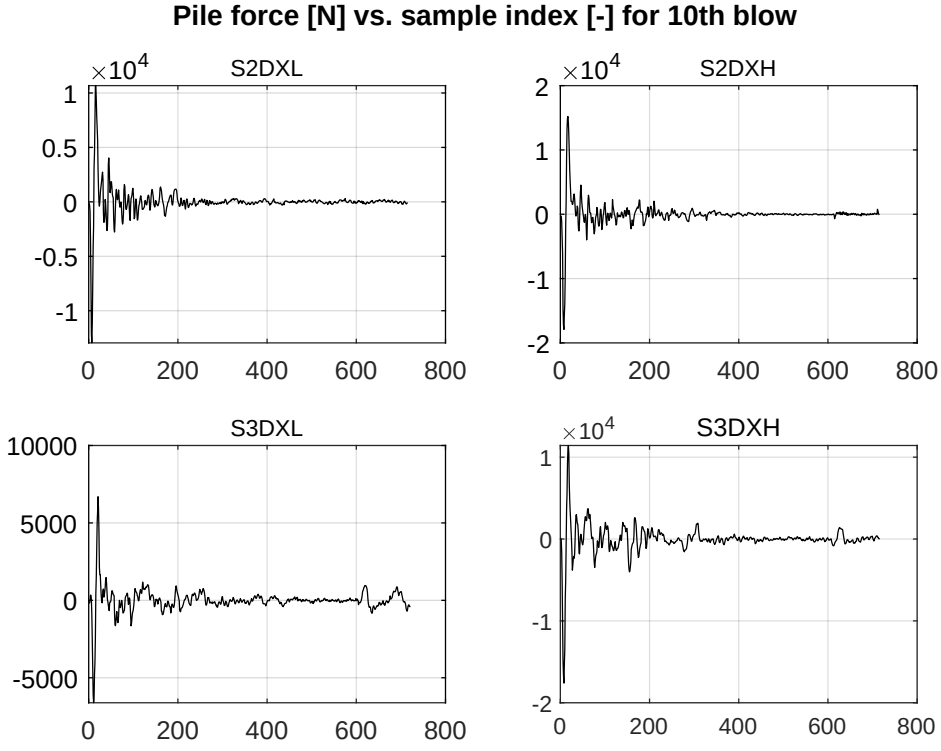

Figure 7.1: Load cell signals (pile force [N] versus sample index [-]) for the 10th blow of the four repeated single blow tests on **dry** soil specimens.

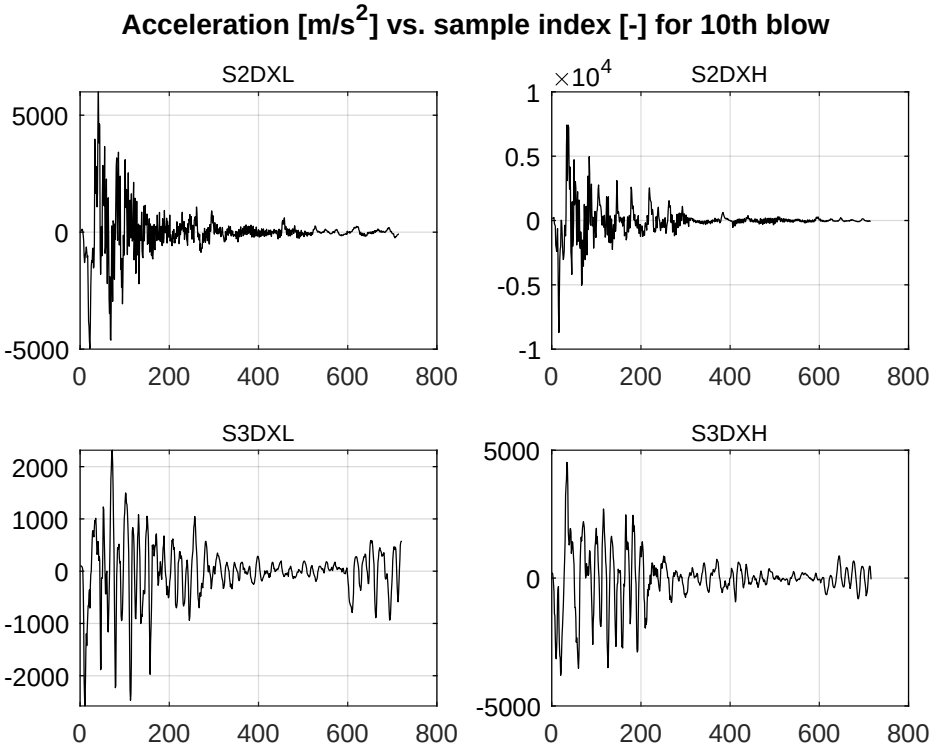

Figure 7.2: Accelerometer signals (acceleration $[m/s^2]$ versus sample index [-]) for the 10th blow of the four repeated single blow tests on **dry** soil specimens.

from Figures 7.1 and 7.2, sensory excitation returns to <5% of the steady state condition at the end of final sample index. Both the load cell and accelerometer were sampled at a rate of 230 *kHz* on the fast ADC system. Due to memory restrictions, sensor output was not continuously recorded but in bursts of 800 samples. A threshold value of 200 *bits* for the output of the load cell was used to determine when a sampling burst should be initiated. Considering the maximum signal length and the measurement frequency, each signal represents a time frame of ≈3.5 *ms* (before trimming). This is ≈1% of the time interval between subsequent blows. Consequently, it stated that stress wave reflections in the pile and driving system are dissipated by the time the next blow is initiated.

Apart from the time associated with the dissipations of wave reflections, Figure 7.1 provides several other interesting insights. The first observation considers the clear effect of the increment in falling height between S2DXL and S2DXH as well as S3DXL and S3DXH. In both instances the magnitude of the initial compression peak is 100-200% larger when the falling height is increased. This observation is in line Equation 4.17, which ensued from the work of Smith (1960) [105] and describes the dependency of the initial peak force to the impact speed (which, in turn, is related to falling height). The second observation relates to the shape of the load cell signals as shown in Figure 7.1. For all signals, the compressive force peak which marks the beginning of the signal, is followed by a tensile peak of approximately the same magnitude. The duration of both peaks is comparable and amounts to ≈35 μs, which is about 50% of the anticipated time for the reflection of initial strain wave to reach the sensors (mounted at the top of the pile). Apart from the seemingly compressed time scale of the aforementioned peaks, the magnitude of the tensile force peak by itself is another oddity as it implies that the incoming strain wave is nearly fully reflected at the pile's tip. Following the conclusions of Massarsch *et al.* (2008) ([78]), similar measurements are exclusively recorded in the absence of both shaft and tip resistance. Naturally, the latter is impossible and consequently

gives reason to believe that an issue with the load cell itself lies at the heart of the observed oddities.

The previously mentioned hypothesis is strengthened by the fact that signals from the load cell mounted to the pile used for saturated experiments, does not display the same type of behavior. Te aforementioned pile was installed during test S3SXH and one of the recorded signals is depicted by the bottom left frame of Figure 7.3. Here, the amplitude of the tensile strain peak is decreased to a reasonable level, which explicates the effect of soil resistance during driving. Moreover, the onset of tensile strain peak occurs ≈70 μs after the anvil-pile system was struck by the ram mass, which coincides with the theoretical estimate based on the phase velocity (see Equation 3.9) and the length of the pile. However, the magnitude of the compressive peak, as well as the total excitation time of the sensor, are comparable between the two load cells. Therefore, although the shape of the load cell signal is arguably not representative of reality, quantitatively the signal is deemed realistic.

Now, considering the accelerometer signals as shown in Figure 7.2, the inspection of shape and magnitude of the obtained signals is repeated. Clearly, the accelerometer signals are more volatile than those of the load cell. This kind of behavior is also seen for the PDA systems which are used in during the installation of monopiles in reality. Additionally, the shape of the obtained signals expresses a larger degree of variation. However, similar to the load cell, a negative sensory spike consistently marks the initiation of the signal. Similar to the load cell, pile accelerations also demonstrates a clear positive correlation with impact velocity. The negative acceleration corresponding to the leading spike, describes the brief instant where the top of the pile assumes the same particle velocity as the ram mass. Following the initial excitation of the sensor, complex wave patterns develop which not of interest to this research. Yet, the magnitude of the acceleration signal is of importance. Through multiplication of force and acceleration and subsequent integration over the dwell time, it is theoretically possible to compute the energy transferred to the pile. However, upon inspection of the signals shown in 7.2 it is clear that the amplitude of the recorded acceleration (≈200 g) is limited. Provided that amplitude of the load cell is of the right magnitude, it is determined that recorded acceleration is one order of magnitude too small. Consequently, the quantification of the piling energy along the lines of the Equation 4.26, does not yield satisfactory results. The aforementioned analysis found a driver system efficiency η_{ds} (see Equation 4.27) of <1%. It is expected that by mounting of accelerometer on an extruded, aluminum block, the acceleration of the pile is not accurately captured. As a result of a non-rigid connection between the pile and the extruded block, the pile and mounting block form a two-bodied system. Differences in geometry and impedance of the two bodies make that the behavior of the second body (to which the accelerometer is mounted) is not representative of that of the first (the pile).

7.3.2. Saturated, (repeated) single blow tests

Similar to the dry, repeated single blow tests, the legitimacy of the claim that steady state conditions prevail at the time of impact is verified for the saturated, (repeated) single blow experiences. To this end, load cell, accelerometer and SPFPS signals are closely inspected. As besides four repeated single blow tests, another four regular single blow tests were carried out, the respective results are separately discussed in the paragraphs below.

Saturated, repeated single blow tests As is clear form Table 7.1, the SPFPS which record PFP during the execution of the four, saturated, repeated single blow tests, only captured meaningful data for tests S2SXL and S3SXL. Consequently, only SPFPS data is presented for aforementioned two tests. Yet, both load cell and accelerometer data is presented for all experiments, respectively in Figure 7.3 and 7.4. As expected, the observation made with regard to the results form the load cell and accelerometer also apply to saturated test conditions. With the exception of the load cell data for test S3SXH, all tests explicate a tensile force spike of inexplicable magnitude (following the impact of the ram mass) as well as the apparent doubling of the phase velocity in the pile. As indicated

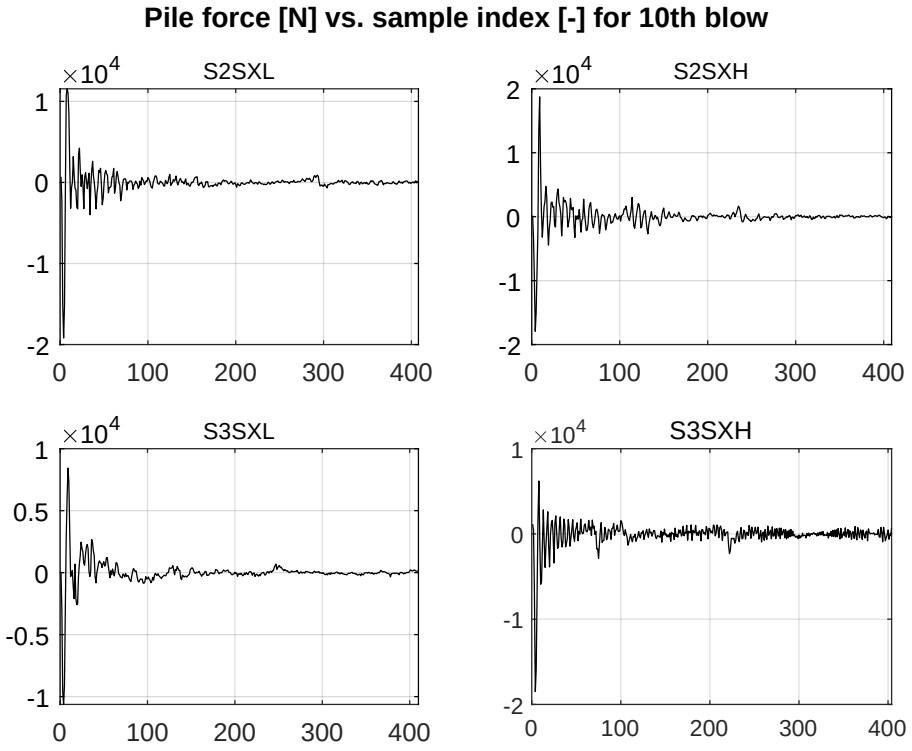

Figure 7.3: Load cell signals (pile force [N] versus sample index [-]) for the 10th blow of the four repeated single blow tests on **saturated** soil specimens.

in 7.3.1, both observations arguably point towards an intrinsic flaw of the load cell itself. This hypothesis is further strengthened by as the model pile intended of dry soil conditions was also used for the following saturated tests: S2SXL, S2SXH and S3SXL. As based on Figure 7.3, the shape of the force signal is seemingly not affected by the saturation of the soil sample. Hence, it is unlikely that shape alterations of the force trace corresponding to test S3SXH, are exclusively due to saturated test conditions. Yet, despite the oddities in the signal of dry load cell, two aspects of the signal are deemed representative: (I) the global magnitude of the force signal; (II) the clear increase in peak compressive force as a result of the increase in falling height, as demonstrated by the bottom two frames of Figure 7.3.

Behavioral trends of the accelerometer also largely coincide with those regarding the repeated single blow tests on dry samples. As shown in Figure 7.4, all signals are initiated by a large negative peak, signifying the brief moment where the top section of the pile assumes the same velocity as the ram mass. Subsequently, a more chaotic acceleration pattern emerges which is characteristic of accelerometers used to record accelerations during pile driving. In terms of magnitude, the signals seems unrelated to the type of ram mass. However, a clear correlation with falling height is observed, as was also the case for the load cell data (present in Figure 7.3). The latter observation is logically compatible with the increased falling height, which augments the impact velocity of the ram mass. Though this trend is clearly visible from the data, like before in 7.3.1, the absolute magnitude of the obtained signals is too low and does not yield reasonable results when used to quantify efficiency of the energy transfer between hammer and pile η_{ds}.

The SPFP data for test S2SXL and S3SXL were recorded continuously at a apparent frequency of 1 *kHz*. Due to minor differences in the global PFP trends captured by the SPFPS during aforementioned tests, solely the the data realting to test S2SXL is addressed in the following. Figure 7.5

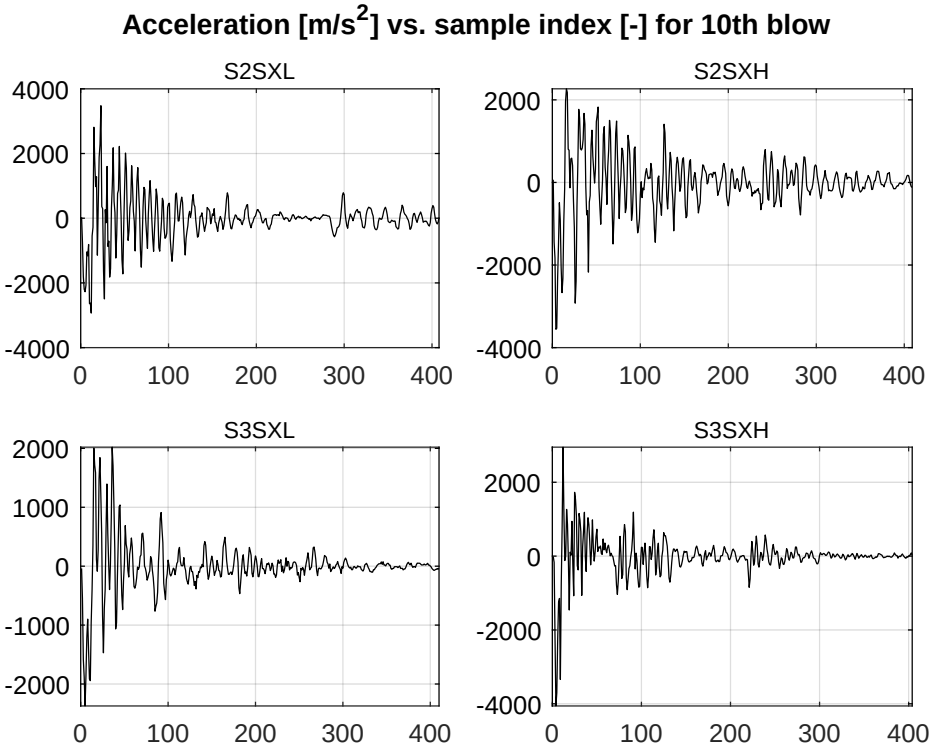

Figure 7.4: Accelerometer signals (acceleration $[m/s^2]$ versus sample index [-]) for the 10th blow of the four repeated single blow tests on **saturated** soil specimens.

show the evolution of PFP as a function of model time for test S2SXL. The portrayed pressures are recorded by three sensors embedded a fixed distances from the upper extremity of the strongbox. Moreover, the sensors are located at three distinct radial distances r_{min} from the pile shaft. Further details on the properties and placement of the SPFPs is provided by 5.2.3. Form Figure 7.5 it follows that over the course of the experiment, the net change in PFP equals 0 *kPa*. Evidently, in absence of accumulation of deviatoric PFP for all three sensors, the prevalence of steady state conditions prior to announcement of the subsequent blow is warranted. Moreover, large compressive and tensile PFP spikes are recorded directly after impact of the ram mass. Both are arguably related to the transmittance of P- or S-waves and possibly associated reflections from the strongbox boundaries. Due to the data logging frequency of 1 *kHz*, the Nyquist frequency is limited to 0.5 *kHz*. Provided the a lower boundary estimate of the propagation speed of P- and S-waves in wet sand, respectively 1500 and 400 *m/s* [79]; and a nominal sample radius of 0.15 *m*, the timescales associated with the propagation of these waves lie well above the Nyquist frequency. Due to aliasing it is therefore impossible to say which (combination of) event(s) lies at the heart of the aforementioned observation. Additionally, due to measurement frequency limitations, both the tensile and compressive spike are not consistently present in the signals shown in Figure 7.5. The latter is also illustrated by Figure 7.6, where the compressive PFP spike is not present in the signal corresponding the shallowest SPFPS for the 10th blow of test S2SXL. Additionally, the single blow data demonstrates the temporal generation of deviation PFP following the impact of the ram mass. As is clear form Figure 7.6, the recorded soil response differs between sensors. Where SPFPS1 and SPFPS2 record compressive PFP, SPFPS3 explicates the development of tensile PFP. The aforementioned observations are seemingly in line with the general expectation pattern, namely: dilation of the dense soil matrix for regimes with low overburden pressure and net contraction (excess PFP development) for high overburden pressures.

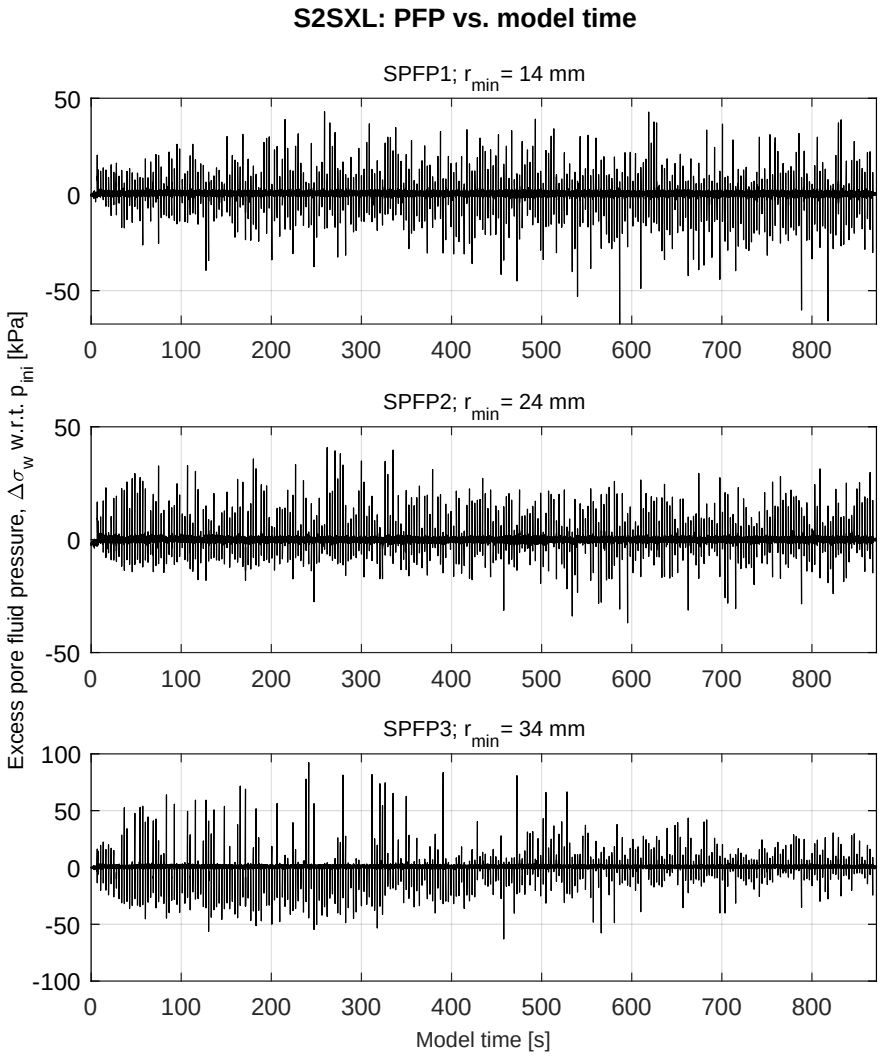

Figure 7.5: Deviatoric pore fluid pressure (w.r.t. hydrostatic pressure at the depth of embedment) as a function of model time for test S2SXL. Data was recorded at 1 *kHz*.

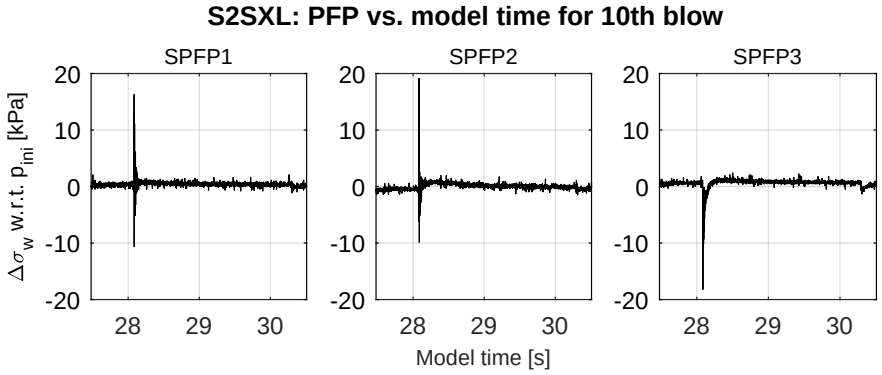

Figure 7.6: Deviatoric pore fluid pressure (w.r.t. hydrostatic pressure at the depth of embedment) for 10th blow of test S2SXL. Data was recorded at 1 *kHz*.

Yet, due to the limited distance between the sensors of 20 *mm* (model scale), which equates to 1 *m* at prototype scale; the increase in overburden pressure is limited. Moreover, following the conclusion of Azua-Gonzalez (2017) [12], pronounced fluctuations of PFP related to undrained shear associated with pile driving, are exclusively expected in the near field. Further strengthening the believe that the constrained dilation underlying the tensile PFP measured by SPFPS3, is related to local shear planes in the vicinity of the sensor. Although not part of this report, the aforementioned notion is supported by the observation of abrupt PFP deviations during spin-up of the centrifuge. Considering that samples were densified through shock wave compaction (as discussed in 5.4.2) and provided the dimensions of the SPFPS (20x20x20 *mm*), a decreased level of in the vicinity of the SPFPS is a real possibility.

Provided the aforementioned information, it is impossible to ascertain the representativity of compressive nor dilative soil behavior in the far field and its underlying causes when based solely on the information following from Figure 7.6. Therefore, focus is shifted towards the timescale associated with full dissipation of the PFP fluctuations from the SPFPS closest to the pile. Foremost based on the frame corresponding to SPFPS2form Figure 7.6, the dissipative timescale equates to approximately 1-1.5 *s* (model time) following impact. Translated to prototype scale, full dissipations under similar soil conditions takes 50-75 *s*. Based on the latter statement, the undrained response of the soil opens a window for accumulation of deviatoric PFP, provided an excitation interval is <1 *s* at model scale. Consequently, the blow frequency must exceed 1 *Hz* or 1.2 *blow/min* at prototype scale.

Saturated single blow tests In this section the PFP measurements corresponding to four saturated single blow tests are discussed. Details of the test configuration for the aforementioned tests are listed in Table 6.2. Details regarding the use of sensory equipment are included in Table 7.1. Like the repeated single blow tests on saturated samples, data is measured continuously using BOX2 of the Fast ADC at a rate of 1 *kHz*. PFP data is presented for each test individually. Hence, Figure 7.7, 7.8, 7.9 and 7.10, respectively show the PFP data obtained for test T2SXL, T3SXL.I, T3SXL.II and T3SXH. In the following, the data corresponding to SPFPS1 from test T3SXL.II (Figure 7.9) is disregarded.

Upon in inspection of Figure 7.7, 7.8, 7.9 and 7.10, the most striking communality interests the compressive PFP which is recored by all sensors following the impact of the ram mass. With respect to antecedent hydrostatic conditions, recorded PFP increments are generally higher than those recorded for the repeated single blow tests also discussed in 7.3.2. Specifically for test T3SXL.I and T3SXH, the increment amounts to >15 *kPa*. Especially for an R_d of ≈80%, it is not likely that the observed stressed are due to undrained shearing of highly compacted sand. Instead, it is believed that micro failures were triggered in the zones around the SPFPS upon impact of the hammer. Due to contraction of the soil matrix, as a result of a lesser degree of compaction in the vicinity of the pore fluid sensors, high excess PFP were generated. Similar PFP fluctuation were observed for the leading ±5 blows of the repeated single blow tests on saturated samples, which points towards the presence of weak zones in the sample following the completion of the spin-up procedure. Thereafter, following the start of driving, P- and S-waves emitted from the pile initiate the contraction of weaker zones in of the soil skeleton, leading to a local increase of PFP. Hence, although the observations are explainable, they are arguably not representable of soil behavior associated with dynamic pile driving.

Although the representativity of the qualitative results in under debate, the data from the saturated single blow tests does contain valuable informations relating to the recovery of hydrostatic pressure conditions following the end of driving. Particularly Figure 7.8 and 7.10 show dissipation times within the 1-1.5 *s* range, which is comparable to the results obtained for the repeated single blow tests despite of a significant differences in initial deviatoric pressure. As the dissipation of deviatoric PFP is governed by an exponential decay, the limited variation in the total dissipation time

is reasonable. However, dissipation times inferred from the signals of SPFP2 and SPFP3 associated with T2SXL and T3SXL.II are estimated to be about 30% larger than previously discussed. Judging by Figure 7.7 and 7.9, the majority of this increase is accounted for by the delayed onset of excess PFP following impact of the ram mass. The latter has two likely explanations: (I) the sensors is located close to a zone of net contraction, leading to a delayed perception of the associated PFP fluctuation. (II) The soil matrix around the sensors is distorted due to the effects of contraction; yet, due to a more substantial distance from the epicenter, the soil skeleton is deformed gradually instead of abrupt.

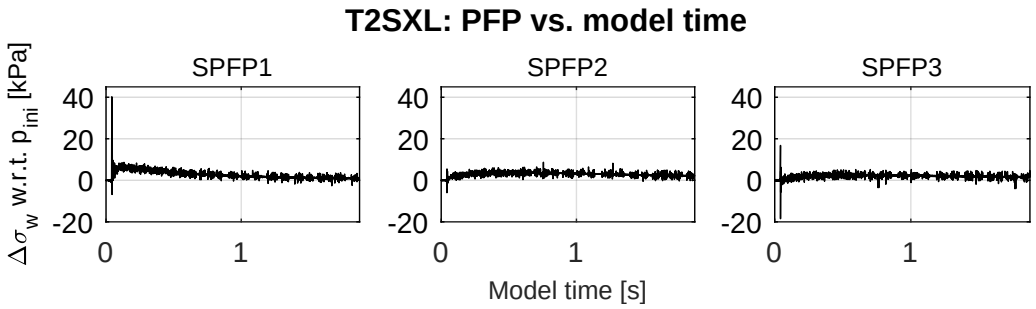

Figure 7.7: Deviatoric pore fluid pressure (w.r.t. hydrostatic pressure at the depth of embedment) for test T2SXL.

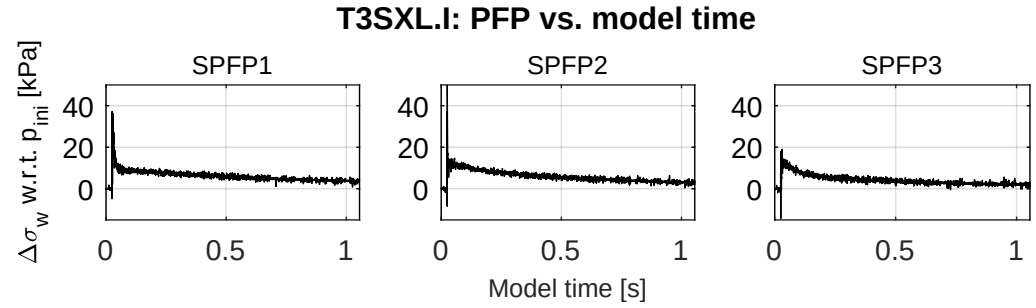

Figure 7.8: Deviatoric pore fluid pressure (w.r.t. hydrostatic pressure at the depth of embedment) for test T3SXL.I.

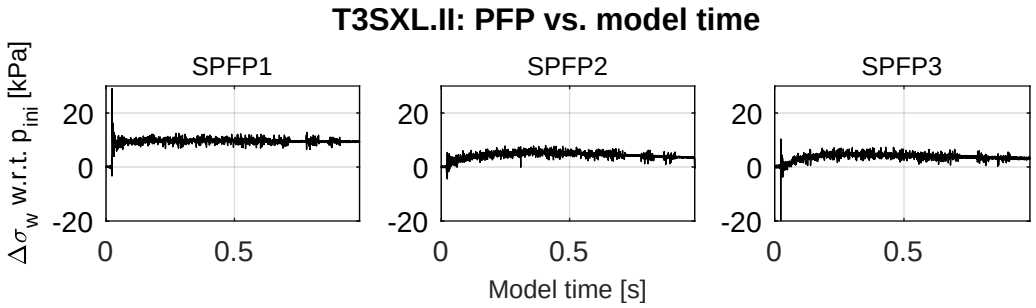

Figure 7.9: Deviatoric pore fluid pressure (w.r.t. hydrostatic pressure at the depth of embedment) for test T3SXL.II.

7.3.3. Concluding remarks

Based on the results discussed in the foregoing sections, several conclusions are drawn relating to both the effectiveness and the quality of the associated tests. Firstly, it is evident that the dissipation time regarding the reflection of strain waves in the pile as well as movement of the pile itself, plays out on minute timescale directly following the start of driving. Judging by the observations, afore-

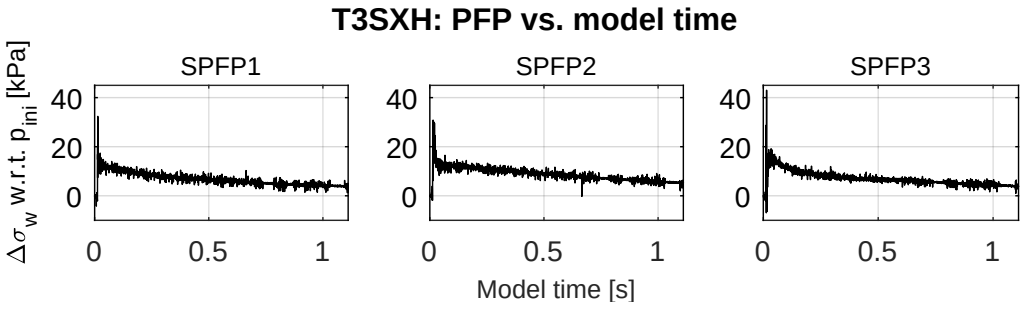

Figure 7.10: Deviatoric pore fluid pressure (w.r.t. hydrostatic pressure at the depth of embedment) for test T3SXH.

mentioned effects dissipate in <4 *ms*. The latter implies the penetration of the pile also happens within the first few *ms* following impact. Consequently, the large shear rates are exerted on the material surrounding the shaft. For a hypothetical scenario in which the pile moves 0.5 *mm* following impact, the average particle velocity amounts to 0.125 *m/s*. According to Garnier & Konig (1998) [41] the typical shear band thickness is equals $10 \cdot d_{50}$. For GEBA sand, this yields a shear band thickness of 1.03 *mm*. Now, assuming the particles of the outer shear band extremity remain stationary whilst those closest to the pile follow its respective movement, the shear rate (quotient of particle velocity over the shear band thickness) equals ≈120 *1/s*. Conclusions by Quinten (2019) ([92]) indicate that at a nominal shear rate of 120 *1/s* a >10% decrease in the apparent viscosity of the HPMC viscous fluid used for the experiments is expected. This leads to a temporal mismatch in scaling of dynamic time and dissipation of deviatoric PFP, unrealistically promoting the dissipative processes. As a consequence, the generation of devaitoric PFP is arguably disadvantaged, which could explain the modest changes in PFP. Yet, it is safe to state that the full dissipation of strain waves seized prior to the initiation of the subsequent blow.

Similar conclusions are drawn regarding the dissipation of generated deviatoric PFP in the soil body surrounding the pile. Although arguably influenced by the shear thinning of vicious fluid, nominal timescales relating to the aforementioned process equate to 1-1.5 *s*. The latter indicates that the blow frequency allows for full dissipation of deviatoric PFP between blows, which is confirmed by the experimental results as no accumulative effects are visible in Figure 7.5. Additionally, it is observed that large the dissipation of larger pressure fluctuations do not take noticeably longer than small ones. This observation is linked to the exponential decay of deviatoric PFP over time; which also strengthens the believe that (if present) excessive dissipation of PFP due to scaling inconsistencies would have had a minor effect on the determined dissipative timescale. Following this observation, the anticipated frequency required for accumulation of deviatoric PFP is set at >1 *Hz*, which translates to 1.2 *blow/min* at prototype scale. The latter notion increases the likelihood of observing accumulated PFP for both 10 and 15 *Hz* experiments as indicated in Table 6.1.

Quantitatively, the most representable results were obtained by the load cells on both the dry and saturated pile. Signals recorded by the former load cell show an unfamiliar particularity in the form of large tensile strain peaks following the initial excitation of the system. Moreover, the timescale relating to the relevance of the aforementioned tensile strain peak, is ≈35 μs after striking the pile. Phase velocity in the pile is underestimated by a factor of 2 in the latter case, which is unlikely. Moreover, the tensile peak in similar magnitude as the leading compressive spike. Following the observations by Massarsch *et al.* (2008) [78], this indicates limited soil resistance of at both the shaft and tip of the pile, which is also refutable. The latter leads to the believe that unlike the load cell mounted to the pile for saturated experiments, the dry load cell is faulty in terms of signal shape.

Although data recorded by the SPFPS is not faulty, it is seemingly distorted due to local soil failures in the vicinity of the sensors. Due to the sizable dimensions of the SPFPS, the effectiveness of shock wave compaction in the vicinity of the sensors was likely affected, creating zones of low

D_r in the soil body. Both during spin-up of the centrifuge and administration of the first (repeated) single blows, excess PFP were recorded, which is a clear indication of contractive soil behavior. This hypothesis was strengthened as identical behavior was observed in the far-field too. Findings of Azua-Gonzalez (2017) [12] indicate that the PFP response is exclusively affected by soil shearing when recored in the vicinity of shear zones associated with dynamic pile driving (most notably those along the shaft and surrounding the toe). The effects of soil shearing were however also noticed in the signals from SPFPS located in the far-field, pointing towards the unthought-of source.

Finally, the quantitative results of the accelerometer are about one order of magnitude too small. The latter inhibits the combined use of load cell and accelerometer signals to determine the energy transmitted to the pile and associated η_{ds}. The rigidity of the connection between the mounting block for the accelerometer and the pile shaft is arguably the source of the aforementioned discrepancy. The accelerometer signal is distorted due to the degraded rigidity of the connection between the mounting block an the pile shaft, due to differences in geometry and impedance between of the resulting two-bodied system, the true pile response is lost.

7.4. Evolution of PFP during multi-blow experiments

In this section, the PFP measurements obtained during the execution of the saturated multi-blow experiments from Table 6.1 are presented. Despite of the modifications which were made to Table 6.1 to guarantee proper operation of the actuator, it was found that the penetration rates associated with the execution of test M2SHH and M3SHH were of such magnitude that the servo-system failed to track the penetration of the pile in a satisfactory manner. Consequently, test M2SHH and M3SHH were not performed. Hence, the results of six multi-blow experiments are discussed in the following. As the PFP results between tests are comparable to a large extend; in the following, the data analysis and interpretation are solely considers test M2SLL. Figures corresponding to the remaining five tests are part of Appendix B. In 7.4.1 various plots are presented to infer the evolution of PFP as a function of time and radial distance. General conclusions with regard to the aforementioned PFP trend in both space and time and their respective influence on the driving operation are part of 7.4.2. The locations of installation of the SPFPS w.r.t. the upper extremity of the sample container, as well as (radially to the projection of) the pile shaft are provided by Table 5.4.

7.4.1. PFP analysis for test M2SLL

As part of the verification process of the SPFPS, readings the PFP recorded at 50g under static conditions is compared to expected PFP derived from theory. The aforementioned comparison is illustrated by Figure 7.11, where the total stress, effective stress, and the hydrostatic PFP distribution are presented. Please consider that due to the effects of the gravity curve, pressures are not linearly dependent on on the height of a fluid or soil column. Based on Figure 7.11 is it clear that for all sensors, the deviation between anticipated and measured PFP is limited and within the acceptable margin. This statement also applies to the PFP data recorded by the SPFPS for the other saturated multi-blow experiments, corresponding figures are provided in Appendix B. Consequently, it is inferred that SPFPS are performing as supposed and provide realistic insight into the distribution of PFP in the soil sample.

During the experiments the data of the SPFPS was recorded by two separate measurement systems, namely: (I) a low frequency data acquisition system which works with s program called MP3, the nominal frequency of measurements equals 2 *Hz*; (II) a high frequency data acquisition system operating at 1 *kHz*. Although the value of the low frequency measurements is limited for analysis purposes, it does provide insight into the global evolution of PFP over the duration of the test. Consequently, a plot displaying the evolution of PFP as a function of radial distance is include as Figure

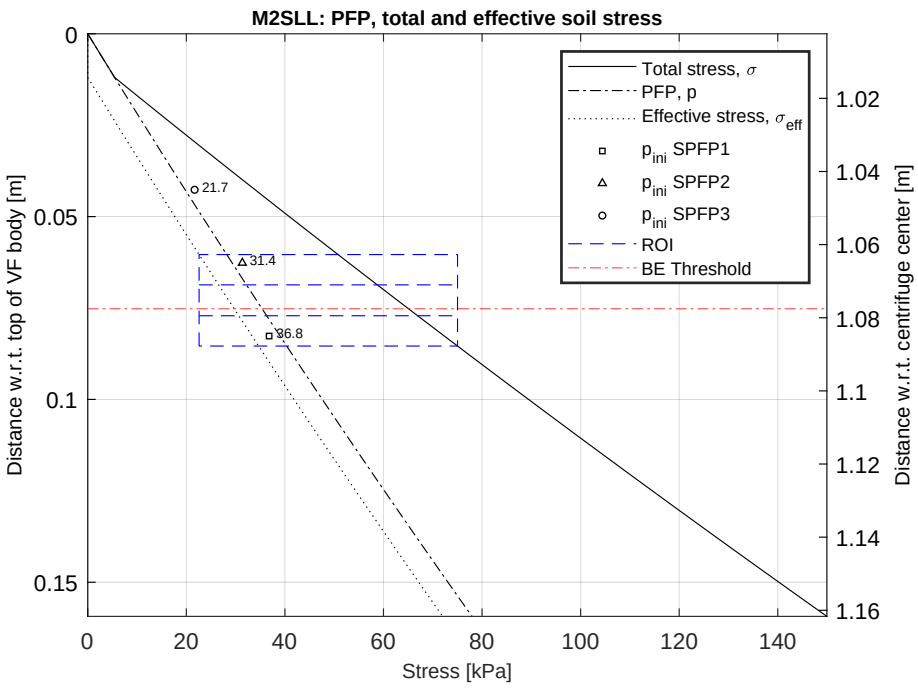

Figure 7.11: Evolution of total stress, effective stress and PFP with depth for M2SLL provided a static test condition at 50g in the centrifuge. For completeness, the radial distance with respect to the center of the centrifuge is shown on the left y-axis.

7.12. The radial distance δ_r is calculation in accordance with Equation 7.1.

$$\delta_r = \sqrt{dr^2 + \delta_z^2} \tag{7.1}$$

Where dr is the radial distance between the tip of the SPFPS and the (projection of the) pile shaft. Unlike δ_r, dr is always perpendicular to the (projection of the) pile shaft. Furthermore, δ_z is the vertical distance between the plane perpendicular to the pile tip at any given moment during pile driving, and the plane which horizontally dissects the considered SPFPS in two equal parts. In order to comprehensively illustrate the evolution of PFP as a function of radial distance, Equation 7.1 is slightly modified. The result is depicted as Equation 7.2. Figure 7.12 employs the distance computed by Equation 7.2 and plots it against the respective deviatoric PFP measurement. The deviatoric PFP is the deviation of the PFP measured during driving, relative to the hydrostatic pressure at the start of the test, which is quantified for all three SPFPS (as p_{ini} in Figure 7.11).

$$\delta_r^* = \begin{cases} \sqrt{dr^2 + \delta_z^2} - dr, & \text{for } \delta_z \geq 0 \\ \sqrt{dr^2 + \delta_z^2} + dr, & \text{for } \delta_z < 0 \end{cases} \tag{7.2}$$

Based on the spacing between the markers in the subplots of Figure 7.12, it is evident that pile penetration is highest right after the initiation of the driving procedure. As the pile penetrates further into the soil, the penetration rate decreases as a result of a larger resisting force along the shaft and at the tip. Consequently, the distance covered in the fixed measurement interval is decreased, explaining the smaller spacing between the markers. Right after the first blow, all SPFPS record an increase of ≈ 10 *kPa* with respect to the initial hydrostatic pressure condition. The magnitude of the global increase in PFP is evidently related to the driving frequency. For test M2SHL (Figure B.5), which is executed at 15 *Hz* instead of 10 *Hz*, the global increase amounted to $approx16$ *kPa*. Hence, it seems that the reduction of the available time to dissipate excess PFP, allows for further accumulation of

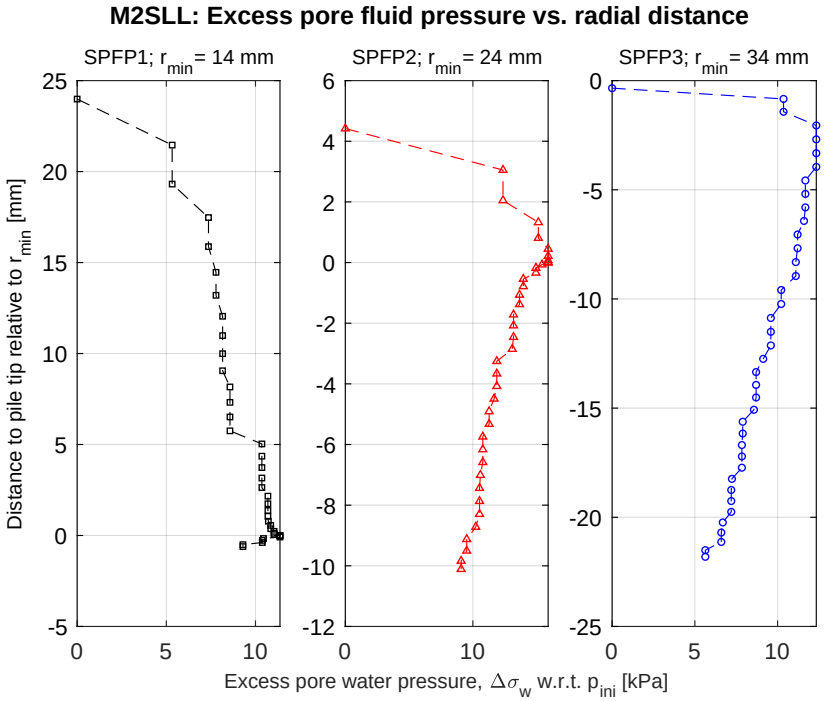

Figure 7.12: δ_r^* versus deviatoric PFP (measured at low frequency). Please observe that through the definition of δ_r^*, the y-value is negative when the pile tip has surpassed the level at which the sensor is installed. r_{min}, as depicted above each subplot, is equivalent to the variable *dr* used in the report.

PFP up to point where a new equilibrium is reached between generative and dissipative processes. As comparable PFP are recorded by all SPFPS (at various locations in the soil body), the excess PFP are likely generated by a single, centralized source which affects the entire soil mass in a similar fashion. In this respect, the P- and S-waves propagating from the pile are arguably the source of the observations. Hwang *et al.* (2001) ([57]), also states that compressions due to stress waves lead to the generation of excess PFP throughout the surrounding soil mass. As the all SPFPS are relatively close to the pile, it is sensible that the observed PFP deviations are about the same for all sensors. However, when the deviatoric pressure is expressed as a quotient of effective stress under hydrostatic conditions, it is found that the excess PFP ratio R_u decreases with depth. The latter indicates that liquefaction potential is highest in the upper region of the soil mass. Judging by the increase in PFP for higher driving rates, there is a real possibility that a state of liquefaction is reached in the upper soil regions for frequencies which were not explored by the test plan.

Apart from the relatively constant deviatoric PFP recorded at different depth and radial distances from the pile, all three SPFPS show an increase in deviatoric PFP while the pile tip moves towards the sensor ($\delta_z \geq 0$ for Equation 7.2). The gradual increase of PFP for consecutive blows was also observed by Iskander (2010) ([58]). Right at the point where the depth of the pile coincides with the depth of the sensor, the deviatoric PFP reaches a maximum. Under continued penetration, this behavior is reversed an the deviatoric PFP reduces as the pile distances itself from the sensor. Arguably, the energy content of the P-waves emitted from the tip of the pile is direction dependent, where waves which propagate deeper into the soil have a higher energy content than those emitted upward in the soil column.

For a more detailed picture of PFP development over the course of the driving operation, the high frequency measurements of the SPFPS are analyzed in a similar fashion. Figure 7.14 explicates the high frequency PFP recording from the three SPFPS on the same set of axis as Figure 7.12. Globally, Figure 7.14 shows the same trend with regard to the evolution of deviatoric PFP during

driving as Figure 7.12. As was also observed for the high frequency recording of the SPFPS for the repeated single blow tests in 7.3.2, each blow causes introduces narrow spikes of large magnitude on in the PFP signal, which appear so rapidly that at the current sampling rate of 1 *kHz*, they are not consistently recorded. Due to the limited sampling frequency it is impossible to distinguish which phenomena is responsible for the observation of these spikes. However, the most likely candidates are P- and S-waves. For both waves types, the propagation velocity is too high to make a differentiation based on the available PFP measurement.

Arguably, what follows after the observation of the spikes is more relevant to this research. Particularly the the high frequency measurement of SPFPS1 shows a relatively strong decrease of deviatoric PFP right after impact. This behavior is most for $10 \leq \delta_r^* \leq 18$ and implies the occurrence of constrained dilation within the aforementioned zone. This observation is related to the high state of compaction as well as the relatively large shear stresses associated with these planes. The observations are relateable to the presence of failure plains which fan out from the pile tip into lower regions of the soil body; the shear rate concentrations in these zones, together with the high relative density of the sample, favor dilation. Provided the sensor is close enough, the generation of tensile PFP in the vicinity of the failure planes is registered. Based on the range of δ_r^*, it is established that observations coincide with $17 \leq \delta_z \leq 29$ *mm*, of which the upper bound provides a rough indication of the depth to which failure planes extend for open-ended piles. This values equates to ≈35% of the depth at which the onset of bottom boundary effects is reported for closed-ended piles by Prakasha *et al.* (2005) ([91]). At larger radial distances, SPFPS2 and SPFPS3 demonstrate the generation of excess PFP during the first blows. As the tip of the sensor is closer to the bulky housing of the sensor, the recorded excess PFP can also be related to soil compaction around the housing due to a lower degree of compaction. Yet, as soon as the pile surpasses the embedment level of the sensor, the skewed PFP recordings (either towards dilative or contractive deviatoric PFP) are substituted for symmetric PFP fluctuations around a slightly elevated value with respect to hydrostatic conditions. The aforementioned behavior is maintained by R-waves radiating outward from the pile over consecutive blows.

Finally, deviatoric PFP are recorded at the pile shaft by means of optical PFP sensors (OFPFS). The OFPFS inserted into capillary tubes, which in turn are partially embedded in the pile shaft. The capillaries are filled with silicon oil and the top sealed off using water resistant polymer glue. Provided the capillary if fully sealed, the incompressibility of the oil enables the full transfer of pressures fluctuations at the interface to the OPFPS. However, under the influence of the high g-levels, oil was forces from the capillaries, yielding unusable measurements. The aforementioned effect is clearly visible for OPFPS3 in Figure 7.13. Upon the completion of the spin-up of the centrifuge, oil is forced out of the capillary; the resulting pressure dissipation is captured by the sensor. Yet, OPFPS2 proves that the method of installation has potential, as the reading remains stable after reaching 50g. Additionally, despite of the limited sample rate, OPFPS2 captures the accumulation of tensile PFP at the interface over a set of consecutive blows. At its peak, the under-pressure is ≈40 *kPa*, a decrease of about 80% with respect to hydrostatic conditions. Hence, it is cautiously stated that for samples with D_r=80%, as used for this research, the accumulation of excess pore water pressures in the vicinity of the pile is non-existent. Hence, a state of soil liquefaction is seems to be ruled out. Additionally, sensory results indicate that the accumulation of tensile PFP is a real possibility. Consequently, the suitability of high frequency driving in very dense sand arguably results in lower piling rates due to the progressive increase of the effective soil regime in the direct vicinity of the pile. Unfortunately, the limited resolution of the OPFPS inhibits the further exploration of the tensile PFP generation at the interface.

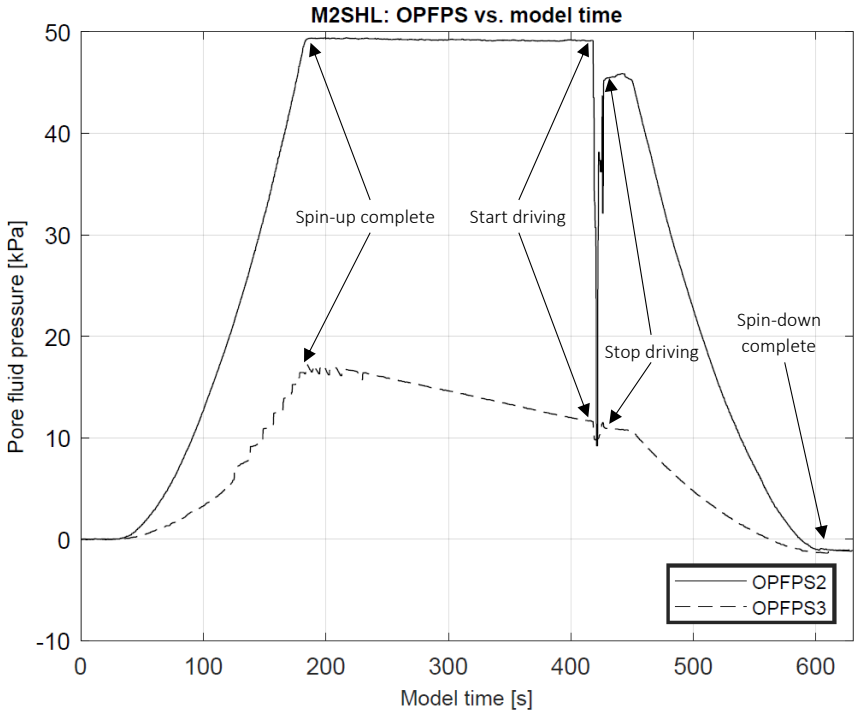

Figure 7.13: Evolution of PFP as measured by OPFPS2 and OPFPS3 for test M2SHL.

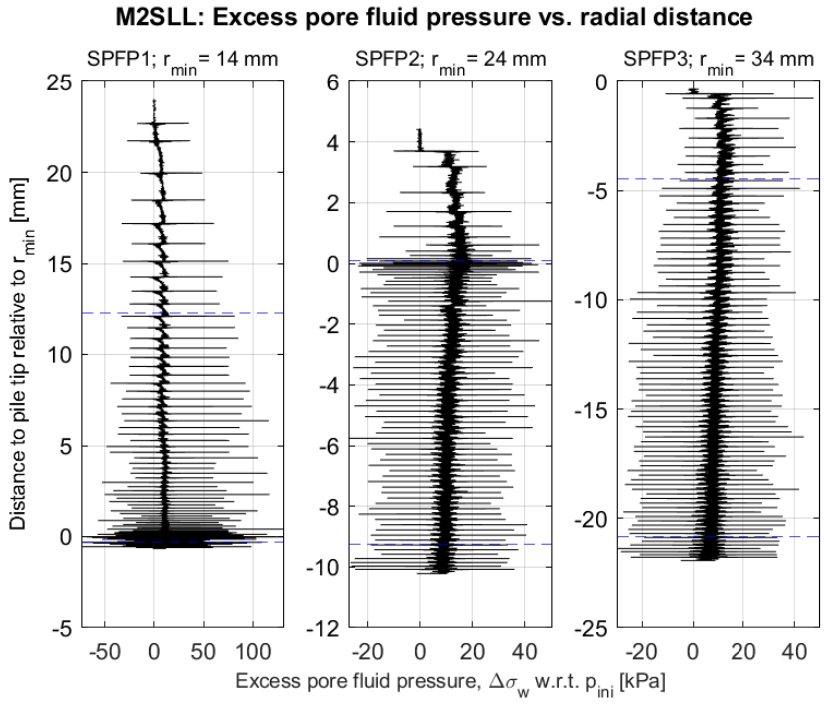

Figure 7.14: Radial distance δ_r^* versus deviatoric PFP (measured at 1 *kHz*). lease observe that through the definition of δ_r^*, the y-value is negative when the pile tip has surpassed the level at which the sensor is installed. r_{min}, as depicted above each subplot, is equivalent to the variable *dr* used in the report. Dashed lines indicated the ROI as determined in accordance with C.2 for the respective test.

7.4.2. Concluding remarks

The results of both low and high frequency SPFPS measurements as well as low frequency OPFPS data related to the execution of multi-blow experiments, yield valuable insights with regard to processes underlying observed PFP fluctuations during impact pile driving. At larger radial distances, the global trend in the evolution of PFP during the piling operation is adequately captured by low frequency measurements. Aforementioned measurements demonstrate a rather uniform increase of the PFP with respect to hydrostatic conditions in the soil body surrounding the pile, which more importantly exhibits a clear correlation to driving frequency. The uniform increase in PFP is likely due to the combined effect of P- and S-waves, which compress the soil skeleton and thereby enable the generation of excess PFP. In this respect, Hwang *et al.* (2001) ([57]) reached comparable conclusions.

Additionally, there is a directional dependency between pile displacement and the net change in excess PFP. Excess PFP are consistently increased up to the point where the depth of the pile coincides with the installation depth of the sensor. Under the effect of continued pile driving, the net increase in excess PFP makes room for a net decrease. The aforementioned effect is observable up to a radial distance of at least 34 mm (with respect to the pile shaft) and 55 mm (with respect to the center of the pile). Arguably, the observed trend is related to a directional dependency of the energy content of the P-waves, emitted from the pile's tip. Based on the observations, there is reason to believe that P-waves which propagate deeper into the soil body have have a higher energy content than waves which travel towards the soil surface.

Similar to the high frequency measurements of PFP for repeated single blow tests, signals show an abrupt spike in PFP directly following impact of the ram mass. A time scale analysis indicates that the most P- and S-waves are likely to lie at the heart of this observation. Yet, arguably, the PFP trends which follow after short-lived spike are more indicative of soil behavior relevant to the pile driving operation. For SPFPS1, which is installed closest to the pile, tensile PFP are observed as the pile progresses towards the sensor. The effect is best observed in for $10 \leq \delta_r^* \leq 18$ and fades for continued pile penetration. Arguably, for the aforementioned range, the sensor lies within of close to a shear plane related to the failure mechanism below the pile. Based on the observations, it is likely the onset of bottom boundary effects in about 50% lower than advocated by Prakasha et al. (2005) ([91]). Hence, at about one pile diameter.

Finally, through the use of OPFPS, it is inferred that constrained dilation occurs at the pile interface while driving. Although based a single observation, there is reason to believe that for high R_d samples, that accumulation of tensile PFP is a real effect. Due to this accumulation, radial soil stresses are temporarily increased resulting in higher resisting forces during driving and arguable lower penetration rates. Contrary to the anticipated benefits of high frequency driving with regard to liquefaction, as stated by hypothesis III, it seems that R_d plays a key role in the determination of the best pile driving technique. In this sense, HiLo driving is not a generic tool to improve pile drivability under all circumstances.

7.5. Pile drivability analysis

As mentioned in 6.3, three hypothesis were formulated to explain the ostensible efficiency improvement of dynamic pile installation through the use of HiLo driving techniques, as implied by the observation relating to a case study on pile drivability conducted by Anusic *et al.* (2016) ([6]). The hypotheses, which are founded on an extensive literature study targeting pile drivability, are concisely listed below:

- Improved drivability through the accumulation of excess PFP, which decreases effective stresses in the vicinity of the pile; consequently lowering driving resistance.
- Implementation of the HiLo technique entails the simultaneous decrease of energy per blow and increase driving frequency while maintaining the total energy input, as illustrated by

Equation 7.3.

$$E_{\text{Conv}} = E_{\text{HiLo}} \implies f_{\text{Conv}} \cdot E_{\text{Conv}} = f_{\text{HiLo}} \cdot E_{\text{HiLo}} \implies \frac{E_{\text{Conv}}}{E_{\text{HiLo}}} = \frac{f_{\text{HiLo}}}{f_{\text{Conv}}} \tag{7.3}$$

Where E and f, respectively denote energy per blow and frequency. Additionally, subscript $_{\text{Conv}}$ and $_{\text{HiLO}}$ indicated whether the aforementioned parameter applies to conventional of HiLo driving. It is expected that the increased driving frequency (for HiLo driving), the exposes the soil to a higher number of load cycles which arguably aid the degradation of shaft resistance through a process called friction fatigue.

- As a result of lower energy input per blow, the particle velocity of the pile following impact is reduced. Consequently, the development of (velocity related) dynamic soil resistance is reduced with respect to conventional driving techniques which employ larger hammer strokes. The latter implies more the efficient, ameliorating pile drivability.

To assess the validity of the hypotheses listed above, the intended interpretation methodology is discussed in 6.6. The approach entails a significant number of test-by-test comparison to differentiate between the respective effects on drivability of: (I) frequency fluctuation; (II) falling height adjustment; (III) hammer type; (IV) HiLo vs. conventional driving technique. However, during execution of the tests it was found that practical challenges complicated both the achievement and retention the intended test parameters. The aforementioned statement chiefly applies to driving frequency and impact velocity. Respectively, both parameters where unwillingly influenced by the following phenomena: (I) a reduction of the driving frequency following the release of the ram mass. As the frequency controller is bound by a tuning response time to adapt to the situation where the ram mass is displaced by the flywheel, blow frequency is not constant for a substantial part of the test; (II) Due to lag between pile movement and servo-system response as well as friction variation between the guiding rod and ram mass, the kinetic energy carried by the ram mass at an infinitesimal instant before impact, varies within and between tests. The influence of both processes makes it impossible to draw unambiguous conclusions relating to the influence of the variation of a single driving parameter. Consequently, it is decided collectively assess the influence of energy per blow and driving frequency on drivability through contour plots. This process is conducted separately for dry and saturated experiments. Additionally, to differentiate between the influence of the type of hammer used, aforementioned plots are drafted independently for ram mass II and III.

As data from a large number of tests is simultaneously compared in each contour plot, the inherent differences between tests are appreciated through the calculation of a normalized, non-dimensional drivability coefficient Ψ. Section 7.5.1 provides further background in relation to the definition and determination of Ψ. To enable a fair comparison between experiments, it is important that penetration intervals on the basis of which Ψ is calculated are comparable in terms of soil stress conditions (and consequently stress-dependent soil parameters). The aforementioned interval is henceforth referred to a the region of interest (ROI). Section C.2 elaborates upon the general definition of the ROI as well as its respective determination for all tests from Table 6.1 (excluding M2SHH and M3SHH). To maximize the sample population for the contour plots, the ROI is divided into three subsections for which Ψ is calculated. Consequently, the other two contour plot parameters should be computed for each of the ROI segments too. The specific parameters are: (I) the mean driving frequency, $\overline{f}$; (II) the mean impact (kinetic) energy per blow, $\overline{E}_{kin}$. The associated determination processes are described in 7.5.2 and 7.5.3 respectively. Following the definition of all contour plot parameters, the contour plots themselves are presented and discussed in 7.5.4. Finally, 7.5.5 provides concluding remarks with regard to the obtained contour plots and the preceding data analysis.

7.5.1. Normalization and nondimensionalization of pile drivability

Following the establishment of the ROI in accorandance with C.2, focus is now shifted towards the normalization and nondimensionalization of pile driavability. As mentioned before, this process in conducted both for the entire penetration interval and the ROI corresponding to each experiment form Table 6.1. For most tests, fluctuations of driving frequency and energy per blow fluctuations are observed. As both parameters arguably have an influence on pile drivability, the ROI is subdivided into three segments of equal length. This has several advantages, most predominantly: (I) due to the definition of several subintervals, averaging of the driving frequency and energy per blow over the interval yields more representative results. Both of the aforementioned parameters are used when drafting the contour plots; (II) Instead of a single drivability coefficient for the entire ROI, three separate coefficients are obtained, each respectively relating to a subsection of the ROI. Consequently, the number of data points to draft the contour plot triples, resulting in better mesh definition.

The drivability coefficient Ψ is determined in accordance with Equation 7.4 and has no physical dimension.

$$\Psi = \tilde{p} \cdot \frac{\overline{\sigma}'}{\overline{\sigma}^*} \cdot \frac{\overline{w}}{\overline{w}^*} \tag{7.4}$$

Where $\tilde{p}$ is the non-dimensional pile penetration rate in [-], as calculated in accordance with Equation C.3 from C.3.1. Furthermore, $\overline{\sigma}'$ and $\overline{\sigma}^*$ respectively concern: the mean (effective) stress at the center of the considered (full) penetration interval or ROI segment; the reference total stress corresponding to the center of the entire ROI. Where the ROI is defined as a depth profile of length dw_{norm} of which the upper extremity coincides with $w_{adj,\,ini}$. This definition is also used for tests where due to limitations in dw_h, $w_{adj,\,ini}$ was reduced to accommodate for dw_{norm}. Finally $\overline{w}$ and $\overline{w}^*$ represent: the mean penetration depth of the pile at the center of the considered (full) penetration interval of ROI segment; the reference penetration depth corresponding to the center of the entire ROI.

Due to the way in which Ψ is defined, both the depth trend in the (effective) stress and the increase of shaft surface taking part in interaction with the surrounding soil body, are accounted for. Additionally, due to the definition of the ROI with respect to the SSL, $\overline{\sigma}^*$ is highly comparable between tests whereas $\overline{w}^*$ is constant. It should be noted that $\overline{\sigma}^*$ is always determined based on the dry bulk weight of the soil. The latter is done to enable the comparison of the drivability coefficient between dry and saturated experiments. As the bulk density of saturated material is higher, this would increase the total stress and thus influence negatively impact the second quotient of Equation 7.4. However, if this effect is unaccounted for, the drivability of saturated tests is disproportionately reduced (compared to dry tests) and thereby introduces ambiguity in the comparison of dry and saturated experiments. Furthermore, it is noted that Equation 7.4 does not account for stress dependency of soil parameters between dry and saturated tests. Hence, to some extend ambiguity is an inherent part of the comparison of experimental data associated with dry and saturated tests.

7.5.2. Determination of mean driving frequency

In this section the determination of the mean driving frequency $\overline{f}$ for each segment of the ROI is discussed. As mentioned in the introduction of 7.5, the ability of the frequency controller to readily adapt to changes in the power demand by the engine, is bound by a tuning response time of a few dozens of blows. Consequently, the blow frequency is not constant and below the ideal value for a significant part of the experiment. The latter statement is clearly explicated by the figures relating to blow frequency for multi-blow tests in C.4. Globally the frequency decrease following the release of the ram mass is in the order of 40-60% with respect to the ideal frequency. Independent of the desired blow frequency (either 10 or 15 *Hz*), the ideal frequency is achieved 70-100 blows after the release of the ram mass. Due to the long adaptation period, the ROI often resides partially in range where the frequency is not constant. As it is attempted to relate the normalized, nondimen-

sionalized drivability coefficient to driving frequency per ROI subsection, the observed fluctuations complicate this process as the frequency is not constant over the considered interval. It was found that by setting the length of the ROI subsections to 25/3 *mm*, the inherent fluctuation of blow frequency is within reasonable bounds. Additionally, the length of the ROI is sufficient to restrict the influence of faulty measurements of $\overline{f}$. Consequently, $\overline{f}^{j}$ is calculated in accordance with Equation 7.5 for each ROI segment (indexed by *j*).

$$\overline{f}^{j} = \frac{\sum_{i=1}^{n} f^{\mathrm{i,j}}}{n} \tag{7.5}$$

Where $f^{i,j}$ is the frequency corresponding to blow i of ROI subsection j and n is the total number of blows required to bridge the distance between the upper and lower boundary of the *j-th* ROI subinterval.

Another observation, independent of the variable driving frequency over the experiment, considers stabilization of the driving frequency before the desired frequency is reached. From C.4, this behavior is exemplified by (amongst others) Figure C.61, C.85 and C.73. Globally, the frequency deficiency is in the order of 15% when compared to the ideal value. However, expressed as a percentage of the frequency difference between the low (10 *Hz*) and high (15 *Hz*) frequency experiments, it amounts to ≈40%. The latter raises some concerns about the ability to truly investigate drivability as a function of driving frequency. As after accounting for the aforementioned effect, a very small difference of about 3 *Hz* remains between high and low frequency experiments. Arguably, a lower than anticipated battery voltage explains the frequency deficiency observed for several experiments as voltage is directly related to the amount power directed towards the engine.

7.5.3. Determination of mean kinetic energy per blow

In this section the determination of the mean kinetic energy per blow $\overline{E}_{kin}$ for each segment of the ROI is elaborated upon. Judging by the results presented in C, specifically C.4.2, it is clear that $\overline{E}_{kin}$ explicates a significant degree of variation. The aforementioned variation is both present between individual blows of the same experiment and between experiments. Several contributing factors are identified with respect to the latter observation, chiefly:

- Due to a time delay between the penetration of the pile and response of the servo-system, which is most pronounced at the start of the experiment, the stroke of the hammer deviates significantly from its ideal during the experiment. Due to the effective increase of hammer stroke, the impact velocity v_0 is influenced. This effect, in turn, causes fluctuations of the administered energy per blow.
- The friction between the ram mass and guiding rod is not constant over all experiments. For the repeated single blow experiments, unhardened steel guiding rods were used which explicated significantly wear. Consequently, it was decided to exchange the plain steel guiding rods for hardened examples. This change proved very effective as the abrasion of the guiding rods was significantly reduced. However, the decrease in abrasion seemingly influenced the efficiency of the hammer η_h as the aforementioned value lies at ≈45% for repeated single blow experiments, whereas the nominal efficiency of multi-blow experiments is ≈90%. It should be noted that the efficiency of the repeated single blow tests is based on a single tests as for all other tests, the quality of the signals used to compute v_0 was of inferior quality. Attempts to estimate v_0 for the affected tests by savaging parts of the signals were pointless, as is also explained in C.4.1. Yet, intuitively, the decrease in η_h as a result of abrasion of the guiding rod is sensible.
- Intrinsically, as a direct consequence of testing in the centrifuge, a gradual increase of v_0 is expected due to the radial dependency of centrifugal acceleration. As the pile penetrates the

soil during testing, it effectively distances itself form the centrifuge center. The same is true for the motor housing which drives the hammer as it is displaced by the servo-system in order to maintain hammer stroke during the test. Hence, effectively, the gravitational acceleration (integrated over the falling height) increases for a larger penetration depth. Consequently, the impact velocity of the hammer is also gradually increased.

Due to the influence of the aforementioned effects on v_0 it is sensible to average this value over a number of blows to obtain a representative estimate. In this respect, it is important that the interval is long enough to be relatively unaffected any outliers; yet, it should be short enough to have a negligible influence by global trends. Through consideration of both factors, the length of ROI subsections was eventually set to 25/3 *mm* (consult C.2 for the full ROI definition process). For each ROI subsection of each experiment, $\overline{E}^{j}_{kin}$ is computed in accordance with Equation 7.6.

$$\overline{E}^{j}_{\text{kin}} = \frac{\sum_{i=1}^{n} E^{i,j}_{\text{kin}}}{n} \tag{7.6}$$

Where $E^{i,j}_{kin}$ is the kinetic energy corresponding to blow i of ROI subinterval j and n is the total number of blows required to bridge the distance between the upper and lower boundary of the *j-th* ROI subsection.

7.5.4. Drivability contour plots

Following the establishment of a comprehensive framework with regard to the variables at the heart of the drivability analysis, specifically Ψ, $\overline{f}$ and $\overline{E}_{kin}$, respectively in 7.5.1, 7.5.2 and 7.5.3, contour plots are drafted. As was previously mentioned, the influence of energy per blow and driving frequency on drivability is conducted separately for dry and saturated experiments. Additionally, to differentiate between the influence of the type of hammer used, contour plots are drafted independently for ram mass II and III. Consequently, a total of four figures is presented in this section. Respectively, Figure 7.15, 7.16, 7.17 and 7.18 correspond to the following experimental subsets: (I) dry tests with ram mass II; (II) dry tests with ram mass III; (III) saturated experiments employing ram mass II; (IV) saturated experiments conducted with ram mass III. All variables required to draft the aforementioned figures are conveniently listed together in four tables. Respectively, Table 7.2, 7.3, 7.4 and 7.5 illustrate the data for experimental subsets I, II, III and IV.

Dry tests using ram mass II Figure 7.15 shows the contour plot for the ROI (segments) of all dry experiments executed with ram mass II. Grid points (x = $\overline{f}$; y = $\overline{E}_{kin}$) for which Ψ is part of Table 7.2 are indicated by an *x*. All 18 ROI subintervals are incorporated in Figure 7.15. For the high frequency tests, it is clear form Figure 7.15 that two distinct driving energies were used, namely: (I) ≈1.7 *J*; (II) ≈2.6 *J*. The aforementioned values are close to the ideal values from Table 6.1, which respectively amount to: (I) 1.87 *J*; (II) 2.80 *J*. Hence it is clear that the hammer efficiency is rather constant at ≈90%, a value which seems independent of the falling height and driving frequency.

Unlike for blow energy, it is impossible to distinguish the two frequency bands, which according to Table 6.1, should be present at: (I) 10 *Hz*; (II) 15 *Hz*. Instead, measurements are more or less evenly distributed over the frequency range 6-14 *Hz*. Hence it is clear that the ROI often lies (partially) within the range where the frequency controller has not yet managed to increase the driving frequency to the desired level of either 10 or 15 *Hz*. As a consequence, it is impossible conduct mutual comparisons between tests as effects of significant (and undesired) frequency fluctuations are distort the respective influence on drivability due to intentional variation of other driving parameters.

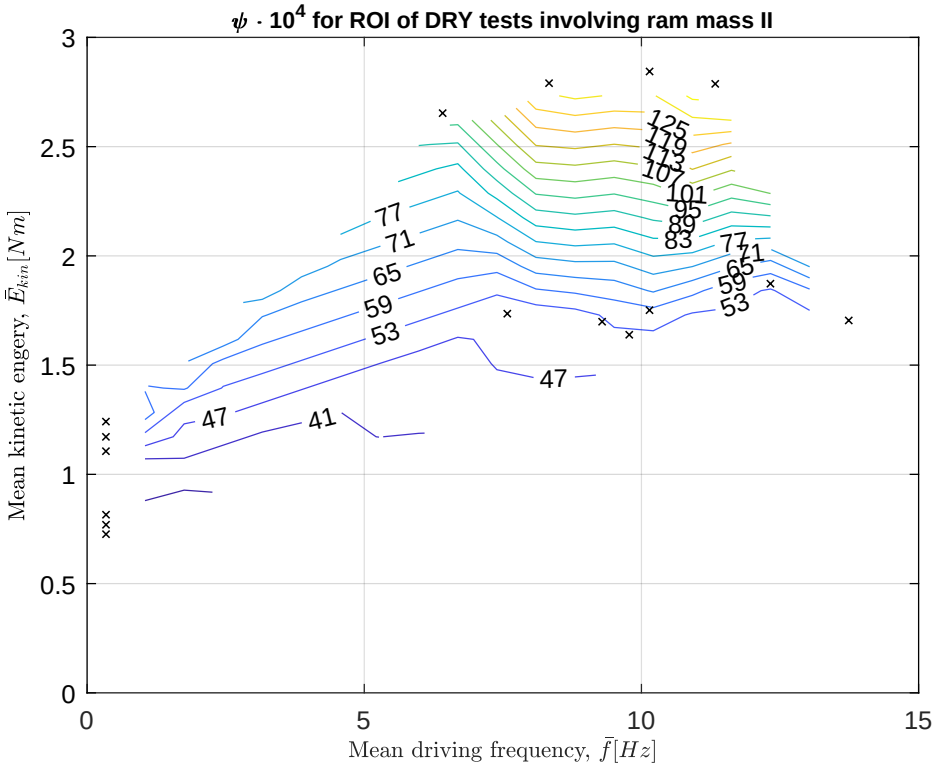

Figure 7.15: Ψ versus driving frequency and kinetic energy per blow for all **DRY** tests with ram mass **II**. *x* indicates combinations of $\overline{f}$ and $\overline{E}_{kin}$ for which Ψ has been computed. Aforementioned values are part of Table 7.2.

From Figure 7.15 is inferred that there is a linear dependency between normalized drivability and the kinetic energy per blow. Additionally, this observation seems independent of blow frequency. Implicitly, the latter statement indicates that an increment of impact velocity, which is associated with higher driving energy, has no appreciable effect on soil resistance as neither contraction nor divergence of contours is evident for higher pile energies. Consequently, the soil behavior inferred from Figure 7.15 does not illustrate a decisive negative correlation between increasing impact velocity and the drivability coefficient, as is implied by hypothesis III.

Additionally, Figure 7.15 does not provide decisive evidence with regard to the presumed increase of the effects of friction fatigue (and thus better drivability) for an increasing number of load cycles (higher frequencies). For the multi-blow experiments, drivability remains relatively constant when the driving frequency is increased from 8 towards 14 *Hz*. Arguably, the latter is due to a too small number of load cycles. However, White & Lehane (2004) ([118]) already perceived the effects of friction fatigue after a few dozens of load cycles, a number which was comfortably attained during the pile driving experiments. However, White & Lehane based their results on cyclic loading of a single specimen. In reality, the pile shaft is effectively lined with similar specimens which a cyclically loaded for each blow. As, the pile penetrates the soil, new elements are added. Consequently, the number of shear cycles experiences by the soil elements decreases as the elements get closer to the tip. Hence, at greater depths, the effects of friction fatigue are less pronounced while radial stresses are elevated. Consequently, the overall decrease is shaft friction, which predominantly occurs in the upper soil regions where radial stresses are the lowest, is arguable of sufficient magnitude yield an observable effect on pile drivability.

Dry tests using ram mass III Figure 7.16 shows the contour plot for the ROI (segments) of all dry experiments executed with ram mass III. Grid points (x = $\overline{f}$; y = $\overline{E}_{kin}$) for which Ψ is part of Table 7.2 are indicated by an *x*. Out of the 18 ROI subintervals, 14 are incorporated in Figure 7.15. Intervals M3DLL.i, M3DLH.i, M3DHL.i and M3DHH.i were excluded as the normalized drivability coefficient is for the first ROI segment is inexplicably high. Arguably, the confining stress condition of the of the pile segment embedded during the sample installation in the centrifuge, is not representative. Consequently, the shaft resistance is lower than anticipated which results in an increase of the normalized drivability coefficient.

Contrastingly to Figure 7.15 where two narrow bands of driving energy where seen, the driving energy for the multi-blow tests which are incorporated into Figure 7.16 is more scattered. The latter notion particularly applies to the low energy tests for which $\overline{E}_{kin}$ varies between 1.2 and 1.7 *J*. Additionally, like the dry experiments involving ram mass II, the frequencies at which the experiments were executed are not consistent and vary between 7 and 13 *Hz*. Lastly, higher driving frequencies, which are favored by the friction fatigue hypothesis, do not decisively yield a larger drivability coefficient.

When drivability coefficients are globally compared between ram mass II and ram mass III, the coefficients corresponding to tests executed with ram mass III tend to be higher for the same energy flux (product of frequency and energy per blow). Consequently, it is clear that more advantageous piling conditions prevail during use of a heavier ram. The latter observation is in line with the scientific consensus as, amongst others, Anusic *et al.* (2016) [6] reached similar conclusions in this respect. Although the aforementioned observation points towards the more efficient transfer of kinetic energy into piling energy for a heavier ram mass, this claim is not verifiable. The latter is due to the unsuitable signals from the accelerometer, which prevent quantification of the piling energy. As is also highlighted in Appendix E, a fair comparison between ram masses is only achieved when the energy delivered to the pile is comparable.

Saturated tests using ram mass II Figure 7.17 shows the contour plot for the ROI (segments) of all saturated experiments executed with ram mass II. Grid points (x = $\overline{f}$; y = $\overline{E}_{kin}$) for which Ψ is part of Table 7.4 are indicated by an *x*. All 15 ROI subintervals are incorporated in Figure 7.17. Similar to the Figure 7.15 and 7.16, Figure 7.17 explicates the use of two driving energy for the multi-blow experiments whereas a clear separation of driving frequencies is entirely absent. Moreover, drivability increases with $\overline{E}_{kin}$ in a practically linear fashion which is independent of the driving rate.

Arguably the most noteworthy observation which is based on Figure 7.17, considers the evident, quantitative decease of normalized drivability when compared to the dry experiments discussed in 7.5.4 and 7.5.4. Following the definition of the normalized, non-dimensional driavbility coefficient, Ψ is corrected for the prevalence of effective stress conditions for the saturated test as these are advantageous with respect to the total stress conditions, applicable to the dry experiments. Under fully drained conditions, an effective stress state favors drivability due to the associated reduction in radial stress. Remarkably, following the normalization of the non-dimensional drivability coefficients $\tilde{p}$, the obtained normalized coefficients are lower than those obtained for dry tests . Globally, the decrease amounts to about 30%. The latter signifies that undrained soil behavior plays an active role dynamic pile driving in saturated, high D_r (≈80%) soil samples. As the saturation of the soil matrix is apparently disadvantageous to Ψ, this implies development of tensile PFP in the vicinity of the pile during driving. Consequently, the radial stresses acting on the pile are enhanced following the increase of the effective stresses, which are a consequence of constrained dilation.

Constrained dilative behavior in know to occur in a highly compacted soil matrix, provided rapid shearing of low permeable soil. Provided the nature of impact pile driving and the sample characteristics, the first two of the aforementioned criteria are unambiguously met. It seems that despite of the sandy soil matrix, which is generally characterized by favorable drainage properties, the rate

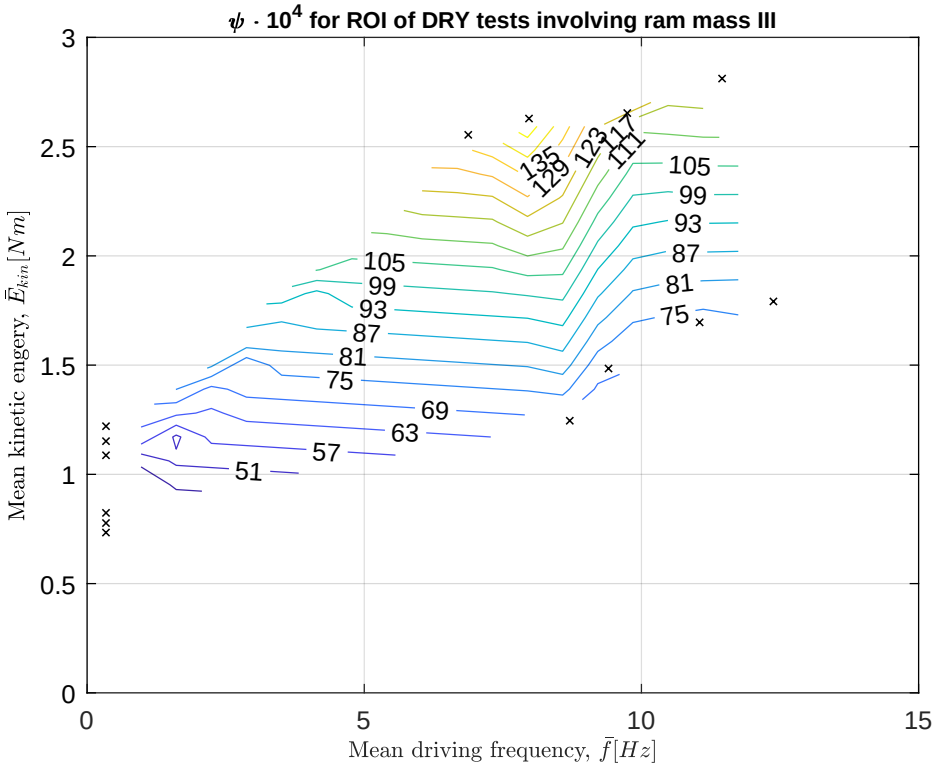

Figure 7.16: Ψ versus driving frequency and kinetic energy per blow for all **DRY** tests with ram mass **III**. *x* indicates combinations of $\overline{f}$ and $\overline{E}_{kin}$ for which Ψ has been computed. Aforementioned values are part of Table 7.3.

of shear is too high to procreate fully drained soil behavior. The observation of soil undrained behavior is in line with the work of Van Zeben (2017) ([112]), who reported the development of excess pore fluid pressures in the soil mass surrounding the pile, during dynamic pile driving experiments in the centrifuge on samples of 50-60% R_d. Although excess PFP were recorded further at larger radial distances, it is clear that the development of tensile pore water pressures in the zone adjacent to the pile shaft dominantly influences drivability for the experiments in this research. The latter is arguably due to the higher D_r of the samples.

Furthermore, judging by Figure 7.18, for driving frequencies <8 *Hz* Ψ expresses little variation due to alteration of $\overline{f}$. Yet, when the frequency is increased to >8 *Hz*, the Ψ is noticeably reduced, provided $\overline{E}_{kin}$ is maintained at a constant value. Hence, possibly, the effects of constrained dilation are accumulated once the time interval between blows is reduced below the critical threshold. Judging by Figure 7.18, the latter occurs at value <0.125 *s* (model time). This trend is opposite to the one indicated by Van Zeben (2017) ([112]), who reports a positive correlation between driving frequency and the build-up of PFP, possibly towards a zero effective stress state. Contrastingly, the corresponding numerical model, which was developed by Azua-Gonzalez (2017) [12], states that liquefaction exclusively reserved to experiments which involve dynamic pile driving under fully undrained conditions of lowly compacted samples of $D_r \approx 30\%$.

Saturated tests using ram mass III Figure 7.18 shows the contour plot for the ROI (segments) of all dry experiments executed with ram mass II. Grid points (x = $\overline{f}$; y = $\overline{E}_{kin}$) for which Ψ is part of Table 7.5 are indicated by an *x*. All 15 ROI subintervals are incorporated in Figure 7.18. For the multi-blow experiments, it is clear form Figure 7.18 that there is more variation in the $\overline{E}_{kin}$ as instead of three driving energy bands are visible, respectively at: (I) 1.0 *J*; (II) 1.7 *J*; (III) 2.4 *J*. Here, the lowest

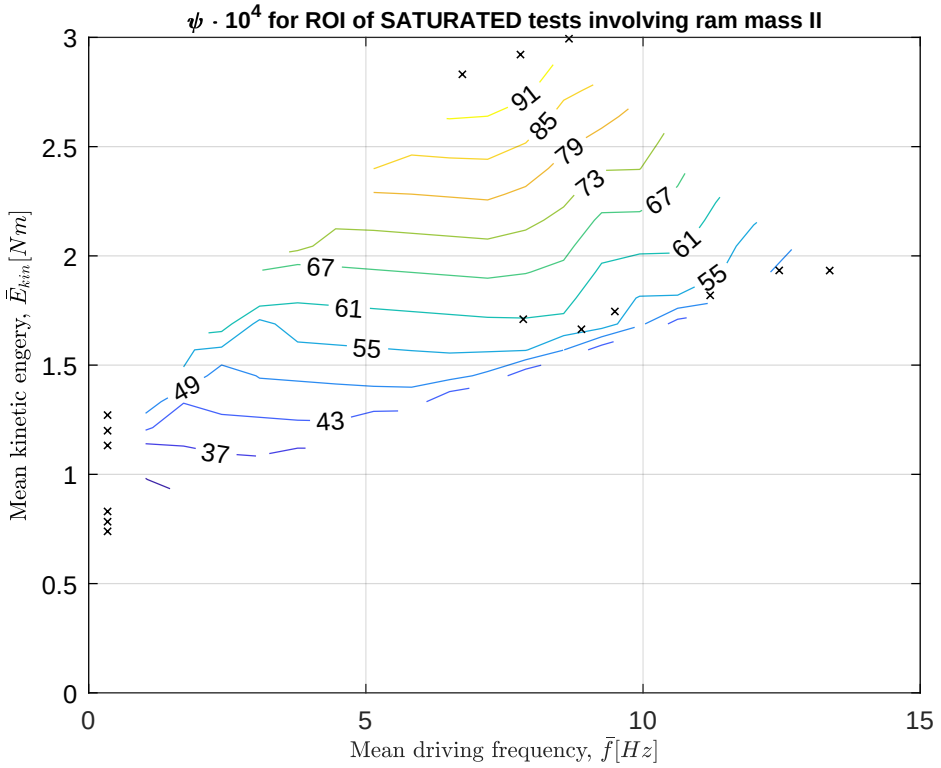

Figure 7.17: Ψ versus driving frequency and kinetic energy per blow for all **SATURATED** tests with ram mass **II**. x indicates combinations of $\overline{f}$ and $\overline{E}_{kin}$ for which Ψ has been computed. Aforementioned values are part of Table 7.4.

driving energy corresponds to test M3SLL, which for unknown reasons yielded a hammer efficiency of ≈50%, which is significantly lower than the other multi-blow tests. However, as there is no clear indication that the obtained measurements are faulty, test M3SLL is considered in the analysis.

Similar to the observations relating to Figure 7.16; globally, the normalized drivability coefficient is higher for experiments which are executed with ram mass III. Currently, it is not possible two differentiate between the two probable causes relating to the aforementioned observation, namely: (I) the efficiency of the overall driving system η_{ds}, which is composed of the hammer, anvil and pile, is higher when a heavier ram mass is used; (II) The efficiency of the driving system η_{ds} is independent of the employed ram mass, however the subsequent soil-structure interaction is more favorable due to the use of a heavier hammer. In the latter case, subtle variations of the application of piling energy to the soil, lie at the heart of the more favorable piling conditions for heavy hammers. In case the latter option is true, the administration of energy takes place in a more gradual manner over a longer period of time. As also indicated in Appendix E, the latter causes less abrupt shearing of the soil along the shaft. As a result, the tendency for dilative soil behavior (hardening behavior) is less pronounced, yielding more favorable radial stress conditions along the pile shaft. Moreover, the due to the increased dwell time, more deviatoric PFP are dissipated over the time interval in which the soil is subjected to shear. The latter is also beneficial with regard to the limitation of adverse effects associated with tensile pore fluid pressure development along the pile shaft for impact driving in high D_r sandy soils. Additionally, like observations regarding Figure 7.17, Ψ reaches an optimum at a driving frequency of about 8 *Hz*.

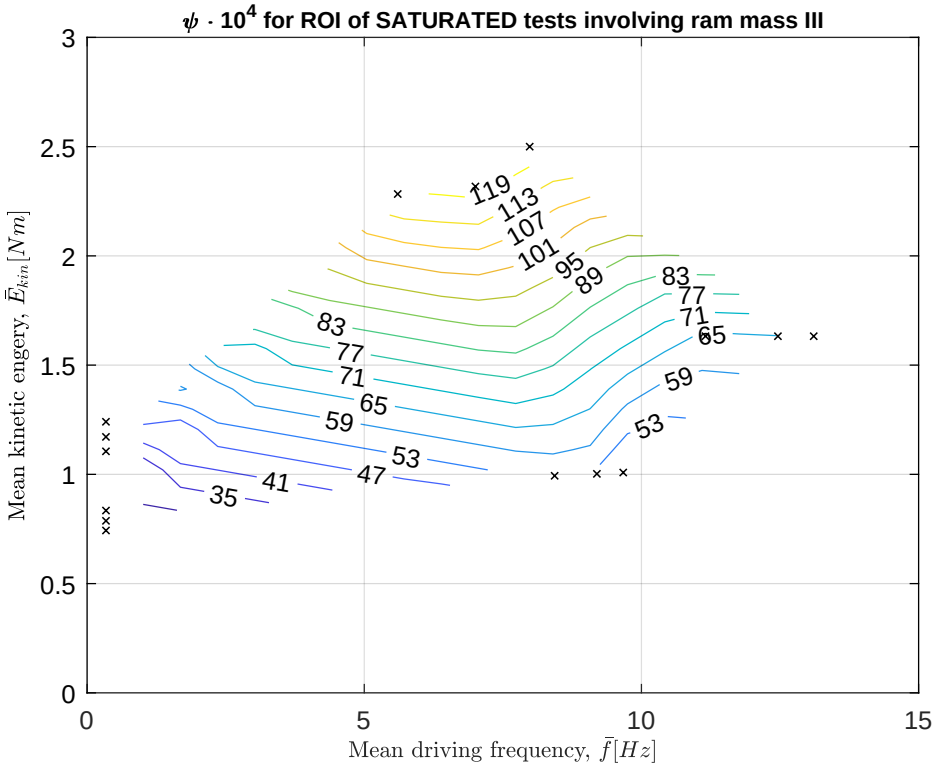

Figure 7.18: Ψ versus driving frequency and kinetic energy per blow for all **SATURATED** tests with ram mass **III**. *x* indicates combinations of $\overline{f}$ and $\overline{E}_{kin}$ for which Ψ has been computed. Aforementioned values are part of Table 7.5.

7.5.5. Concluding remarks

Based on the interpretation of the contour plots, several important conclusions are drawn with respect to the validity of the three hypotheses aimed a explaining the apparent improvement of drivability when employing HiLO driving techniques. Firstly, through mutual comparison of the drivability coefficients of dry and saturated tests, it is established that saturation of the soil matrix has an adverse effect on normalized pile drivability. This observation implicates that during pile driving tensile pore water pressures are developed in the soil as a consequence of untrained behavior in the form of constrained dilation. Consequently, the effective stress regime in the direct vicinity of the pile in enhanced, leading to greater radial stresses which hampers pile displacement during driving to some extend. Thereby the observed behavior does not coincide with the observation made by Van Zeben (2017) ([112]), who established the accumulation of excess (contractive) PFP over the course of the driving operation. Arguably the difference in D_r in the of the soil samples used in the this and the aforementioned research which are respectively 80% and 50-60%, explains the mirrored typed of undrained behavior. Provided presumably dilative soil behavior in the vicinity of the pile, soil liquidation is not realized. Moreover, the contour plots relating to saturated experiment indicate a further decrease of drivability for driving frequencies above 8 *Hz*. Arguable accumulation of tensile PFP occurs above this point. Yet, this statement is difficult to verify due to the narrow range of frequencies at which the experiments were conducted.

Secondly, there is no decisive evidence for the occurrence of enhances friction fatigue (and thus better drivability) for tests executed at lower driving energy, yet higher frequency. Following the conclusions of White & Lehane (2004) ([118]), the number of load cycles experiences by soil elements lining the shaft of the pile is negatively correlated to the radial stress regime surrounding the pile shaft. The observations relating to the absence of the effects of enhanced friction fatigue during the

experiments, are made despite of a comparable number load cycles experienced by the interface layer with respect to the research conducted by White & Lehane. Arguably, due to the penetration of the pile during the driving operation and continuous addition soil which has not yet been exposed to the cyclic loading along the shaft, the effects of friction fatigue are only perceived relevant for the upper region of the embedded pile section. Here, radial soil stresses are lowest due to smaller overburden pressures. Hence, relatively, the decrease in radial stresses resulting from friction fatigue is limited and influential to the overall trends in the obtained results.

Thirdly, it is noted that a more or less linear relationship exists between Ψ and $\overline{E}_{kin}$. Despite of the implied decrease in drivability for higher piling energies, due to larger energy dissipation associated with the occurrence of effects of dynamic soil resistance, the anticipated divergence of contour lines for higher piling energies is not evident from the experimental results. As it is impossible to quantify the differences in particle velocity which are realized by changes of the falling height due to the unusable signals from the accelerometer, the spread of particle velocities between tests in unknown. Additionally, as tests were executed at two driving energies, the observed linear relationship is arguably due to linear interpolation between to respective energies. The execution of tests at three different energy levels would yielded more reliable results with regard to the evolution of dynamic soil resistance as a function of $\overline{E}_{kin}$. However, a reliable observation which also relates to the development of dynamic soil resistance, relates to the effect of using a heavier ram mass. Through mutual comparison of the contour plots corresponding to experiments with ram mass II and III, for both dry and saturated conditions, it is established that the use of a heavier ram mass is beneficial to Ψ. Although it is not possible to rule out the possibility that the η_{ds} is larger for the ram mass (implying that more of the kinetic energy carried by the ram is transferred to the pile), it is hypothesized that the energy is administered more gradually and over an extended time interval (as also indicated in Appendix E). As a result, the tendency for dilative soil behavior (hardening behavior) is reduced, yielding more favorable radial stress conditions along the pile shaft which promote pile installation. Similar conclusions where reached by Anusic *et al.* (2016) ([6]).

Test ID UNIT ⟶	ROI (top) [mm]	ROI (bottom) [mm]	$\overline{\sigma}'$ [kPa]	$\overline{\sigma}^*$ [kPa]	$\overline{w}$ [mm]	$\overline{w}^*$ [mm]	$\tilde{p}$ [-]	Ψ [-]	$\overline{f}$ [Hz]	$\overline{E}_{\text{pot}}$ [J]	$\overline{E}_{\text{kin}}$ [J]	η_h [%]
M2DXL.i	49.9391	58.3147	40.2712	46.6710	0.0541	0.0625	0.0039	0.0029	0.3411	1.8685	*0.8153**	43.6324*
M2DXL.ii	58.3147	66.6832	46.6732	46.6710	0.0625	0.0625	0.0030	0.0030	0.3411	1.8880	*0.7693**	40.7479*
M2DXL.iii	66.6832	75.0075	53.1256	46.6710	0.0708	0.0625	0.0024	0.0031	0.3410	1.9075	*0.7261**	38.0672*
M2DXH.i	49.8162	58.2335	39.8664	46.1358	0.0540	0.0624	0.0072	0.0054	0.3396	2.8454	*1.2415**	43.6324*
M2DXH.ii	58.2335	66.5624	46.1996	46.1358	0.0624	0.0624	0.0055	0.0055	0.3395	2.8755	*1.1717**	40.7479*
M2DXH.iii	66.5624	74.9105	52.5828	46.1358	0.0707	0.0624	0.0045	0.0058	0.3395	2.9055	*1.1060**	38.0672*
M2DLL.i	49.9268	58.3489	40.0284	46.3232	0.0541	0.0625	0.0065	0.0048	7.5802	1.9008	1.7354	91.2818
M2DLL.ii	58.3489	66.6158	46.3873	46.3232	0.0625	0.0625	0.0049	0.0049	9.2906	1.9296	1.6987	88.0455
M2DLL.iii	66.6158	74.9402	52.7964	46.3232	0.0708	0.0625	0.0040	0.0052	9.7801	1.9421	1.6389	84.3883
M2DLH.i	50.1954	58.3570	40.1682	46.5376	0.0543	0.0625	0.0078	0.0058	10.1458	1.9231	1.7515	91.0576
M2DLH.ii	58.3570	66.7208	46.5398	46.5376	0.0625	0.0625	0.0052	0.0052	12.3269	1.9336	1.8727	96.8524
M2DLH.iii	66.7208	74.9295	53.0240	46.5376	0.0708	0.0625	0.0040	0.0052	13.7398	1.9490	1.7045	87.4597
M2DHL.i	49.6865	58.1794	39.8959	46.3125	0.0539	0.0625	0.0126	0.0094	6.4142	2.8995	2.6533	91.5190
M2DHL.ii	58.1794	66.7819	46.2527	46.3125	0.0625	0.0625	0.0085	0.0085	8.2075	2.9052	2.7090	93.2477
M2DHL.iii	66.7819	74.9569	52.6598	46.3125	0.0709	0.0625	0.0070	0.0090	9.1955	2.9351	2.7871	94.9558
M2DHH.i	50.1608	58.6277	39.9369	46.2695	0.0544	0.0625	0.0183	0.0138	8.3333	3.0627	2.7905	91.1938
M2DHH.ii	58.6277	66.7097	46.2717	46.2695	0.0627	0.0625	0.0137	0.0138	10.1469	2.9921	2.8440	95.0709
M2DHH.iii	66.7097	74.8227	52.7184	46.2695	0.0708	0.0625	0.0114	0.0147	11.3311	2.9649	2.7873	94.0153

* Copied from test M3DXL

Table 7.2: Overview of all parameters relevant to the contour plot corresponding to **DRY** tests executed with ram mass **II**. Please note that all *cursive* entries are computed based on an assumed (not measured) variable. To clearly indicate these interdependencies, the same superscripted symbol is used.

Test ID UNIT ⟶	ROI (top) [mm]	ROI (bottom) [mm]	$\overline{\sigma}'$ [kPa]	$\overline{\sigma}^*$ [kPa]	$\overline{w}$ [mm]	$\overline{w}^*$ [mm]	$\tilde{p}$ [-]	Ψ [-]	$\overline{f}$ [Hz]	$\overline{E}_{\text{pot}}$ [J]	$\overline{E}_{\text{kin}}$ [J]	η_h [%]
M3DXL.i	50.0115	58.2712	39.9473	46.2293	0.0541	0.0624	0.0036	0.0027	0.3408	1.8878	*0.8237**	43.6324*
M3DXL.ii	58.2712	66.5944	46.2933	46.2293	0.0624	0.0624	0.0029	0.0029	0.3404	1.9073	*0.7772**	40.7479*
M3DXL.iii	66.5944	75.0138	52.6894	46.2293	0.0708	0.0624	0.0026	0.0033	0.3401	1.9271	*0.7336**	38.0672*
M3DXH.i	49.8083	58.2851	40.0284	46.3232	0.0540	0.0624	0.0078	0.0058	0.3407	2.7976	1.2205	43.6324
M3DXH.ii	58.2851	66.6485	46.3873	46.3232	0.0625	0.0624	0.0057	0.0057	0.3407	2.8272	1.1520	40.7479
M3DXH.iii	66.6485	75.0597	52.7964	46.3232	0.0709	0.0624	0.0048	0.0062	0.3406	2.8567	1.0874	38.0672
M3DLL.i	49.9646	58.1385	40.0180	46.3635	0.0541	0.0625	0.0108	0.0081	6.8212	1.9372	1.1264	58.1525
M3DLL.ii	58.1385	66.7449	46.3657	46.3635	0.0624	0.0625	0.0068	0.0068	8.7074	1.9383	1.2455	64.2438
M3DLL.iii	66.7449	75.0560	52.8255	46.3635	0.0709	0.0625	0.0052	0.0067	9.4062	1.9510	1.4844	76.0838
M3DLH.i	49.5963	58.2473	40.0759	46.4828	0.0539	0.0625	0.0137	0.0102	8.6582	2.0147	1.9458	96.3054
M3DLH.ii	58.2473	66.7410	46.4849	46.4828	0.0625	0.0625	0.0072	0.0072	11.0495	2.0223	1.6957	83.8250
M3DLH.iii	66.7410	74.9193	52.9447	46.4828	0.0708	0.0625	0.0059	0.0076	12.3808	2.0122	1.7914	89.0170
M3DHL.i	50.0657	58.4124	39.9263	46.3092	0.0542	0.0625	0.0248	0.0186	5.8843	2.9281	2.5676	87.6936
M3DHL.ii	58.4124	66.4986	46.3114	46.3092	0.0625	0.0625	0.0138	0.0137	6.8757	2.9287	2.5540	87.2012
M3DHL.iii	66.4986	74.9702	52.7469	46.3092	0.0707	0.0625	0.0119	0.0153	7.9717	2.9930	2.6286	87.8238
M3DHH.i	50.1242	58.4099	39.7730	46.0277	0.0543	0.0625	0.0247	0.0185	9.6814	2.9656	2.6577	89.1581
M3DHH.ii	58.4099	66.5863	46.0914	46.0277	0.0625	0.0625	0.0115	0.0115	9.7443	3.0110	2.6538	88.1394
M3DHH.iii	66.5863	75.0233	52.4597	46.0277	0.0708	0.0625	0.0096	0.0124	11.4551	2.9737	2.8116	94.5417

* Copied from test M3DXH

Table 7.3: Overview of all parameters relevant to the contour plot corresponding to **DRY** tests executed with ram mass **III**. Please note that all *cursive* entries are computed based on an assumed (not measured) variable. To clearly indicate these interdependencies, the same superscripted symbol is used.

Test ID UNIT ⟶	ROI (top) [mm]	ROI (bottom) [mm]	$\overline{\sigma}'$ [kPa]	$\overline{\sigma}^*$ [kPa]	$\overline{w}$ [mm]	$\overline{w}^*$ [mm]	$\tilde{p}$ [-]	Ψ [-]	$\overline{f}$ [Hz]	$\overline{E}_{\text{pot}}$ [J]	$\overline{E}_{\text{kin}}$ [J]	η_h [%]
M2SXL.i	50.0529	58.2270	25.4713	47.2736	0.0541	0.0625	0.0041	0.0019	0.3404	1.9026	*0.8302**	43.6324*
M2SXL.ii	58.2270	66.6501	29.5102	47.2736	0.0624	0.0625	0.0034	0.0021	0.3404	1.9222	*0.7833**	40.7479*
M2SXL.iii	66.6501	74.9511	33.5803	47.2736	0.0708	0.0625	0.0029	0.0024	0.3404	1.9417	*0.7391**	38.0672*
M2SXH.i	48.1304	56.1802	24.3456	46.9974	0.0522	0.0625	0.0096	0.0041	0.3406	2.9136	*1.2713**	43.6324*
M2SXH.ii	56.1802	64.6586	28.3430	46.9974	0.0604	0.0625	0.0078	0.0045	0.3405	2.9441	*1.1997**	40.7479*
M2SXH.iii	64.6586	72.9857	32.4100	46.9974	0.0688	0.0625	0.0064	0.0049	0.3405	2.9744	*1.1323**	38.0672*
M2SLL.i	48.8005	56.9113	24.5701	46.9144	0.0529	0.0625	0.0138	0.0061	7.8391	1.9824	1.7100	86.2809
M2SLL.ii	48.8005	65.2162	28.5933	46.9144	0.0611	0.0625	0.0099	0.0059	8.8885	1.9842	1.6642	83.8728
M2SLL.iii	65.2162	73.5572	32.6478	46.9144	0.0694	0.0625	0.0068	0.0053	9.4918	1.9879	1.7455	87.8021
M2SLH.i	50.2717	58.1663	25.3894	47.1982	0.0542	0.0625	0.0117	0.0055	11.2113	2.0054	1.8194	90.7306
M2SLH.ii	58.1663	66.5379	29.3855	47.1982	0.0624	0.0625	0.0077	0.0048	12.4567	1.9751	1.9334	97.8971
M2SLH.iii	66.5379	74.9408	33.4126	47.1982	0.0707	0.0625	0.0054	0.0043	13.3673	1.9740	1.9328	97.9152
M2SHL.i	50.3072	58.2197	25.2715	46.9017	0.0543	0.0625	0.0209	0.0098	6.7410	3.0177	2.8310	93.8201
M2SHL.ii	58.2197	66.7933	29.2795	46.9017	0.0625	0.0625	0.0157	0.0098	7.7893	3.0157	2.9214	96.8706
M2SHL.iii	66.7933	74.9293	33.3188	46.9017	0.0709	0.0625	0.0114	0.0092	8.6642	3.0316	2.9938	98.7514

* Copied from test M3DXH

Table 7.4: Overview of all parameters relevant to the contour plot corresponding to **SATURATED** tests executed with ram mass **II**. Please note that all *cursive* entries are computed based on an assumed (not measured) variable. To clearly indicate these interdependencies, the same superscripted symbol is used.

Test ID UNIT ⟶	ROI (top) [mm]	ROI (bottom) [mm]	$\overline{\sigma}'$ [kPa]	$\overline{\sigma}^*$ [kPa]	$\overline{w}$ [mm]	$\overline{w}^*$ [mm]	$\tilde{p}$ [-]	Ψ [-]	$\overline{f}$ [Hz]	$\overline{E}_{\text{pot}}$ [J]	$\overline{E}_{\text{kin}}$ [J]	η_h [%]
M3SXL.i	37.8182	46.0254	19.5395	47.1817	0.0419	0.0624	0.0061	0.0017	0.3404	1.9123	*0.8344**	43.6324*
M3SXL.ii	46.0254	54.4170	23.5189	47.1817	0.0502	0.0624	0.0050	0.0020	0.3405	1.9322	*0.7873**	40.7479*
M3SXL.iii	54.4170	62.6929	27.5295	47.1817	0.0586	0.0624	0.0038	0.0021	0.3404	1.9521	*0.7431**	38.0672*
M3SXH.i	27.6339	36.5156	15.0508	47.6438	0.0321	0.0625	0.0192	0.0031	0.3400	2.8434	*1.2406**	43.6324*
M3SXH.ii	36.5156	44.9022	19.0344	47.6438	0.0407	0.0625	0.0143	0.0037	0.3399	2.8749	*1.1715**	40.7479*
M3SXH.iii	44.9022	53.0774	23.0492	47.6438	0.0490	0.0625	0.0108	0.0041	0.3399	2.9039	*1.1054**	38.0672*
M3SLL.i	49.7886	58.1479	25.4911	47.3437	0.0540	0.0625	0.0117	0.0054	8.4343	1.9869	*0.9934***	50.0000**
M3SLL.ii	58.1479	66.7186	29.5537	47.3437	0.0624	0.0625	0.0085	0.0053	9.1964	2.0046	*1.0023***	50.0000**
M3SLL.iii	66.7186	75.0585	33.6092	47.3437	0.0709	0.0625	0.0057	0.0046	9.6716	2.0168	*1.0084***	50.0000**
M3SLH.i	49.7558	58.3023	25.3385	47.0459	0.0540	0.0625	0.0136	0.0063	11.1554	2.1463	1.6324	83.3582
M3SLH.ii	58.3023	66.4981	29.3681	47.0459	0.0624	0.0625	0.0103	0.0064	12.4621	2.0774	1.6324	83.3582
M3SLH.iii	66.4981	74.8687	33.4290	47.0459	0.0707	0.0625	0.0080	0.0064	13.1080	2.1260	1.6324	83.3582
M3SHL.i	49.8569	58.4488	25.1144	46.7689	0.0542	0.0625	0.0256	0.0119	5.6038	2.9862	2.2831	76.4808
M3SHL.ii	58.4488	66.6631	29.1163	46.7689	0.0626	0.0625	0.0196	0.0122	7.0051	2.9802	2.3177	77.6946
M3SHL.iii	66.6631	74.9965	33.1497	46.7689	0.0708	0.0625	0.0153	0.0123	7.9843	2.9908	2.4999	83.5718

* Copied from test M3DXH

** Approximated average hammer efficiency η_h of the blows from test M3SLL for which impact velocity analysis was succesfully performed

Table 7.5: Overview of all parameters relevant to the contour plot corresponding to **SATURATED** tests executed with ram mass **III**. Please note that all *cursive* entries are computed based on an assumed (not measured) variable. To clearly indicate these interdependencies, the same superscripted symbol is used.

8

Conclusions

The results in this section are presented in three part. Respectively, each part relates to one of the three hypothesis which formulated on the basis at the literature study which precedes this research. A complete description of what each hypothesis entails, is provided in 6.3. General conclusions relating to the validity of hypothesis I, II and III, are respectively presented in 8.1, 8.2 and 8.3.

8.1. Hypothesis I - Accumulation of excess pore fluid pressures

To observe an accumulation of excess pore fluid pressures, two criteria should be met, namely: (I) a (fully) undrained shear response; (II) a tendency towards contractive behavior when exposed to shear. Although low soil permeability is important with respect to the former point; for sands, on which is work focused, the rate of loading is of critical importance to the establishment of undrained loading conditions. The latter point implicates that the relative density should accommodate contraction of the soil matrix under shear, which is generally reserved to low or medium compacted soil whereas this research employs high R_d (80%) samples. Yet, under the right conditions (specifically high confining stresses), excess PFP are generated in high D_r material.

As part of the research methodology, the pore fluid pressures (PFP) during driving were recorded by three static pore fluid pressure sensors (SPFPS) and well as three optical pore fluid pressure sensors (OPFPS). The SPFPS sensors are installed at three distinct combinations of depth and radial distance (towards the (projection) of the pile shaft). Results associated to the execution of six multi-blow experiments, indicate a modest increase in PFP of about 10 *kPa* at radial distances between 14 and 34 *mm*. Arguably, as blow frequency exceeds the dissipation time, small compressions of the soil skeleton caused by P- and S-waves, enable the generation of excess PFP. In this respect an self-reinforcing trend is expected for higher driving frequencies. Based on the comparison between 10 and 15 *Hz* experiments, the latter is arguable proven by the observations. The aforementioned relationship is endorsed by Hwang *et al.* (2001) ([57]) who observed also observed the generation of excess PFP during dynamic pile driving.

As the absolute magnitude of the generated excess PFP is globally the same throughout the soil body, the upper regions are most susceptible to liquefaction due to excess PFP generation associated with the emittance of seismic waves. However, in order to approach this state, the driving frequency should be increase well beyond those employed by this research. The relationship between excess PFP generation and piling conditions. Interestingly, SPFPS1, but most notably the OPFPS, observed the effect of (accumulation of) tensile PFP development at the interface. The simultaneous observation of accumulation of both tensile and excess PFP, opens up an interesting possibility. It is hypothesized that under the effect of tensile PFP accumulation along the shaft for increasing driving frequencies, the stiffness of the surrounding soil body is increased. Following the initiation

of the next blow, the stiffer soil response yields a higher dissipation of energy in the form of seismic waves. Consequently, the higher excess PFP in the far-field are further enhanced by the emittance of seismic waves with an higher energy content. This effect could potentially give rise to a situation in which the pile penetrates together with a mass of clinging soil in a partially liquefied soil mass.

It is unlikely that pile drivability is improved in the aforementioned scenario. This also follows from the comparison of the contour plots for dry and saturated experiments. It is evident that the normalized drivability is lowest for under tests executed under fully saturated conditions, independent of the type of ram mass used. This implies that soil dilation under dry conditions has a less pronounced adverse effect than inhibited dilation under fully undrained conditions. Possibly, the latter is related to the low threshold for the accumulation of tensile pore water pressures. This notion is confirmed by the contour plots, from which it follows that it is not advisable to increase the driving frequency above 8 *Hz* as normalized drivability coefficient steadily decreases at higher frequencies. This indicates that the the blow frequency is approaches the time required to realize full dissipation of deviatoric PFP at the interface. In this sense, it is evident that HiLo driving is not a generic tool to improve pile drivability under all circumstances. Moreover, the R_d of the soil requires careful consideration when deciding on the best approach with regard to pile driving.

8.2. Hypothesis II - Enhanced radial stress degradation following from cyclic interface loading

Following the conclusions of White & Lehane (2004) ([118]), the number of load cycles experiences by soil elements lining the shaft of the pile is negatively correlated to the radial stress regime surrounding the pile shaft. It is reported that the effects of friction fatigue are perceived after a few dozens of load cycles. Based on the obtained contour plots, it seems that there is little evidence which points towards the enhancement of friction fatigue for tests executed at low driving energy, yet high frequency. The latter observation is made despite a rather good match between the number of load cycles for which a noticeable influence was reported by White & Lehane, and the number of cycles experienced by the soil over the coarse of the pile driving experiments. However, White & Lehane based their results on cyclic loading of a single specimen. In reality, the pile shaft is effectively lined with similar specimens which a cyclically loaded for each blow. As the pile penetrates the soil, new elements are added continuously. Consequently, the number of shear cycles to which soil elements were exposed, decreases as the elements get closer to the tip. Hence, at greater depths, the effects of friction fatigue are less pronounced while radial stresses are elevated as a result of the depth trend. Consequently, the overall decrease is shaft friction, which predominantly occurs in the upper soil regions, where radial stresses are the lowest, is of sufficient magnitude yield an observable effect on pile drivability.

Alternatively, the reason for the absence of the effect of friction fatigue lies in the chosen method of analysis. Due to unintended fluctuation of driving parameters, predominantly the driving frequency and (to a lesser extend) impact velocity, the contour plots are based on short pile driving intervals where the variation is driving parameters is small enough to justify averaging over the interval. In this sense, the contour plots are based on a large number of short tests, executed at various depths, frequencies and piling energies. The limited number of load cycles which is represented by each of these segments undoubled falls short of the number of cycles needed to appreciate the effect of friction fatigue. Consequently, its seems that the effect of cyclic loading of the interface is incompletely captured and hence warrants further exploration, provided better controllability of the driving parameters.

8.3. Hypothesis III - Reduced dynamic soil resistance related to lower particle velocities

A relationship on which pile drivability models heavily rely, considers the dependence of soil resistance on the particle velocity. As the particle velocity of the pile is related to the impact velocity of the hammer v_0, larger falling height and thus higher piling energies presumably affect the drivability of the pile in a disadvantageous manner. Based on the obtained contour plots, it is noted that a more or less linear relationship exists between Ψ and $\overline{E}_{kin}$. Consequently, despite of the implied decrease in drivability for higher piling energies, due to larger energy dissipation associated with the occurrence of effects of dynamic soil resistance, the anticipated divergence of contour lines for higher piling energies is not observed in the experimental results.

However, as tests were executed at two different driving energies, the observed linear relationship between drivability and piling energy, is arguably due to the linear interpolation used to determine the positions of the contour lines. In this respect, the execution of experiments at three different energy levels would arguably yield more reliable results with regard to the evolution of dynamic soil resistance as a function of $\overline{E}_{kin}$. Additionally, the quantification of particle velocity through analysis of data from the accelerometer and load cell would arguably provide more insight in how impact velocity is converted to particle velocity through the anvil, which remains a black box at this point in time. By totally eliminating this influence, by inferring particle velocity directly from measurements, the chance of finding a satisfactory, qualitative description of the relation between dynamic soil resistance and particle velocity, is undoubtedly improved.

Yet, by means of a drivability comparison between ram mass II and III respectively, for both dry at saturated conditions, the correlation between v_0 and dynamic soil resistance is further investigated. For both dry and saturated experiments, it was found that the global drivability improved through the use of a heavier ram mass, which has a lower impact velocity compared to its lighter counterpart. The latter observation is in line with scientific consensus as, amongst others, Anusic *et al.* (2016) [6] reached similar conclusions in this respect. Although the aforementioned observation points towards the more efficient transfer of kinetic energy into piling energy for a heavier ram mass, this claim is not verifiable. The latter is due to the unsuitable signals from the accelerometer, which inhibits the differentiation between the two possible explanations, namely: (I) the efficiency of the overall driving system η_{ds}, which is composed of the hammer, anvil and pile, is higher for a heavier ram mass; (II) the efficiency of the driving system η_{ds} is independent of the employed ram mass; however, the subsequent soil-structure interaction is more favorable due to the use of a heavier hammer. In the latter case, subtle variations of the application of piling energy to the soil, lie at the heart of the more favorable piling conditions for heavy hammers. Provided the latter option is true, the administration of energy takes place in a more gradual manner over a longer period of time. As also indicated in Appendix E, the latter causes less abrupt shearing of the soil along the shaft. As a result, the tendency for dilative soil behavior (hardening behavior) is less pronounced, yielding more favorable radial stress conditions along the pile shaft which improve drivability. Moreover, due to the increased dwell time, more deviatoric PFP are dissipated over the time interval in which the soil is subjected to shear. The latter is also beneficial with regard to the limitation of adverse effects associated with tensile pore fluid pressure development along the pile shaft for impact driving in high D_r, sandy soils.

9

Recommendations and future research

Significant improvements were made to the actuator over the course of this project. The current set-up is highly versatile as it provided the possibility to conduct experiments over a very wide range of driving frequencies, provides full control over the falling height and allows for the experimentation with different hammers. Additionally, several new sensors were developed which aid the quantification of important driving parameters such as impact velocity, pile force and pore fluid pressures. However, there is evidently room for further improvement, which is discussed in this section.

Provided that this research initially aimed to quantitatively investigate the soil behavior surrounding HiLo driving, the decisions to scale back the driving frequencies due to limitations of the servo-system was highly unsatisfactory. Although servo-system undoubtedly proved itself in terms of reliability and robustness, its operational threshold lies at an energy flux of approximately 27 *Nm/s*. Consequently, the quality of the experiments is guaranteed up to a frequency of 15 *Hz* while operating ram mass II at about 70% capacity. Hence, at prototype scale the actuator can simulate pile driving tests to about 18 *blow/min*. Roughly, this number translates to 50% of the conventional driving rate and about 30% of driving rates associated with HiLo driving. To truly develop a better understanding of the processes which occur in the subsoil during the real-life implementation of these driving techniques, it is important to ameliorate the performance of the servo system. Th best but arguable also the most elaborate way to do so is through a mechanical overhaul of the system, where the current stepper engine is exchanged for a stronger model.

Additionally, time should be dedicated to decrease the tuning response time of the frequency controller of the fast engine. Although the system works, it takes too long to get the engine to run at the desired frequency. Even now, at rather low driving frequencies of about 15 *Hz*, the system was performing optimally by the time the experiment was about to be terminated. The ability of truly independently vary parameters is essential to the conductance of a high quality parameter study, which eventually yields unambiguous results.

Furthermore, based on the results, there is reason to believe that the manual embedment of the pile is disruptive to the obtained results. Ideally, the set-up is modified to eliminate the need to manually embed a portion of the pile. To this end the spacers which are installed on top of the motor housing can be removed entirely. This modification also entails the removal of the upper end-switch. Consequently about 3 *cm* of additional space is created. Provided the pile clamp can provide enough support, the pile could be positioned op top of the soil surface. Subsequently all of the penetration follows from the pile driving operation, thereby removing the a doubtful aspect of the sample preparation from the test procedure.

The use of optical pore fibers to conduct measurements in the centrifuge, has provided some interesting insights with respect to soil behavior at the interface. However, the potential of this type of sensor is not fully realized by this research. Consequently, it is advisory to further develop the

integration of optical fibers in the pile shaft. Here, the largest challenges lie in the area of sensor fixation and the saturation of the capillary tubes, which tended to leak oil during the experiments. Finally, is would be beneficial to increase the measurement frequency of MP3 or connect the sensors to a fast data acquisition channels. In the latter case it should be noted that the intrinsic data logging rate is limited to 125 Hz.

The quantification of the driving system efficiency was unsuccessful due to unreliable signals from the accelerometer. The most likely cause for this observation lies in the mechanical system envisioned to attach the sensor to the pile shaft, which behaves as a separate system instead of an extension of the pile. Conceptually the system has huge potential to be of great value to the continued effort to increase the understanding of the dynamic aspects of impact pile driving. Moreover, the measurement system in the centrifuge can accommodate the high data logging frequencies needed to conduct reliable measurements, which makes it worthwhile ot put some more thought into the proper implementation of this system.

During the sample preparation procedure of the saturated samples, the static pore fluid pressure sensors are already gradually encases in sand. Due to the reasonable dimensions of the sensors, the shockwave compaction is less effective in the direct vincinty. Consequently, a lower state of compaction is reached. During spin-up of the centrifuge, as well as the initiation of the driving operation, local failures occur around the sensors which affect the PFP readings. Hence, the tendency for this type of behavior should be eliminated, either by reducing the dimensions of the sensors or using local compaction methods to obtain the a uniform D_r throughout the entire sample.

Anticipating on the continuation of this research in the future, the scope of research could be extended to incorporate the following areas of interest. As mentioned in the report, currently, the use of the heavy ram mass effectively brings about two simultaneous changes which relate to energy transfer, namely: (I) the alteration of dwell time to due to different geometrical properties; (II) a different degradation coefficient for the energy flux with time, due to the increased mass. Currently, it is impossible to distinguish between the two effects. Hence, it could be of interest design to new pairs of ram masses for which the following holds: (I) the same weight but deviating dimensions (particularly length); (II) the same dimensions, yet a different weight. During this design process, the impedance of the ram masses should be considered at all times.

The soil behavior observed inside of the inner cavity of the pile during impact hammering remains a gray area and is consequently well suited for further research. This research could focus on the distribution of friction between the inner cavity and outer surface of the pile and the observed soil behavior for various soil conditions and driving parameters.

Finally, the simultaneous use of the different data acquisition systems in the centrifuge is an elaborate process which should be improved. As there is no way automatically synchronize the data measurements taken by the different acquisition systems, this is often done by hand following execution of the tests. This process is tedious and highly labor intensive and would benefit significantly from a center interface to start, stop and modify the data acquisition process.

Bibliography

[1] 4C Offshore. Monopiles Support Structures.

[2] Tony M. Allen. Development of the WSDOT Pile Driving Formula and Its Calibration for Load and Resistance Factor Design (LRFD). Technical report, Washington State Department of Transportation, Washington, D.C., 2005.

[3] H.G.B. Allersma. The University of Delft geotechnical centrifuge. In *International Conference Centrifuge 94*, pages 47–52, Signapore, 1994.

[4] Torstein Alm and Liv Hamre. Soil model for driveability predictions. In *Offshore Technology Conference 8835*, Houston, USA, 1998.

[5] Torstein Alm and Liv Hamre. Soil model for pile driveability predictions based on CPT interpretations. In *International Conference on Soil Mechanics and Geotechnical Engineering*, pages 1297–1302, Istanbul, Turkey, 2001.

[6] I Anusic, G.R. Eiksund, and M.A. Liingaard. Comparison of pile driveability methods based on a case study from an offshore wind farm in North Sea. *Proceedings of the 17th Nordic Geotechnical Meeting Challenges in Nordic Geotechnic*, (October 2017):1037–1046, 2016.

[7] Ivana Anusic, Gudmund R. Eiksund, Sandra Meissl, and Morten A Liingaard. Study of a new installation technique for large diameter monopiles. In *Proceedings of the 19th International Conference on Soil Mechanics and Geotechnical Engineering*, pages 2261–2264, Seoul, 2017.

[8] A. Askarinejad. *Failure mechanisms in unsaturated silty sand slopes triggered by rainfall*. Phd thesis (no. 21423), ETH Zurich, 2013.

[9] A Askarinejad, J Laue, A Zweidler, M Iten, E Bleiker, H Buschor, and S M Springman. Physical modelling of rainfall induced landslides under controlled climatic conditions Physical modelling of rainfall induced landslides under controlled climatic conditions. (April 2012), 2012.

[10] A. Askarinejad, A Philia Boru Sitanggang, and F. Schekeveld. Effect of pore fluid on the cyclic behavior of laterally loaded offshore piles modelled in centrifuge Effect of pore fluid on the behavior of laterally loaded offshore piles modelled in centrifuge. In W. Lee, J.S. Lee, H.K. Kim, and D.S. Kim, editors, *Proceedings of the 19th International Conference on Soil Mechanics and Geotechnical Engineering, Seoul 2017*, volume 2, pages 897–900, 2017.

[11] G. Axelsson. Long-term increase in shaft capacity of driven piles in sand. In *Proc. of 4th Int. Conf. on Case Histories in Geotechnical Engineering*, pages 301–308, St. Louis, Missouri, 1998.

[12] C. Azúa-Gonzalez. *Dynamic finite element analysis of impact pile driving centrifuge tests*. Msc. thesis, Delft University of Technology, 2017.

[13] A. Beijer Lundberg. *Displacement pile installation effects in sand*. PhD thesis, Delft University of Technology, 2015.

[14] Lars Beuth. Numerical Studies of Offshore Monopile Installation. 2016.

[15] T De Blaeij. On the modelling of installation effects on laterally cyclic loaded monopiles. 2013.

[16] M.D. Bolton and C.K. Lau. Scale effects arising from particle size. In *Centrifuge 98*, pages 127–131, 1988. ISBN 9061918138.

[17] M Boulon and P. Foray. Physical and Numerical simulation of lateral shaft friction along offshore piles in sand. In *Proc. of the 3rd Int. Conf. on Numerical methods in Offshore piling*, pages 127–147, Nantes, France, 1986.

[18] J.L. Briaud and E. Garland. Pile response to dynamic loads. Technical report, Texas A&M University, Bryan, TX, 1984.

[19] F. Brucy, J. Meunier, and J-F. Nauroy. Behaviour of a pile plug in sandy soils during and after driving. *Offshore Technology Conference*, (1):145–154, 1991.

[20] D Bruno. *Dynamic and static load testing of driven piles in sand.* Ph.d. thesis, University of Western Australia, 1999.

[21] L.G. Buitendijk. Floating installation of offshore wind turbine foundations. 2016.

[22] P.J. Bullock, J.H. Schmertmann, M.C. McVay, and F.C. Townsend. Side shear setup. I: Test piles driven in Florida. *Journal of Geotechnical and Geoen- vironmental Engineering*, 131(3):292–300, 2005.

[23] F. Chow. *Investigations into the behaviour of displacement piles for offshore foundations*. Ph.d. thesis, University of London (Imperial College), UK, 1996.

[24] F.C. Chow. Field measurements of stress interactions between displacement piles in sand. *Ground Engineering*, 28(6):36–40, 1995.

[25] Günther Clauss, Eike Lehmann, and Carsten Östergaard. *Meerestechnische Konstruktionen Teil 2*. Springer, 1988. ISBN 0387189645.

[26] Harry M. Coyle and Gary C. Gibson. Empirical damping constants for sands and clays. *Journal of the Soil Mechanics and Foundations Division*, 96(3):949–965, 1970.

[27] CUR. Report 2001-8: Bearing capacity of steel pipe piles. Technical Report December, Centre for Civil Engineering Research and Codes, Gouda, The Netherlands., 2001.

[28] Jason T. De Jong, Mark F. Randolph, and David J. White. Interface Load Transfer Degradation During Cyclic Loading: a Microscale Investigation. *Soils and Foundations*, 43(4):81–93, 2003. ISSN 1341-7452. doi: 10.3208/sandf.43.4_81.

[29] D. A. De Lange, A. F. Van Tol, J. Dijkstra, A. Bezuijen, and R. Stoevelaar. Set-up effects of piles in sand tested in the centrifuge. *Physical Modelling in Geotechnics - Proceedings of the 8th International Conference on Physical Modelling in Geotechnics 2014, ICPMG 2014*, 2:721–727, 2014.

[30] L de Neef, P Middendorp, and J Bakker. Installation of monopiles by vibrohammers for the Riffgat Project. *Piling Symposium*, pages 1–14, 2015.

[31] A De Nicola. *The performance of pipe piles in sand.* Ph. d. thesis, University of Western Australia, 1996.

[32] a. De Nicola and M. F. Randolph. The plugging behaviour of driven and jacked piles in sand. *Géotechnique*, 47(4):841–856, 1997. ISSN 0016-8505. doi: 10.1680/geot.1997.47.4.841.

[33] A. J. Deeks. *Numerical Analysis of Pile Driving Dynamics*. Ph.d. thesis, University of Western Australia, 1992.

[34] A. J. Deeks and M. F. Randolph. Analytical modelling of hammer impact for pile driving. *International Journal for Numerical and Analytical Methods in Geomechanics*, 17(5):279–302, 1993. ISSN 10969853. doi: 10.1002/nag.1610170502.

[35] EIA. International Energy Outlook 2017 Overview. *U.S. Energy Information Administration*, IEO2017(2017):143, 2017. ISSN 0163660X. doi: www.eia.gov/forecasts/ieo/pdf/0484(2016).pdf.

[36] European Commission. Green Paper - A 2030 framework for climate and energy policies. *COM(2013) 169 final*, pages 1–16, 2013.

[37] European Commission. A policy framework for climate and energy in the period from 2020 up to 2030, 2014. ISSN 1935-5130.

[38] European Commission. Proposal for a directive of the European Parliament and of the council on the promotion of the use of energy from renewable sources (recast). *Official Journal of the European Union*, 0382(2016), 2017.

[39] EWEA. Wind Energy Scenarios For 2030. (August):16, 2015.

[40] J D Frost, Gregory L Hebeler, T Matthew Evans, and J T DeJong. Interface behavior of granular soils. In *Ninth Biennial Conference on Engineering, Construction, and Operations in Challenging Environments*, pages 65–72, Houdson, 2004.

[41] J Garnier and D. Konig. Scale effects in piles and nails loading tests in sand. *Centrifuge 98*, 98: 205–210, 1998.

[42] J. Garnier, C. Gaudin, S.M. Springman, P.J. Culligan, D. Goodings, D. Konig, B. Kutter, R. Phillips, M.F. Randolph, and L. Thorel. Catalogue of scaling laws and similitude questions in geotechnical centrifuge modelling. *International Journal of Physical Modelling in Geotechnics*, 7(3):01–23, 2007. ISSN 1346-213X. doi: 10.1680/ijpmg.2007.070301.

[43] M. Gates. Empirical Formula For Predicting Pile Bearing Capacity. *Civil Engineering*, 27(3): 65–66, 1957.

[44] Kenneth Gavin, David Igoe, and Paul Doherty. Piles for offshore wind turbines: a state-of-the-art review. *Proceedings of the Institution of Civil Engineers - Geotechnical Engineering*, 164(4): 245–256, 2011. ISSN 1353-2618. doi: 10.1680/geng.2011.164.4.245.

[45] G.G. Goble and F. Rausche. Wave Equation Analysis of Pile Driving - WEAP Program. Technical report, U.S. Department of Transportation, Federal Highway Administration, Office of Research and Development, Washington, D.C., 1976.

[46] G.G. Goble, J.J. Tomko, F. Rausche, and P.M. Green. Dynamic studies on the bearing capacity of piles (Report No. 31, Vols. 1 and 2). Technical report, Case Western Reserve University, Division of Solid Mechanics, Structures, and Mechanical Design, 1968.

[47] G.G. Goble, F. Rausche, and G. Likins. The analysis of pile driving—a state-of-the-art. In *Proceedings of the 1st International Seminar of the Application of Stress-Wave Theory to Piles*, pages 131–162, Stockholm, 1980. A.A. Balkema Publishers Rotterdam.

[48] Inc. Goble, Rausche, Linkins and Associates. GRLWEAP Users Manual. Technical report, Cleveland, Ohio, 1996.

[49] S.R. Gudavalli, O. Safaqah, and H. Seo. Effect of Soil Plugging on Axial Capacity of Open-Ended Pipe Piles in Sands. In *Proceedings of the 18th International Conference on Soil Mechanics and Geotechnical Engineering*, pages 1487–1490, Paris, 2013.

[50] Patrick J. Hannigan, Frank Rausche, Garland E. Likins, Brent P. Robinson, and Matthew L. Becker. Design and Construction of Driven Pile Foundations – Volume II. Technical report, Federal Highway Administration, U.S. Dept. of Transportation., Washington, D.C., 1998.

[51] Mads Helsager Harpoth. *Development of driveability model for piles for offshore wind turbines*. M.sc. thesis, Aalborg University, 2017.

[52] Edward P. Heerema. Predicting Pile Driveability: Heather As an Illustration of the 'Friction Fatigue' Theory. *Ground Engineering*, 13(3):15–20, 1980. ISSN 00174653. doi: 10.1016/0148-9062(80)90719-6.

[53] Het Parool. Nuon wint subsidievrij windpark Noordzee, mar 2018.

[54] T.J. Hirsch, L. Carr, and L.L. Lowery. TTI Program. Technical report, U.S. Department of Transportation, Federal Highway Administration, Offices of Research and Development, Washington, D.C., 1976.

[55] T. Y. K. Ho, R. J. Jardine, and N. Anh-Minh. Large-displacement interface shear between steel and granular media. *Geotechnique*, 61(3):221–234, 2010.

[56] P. Hölscher, A. F. Van Tol, and N. Q. Huy. Rapid pile load tests in the geotechnical centrifuge. *Soils and Foundations*, 52(6):1102–1117, 2012. ISSN 00380806. doi: 10.1016/j.sandf.2012.11.024.

[57] Jin-Hung Hwang, Neng Liang, and Cheng-Hsing Chen. Ground Response during Pile Driving. *Journal of Geotechnical and Geoenvironmental Engineering*, 127(11):939–949, 2001. ISSN 1090-0241. doi: 10.1061/(ASCE)1090-0241(2001)127:11(939).

[58] Magued Iskander. *Behavior of pipe piles in sand*. Springer, New York, 2010. ISBN 9783642131073. doi: 10.1007/978-3-642-13108-0.

[59] T. Iwanowski and A. Bodare. On soil damping factor used in wave analysis of pile driving. In B.H. Fellenius, editor, *International conference on Application of Stress-wave Theory to Piles*, pages 343–352, Ottawa, Canada, 1988.

[60] R Jardine, F Chow, R Overy, and J Standing. *ICP design methods for driven piles in sands and clays*. Thomas Telford Publishing, London, UK, 2005. ISBN 0727732722. doi: 10.1680/idmfdpisac.32729.

[61] R. J. Jardine and F. C. Chow. *New design methods for offshore piles (MTD publication)*. Marine Technology Directorate, 1996.

[62] R J Jardine, Z X Yang, P Foray, and Bt Zhu. Interpretation of stress measurements made around closed-ended displacement piles in sand. *Géotechnique*, 63(8):613–627, 2013. ISSN 0016-8505. doi: 10.1680/geot.9.P.138.

[63] R. J. RJ Jardine, BM B.M. Lehane, and SJ S.J. Everton. Friction coefficients for piles in sands and silts. In *Proc. Int. Conf. on Offshore Site Investigation and Foundation Behaviour*, volume 28, pages 661–677, London, UK, 1993. ISBN 0952-1798. doi: 10.1007/978-94-017-2473-9_31.

[64] R Kelly. Development of a large diameter ring shear apparatus and its use. Ph.D thesi (September), 2001.

[65] E.U. Klotz and M.R. Coop. An investigation of the effect of soil state on the capacity of driven piles in sands. *Géotechnique*, 51(9):733–751, 2002. ISSN 0016-8505. doi: 10.1680/geot.2002.52.8.620.

[66] Clemens Krapfenbauer. *Experimental Investigation of Static Liquefaction in Submarine Slopes*. Msc thesis, ETH Zurich, 2016.

[67] Bruce L Kutter. Dynamic centrifuge modeling of geotechnical structures. *Transportation research record*, (1336):24–30, 1992. ISSN 0309051746.

[68] P.C. Lambe and R.V. Whitman. Scaling for earthquake shaking tests on a centrifuge. In *Conference of Soil Dynamics and Earthquake Engineering*, volume 7, pages 367–378, Southampton, 1982.

[69] B. M. Lehane, C. Gaudin, and J.A. Schneider. Scale effects on tension capacity for rough piles buried in dense sand. *Géotechnique*, 55(10):709–719, 2005. ISSN 0016-8505. doi: 10.1680/geot.2005.55.10.709.

[70] Barry Lehane. *Experimental investigations of pile behaviour using instrumented field piles*. Ph.d. thesis, University of London (Imperial College), UK., 1992.

[71] Barry M. Lehane, James A. Schneider, Jit Kheng Lim, and Giuseppe Mortara. Shaft Friction from Instrumented Displacement Piles in an Uncemented Calcareous Sand. *Journal of Geotechnical and Geoenvironmental Engineering*, 138(11):1357–1368, 2012. ISSN 1090-0241. doi: 10.1061/(ASCE)GT.1943-5606.0000712.

[72] B.M. Lehane and R.J. Jardine. Shaft capacity of driven piles in sand: a new design method. In *In Proceedings of the 7th International Conference on the Behaviour of Offshore Structures*, pages 23–36, Boston, 1994.

[73] B.M. Lehane, R.J. Jardine, A.J. Bond, and R. Frank. Mechanisms of shaft friction in sand from instrumented pile tests. *Journal of Geotechnical Engineering*, 119(1):19–35, 1993.

[74] J. Luking and H. G. Kempfert. Plugging Effect of Open-Ended Displacement Piles. *ISSMGE 2013 Paris*, pages 2363–2366, 2005.

[75] Sanjeev Malhotra. *Selection, Design and Construction of Offshore Wind Turbine Foundations*. 2010. ISBN 978-953-307-221-0.

[76] D. Masin. *Report on the triaxial tests on GEBA sand carried out for client : IHC IQIP, NL*. Technical report, 2017.

[77] K R Massarsch. Ground Vibrations Caused by Impact Pile Driving. In *Proceedings, Environmental Vibrations: Prediction, Monitoring, Mitigation and Evaluation (ISEV 2005)*, number Isev, pages 369 – 379, Okayama University, Japan, 2005. Taylor & Francis.

[78] K Rainer Massarsch and Bengt H Fellenius. GROUND VIBRATIONS INDUCED BY IMPACT PILE DRIVING. *International Conference on Case Histories in Geotechnical Engineering.*, 2008.

[79] Gary Mavko. Conceptual Overview of Rock and Fluid Factors that Impact Seismic Velocity and Impedance. Technical report, 2005.

[80] P. C. Meijers, A. Tsouvalas, and A. V. Metrikine. The Effect of Stress Wave Dispersion on the Drivability Analysis of Large-Diameter Monopiles. *Procedia Engineering*, 199:2390–2395, 2017. ISSN 18777058. doi: 10.1016/j.proeng.2017.09.272.

[81] Christopher Mone, Maureen Hand, Mark Bolinger, Joseph Rand, Donna Heimiller, Jonathan Ho, Christopher Mone, Maureen Hand, Mark Bolinger, and Joseph Rand. 2015 Cost of Wind Energy Review. Technical Report May, National Renewable Energy Laboratory (NREL), 2015.

[82] G. Mortara. *An elasto-plastic model for sand-structure interface behavior under monotonic and cyclic loading*. Ph.d. thesis, Politecnico di Torino, Italy, 2001.

[83] C T Nguyen. Centrifuge modelling of rapid load tests with piles in silt and sand. *Frontiers in Offshore Geotechnics II, ISFOG 2010 - Proceedings*, (Taylor 2005):537–542, 2010. doi: doi: 10.1201/b10132-7010.1201/b10132-70.

[84] R. E. Olson and K. S. Flaate. Pile-Driving Formulas for Friction Piles in Sand. *Journal of the Soil Mechanics and Foundations Division*, 93(SM6):279–296, 1967.

[85] N.K. Oveson. The use of physical models in design. In *Proceedings of the 7th ECSMFE*, Brighton, 1979.

[86] Erdem Ozsu, An-Ninh Ta, Bruno Stuyts, and Christophe Jaeck. Optimizing Pile Driving Fatigue for Offshore Foundations in Very Dense Sand: A Case Study. *Volume 6: Polar and Arctic Sciences and Technology; Offshore Geotechnics; Petroleum Technology Symposium*, 6(June): V006T10A026, 2013. doi: 10.1115/OMAE2013-10664.

[87] K.H. Paik and S.R. Lee. Behavior of Soil Plugs in Open-Ended Model Piles Driven into Sands. *Marine Georesources and Geotechnology*, 11:353–373, 1993.

[88] S. G. Paikowsky and L. R. Chernauskas. Energy approach for capacity evaluation of driven piles, 1992.

[89] S.G. Paikowsky, R.V. Whitman, and M.M. Baligh. A new look at the phenomenon of offshore pile plugging. *Marine Geotechnology*, 8(3):213–230, 1989. doi: https://doi.org/10.1080/10641198909379869.

[90] PDI Pile Dynamics. GRLWEAP Procedures and Models. Technical report, Pile Dynamics Inc., Cleveland, OH, 2010.

[91] K. S. Prakasha, H. a. Joer, and M. F. Randolph. Establishing a model testing capability for deep water foundation systems. In *Frontiers in Offshore Geotechnics, ISFOG 2005 - Proceedings of the 1st International Symposium on Frontiers in Offshore Geotechnics*, pages 309–315, Seoul, 2005. ISBN 0415390648. URL `http://www.scopus.com/inward/record.url?eid=2-s2.0-33947526196{&}partnerID=tZOtx3y1`.

[92] T O Quinten. Experience on the preparation of HPMC viscous fluid for physical modeling in the geocentrifuge. Technical report, Delft University of Technology, Delft, 2019.

[93] M. F. Randolph, E. C. Leong, and G. T. Houlsby. One-dimensional analysis of soil plugs in pipe piles. *Géotechnique*, 41(4):587–598, 1991. ISSN 0016-8505. doi: 10.1680/geot.1991.41.4.587.

[94] M. F. Randolph, J. Dolwin, and R. Beck. Design of driven piles in sand. *Geotechnique*, 44(3): 427–448, 1994. ISSN 00168505. doi: 10.1680/geot.1994.44.3.427.

[95] M.F. Randolph. The axial capacity of deep foundations is calcareous soils (state-of-the-art report). *Proc. Int. Conf. Calcareous Sediemnts, Perth, Vol. 2*, 2:837–857, 1988.

[96] F. Rausche. Pile Driving Equipment: Capabilities, and Properties. In *Sixth Conference on the Application of Stress-wave Theory to Piles*, pages 75 – 98, Sao Paulo, Brazil, 2000.

[97] F. Rausche, G.G. Goble, and G.E. Likins. Investigation of dynamic soil resistance on piles using GRLWEAP. In *Proceedings of the 3rd International Conference on the Application of Stress-Wave Theory to Piles*, pages 137–142, Rotterdam, Netherlands, 1992.

[98] F. Rausche, G. Likins, and G. Goble. A Rational and Usable Wave Equation Soil Model Based on Field Test Correlation. In *Proc. Int. Conf. Design and Construction of Deep Foundations*, Orlando, FL, 1994.

[99] J Rietdijk, F M Schenkeveld, P E L Schaminee, and a Bezuijen. The drizzle method for sand sample preparation. In *7th International Conference on Physical Modelling in Geotechnics*, volume 1, pages 267–272, London, UK, 2010. Taylor & Francis. ISBN 9780415592888.

[100] Arunjyoti Sarkar and Ove T Gudmestad. Installation of Monopiles for Offshore Wind Turbines – By Using End-Caps and a Subsea Holding Structure. *Connect*, (February 2016):1–7, 2011. doi: 10.1115/OMAE2011-49129.

[101] Steve Sawyer, Sven Teske, and Morten Dyrholm. The Global Wind Energy Outlook. *Gwec*, 2016.

[102] A.N. Schofield. Cambridge Geotechnical Centrifuge Operations. *Geotechnique*, 30(3):227–268, 1980.

[103] Siemens. What is the real cost of offshore wind? *Consumer Policy Review*, 15(3):1–7, 2014.

[104] R Skov and H Denver. Time-dependence of bearing capacity of piles. In *Proceedings 3rd Int. Conf. on App. Stress-wave theory to piles*, pages 879–888, Ottawa, Canada, 1988.

[105] E.A.L. Smith. Pile Driving Analysis by Wave Equation, 1960.

[106] I. M. Smith and Y. K. Chow. Three dimensional analysis of pile drivability. In *Proc. 2nd Int. Conf. on Numerical Methods in Offshore Piling*, pages 1–19, Austin, Texas, 1982.

[107] Brian Snyder and Mark J. Kaiser. Ecological and economic cost-benefit analysis of offshore wind energy. *Renewable Energy*, 34(6):1567–1578, 2009. ISSN 09601481. doi: 10.1016/j.renene.2008.11.015.

[108] RS Stevens, EA Wiltsie, and TH Turton. Evaluating Drivability for Hard Clay Very Dense Sand and Rock. In *Offshore Technology Conference*, pages 465–482, Houston, USA, 1982. doi: http://dx.doi.org/10.4043/4205-MS.

[109] R.N. Taylor. *Geotechnical Centifuge Technology*. Blackie Academic & Professional, London, 1995. ISBN 9780751400328.

[110] F. E. Toolan, M. L. Lings, and U. A. Mirza. An appraisal of API RP2A recommendations for determining skin friction of piles in sand. In *Proceedings of the 22nd Annual Offshore Technology Conference*, pages 33–42, Houston, USA, 1992.

[111] FE TOOLAN and DA FOX. Geotechnical Planningof Piled Foundations for Offshore Platforms. In *Proceedings of the Institution of Civil Engineers*, volume 62, pages 221–244, London, UK, 1977. doi: 10.1680/iicep.1977.3224.

[112] J. Van Zeben. *Physical modelling of pore pressure development during impact pile driving using geo-centrifuge*. Msc. thesis, Delft University of Technology, 2017.

[113] Vattenfall. Kriegers flak offshore wind farm-design basis foundations. Technical report, Vattenfall Vindkracft AB, 2008.

[114] A Verruijt. Waves in Piles. *An Introduction to Soil Dynamics*, pages 17–44, 2010. doi: 10.1007/978-90-481-3441-0_2.

[115] D. J. White. *A general framework for shaft resistance on displacement piles in sand*. Taylor and Francis, 2005.

[116] D J White and M D Bolton. Observing friction fatigue on a jacked pile. *Centrifuge and constitutive modelling: Two extremes*, (Equation 1):346–354, 2002.

[117] D. J. White and M. D. Bolton. Displacement and strain paths during plane-strain model pile installation in sand. *Géotechnique*, 54(6):375–397, 2004. ISSN 0016-8505. doi: 10.1680/geot.2004.54.6.375.

[118] D. J. White and B. M. Lehane. Friction fatigue on displacement piles in sand. *Géotechnique*, 54(10):645–658, 2004. ISSN 0016-8505. doi: 10.1680/geot.2004.54.10.645.

[119] Wind Energy Update (WEU). Offshore Foundations and Supporting Structures. Technical report, 2015.

[120] Wind Europe. Wind in power 2016 European Statistics. *Wind Europe*, (February):1–24, 2016. ISSN 09574522. doi: 10.1007/s10854-007-9177-9.

[121] WindEurope. Offshore Wind in Europe, Key Trends and Statistics 2017. Technical report, 2017.

[122] WindEurope and BVG Associates. Unleashing Europe's offshore wind potential. (June):64, 2017.

[123] A Wood Muir and P Knight. Site investigation and geotechnical design strategy for offshore wind development. *Proc. 18th ICSMGE.*, pages 2375–2378, 2013.

[124] X. Xu, B. M. Lehane, and J. a. Schneider. Evaluation of end-bearing capacity of open-ended piles driven in sand from CPT data. *Frontiers in Offshore Geotechnics, ISFOG 2005 - Proceedings of the 1st International Symposium on Frontiers in Offshore Geotechnics*, n/a:725–731, 2005. URL `http://www.scopus.com/inward/record.url?eid=2-s2.0-84863179092{&}partnerID=tZOtx3y1`.

A

Test matrix revision

The original test matrix of this research is presented in Table A.1. As challenges relating to the operation of the actuator, inhibited the execution of multi blow tests as specified in Table A.1. Consequently, several alterations were made to the test matrix. The definitive test matrix is included in the main report as Table 6.1 alongside an complementary set of four tests, which were also not part of the original test plan. Specifics relating to the aforementioned tests are included in Table 6.2. Causes underpinning the necessity of test matrix adjustments, as well as the reasoning behind the chosen method of revision are comprehensively discussed below.

Due to far-reaching improvements to the centrifuge actuator which was designed by Van Zeben (2017) ([112]), in excess of 50 centrifuge experiments were performed to verify the workings of newly added features and improvements to existing parts. These tests were predominantly related to the verification of (I) A newly designed (feedback-controlled) servo system to maintain the stroke of the hammer while driving; (II) the implementation of a stepper engine to extend the available range of driving frequencies towards lower frequencies, a modification which was required to execute the repeated single blow tests. Due to the use of an open-ended pile in the experiments, the driving resistance can almost exclusively be attributed to the friction component along the shaft of the pile. The shaft friction originates from shear stress applied by the soil exclusively, as fluids can generally not transmit shear forces. Hence, the magnitude of the shear force depends solely on the lateral pressure exerted onto the pile by the soil. Contrary to fluids, soils are anisotropic. Consequently, the coefficient which relates axial and lateral stress is less than unity. As axial soil stresses are related to the unit weight of the granules, so are the lateral stresses. However, when introducing a fluid to the soil matrix, the law of Archimedes states that the reprieved weight of the granules is reduced form a dry to an effective weight. Thereupon, both the axial and (consequently) lateral soil stresses are reduced. In turn, the latter reduces the soil resistance as perceived by the pile during driving and leading to larger penetration rates.

Predominantly, the increased penetration rate implicates higher operational strain on the servo system. Consequently, higher rotational velocities of the required to maintain hammer stroke during piling. Due to the favorable properties of stepper engines, specifically stability and controllability, this type of engine was the best-suited candidate to incorporate into the servo-system. By means of a linkage piece the motor's axle is connected to a worm-wheel. This combination yields a total mechanical advantage of $\approx$40, which means the system can theoretically mobilize several hundreds of kilograms. The mechanical advantage of the system follows from the quotient of the circumference of the thread over the winding pitch (vertical displacement per full rotation). Both of the aforementioned parameters are mechanical constants which are not straightforwardly adjusted. Therefore, maintaining a constant stroke at higher piling velocities requires a higher engine RPM. Here, at high operational velocities (RPM), the disadvantageous characteristic of stepper en-

Test [-]	Acceleration [g]	Type [SINGLE /MULTI]	Ram mass [-]	Frequency [Hz]	Energy/blow* [J] (Capacity [%])	Energy flux [J/s]	Relative packing [LOOSE/DENSE]	Saturation [%]	Repeat [NO/PREF/YES]
S2DXL	50	SINGLE	II; 140 g	n.a.	1.87 (67%)	n.a.	DENSE	0	PREF
S2DXH	50	SINGLE	II; 140 g	n.a.	2.80 (100%)	n.a.	DENSE	0	PREF
S2SXL	50	SINGLE	II; 140 g	n.a.	1.87 (67%)	n.a.	DENSE	100	PREF
S2SXH	50	SINGLE	II; 140 g	n.a.	2.80 (100%)	n.a.	DENSE	100	PREF
S3DXL	50	SINGLE	III; 220 g	n.a.	1.87 (42%)	n.a.	DENSE	0	PREF
S3DXH	50	SINGLE	III; 220 g	n.a.	2.80 (67%)	n.a.	DENSE	0	PREF
S3SXL	50	SINGLE	III; 220 g	n.a.	1.87 (42%)	n.a.	DENSE	100	PREF
S3SXH	50	SINGLE	III; 220 g	n.a.	2.80 (67%)	n.a.	DENSE	100	PREF
M2DLL	50	MULTI	II; 140 g	20	1.87 (67%)	33	DENSE	0	PREF
M2DLH	50	MULTI	II; 140 g	20	2.80 (100%)	56	DENSE	0	PREF
M2DHL	50	MULTI	II; 140 g	30	1.87 (67%)	56	DENSE	0	PREF
M2DHH	50	MULTI	II; 140 g	30	2.80 (100%)	84	DENSE	0	PREF
M2SLL	50	MULTI	II; 140 g	20	1.87 (67%)	33	DENSE	100	PREF
M2SLH	50	MULTI	II; 140 g	20	2.80 (100%)	56	DENSE	100	PREF
M2SHL	50	MULTI	II; 140 g	30	1.87 (67%)	56	DENSE	100	PREF
M2SHH	50	MULTI	II; 140 g	30	2.80 (100%)	84	DENSE	100	PREF
M3DLL	50	MULTI	III; 220 g	20	1.87 (42%)	33	DENSE	0	PREF
M3DLH	50	MULTI	III; 220 g	20	2.80 (67%)	56	DENSE	0	PREF
M3DHL	50	MULTI	III; 220 g	30	1.87 (42%)	56	DENSE	0	PREF
M3DHH	50	MULTI	III; 220 g	30	2.80 (67%)	84	DENSE	0	PREF
M3SLL	50	MULTI	III; 220 g	20	1.87 (42%)	33	DENSE	100	PREF
M3SLH	50	MULTI	III; 220 g	20	2.80 (67%)	56	DENSE	100	PREF
M3SHL	50	MULTI	III; 220 g	30	1.87 (42%)	56	DENSE	100	PREF
M3SHH	50	MULTI	III; 220 g	30	2.80 (67%)	84	DENSE	100	PREF
H2SLH	50	HALF PILE	II; 140 g	20	2.80 (67%)	56	DENSE	100	PREF
H2SHH	50	HALF PILE	II; 140 g	30	2.80 (100%)	84	DENSE	100	PREF
H3SHL	50	HALF PILE	III; 220 g	30	1.87 (42%)	56	DENSE	100	PREF
H3SHH	50	HALF PILE	III; 220 g	30	2.80 (67%)	84	DENSE	100	PREF

* Please note that this is the kinetic energy carried by the ram mass at an infinitesimal instant before impact (assuming no friction during fall). Hence, it is not equal to the net energy administered to the pile E_T. Theoretically, if driver system efficiency η_{ds} and the friction regime during the drop is the same, values for E_T should coincide. Experiments should establish whether the latter statement holds or if hammer stroke should be reevaluated

Table A.1: Test matrix

gines becomes perceivable: a negative correlation between RPM and engine efficiency, leading to the progressive reduction of available torque to regulate the displacement of the motor housing.

For low driving frequencies, as is the case for the repeated single blow tests, the low driving frequency provides the servo-system with a spacious interval to reevaluate the position of the motor housing. Consequently, the previously discussed increased piling rate in saturated conditions is surmountable at low frequencies. However, upon increasing the driving frequency (and reducing time interval for positional adjustment of the motor housing), operational margins are rapidly depleted. For the ultimate energy flux of 84 *J/s* (see Table A.1), the servo-system struggled to maintain the hammer's stroke during experiments of dry sand, executed at 20 *Hz*. Hence, the likelihood of exceeding the operational threshold of the servo-system, either during high frequency driving (30 *Hz*) or while conducting tests on saturated samples, is significant. In an attempt to increase the operational efficiency of the servo-system, three hypothesis relating to the cause of the observed limitation were formulated, specifically:

- Excessive friction between the worm-wheel and the threaded connection on the motor housing as a result of misalignment or lack of lubrication;
- Exceedance of the maximum axial load on the stepper engine when the ram mass is picked up by the notch on the flywheel. Due to the increase in rotational velocity of the flywheel for higher frequencies, the force generated upon impact could be of sufficient magnitude to overload the servo and temporarily drain momentum servo-system;
- Due to higher operating velocities as a result of increased driving rates, the efficiency of the stepper engine is reduced beyond the minimum threshold. As a result the torque applied on the worm-wheel by the engine is reduced to such an extend that movement of the motor housing insufficient for testing purposes or ultimately seized altogether.

Solutions corresponding to the three aforementioned hypothesis were rapidly drafted and entail the following countermeasures (please observe that the previously used order of listing is maintained):

- Minimization of operational friction was established through a complete realignment of the stepper engine, worm-wheel and motor housing was conducted. In addition, lubricant was applied on the worm-wheel;
- The compensate for the dynamic forces generated upon lifting the the ram mass, the balance of the motor housing and counterweight was re-evaluated. By adding mass to the counter weight, compressive stress on the axle of the stepper engine was decreased. This measure would provide more increase bandwidth of the compressive load buffer, which was possibly exceeded priorly upon impact of the flywheel notch and the ram's lifting pin;
- Most stepper engines can operate at different power inputs. Manufactures provide a maximum input voltage and current, which can be leveraged to boost the output torque of the engine. Although the negative correlation between torque and RPM remains, maximizing input voltage and current can increase torque at any given RPM up to several tens of percent. Alteration of the operational engine parameters (to be adjusted through manufacturer-provided software) can further help to maximize the engine's output. Parameters which were adjusted for this research include: (I) acceleration and deceleration of the engine [steps/s^2] (governs how fast the engine accelerates/decelerates to the desired velocity and thereby of influence to the engine's responsiveness); (II) holding current, A_{hold} [A]; which is the power supplied to the when idle and can help shorten response time; (III) maximum number of rotations per second (RPS) [*rev/s*] at full power, which govern the maximum rate of displacement of the motor housing (provided the stepper engine's torque is adequate to operate at the provided RPM under applicable loading conditions).

The solutions listed above were individually implemented and tested on their respective effectiveness to improve the operation of the servo-system. It was found that friction minimization,

together with re-evaluation of the motor-counterweight balance, were the most advantageous to the performance of the system. Increasing the input voltage to the stepper engine from $24V$ to $48V$ (despite the projected torque increase of 60%), yielded no noteworthy improvement. Due to the combined effect of the first two measures of the list above, it is likely that the torque capacity of the stepper engine became the limiting factor in its performance, disclosing the potential benefits of the input voltage increase. Further noticeable improvement of the performance of the actuator could possibly be established by the installation of more powerful (stepper) engine.

Despite the aforementioned measures and their respective effect on the performance of servo-system. In was proven impossible to realize the tests in Table A.1 in both dry and saturated conditions at the desired frequencies of 20 and 30 *Hz*. Hence, two possibilities to proceed remained: (I) re-design the servo system and incorporate a stronger (stepper) engine; (II) adjust the test matrix in such a way that the test lie within the operational range of the (optimized) servo-system. Eventually, a consensus was reached to proceed with the second alternative, which meant reducing the product of frequency and energy per blow, or energy flux in Table A.1. Consequently, two alternatives remained: (I) reduce the driving frequency; (II) reduce the energy per blow by re-evaluating the falling height of the ram mass. When translated to prototype scale, both options entailed the following respectively: (I) A reduction of driving frequency form 36 to 18 *blow/min* (for high frequency experiments) and from 24 to 12 *blow/min* for low frequency experiments; (II) Reducing the operational capacity of the **light** hammer (Ram mass II) from 67% and 100% (respectively for the corresponding minimum and maximum falling height) to 34% and 50%. Similarly for the **heavy** hammer (Ram mass III), operational capacity is decreased from 42% and 67% (respectively for the corresponding minimum and maximum falling height) to 21% and 34%.

As the driving frequency is not varied for the repeated single blow tests, aforementioned tests would not require re-execution in case the driving frequency for multi blow experiments was reduced, while the latter was not true in case the falling height was re-evaluated. Consequently, the frequency adjustment was labeled as the best alternative. Additionally, it was decided to eliminate the half pile tests from the matrix as the execution was no longer viable, provided the remaining time window for project completion. The latter entails that the qualitative investigation into dependency of the observed failure mechanism at the tip, as a function of driving frequency (M2SLH & M2SHH), energy per blow (M3SHL & M2SHH) and HiLo versus conventional driving (M2SLH & M3SHL), is omitted.

B

Complementary figures relating to PFP development for multi-blow experiments

This chapter complements the analysis of the PFP development for multi-blow experiments, which is part of the main report as 7.4. Due to the large overlap between observed trends in the PFP development for the six saturated, multi-blow experiments, the decision was made to solely focus of test M2SLL in the main report. However, in other to provide the full picture, relevant figures for the five remaining experiments are part of this Appendix. For clarity, the figures associated with each experiment are clustered in their own respective section. Consequently, test M2SLL, M2SLH, M3SLL, M3SLH and M3SHL are respectively highlighted in B.1, B.2, B.3, B.4 and B.5. In each section, there are the two figures which display deviatoric PFP as a function of radial distance to the pile tip, hence it is important to establish a reference for the pressures. This reference level is denoted as p_{ini} and is quantified in the soil stress plot corresponding the considered experiment (which is included in the respective section). Additionally, the meaning of the abbreviations used in the Figures is listed below:

- PFP = Pore Fluid Pressure;
- VF = Viscous Fluid;
- ROI = Region Of Interest;
- BE = Boundary Effects;
- SPFPS = Static Pore Fluid Pressure Sensor;

B.1. M2SLH

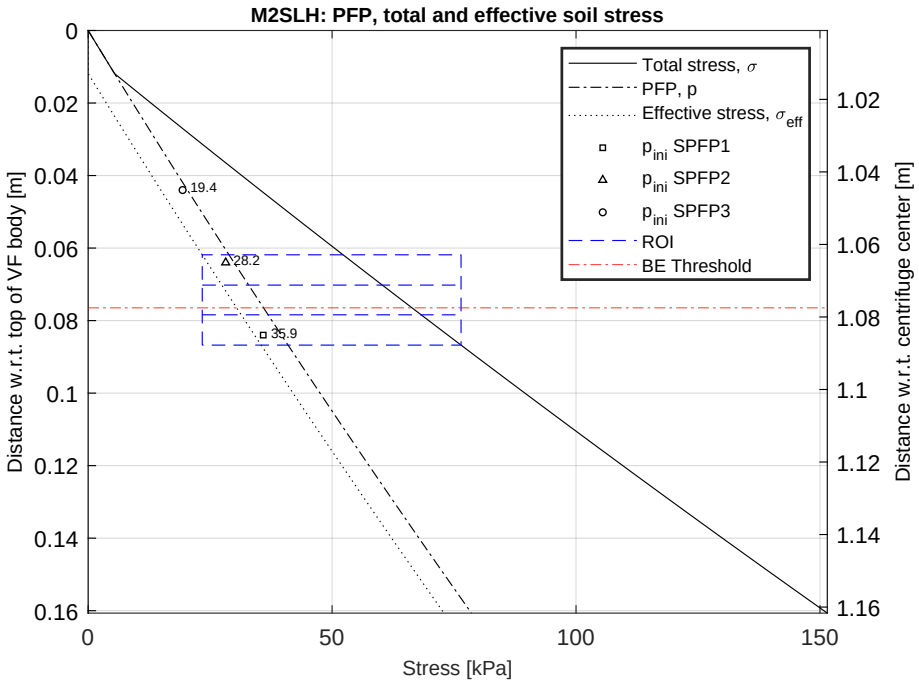

Figure B.1: Evolution of total stress, effective stress and PFP with depth for M2SLH provided a static test condition at 50g in the centrifuge. For completeness, the radial distance with respect to the center of the centrifuge is shown on the left y-axis.

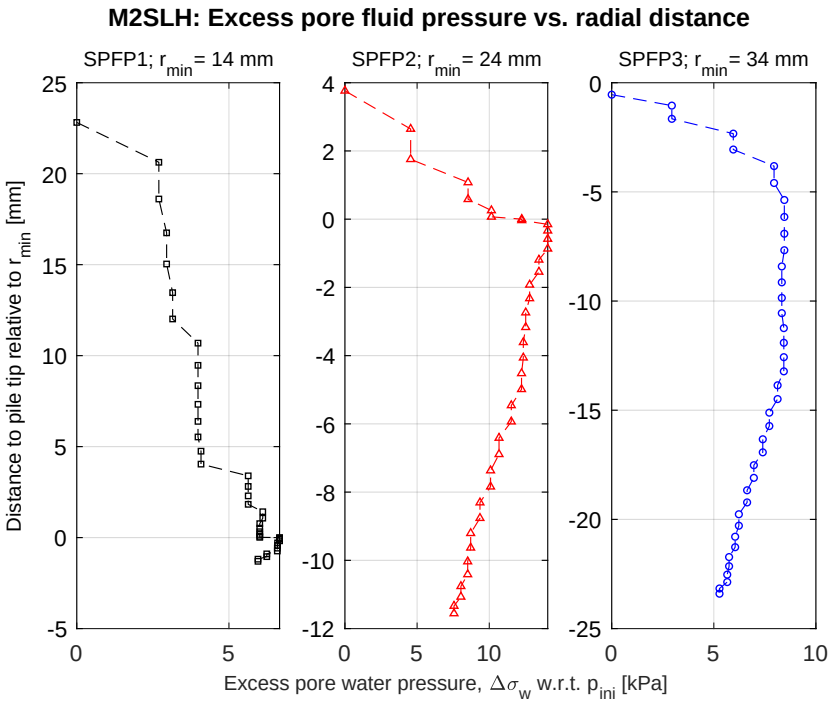

Figure B.2: δ_r^* versus deviatoric PFP (measured at low frequency). Please observe that through the definition of δ_r^*, the y-value is negative when the pile tip has surpassed the level at which the sensor is installed. r_{min}, as depicted above each subplot, is equivalent to the variable *dr* used in the report.

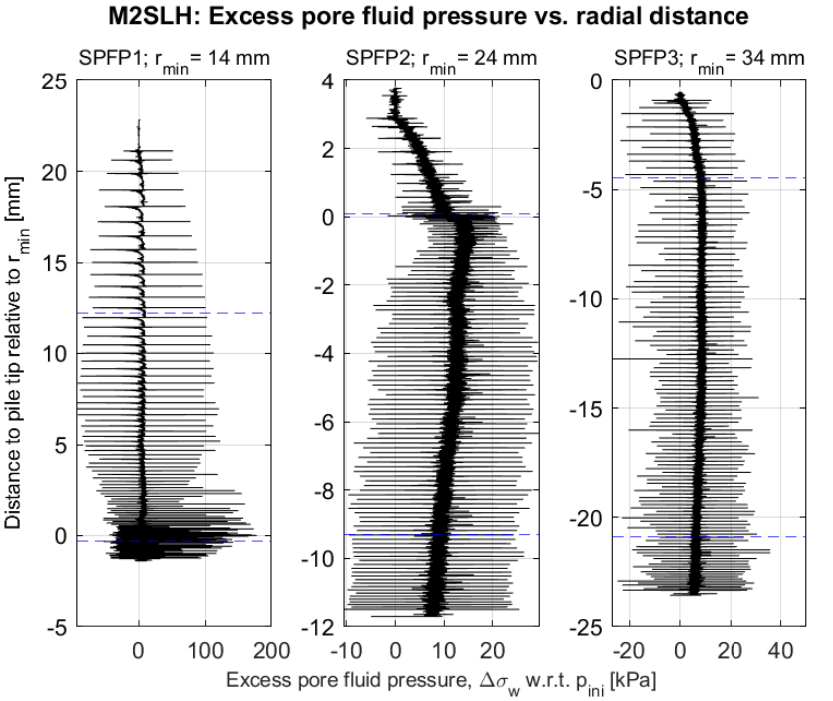

Figure B.3: Radial distance δ_r^* versus deviatoric PFP (measured at 1 *kHz*). Please observe that through the definition of δ_r^*, the y-value is negative when the pile tip has surpassed the level at which the sensor is installed. r_{min}, as depicted above each subplot, is equivalent to the variable *dr* used in the report. Dashed lines indicated the ROI as determined in accordance with C.2 for the respective test.

B.2. M2SHL

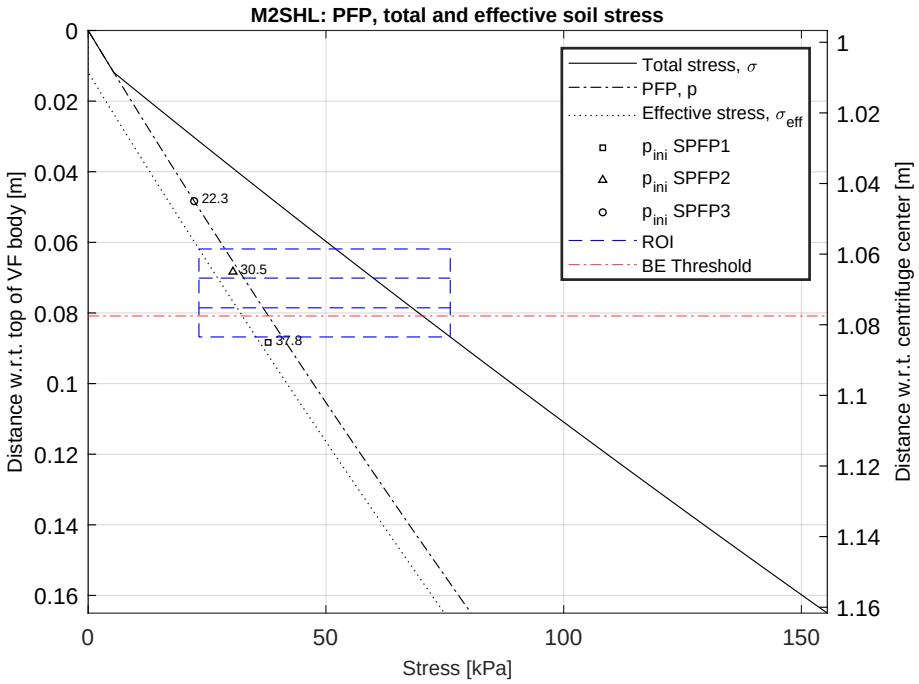

Figure B.4: Evolution of total stress, effective stress and PFP with depth for M2SHL provided a static test condition at 50g in the centrifuge. For completeness, the radial distance with respect to the center of the centrifuge is shown on the left y-axis.

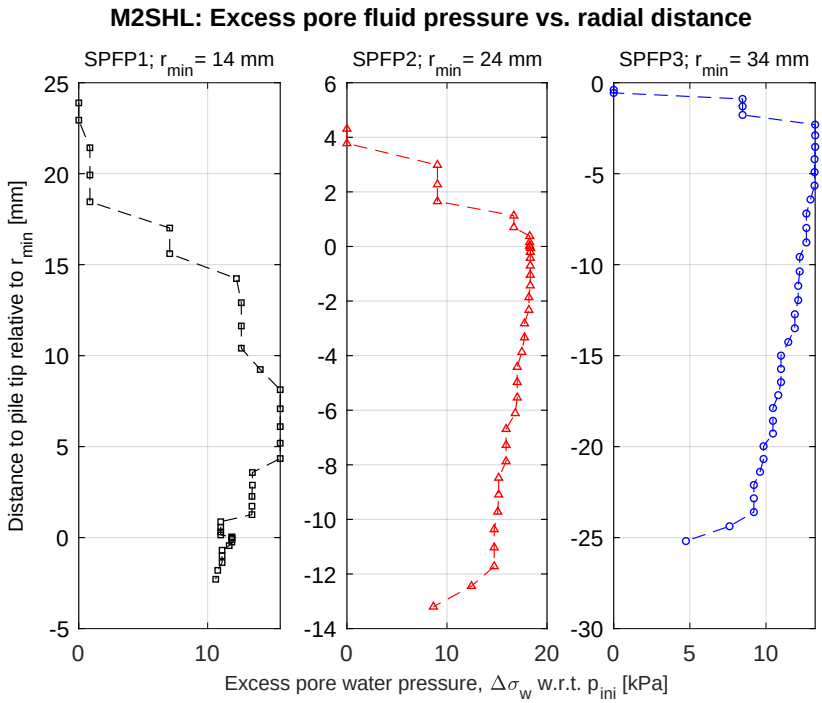

Figure B.5: δ_r^* versus deviatoric PFP (measured at low frequency). Please observe that through the definition of δ_r^*, the y-value is negative when the pile tip has surpassed the level at which the sensor is installed. r_{min}, as depicted above each subplot, is equivalent to the variable *dr* used in the report.

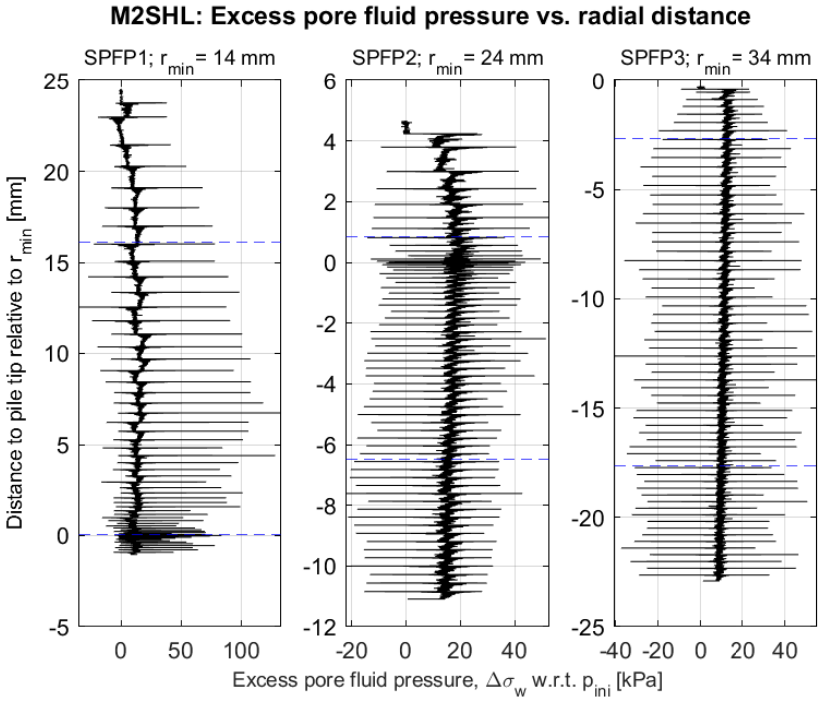

Figure B.6: Radial distance δ_r^* versus deviatoric PFP (measured at 1 *kHz*). Please observe that through the definition of δ_r^*, the y-value is negative when the pile tip has surpassed the level at which the sensor is installed. r_{min}, as depicted above each subplot, is equivalent to the variable *dr* used in the report. Dashed lines indicated the ROI as determined in accordance with C.2 for the respective test.

B.3. M3SLL

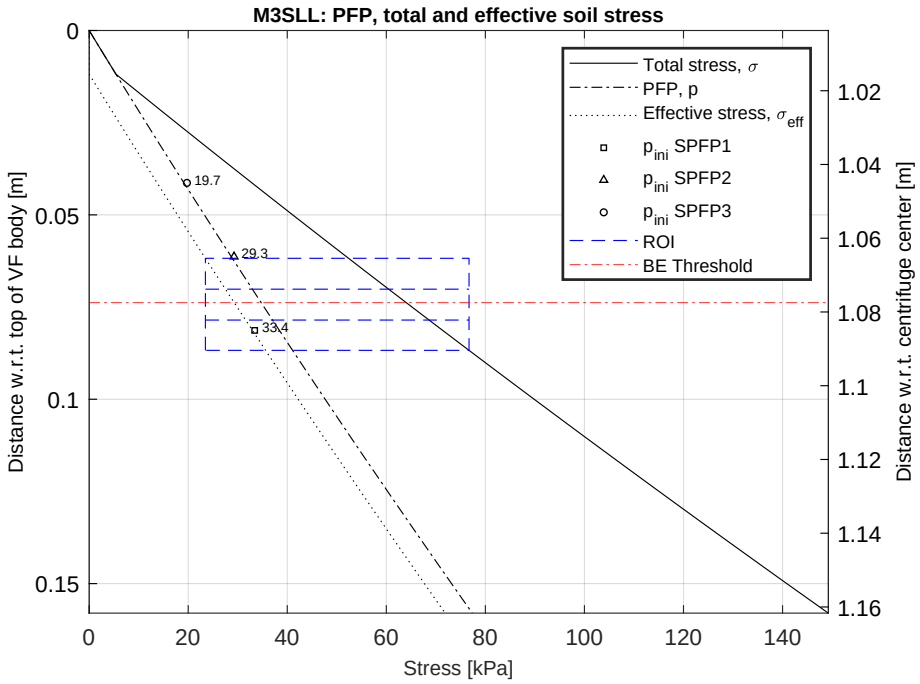

Figure B.7: Evolution of total stress, effective stress and PFP with depth for M3SLL provided a static test condition at 50g in the centrifuge. For completeness, the radial distance with respect to the center of the centrifuge is shown on the left y-axis.

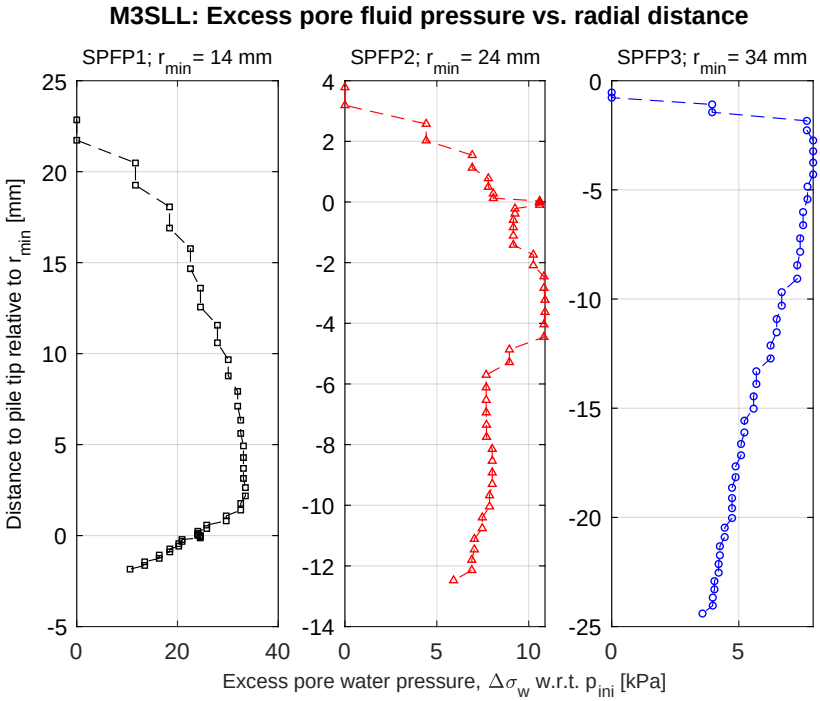

Figure B.8: δ_r^* versus deviatoric PFP (measured at low frequency). Please observe that through the definition of δ_r^*, the y-value is negative when the pile tip has surpassed the level at which the sensor is installed. r_{min}, as depicted above each subplot, is equivalent to the variable *dr* used in the report.

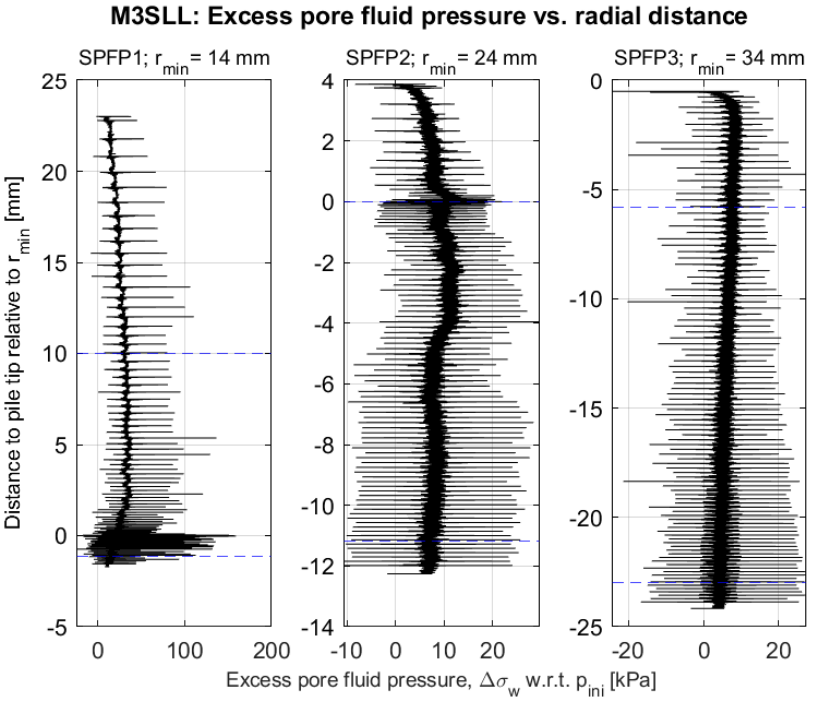

Figure B.9: Radial distance δ_r^* versus deviatoric PFP (measured at 1 *kHz*). Please observe that through the definition of δ_r^*, the y-value is negative when the pile tip has surpassed the level at which the sensor is installed. r_{min}, as depicted above each subplot, is equivalent to the variable *dr* used in the report. Dashed lines indicated the ROI as determined in accordance with C.2 for the respective test.

B.4. M3SLH

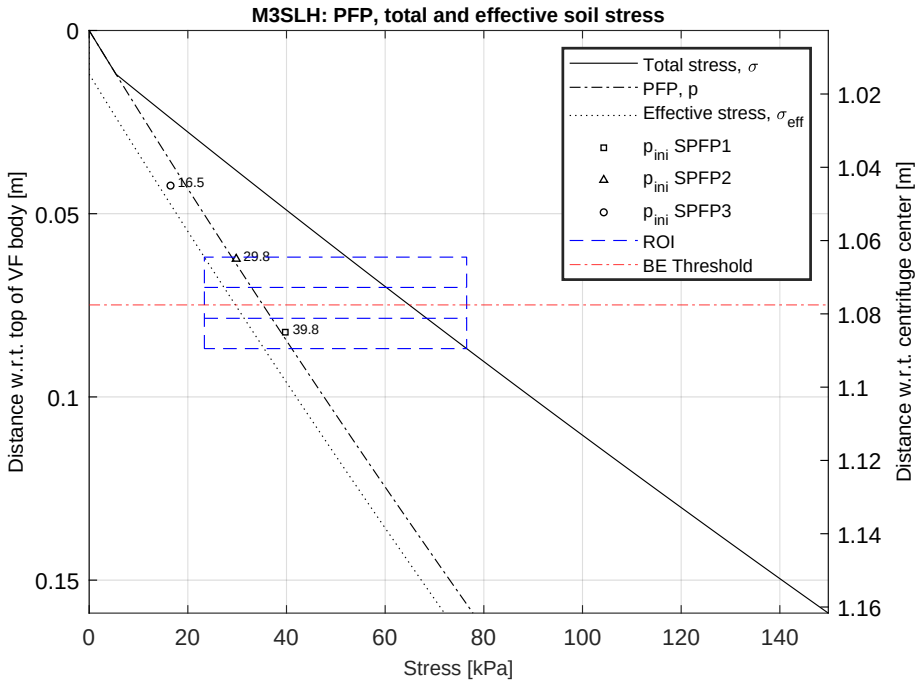

Figure B.10: Evolution of total stress, effective stress and PFP with depth for M3SLH provided a static test condition at 50g in the centrifuge. For completeness, the radial distance with respect to the center of the centrifuge is shown on the left y-axis.

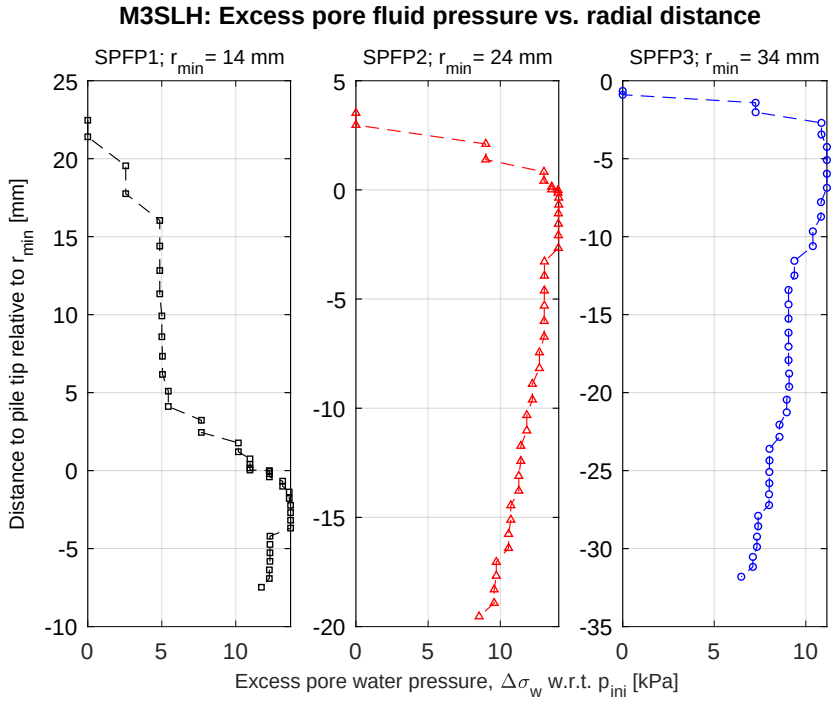

Figure B.11: δ_r^* versus deviatoric PFP (measured at low frequency). Please observe that through the definition of δ_r^*, the y-value is negative when the pile tip has surpassed the level at which the sensor is installed. r_{min}, as depicted above each subplot, is equivalent to the variable *dr* used in the report.

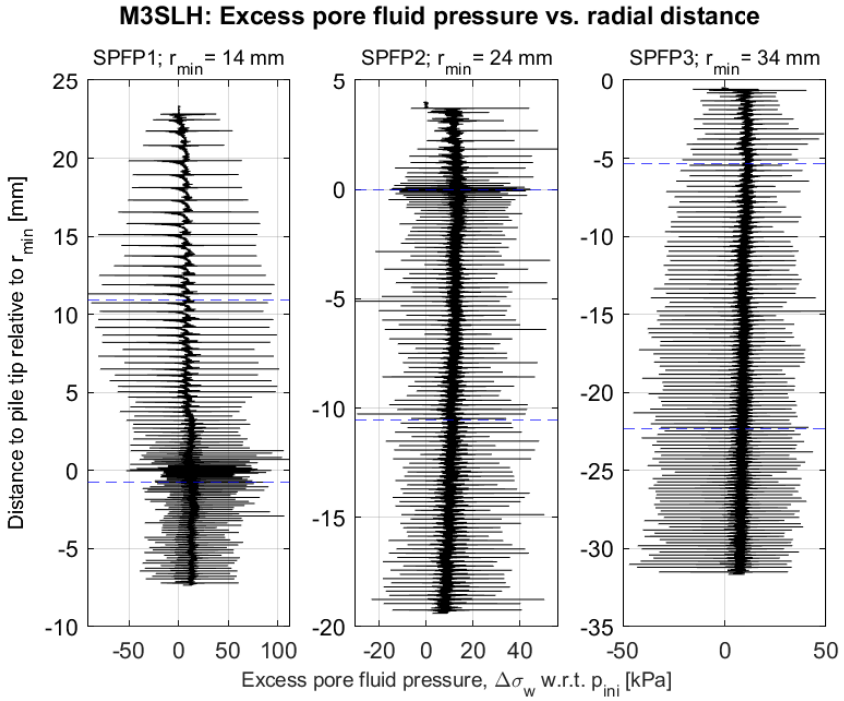

Figure B.12: Radial distance δ_r^* versus deviatoric PFP (measured at 1 *kHz*). Please observe that through the definition of δ_r^*, the y-value is negative when the pile tip has surpassed the level at which the sensor is installed. r_{min}, as depicted above each subplot, is equivalent to the variable *dr* used in the report. Dashed lines indicated the ROI as determined in accordance with C.2 for the respective test.

B.5. M3SHL

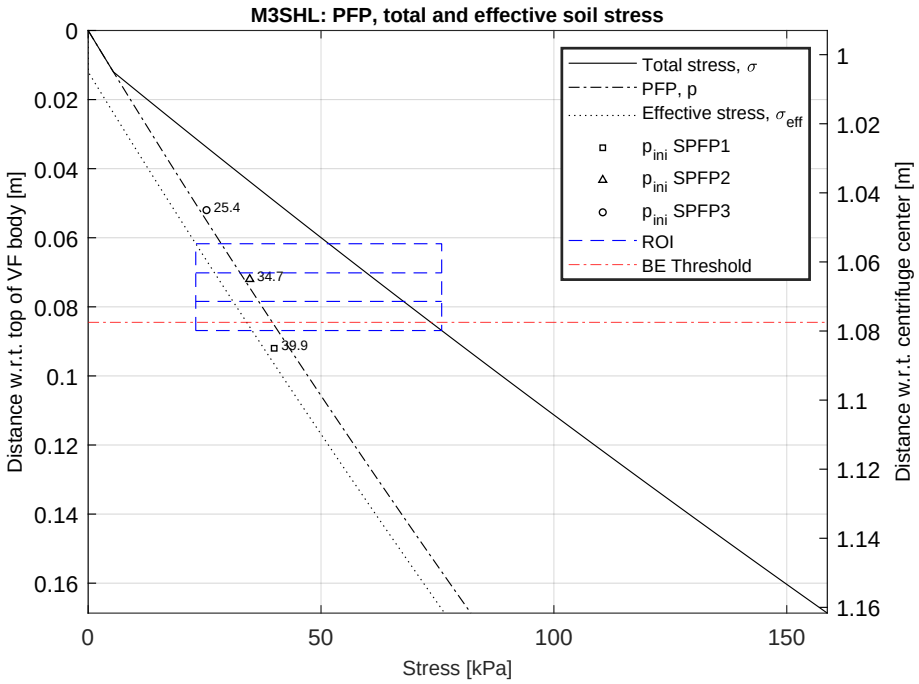

Figure B.13: Evolution of total stress, effective stress and PFP with depth for M3SHL provided a static test condition at 50g in the centrifuge. For completeness, the radial distance with respect to the center of the centrifuge is shown on the left y-axis.

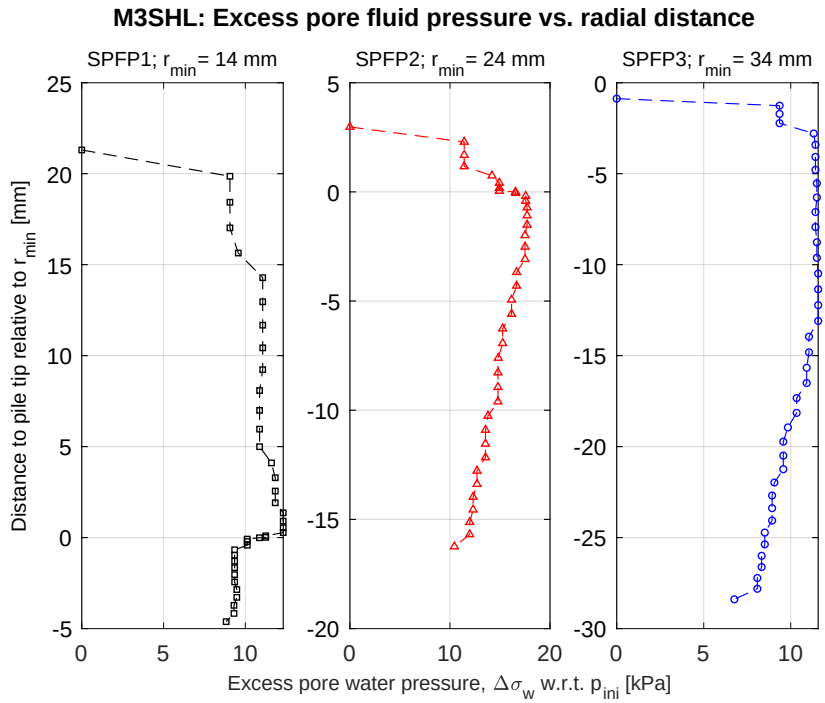

Figure B.14: δ_r^* versus deviatoric PFP (measured at low frequency). Please observe that through the definition of δ_r^*, the y-value is negative when the pile tip has surpassed the level at which the sensor is installed. r_{min}, as depicted above each subplot, is equivalent to the variable *dr* used in the report.

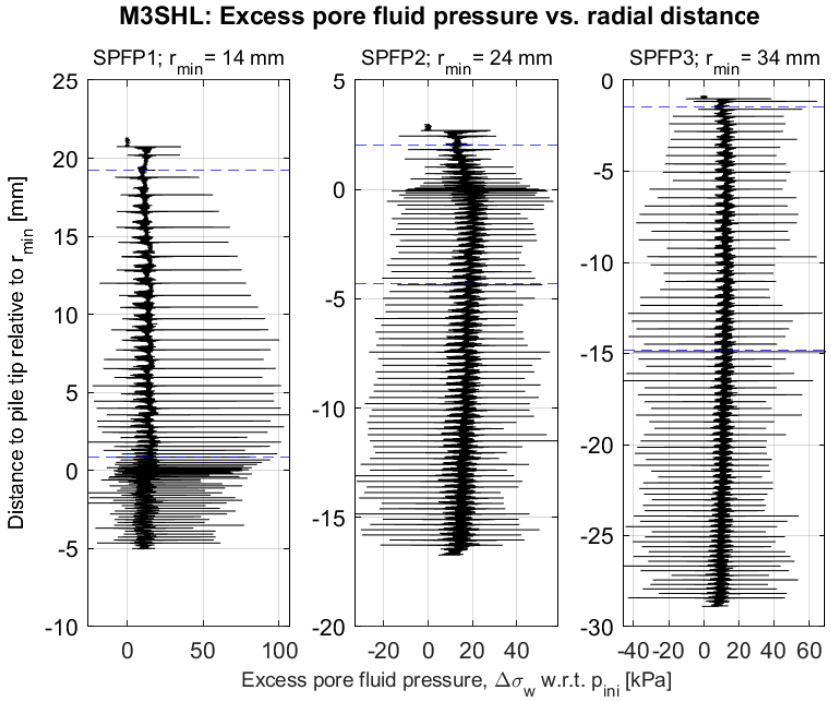

Figure B.15: Radial distance δ_r^* versus deviatoric PFP (measured at 1 *kHz*). Please observe that through the definition of δ_r^*, the y-value is negative when the pile tip has surpassed the level at which the sensor is installed. r_{min}, as depicted above each subplot, is equivalent to the variable *dr* used in the report. Dashed lines indicated the ROI as determined in accordance with C.2 for the respective test.

C

ROI definition and determination of driving parameters

C.1. Introduction

In the beginning, this chapter addresses the definition of the region of interest (ROI) and its respective determination for all experiments listed in Table 6.1 and is described in detail in C.2. Secondly, the procedure used to infer important driving parameters from the experimental data is elaborated upon in C.3. The aforementioned driving parameters include: (I) the non-dimensional pile penetration rate; (II) the theoretical impact velocity of the ram mass; (III) the measured impact velocity of the ram mass; (IV) The impact (kinetic) energy of the ram mass and hammer efficiency; (V) the driving frequency. Respectively, the full definition of all five parameters as well as the quantification process is discussed in C.3.1, C.3.2, C.3.2, C.3.3 and C.3.4. It should be noted that the all of the aforementioned parameters are defined for one specific test, namely: M2SLL. Therefore, this chapter essentially discusses the entire data processing work-flow on the basis of a single case study. However, the analysis described in the following was in fact executed all experiments from Table 6.1, with the exception of M2SHH and M3SHH. The corresponding results are included in the final section of this chapter, C.4.

C.2. ROI determination

Despite efforts to completely homogenize the specimens, as discussed in 7.2.1 and 7.2.2, some differences remained. Aforementioned differences are predominantly related to: (I) the distance of soil surface level with respect upper extremity of the strongbox; (II) the initial pile embedment level, relative to the centrifuge's center. Due to these small deviations a true one-to-one comparison between tests cannot be achieved. To produce optimal result despite of these intrinsic shortcomings, a normalized region of interest (ROI) is drafted to aid the cross-checking process. The delimitations to the aforementioned normalized penetration interval are as follows: (I) The upper boundary of the ROI is delimited by the maximum initial pile embedment (the distance between the pile tip and the soil surface level) of the ensemble of all 24 experiments form Table 6.1, with the exception of M2SHH and M3SHH. Henceforth, this value is denoted as the adjusted, initial penetration depth $w_{adj,\,ini}$. For the majority of experiments, the initial pile embedment w^*_{ini} is smaller than $w_{adj,\,ini}$. In this case, penetration data is disregarded up to the point where $w_{adj,\,ini}$ is surpassed; (II) The lower boundary of the ROI is defined as the minimum difference between $w_{adj,\,ini}$ and the final penetration depth of the ensemble of experiments. Respectively, the difference between the upper and lower ROI boundary is denoted as dw_{norm}. Consequently, dw_{norm} defines the bandwidth of the ROI. It is important to realize that the aforementioned interval is positioned relative to the soil surface

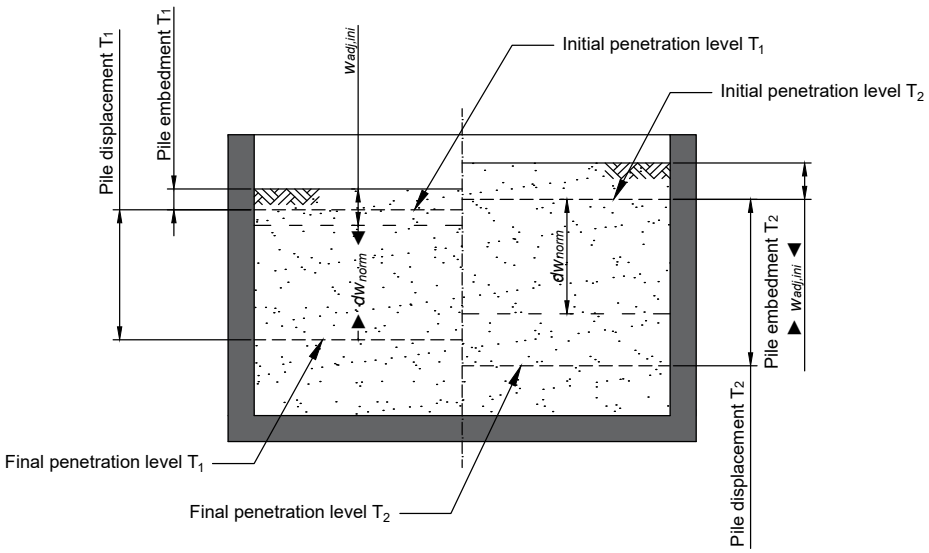

Figure C.1: Schematic overview of the determination of the region of interest (ROI) of penetration for comparative purposes. Left-hand side of the Figure corresponds to fictive test T_1, the right-hand side to T_2

level (SSL), of which the absolute distance to the center of the centrifuge may fluctuate between tests due small inconsistencies during sample preparation. To further illustrate the definition of the ROI, Figure C.1 describes its determination for two fictive tests, T_1 and T_2. Through definition of the ROI, the introduction of bias while comparing results between tests is kept to a minimum due to largely coinciding stress conditions and associated stress-dependant soil parameters; predominantly the internal friction angle ϕ. By means of an exemplary calculation, the importance of normalizing the pile embedment between tests is further substantiated. Reconsidering the two fictive tests T_1 and T_2, the implications of a deviation Δr from a hypothetical target embedment level are quantitatively assessed by deriving proportionality relationships for potential energy of the ram mass E_{pot} and soil resistance R_s. The corresponding relationships are respectively shown as Equations C.1 and C.2.

$$E_{\text{pot}} = mgh \Longrightarrow E_{\text{pot, 1}} \longleftrightarrow \frac{E_{\text{pot,2}}}{1+\Delta r} \tag{C.1}$$

$$R_s = \frac{1}{2}\rho g h^2 \cdot C_p \cdot K_n \cdot \tan(\delta_f) \Longrightarrow (\omega^2 r_1) \cdot {h_1}^2 \longleftrightarrow (\omega^2 (r_1+\Delta r)) \cdot (h_1+\Delta r)^2 \tag{C.2}$$

Where, C_p represents the circumference of the pile, K_n is the neutral lateral earth pressure coefficient and δ_f is the soil-structure friction angle. As follows from Equations C.1 and C.2, the soil resistance is most sensitive to deviations in the initial pile embedment w^*_{ini}. The latter justifies the approach where the ROI in defined such that R_s is comparable between tests by prescribing a minimum embedment level in the form of $w_{adj,\,ini}$. However, although the advocated normalization method is arguably the most advantageous, some minor negative implications should be appreciated. Most notably; as a result of embedment normalization, the number of load cycles experienced by the soil when the pile tip is level with the top of the ROI, deviate from test to test. Experiments for which it holds $w^*_{ini} < w_{adj,\,ini}$, the embedment difference is compensated by the penetration increment realized during the first blows of the driving sequence. Consequently, although limited, the effect of friction fatigue and accumulation of pore fluid pressures are likely to be more pronounced for tests which require a significant correction of initial pile embedment w^*_{ini}. Moreover, it could be that a section of the ROI extends beyond the threshold for bottom boundary effects as defined in

5.1.6. Moreover, as ROI is defined relative to the SSL, the degree of the exceedance of the threshold may very too. Although the recommendation with regard to the onset of bottom boundary effects was derived by Prakasha *et al.* (2005) ([91]) based on a set of experiments with a closed-ended pile (whereas this research employs an open-ended pile), the potential influence of boundary effects should be kept in mind. Finally, the correction of pile embedment introduced slight differences in the centrifugal acceleration perceived by the actuator during pile pile driving in the ROI. Amongst other things, this has an effect on the potential energy accumulated during lifting of the ram (as demonstrated by Equation C.1).

To maximize the comparability of the tests listed in Table 6.1, $w_{adj,\,ini}$ and dw_{norm} are sourced from the ensemble of all 22 tests. For clarity, the normative values for $w_{adj,\,ini}$ and dw_{norm} are highlighted in **boldface** and respectively equate to 49.97 mm and 4.05 mm. However, as dw_{norm}=4.05 mm does yield a representative comparison of ROI data, w_{norm} is set to 25 mm. As results of dry and saturated experiments are assessed separately, the parameters relating to the determination of the ROI are presented not presented in a single table. Instead, Table C.1 considers dry experiments, whereas Table C.2 addresses saturated tests. Below, parameters listed in both table C.1 and C.2 are defined. Moreover, relation between individual parameters is elucidated. Please observe that the parameters are listed by order of appearance (from left to right) in table C.1 and C.2.

1. *Test ID*, corresponds to the test ID as mentioned in the test matrix, Table 6.1;
2. *Sample ID*, relates to the sample used to conduct the particular test;
3. SSL_{SB}, the distance from the SSL to the upper extremity of the strongbox (SB) in [mm], which is respectively located at 0.985 m from the centrifuge center (CC);
4. SSL_{CC}, the distance from the SSL to the CC in [mm];
5. dw_{corr}, deviation of the actual embedment level of the pile with respect to the ideal embedment of 1.029 m from CC in [mm]. Exemplary causes for this deviation include: (I) the execution of a single blow test on the same sample prior to the initiation of the multi-blow test; (II) pile installation error; (III) a deliberate increase of the initial pile embedment. The latter is the case for all multi-blow tests, where the ideal embedment level increased to 1.049 m due to limitations relating to the operating velocity of the servo-system;
6. dw_{sw}, pile settlement due to spin-up of the centrifuge in [mm]. The value is calculated as the difference between: (I) apparent soil set-up while spinning down the centrifuge; (II) the apparent increase in penetration during centrifuge spin-up. The majority of both phenomena is due to effect of wind load on the potentiometer which records pile displacement, whatever remains is regarded as genuine pile settlement during spin-up;
7. $r_i ni^*$, the distance of the pile tip from the center of the centrifuge following full spin-up of the centrifuge in [mm]. In this sense $r_i ni^*$ equals the sum of the ideal penetration level (which, respectively for single and multi-blow tests, equates to 1.029 m and *1.049 m*), dw_{corr} and dw_{sw};
8. $w_i ni^*$, the embedment of the pile with respect to SSL following completion of the centrifuge spin-up in [mm];
9. dw_h, the total pile displacement achieved during impact driving in [mm];
10. $d\tilde{w}_h$, required penetration increment (realized though pile hammering) to attain $w_{adj,\,ini}$ in [mm];
11. dw_h^*, remaining length of the dw_h following achievement of the desires embedment $w_{adj,\,ini}$ in [mm].
12. dw_{norm}, length of the normalized pile penetration interval in mm;
13. r_{ini}, distance to the top of the ROI as seen from CC in [mm];
14. $w_{adj,\,ini}$, pile embedment at the top of the ROI in mm. In case $dw_h^* < dw_{norm}$, $w_{adj,\,ini}$ is reduced to fully accommodate dw_{norm}. The latter is the case for tests S2SXH, S3SXL, S3SXH and M2SLL.

Test ID	Sample ID	SSL_{SB}	SSL_{CC}	dw_{corr}	dw_{sw}	r^*_{ini}	w^*_{ini}	dw_h	$d\tilde{w}_h$	dw^*_h	dw_{norm}	r_{ini}	$w_{adj,\,ini}$
Unit	[-]	[mm]	[mm]	[mm]	[mm]	[mm]	[mm]	[mm]	[mm]	[mm]	[mm]	[mm]	[mm]
S2DXL	Dry82Y1	16.33	1001.33	0	0.64	1029.94	28.61	68.79	21.36	47.43	25	1051.30	49.97
S2DXH	Dry78X2	15.00	1000.00	0	1.59	1030.89	30.89	67.13	19.08	48.05	25	1049.97	49.97
S3DXL	Dry79Y2	15.00	1000.00	0	0.35	1029.65	29.65	68.05	20.33	47.72	25	1049.97	49.97
S3DXH	Dry80X4	15.00	1000.00	0	0.05	1029.35	29.35	68.53	20.62	47.90	25	1049.97	49.97
M2DLL	Dry80X19	15.00	1000.00	20	0.00	1049.30	49.30	45.22	0.67	44.55	25	1049.97	49.97
M2DLH	Dry82Z8	15.00	1000.00	20	0.05	1049.35	49.35	42.13	0.62	41.51	25	1049.97	49.97
M2DHL	Dry79X18	14.67	999.67	20	0.05	1049.35	49.69	44.24	0.29	43.95	25	1049.64	49.97
M2DHH	Dry79X16	15.33	1000.33	20	0.00	1049.30	48.97	49.13	1.01	48.12	25	1050.31	49.97
M3DLL	Dry80X17	15.33	1000.33	20	0.00	1049.30	48.97	32.10	1.01	31.10	25	1050.31	49.97
M3DLH	Dry81Z6	15.33	1000.33	20	0.29	1049.59	49.25	45.27	0.72	44.55	25	1050.31	49.97
M3DHL	Dry79Y4	15.67	1000.67	20	0.00	1049.30	48.63	38.27	1.34	36.93	25	1050.64	49.97
M3DHH	Dry77Z7	14.67	999.67	20	0.34	1049.64	**49.97**	46.39	0.00	46.39	25	1049.64	49.97

Table C.1: Summary of all relevant variables for the determination of the region of interest (ROI) for all dry tests from Table 6.1.

Test ID	Sample ID	SSL_{SB}	SSL_{CC}	dw_{corr}	dw_{sw}	r^*_{ini}	w^*_{ini}	dw_h	$d\tilde{w}_h$	dw^*_h	dw_{norm}	r_{ini}	$w_{adj,\,ini}$
Unit	[-]	[mm]	[mm]	[mm]	[mm]	[mm]	[mm]	[mm]	[mm]	[mm]	[mm]	[mm]	[mm]
S2SXL	Sat82Y2	30.00	1015.00	2.00	0.66	1031.96	16.96	59.32	33.02	26.30	25.00	1064.97	49.97
S2SXH	Sat79Z1	30.03	1015.03	0.00	1.42	1030.72	15.69	58.24	34.28	23.95	25.00	1063.96	47.93
S3SXL	Sat80X1	33.33	1018.33	0.00	0.44	1029.74	11.41	52.32	38.57	13.75	25.00	1057.06	37.73
S3SXH	Sat80Y1	42.67	1027.67	0.00	3.23	1032.53	4.86	49.17	45.11	**4.05**	25.00	1056.70	28.03
M2SLL	Sat79X2	29.33	1014.33	20.00	0.30	1049.60	35.27	39.30	14.70	24.59	25.00	1063.90	48.57
M2SLH	Sat81X6	28.00	1013.00	21.50	0.00	1050.80	37.80	40.15	12.17	27.98	25.00	1062.97	49.97
M2SHL	Sat81Y3	23.67	1008.67	20.00	0.83	1050.13	41.46	39.37	8.51	30.86	25.00	1058.64	49.97
M2SHH	NA	NA	NA	NA	NA	NA	NA	NA	NA	NA	NA	NA	NA
M3SLL	Sat82X5	30.67	1015.67	21.70	0.07	1051.07	35.41	40.61	14.57	26.04	25.00	1065.64	49.97
M3SLH	Sat80Y4	29.67	1014.67	21.60	0.77	1051.67	37.00	49.17	12.97	36.20	25.00	1064.64	49.97
M3SHL	Sat81X4	20.00	1005.00	23.00	0.27	1052.57	47.57	44.30	2.41	41.89	25.00	1054.97	49.97
M3SHH	NA	NA	NA	20.00	NA	NA	NA	NA	NA	NA	NA	NA	NA

Table C.2: Summary of all relevant variables for the determination of the region of interest (ROI) for all saturated tests from Table 6.1. Please observe that test M2SLL and M3SLL were both not executed as a consequence of capacity issues of the servo-system.

As is observed in Table C.1 and C.2, $w_{adj,\,ini}$ is not directly retractable to specific tabular value. This is due to the existence of tests (critically S3SXL and S3SXH) where the penetration increment required to attain $w_{adj,\,ini}$ would reduce dw_{norm} to a few millimeters. Hence, dw_{norm} is set to 25 mm. The choice for this particular value is based on: (I) 25 mm is directly compatible with most tests; (II) the ensures that the length of the interval is sufficient to draw meaningful conclusions based on penetration data from the ROI. In case the total penetration achieved during a test dw_h is insufficient to satisfy both $w_{adj,\,ini}$ and dw_{norm}, $w_{adj,\,ini}$ is reduced to the level where it is possible to accommodate dw_{norm}. As the position of the ROI is shifted towards the SSL, mean soil resistance is reduced with respect to experiments for which $w_{adj,\,ini}$ = 49.97 mm is maintained. Consequently, higher penetration rates are expected for experiments where the ROI is closer to the SSL. This effect is compensated during the normalization and nondimensionalization of the penetration rate, of which the associated procedure is discussed in 7.5.1 of the main report.

C.3. Determination of driving parameters

In this section, the determination of five important driving parameter is discussed. The parameter and the respective section in which it is discussed are a follows: (I) pile penetration rate, C.3.1; (II) theoretical impact velocity, C.3.2; (III) Experimental impact velocity, C.3.2; (IV) Kinetic enegery and hammer efficiency, C.3.3; (V) driving frequency, C.3.4.

C.3.1. Quantification of pile penetration rate

A parameter which plays an important role in the mutual comparison of the experiments concerns pile penetration. As this research exhibits a strong focus on the time-wise optimization of the driving operation, the rate of pile penetration is arguably more relevant. Generally, the pile penetration rate equals the time derivative of displacement. However, time derivation is ambiguous as it discloses nothing about the number of blows applied over the time interval. As this number is directly related to the number of load cycles experienced by the soil as stated by White and Bolton (2004) [117], seeking a definition which preserves the aforementioned relationship is arguably more insightful. Consequently, the definition of pile penetration rate for this research is provided by Equation C.3.

$$\tilde{p} = \frac{\Delta \tilde{w}}{n} \tag{C.3}$$

Where $\tilde{p}$ is the nondimensionalized pile penetration rate. $\Delta\tilde{w}$ is defined as the quotient of an arbitrary pile penetration increment Δw and the pile diameter Φ_p. Finally, n is the number of blows required to bridge the length of the arbitrary penetration interval.

In reality, the length of the considered penetration interval is not arbitrary but defined as the ROI. As discussed in C.2, use of an ROI enables fair comparison of experimental results as both soil stress conditions and stress-dependent soil parameters are comparable. Ideally, the ROI fixed with respect to the SSL. However due to limitation regarding the total pile penetration achieved during several tests of Table 6.1, the ROI is shifted towards the SSL in some instances. The latter ensures the comparative penetration interval is of equal length for all tests. As the penetration data from the ROI is ultimately used in contour plots, it is devised into three different subsections which are indicated in the third frame (as seen from the top) of Figure C.4. For each of the respective segments, the nondimensionalized penetration rate is computed through the use of Equation C.3. This method of analysis yields three values for $\tilde{p}$ per tests, thereby providing a larger sample population which is beneficial to the reliability of the contour plots.

C.3.2. Theoretical estimation of impact velocity

The determination of starts with processing the pile penetration (PP) and motor displacement (MD) data from each experiment, which are measured by two potentiometers: (I) connected to the shaft

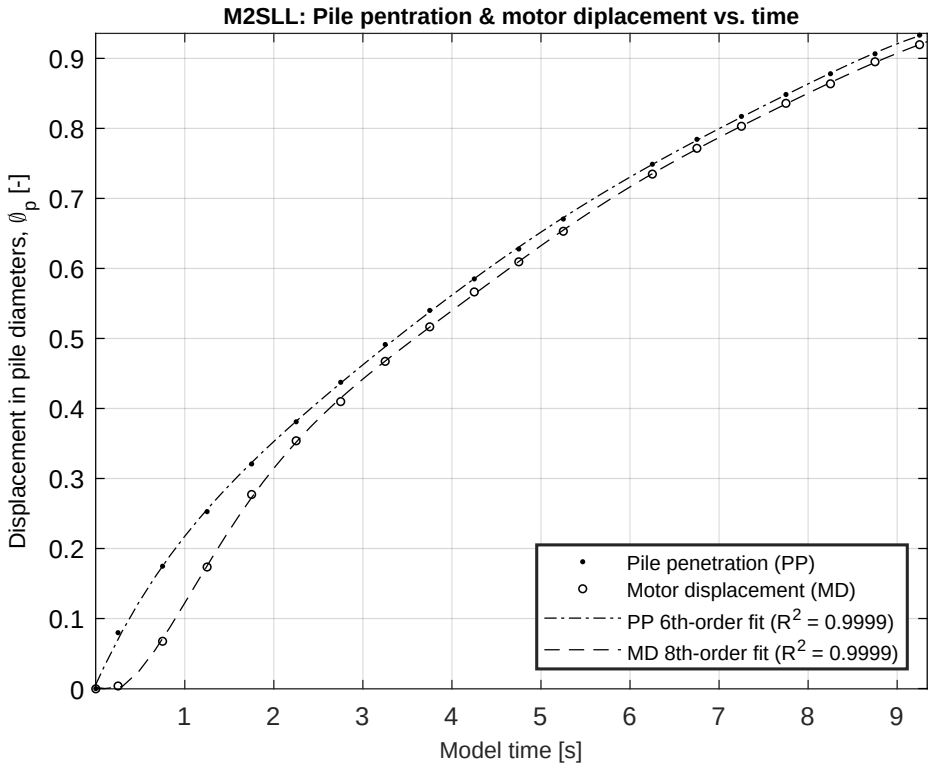

Figure C.2: Measured and approximated normalized (by pile diameter Φ_p) pile penetration (PP) and motor displacement (MD) as a function of model time for M2SLL.

of the pile to determine pile displacement; (II) connected to the back of the motor housing to infer the response of the servo-system due to movement of the pile. The data of both potentiometer is measured at flow frequency, the sampling interval is equal to ≈0.5 *s*. This is sufficient individually capture the displacement related to each blow for (repeated) single blow experiments. However, for multi-blow experiments where the driving frequency is between 10 and 15 *Hz*, the sampling frequency is inadequate. Consequently, it is decided to approximate both the recored pile penetration and motor displacement by means of a polynomial fit. Depending on the results, the order of both polynomials varies between 4, 6 and 8 for individual tests. The degree of polynomial is chosen such that the determination coefficient R^2 is maximized. For Test M2SLL, Figure C.2 shows normalized measurements from both potentiometers alongside their respective polynomial fitting expressions and associated determination coefficients. As both PP and MD are approximated by polynomials, the starting value (for t = 0) does not necessarily equal zero. If applicable, all values within the domain where the approximation yields a negative value for the normalized pile penetration (not representative of reality), are forced to zero. Contrastingly, if the initial value of the approximation is well above zero, the first eight points of the signal are replaced through spline interpolation, which forces the approximation through the origin. Both of aforementioned corrections are visible in Figure C.2. Finally, the deflecting trend of the PP measurements, is line with expectations. Due to increasing pile embedment during driving, both shaft and tip resistance increase; respectively due to: (I) the increase of lateral earth pressure with depth; (II) the increase of soil bearding capacity due to larger overburden pressure. Provided a constant piling energy, both of the aforementioned effects cause the deflecting trend in the PP measurement.

Following the determination of the fitting relationships for PP and MD as a function of model time, both are evaluated at the instances where the load cell recorded the impact of the ram mass.

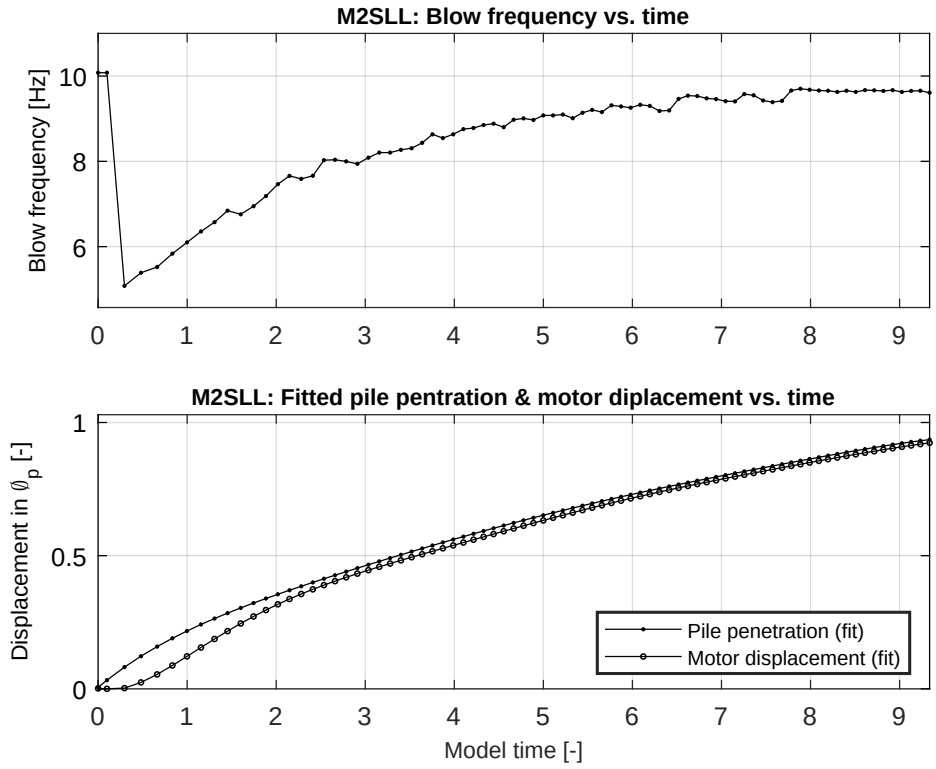

Figure C.3: (TOP) Driving frequency evaluated per blow as a function of model time for test M2SLL. As the frequency in inferred based on time intervals between triggers of the load cell, the frequency for the first blow cannot be determined. Instead, it is equaled to the frequency estimate for the second blow. (BOTTOM) Fitted expressions for PP and MD, evaluated per blow as a function of model time for M2SLL

The result of this procedure is shown in the lower frame of Figure C.3. Here, each dot corresponds to the respective value of PP and MD at the moment of load cell excitation. As is observed in the bottom frame of Figure C.3, there is a delay between the penetration of the pile and the corresponding displacement of the motor housing by the servo system. By the time the servo system registers the convergence of pile and motor position, several blows have already been executed. As a consequence, the stroke of the hammer effectively increases form its intended value. At the point of maximum deviation, the stroke increment is ≈4.6 *mm*, a 14% increase with respect to the intended 32 *mm* stoke for test M2SLL. However, once the servo-system is operational, the divergence between PP and MD is largely corrected. Towards the end of the tests, the absolute difference amounts to ≈1.7 *mm*. Relative to the ideal stroke, this difference amounts to 5%, which is acceptable.

By evaluating the difference between PP and MD per blow, through subtraction of the estimates provided by the fitted polynomials respectively, the effective hammer stroke as a function of blow number is obtained. The resulting graph is shown as the second frame of Figure C.4. Form Figure C.4, the increase in stroke at the beginning of the test due to the regulatory delay of the servo-system is clearly visible. Additionally, from the location of the inflection point at the left hand side of the leading concave, it is inferred that the reaction time of the servo is ≈0.2 *s*. Respectively, ≈0.3 *s* later the performance of the servo system is optimal.

Knowing the evolution of the hammer stroke as function of blow number, it is possible to estimate the impact velocity of the ram mass at an infinitesimal instant prior to impact of the ram mass. The latter is done on the basis of a numerical integration script which infers impact velocity from the initial and final position of the ram mass with respect to the centrifuge center. To this end, the falling height of the trajectory covered by the center of mass (COM) of the ram mass is dis-

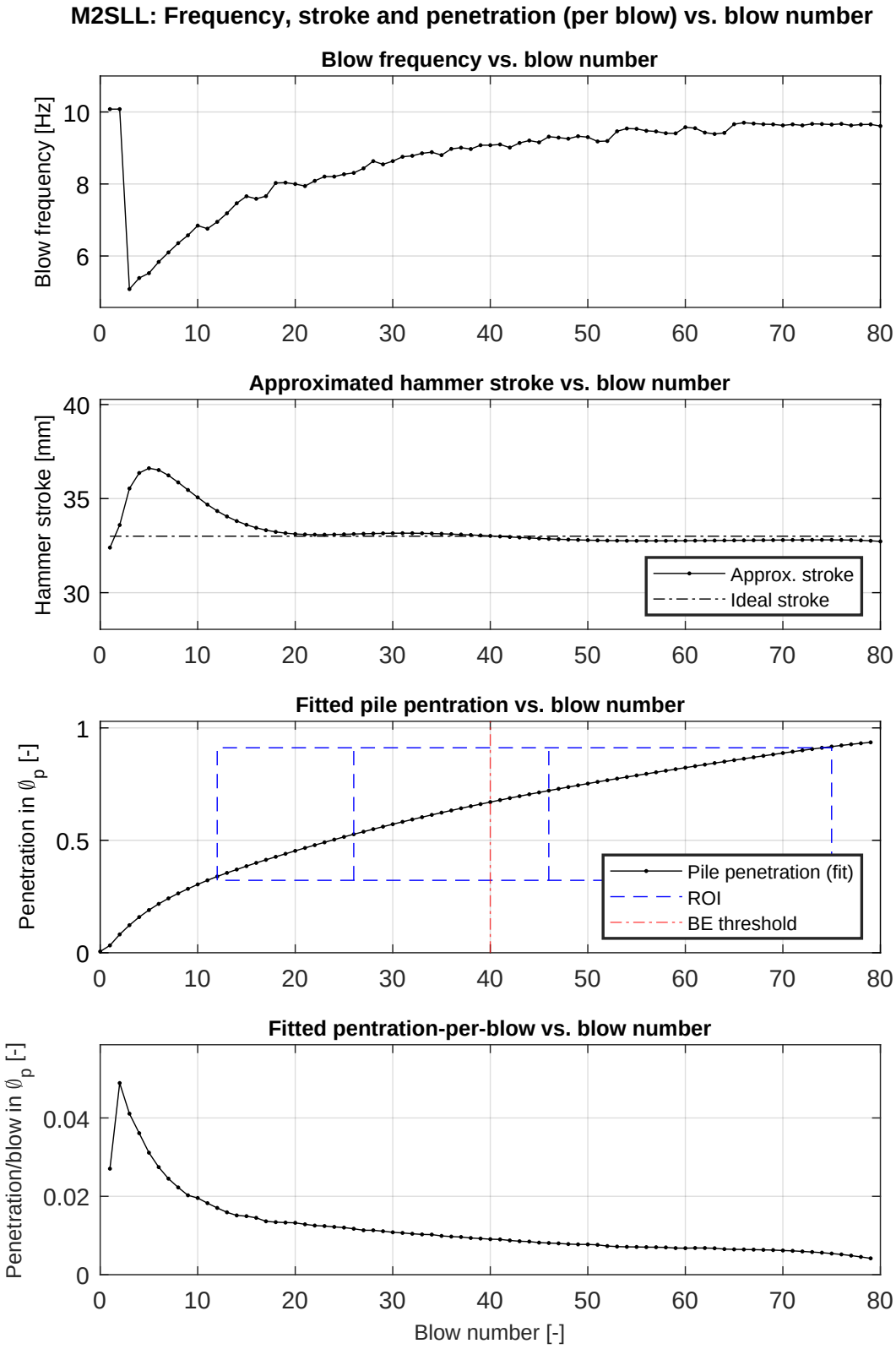

Figure C.4: From top to bottom: (I) blow frequency; (II) effective hammer stroke; (III) cumulative pile penetration, with graphical annotation of the ROI; (IV) pile penetration-per-blow. All are plotted a function of blow number for test M2SLL.

cretized into 1000 segments of equal length. The length of the each discretization interval equals δr. For each of the nodes of the discretized falling height, the centrifuge acceleration is computed as follows:

$$a_i = r_i \cdot \omega^2 \tag{C.4}$$

Here, a_i is the centrifuge acceleration in node i (for the first note i = 1). Similarly, r_i is the distance from the node to the center of the centrifuge center. Lastly, ω denoted the angular velocity of the centrifuge which is calculated to achieve 50g acceleration in the middle of the soil sample. Consequently it follows ω=206 *rad/s*. The initial conditions of the model relating to time are provided by Equation C.5.

$$\begin{aligned} t_1 &= 0; \\ t_2 &= \sqrt{\frac{2 \cdot \delta r}{\frac{a_2 + a_1}{2}}} \end{aligned} \tag{C.5}$$

Similarly, initial conditions with respect to velocity are shown as Equation C.6.

$$\begin{aligned} v_1 &= 0; \\ v_2 &= \frac{a_2 + a_1}{2} \cdot t_2 \end{aligned} \tag{C.6}$$

Following the definition of the initial conditions; for all remaining nodes, t_i and v_i are computed using a numerical predictor-corrector scheme. The predictor step for both variables is provided by Equation C.7.

$$\begin{aligned} t_i^* &= t_{i-1} + \frac{\delta r}{v_{i-1}}; \\ v_i^* &= v_{i-1} + \frac{a_i + a_{i-1}}{2} \cdot (t_i^* - t_{i-1}) \end{aligned} \tag{C.7}$$

Furthermore, Equation C.8 explicates the corrector step of the numerical scheme.

$$\begin{aligned} t_i &= t_{i-1} + \frac{v_i^* + v_{i-1}}{2}; \\ v_i &= v_{i-1} + \frac{a_i + a_{i-1}}{2} \cdot (t_i - t_{i-1}) \end{aligned} \tag{C.8}$$

After each blow, the pile position is updated based on the recorded pile penetration and the final position of the ram's COM for the next blow is determined. The corresponding stroke is used to determine the upper extremity of the COM trajectory. The latter is subsequently discretized after which the velocity profile is computed. This process is repeated up to the point where evolution of ram velocity is known for all blows. Three specific velocities are extracted from the full profile, specifically: (I) the final value or impact velocity $v_{0,t}$ of the ram mass; (II) the average velocity between the nodes corresponding to the respective positions of the hall sensors (HS) and light sensors (LS), $\overline{v}_{HS,\,t}$ and $\overline{v}_{LS,\,t}$ respectively. Based on the three aforementioned variables, two proportionality quotients (ξ_{HS} and ξ_{LS}) are defined for both hall and light sensors, respectively denoted by Equation C.9 and C.10.

$$\xi_{HS} = \frac{\overline{v}_{\mathrm{HS,\,t}}}{v_{0,t}} \tag{C.9}$$

$$\xi_{LS} = \frac{\overline{v}_{\mathrm{LS,\,t}}}{v_{0,t}} \tag{C.10}$$

The proportionality coefficients, as provided by Equation C.9 and C.10, are used to transform the average velocity measured over the interval between either the hall or light sensors, to the (estimated) impact velocity v_0.

Practical computation of impact velocity To determine the efficiency of the hammer, the theoretical velocity measurement is compared to the measured impact velocity. Determination of the latter quantity relies on the signals obtained from either: (I) a pair of hall sensors, which react to change in polarity associated with the passage of the magnets embedded in bottom section of the the ram mass. As the output of the sensors is maximized when the magnet is right in front of the sensor, it is possible to infer when the ram mass passed each sensor; (II) a pair of light sensors, of which either sensor consist of a combination of: (i) a photoelectric sensor; (ii) an LED. When the ram mass passes the one of the sensors, the light emitted from the LED is blocked. The subsequent response of the photoelectic sensor is traceable in the output signal. Respectively, Figure C.5a and C.5b illustrate the signals obtained from the hall and light sensors. Respectively, 'Trigger 1' and 'Trigger 2' indicate the instant where the ram mass passes the first (top) sensor and second (bottom) sensor respectively. The third legend entry ('Transition point') for the last bottom frame of Figure C.5a, marks the point where the shape of the signal (which is a combination of the output of both sensors) is predominantly influenced by the output of the second (bottom) hall sensor. For both the hall sensors and light sensors, the following distances are known: (I) the distance between the two individual sensors; (II) the distance from the bottom sensor to the top of the anvil. For the hall sensors and light sensors respectively, aforementioned values correspond to 13 & 8 mm and 15.5 & 5.5 mm. Provided aforementioned constants, the average velocity over the measurement interval is inferred in accordance with Equation C.11 whenever HS are employed, whereas Equation C.12 is used in case velocity measurement is conducted by LS.

$$\overline{v}_{\mathrm{HS}} = \frac{\Delta h_{\mathrm{HS}}}{\Delta t_{\mathrm{HS}}} \tag{C.11}$$

$$\overline{v}_{\mathrm{LS}} = \frac{\Delta h_{\mathrm{LS}}}{\Delta t_{\mathrm{LS}}} \tag{C.12}$$

Now, through use of the proportionality quotients as calculated in C.3.2, the average velocities are transformed to impact velocity estimates. This transformation involves the use of Equation C.13 and C.14 for HS and LS respectively.

$$v_0 = \overline{v}_{\mathrm{HS}} \cdot \xi_{HS} \tag{C.13}$$

$$v_0 = \overline{v}_{\mathrm{LS}} \cdot \xi_{LS} \tag{C.14}$$

For some tests, it was impossible to determine in impact velocity along the lines of the methodology described above. C.4.1 discusses the approach aimed at the determination of impact velocity for experiments where the obtained HS velocity signals where of lower quality than the signals depicted by Figure C.5a, is discussed. The aforementioned analysis relies on the assumption that the shape of the HS signals in uniform. In this case, the quotients of horizontal distances between annotated points can be used to infer impact velocity if an incomplete velocity signal was obtained.

C.3.3. Efficiency and driving energy calculation

Following the determination of the theoretical and practical estimate of impact velocity v_0, it is possible to compute the hammer efficiency as well as the Kinetic energy carried by the ram mass at an infinitesemal instant before impact with the anvil. The the upper frame of Figure C.6, the theoretical and practical estimate of v_0 and plotted against blow number. Please consider that for the associated experiment (M2SLL), the practical estimation of v_0 was conducted on the basis of light sensor measurements. Due to the presence of faulty measurement it is not possible to conduct a velocity analysis for all blows. Consequently, these values are disregarded. Similarly, blows for which it holds $v_0 > v_{0,t}$ are disregarded. The number of times a signal is rejected on the basis of the two aforementioned observations, are respectively denoted as n^*_{sig} and n^*_{eff}. The total number of

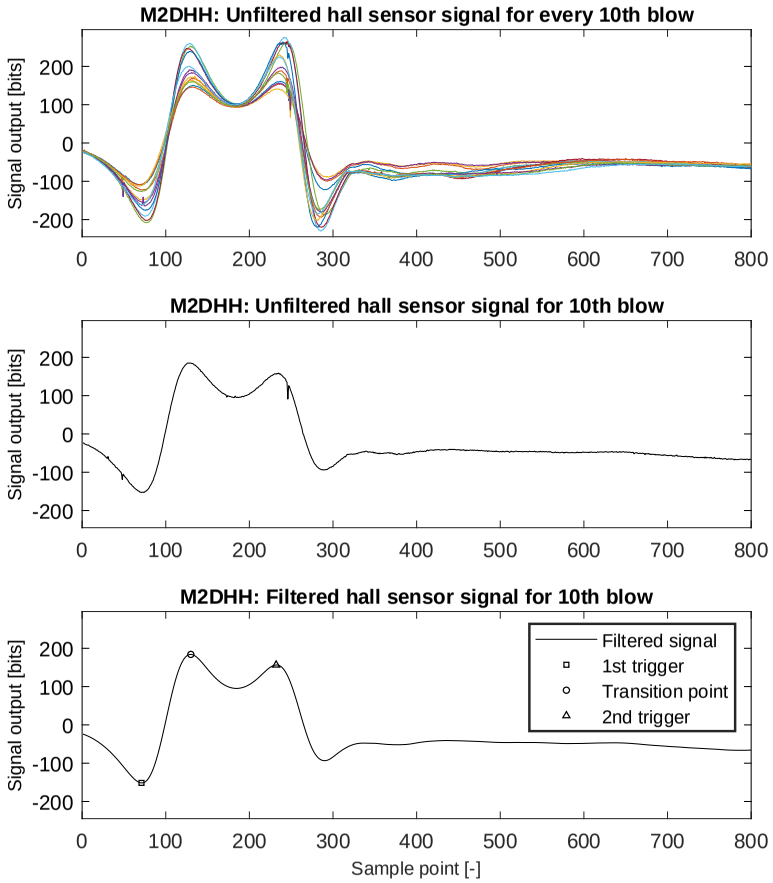

(a) Exemplary signals obtained from triggered measurement of the light sensors. Signals are used velocity measurement of the ram mass. From top to bottom: (I) Unprocessed signals for every 10th blow of test M2DHH; (II) Filtered signal for the 10th blow of test M2DHH; (III) Filtered and allocated signal for the 10th blow of test M2DHH.

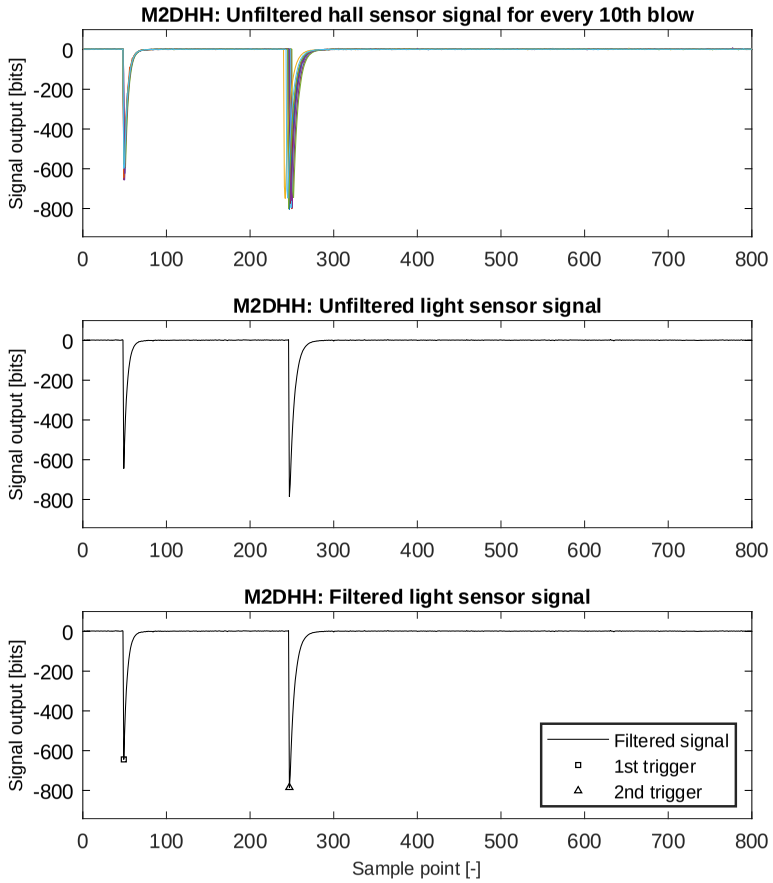

(b) Exemplary signals obtained from triggered measurement of the light sensors. Signals are used velocity measurement of the ram mass. From top to bottom: (I) Unprocessed signals for every 10th blow of test M2DHH; (II) Filtered signal for the 10th blow of test M2DHH; (III) Filtered and allocated signal for the 10th blow of test M2DHH.

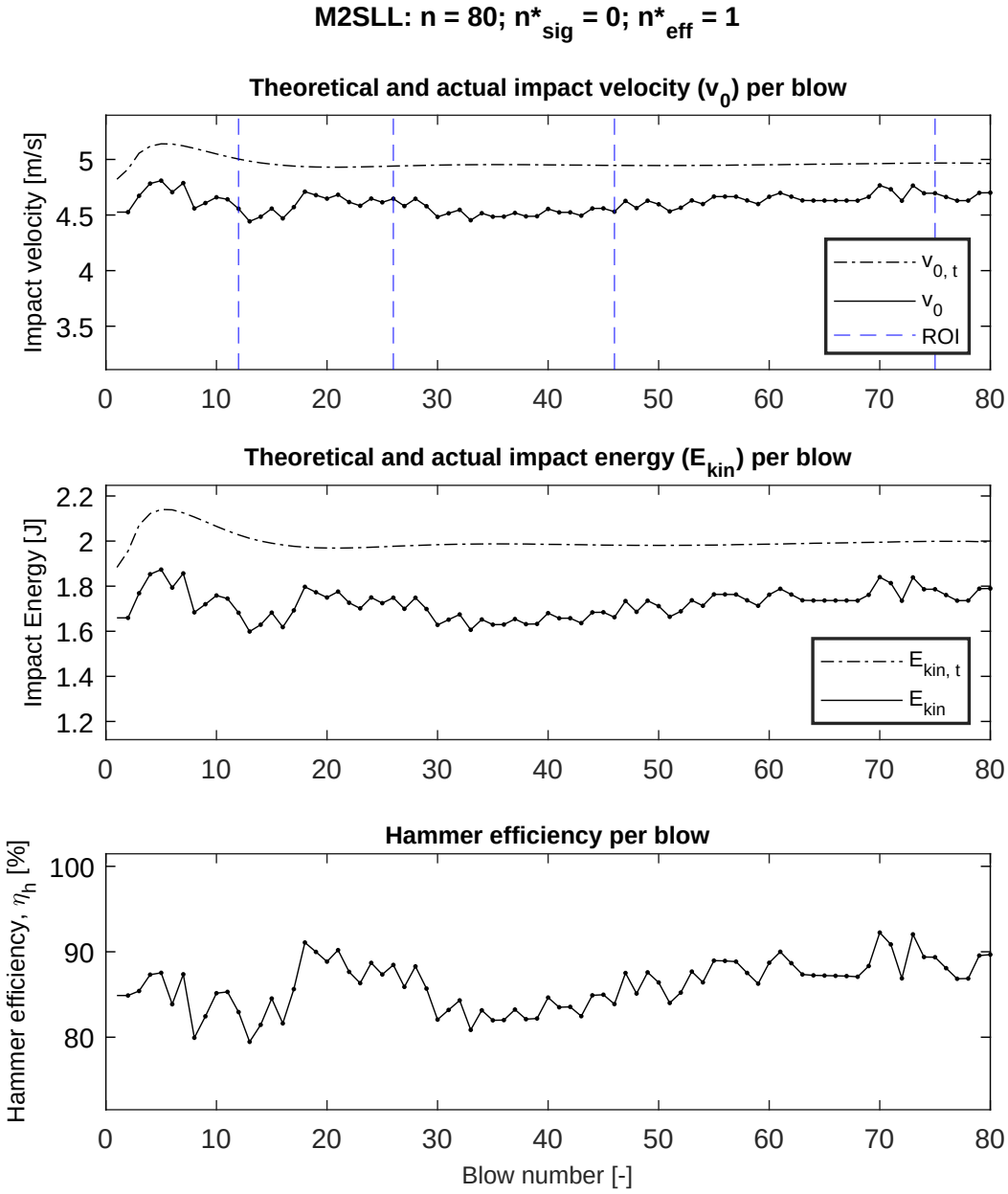

Figure C.6: For test M2SLL, from top to bottom: (I) theoretical and measured impact velocity v_0 versus blow number; (II) Theoretical and calculated impact energy versus blow number; (III) Hammer efficiency η_h versus blows number. Dots indicate blows for which the signal of the LS was approved and the subsequent velocity analysis yielded satisfactory results.

blows is indicated as n. Each of the three previously mentioned parameters is defined at the top of Figure C.6. Linear interpolation is used to replace measurements corresponding to rejected blows.

For the $v_{0,t}$ and v_0, theoretical and practical kinetic energy estimates are inferred. The latter is done is accordance with Equation C.15.

$$E_{\text{kin}} = \begin{cases} 1/2 \cdot m_h \cdot v_0^2, & \text{for measured velocities} \\ 1/2 \cdot m_h \cdot v_{0,t}^2, & \text{for theoretical velocities} \end{cases} \tag{C.15}$$

Results corresponding to the employment of Equation C.15 are shown (as a function of blow number) in the second frame of Figure C.6.

Finally, from the theoretical and practical estimates for impact energy, the hammer efficiency is calculated in accordance with Equation C.16.

$$\eta_h = \frac{1/2 \cdot m_h \cdot v_0^2}{1/2 \cdot m_h \cdot v_{0,t}^2} \tag{C.16}$$

Where m_h is the mass of the hammer in $[kg]$. Corresponding results are shown in the bottom frame of Figure C.6 for test M2DLL. As unrepresentative velocities were removed from the results, the η_h is below 100% for all blows, which conforms to the general expectation. Quantitatively, for test M2DLL the hammer efficiency amounts to ≈90%. At prototype scale, the nominal efficiency of Hydrohammer® is in the neighborhood of 95% [96]. Hence, the deviation between model and prototype in terms of efficiency is limited.

C.3.4. Determination of driving frequency

The driving frequency is calculated from the time interval between subsequent blows as is accordance with Equation C.17.

$$f_{h,i} = \frac{1}{t_{b,i} - t_{b,i-1}} \tag{C.17}$$

Where, $f_{h,i}$ is the driving frequency corresponding to blow i, $t_{b,i}$ is the time of initiation of blow i and similarly, $t_{b,i-1}$ is the time of initiation of blow *i-1*.The time corresponding to the initiation of each blow are taken from the load cell measurements. Primarility beacuse: (I) the load cell is a reliable sensor which consistently captures the initiation of a blow; (II) as the load cell is recorded using triggered measurements, the time of impact is straightforwardly determined. The upper frame of Figure C.3 depicts the evolution of blow frequency as a function of time. Similarly, the top frame of Figure C.4 plots the blow frequency against blow number. Despite of the change of axis, both Figure C.3 and C.4 demonstrate a clear decrease in the blow frequency following the release of the ram mass of ≈50%. The frequency controller, which regulates the flow of power to the engine, requires some time to achieve the power requirement to maintain the driving operation at the intended frequency. Quantitatively, this adjustment time translates to about 70 blows, which means that the blow frequency is below the ideal value for effectively the entire experiment.

C.4. Complementing figures & v_0 estimation using partial HS signals

In this section, figures corresponding to the analysis aimed at the determination of the previously discussed driving parameters, are presented. These figures were drafted for all experiments from Table 6.1, excluding M2SHH and M3SHH. For clarity, all figures which correspond to the same tests are plotted together. Hence, all plots corresponding to a particular experiment are accommodated in their own respective paragraph of C.4.2. Additionally, as indicated in C.3.2, section C.4.1 is dedicated to the methodology to a infer velocity measurement from incomplete HS signals. This process was drafted under the assumption that the shape HS signal, as demonstrated in Figure C.5a, is uniform. This would imply that quotients of distances between characteristic points of the signal are constant.

Test ID	$\varphi_{LS\text{-}HS}$	φ^*_{LS}	φ^*_{HS}
M2DLL	1.2137	1.8693	1.5417
M2DLH	1.2028	2.2134	1.8408
M2DHL	1.1363	2.3195	2.0422
M2DHH	1.1973	1.8893	1.5756
M3DLL	1.1655	2.9255	2.5000
M3DLH	1.1955	2.0086	1.6826
M3DHL	1.2075	1.9644	1.6289
M3DHH	1.1800	2.5828	2.1891
μ [-]	1.1873	2.2216	1.8751
s_u [-]	0.025752	0.37448	0.34158
COV [%]	2.1689	16.856	18.216

Table C.3: Quotients used to infer the correlation between the different time intervals enclosed by characteristic points of HS and LS signals.

C.4.1. Velocity estimation based on partial HS signals

For the following tests, triggered sampling of the HS yielded signals unsuitable for the analysis described in C.3.2: (I) S2DXL; (II) S2DXH; (III) S3DXL; (IV) S2SXL; (V) S2SXH; (VI) S3SXL; (VII) S3SXH. For all of the aforementioned experiments, 'Trigger 1' as shown in Figure C.5a was not present in the obtained HS signal. Hence, it is investigated whether, instead of the respective time interval between 'Trigger 1' and 'Trigger 2' $\Delta t_{HS,\,1\text{-}2}$, the interval between the 'Transition point' and 'Trigger 2' $\Delta t_{HS,\,T\text{-}2}$ is suitable to reliably determine the average velocity over the measurement interval. Based on the assumption that the 'Transition point' is a characteristic point of the HS signal, Equation C.18 was used to calculate φ^*_{HS} for all blows of eight multi-blow experiments (M2DLL, M2DLH, M2DHL, M2DHH, M3DLL, M3DLH, M3DHL and M3DHH). Respectively, Figure C.7a, C.8a, C.9a, C.10a, C.11a, C.12a, C.13a and C.14a, provide a selection of HS signals which where obtained for the aforementioned tests. Subsequently, the average φ^*_{HS} was determined per experiment. The resulting coefficient per test is plotted in Table C.3. In order to objectively quantify the variability of the obtained coefficients; the mean μ, sample standard deviation s_u and the coefficient of variation (COV) are also provided by Table C.3.

$$\varphi^*_{\mathrm{HS}} = \frac{\Delta t_{\mathrm{HS,\,1\text{-}2}}}{\Delta t_{\mathrm{HS,\,T\text{-}2}}} \tag{C.18}$$

From Table C.3 it is evident that that φ^*_{HS} varies substantially between tests. Hence it is ill-advised to employ φ^*_{HS} to scale $\Delta t_{HS,\,T\text{-}2}$ as an approximation for $\Delta t_{HS,\,1\text{-}2}$.

Provided the previous attempt was unsuccessful, it is endeavored to relate $\Delta t_{HS,\,T\text{-}2}$ to the time interval between 'Trigger 1' and 'Trigger 2' for LS signals $\Delta t_{LS,\,1\text{-}2}$ in a similar fashion. Equation C.19 is used to determine the φ^*_{LS} form the aforementioned time intervals. Once more, the analysis focuses on the results obtained for tests M2DLL, M2DLH, M2DHL, M2DHH, M3DLL, M3DLH, M3DHL and M3DHH. An overview of obtained LS signals for the respective experiments is provided by Figure C.7b, C.8b, C.9b, C.10b, C.11b, C.12b, C.13b and C.14b.

$$\varphi^*_{\mathrm{LS}} = \frac{\Delta t_{\mathrm{LS,\,1\text{-}2}}}{\Delta t_{\mathrm{HS,\,T\text{-}2}}} \tag{C.19}$$

Individual values of φ^*_{LS} as well as μ, s_u and COV are presented in Table C.3. The results are highly comparable to those obtained for φ^*_{HS}, verifying the observation that the location of the 'Transition point' varies significantly from test to test. However, conformity between the COV for φ^*_{HS} and φ^*_{LS}, implicates that the quotient of $\Delta t_{LS,\,1\text{-}2}$ over $\Delta t_{HS,\,1\text{-}2}$ expresses a limited degree variation. To prove

this, the aforementioned quotient is computes in accordance with equation C.20.

$$\varphi_{\text{LS-HS}} = \frac{\Delta t_{\text{LS, 1-2}}}{\Delta t_{\text{HS, 1-2}}} \tag{C.20}$$

Numerical values of $\varphi_{LS\text{-}HS}$ are presented in Table C.3 alongside μ, s_u and COV. As is observed, the coefficient of variation of $\varphi_{LS\text{-}HS}$ is significantly smaller than the COV corresponding to φ^*_{HS} and φ^*_{LS}. Hence, unlike the latter two parameters, the location of $\Delta t_{LS,\,1\text{-}2}$ with respect to $\Delta t_{HS,\,1\text{-}2}$ is largely fixed. From this observation it is concluded that velocity estimation based on HS or LS are largely equivalent and both yield representative results. The fact that the $varphi_{LS\text{-}HS}$ follows from the different heights at which the sensors are installed. Specifics with regard to the positioning of the sensors are provided in C.3.2. Moreover, it is also concluded that it is impossible to infer velocity based on a partial HS signal. Consequently, it is impossible to reliably determine the impact velocity of the ram mass for the seven repeated single blow tests, as listed at the beginning of this section. Hence, estimates of the impact velocity are drafted on the assumption that the recorded hammer efficiency η_h for test S3DXH, computed according to the methodology described in C.3.3, is representative for all other experiments. As $v_{0,t}$ and $E_{kin,\,t}$ are determined despite of unusable HS signals, it is possible to estimate v_0 and E_{kin} provided η_h.

C.4.2. Complementing figures to the deterimation of drivability parameters

This section contains figures used for the determination of important driving parameters for all experiments form Table 6.1 (with exception of M2SHH and M3SHH). For clarity, all figures corresponding to a specific test are clustered in a paragraph allocated specifically to the considered test. The process underlying the creation of the presented figures as well as their respective relevance is discussed in the precedent paragraphs of C.3.

For some tests, velocity measurements of the ram mass are not provided. This is due unusable signals which were obtained for these tests. If the latter is true, is not possible to compute the hammer efficiency η_h, consequently the graph which would normally correspond to its respective determination is left out.

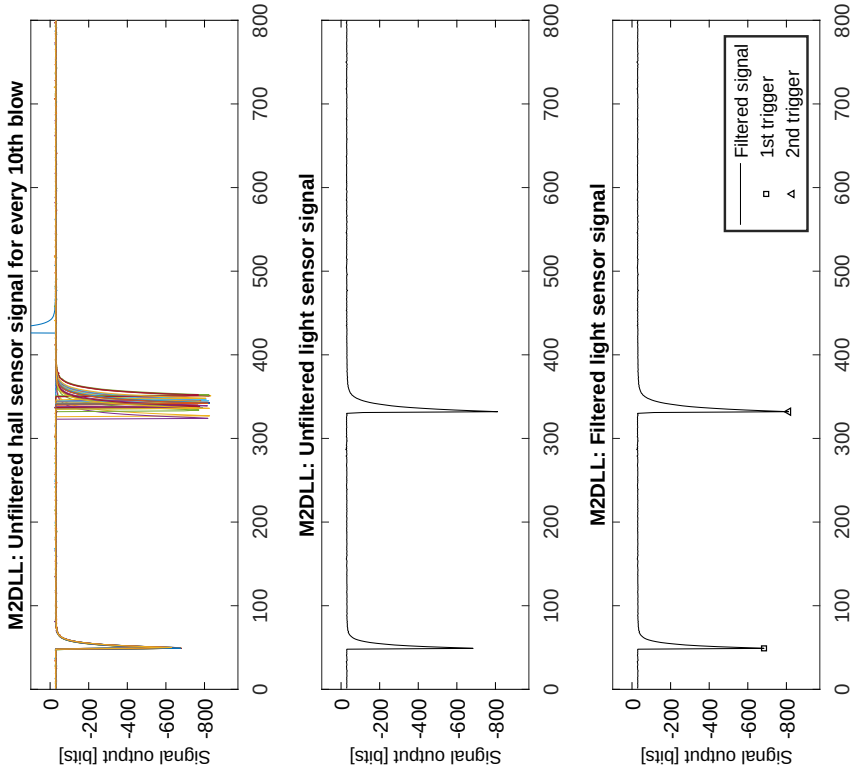

(b) LS signals for test M2DLL

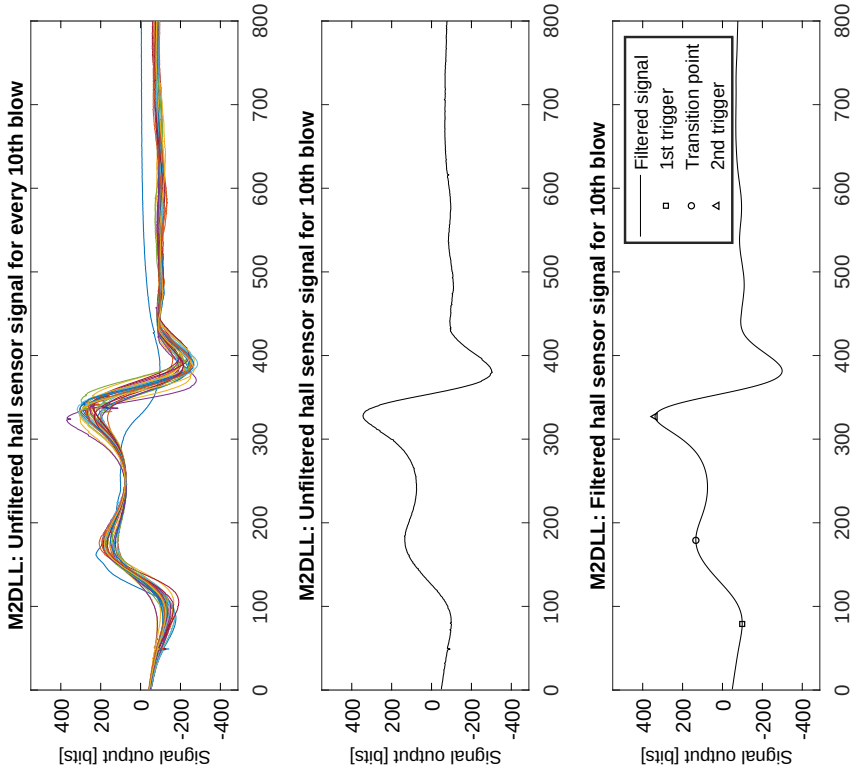

(a) HS signals for test M2DLL

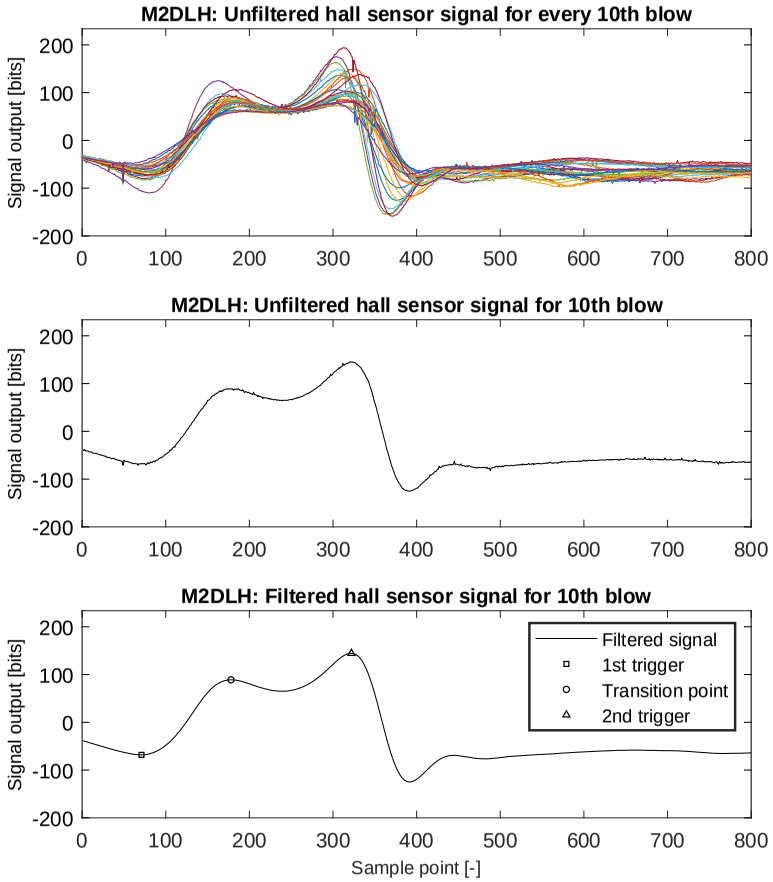

(a) HS signals for test M2DLH

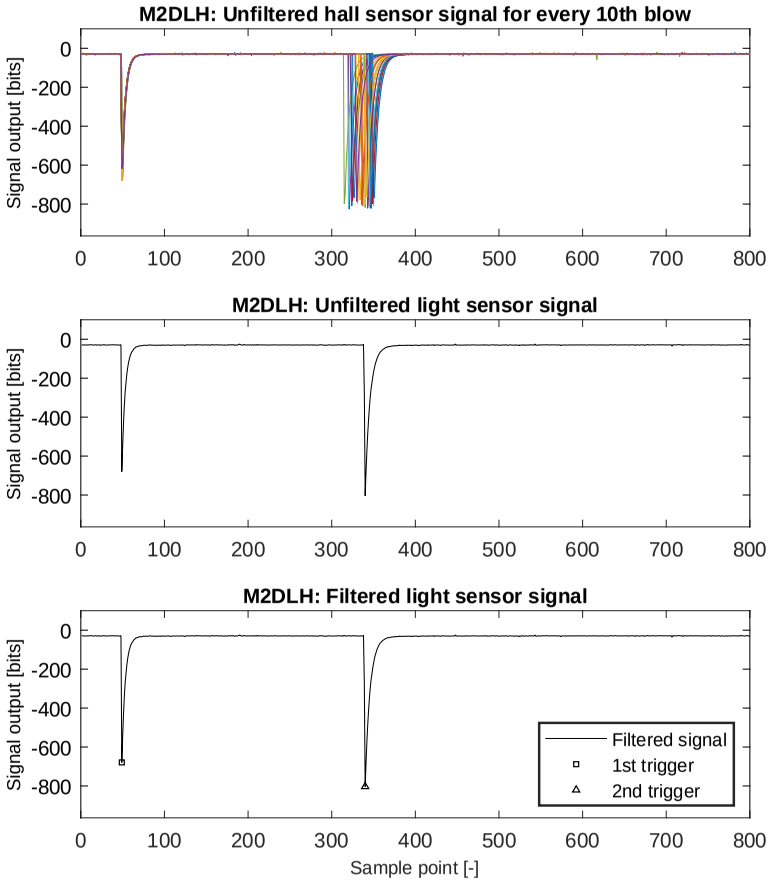

(b) LS signals for test M2DLH

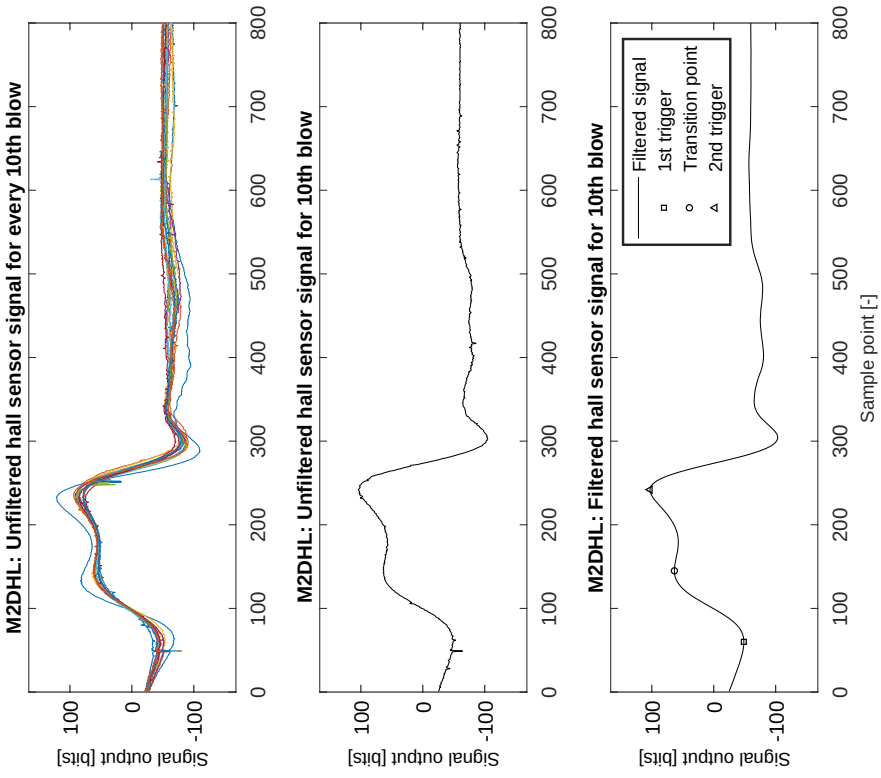

(a) HS signals for test M2DHL

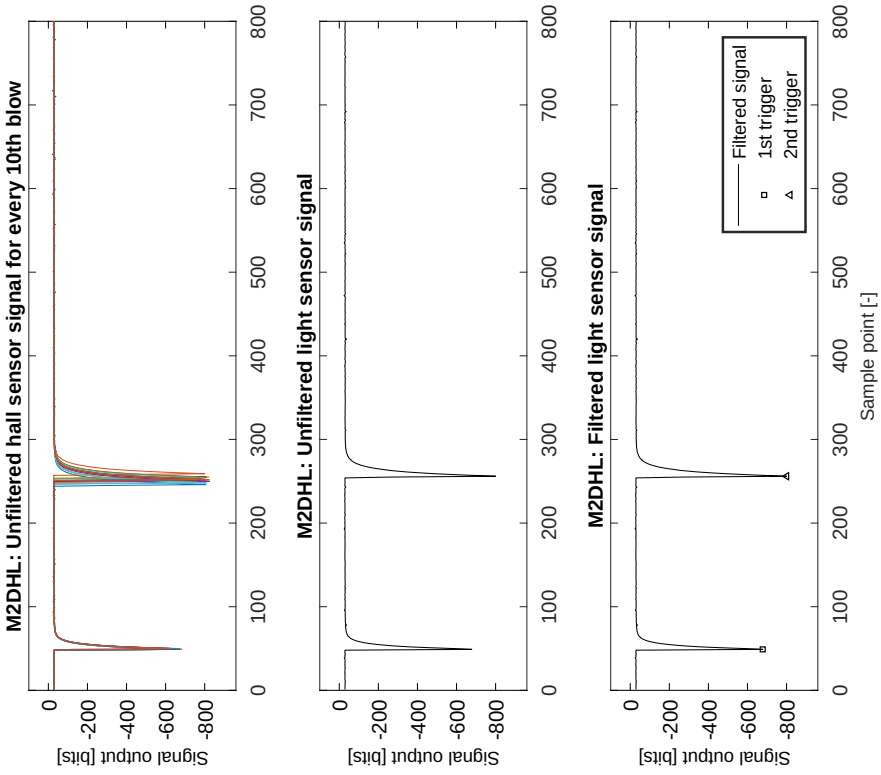

(b) LS signals for test M2DHL

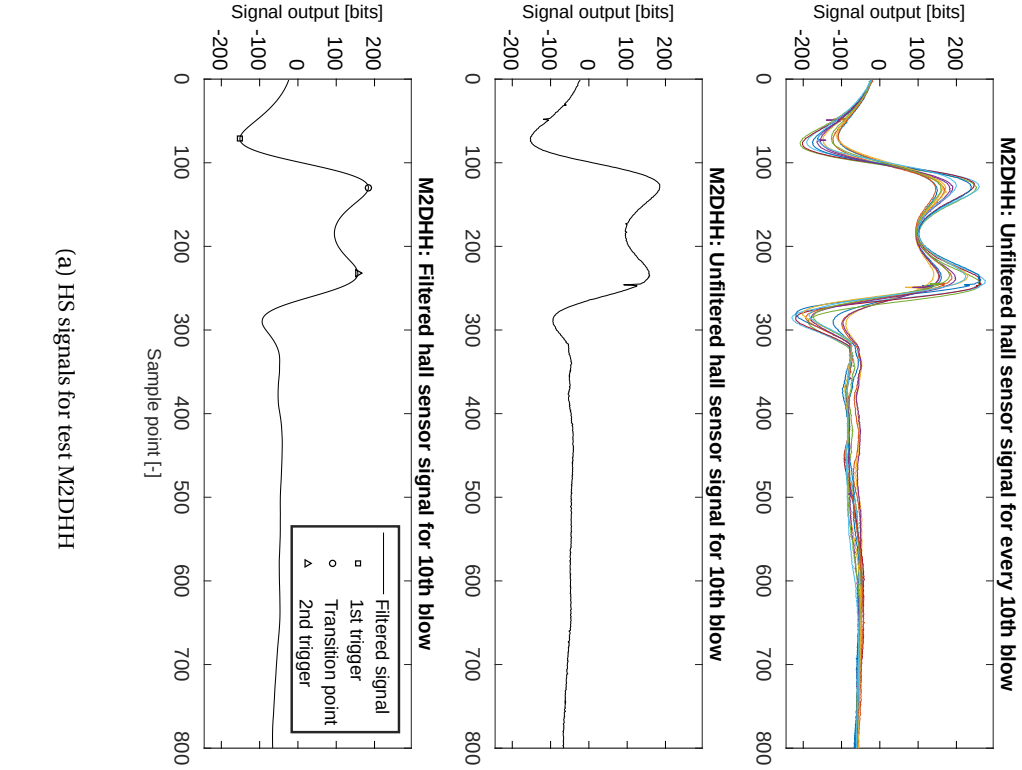

(a) HS signals for test M2DHH

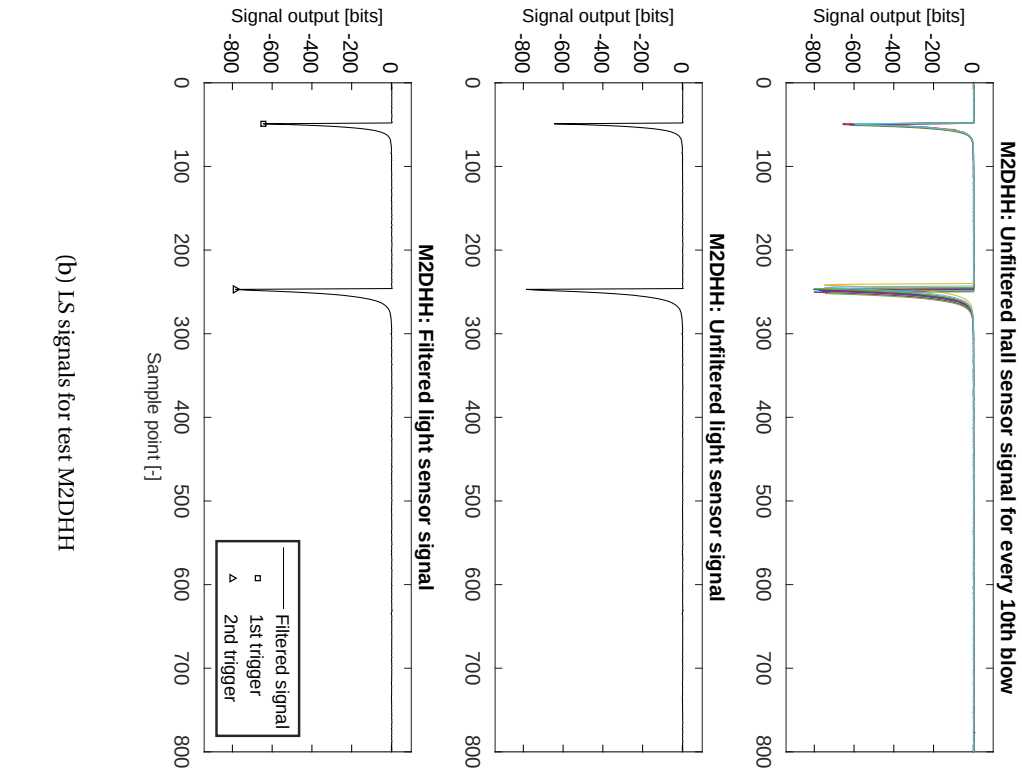

(b) LS signals for test M2DHH

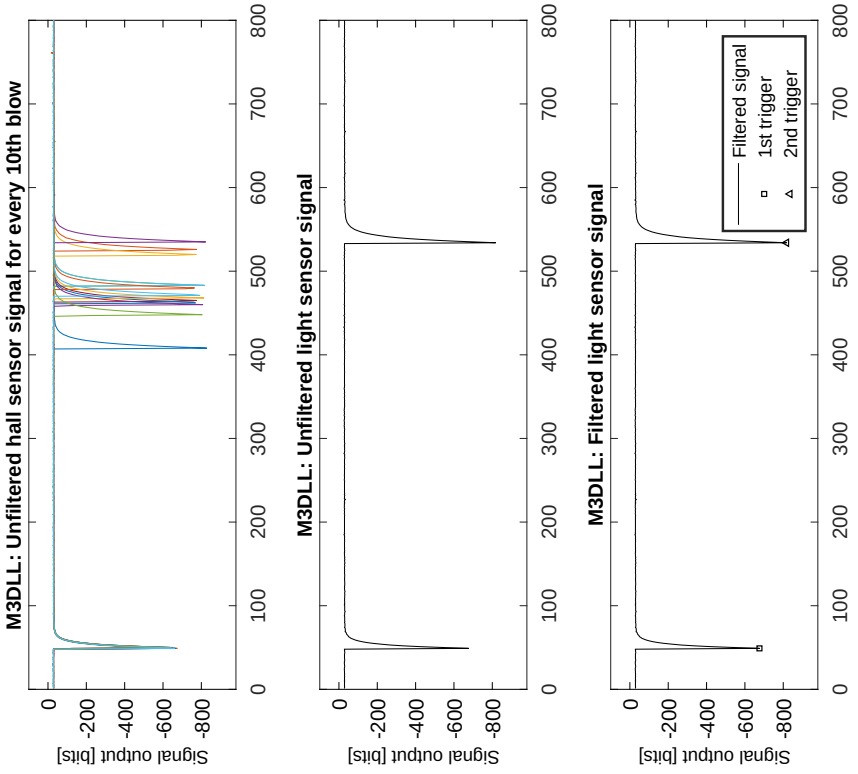

(b) LS signals for test M3DLL

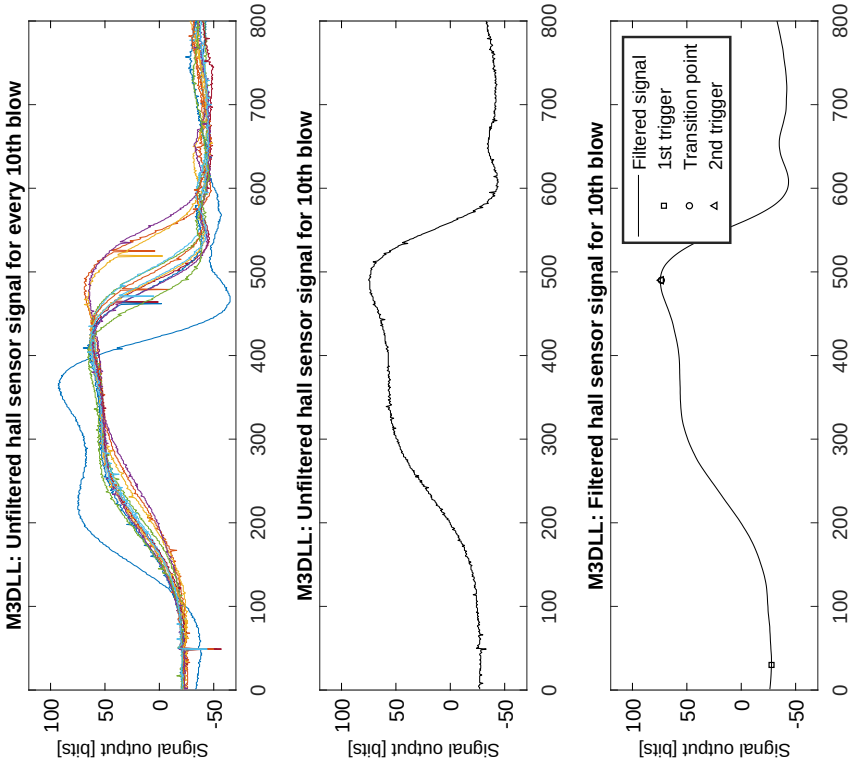

(a) HS signals for test M3DLL

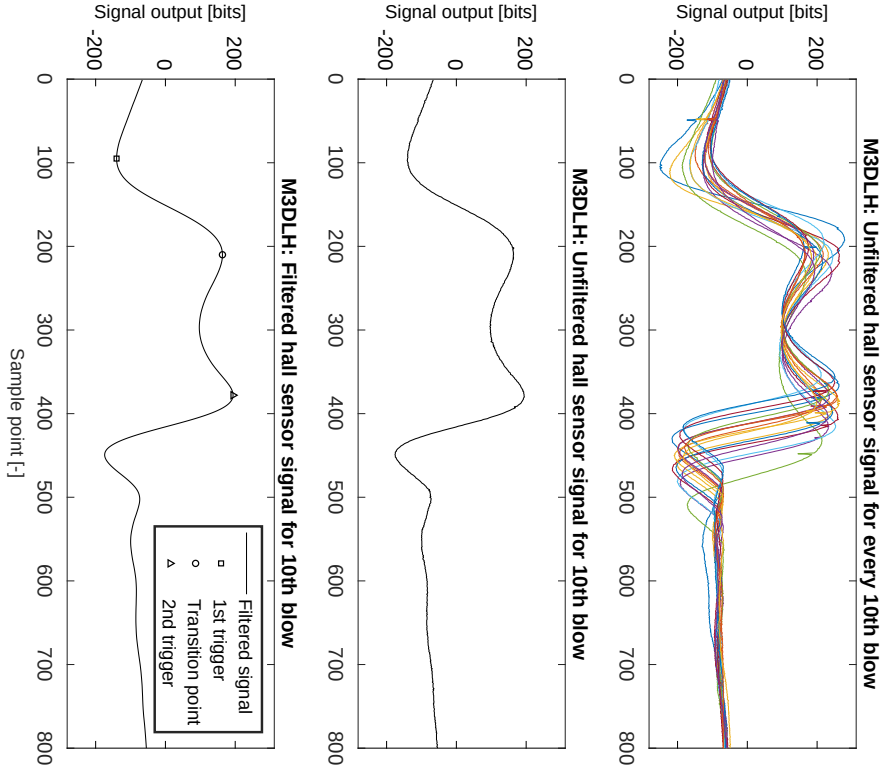

(a) HS signals for test M3DLH

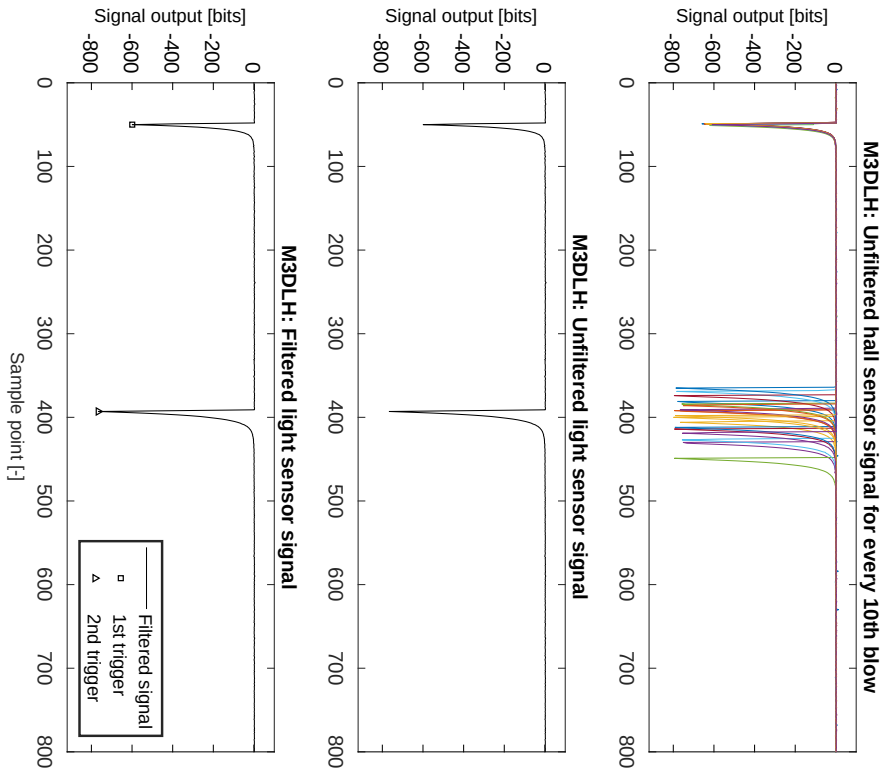

(b) LS signals for test M3DLH

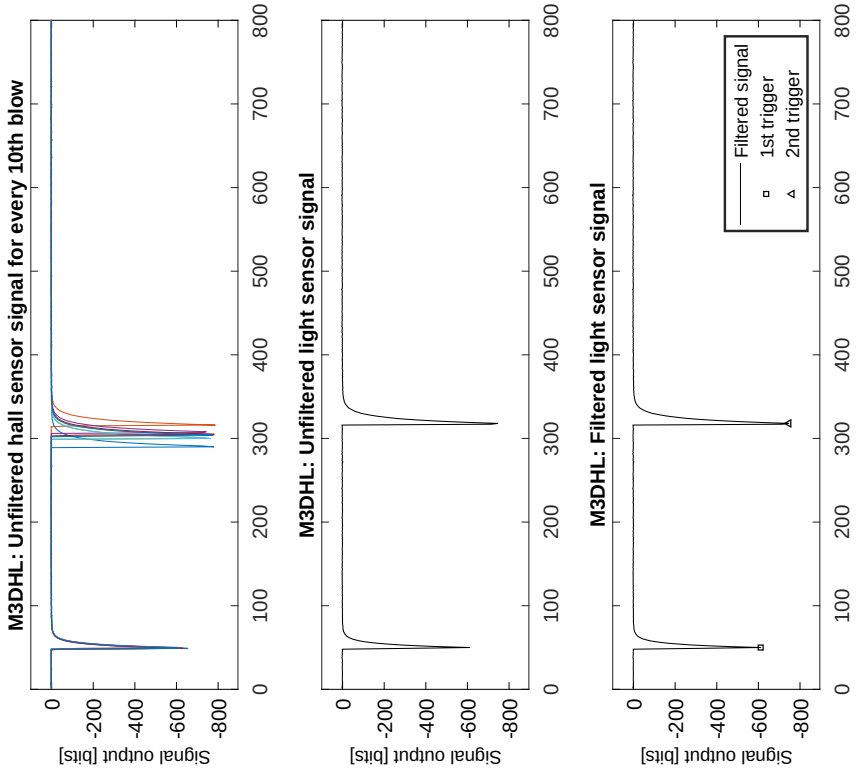

(b) LS signals for test M3DHL

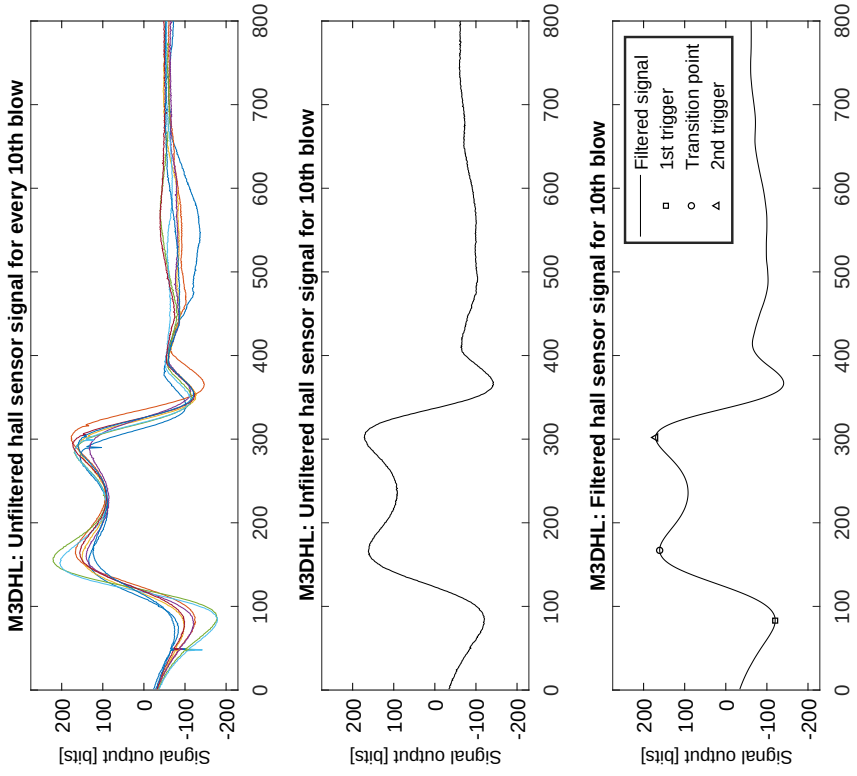

(a) HS signals for test M3DHL

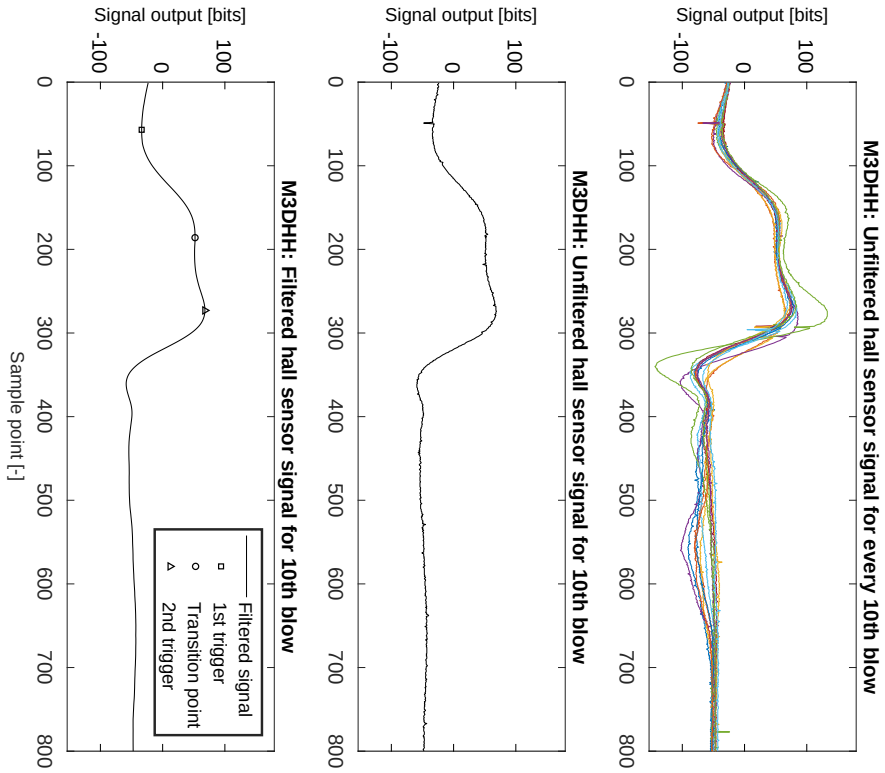

(a) HS signals for test M3DHH

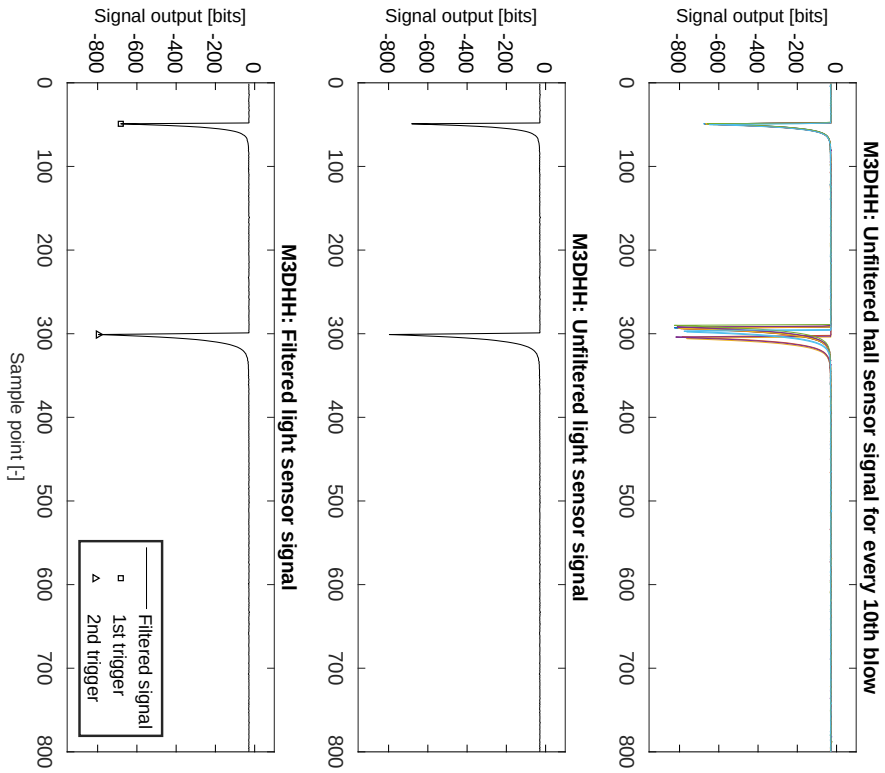

(b) LS signals for test M3DHH

S2DXL

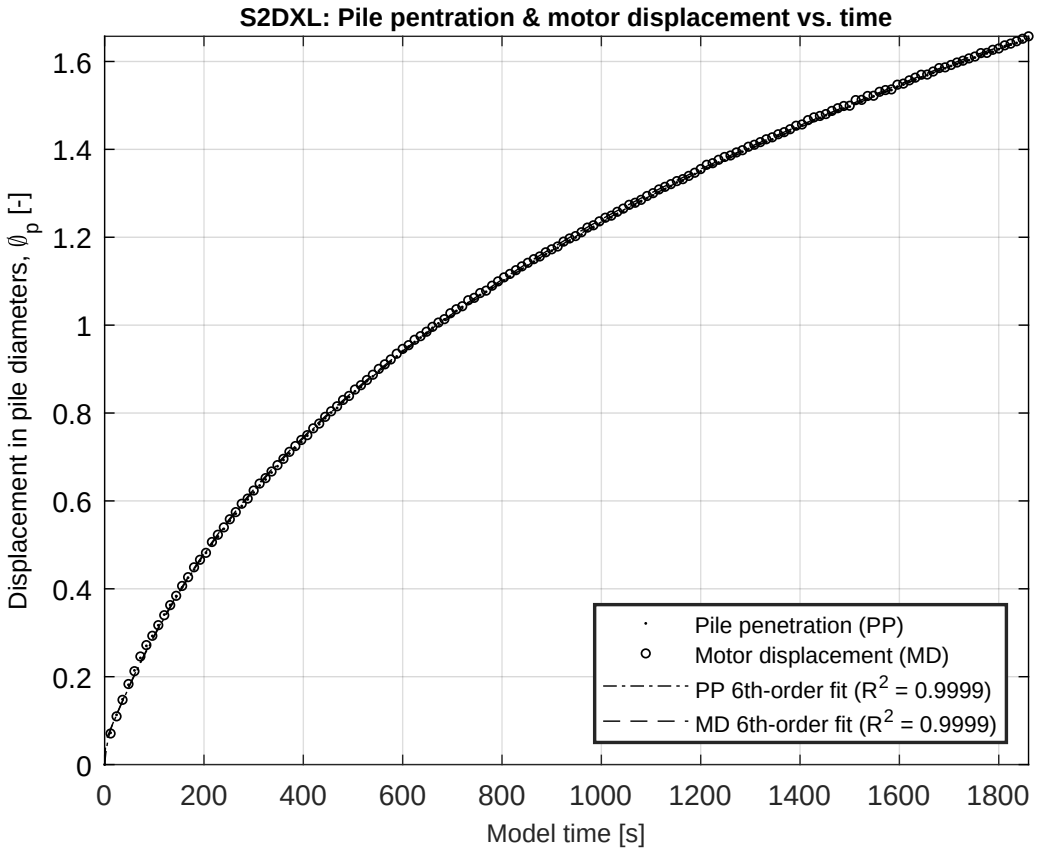

Figure C.15: Measured and approximated normalized (by pile diameter Φ_p) pile penetration (PP) and motor displacement (MD) as a function of model time for S2DXL.

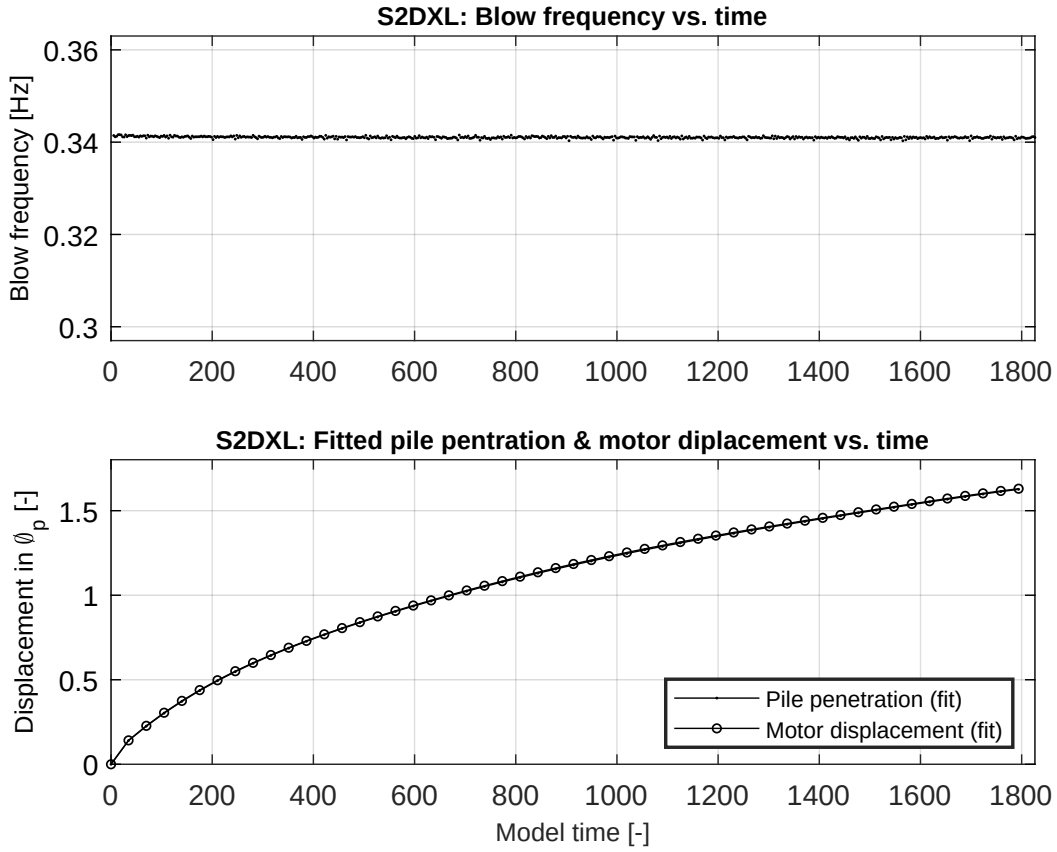

Figure C.16: (TOP) Driving frequency evaluated per blow as a function of model time for test S2DXL. As the frequency in inferred based on time interval between triggers of the load cell, the frequency for the first blow cannot be determined. Instead, it is equaled to the frequency estimate for the second blow. (BOTTOM) Fitted expressions for PP and MD, evaluated per blow as a function of model time for S2DXL

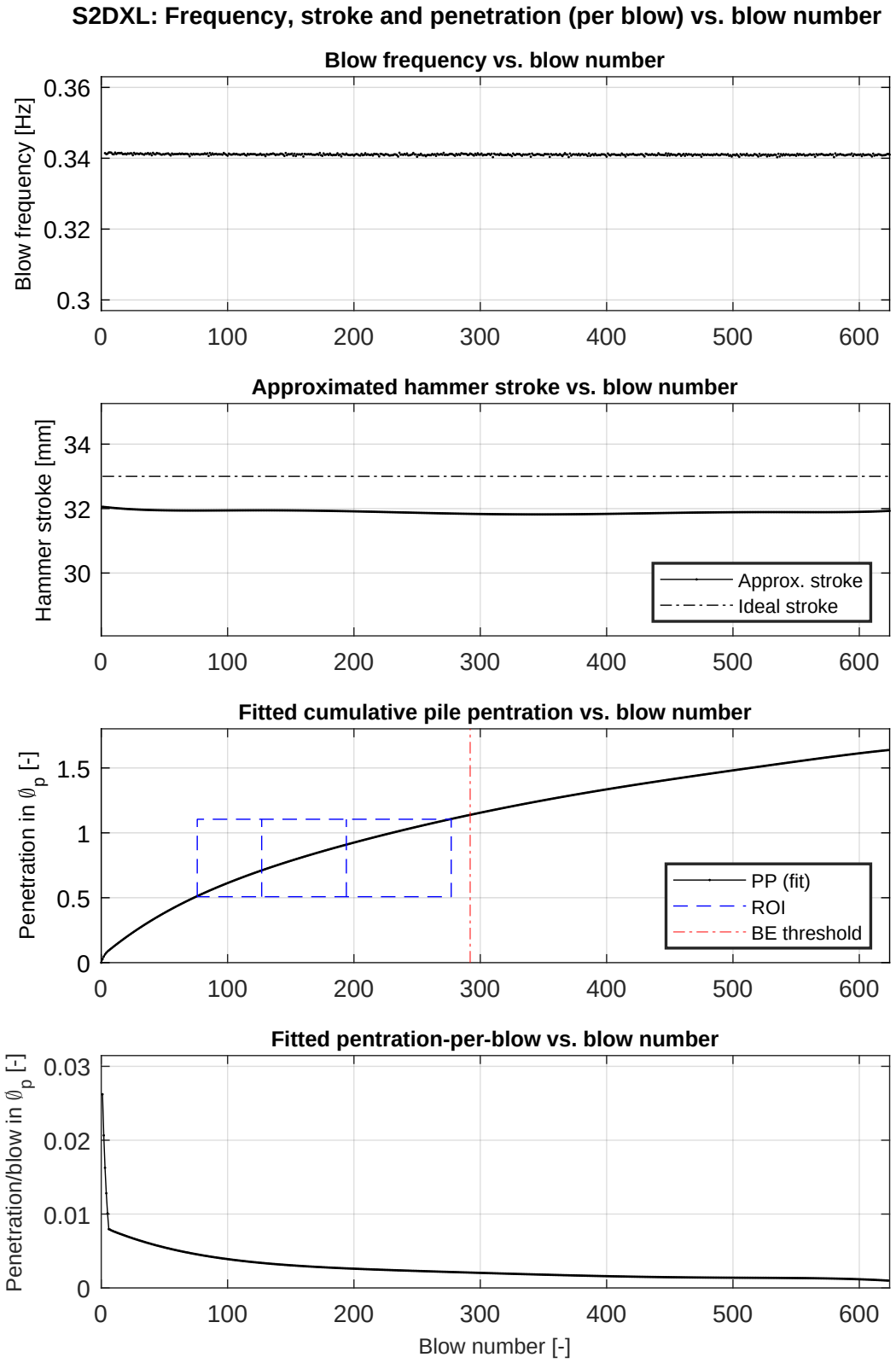

Figure C.17: From top to bottom: (I) blow frequency; (II) effective hammer stroke; (III) cumulative pile penetration, with graphical annotation of the ROI; (IV) pile penetration-per-blow. All are plotted a function of blow number for test S2DXL.

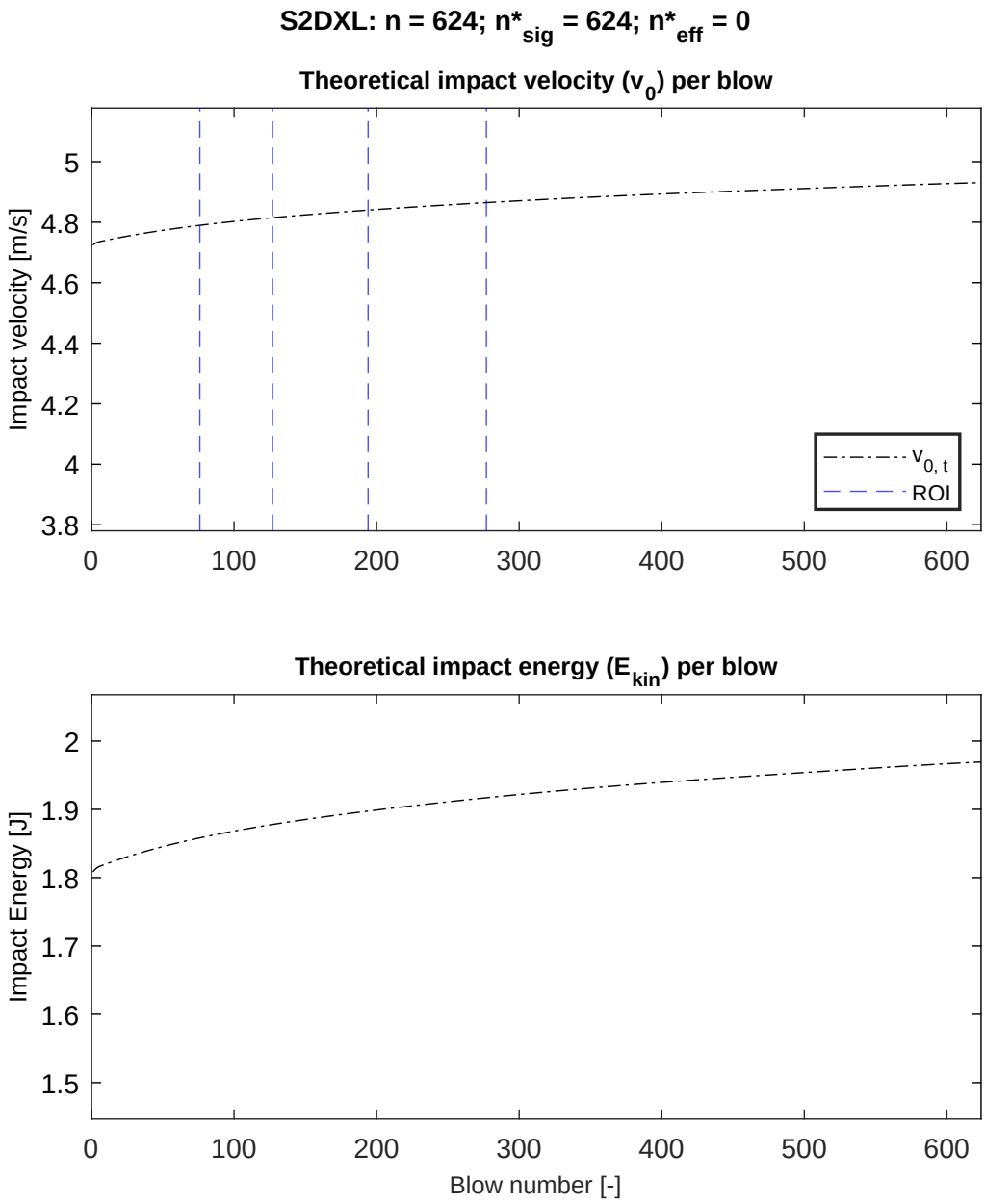

Figure C.18: For test S2DXL, from top to bottom: (I) theoretical and measured impact velocity v_0 versus blow number; (II) Theoretical and calculated impact energy versus blow number; (III) Hammer efficiency η_h versus blows number. Dots indicate blows for which the signal was approved and the subsequent velocity analysis yielded satisfactory results. Out of the total number of blows n, the number for which the latter was found to be true is indicated as n^*_{sig}. Finally, the number of blows which were disregarded (despite of usable velocity signaNA) as they yielded an efficiency >100% is denoted by n^*_{eff}

S2DXH

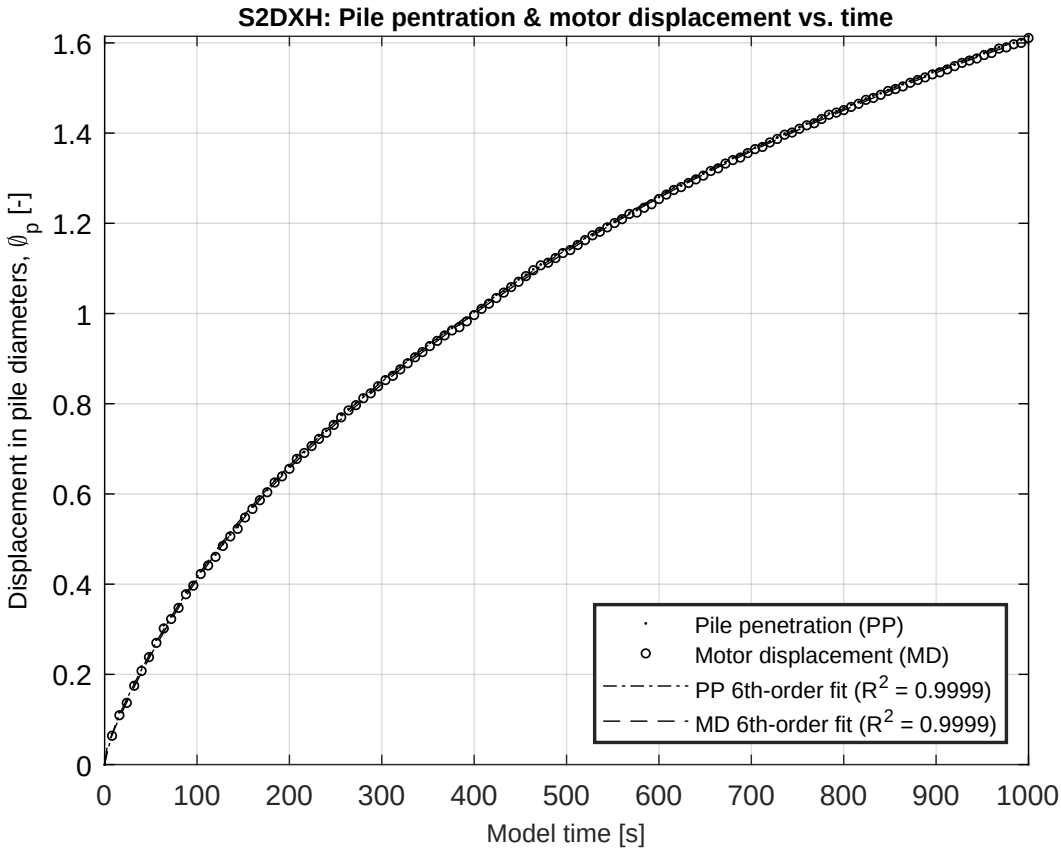

Figure C.19: Measured and approximated normalized (by pile diameter Φ_p) pile penetration (PP) and motor displacement (MD) as a function of model time for S2DXH.

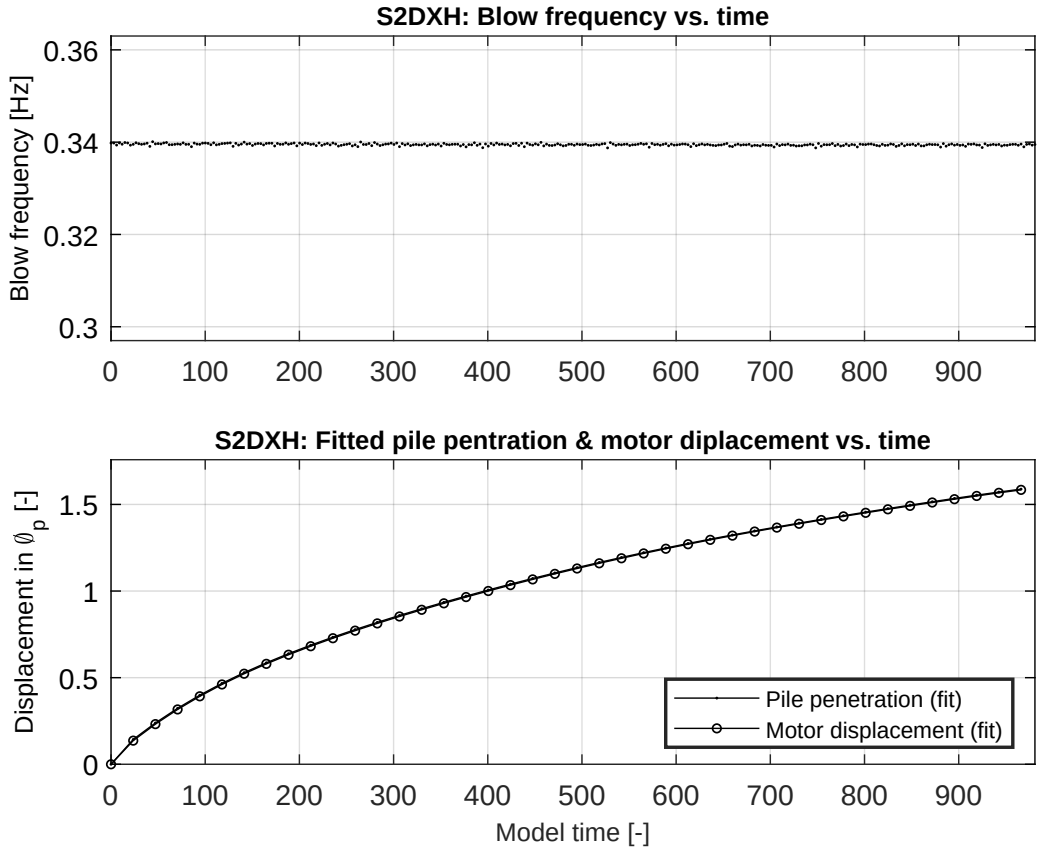

Figure C.20: (TOP) Driving frequency evaluated per blow as a function of model time for test S2DXH. As the frequency in inferred based on time interval between triggers of the load cell, the frequency for the first blow cannot be determined. Instead, it is equaled to the frequency estimate for the second blow. (BOTTOM) Fitted expressions for PP and MD, evaluated per blow as a function of model time for S2DXH

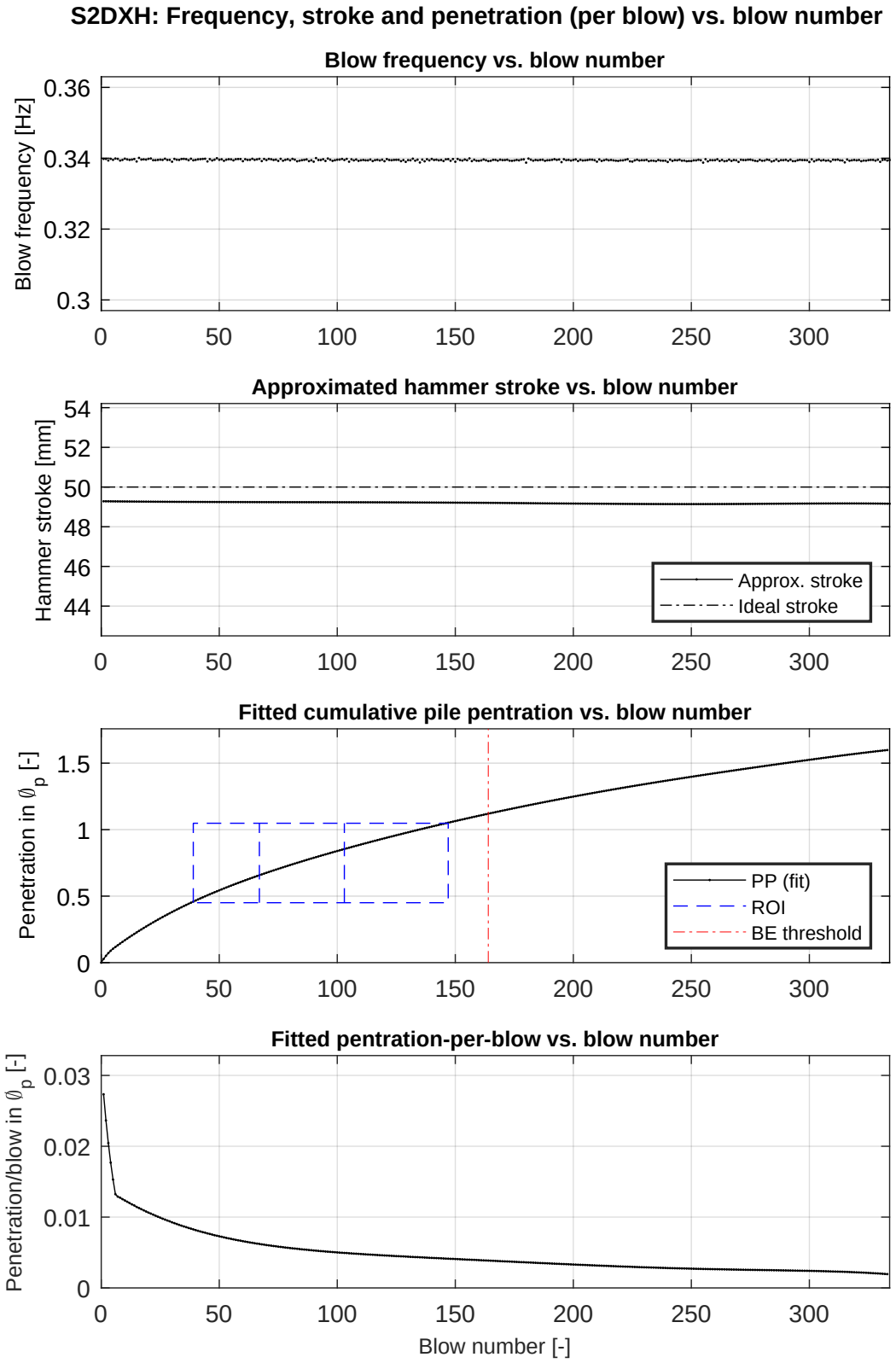

Figure C.21: From top to bottom: (I) blow frequency; (II) effective hammer stroke; (III) cumulative pile penetration, with graphical annotation of the ROI; (IV) pile penetration-per-blow. All are plotted a function of blow number for test S2DXH.

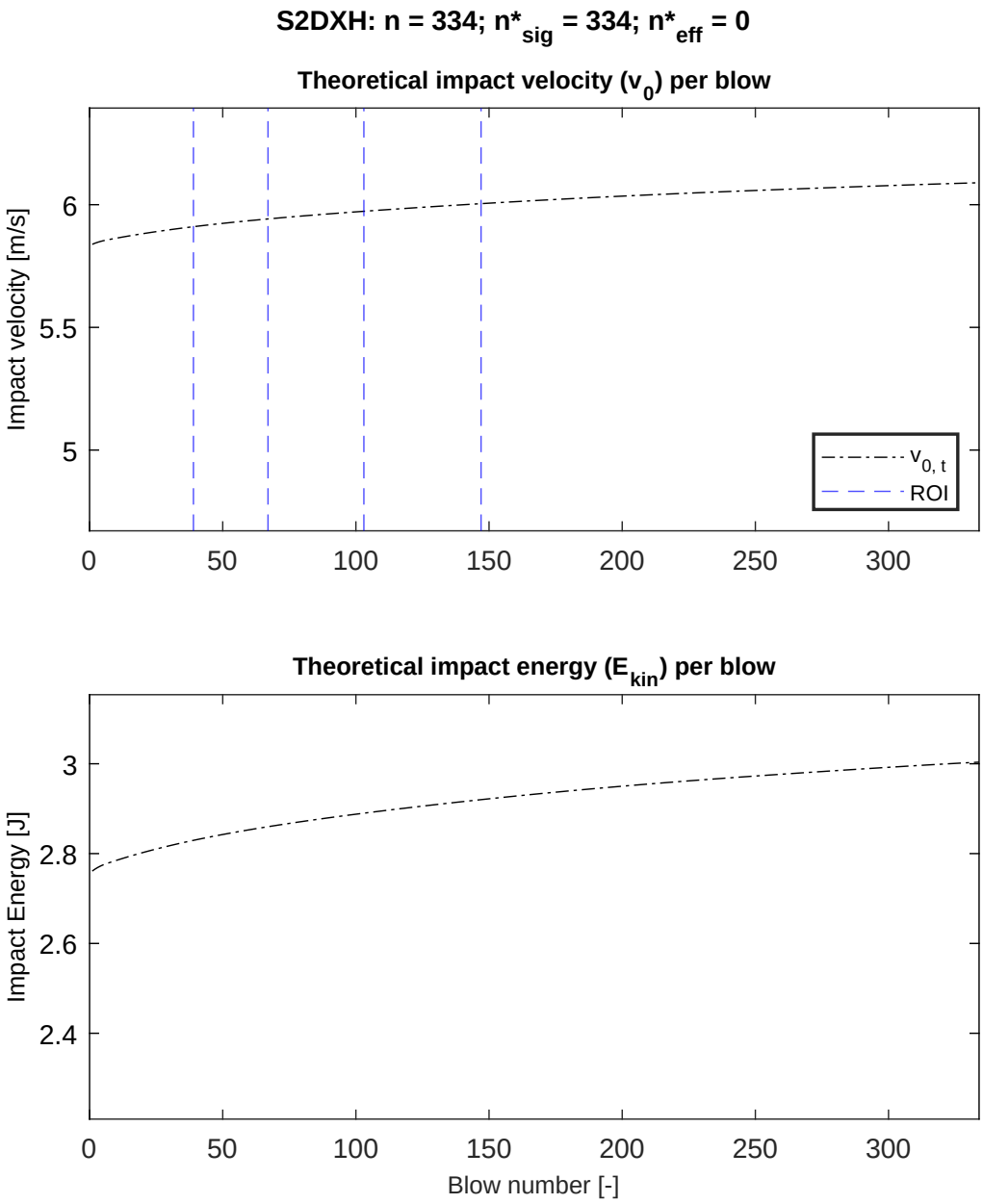

Figure C.22: For test S2DXH, from top to bottom: (I) theoretical and measured impact velocity v_0 versus blow number; (II) Theoretical and calculated impact energy versus blow number; (III) Hammer efficiency η_h versus blows number. Dots indicate blows for which the signal was approved and the subsequent velocity analysis yielded satisfactory results. Out of the total number of blows n, the number for which the latter was found to be true is indicated as n^*_{sig}. Finally, the number of blows which were disregarded (despite of usable velocity signaNA) as they yielded an efficiency >100% is denoted by n^*_{eff}

S3DXL

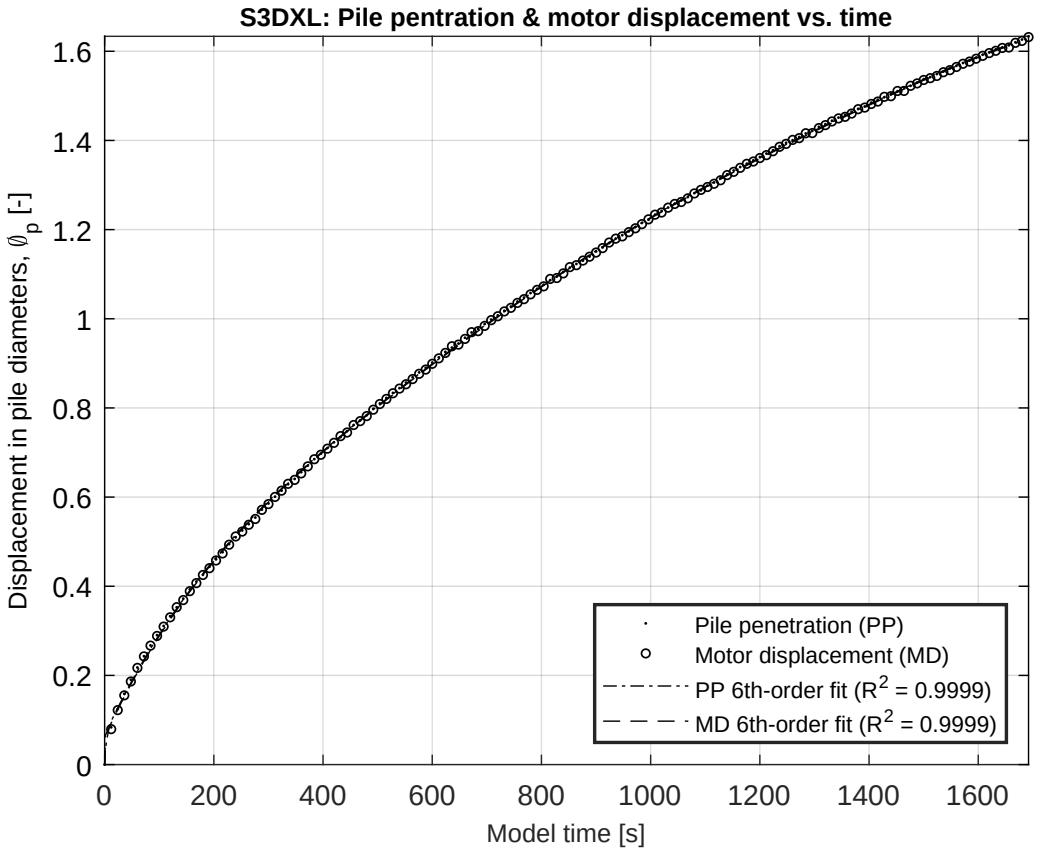

Figure C.23: Measured and approximated normalized (by pile diameter Φ_p) pile penetration (PP) and motor displacement (MD) as a function of model time for S3DXL.

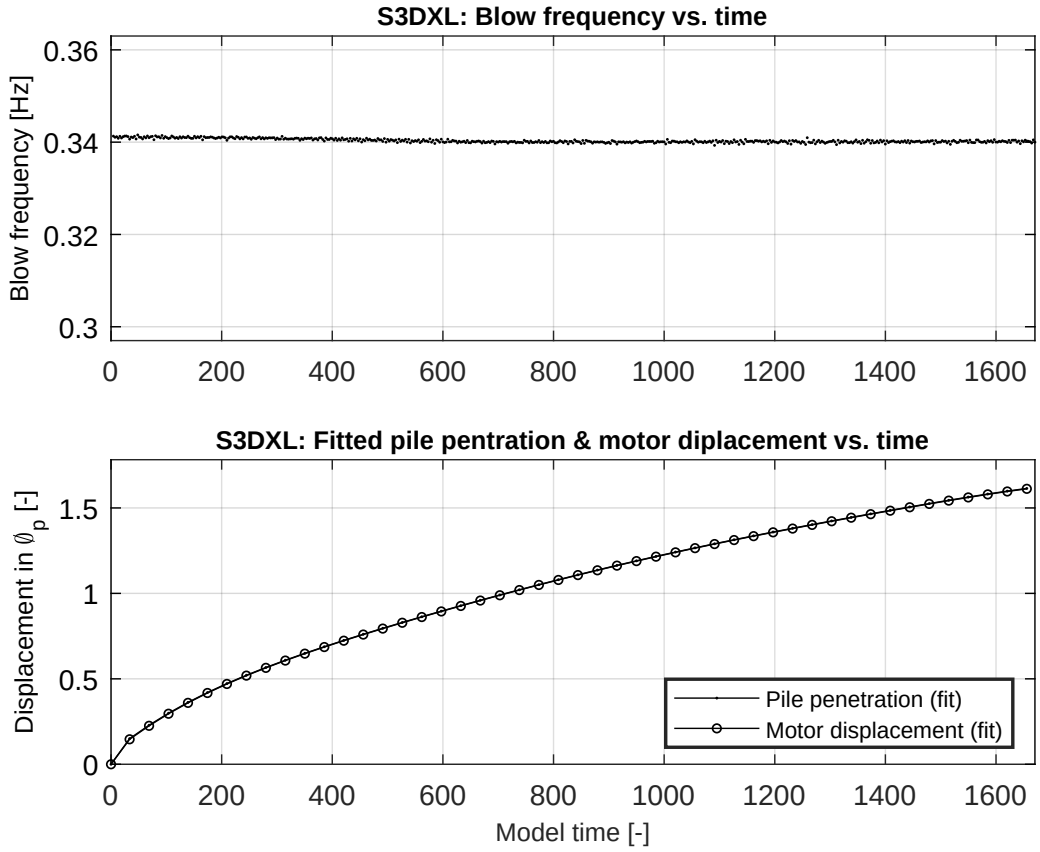

Figure C.24: (TOP) Driving frequency evaluated per blow as a function of model time for test S3DXL. As the frequency in inferred based on time interval between triggers of the load cell, the frequency for the first blow cannot be determined. Instead, it is equaled to the frequency estimate for the second blow. (BOTTOM) Fitted expressions for PP and MD, evaluated per blow as a function of model time for S3DXL

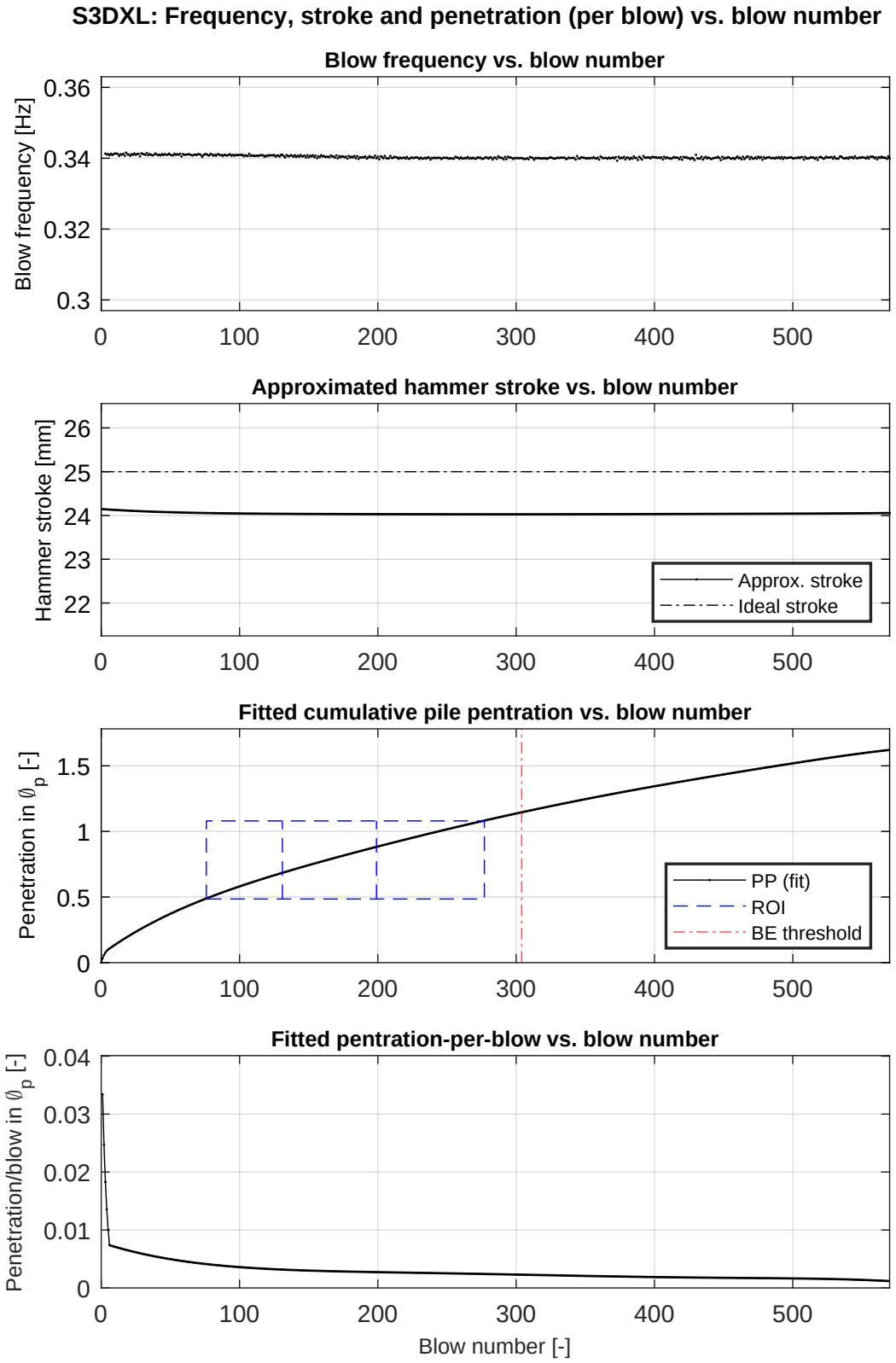

Figure C.25: From top to bottom: (I) blow frequency; (II) effective hammer stroke; (III) cumulative pile penetration, with graphical annotation of the ROI; (IV) pile penetration-per-blow. All are plotted a function of blow number for test S3DXL.

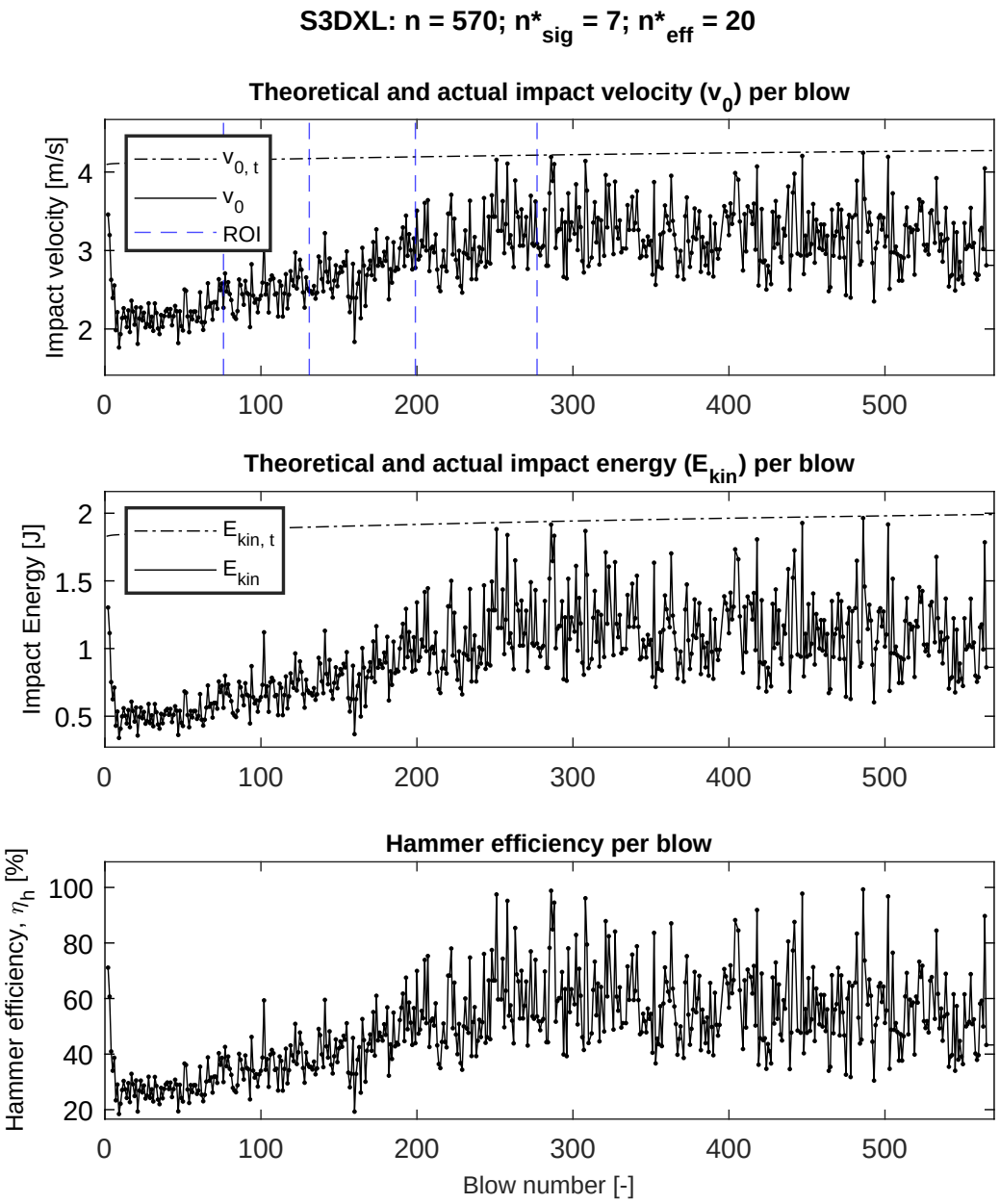

Figure C.26: For test S3DXL, from top to bottom: (I) theoretical and measured impact velocity v_0 versus blow number; (II) Theoretical and calculated impact energy versus blow number; (III) Hammer efficiency η_h versus blows number. Dots indicate blows for which the signal of the HS was approved and the subsequent velocity analysis yielded satisfactory results. Out of the total number of blows n, the number for which the latter was found to be true is indicated as n^*_{sig}. Finally, the number of blows which were disregarded (despite of usable velocity signaHS) as they yielded an efficiency >100% is denoted by n^*_{eff}.

S3DXH

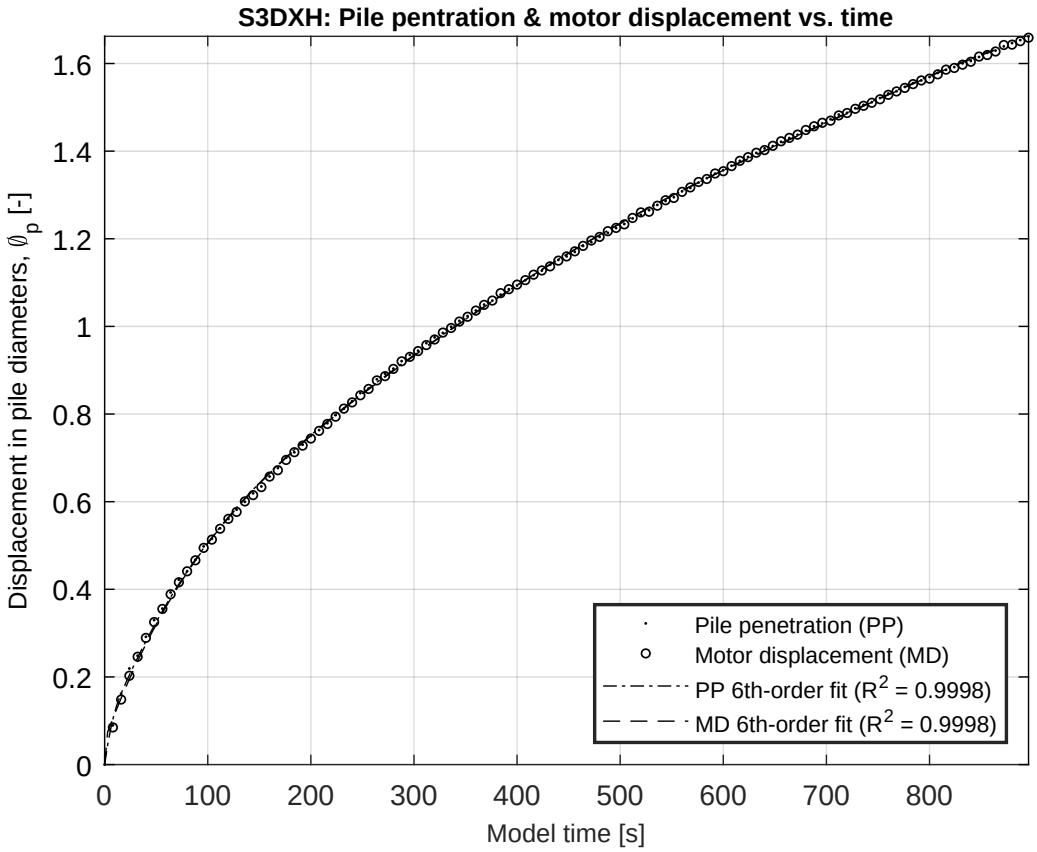

Figure C.27: Measured and approximated normalized (by pile diameter Φ_p) pile penetration (PP) and motor displacement (MD) as a function of model time for S3DXH.

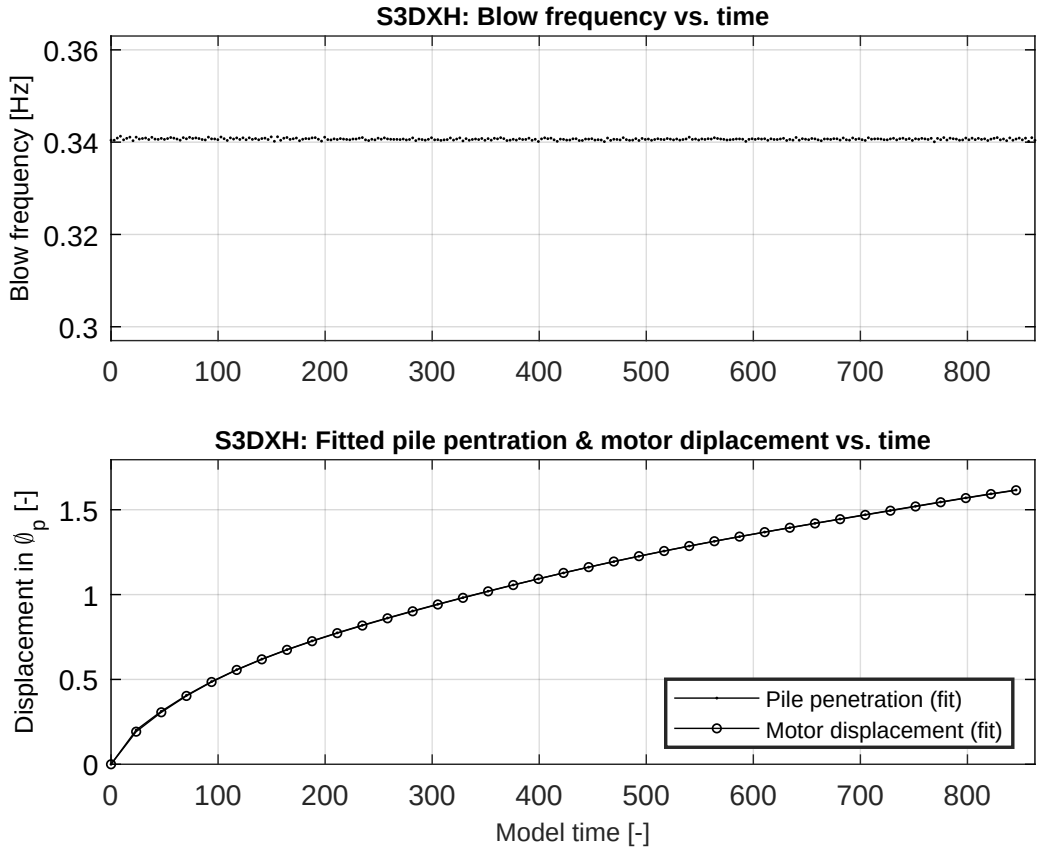

Figure C.28: (TOP) Driving frequency evaluated per blow as a function of model time for test S3DXH. As the frequency in inferred based on time interval between triggers of the load cell, the frequency for the first blow cannot be determined. Instead, it is equaled to the frequency estimate for the second blow. (BOTTOM) Fitted expressions for PP and MD, evaluated per blow as a function of model time for S3DXH

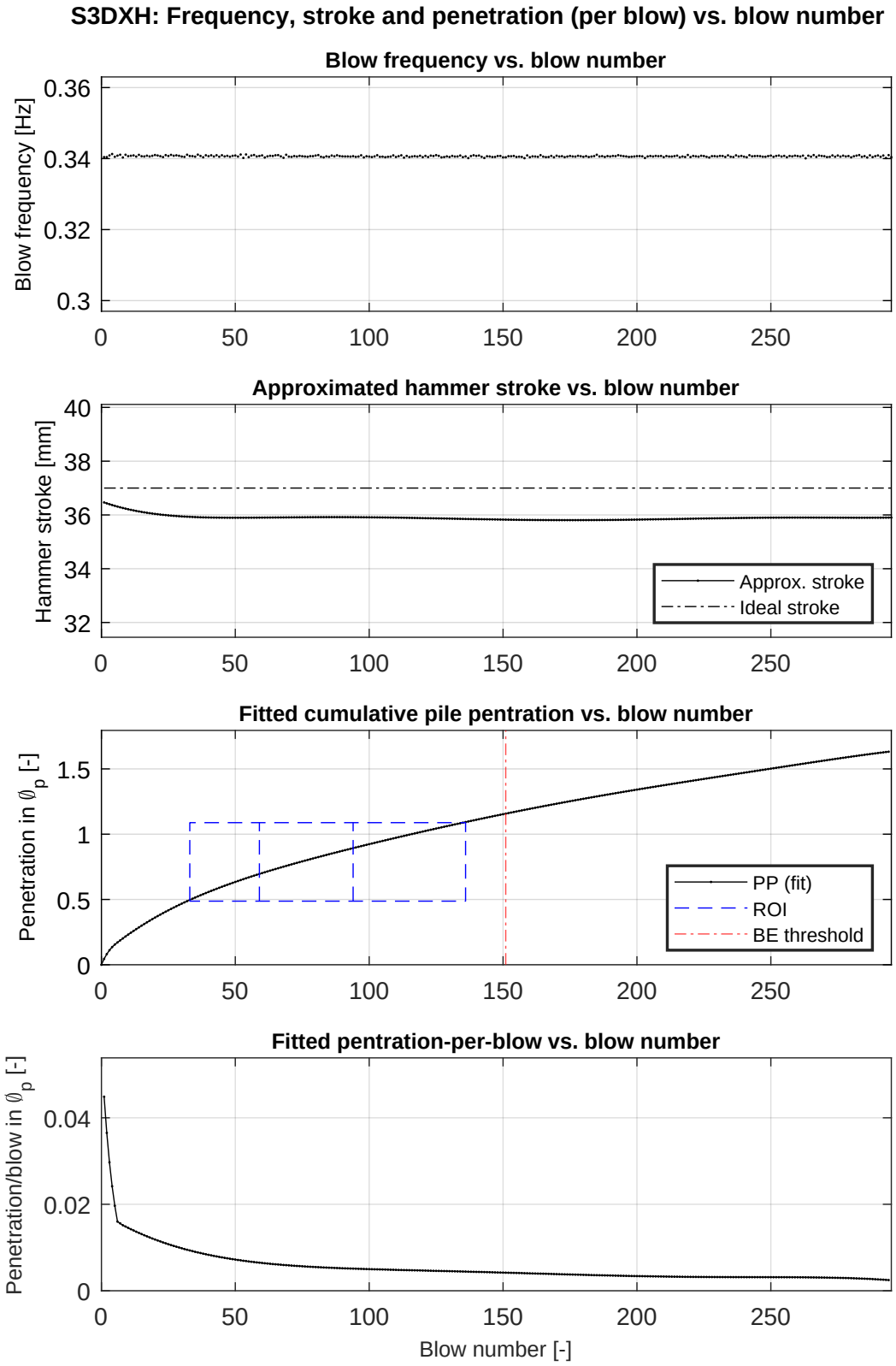

Figure C.29: From top to bottom: (I) blow frequency; (II) effective hammer stroke; (III) cumulative pile penetration, with graphical annotation of the ROI; (IV) pile penetration-per-blow. All are plotted a function of blow number for test S3DXH.

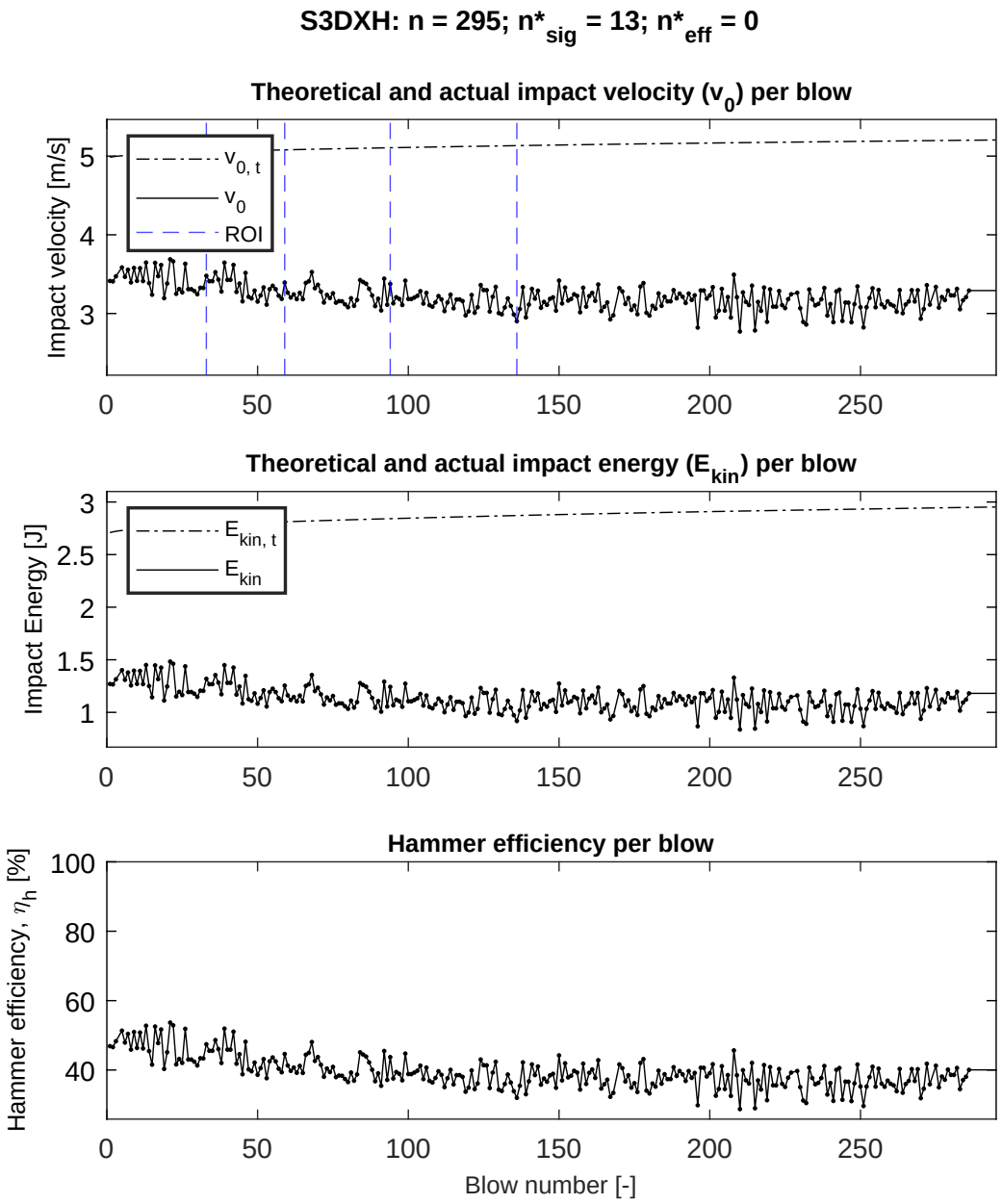

Figure C.30: For test S3DXH, from top to bottom: (I) theoretical and measured impact velocity v_0 versus blow number; (II) Theoretical and calculated impact energy versus blow number; (III) Hammer efficiency η_h versus blows number. Dots indicate blows for which the signal of the HS was approved and the subsequent velocity analysis yielded satisfactory results. Out of the total number of blows n, the number for which the latter was found to be true is indicated as n^*_{sig}. Finally, the number of blows which were disregarded (despite of usable velocity signaHS) as they yielded an efficiency >100% is denoted by n^*_{eff}.

S2SXL

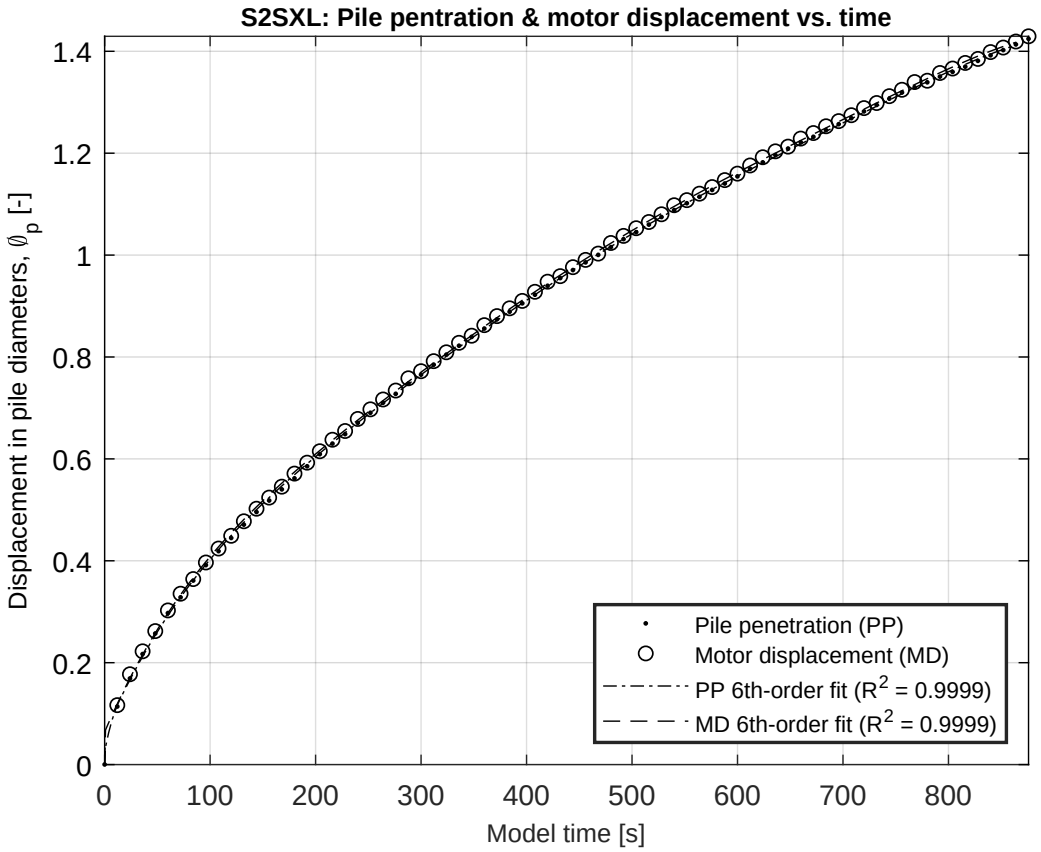

Figure C.31: Measured and approximated normalized (by pile diameter Φ_p) pile penetration (PP) and motor displacement (MD) as a function of model time for S2SXL.

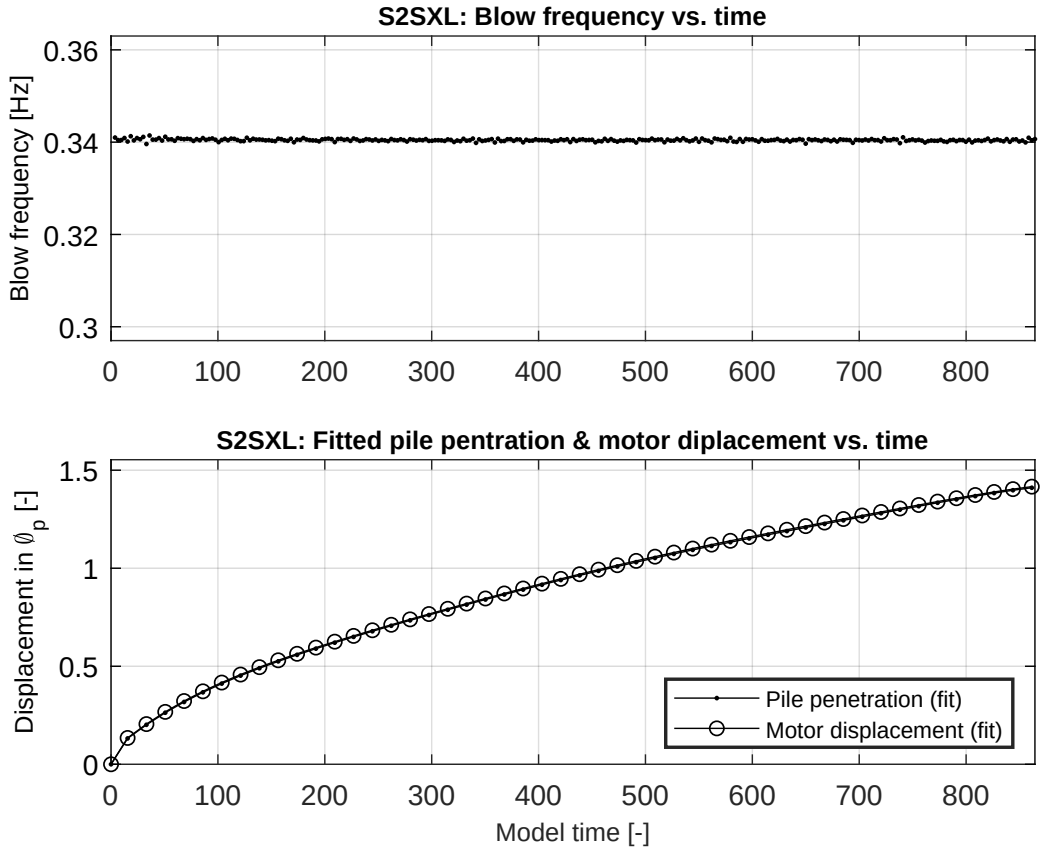

Figure C.32: (TOP) Driving frequency evaluated per blow as a function of model time for test S2SXL. As the frequency in inferred based on time interval between triggers of the load cell, the frequency for the first blow cannot be determined. Instead, it is equaled to the frequency estimate for the second blow. (BOTTOM) Fitted expressions for PP and MD, evaluated per blow as a function of model time for S2SXL

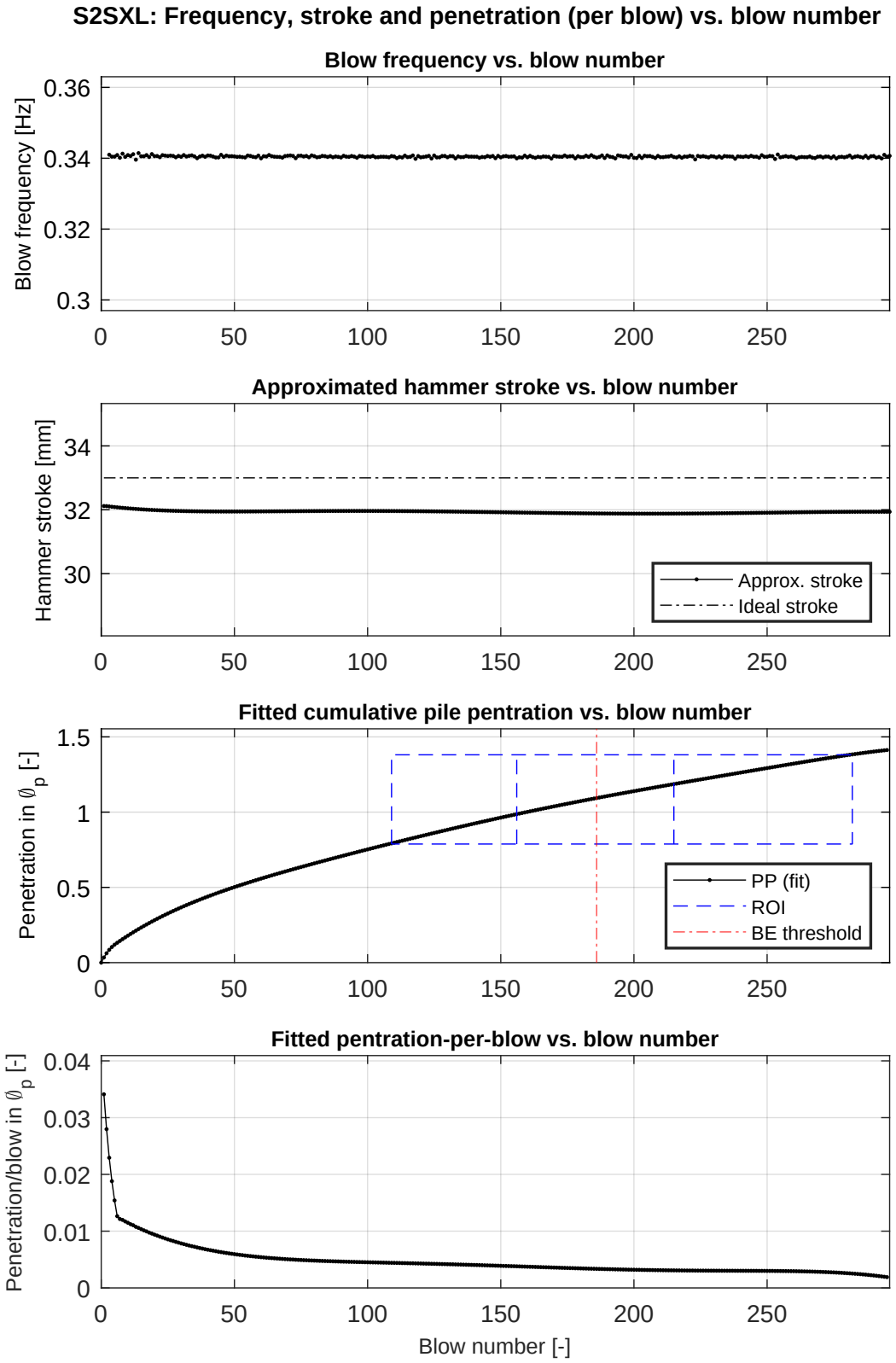

Figure C.33: From top to bottom: (I) blow frequency; (II) effective hammer stroke; (III) cumulative pile penetration, with graphical annotation of the ROI; (IV) pile penetration-per-blow. All are plotted a function of blow number for test S2SXL.

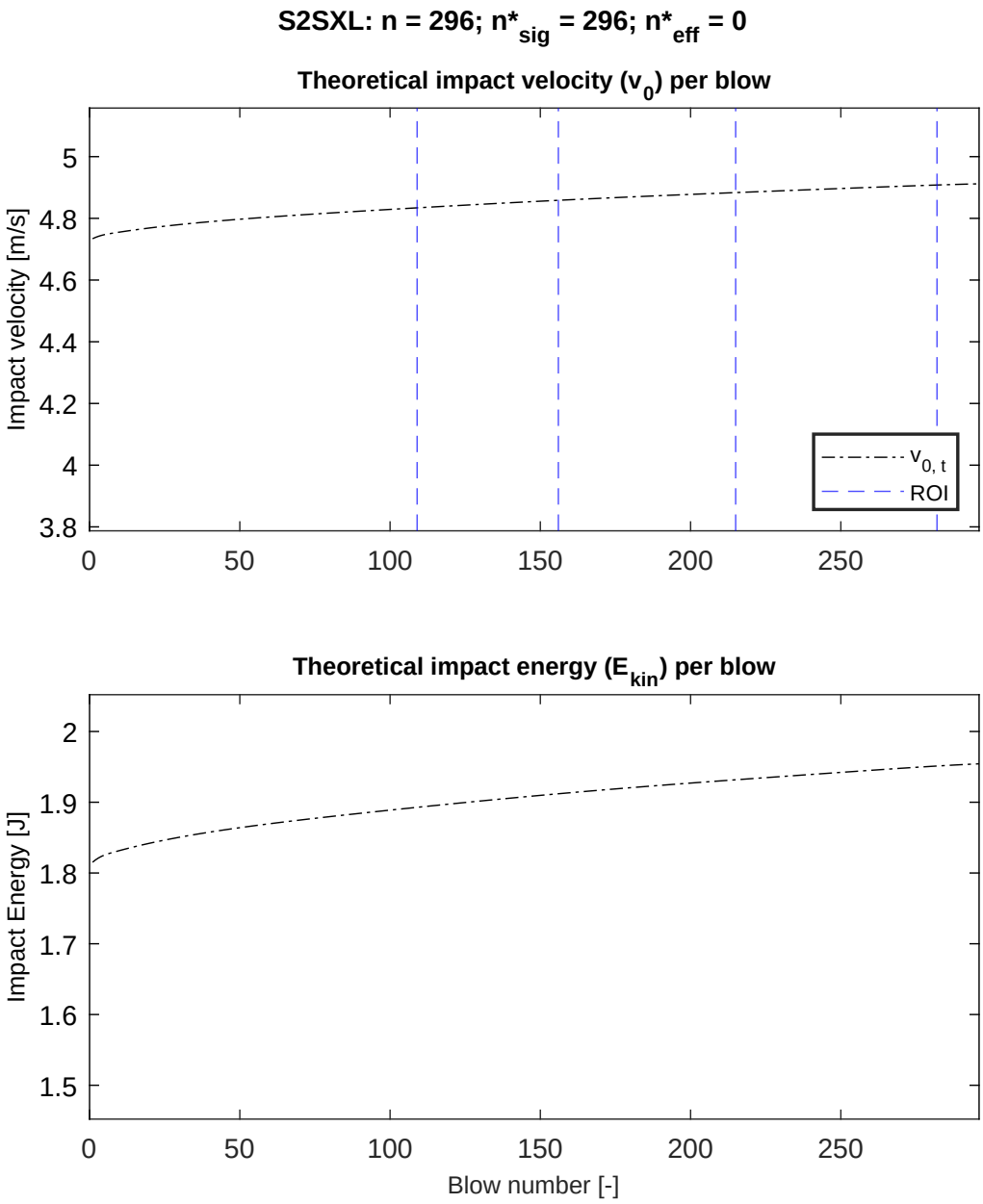

Figure C.34: For test S2SXL, from top to bottom: (I) theoretical and measured impact velocity v_0 versus blow number; (II) Theoretical and calculated impact energy versus blow number; (III) Hammer efficiency η_h versus blows number. Dots indicate blows for which the signal was approved and the subsequent velocity analysis yielded satisfactory results. Out of the total number of blows n, the number for which the latter was found to be true is indicated as n^*_{sig}. Finally, the number of blows which were disregarded (despite of usable velocity signaNA) as they yielded an efficiency >100% is denoted by n^*_{eff}

S2SXH

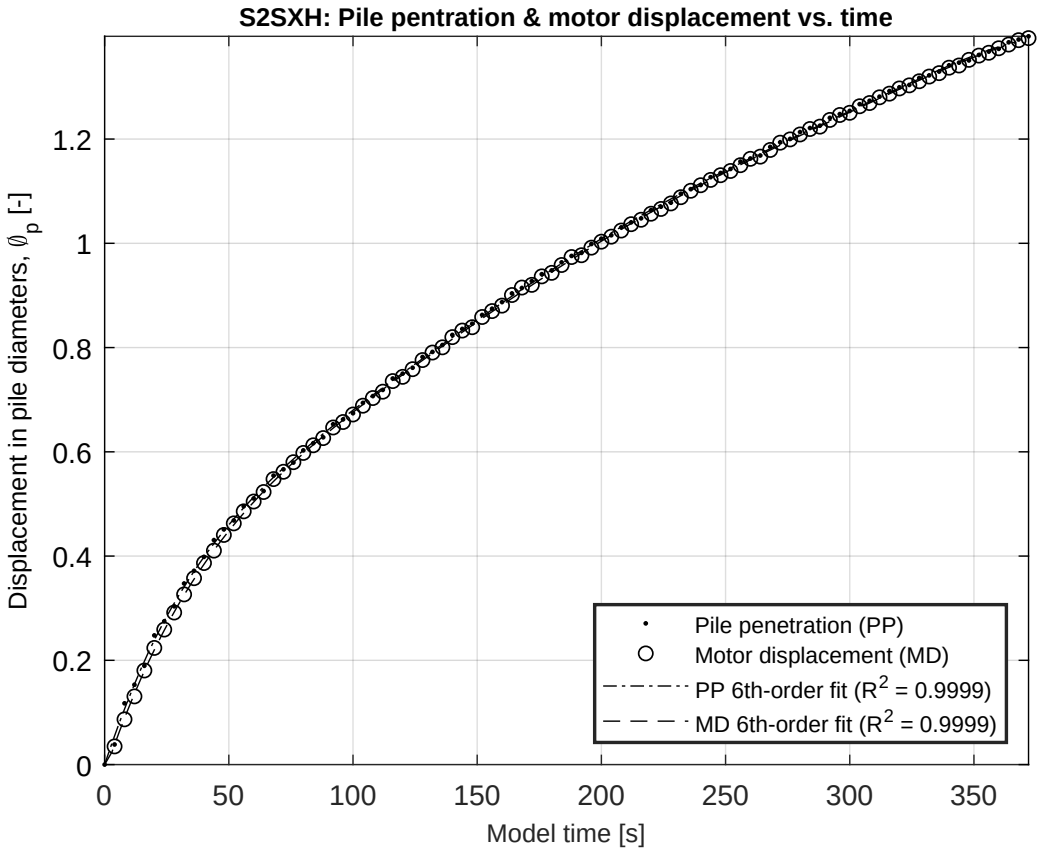

Figure C.35: Measured and approximated normalized (by pile diameter Φ_p) pile penetration (PP) and motor displacement (MD) as a function of model time for S2SXH.

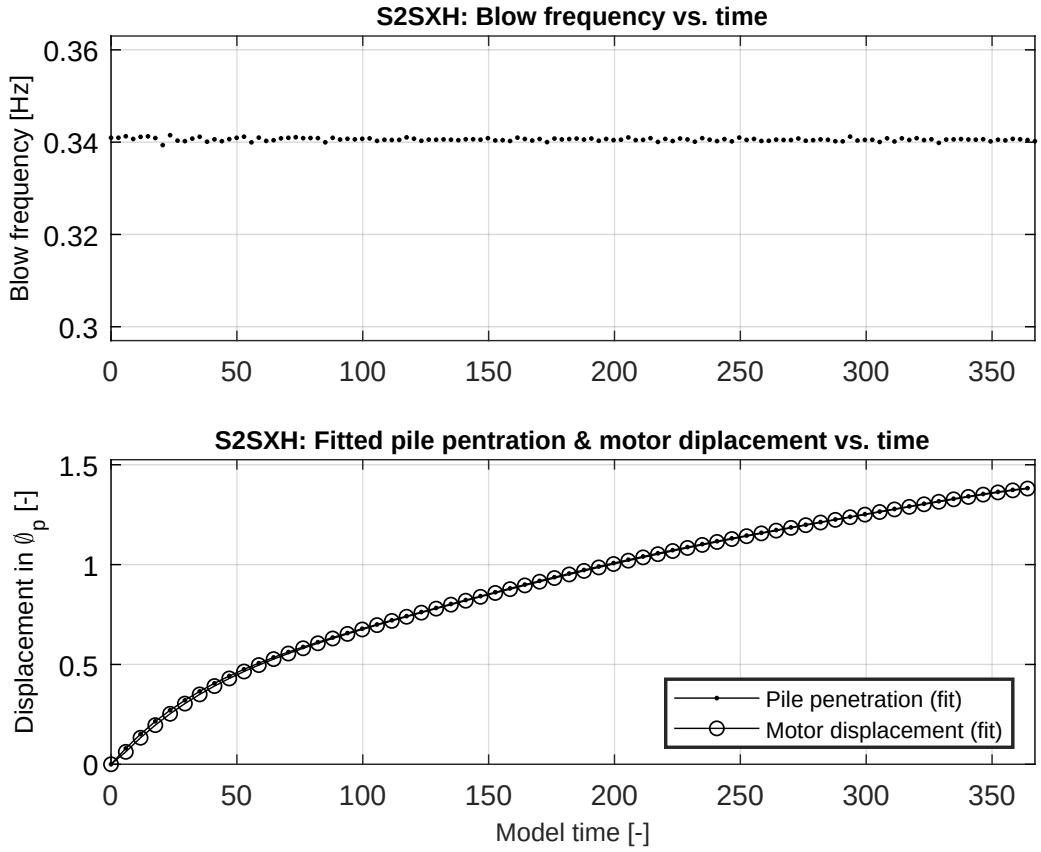

Figure C.36: (TOP) Driving frequency evaluated per blow as a function of model time for test S2SXH. As the frequency in inferred based on time interval between triggers of the load cell, the frequency for the first blow cannot be determined. Instead, it is equaled to the frequency estimate for the second blow. (BOTTOM) Fitted expressions for PP and MD, evaluated per blow as a function of model time for S2SXH

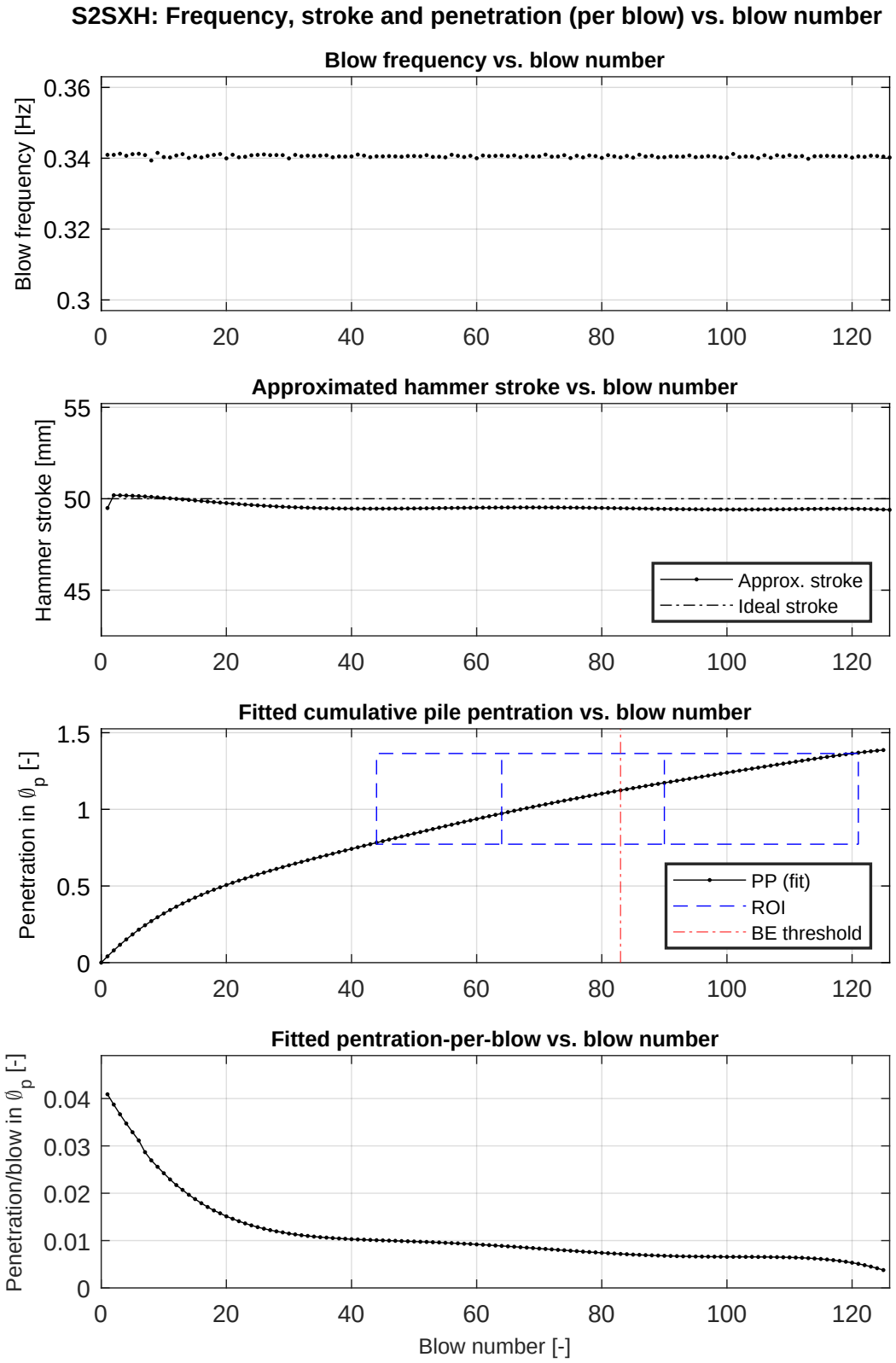

Figure C.37: From top to bottom: (I) blow frequency; (II) effective hammer stroke; (III) cumulative pile penetration, with graphical annotation of the ROI; (IV) pile penetration-per-blow. All are plotted a function of blow number for test S2SXH.

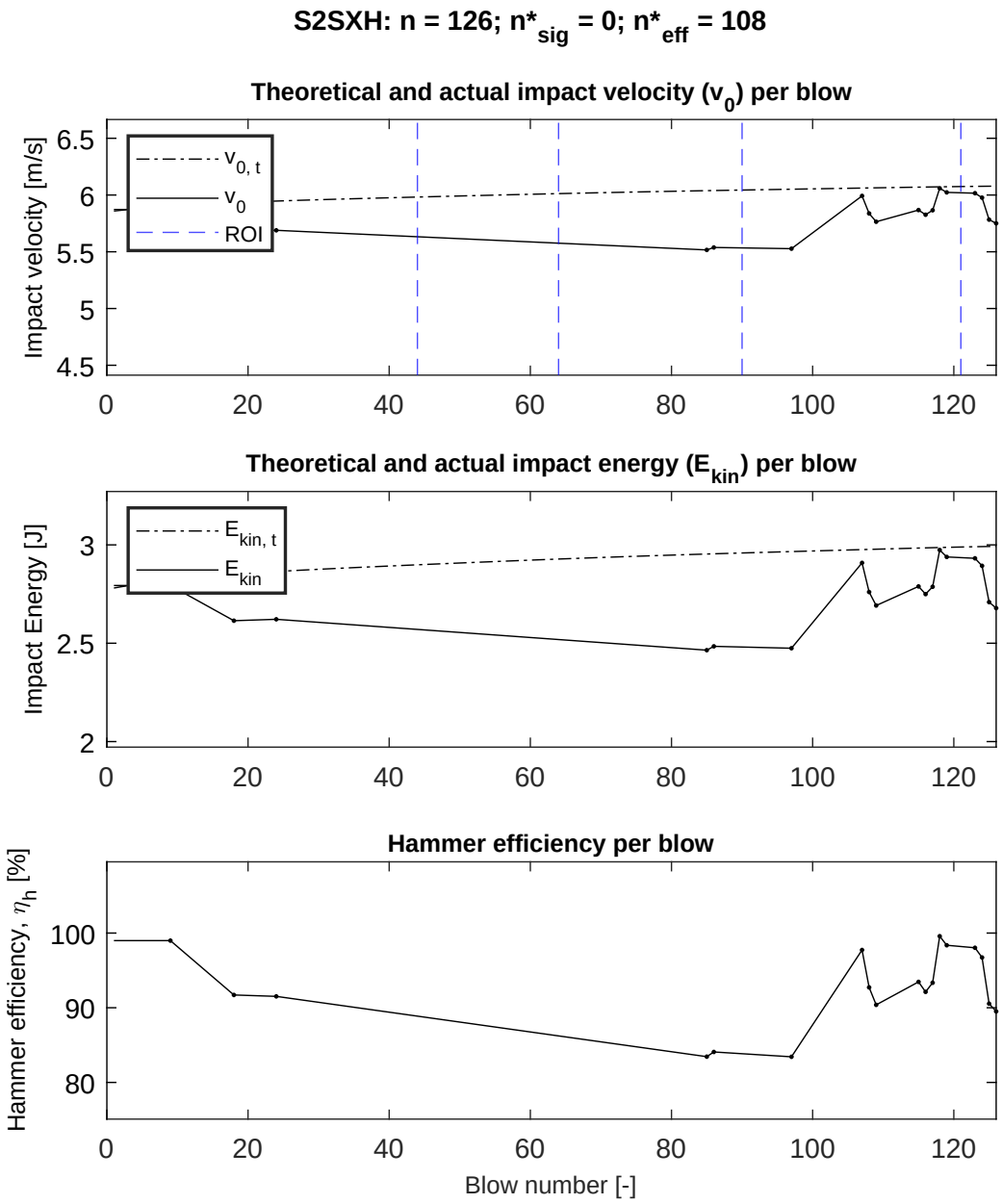

Figure C.38: For test S2SXH, from top to bottom: (I) theoretical and measured impact velocity v_0 versus blow number; (II) Theoretical and calculated impact energy versus blow number; (III) Hammer efficiency η_h versus blows number. Dots indicate blows for which the signal of the HS was approved and the subsequent velocity analysis yielded satisfactory results. Out of the total number of blows n, the number for which the latter was found to be true is indicated as n^*_{sig}. Finally, the number of blows which were disregarded (despite of usable velocity signaHS) as they yielded an efficiency >100% is denoted by n^*_{eff}.

S3SXL

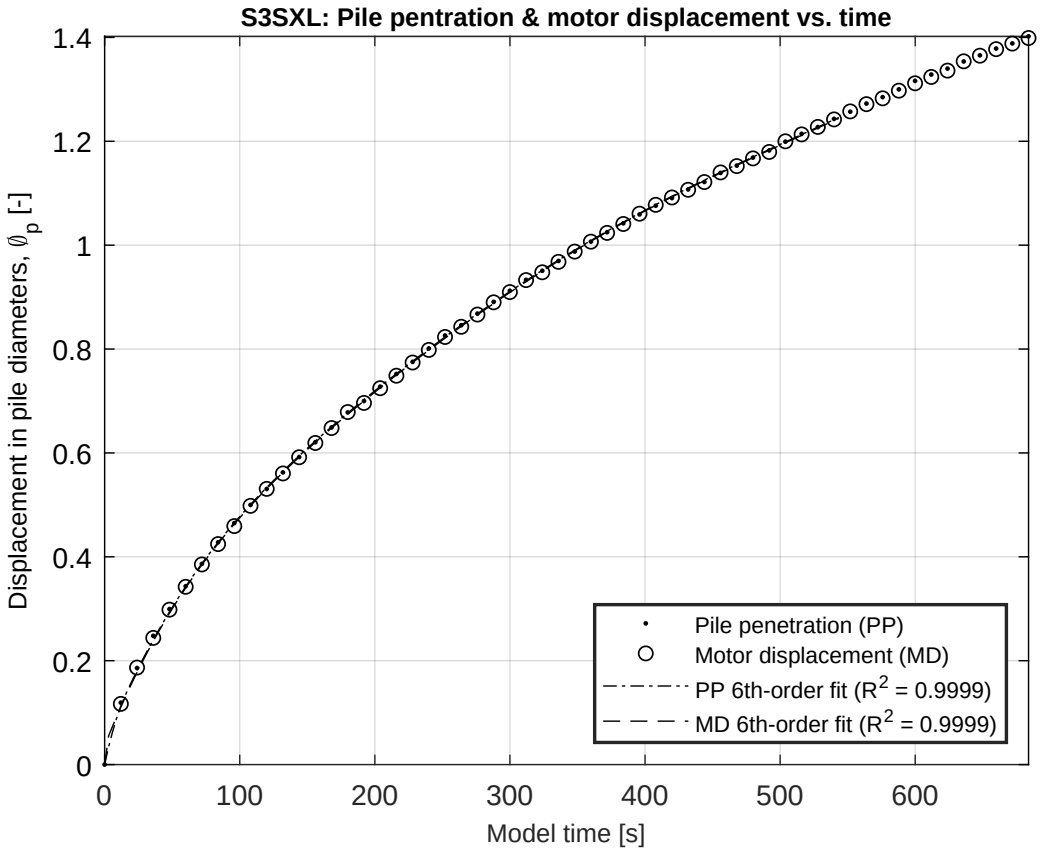

Figure C.39: Measured and approximated normalized (by pile diameter Φ_p) pile penetration (PP) and motor displacement (MD) as a function of model time for S3SXL.

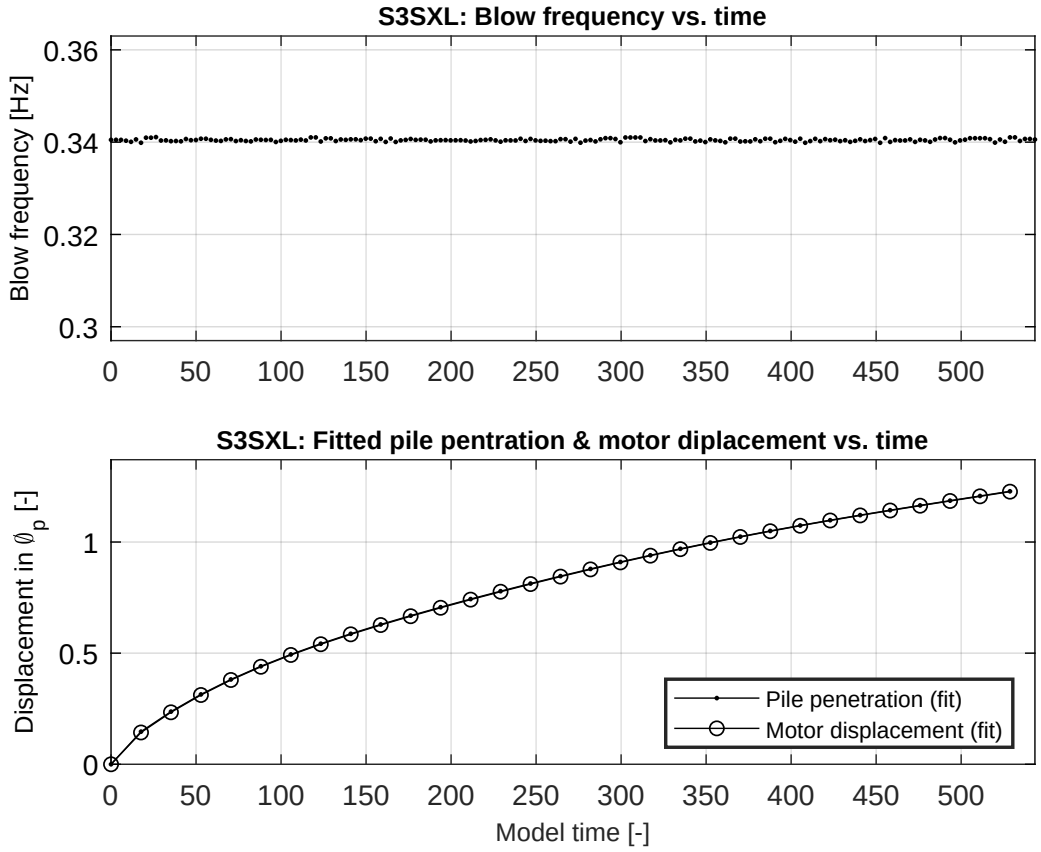

Figure C.40: (TOP) Driving frequency evaluated per blow as a function of model time for test S3SXL. As the frequency in inferred based on time interval between triggers of the load cell, the frequency for the first blow cannot be determined. Instead, it is equaled to the frequency estimate for the second blow. (BOTTOM) Fitted expressions for PP and MD, evaluated per blow as a function of model time for S3SXL

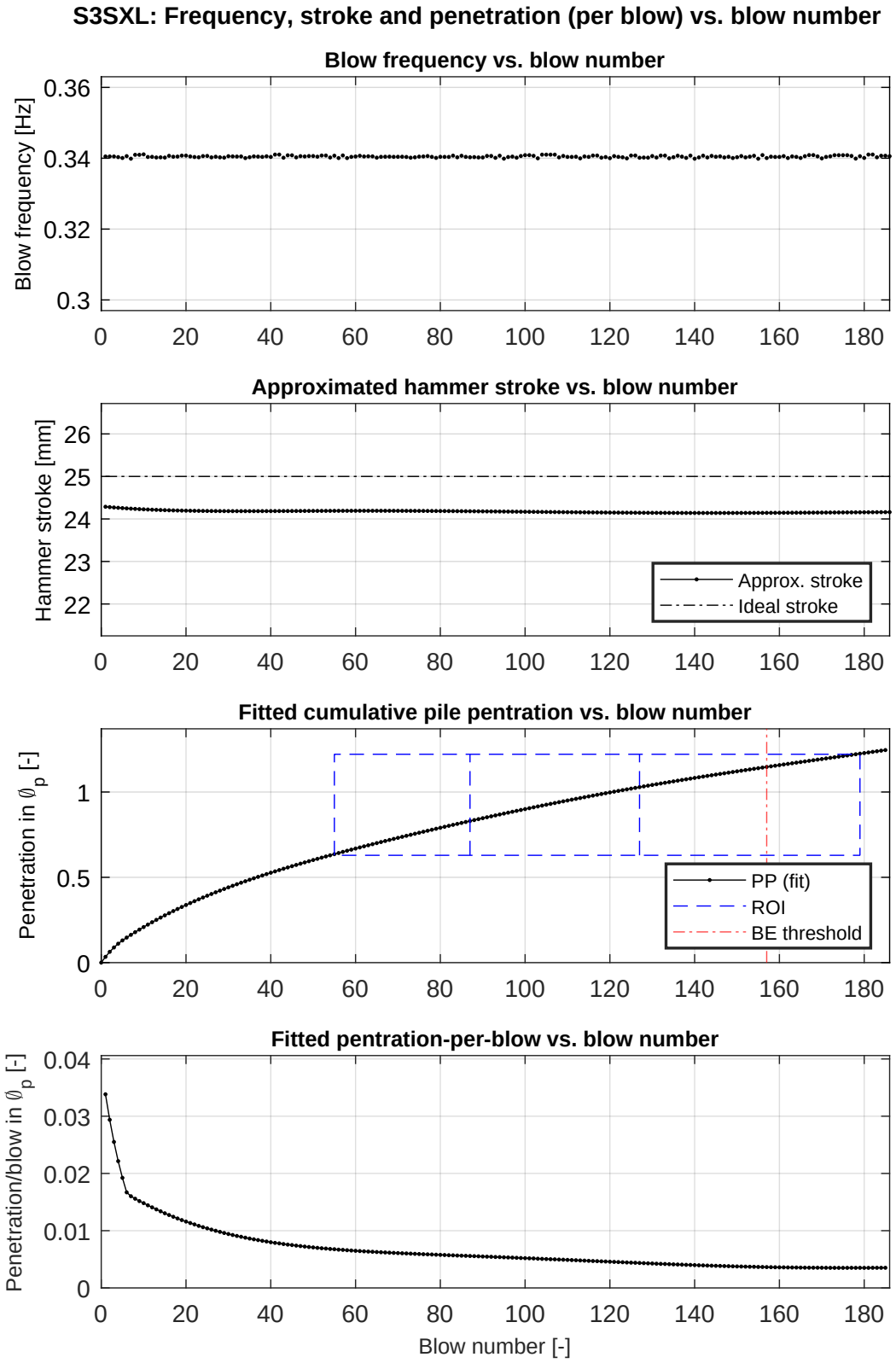

Figure C.41: From top to bottom: (I) blow frequency; (II) effective hammer stroke; (III) cumulative pile penetration, with graphical annotation of the ROI; (IV) pile penetration-per-blow. All are plotted a function of blow number for test S3SXL.

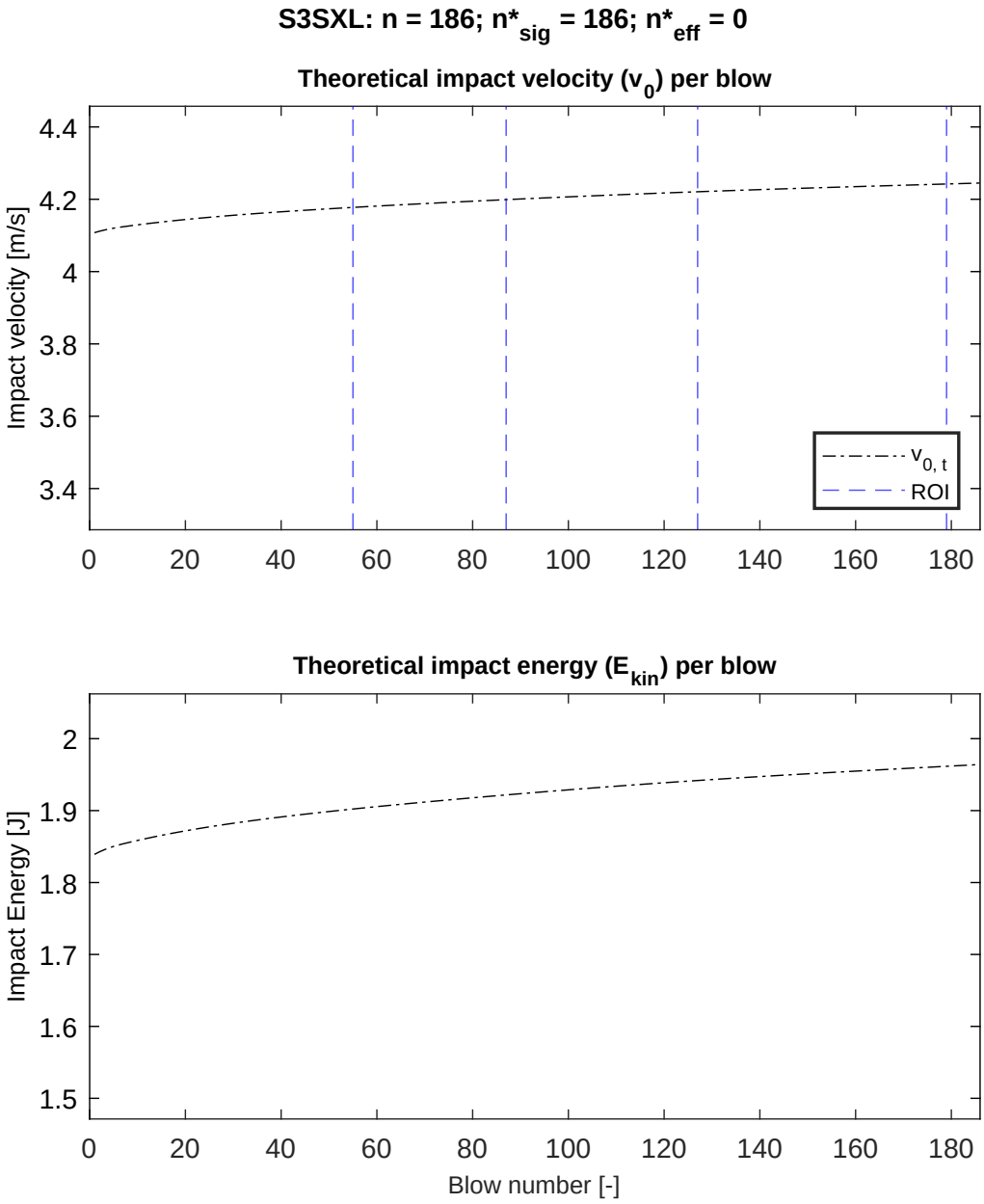

Figure C.42: For test S3SXL, from top to bottom: (I) theoretical and measured impact velocity v_0 versus blow number; (II) Theoretical and calculated impact energy versus blow number; (III) Hammer efficiency η_h versus blows number. Dots indicate blows for which the signal was approved and the subsequent velocity analysis yielded satisfactory results. Out of the total number of blows n, the number for which the latter was found to be true is indicated as n^*_{sig}. Finally, the number of blows which were disregarded (despite of usable velocity signaNA) as they yielded an efficiency >100% is denoted by n^*_{eff}

S3SXH

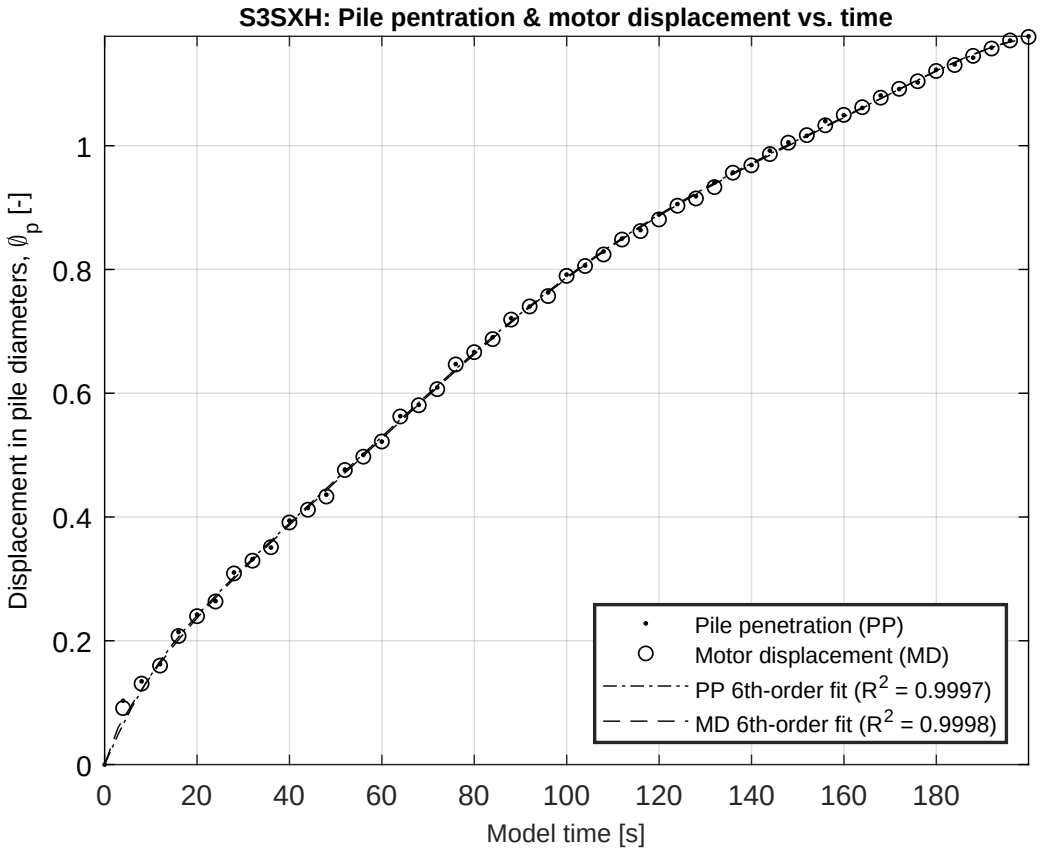

Figure C.43: Measured and approximated normalized (by pile diameter Φ_p) pile penetration (PP) and motor displacement (MD) as a function of model time for S3SXH.

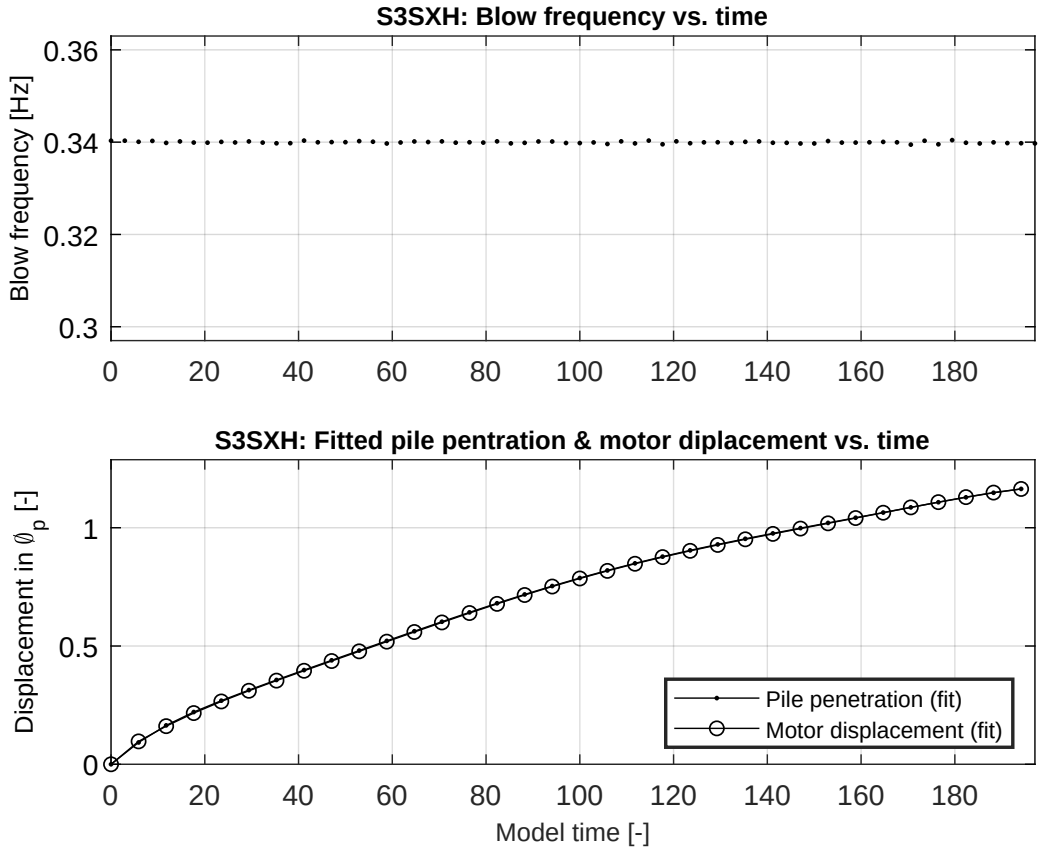

Figure C.44: (TOP) Driving frequency evaluated per blow as a function of model time for test S3SXH. As the frequency in inferred based on time interval between triggers of the load cell, the frequency for the first blow cannot be determined. Instead, it is equaled to the frequency estimate for the second blow. (BOTTOM) Fitted expressions for PP and MD, evaluated per blow as a function of model time for S3SXH

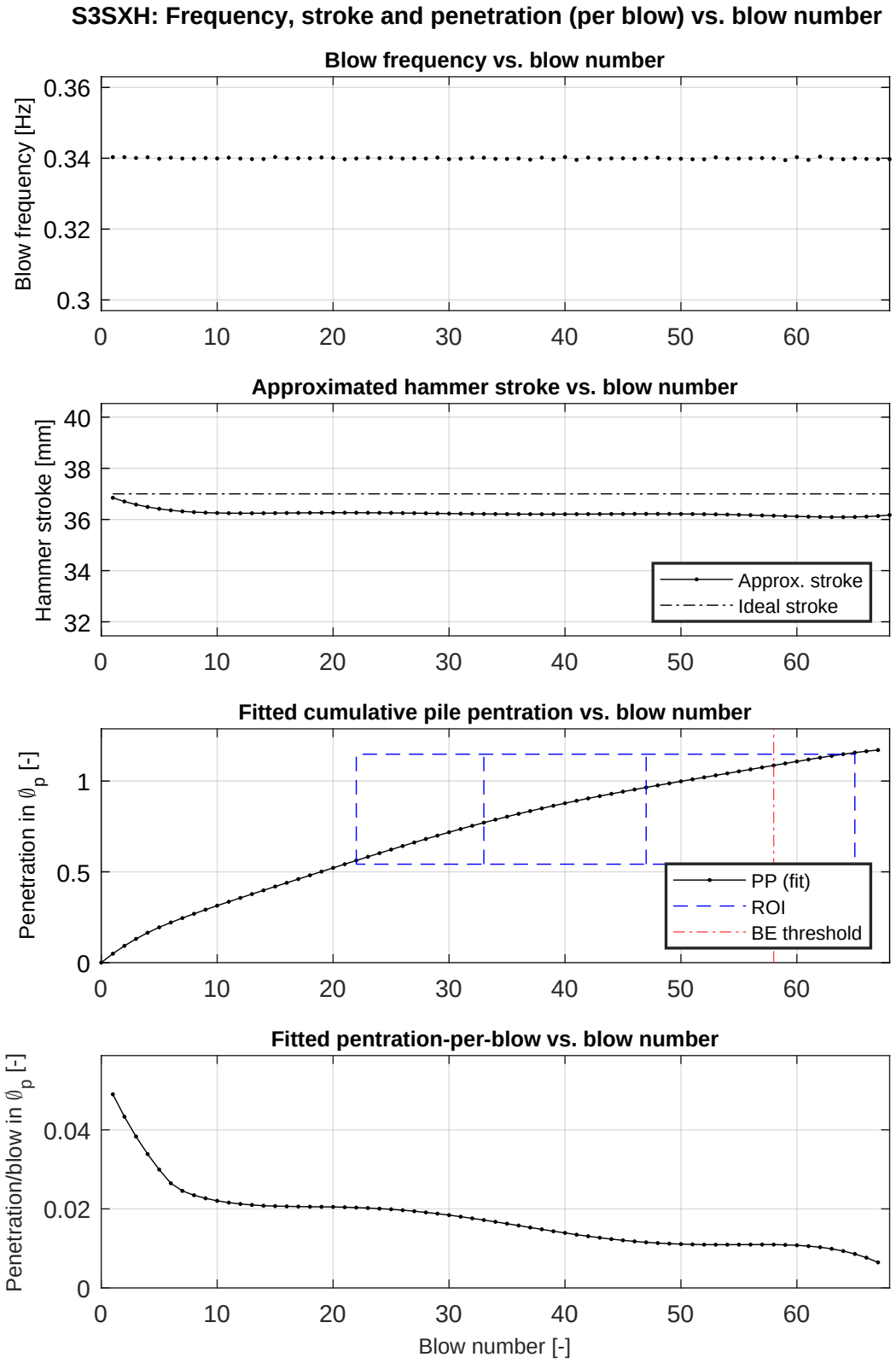

Figure C.45: From top to bottom: (I) blow frequency; (II) effective hammer stroke; (III) cumulative pile penetration, with graphical annotation of the ROI; (IV) pile penetration-per-blow. All are plotted a function of blow number for test S3SXH.

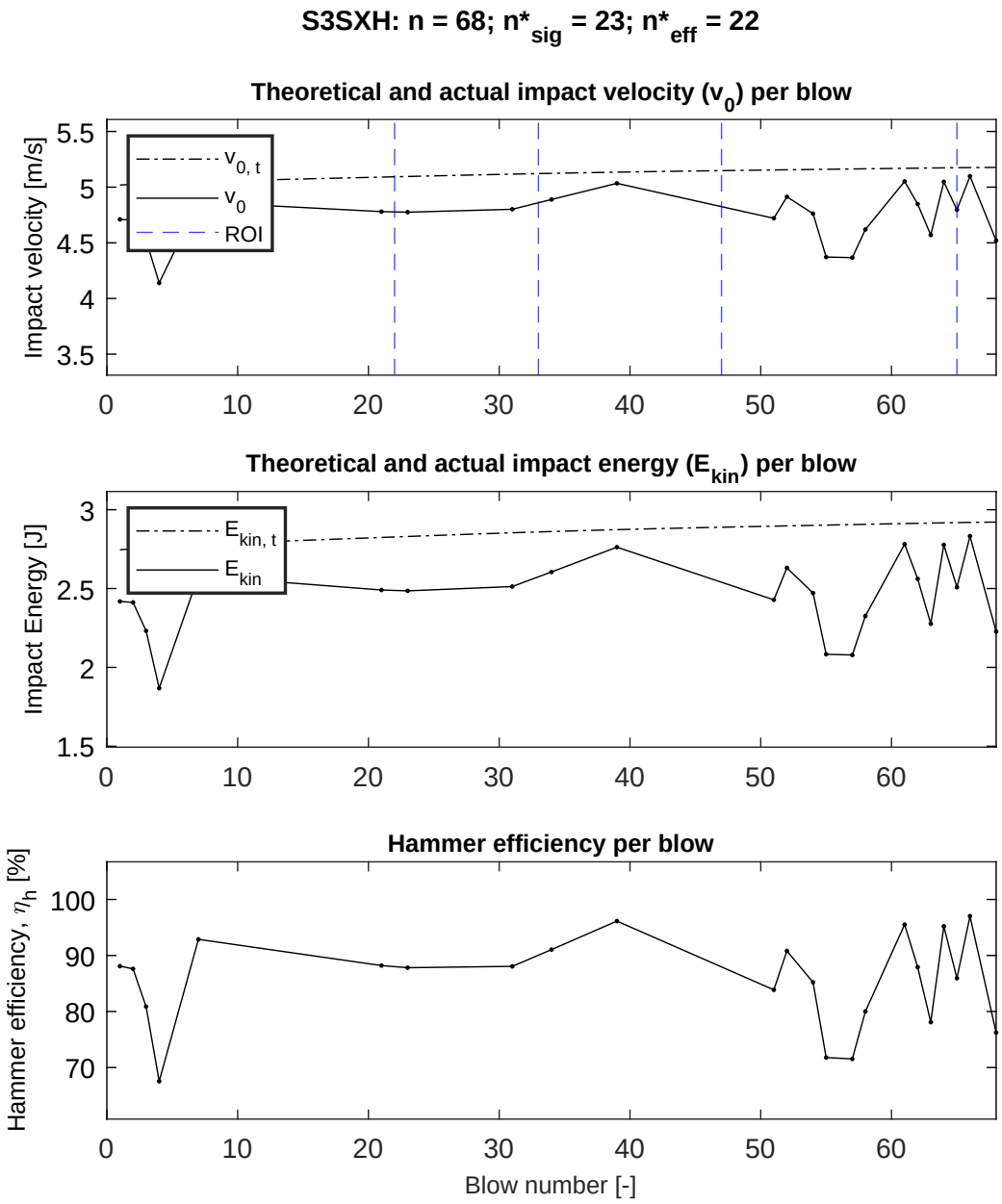

Figure C.46: For test S3SXH, from top to bottom: (I) theoretical and measured impact velocity v_0 versus blow number; (II) Theoretical and calculated impact energy versus blow number; (III) Hammer efficiency η_h versus blows number. Dots indicate blows for which the signal of the HS was approved and the subsequent velocity analysis yielded satisfactory results. Out of the total number of blows n, the number for which the latter was found to be true is indicated as n^*_{sig}. Finally, the number of blows which were disregarded (despite of usable velocity signaHS) as they yielded an efficiency >100% is denoted by n^*_{eff}.

M2DLL

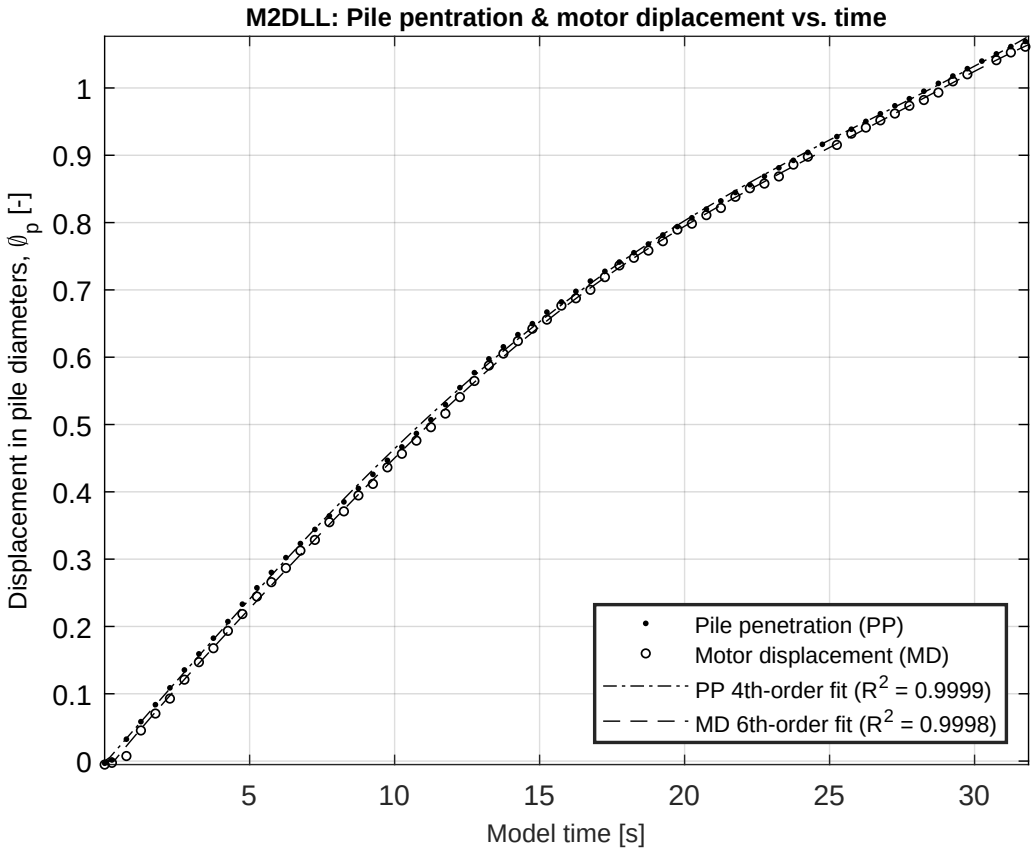

Figure C.47: Measured and approximated normalized (by pile diameter Φ_p) pile penetration (PP) and motor displacement (MD) as a function of model time for M2DLL.

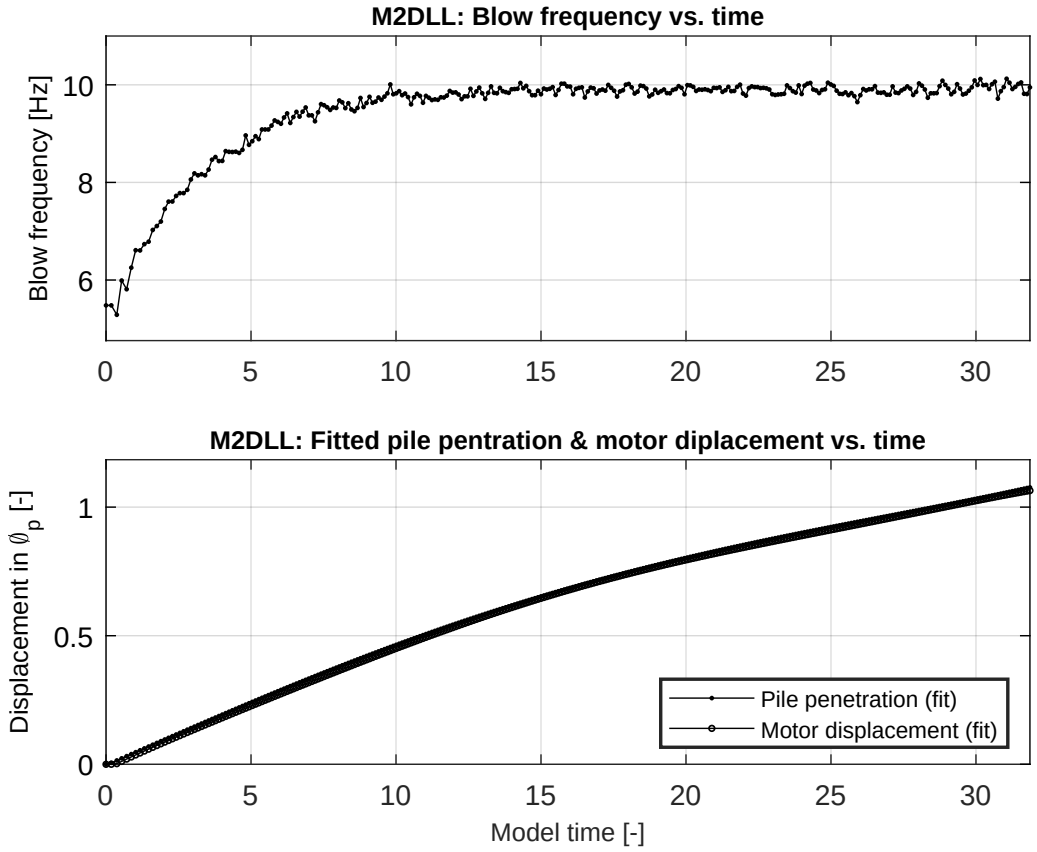

Figure C.48: (TOP) Driving frequency evaluated per blow as a function of model time for test M2DLL. As the frequency in inferred based on time intervals between triggers of the load cell, the frequency for the first blow cannot be determined. Instead, it is equaled to the frequency estimate for the second blow. (BOTTOM) Fitted expressions for PP and MD, evaluated per blow as a function of model time for M2DLL

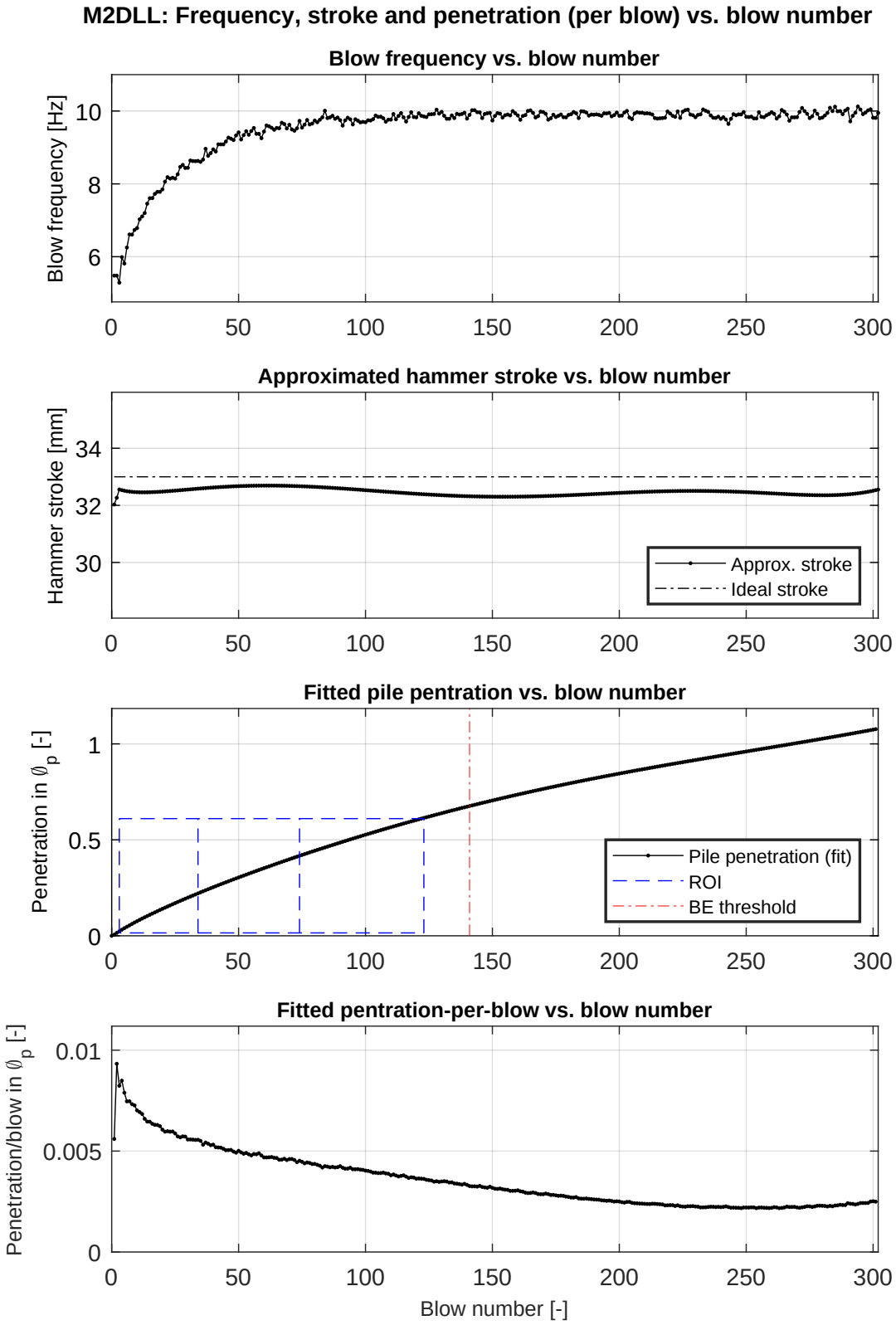

Figure C.49: From top to bottom: (I) blow frequency; (II) effective hammer stroke; (III) cumulative pile penetration, with graphical annotation of the ROI; (IV) pile penetration-per-blow. All are plotted a function of blow number for test M2DLL.

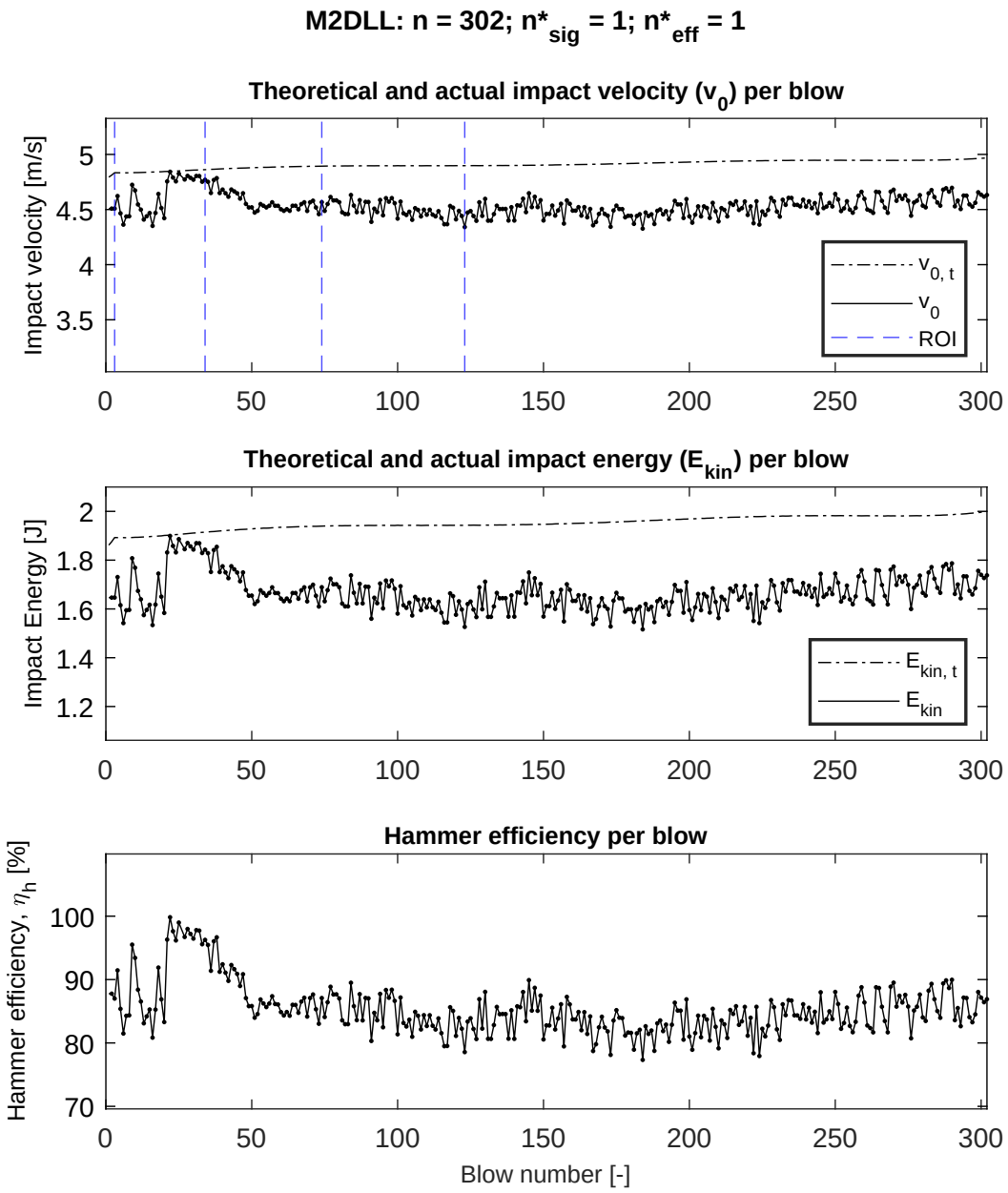

Figure C.50: For test M2DLL, from top to bottom: (I) theoretical and measured impact velocity v_0 versus blow number; (II) Theoretical and calculated impact energy versus blow number; (III) Hammer efficiency η_h versus blows number. Dots indicate blows for which the signal of the LS was approved and the subsequent velocity analysis yielded satisfactory results. Out of the total number of blows n, the number for which the latter was found to be true is indicated as n^*_{sig}. Finally, the number of blows which were disregarded (despite of usable velocity signals) as they yielded an efficiency >100% is denoted by n^*_{eff}.

M2DHL

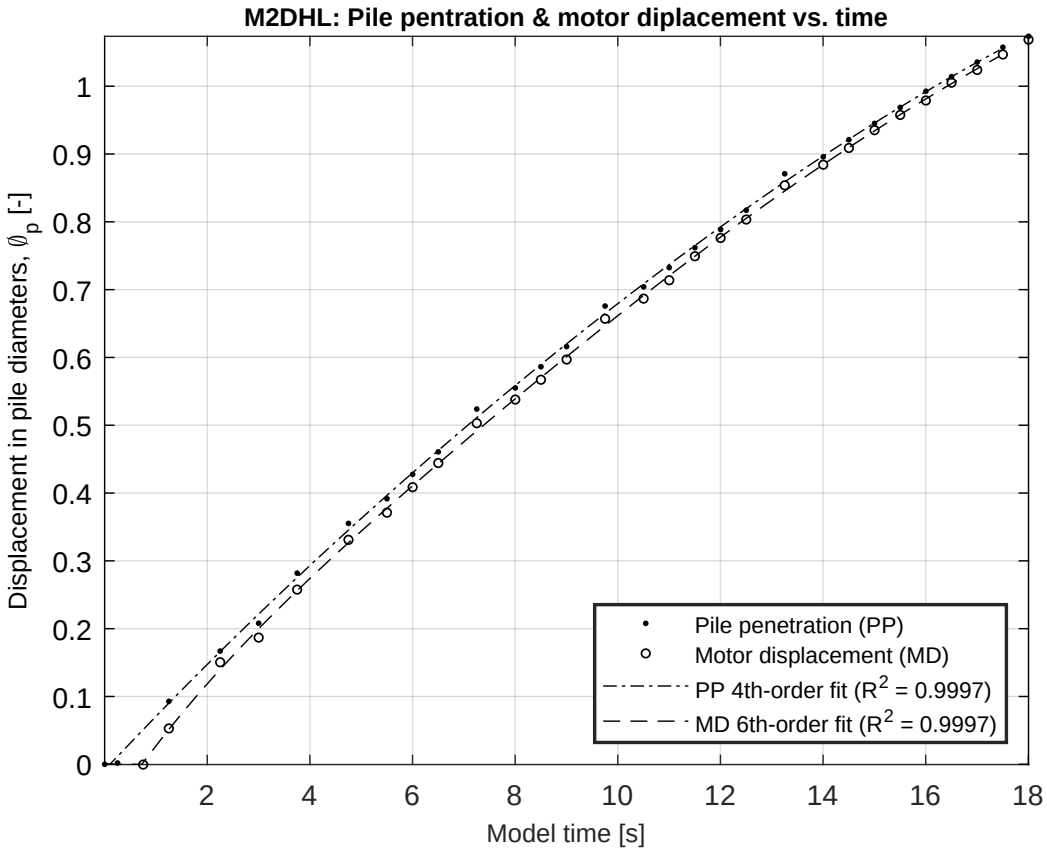

Figure C.51: Measured and approximated normalized (by pile diameter Φ_p) pile penetration (PP) and motor displacement (MD) as a function of model time for M2DHL.

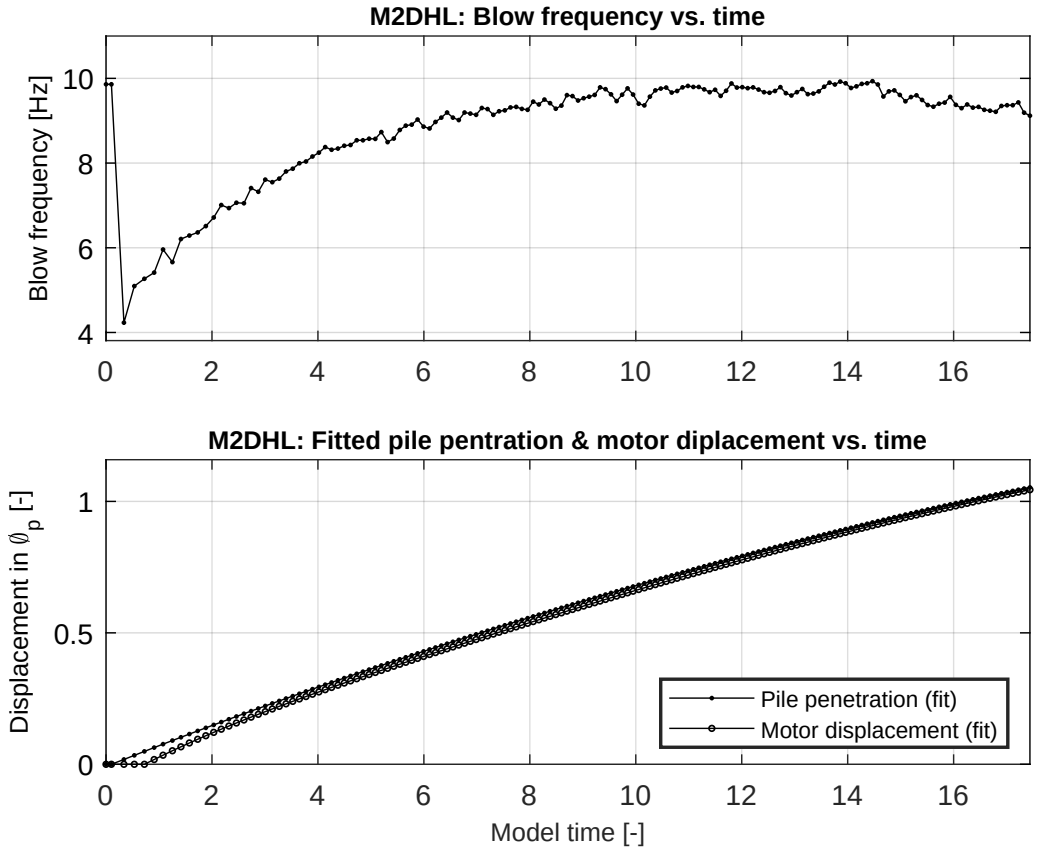

Figure C.52: (TOP) Driving frequency evaluated per blow as a function of model time for test M2DHL. As the frequency in inferred based on time intervals between triggers of the load cell, the frequency for the first blow cannot be determined. Instead, it is equaled to the frequency estimate for the second blow. (BOTTOM) Fitted expressions for PP and MD, evaluated per blow as a function of model time for M2DHL

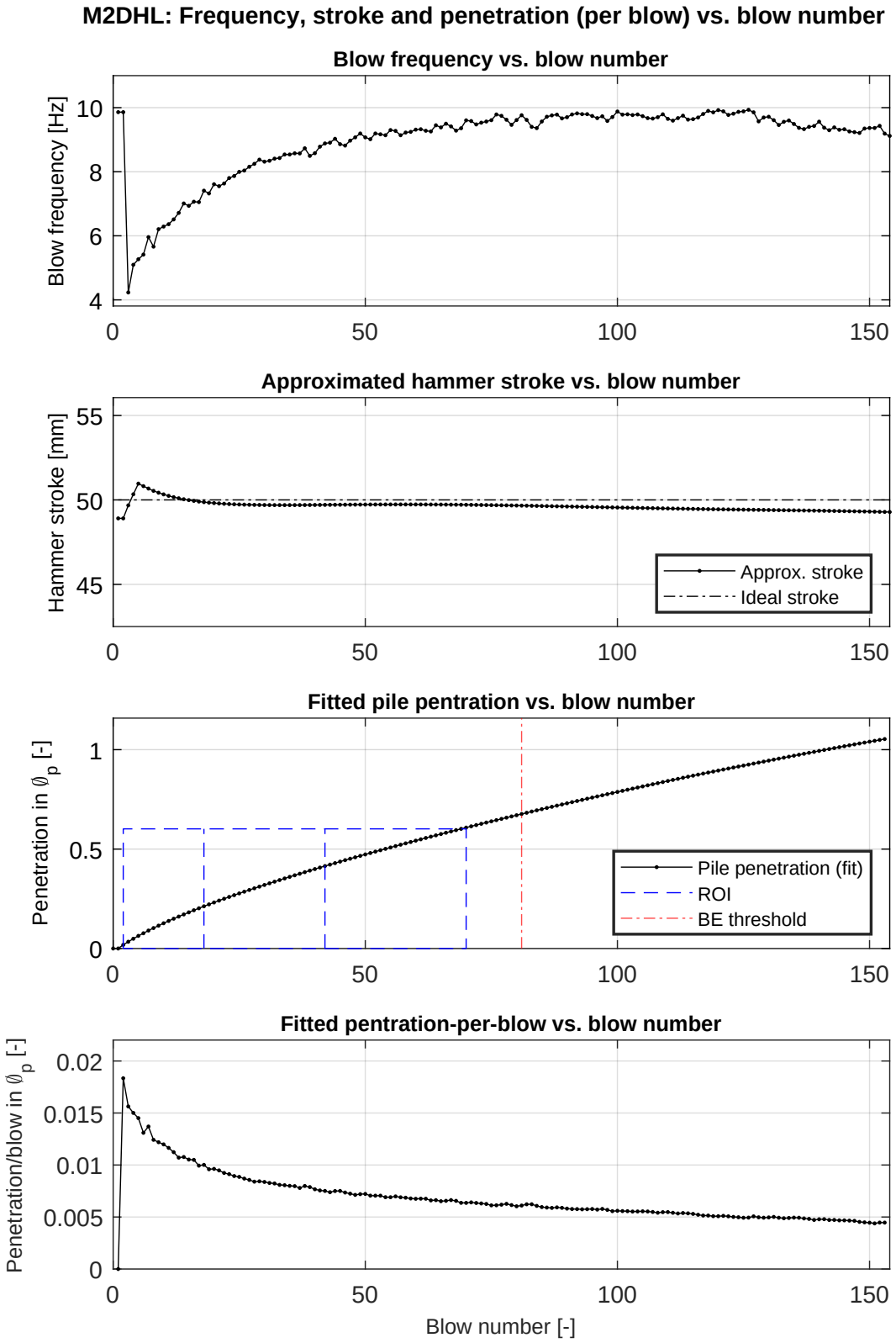

Figure C.53: From top to bottom: (I) blow frequency; (II) effective hammer stroke; (III) cumulative pile penetration, with graphical annotation of the ROI; (IV) pile penetration-per-blow. All are plotted a function of blow number for test M2DHL.

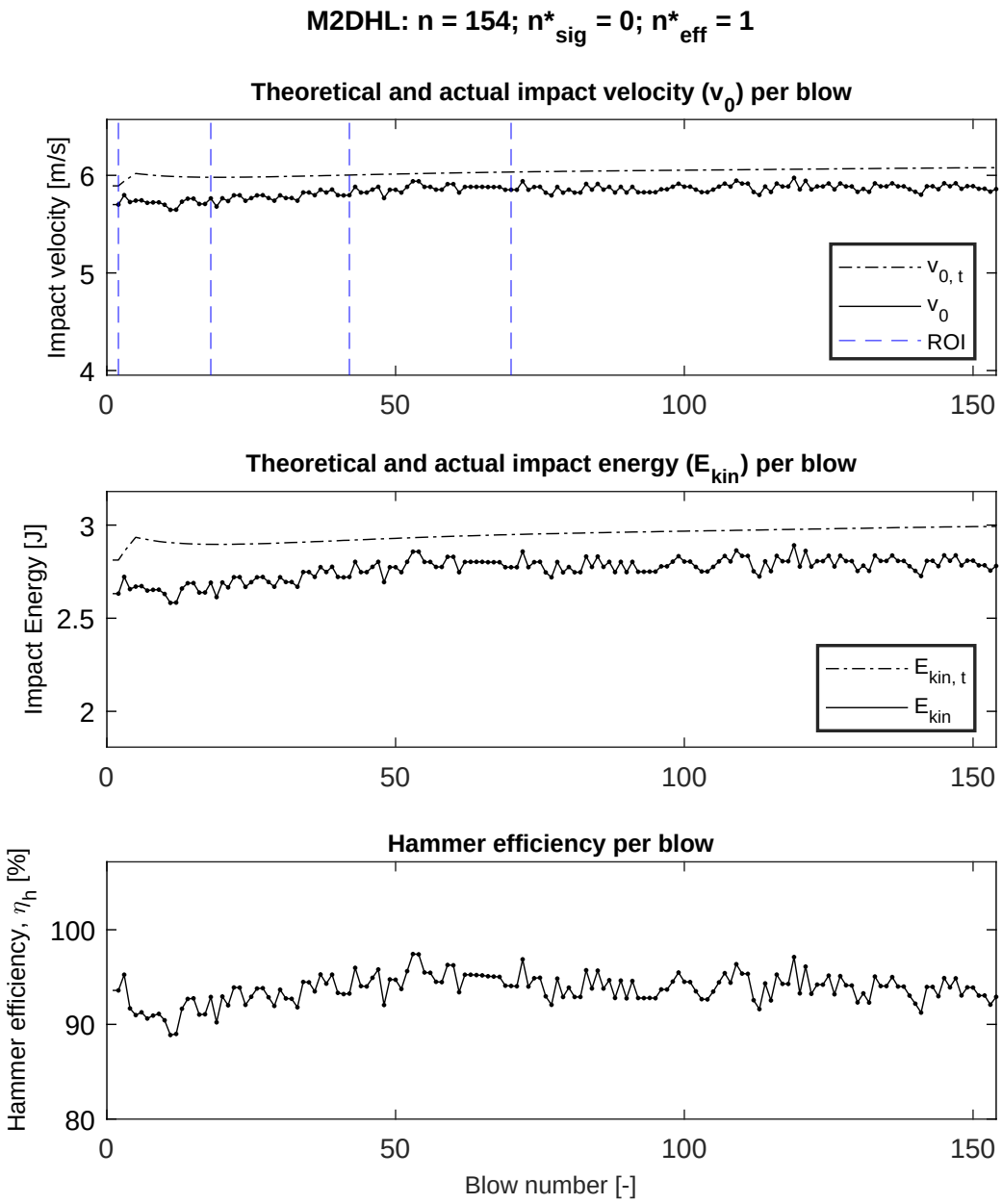

Figure C.54: For test M2DHL, from top to bottom: (I) theoretical and measured impact velocity v_0 versus blow number; (II) Theoretical and calculated impact energy versus blow number; (III) Hammer efficiency η_h versus blows number. Dots indicate blows for which the signal of the LS was approved and the subsequent velocity analysis yielded satisfactory results. Out of the total number of blows n, the number for which the latter was found to be true is indicated as n^*_{sig}. Finally, the number of blows which were disregarded (despite of usable velocity signals) as they yielded an efficiency >100% is denoted by n^*_{eff}.

M2DLH

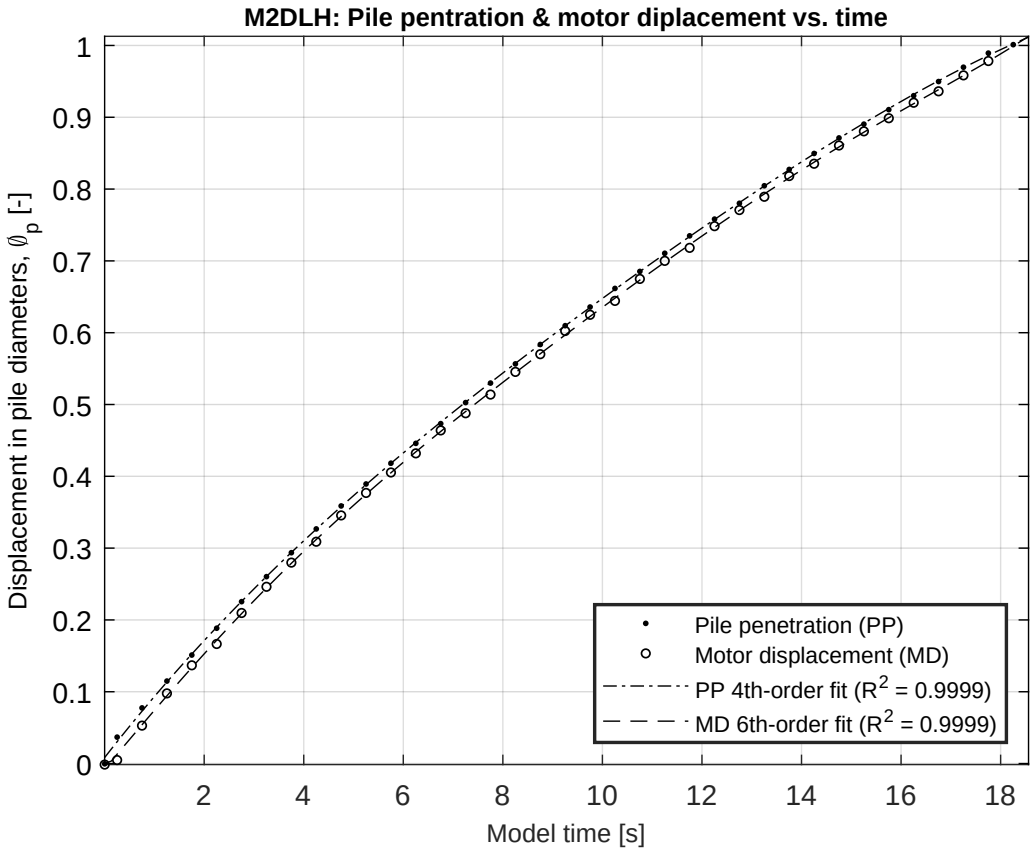

Figure C.55: Measured and approximated normalized (by pile diameter Φ_p) pile penetration (PP) and motor displacement (MD) as a function of model time for M2DLH.

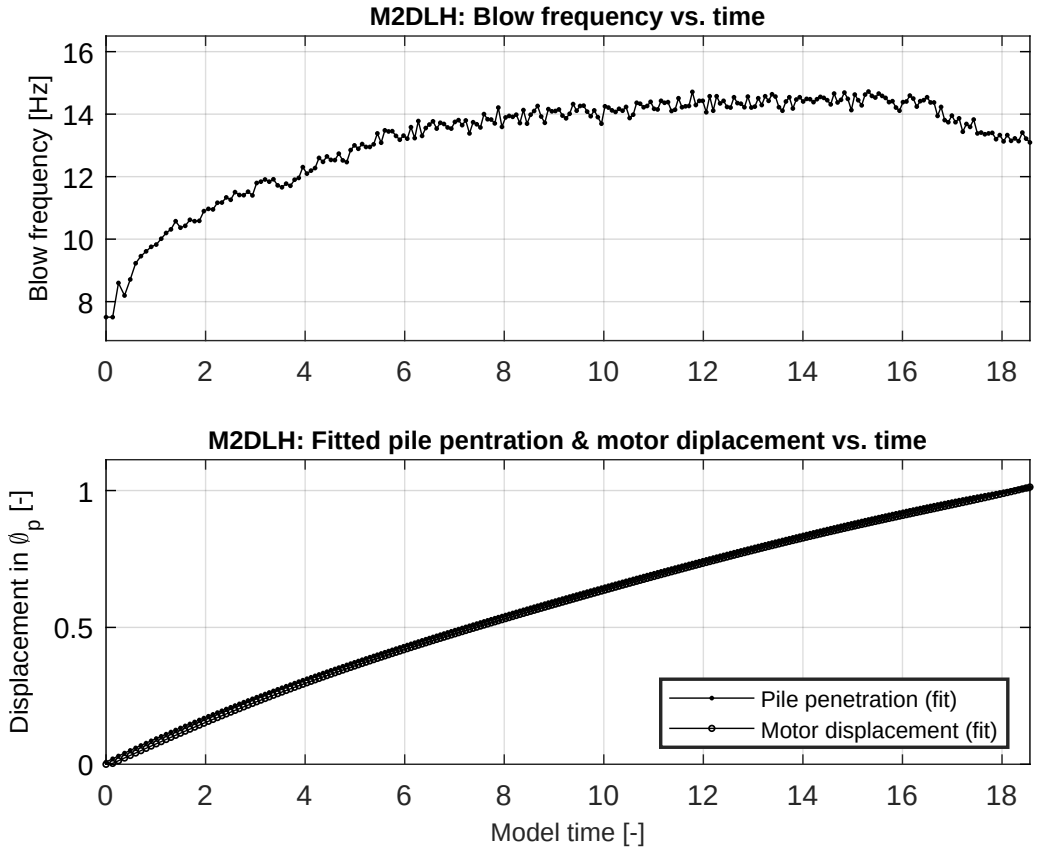

Figure C.56: (TOP) Driving frequency evaluated per blow as a function of model time for test M2DLH. As the frequency in inferred based on time intervals between triggers of the load cell, the frequency for the first blow cannot be determined. Instead, it is equaled to the frequency estimate for the second blow. (BOTTOM) Fitted expressions for PP and MD, evaluated per blow as a function of model time for M2DLH

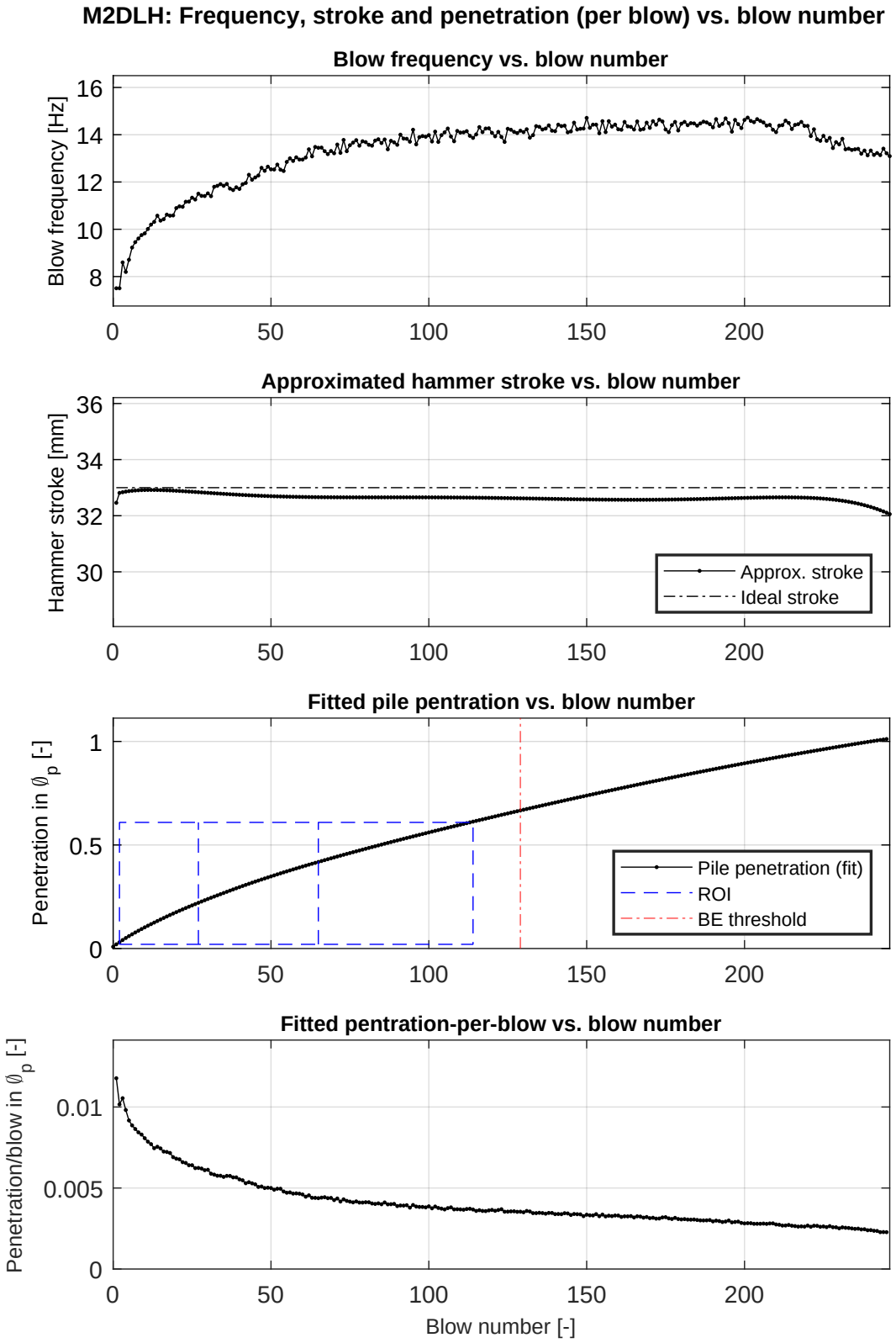

Figure C.57: From top to bottom: (I) blow frequency; (II) effective hammer stroke; (III) cumulative pile penetration, with graphical annotation of the ROI; (IV) pile penetration-per-blow. All are plotted a function of blow number for test M2DLH.

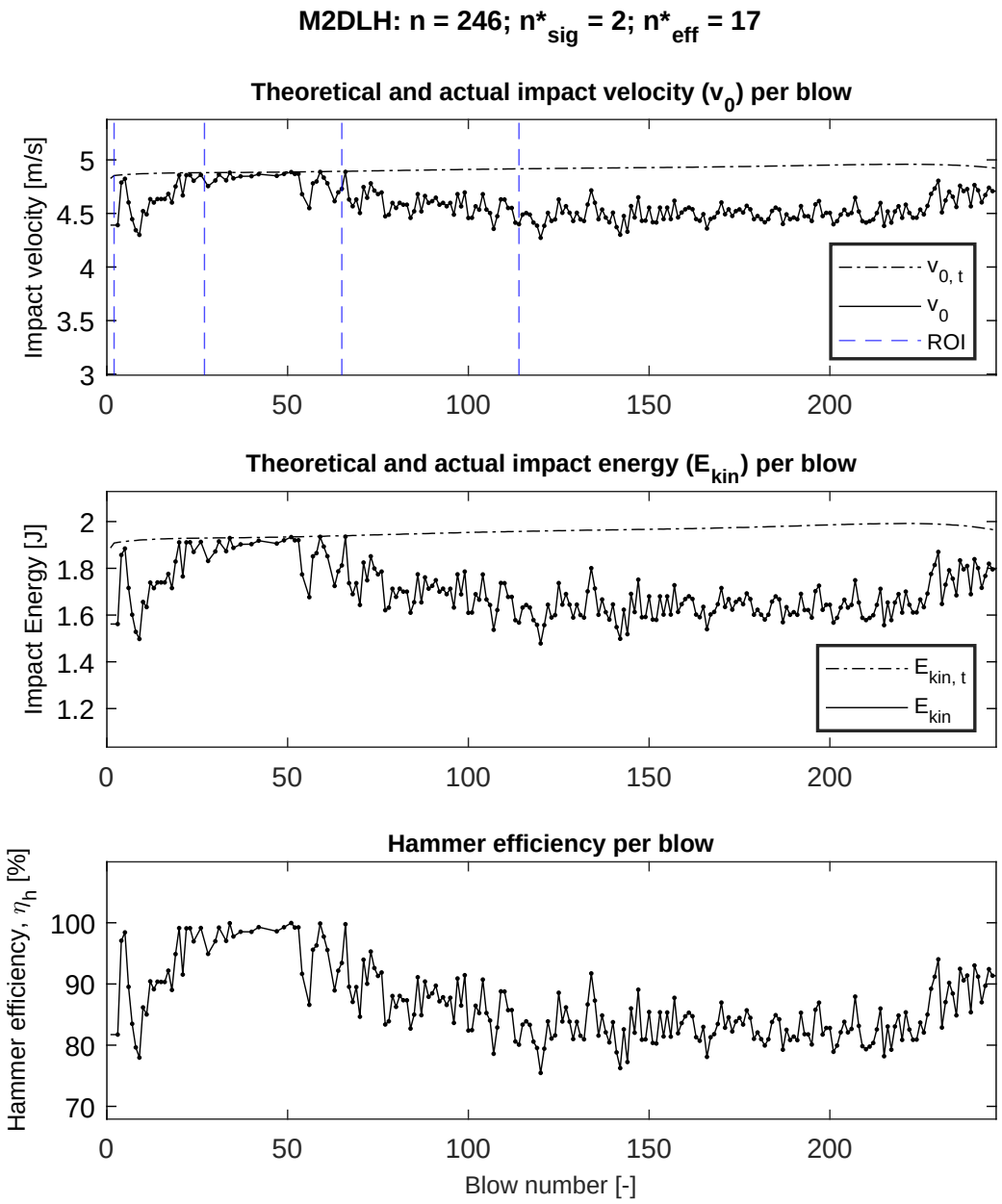

Figure C.58: For test M2DLH, from top to bottom: (I) theoretical and measured impact velocity v_0 versus blow number; (II) Theoretical and calculated impact energy versus blow number; (III) Hammer efficiency η_h versus blows number. Dots indicate blows for which the signal of the LS was approved and the subsequent velocity analysis yielded satisfactory results. Out of the total number of blows n, the number for which the latter was found to be true is indicated as n^*_{sig}. Finally, the number of blows which were disregarded (despite of usable velocity signals) as they yielded an efficiency >100% is denoted by n^*_{eff}.

M2DHH

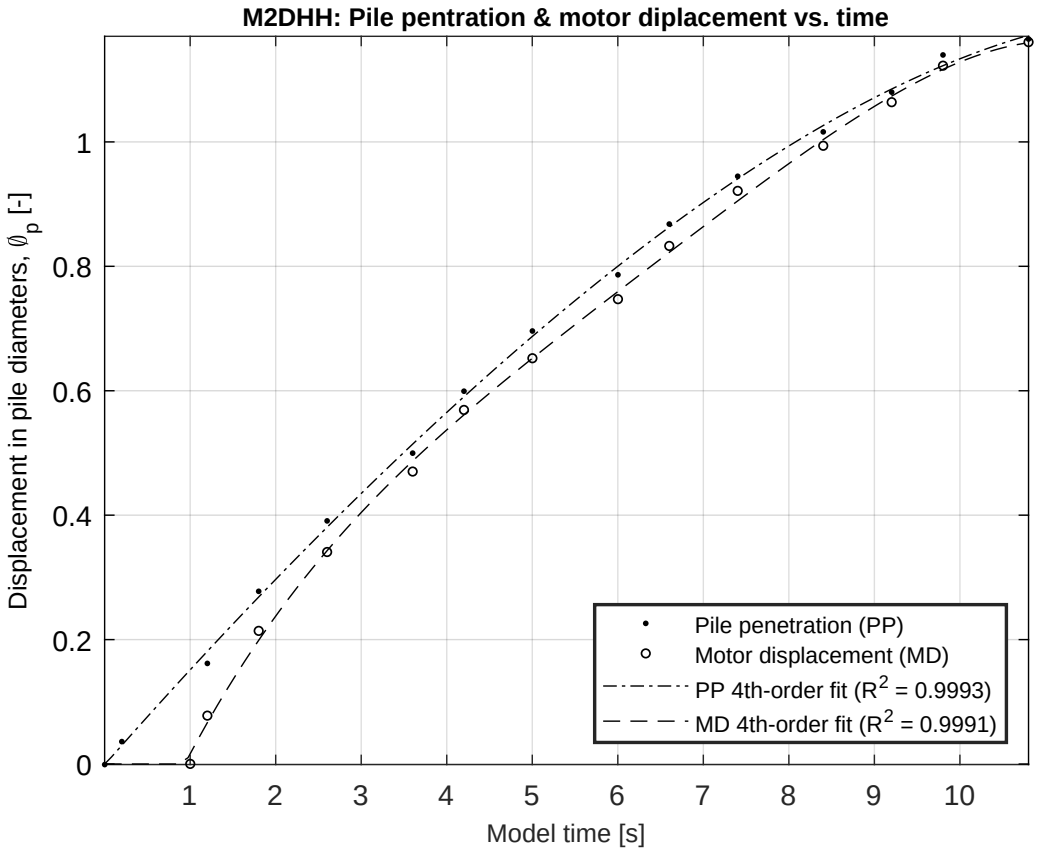

Figure C.59: Measured and approximated normalized (by pile diameter Φ_p) pile penetration (PP) and motor displacement (MD) as a function of model time for M2DHH.

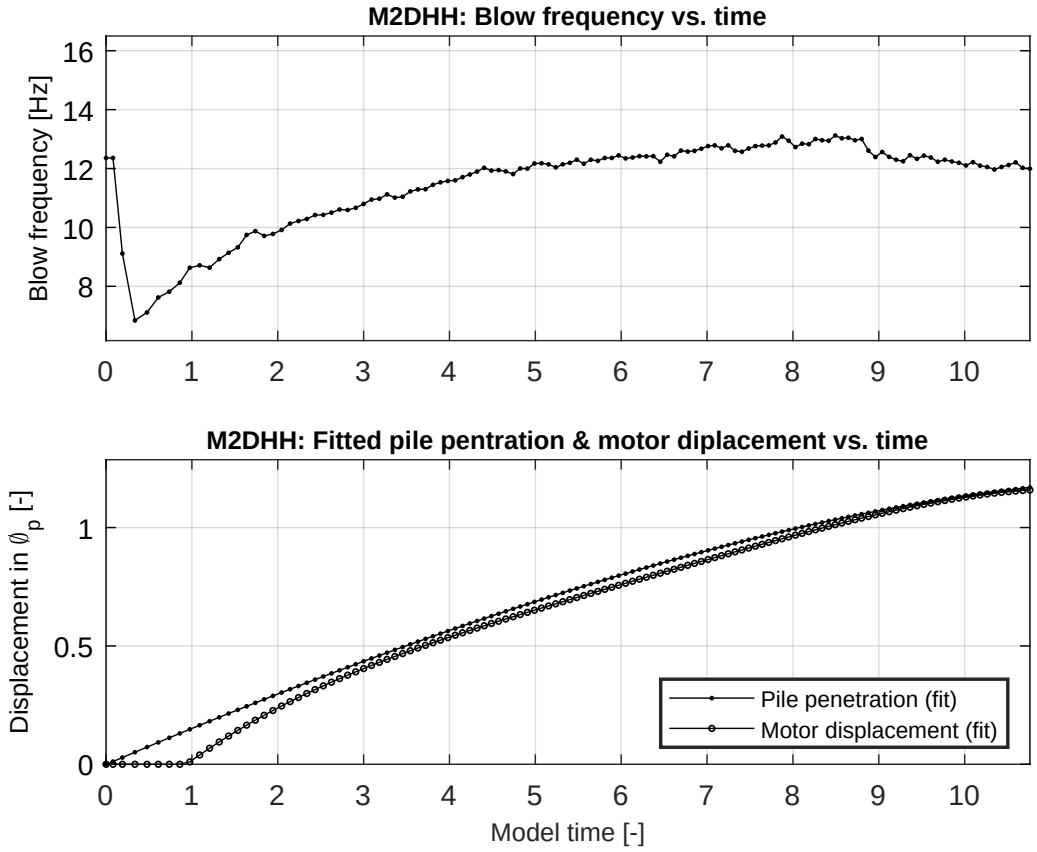

Figure C.60: (TOP) Driving frequency evaluated per blow as a function of model time for test M2DHH. As the frequency in inferred based on time intervals between triggers of the load cell, the frequency for the first blow cannot be determined. Instead, it is equaled to the frequency estimate for the second blow. (BOTTOM) Fitted expressions for PP and MD, evaluated per blow as a function of model time for M2DHH

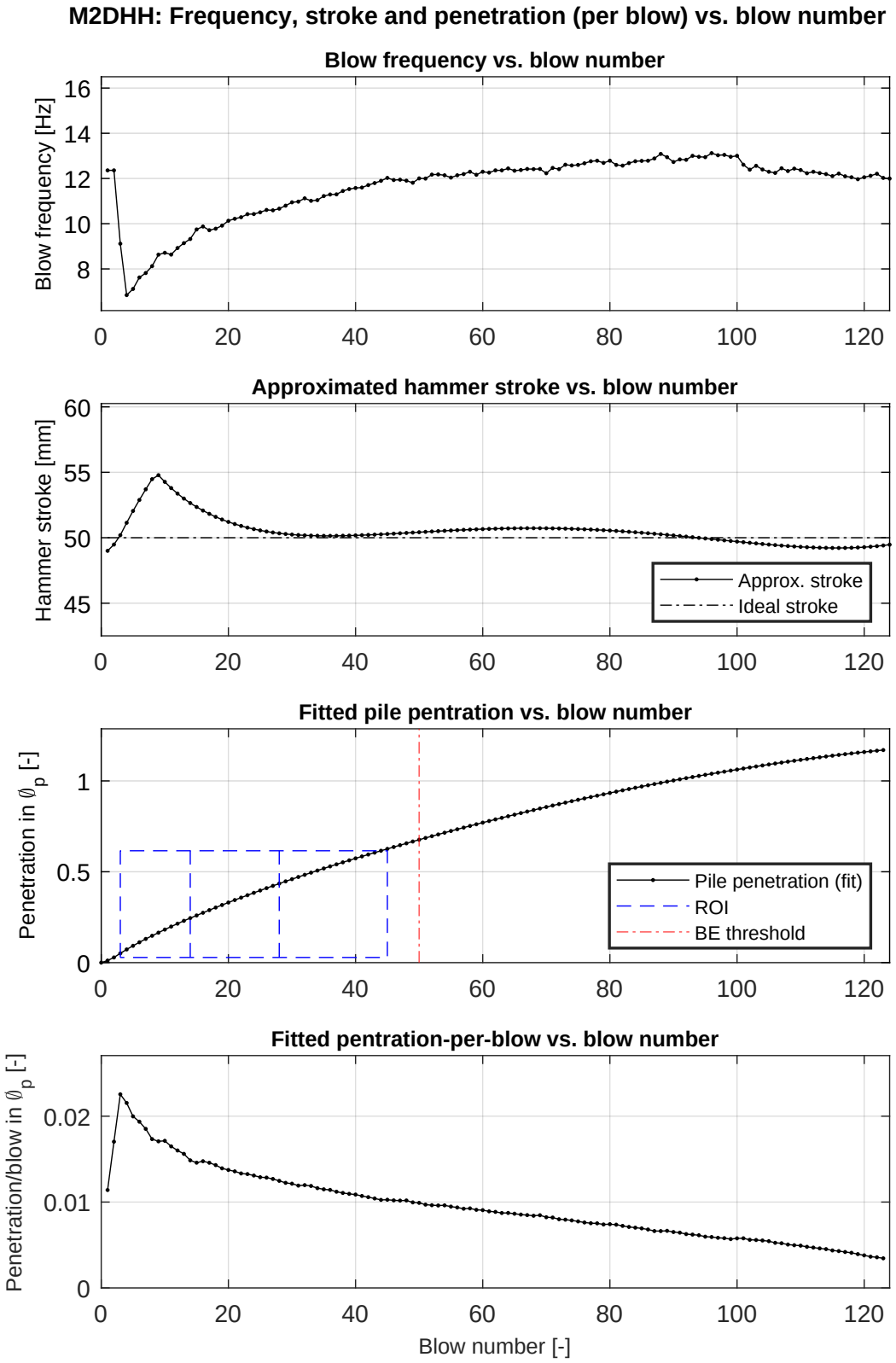

Figure C.61: From top to bottom: (I) blow frequency; (II) effective hammer stroke; (III) cumulative pile penetration, with graphical annotation of the ROI; (IV) pile penetration-per-blow. All are plotted a function of blow number for test M2DHH.

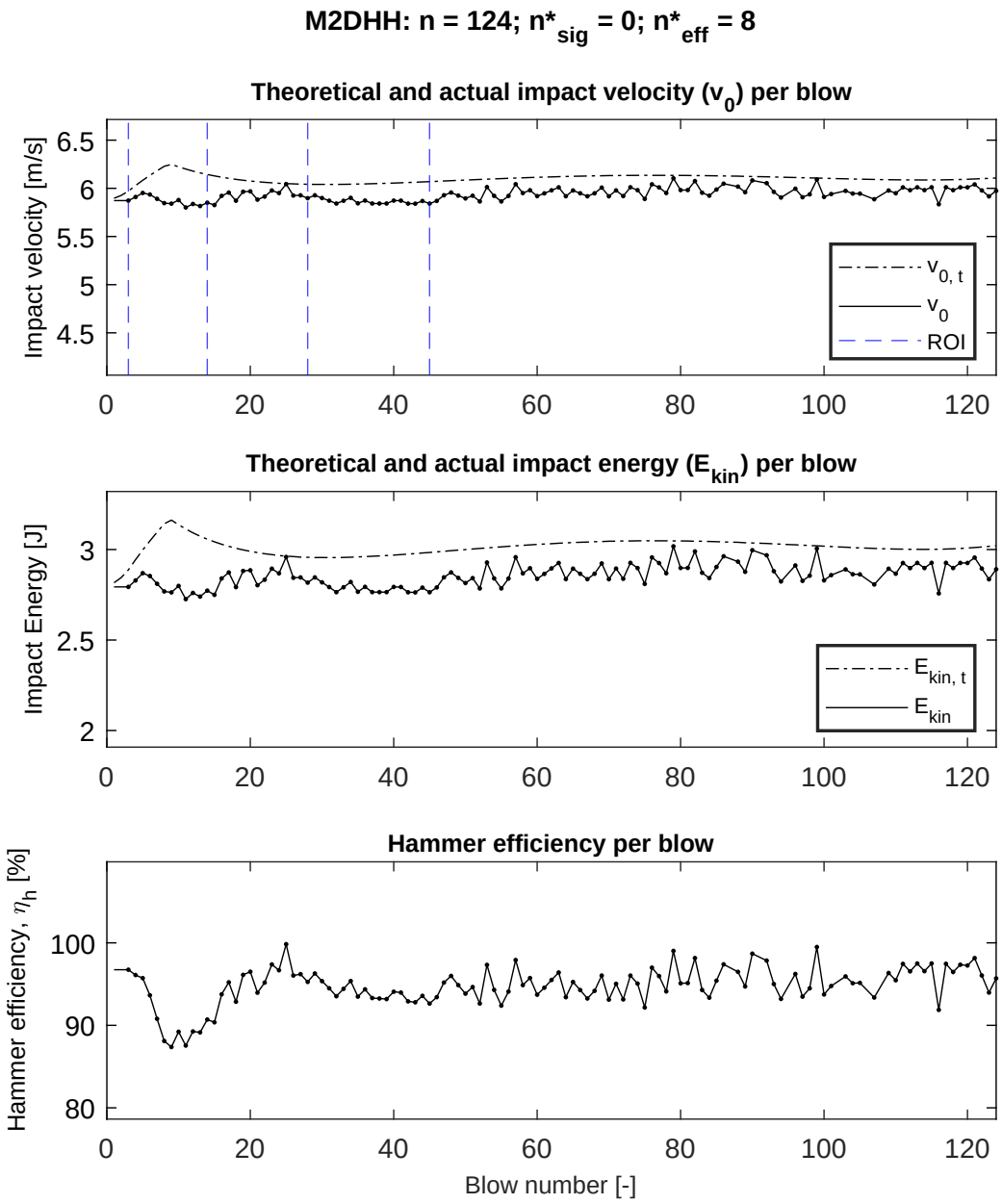

Figure C.62: For test M2DHH, from top to bottom: (I) theoretical and measured impact velocity v_0 versus blow number; (II) Theoretical and calculated impact energy versus blow number; (III) Hammer efficiency η_h versus blows number. Dots indicate blows for which the signal of the LS was approved and the subsequent velocity analysis yielded satisfactory results. Out of the total number of blows n, the number for which the latter was found to be true is indicated as n^*_{sig}. Finally, the number of blows which were disregarded (despite of usable velocity signals) as they yielded an efficiency >100% is denoted by n^*_{eff}.

M3DLL

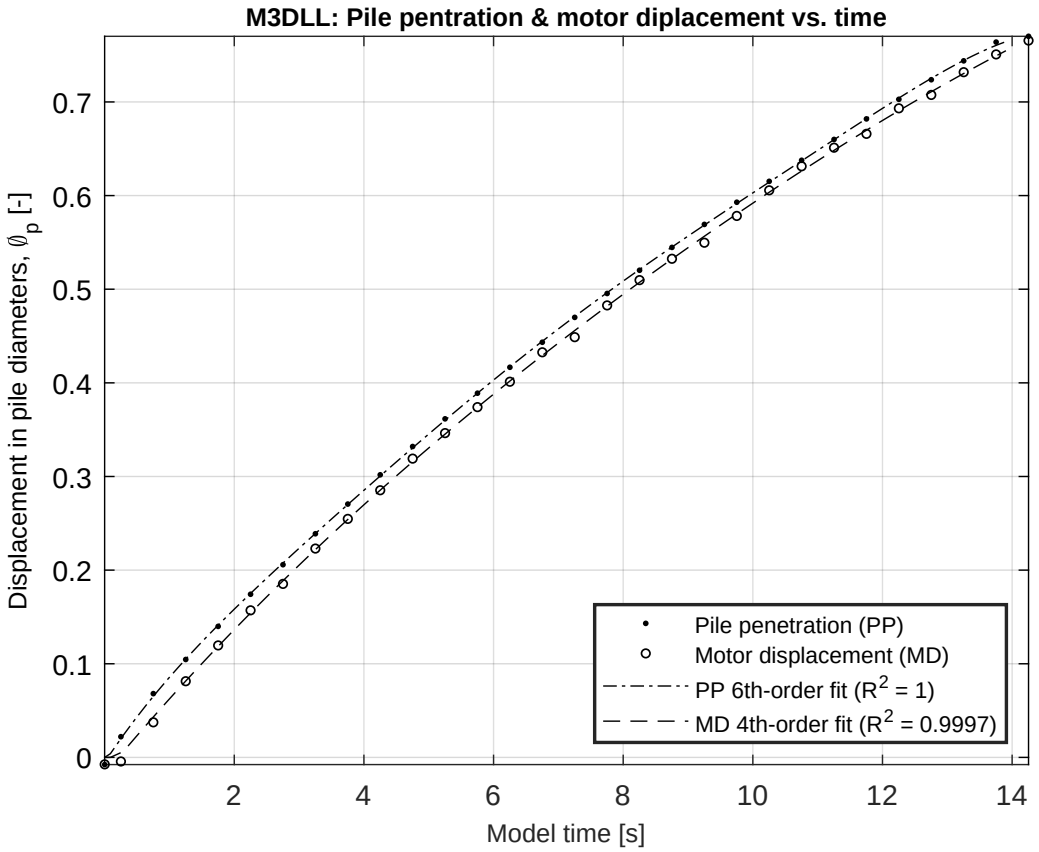

Figure C.63: Measured and approximated normalized (by pile diameter Φ_p) pile penetration (PP) and motor displacement (MD) as a function of model time for M3DLL.

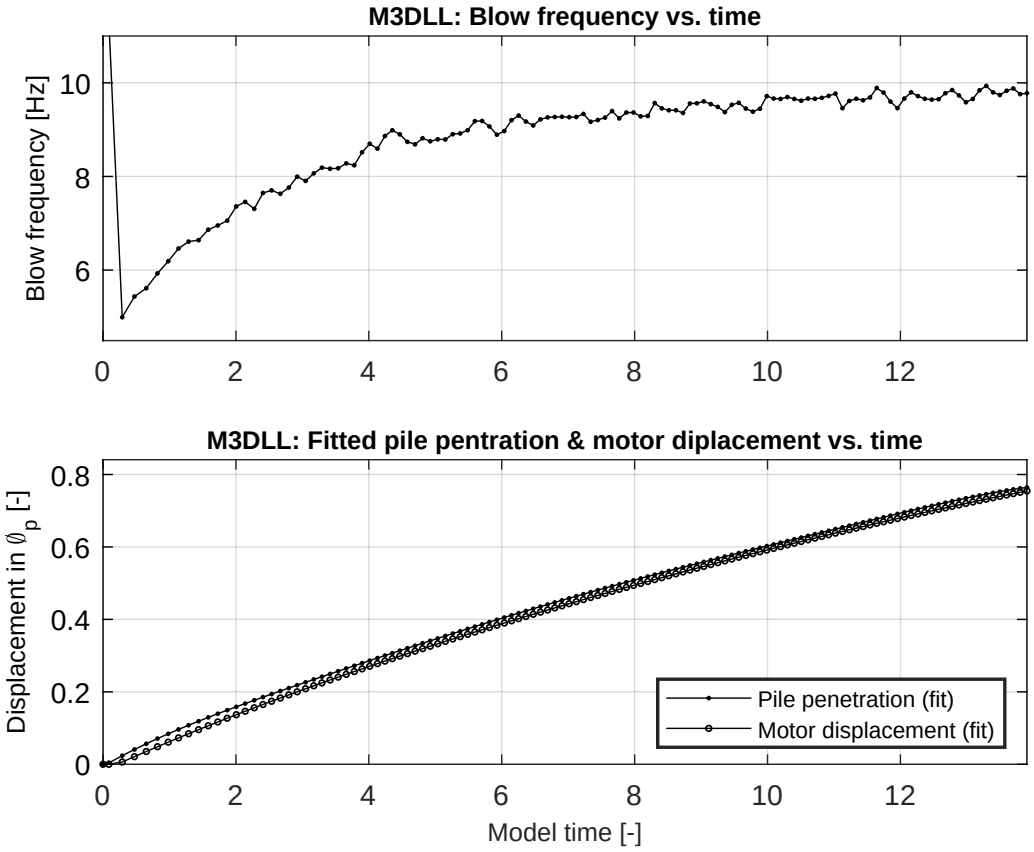

Figure C.64: (TOP) Driving frequency evaluated per blow as a function of model time for test M3DLL. As the frequency in inferred based on time intervals between triggers of the load cell, the frequency for the first blow cannot be determined. Instead, it is equaled to the frequency estimate for the second blow. (BOTTOM) Fitted expressions for PP and MD, evaluated per blow as a function of model time for M3DLL

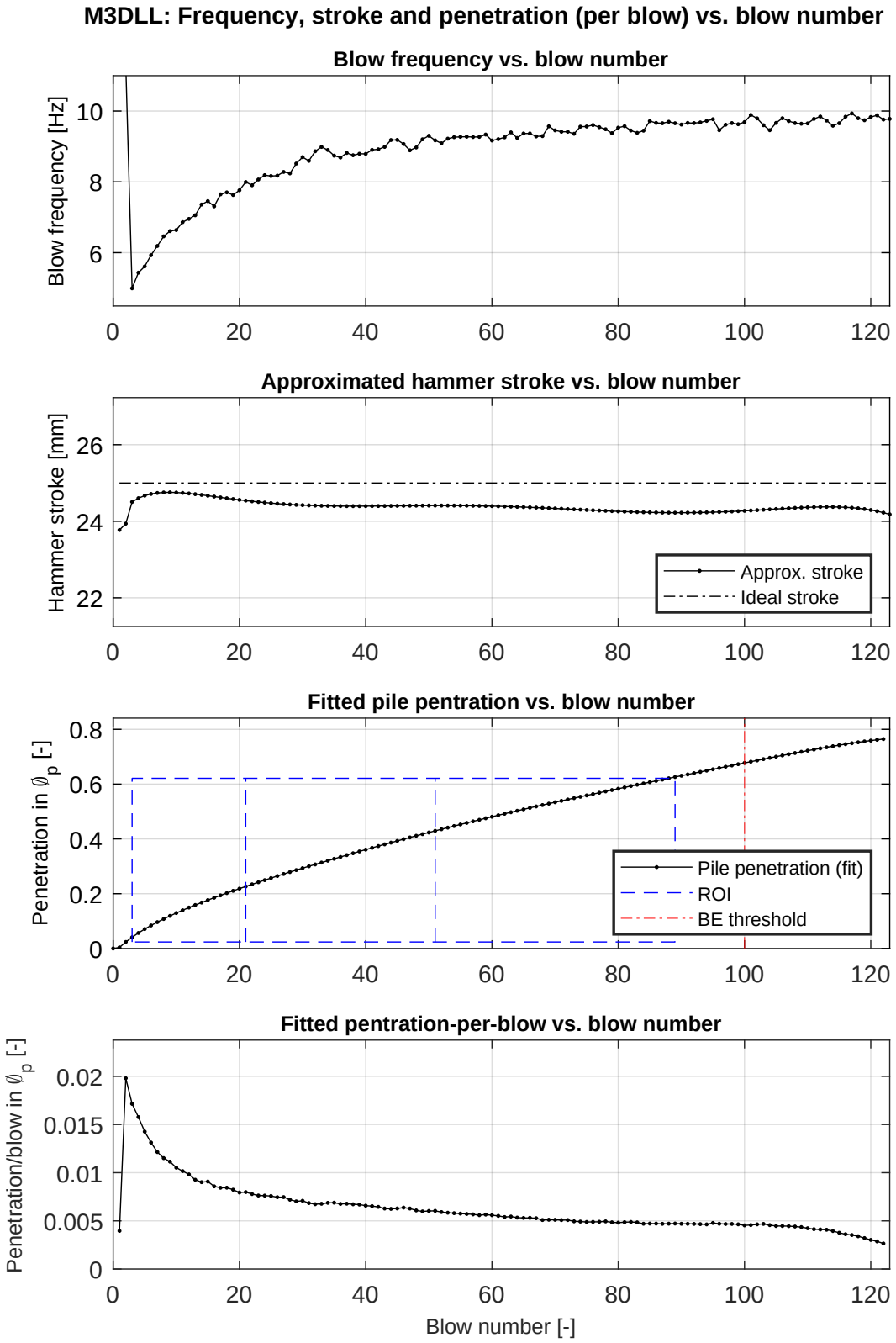

Figure C.65: From top to bottom: (I) blow frequency; (II) effective hammer stroke; (III) cumulative pile penetration, with graphical annotation of the ROI; (IV) pile penetration-per-blow. All are plotted a function of blow number for test M3DLL.

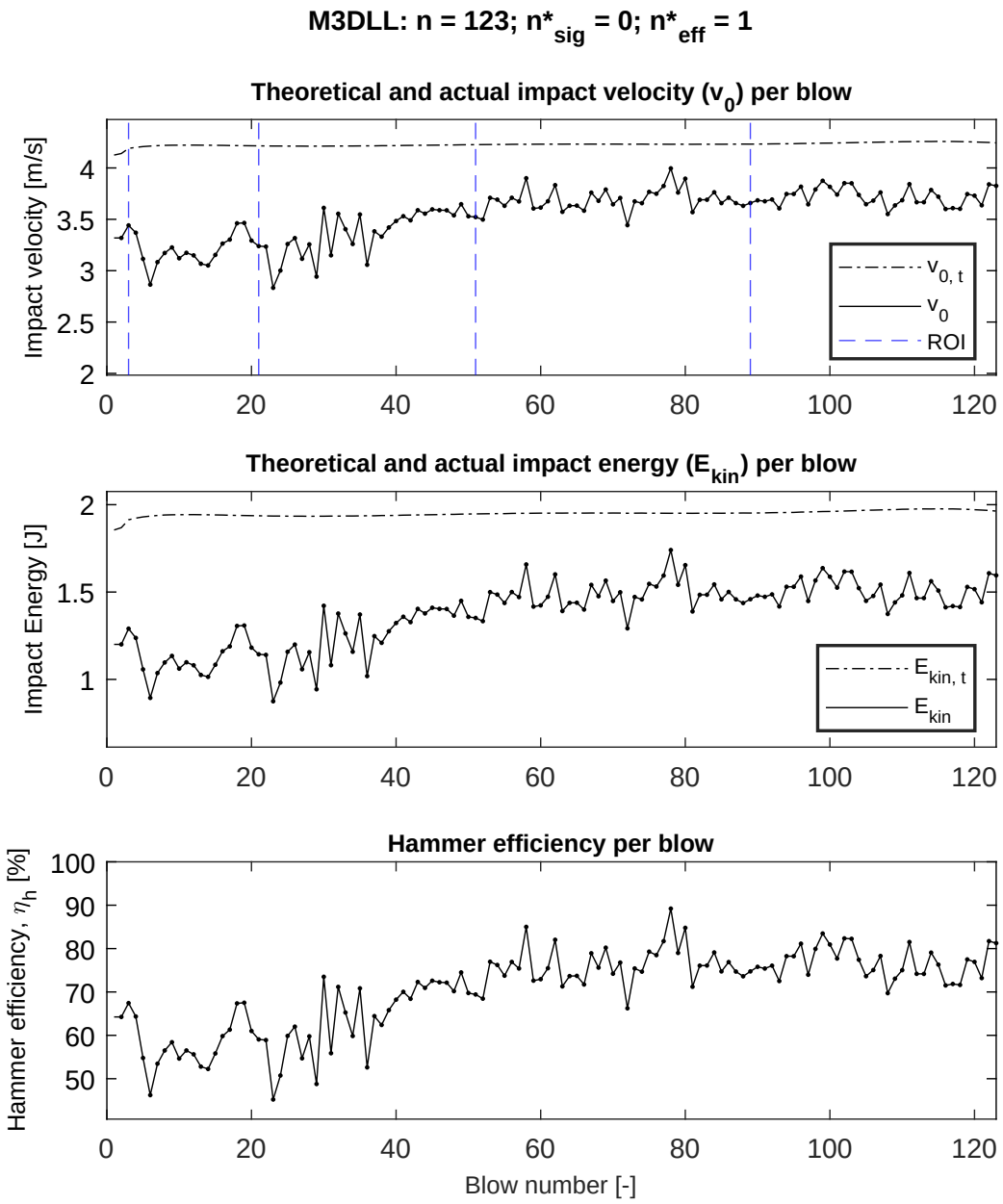

Figure C.66: For test M3DLL, from top to bottom: (I) theoretical and measured impact velocity v_0 versus blow number; (II) Theoretical and calculated impact energy versus blow number; (III) Hammer efficiency η_h versus blows number. Dots indicate blows for which the signal of the LS was approved and the subsequent velocity analysis yielded satisfactory results. Out of the total number of blows n, the number for which the latter was found to be true is indicated as n^*_{sig}. Finally, the number of blows which were disregarded (despite of usable velocity signals) as they yielded an efficiency >100% is denoted by n^*_{eff}.

M3DLH

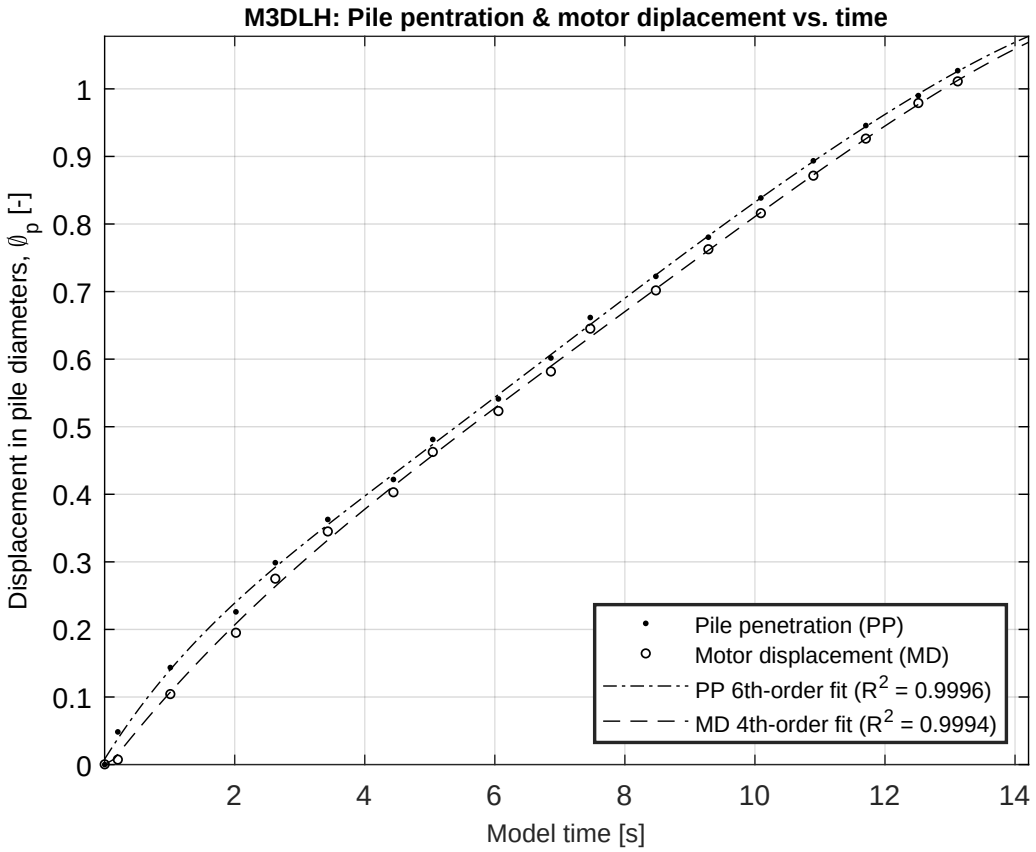

Figure C.67: Measured and approximated normalized (by pile diameter Φ_p) pile penetration (PP) and motor displacement (MD) as a function of model time for M3DLH.

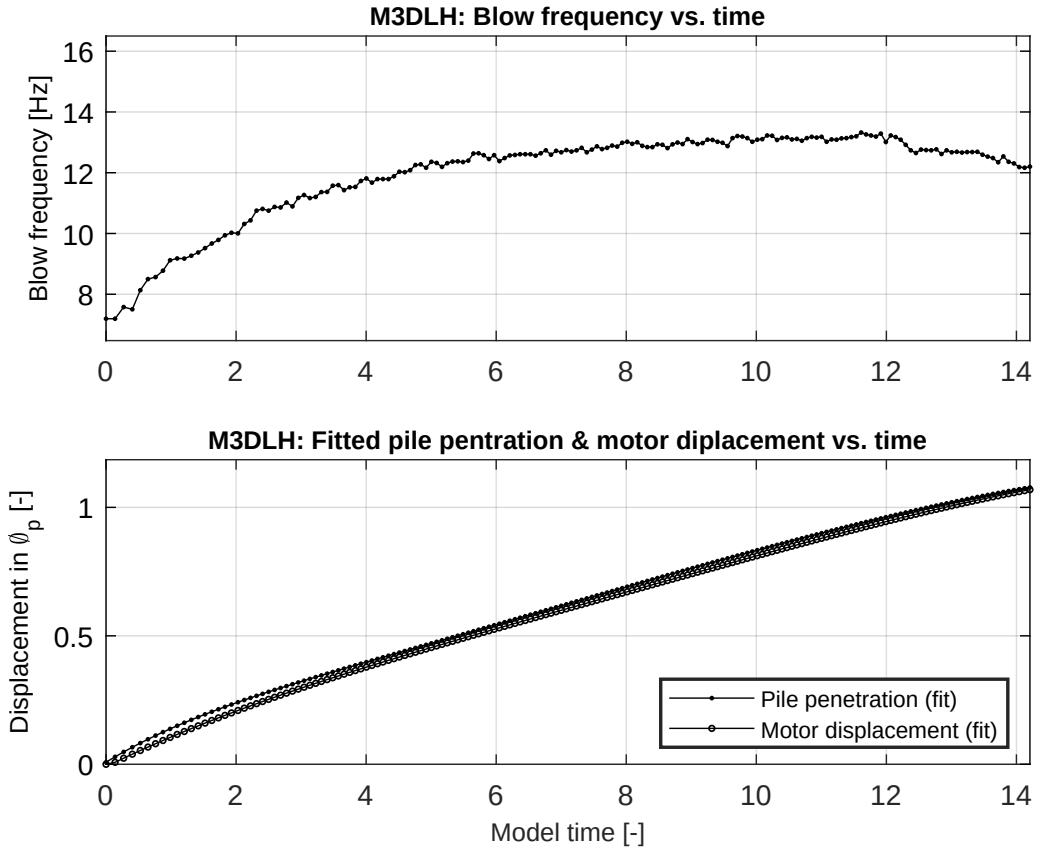

Figure C.68: (TOP) Driving frequency evaluated per blow as a function of model time for test M3DLH. As the frequency in inferred based on time intervals between triggers of the load cell, the frequency for the first blow cannot be determined. Instead, it is equaled to the frequency estimate for the second blow. (BOTTOM) Fitted expressions for PP and MD, evaluated per blow as a function of model time for M3DLH

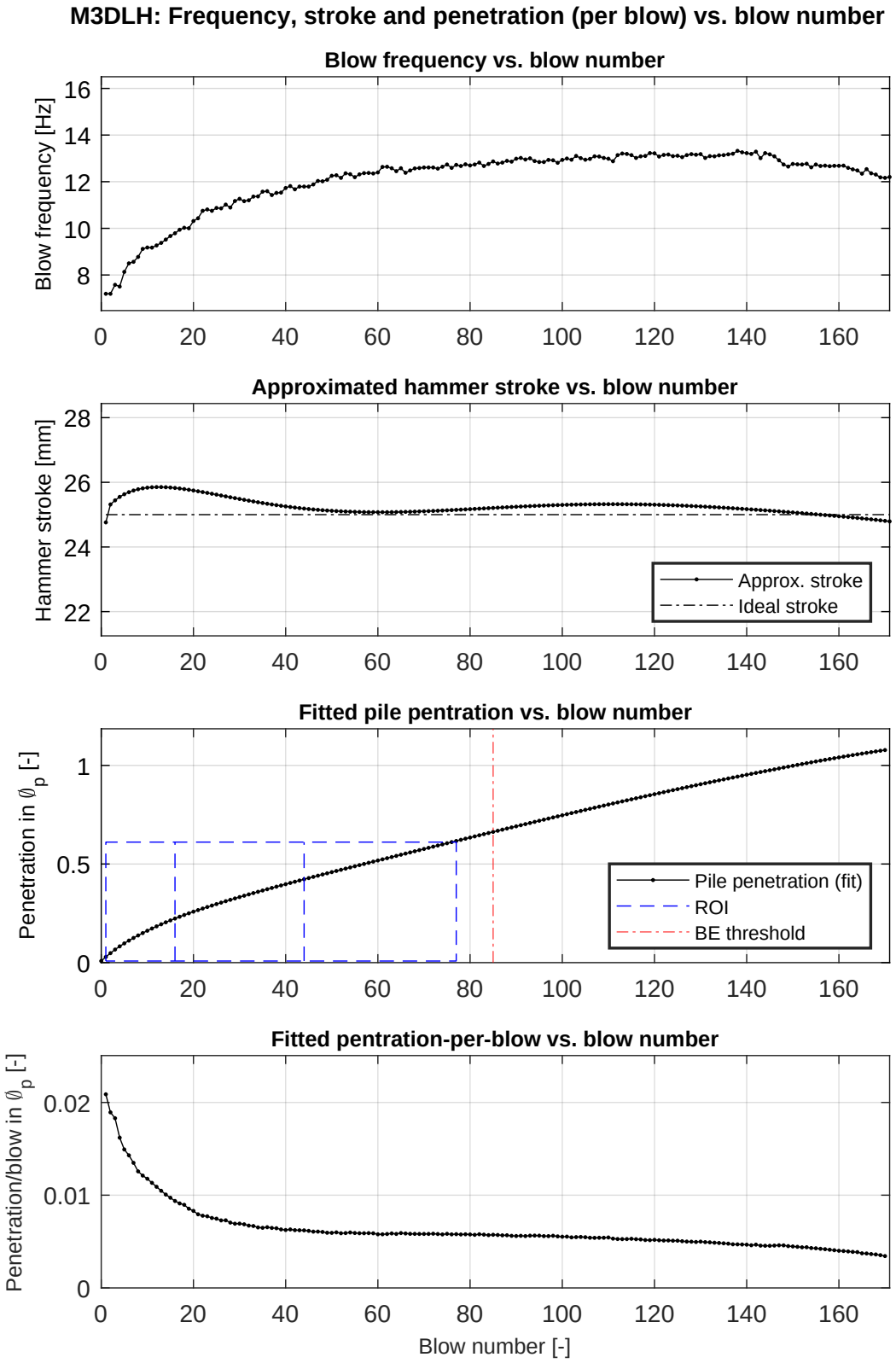

Figure C.69: From top to bottom: (I) blow frequency; (II) effective hammer stroke; (III) cumulative pile penetration, with graphical annotation of the ROI; (IV) pile penetration-per-blow. All are plotted a function of blow number for test M3DLH.

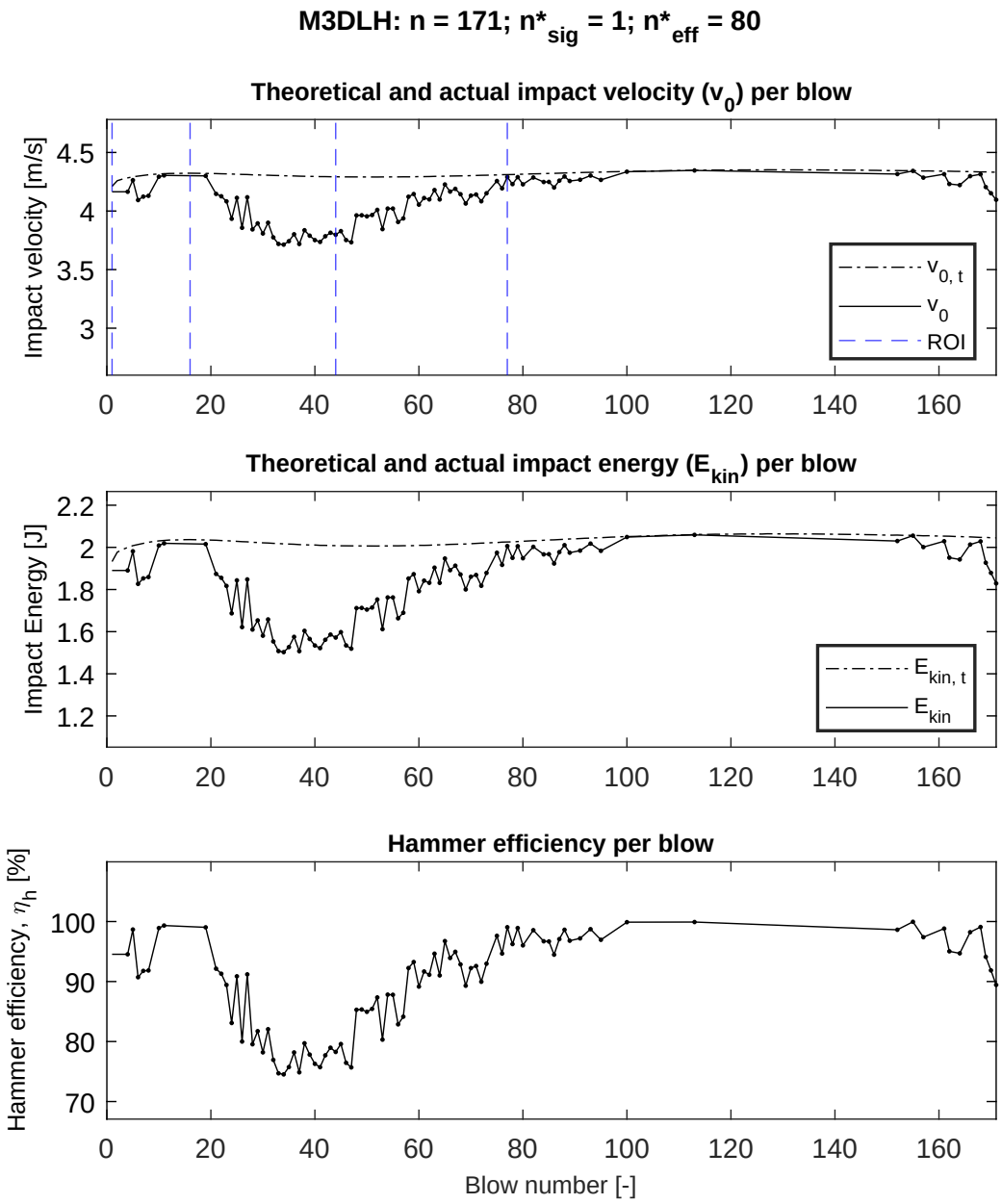

Figure C.70: For test M3DLH, from top to bottom: (I) theoretical and measured impact velocity v_0 versus blow number; (II) Theoretical and calculated impact energy versus blow number; (III) Hammer efficiency η_h versus blows number. Dots indicate blows for which the signal of the LS was approved and the subsequent velocity analysis yielded satisfactory results. Out of the total number of blows n, the number for which the latter was found to be true is indicated as n^*_{sig}. Finally, the number of blows which were disregarded (despite of usable velocity signals) as they yielded an efficiency >100% is denoted by n^*_{eff}.

M3DHL

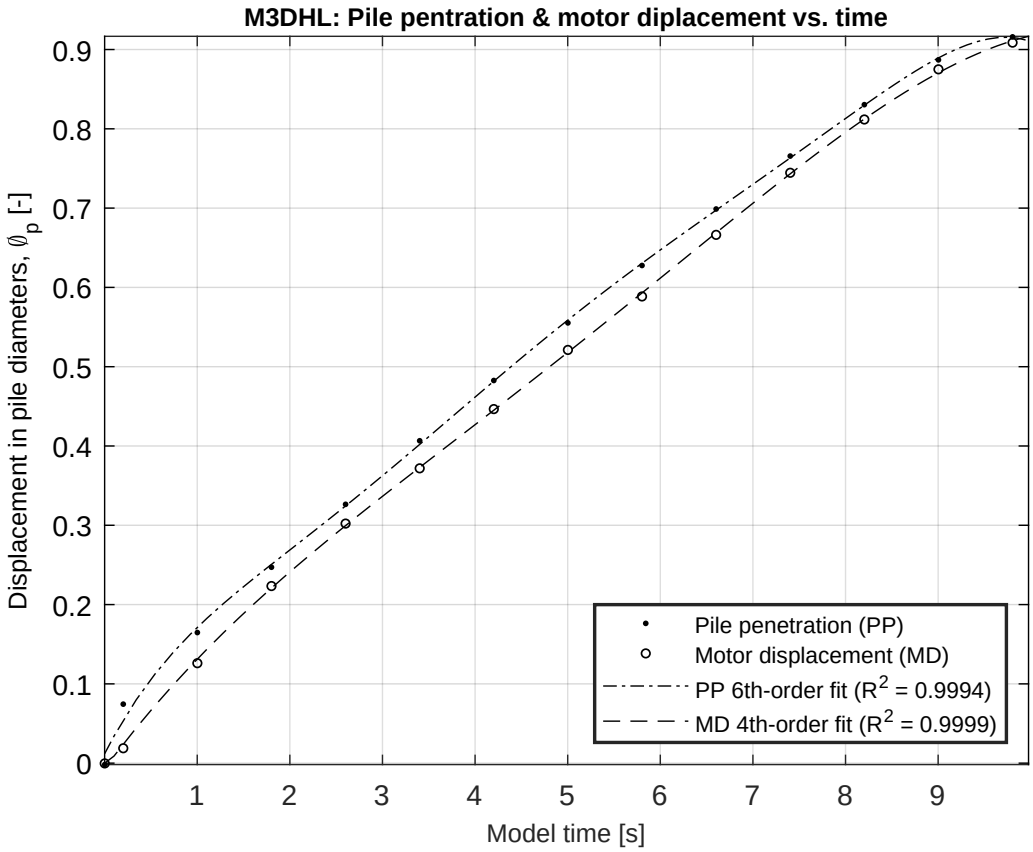

Figure C.71: Measured and approximated normalized (by pile diameter Φ_p) pile penetration (PP) and motor displacement (MD) as a function of model time for M3DHL.

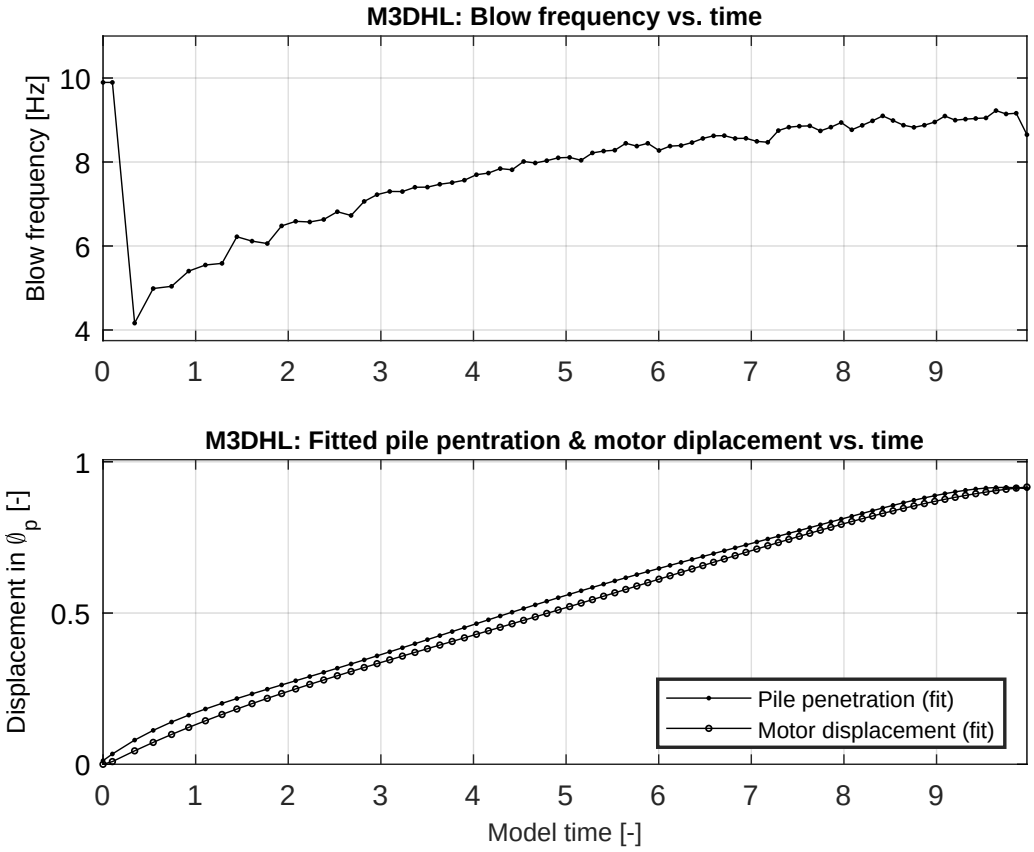

Figure C.72: (TOP) Driving frequency evaluated per blow as a function of model time for test M3DHL. As the frequency in inferred based on time intervals between triggers of the load cell, the frequency for the first blow cannot be determined. Instead, it is equaled to the frequency estimate for the second blow. (BOTTOM) Fitted expressions for PP and MD, evaluated per blow as a function of model time for M3DHL

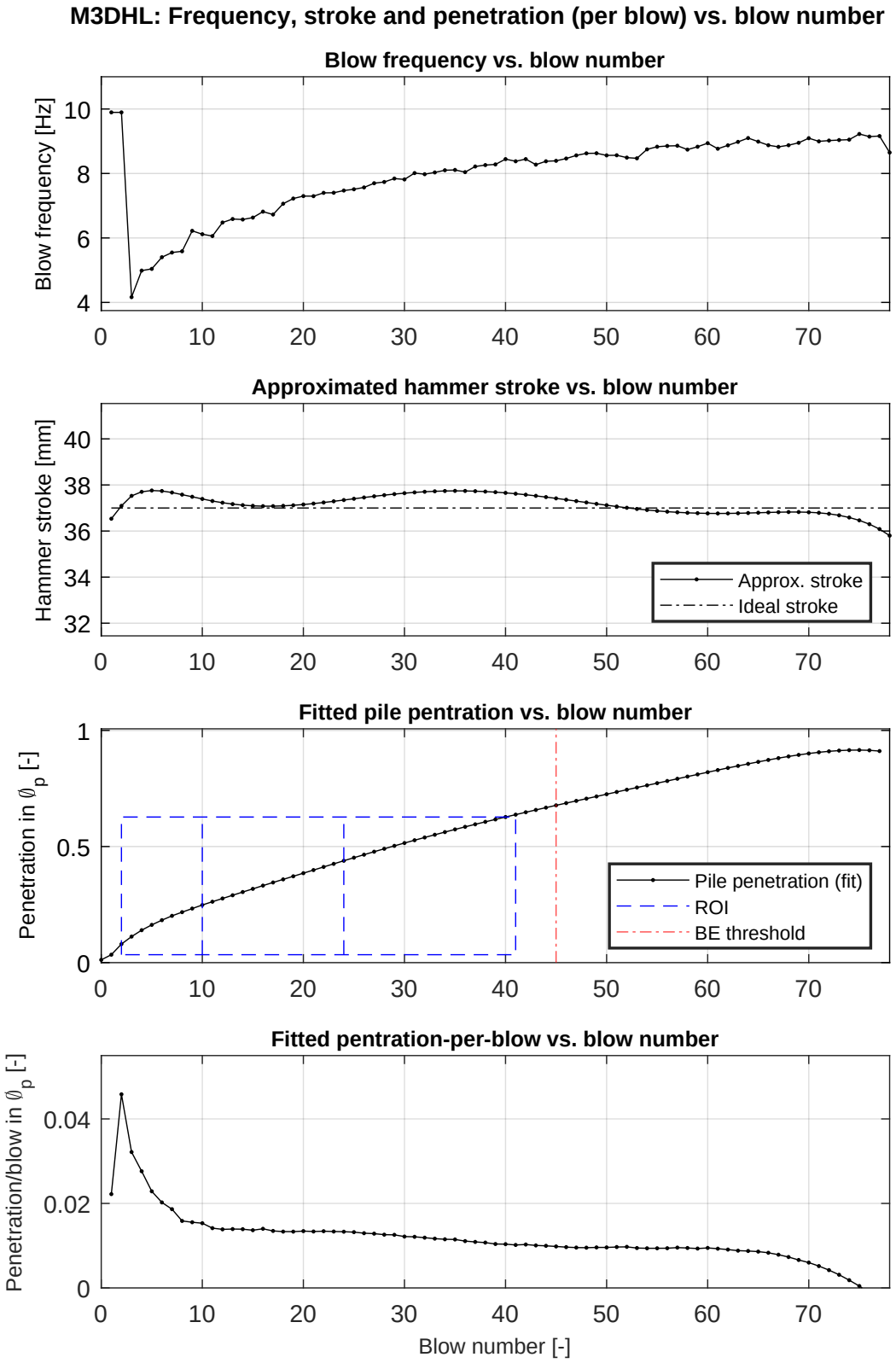

Figure C.73: From top to bottom: (I) blow frequency; (II) effective hammer stroke; (III) cumulative pile penetration, with graphical annotation of the ROI; (IV) pile penetration-per-blow. All are plotted a function of blow number for test M3DHL.

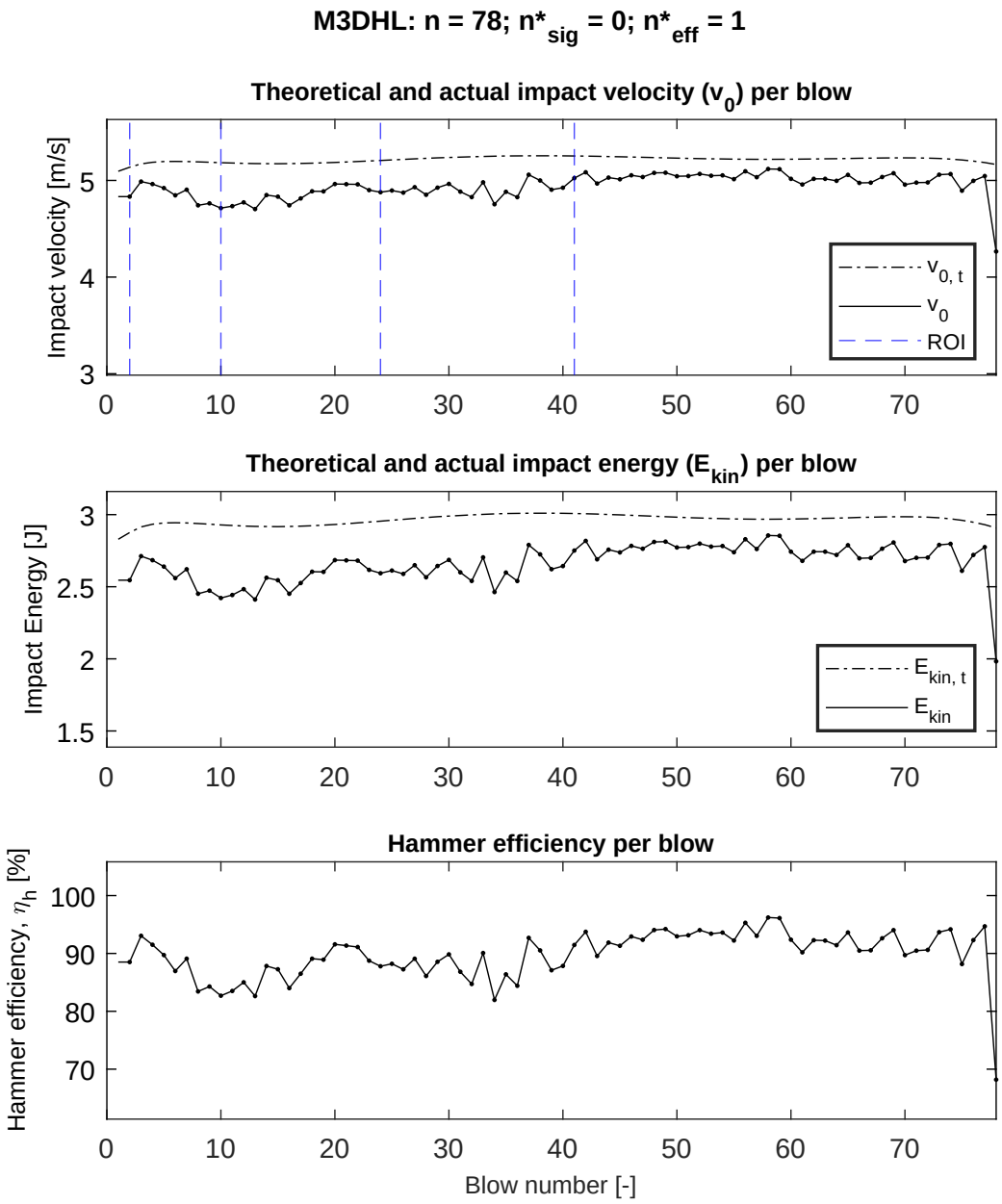

Figure C.74: For test M3DHL, from top to bottom: (I) theoretical and measured impact velocity v_0 versus blow number; (II) Theoretical and calculated impact energy versus blow number; (III) Hammer efficiency η_h versus blows number. Dots indicate blows for which the signal of the LS was approved and the subsequent velocity analysis yielded satisfactory results. Out of the total number of blows n, the number for which the latter was found to be true is indicated as n^*_{sig}. Finally, the number of blows which were disregarded (despite of usable velocity signals) as they yielded an efficiency >100% is denoted by n^*_{eff}.

M3DHH

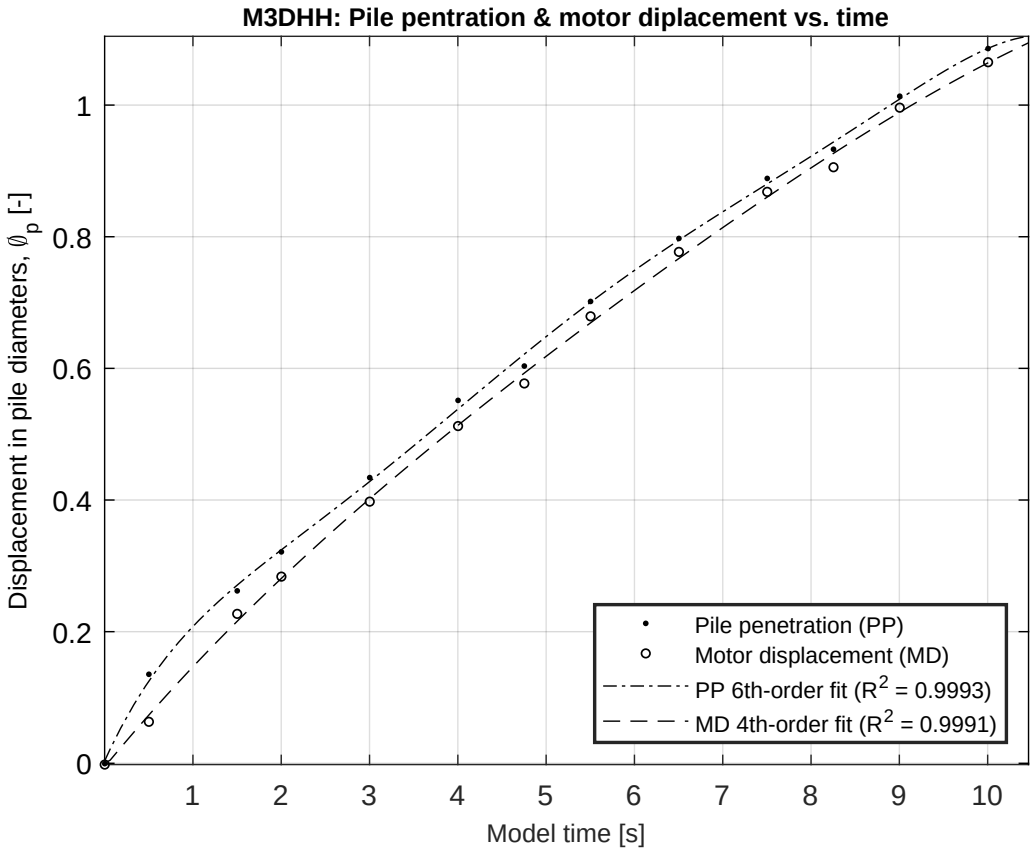

Figure C.75: Measured and approximated normalized (by pile diameter Φ_p) pile penetration (PP) and motor displacement (MD) as a function of model time for M3DHH.

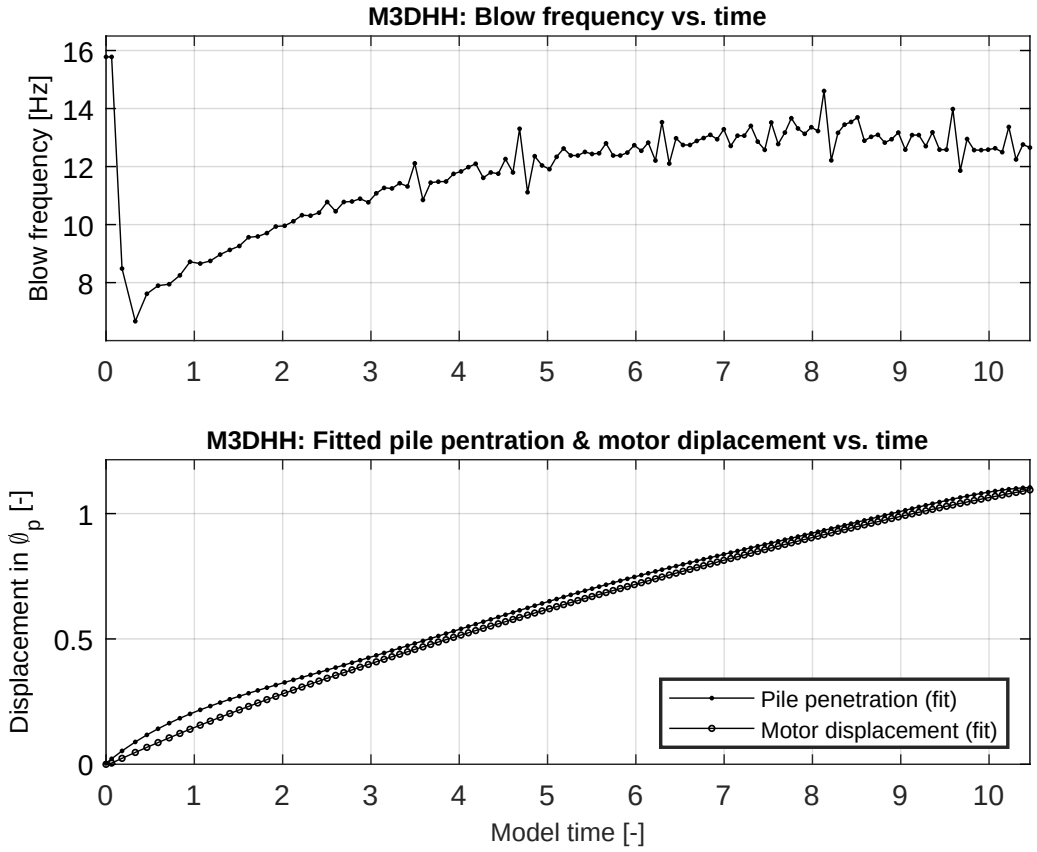

Figure C.76: (TOP) Driving frequency evaluated per blow as a function of model time for test M3DHH. As the frequency in inferred based on time intervals between triggers of the load cell, the frequency for the first blow cannot be determined. Instead, it is equaled to the frequency estimate for the second blow. (BOTTOM) Fitted expressions for PP and MD, evaluated per blow as a function of model time for M3DHH

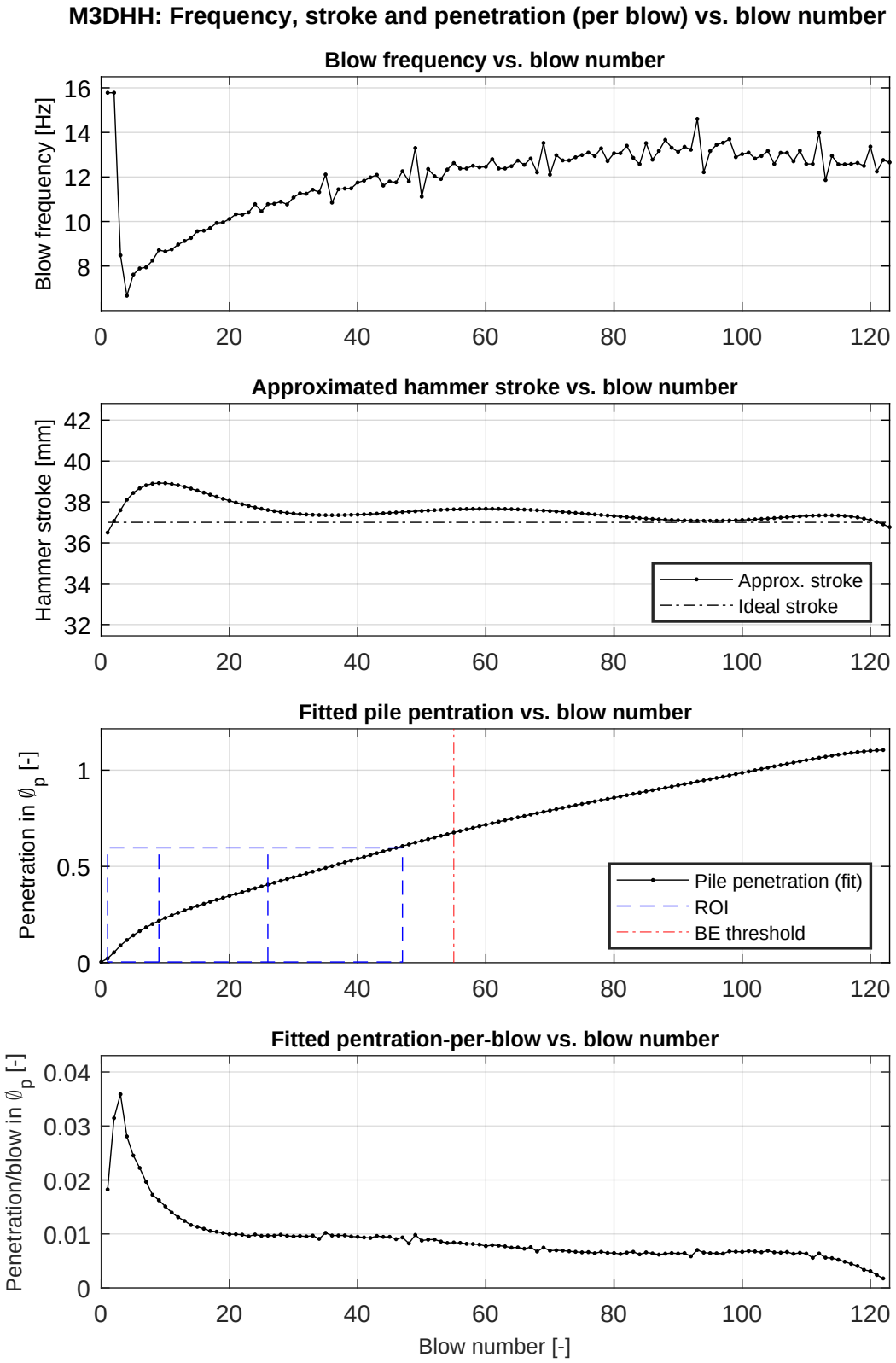

Figure C.77: From top to bottom: (I) blow frequency; (II) effective hammer stroke; (III) cumulative pile penetration, with graphical annotation of the ROI; (IV) pile penetration-per-blow. All are plotted a function of blow number for test M3DHH.

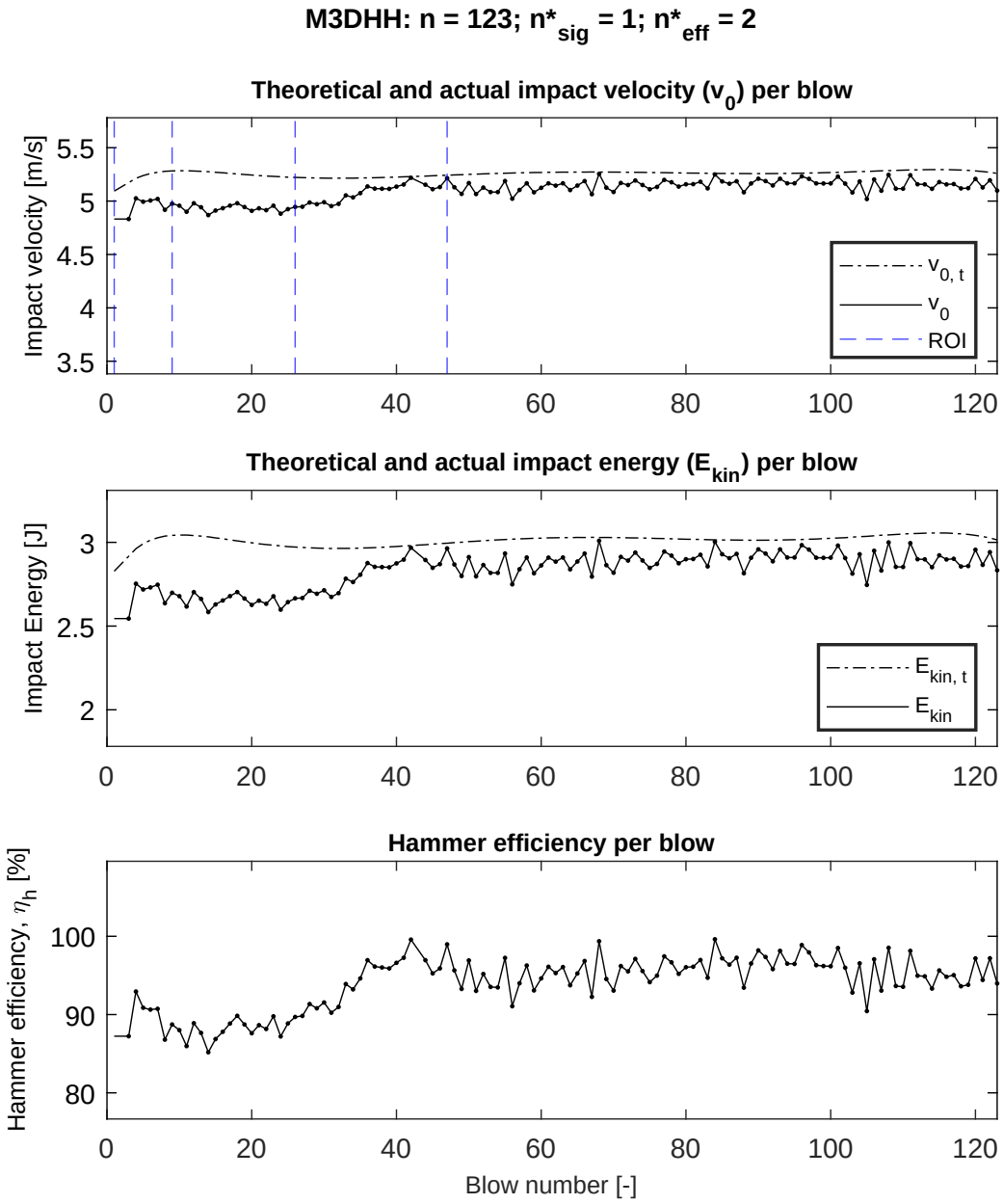

Figure C.78: For test M3DHH, from top to bottom: (I) theoretical and measured impact velocity v_0 versus blow number; (II) Theoretical and calculated impact energy versus blow number; (III) Hammer efficiency η_h versus blows number. Dots indicate blows for which the signal of the LS was approved and the subsequent velocity analysis yielded satisfactory results. Out of the total number of blows n, the number for which the latter was found to be true is indicated as n^*_{sig}. Finally, the number of blows which were disregarded (despite of usable velocity signals) as they yielded an efficiency >100% is denoted by n^*_{eff}.

M2SLL

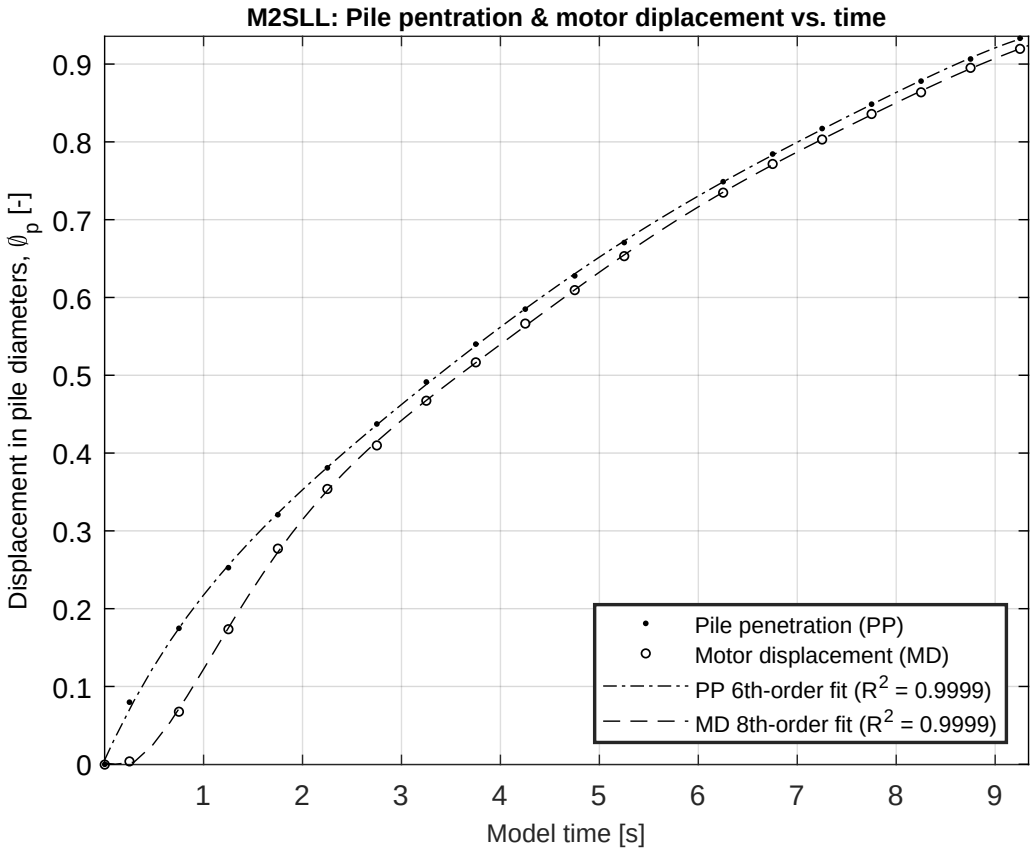

Figure C.79: Measured and approximated normalized (by pile diameter Φ_p) pile penetration (PP) and motor displacement (MD) as a function of model time for M2SLL.

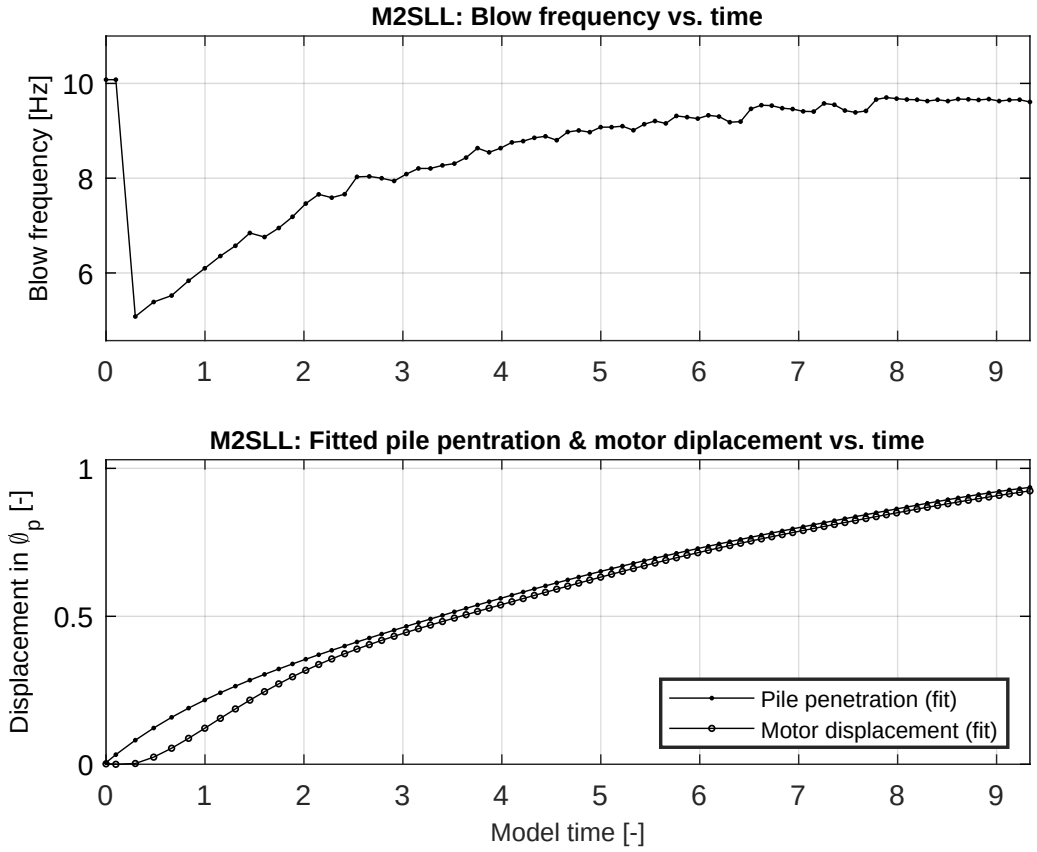

Figure C.80: (TOP) Driving frequency evaluated per blow as a function of model time for test M2SLL. As the frequency in inferred based on time intervals between triggers of the load cell, the frequency for the first blow cannot be determined. Instead, it is equaled to the frequency estimate for the second blow. (BOTTOM) Fitted expressions for PP and MD, evaluated per blow as a function of model time for M2SLL

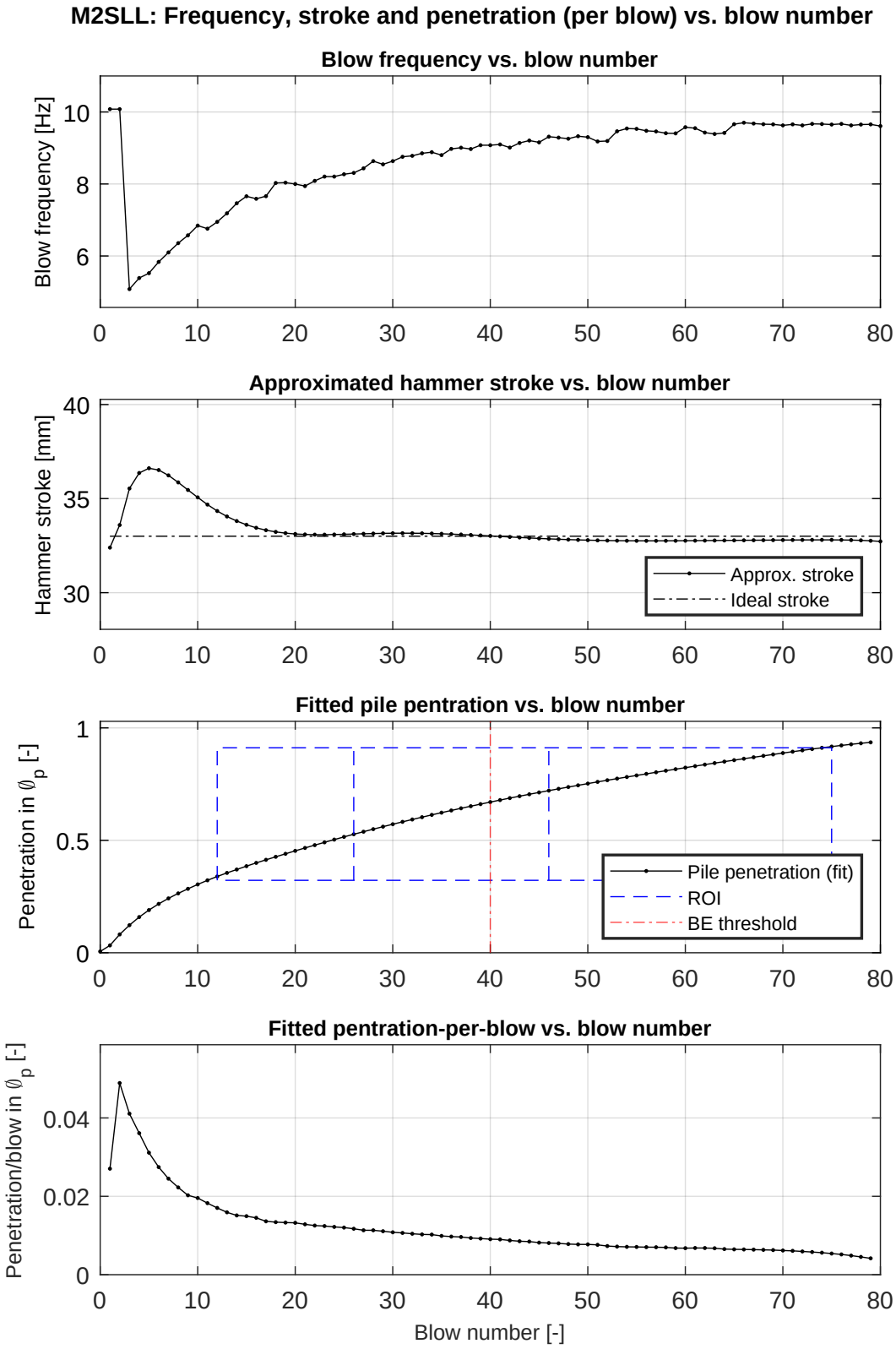

Figure C.81: From top to bottom: (I) blow frequency; (II) effective hammer stroke; (III) cumulative pile penetration, with graphical annotation of the ROI; (IV) pile penetration-per-blow. All are plotted a function of blow number for test M2SLL.

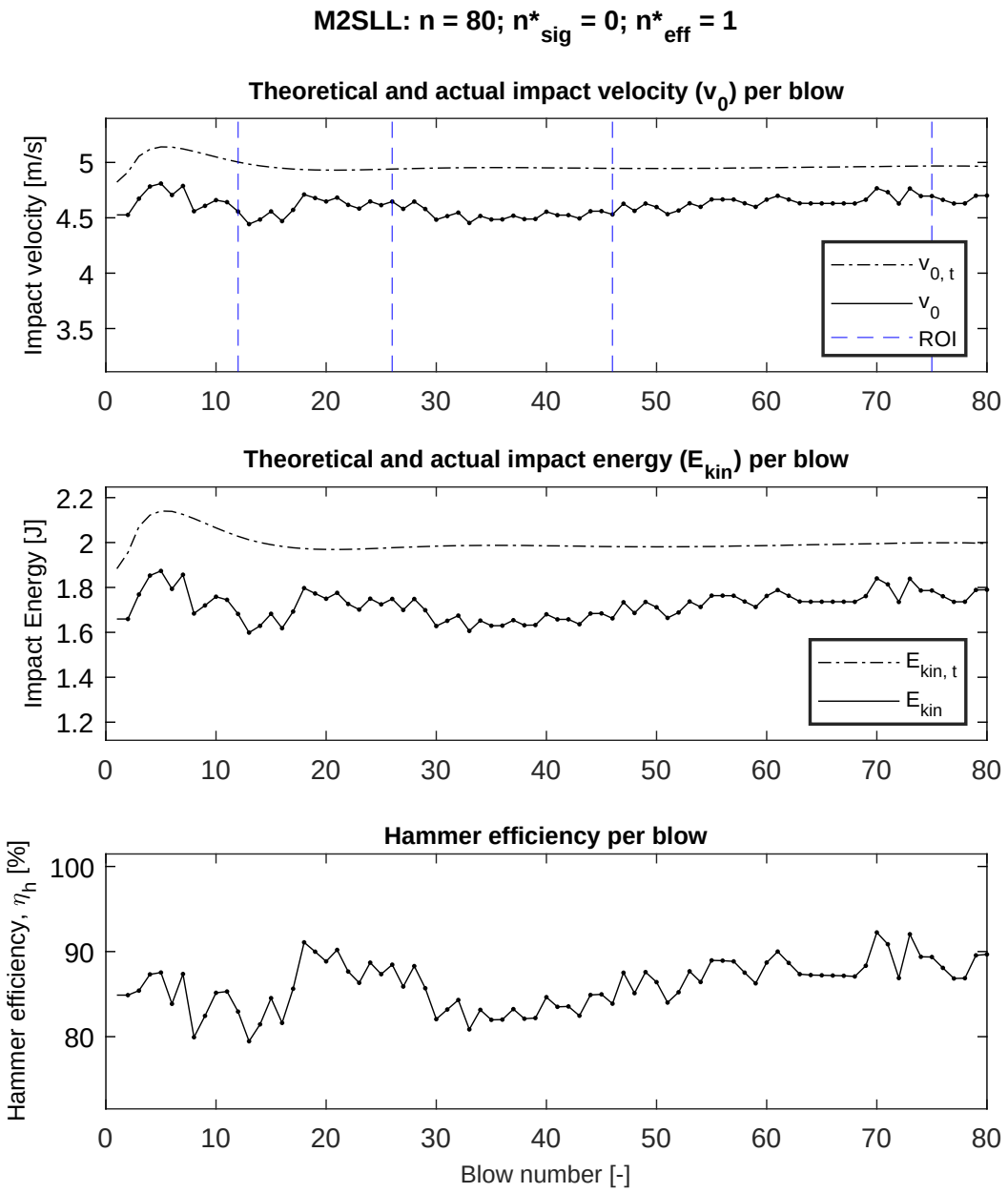

Figure C.82: For test M2SLL, from top to bottom: (I) theoretical and measured impact velocity v_0 versus blow number; (II) Theoretical and calculated impact energy versus blow number; (III) Hammer efficiency η_h versus blows number. Dots indicate blows for which the signal of the LS was approved and the subsequent velocity analysis yielded satisfactory results. Out of the total number of blows n, the number for which the latter was found to be true is indicated as n^*_{sig}. Finally, the number of blows which were disregarded (despite of usable velocity signals) as they yielded an efficiency >100% is denoted by n^*_{eff}.

M2SLH

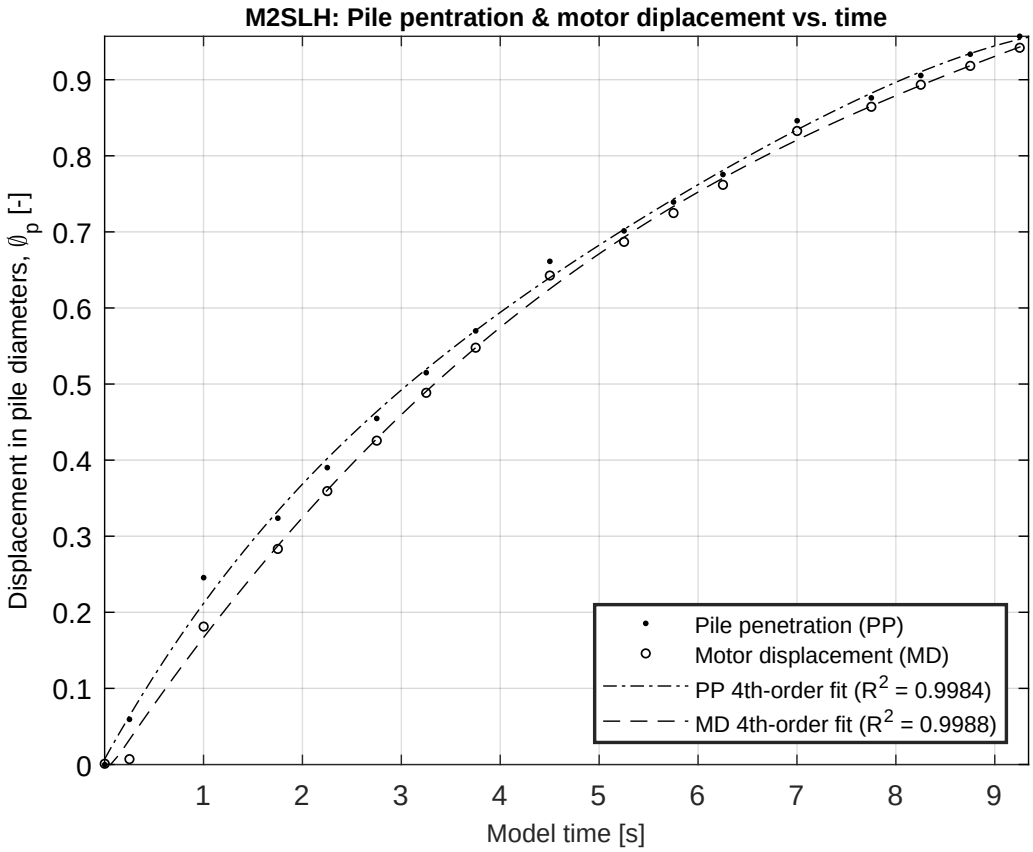

Figure C.83: Measured and approximated normalized (by pile diameter Φ_p) pile penetration (PP) and motor displacement (MD) as a function of model time for M2SLH.

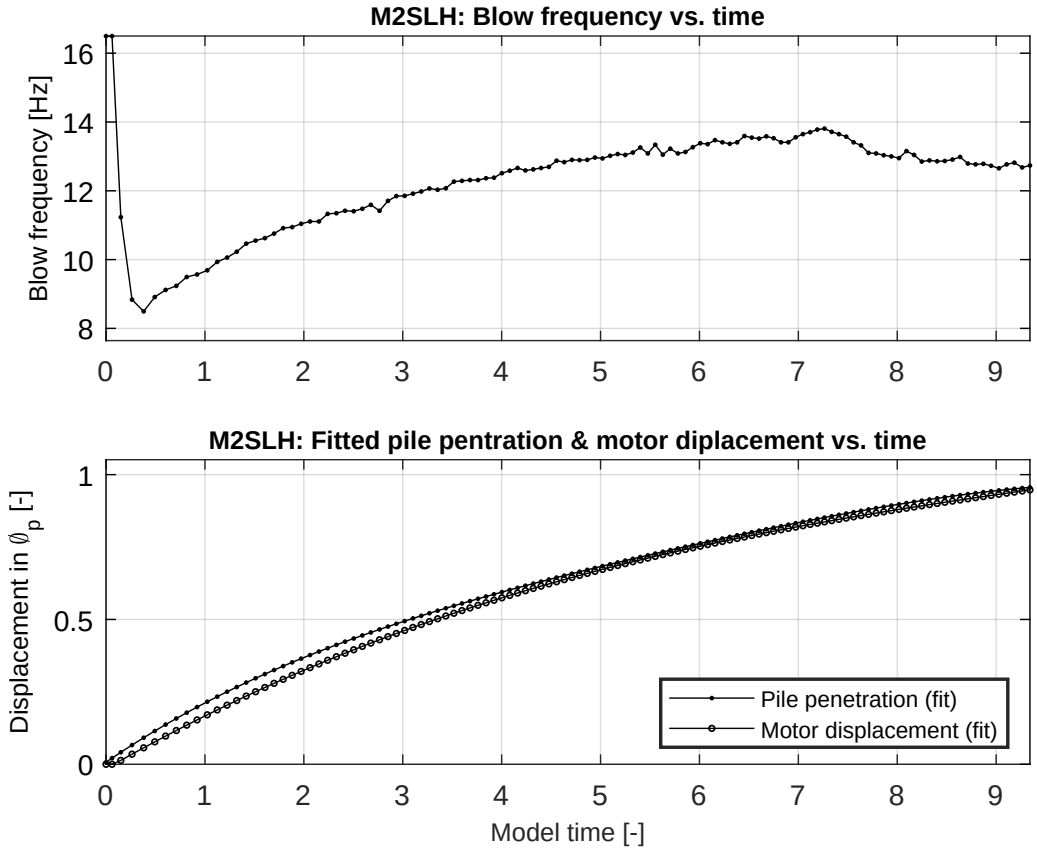

Figure C.84: (TOP) Driving frequency evaluated per blow as a function of model time for test M2SLH. As the frequency in inferred based on time intervals between triggers of the load cell, the frequency for the first blow cannot be determined. Instead, it is equaled to the frequency estimate for the second blow. (BOTTOM) Fitted expressions for PP and MD, evaluated per blow as a function of model time for M2SLH

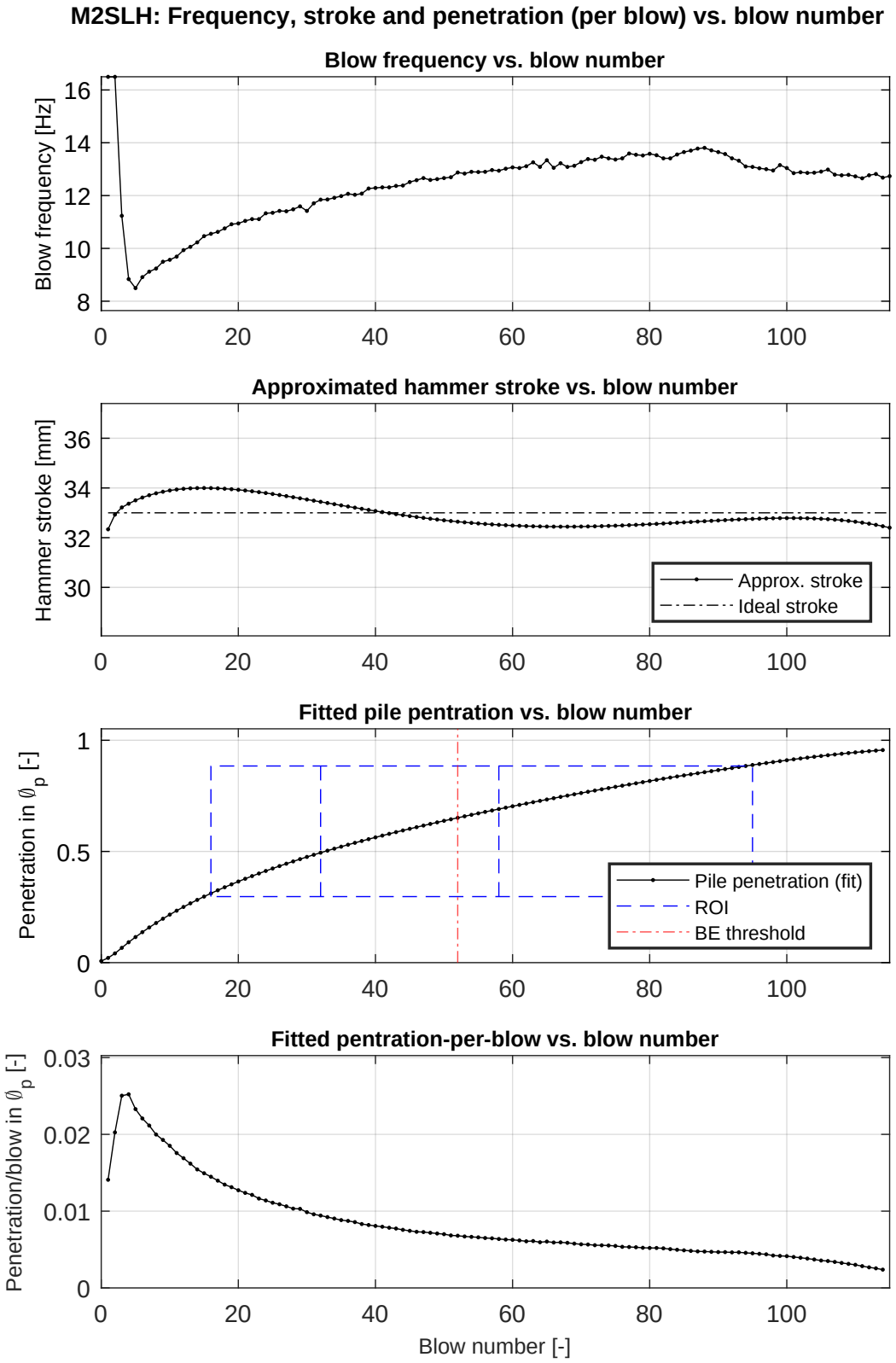

Figure C.85: From top to bottom: (I) blow frequency; (II) effective hammer stroke; (III) cumulative pile penetration, with graphical annotation of the ROI; (IV) pile penetration-per-blow. All are plotted a function of blow number for test M2SLH.

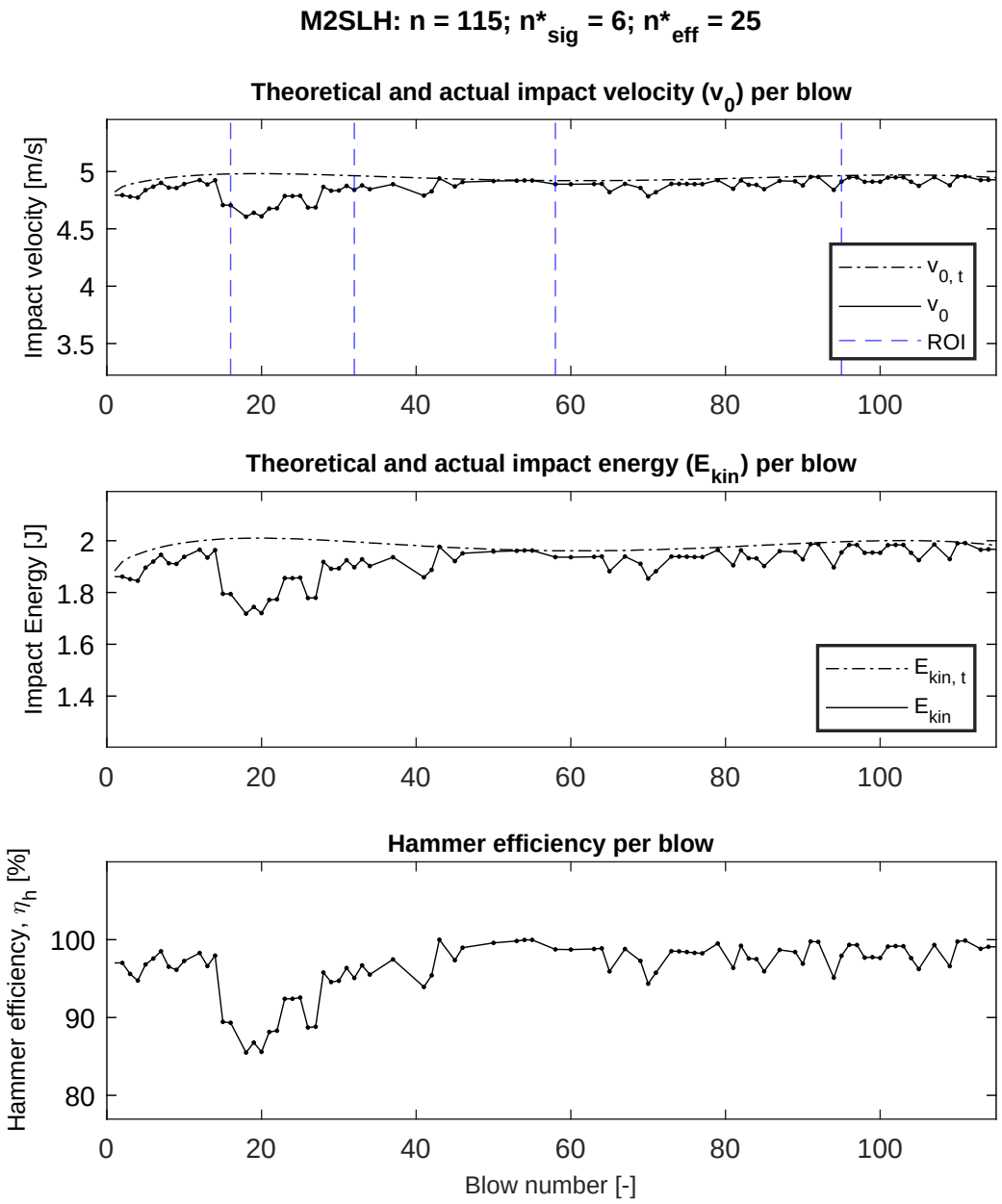

Figure C.86: For test M2SLH, from top to bottom: (I) theoretical and measured impact velocity v_0 versus blow number; (II) Theoretical and calculated impact energy versus blow number; (III) Hammer efficiency η_h versus blows number. Dots indicate blows for which the signal of the LS was approved and the subsequent velocity analysis yielded satisfactory results. Out of the total number of blows n, the number for which the latter was found to be true is indicated as n^*_{sig}. Finally, the number of blows which were disregarded (despite of usable velocity signals) as they yielded an efficiency >100% is denoted by n^*_{eff}.

M2SHL

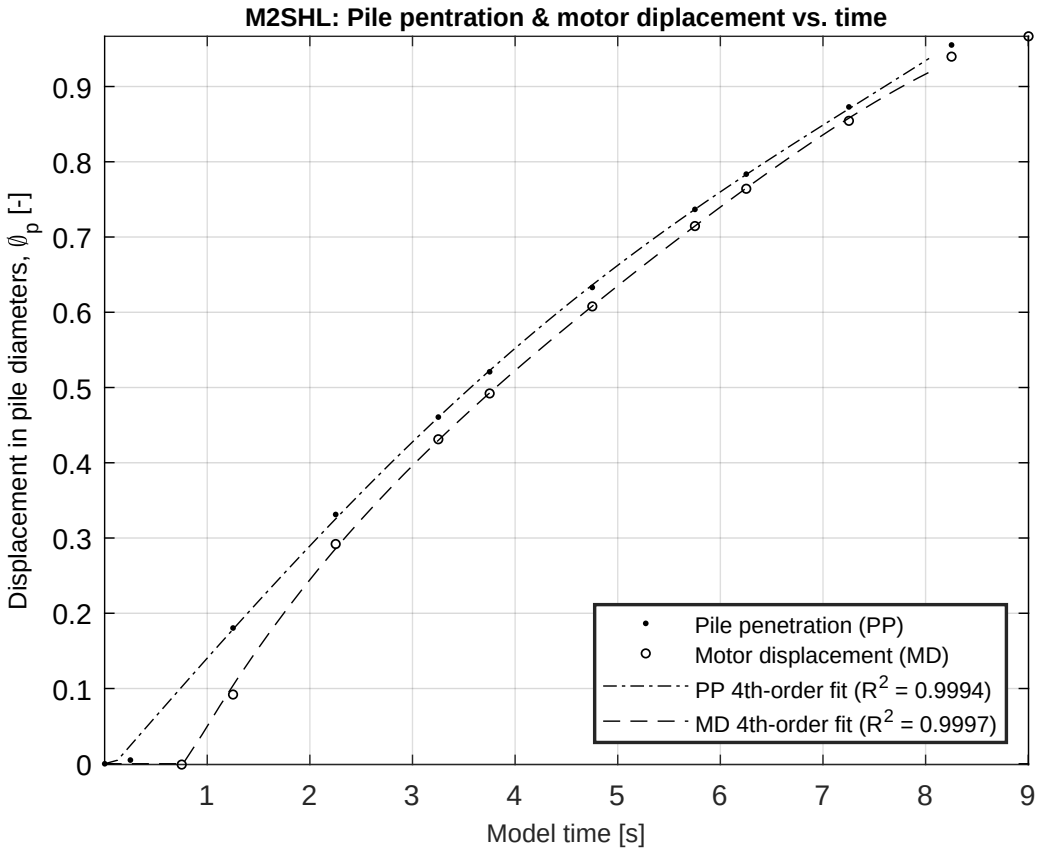

Figure C.87: Measured and approximated normalized (by pile diameter Φ_p) pile penetration (PP) and motor displacement (MD) as a function of model time for M2SHL.

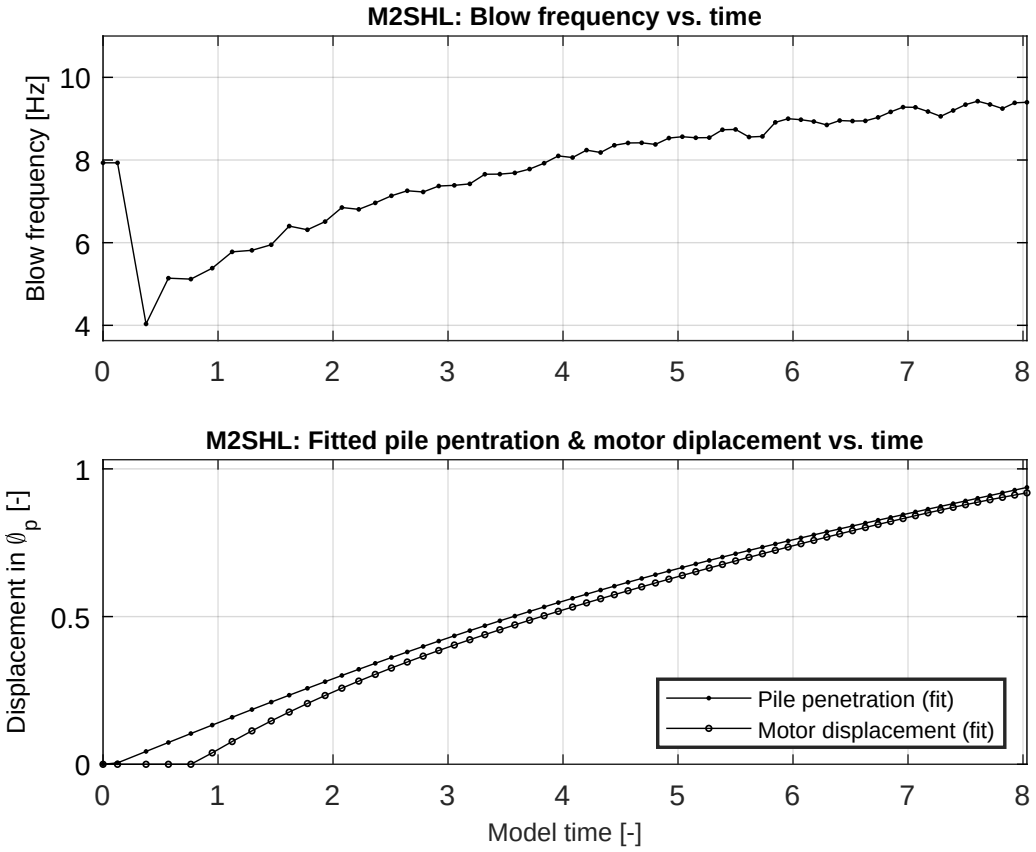

Figure C.88: (TOP) Driving frequency evaluated per blow as a function of model time for test M2SHL. As the frequency in inferred based on time intervals between triggers of the load cell, the frequency for the first blow cannot be determined. Instead, it is equaled to the frequency estimate for the second blow. (BOTTOM) Fitted expressions for PP and MD, evaluated per blow as a function of model time for M2SHL

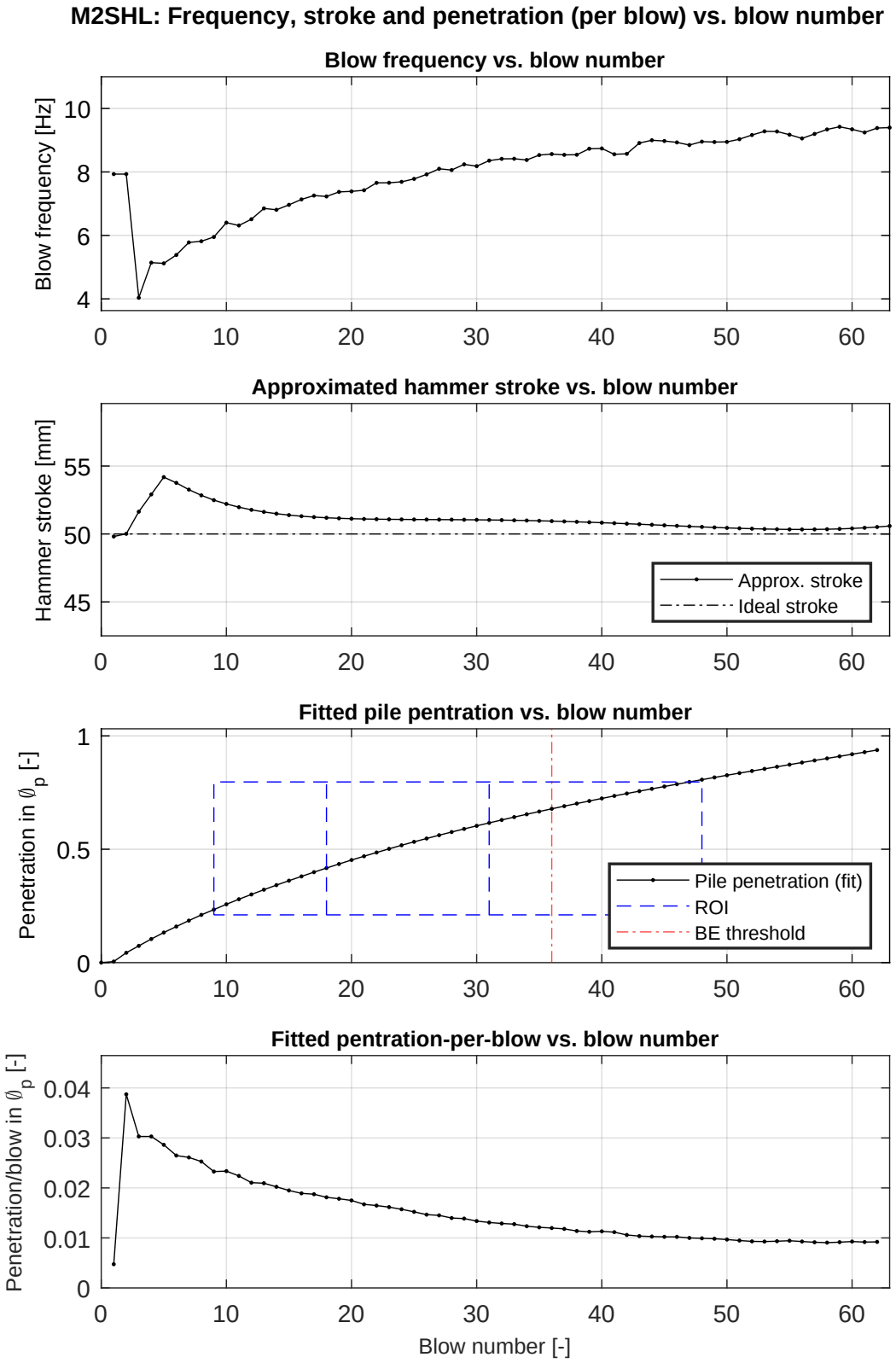

Figure C.89: From top to bottom: (I) blow frequency; (II) effective hammer stroke; (III) cumulative pile penetration, with graphical annotation of the ROI; (IV) pile penetration-per-blow. All are plotted a function of blow number for test M2SHL.

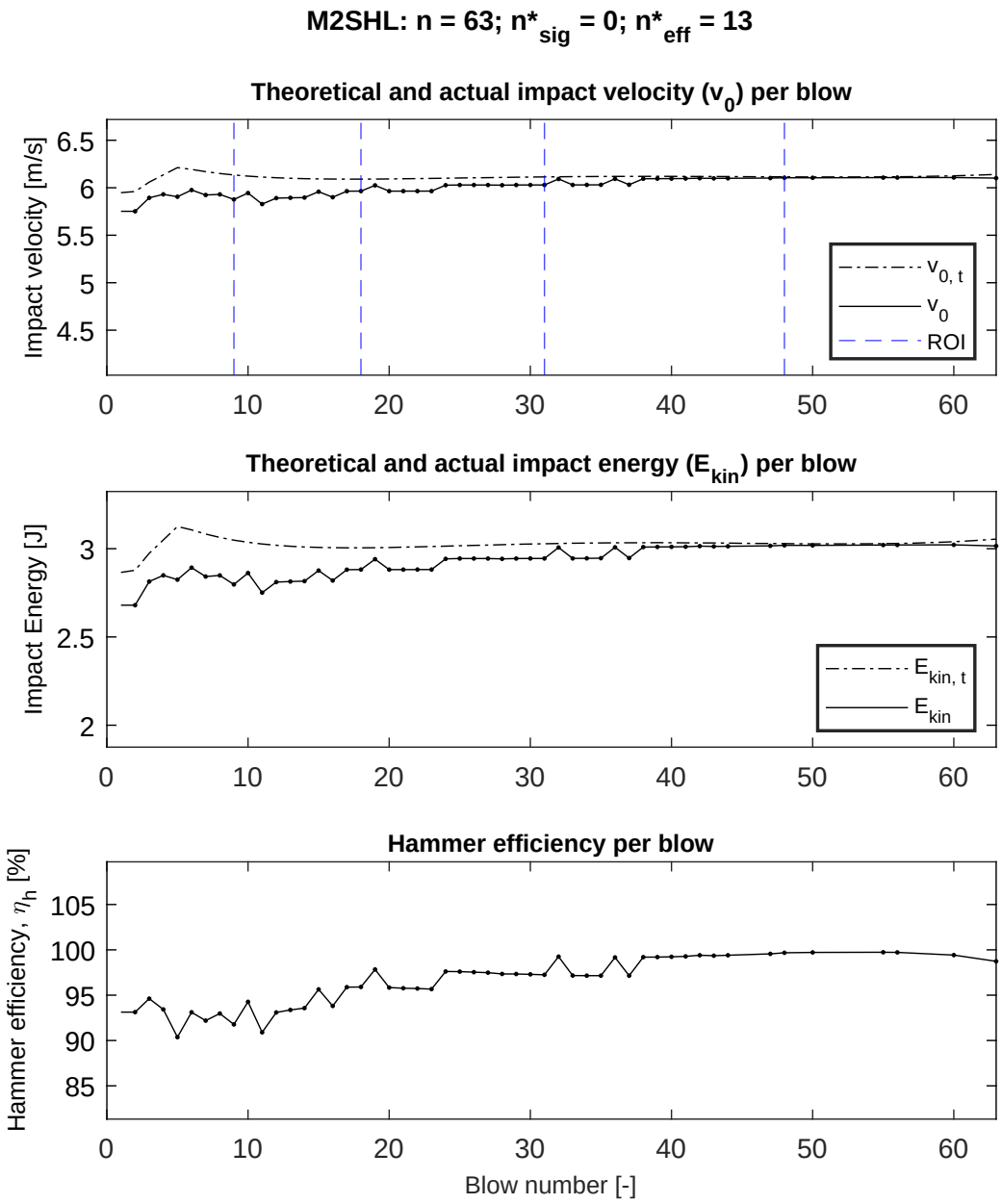

Figure C.90: For test M2SHL, from top to bottom: (I) theoretical and measured impact velocity v_0 versus blow number; (II) Theoretical and calculated impact energy versus blow number; (III) Hammer efficiency η_h versus blows number. Dots indicate blows for which the signal of the LS was approved and the subsequent velocity analysis yielded satisfactory results. Out of the total number of blows n, the number for which the latter was found to be true is indicated as n^*_{sig}. Finally, the number of blows which were disregarded (despite of usable velocity signals) as they yielded an efficiency >100% is denoted by n^*_{eff}.

M3SLL

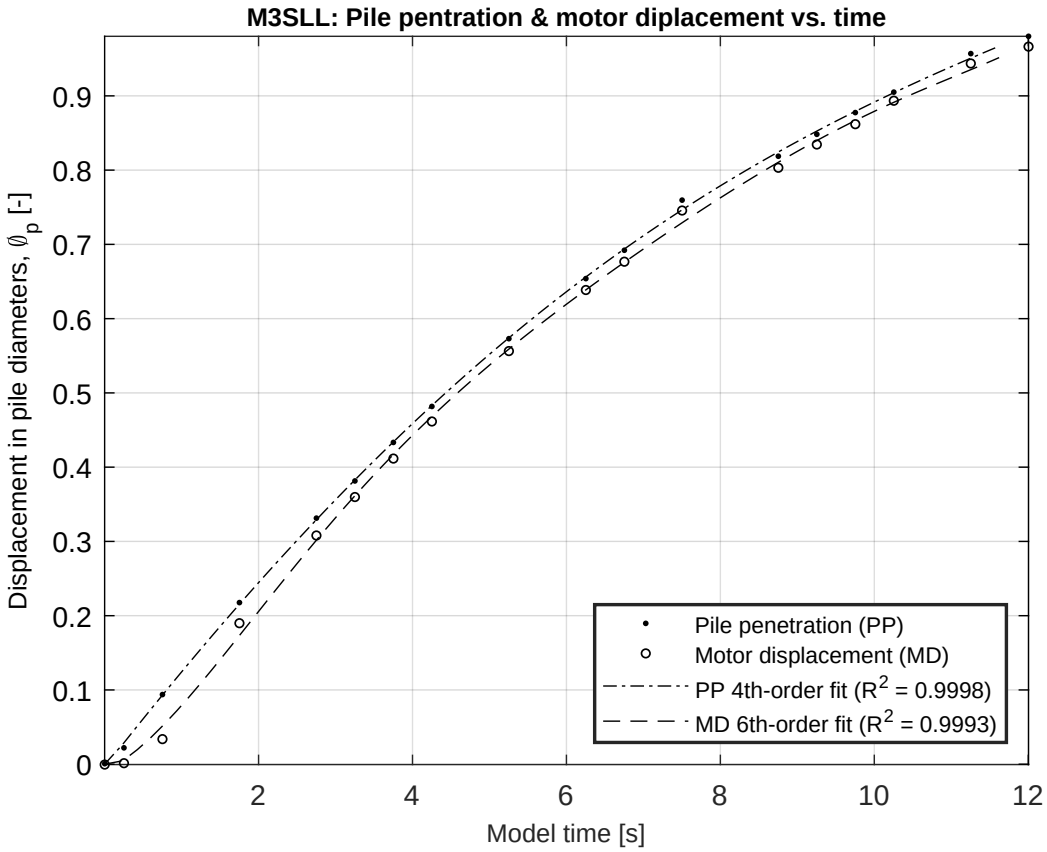

Figure C.91: Measured and approximated normalized (by pile diameter Φ_p) pile penetration (PP) and motor displacement (MD) as a function of model time for M3SLL.

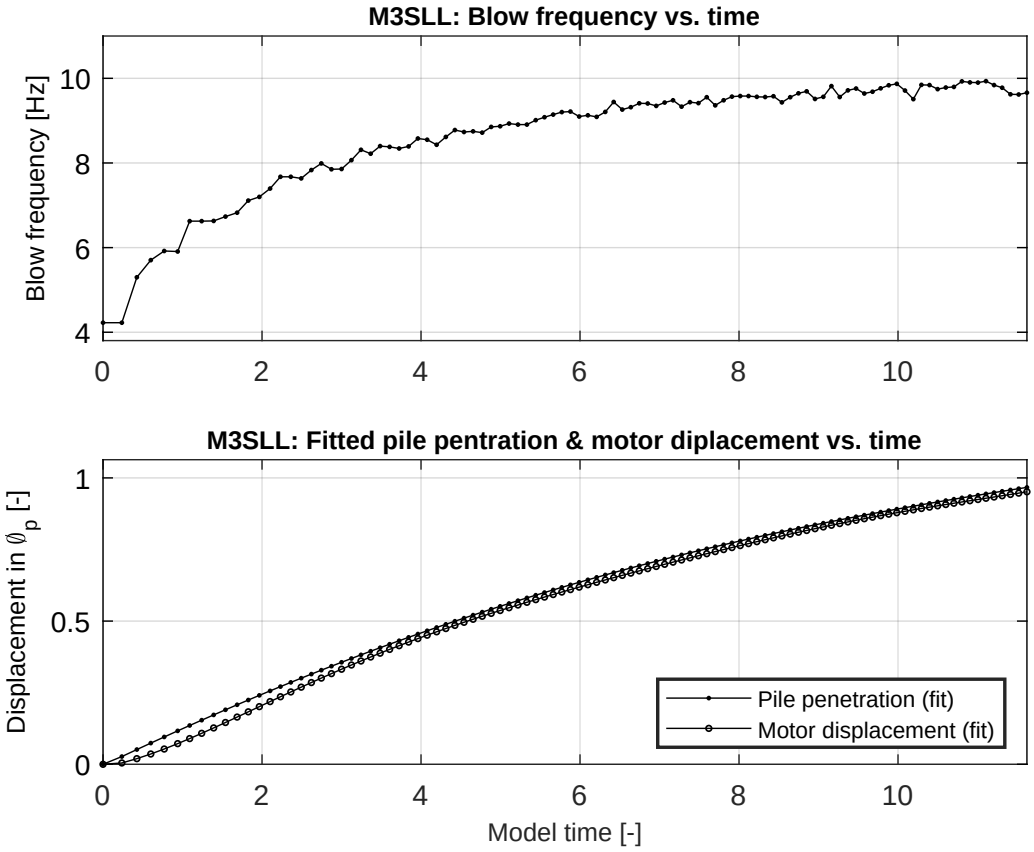

Figure C.92: (TOP) Driving frequency evaluated per blow as a function of model time for test M3SLL. As the frequency in inferred based on time intervals between triggers of the load cell, the frequency for the first blow cannot be determined. Instead, it is equaled to the frequency estimate for the second blow. (BOTTOM) Fitted expressions for PP and MD, evaluated per blow as a function of model time for M3SLL

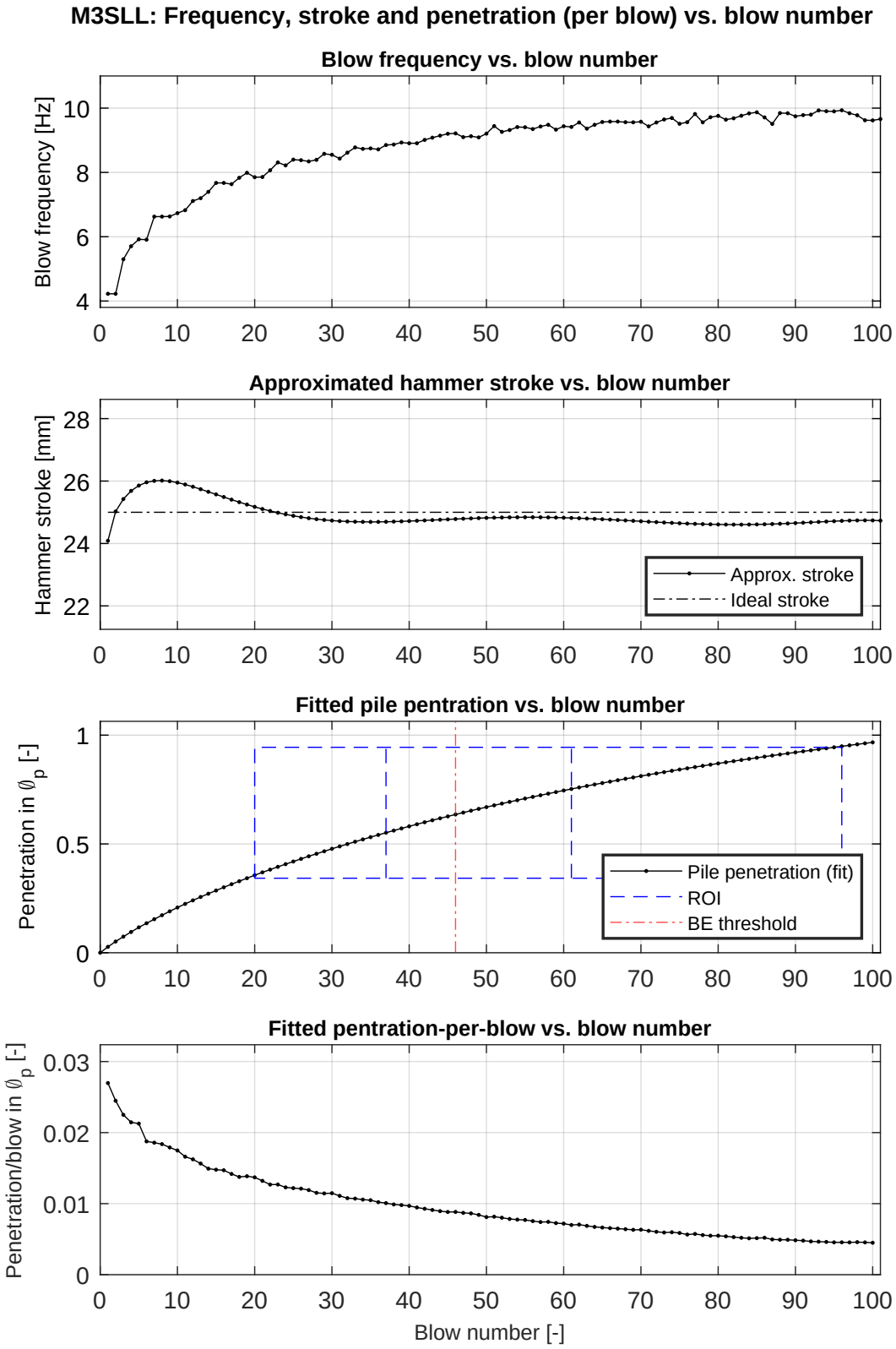

Figure C.93: From top to bottom: (I) blow frequency; (II) effective hammer stroke; (III) cumulative pile penetration, with graphical annotation of the ROI; (IV) pile penetration-per-blow. All are plotted a function of blow number for test M3SLL.

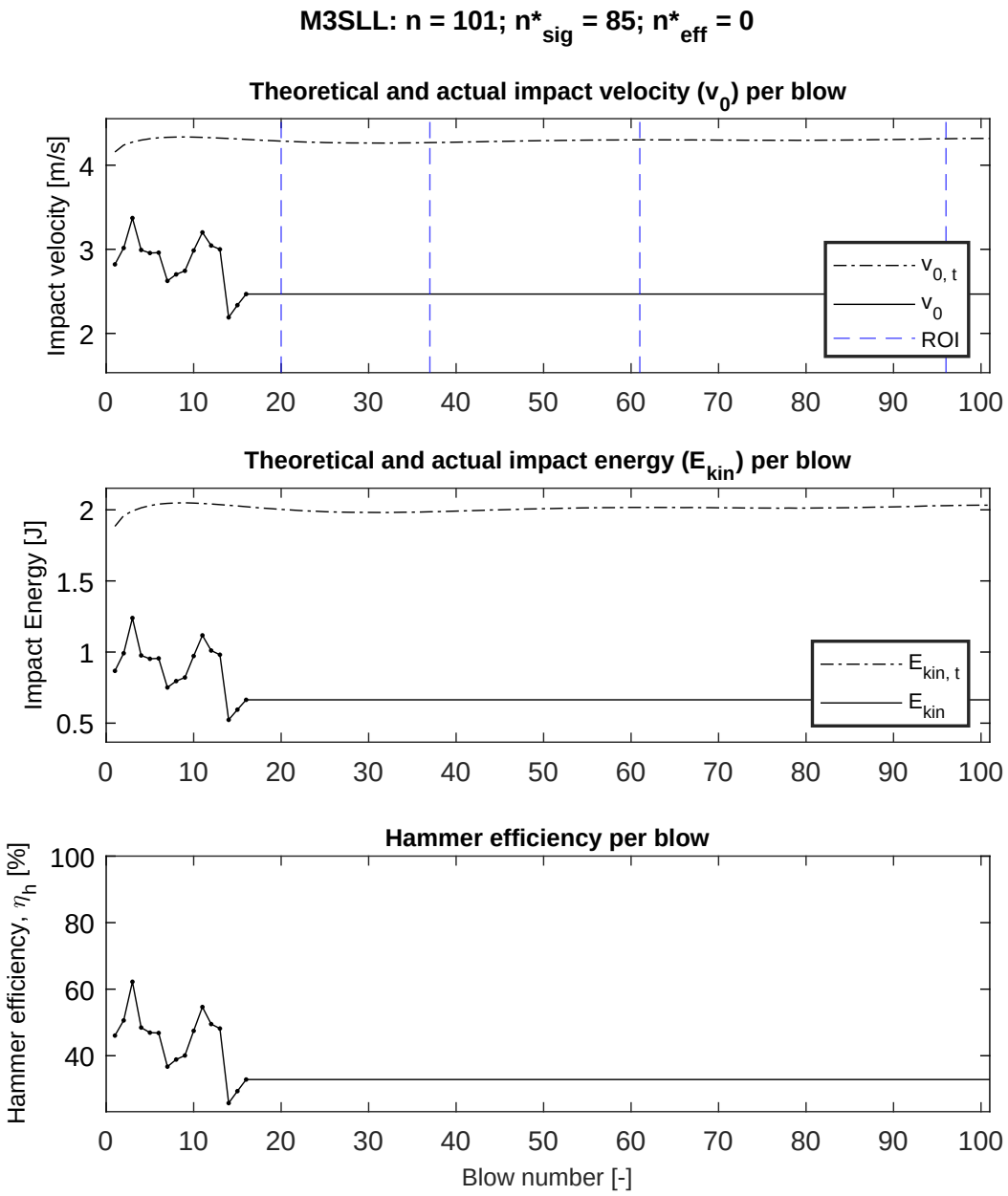

Figure C.94: For test M3SLL, from top to bottom: (I) theoretical and measured impact velocity v_0 versus blow number; (II) Theoretical and calculated impact energy versus blow number; (III) Hammer efficiency η_h versus blows number. Dots indicate blows for which the signal of the LS was approved and the subsequent velocity analysis yielded satisfactory results. Out of the total number of blows n, the number for which the latter was found to be true is indicated as n^*_{sig}. Finally, the number of blows which were disregarded (despite of usable velocity signals) as they yielded an efficiency >100% is denoted by n^*_{eff}.

M3SLH

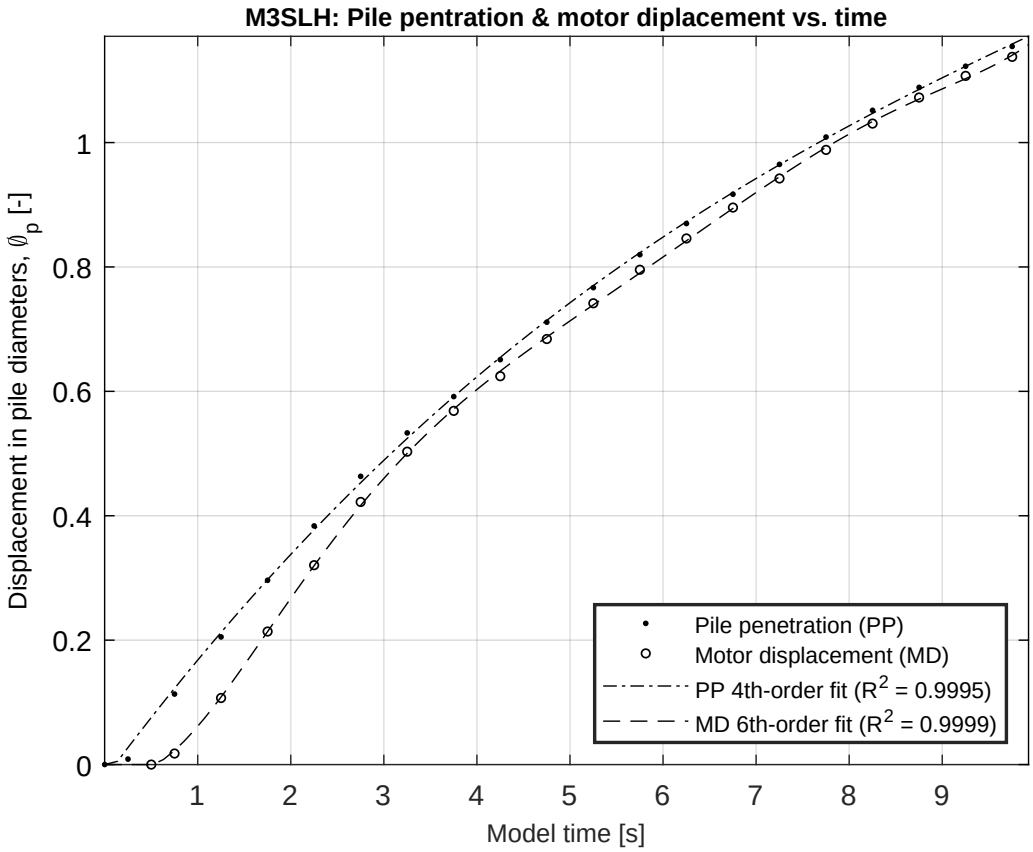

Figure C.95: Measured and approximated normalized (by pile diameter Φ_p) pile penetration (PP) and motor displacement (MD) as a function of model time for M3SLH.

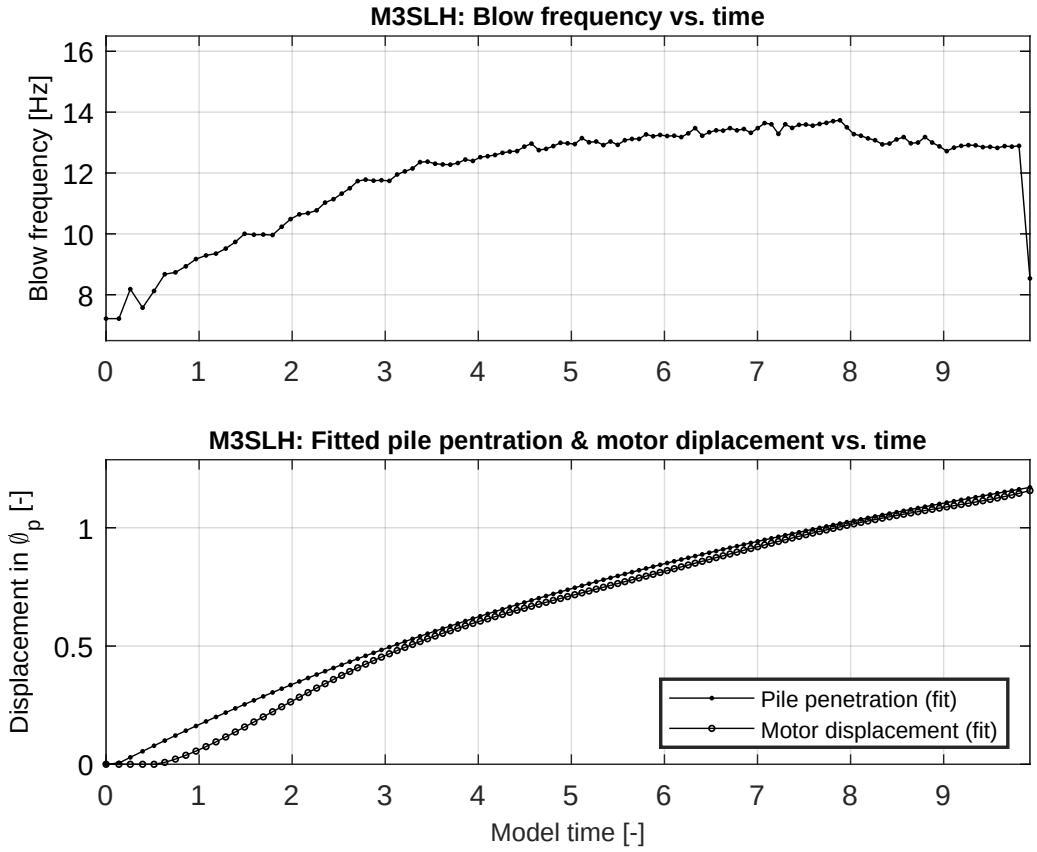

Figure C.96: (TOP) Driving frequency evaluated per blow as a function of model time for test M3SLH. As the frequency in inferred based on time intervals between triggers of the load cell, the frequency for the first blow cannot be determined. Instead, it is equaled to the frequency estimate for the second blow. (BOTTOM) Fitted expressions for PP and MD, evaluated per blow as a function of model time for M3SLH

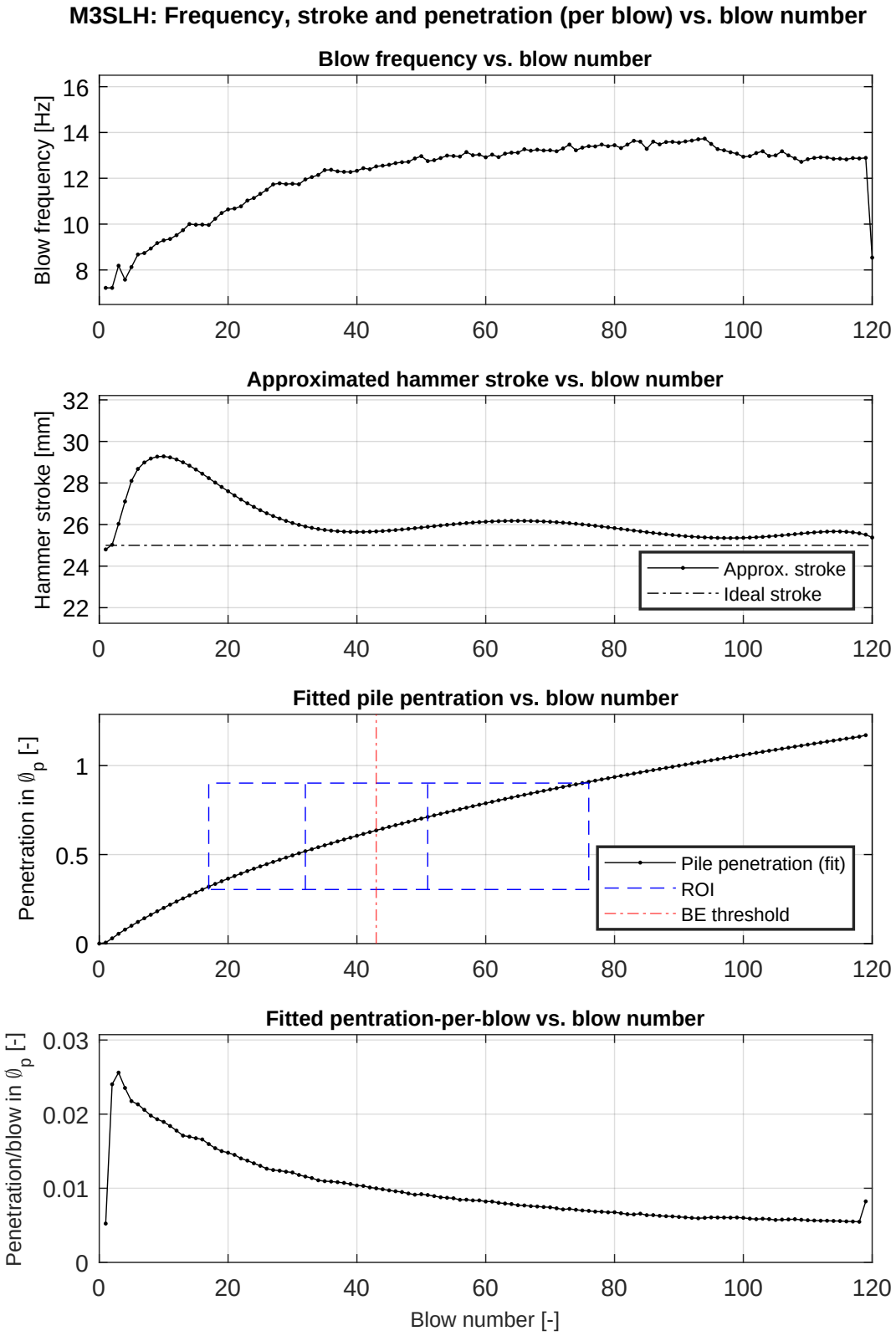

Figure C.97: From top to bottom: (I) blow frequency; (II) effective hammer stroke; (III) cumulative pile penetration, with graphical annotation of the ROI; (IV) pile penetration-per-blow. All are plotted a function of blow number for test M3SLH.

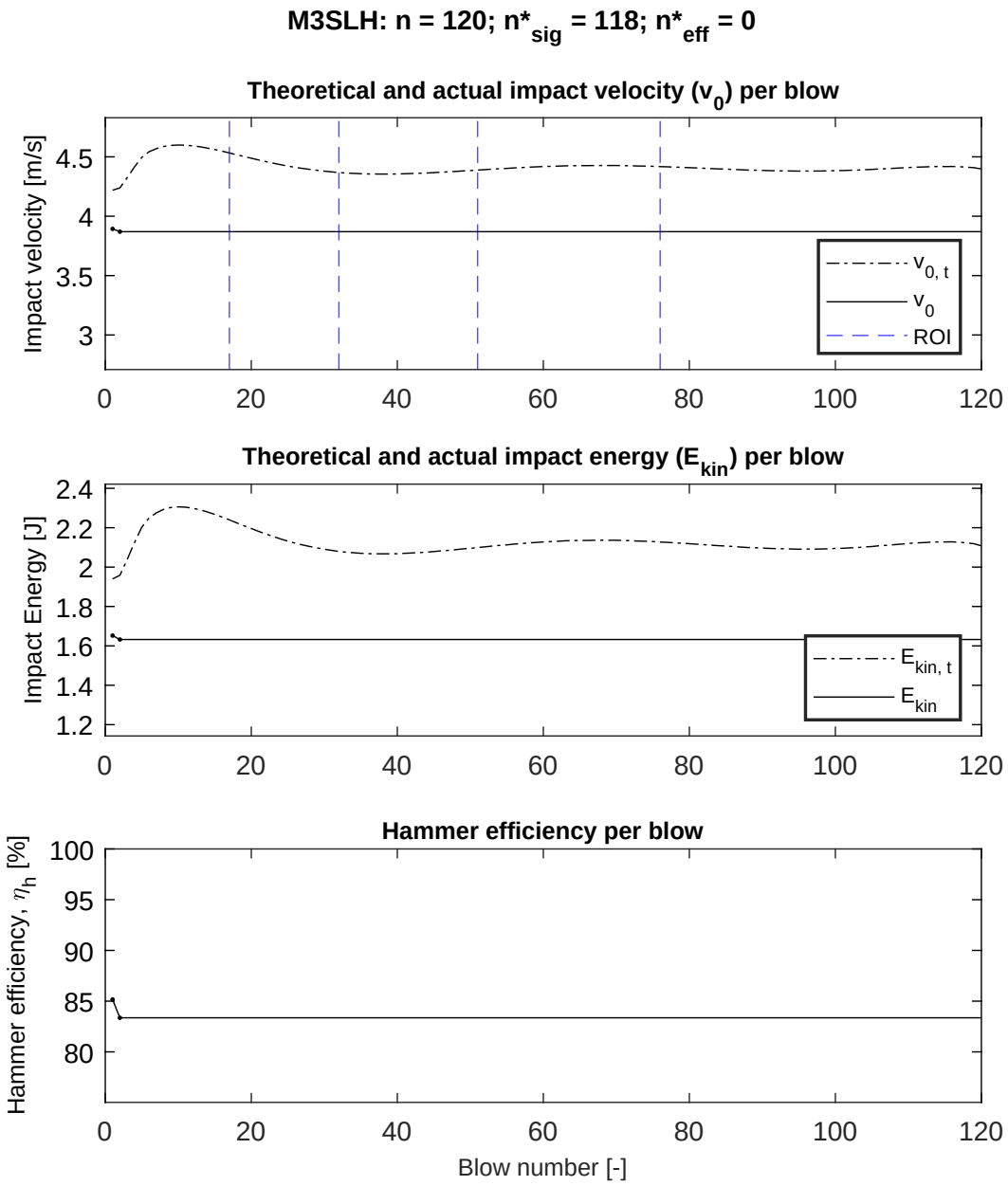

Figure C.98: For test M3SLH, from top to bottom: (I) theoretical and measured impact velocity v_0 versus blow number; (II) Theoretical and calculated impact energy versus blow number; (III) Hammer efficiency η_h versus blows number. Dots indicate blows for which the signal of the LS was approved and the subsequent velocity analysis yielded satisfactory results. Out of the total number of blows n, the number for which the latter was found to be true is indicated as n^*_{sig}. Finally, the number of blows which were disregarded (despite of usable velocity signals) as they yielded an efficiency >100% is denoted by n^*_{eff}.

M3SHL

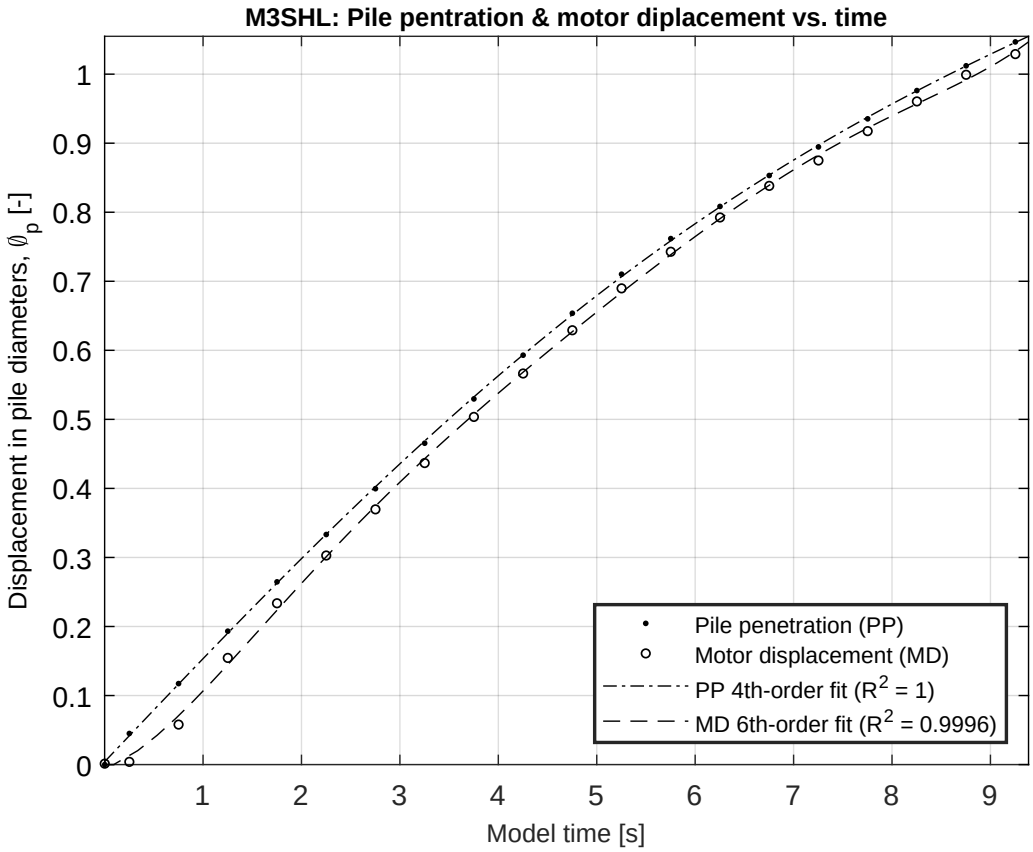

Figure C.99: Measured and approximated normalized (by pile diameter Φ_p) pile penetration (PP) and motor displacement (MD) as a function of model time for M3SHL.

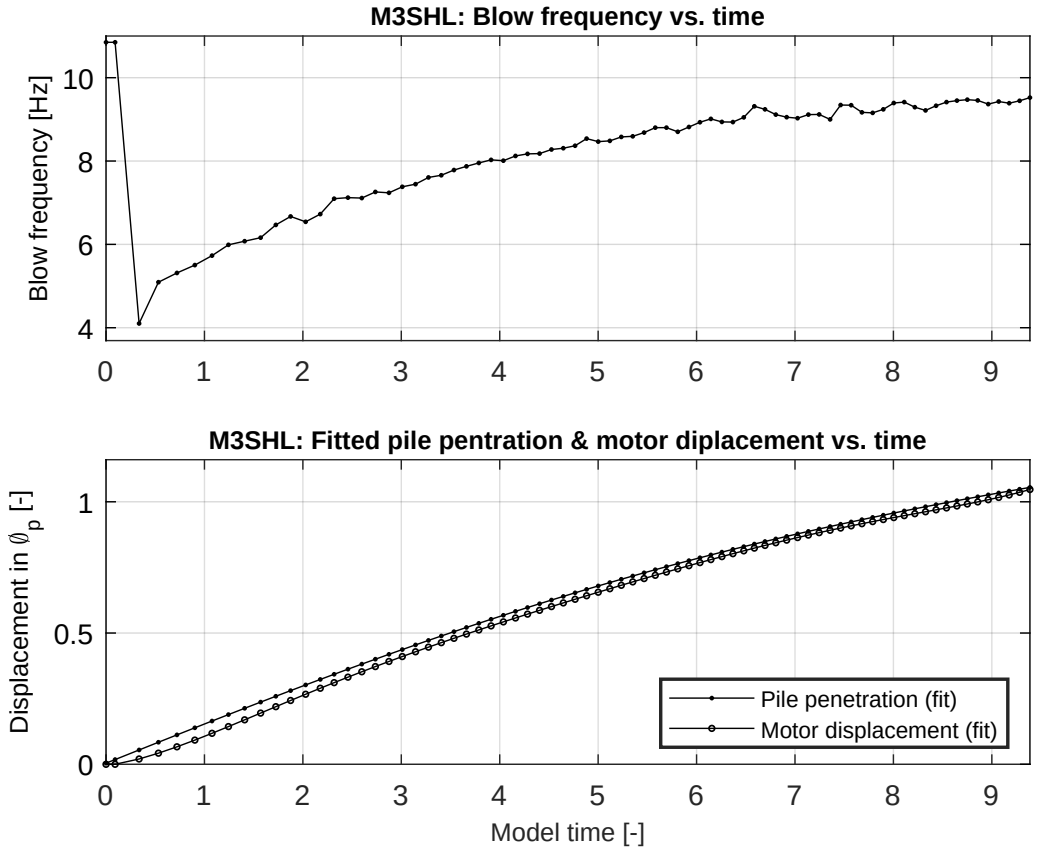

Figure C.100: (TOP) Driving frequency evaluated per blow as a function of model time for test M3SHL. As the frequency in inferred based on time intervals between triggers of the load cell, the frequency for the first blow cannot be determined. Instead, it is equaled to the frequency estimate for the second blow. (BOTTOM) Fitted expressions for PP and MD, evaluated per blow as a function of model time for M3SHL

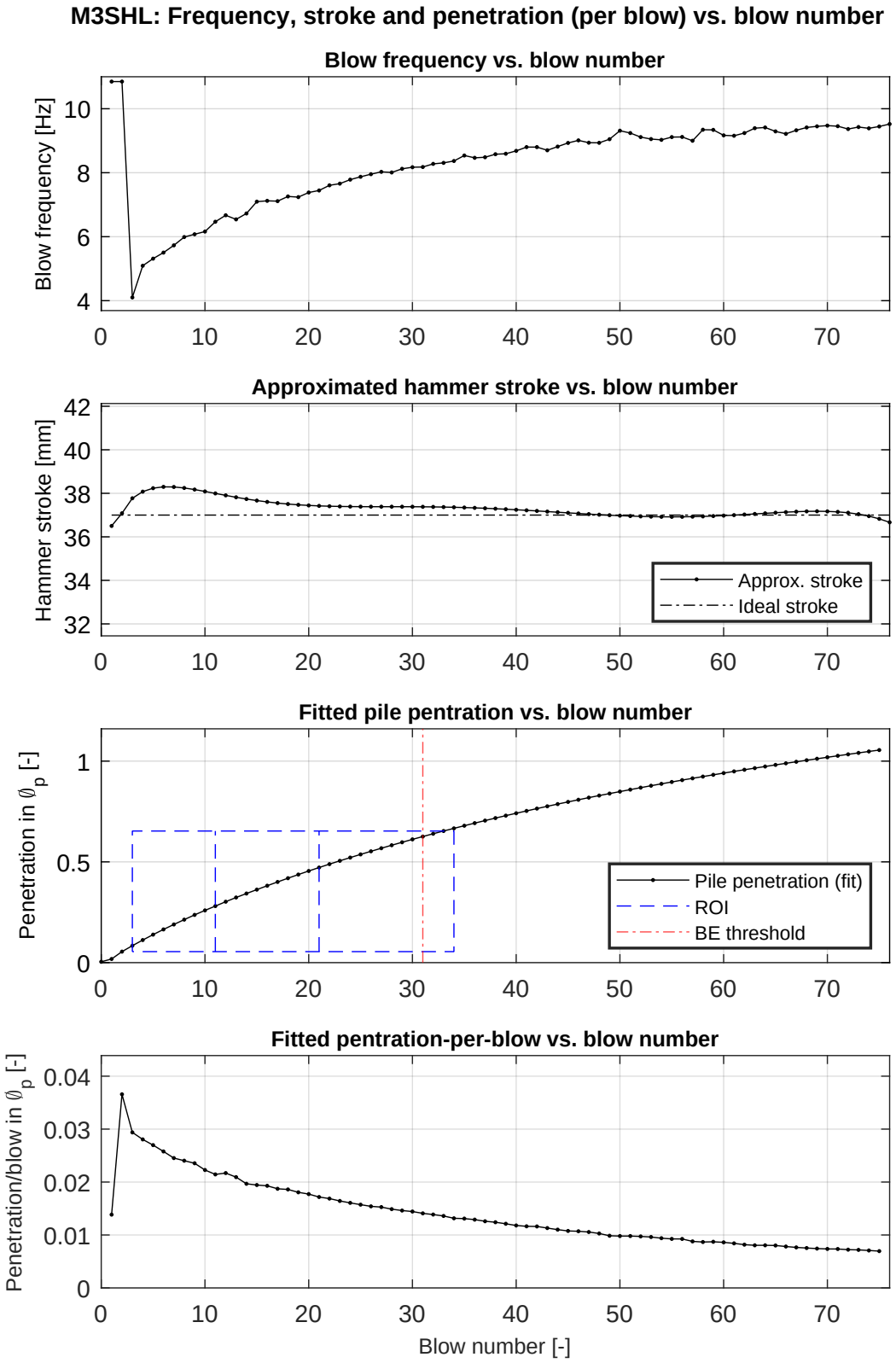

Figure C.101: From top to bottom: (I) blow frequency; (II) effective hammer stroke; (III) cumulative pile penetration, with graphical annotation of the ROI; (IV) pile penetration-per-blow. All are plotted a function of blow number for test M3SHL.

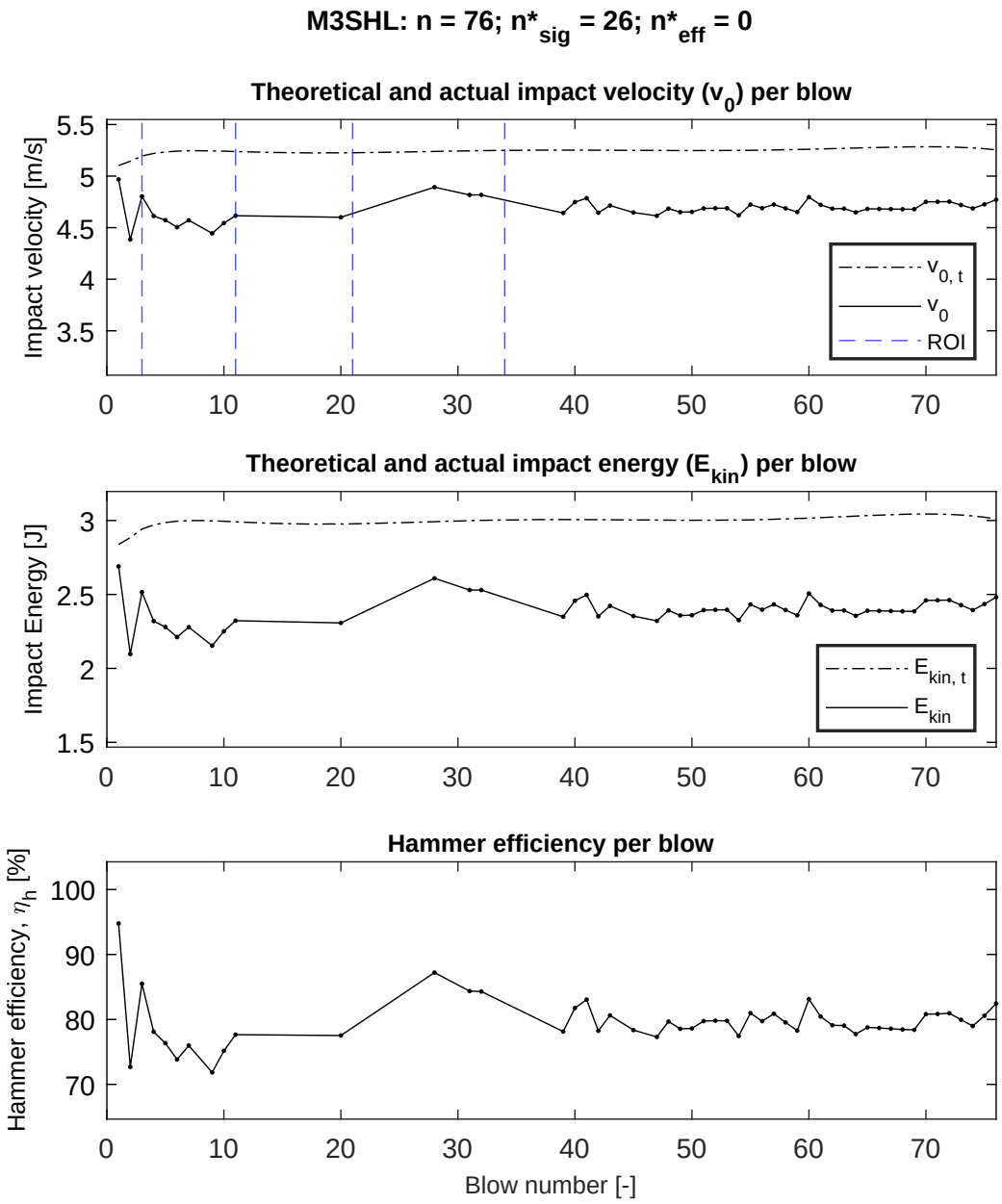

Figure C.102: For test M3SHL, from top to bottom: (I) theoretical and measured impact velocity v_0 versus blow number; (II) Theoretical and calculated impact energy versus blow number; (III) Hammer efficiency η_h versus blows number. Dots indicate blows for which the signal of the LS was approved and the subsequent velocity analysis yielded satisfactory results. Out of the total number of blows n, the number for which the latter was found to be true is indicated as n^*_{sig}. Finally, the number of blows which were disregarded (despite of usable velocity signals) as they yielded an efficiency >100% is denoted by n^*_{eff}.

D

Timing correction of continuous fast ADC measurements

This appendix explores the possibilities to correct data obtained from the second fast ADC in the geo-centrifuge. Due to an unknown cause, data logged by this measurement system when operating in continuous, high frequency mode; were stored with false time labels. Locally, the time interval between individual samples (50 *ms*) matches the user-defined data logging frequency (20 kHz). However, globally, the time interval between any two consecutive blows is too long and thus falls short of the blow frequency maintained by the hammer. As a consequence of the aforementioned abnormality, ram velocities (inferred from the time difference between the passage of the first and second light or hall sensor respectively, as discussed in **??**) are significantly lower than anticipated. In turn, this causes a (aggravated) deviation of the back-calculated impact energies (which vary quadratically with velocity) as well as the hammer efficiency η_h. To ensure a proper comparison between the data from different test, it is of vital importance that the ram velocity data is reliable. In an attempt to quantify the seriousness of the issue and formulate an appropriate way to correct the false data samples, for the six affected tests a full comparison of data obtained from the first and second fast ADC system is carried out. This analysis entails the following steps:

1. *Determination of the driving frequency by analyzing the elapsed time between consecutive load cell triggers.* For all of the affected tests, load cell data was recored at a frequency of 230 *kHz*, while the first fast ADC system operated in so-called 'triggered' mode. In this triggered mode, the system logs 800 data samples at the specified logging frequency (230 *kHz*); As the triggered sampling yields a fragmented data file, each fragment (of 800 samples) is retractable to a specific time span. To this end, sample points are accompanied by time labels, which are referenced with respect to the initiation of the first fast ADC system by a human operator in the centrifuge control room. Now, the blow frequency is inferred by calculating the time interval the first sample of consequences data fragments (or triggers). This process introduces a small error as the sample index corresponding to contact between ram and anvil, may vary between blows. However, due to the high data logging frequency, the associated error is negligible.
2. *Estimation of the driving frequency through time interval analysis between consecutive sets of light sensor excitations due to downward movement (towards the anvil) of the ram mass.* For the considered tests, this data is recored by the second fast ADC system, which operated in a continuous measurement mode at an (apparent) logging frequency of 20 *kHz*. Inherent to the use of the continuous sampling mode, the upward movement of the ram is also captured by the light sensors. This upward movement results a sign change of the the sensory signal, which eases the identification an elimination of such signals form the continuous data log.

Test ID	Mean, μ [-]	STD, σ [-]	COV, C_v [-]
M2SLL	1.5972	0.0069	0.0043
M2SLH	1.5767	0.0187	0.0119
M2SHL	1.6019	0.0078	0.0049
M3SLL	1.5963	0.013	0.0081
M3SLH	1.5766	0.0135	0.00856
M3SHL	1.6003	0.0159	0.00994

Table D.1: Mean, STD and coefficient of variation of 'timing quotient' for all test affected by the time labeling discrepancy of second fast ADC system

Finally, to infer the driving frequency the elapsed time between the first triggers (passage of the first sensor) of two succeeding sets of light sensor excitations is considered. The use of the first trigger out of each set is required as the second trigger was not consequently recored for all blows. Reflections of light within the anvil form a plausible explanation as to why the trigger threshold for the second sensor was not surpassed. A single excitation peak per blow is sufficient to reliably infer the driving frequency.

3. *Calculation of the 'timing coefficient', the quotient of the blow frequency according to the second fast ADC system (light sensor data), over the blow frequency approximation provided by the first fast ADC system (load cell data).* To maximize the reliability of the timing quotient, the data used from the data logging devices should correspond to the same blow. To facilitate this, a MATLAB® script verifies whether the time intervals between blows are in line with evolution of blow frequency over time. High frequency outliers due to a false trigger are deleted from the blow time sequence. Low frequency outliers, caused when the sensory output fluctuation upon passage of the ram mass does (falsely) not surpassed the threshold value, are corrected. To this end, the number of falsely unrecorded blows is estimated based on measured time interval and the expected time interval (based off the global trend in the blow frequency evolution). Subsequently, the (interpolated) time instances corresponding to the missing blows are inserted into the blow time sequence. Finally, estimated driving frequencies are inferred from the time difference between adjacent entries of the post-processed blow time sequence. To distinguish between actual triggers of the measurement system and those added by post-processing algorithms, the former are indicated by black, circular markers.

Data recorded by the second fast ADC was falsely labeled for the following tests from Table 6.1: M2SLL; M2SLH; M2SHL; M3SLL; M3SLH; M3SHL. For these tests, like previously mentioned, the blow frequency from both fast ADC systems is calculated, as well as the resulting 'timing coefficient'. Associated plots can be found as Figures D.1, D.3, D.5, D.7, D.9 and D.11 respectively. Additionally, the timing coefficients are presented in the as histograms (which mean and standard deviations indicated) to gain quantify the variability of the results. Coherent to the order of mention of the affected tests, aforementioned histograms are included as D.2, D.4, D.6, D.8, D.10 and D.12.

As it can reasonably be assumed that the factor by which the timing of the second fast ADC system is off, is constant; the best estimate of the timing coefficient follows from the test with the lowest coefficient of variation C_v. Hence, the mean μ, standard deviation σ and coefficient of variation C_v of the timing quotients of the affected tests are listed in Table D.1. As can be inferred, test M2SLL expresses the lowest degree of variability. **Therefore, time labels for all affected tests are divided 1.5972 as a compensatory measure.** The necessary correction factor points out that data recoded through continuous logging by the second fast ADC system, were sampled at a rate ≈32 *kHz* instead of the anticipated rate of 20 *kHz*.

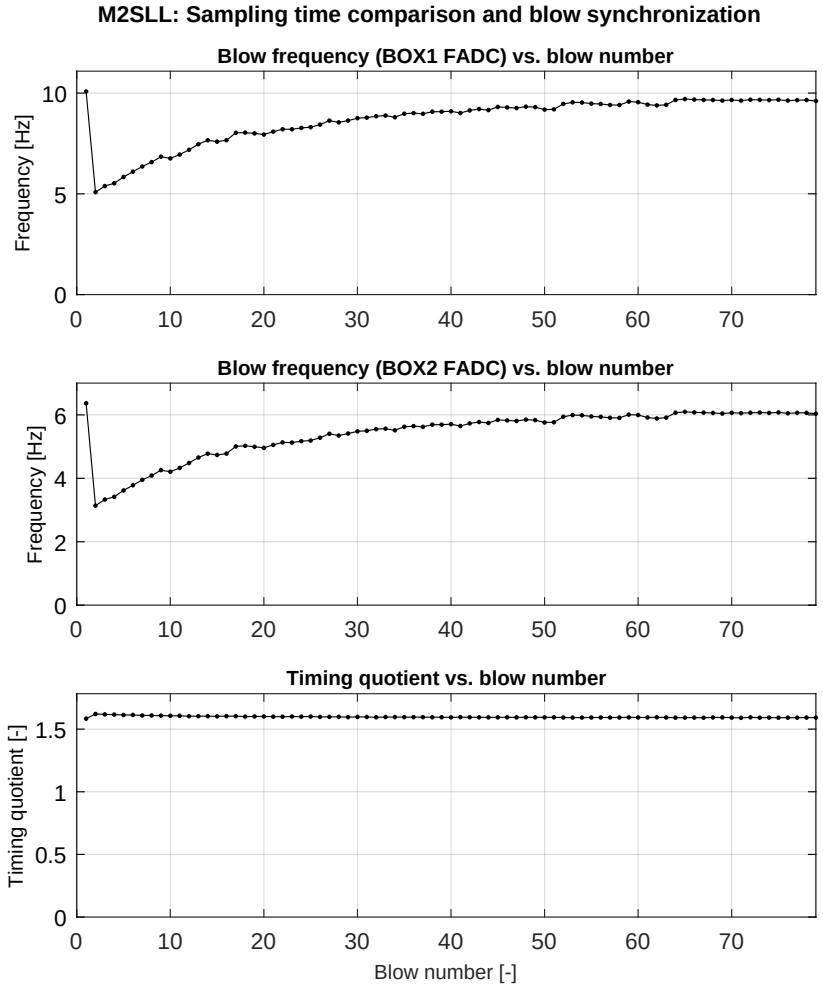

Figure D.1: Blow frequency as recorded by first and second fast ADC system and corresponding timing quotient for test M2SLL

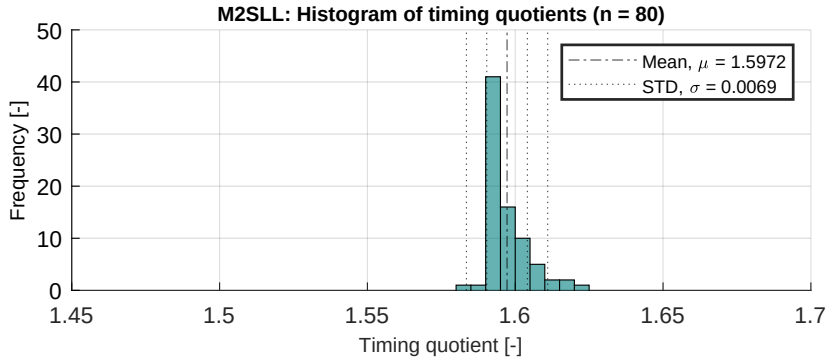

Figure D.2: Histogram of timing quotients, with specified mean μ and standard deviation σ for test M2SLL. n indicates the number of blows for which the timing quotient was calculated.

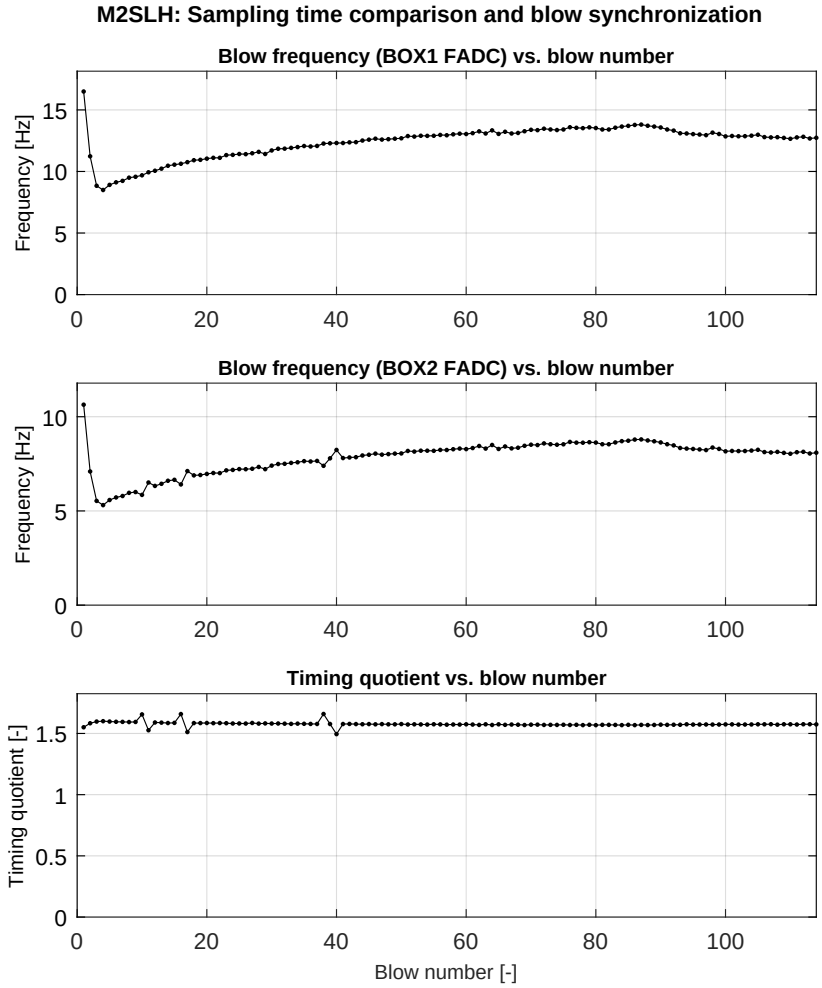

Figure D.3: Blow frequency as recorded by first and second fast ADC system and corresponding timing quotient for test M2SLH

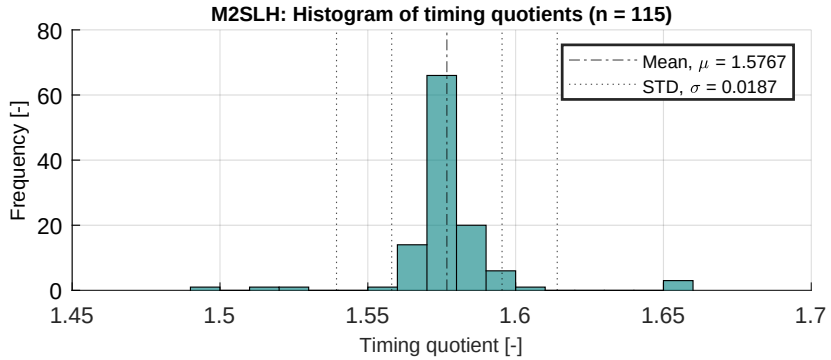

Figure D.4: Histogram of timing quotients, with specified mean μ and standard deviation σ for test M2SLH. n indicates the number of blows for which the timing quotient was calculated.

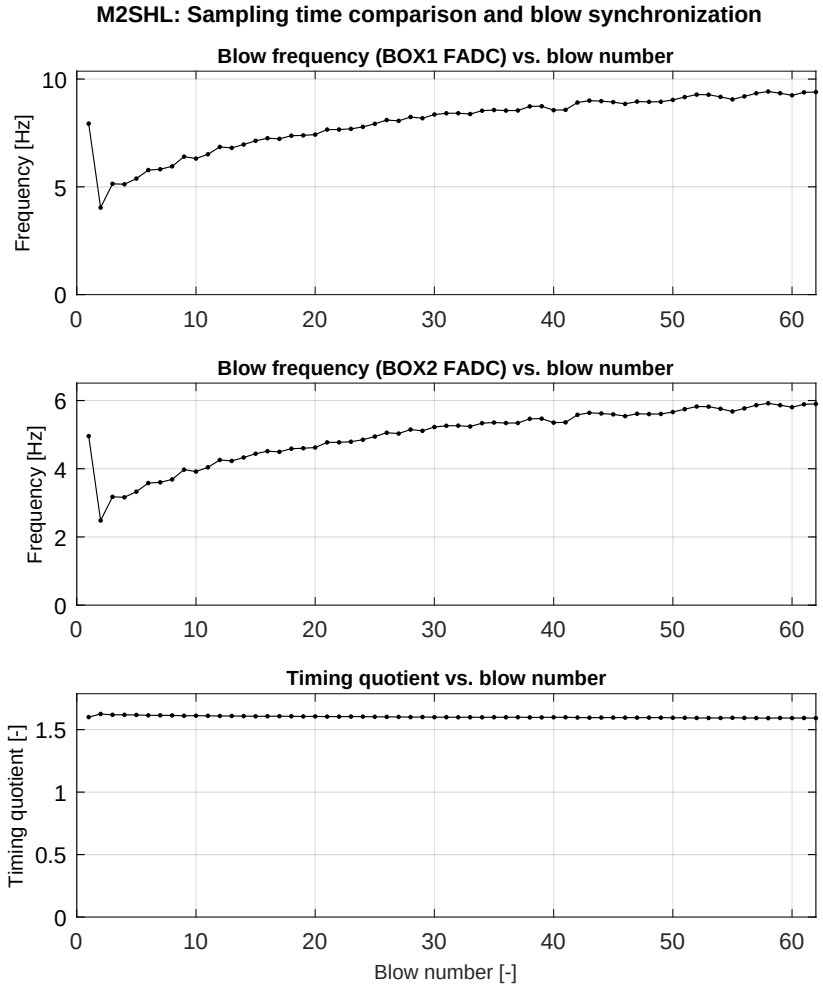

Figure D.5: Blow frequency as recorded by first and second fast ADC system and corresponding timing quotient for test M2SHL

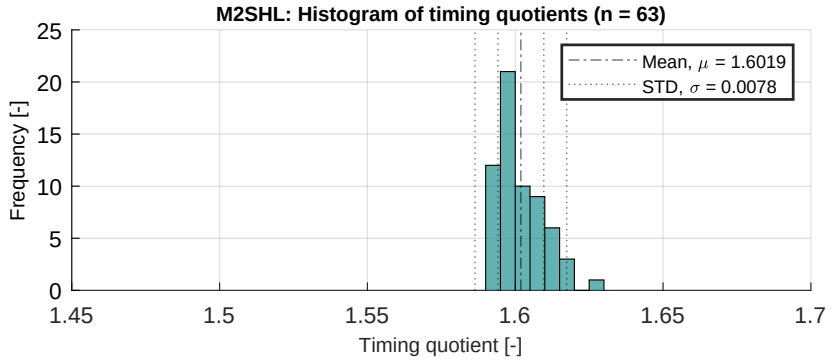

Figure D.6: Histogram of timing quotients, with specified mean μ and standard deviation σ for test M2SHL. n indicates the number of blows for which the timing quotient was calculated.

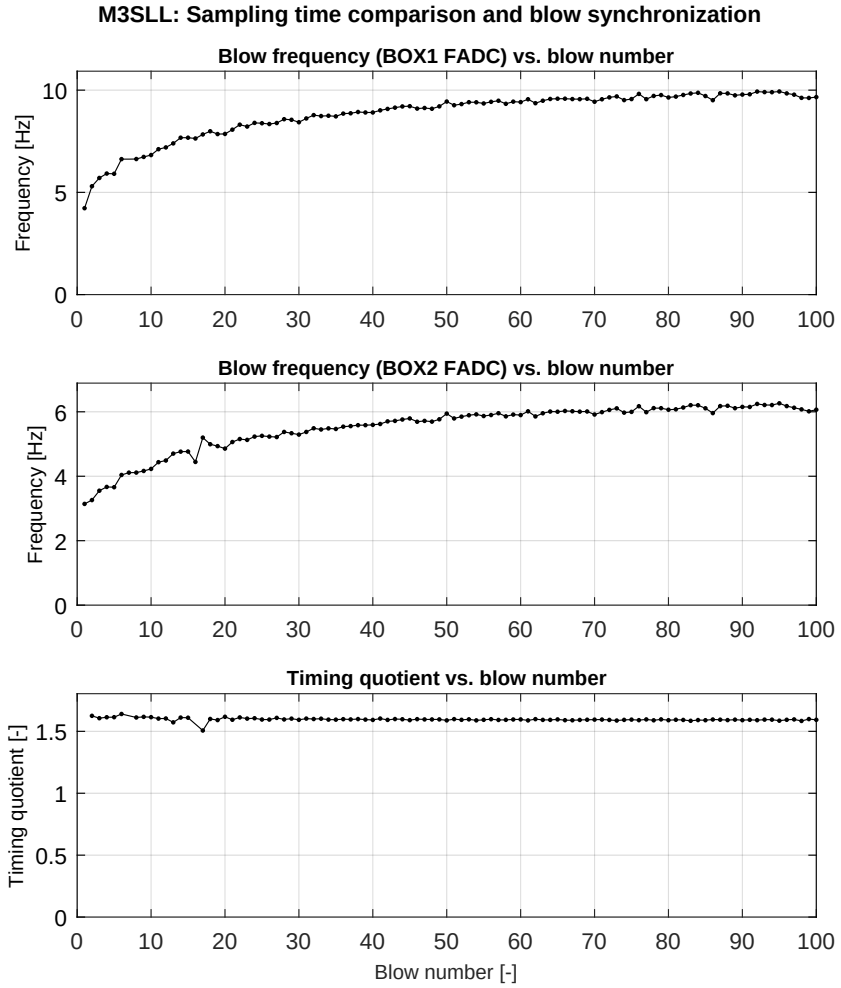

Figure D.7: Blow frequency as recorded by first and second fast ADC system and corresponding timing quotient for test M3SLL

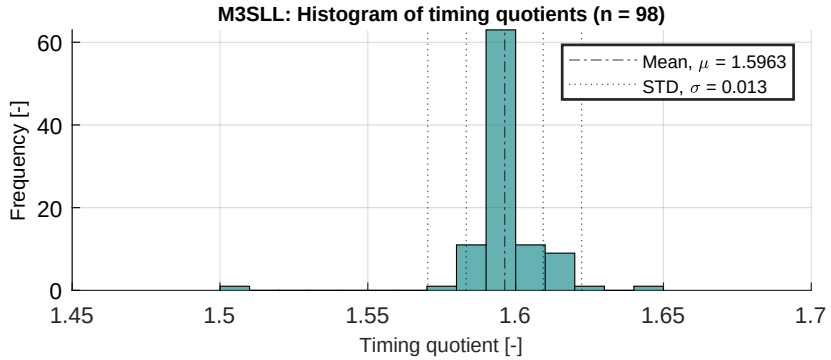

Figure D.8: Histogram of timing quotients, with specified mean μ and standard deviation σ for test M3SLL. n indicates the number of blows for which the timing quotient was calculated.

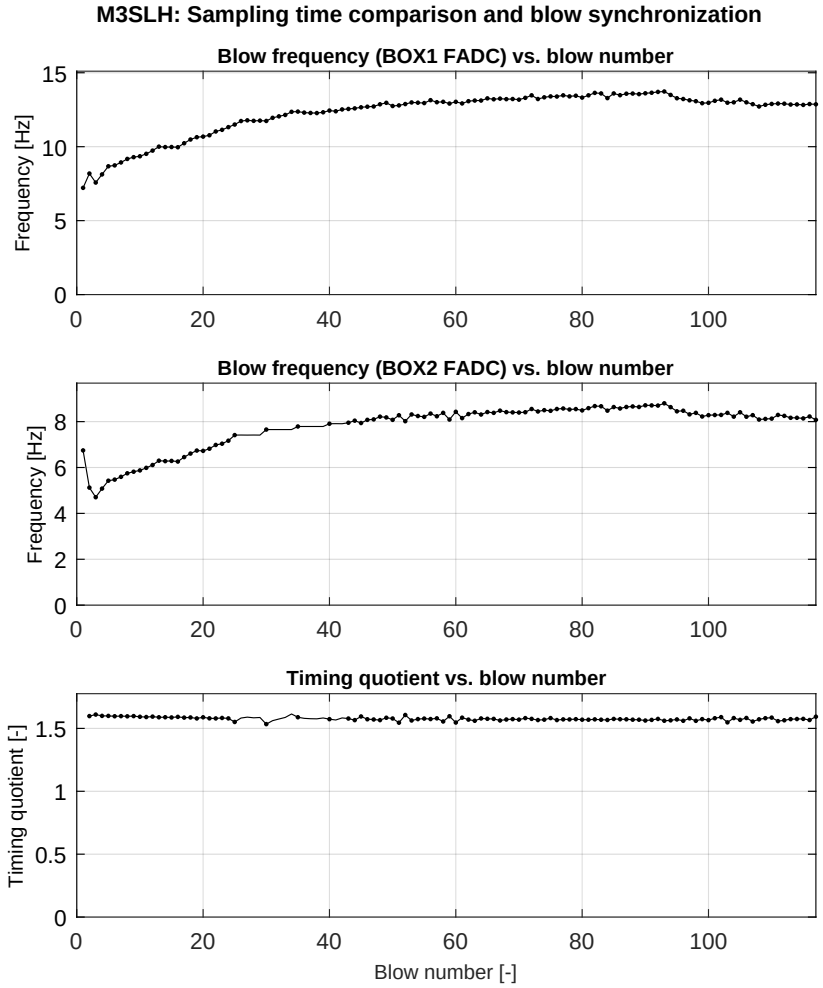

Figure D.9: Blow frequency as recorded by first and second fast ADC system and corresponding timing quotient for test M3SLH

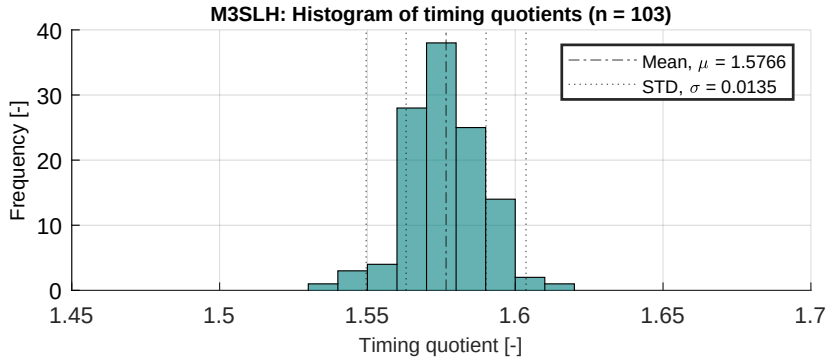

Figure D.10: Histogram of timing quotients, with specified mean μ and standard deviation σ for test M3SLH. n indicates the number of blows for which the timing quotient was calculated.

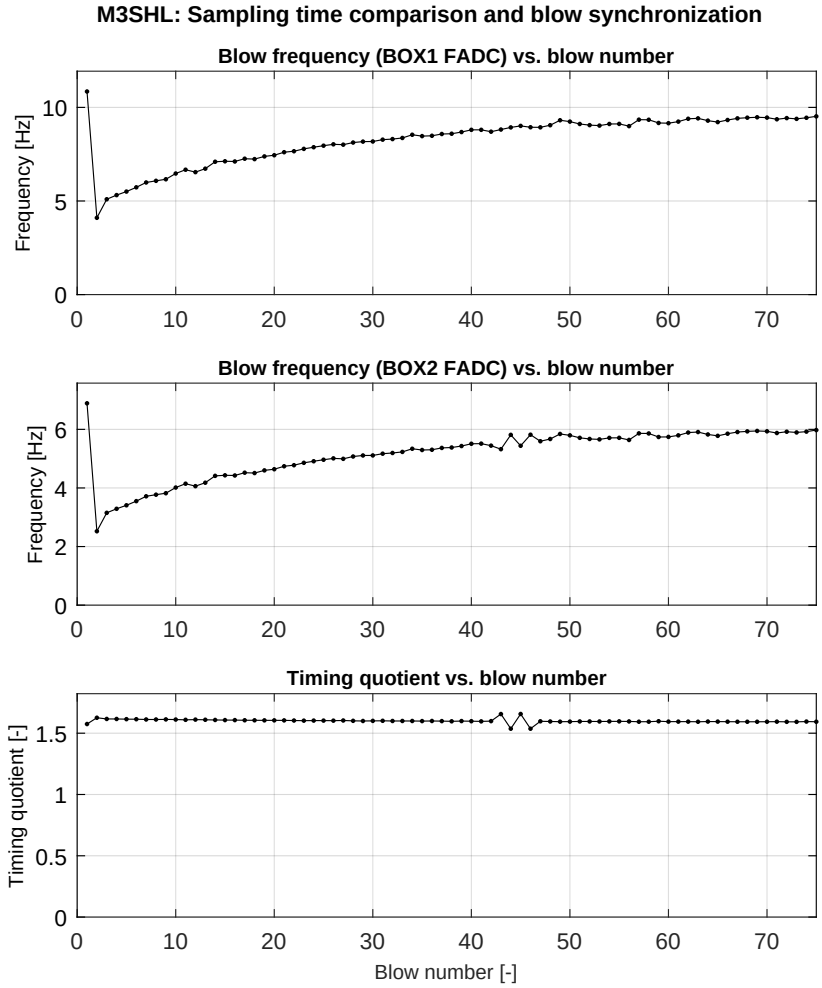

Figure D.11: Blow frequency as recorded by first and second fast ADC system and corresponding timing quotient for test M3SHL

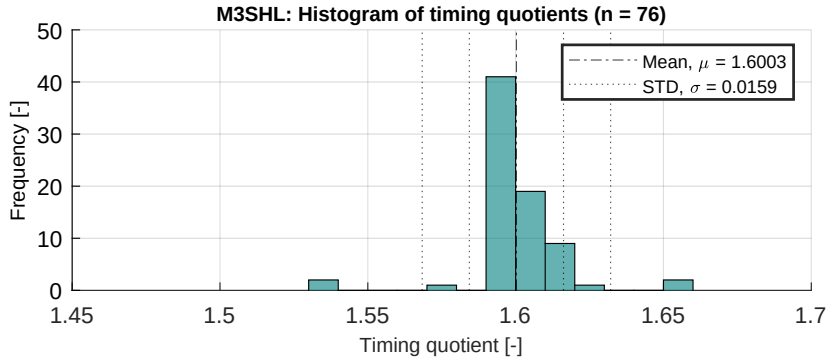

Figure D.12: Histogram of timing quotients, with specified mean μ and standard deviation σ for test M3SHL. n indicates the number of blows for which the timing quotient was calculated.

E

Energy transfer matching

E.1. Conventional vs. Hilo driving with the same ram mass

Researching the differences between conventional driving techniques and and HiLo driving for the same type of hammer, effectively entails assessing the influence of alterations in the energy administration mechanism of the following two cases:

1. high energy per blow $E_{T,1}$, low frequency $f_{T,1}$;
2. low energy per blow $E_{T,1}$, high frequency $f_{T,2}$.

To achieve the latter, it is essential to maintain the total energy administered to the pile E_T per unit of time. In other words: the product of energy per blow and driving frequency should yield the same result for the two cases described above. The single most important parameter is in this case the impact velocity of the ram mass v_0 , which is governed by hammer stroke h, and determines the maximum force amplitude in the pile. Theoretically, for an idealized situation where energy conversion is 100% efficient, this entails decreasing impact inversely proportional to the increase in hammering frequency, as illustrated by the Equation E.1 where the the frequency is respectively increased by a factor α.

$$E_{T,1} \cdot f_{T,1} = E_{T,2} \cdot f_{T,2} \implies E_{T,1} \cdot f_{T,1} = \frac{E_{T,1}}{\alpha} \cdot (f_{T,1} \cdot \alpha) \tag{E.1}$$

To decrease the impact energy, the hammer stroke h needs is reduced to decrease the impact velocity v_0. The latter parameter can be calculated from the energy balance:

$$E_{\text{pot}} = E_{\text{kin}} \implies m_H \cdot g \cdot h = 1/2 \cdot m_H \cdot v_0^2 \implies v_0 = \sqrt{\frac{2 \cdot h}{g}} \tag{E.2}$$

Please note that Equation E.2 only holds for 1g conditions. In the centrifuge, due to the presence of a gravity curve (see Equation 5.1), Equation E.2 needs to be adapted. As mentioned before in Chapter 5, centrifugal acceleration (following from the circular motion around the center of the centrifuge) effectively creates and artificial "gravitational" field, which acts on the small scale model in the carriage. However, unlike gravity, centrifugal acceleration only acts on objects subjected to circular motion around a fixed reference. Although this is true of the majority of components of the actuator and sample container, there is one important exception: the ram mass. Theoretically, up till its moment of release, the ram mass is subjected to centrifugal acceleration, say $r_{ini} \cdot \omega^2$. Hence its weight is equal to $m \cdot r_{ini} \cdot \omega^2$. Now, the ram mass is released. Basic physical state that for an object released from circular motion, the direction of the velocity vector is fixed and equal to

tangent of the circular path at the point of release. As the direction of the velocity vector no longer changes, the effects of centrifugal acceleration are not present anymore. Hence, the object has a weight equal to $m \cdot g$ and velocity v equal to $r \cdot \omega$ (tangential to the circle). Hence, the ram mass has only kinetic and no potential energy (in the direction centrifugal acceleration field). Continuing this line of thought, and stating that the ram mass (coincidentally) lands on top of the anvil, its weight is instantly increased to $m \cdot r_{end} \cdot \omega^2$. However, in reality is practically impossible to create a hammer which consequently lands on top of the anvil without any guidance due to the Coriolis effect. As the top of the anvil is located at a larger distance form the center of the centrifuge (r_{end}) than the ram mass before release (r_{ini}), its rotational velocity is larger. The latter entails that (for an orbit where $r_{end} - r_{ini} << r_{end}$, so the circular path can be approximated as straight line) the tangential distance traveled by the anvil is larger than the distance traveled by the ram mass during its fall. Hence, the ram mass misses the anvil.

To overcome the aforementioned problem, the ram mass moves around a guiding rod. This means that is remains in contract with a stationary part of the carriage while moving through the centrifugal acceleration field. Hence, it remains under its respective influence and energy balance equations remain valid. Therefore, by substitution of Equation 5.1 into Equation E.2 it is found:

$$E_{\text{pot, centrifuge}} = E_{\text{kin, centrifuge}} \implies m_H \cdot (r \cdot \omega^2) \cdot h = 1/2 \cdot m_H \cdot v_0^2 \tag{E.3}$$

The contact between the ram mass and guiding rod, is associated with extreme forces and therefore causes severe abrasion of the guiding rod, which is made from unhardened silversteel. The latter could result in more energy dissipation, resulting in a lower impact velocity. However, this influence can only be quantified by direct measurement of the impact velocity. Hence, the use of a dissipation term in the following but also previous equations has been omitted.

While falling, the ram mass is displaced through the centrifugal acceleration field. Consequently, the distance to the centrifuge's center r and the ram acceleration $r \cdot \omega^2$ are not constant. As no energy dissipatin is considered, either side of Equation E.3 can be discretized to account for the change in r. Approximation of E_{pot} through discretization of the fall height h is the most convenient option and is elaborated upon below.

Firstly, the total fall height is defined as the difference between the end position and initial position of the ram mass, r_{end} and r_{ini} respectively, and subsequently divided into n equal segments of height δh as shown by Equation E.4.

$$\delta h = \frac{h}{n} = \frac{r_{\text{end}} - r_{\text{ini}}}{n} \tag{E.4}$$

As the ram mass moves away from the center of the centrifuge while falling, $r_{end} > r_{ini}$. The latter explains the sequence of the terms in Equation E.4. Secondly, discretization of the left hand side of E.3 yields:

$$E_{\text{pot, centrifuge}} = m_H \cdot \omega^2 \cdot \delta h \sum_{i=0}^{n-1} r_{\text{ini}} + (1/2 + i)\delta h \tag{E.5}$$

By substitution of Equation E.4 into Equation E.5, it is found:

$$E_{\text{pot, centrifuge}} = m_H \cdot \omega^2 \cdot h \sum_{i=0}^{n-1} \frac{r_{\text{ini}} + (1/2 + i)\delta h}{n} \tag{E.6}$$

Where the Riemann sum from Equation E.6 can be evaluated as:

$$\sum_{i=0}^{n-1} \frac{r_{\text{ini}} + (\frac{1}{2} + i)\delta h}{n} = r_{\text{ini}} + 1/2 \cdot \delta h + \frac{(n-1)}{2} \cdot \delta h = \frac{1}{2}(r_{\text{end}} + r_{\text{ini}}) \tag{E.7}$$

Test description	Impact velocity [L/T]	Impact duration [T]	Ram mass [M]
Light	$v_{0,light}$	Δt_{light}	$m_{H,light}$
Heavy	$v_{0,heavy}$	Δt_{heavy}	$m_{H,heavy}$

Table E.1: Variable denotation as used in Figure E.1a and E.1b

Finally, substituting the result of Equation E.7 into E.5, it is found:

$$E_{\text{pot, centrifuge}} = m_H \cdot (\frac{1}{2}(r_{\text{end}} + r_{\text{ini}}) \cdot \omega^2) \cdot h = m_H \cdot \overline{a} \cdot h \tag{E.8}$$

Where $\overline{a}$ is equal to the acceleration averaged over the stroke of the hammer.

E.2. Conventional vs. Hilo driving with different ram masses

To deepen the investigation into the differences between conventional driving and HiLo driving, change of hammer has also been incorporated into the test matrix. Once more, the total energy delivered to the pile per unit time should be maintained. Apart from the need to further decrease hammer stroke h to compensate for the increase in the hammer's mass, two additional effects should be accounted for, namely:

- Deviations in impact time Δt. Impact time is proportional to the height of the ram mass divided by the wave propagation velocity $c = \sqrt{\frac{E}{\rho}}$. Due to deviating dimensions of the hammers, the available time for energy exchange between the driver and pile Δt differs;
- Force degradation rate. The mass of the hammer governs the reduction of stress (and force) in the pile over impact duration . When expressed as a stress reduction coefficient, it is inversely proportional to the hammer's mass m_H. Hence, for a heavier ram mass, stress at the top of the pile degrades slower and is present longer.

Both of the aforementioned effects are known to exist. However, literature provides very little information with respect to the quantification of both effects. Arguably, the influences should therefore be assessed on the basis of an experimental investigation. Yet, the existing theoretical framework can be applied to gain a better understanding of the key variables affected by the aforementioned phenomena. Based on previous research, the latter requires a profound understanding of three parameters which govern the energy transfer between driver and pile, namely:

- Impact velocity v_0, which is governed by hammer stroke h, and determines the maximum force amplitude in the pile;
- Impact time Δt, which proportional to the height of the ram mass divided by the wave propagation velocity for its respective material and designates the available time for energy exchange between the driver and pile Δt;
- Force degradation rate, which is inversely proportional to the hammer's mass m_H and governs the reduction of stress (and force) in the pile over impact duration

Now, consider two hypothetical tests respectively with a light and heavy hammer, coherently named *light* and *heavy*, characterized by the following two sets of test parameters:

1. $v_{0,light}$, Δt_{light}, $m_{H,light}$;
2. $v_{0,heavy}$, Δt_{heavy}, $m_{H,heavy}$.

For an ideal comparison of results, the energy administered to the pile E_T should be equal for of both tests, the following should hold:

$$E_{T,1} = E_{T,2} \tag{E.9}$$

By substitution of Equation 4.25 into Equation E.9, it is found:

$$\int_{T_{\text{impact}}}^{T_{\text{impact}}+\Delta t_{\text{light}}} (F_{(P,m)_{\text{light}}} \cdot v_{(P,m)_{\text{light}}})\ \text{dt} = \int_{T_{\text{impact}}}^{T_{\text{impact}}+\Delta t_{\text{light}}} (F_{(P,m)_{\text{heavy}}} \cdot v_{(P,m)_{\text{heavy}}})\ \text{dt} \tag{E.10}$$

Where $F_{(P,m)_{light}}$ and $F_{(P,m)_{heavy}}$ represent the pile force recorded during pile installation by strain gauges installed on the upper part of the shaft. Similarly, $v_{(P,m)_{light}}$ and $v_{(P,m)_{heavy}}$ designate pile velocity, which is computed through time integration of acceleration (measured by an accelerometer installed at the aforementioned location). The relevance of impact velocity v_0 and the hammer's mass m_H is illustrated in Figures E.1a and E.1b for test 1 and 2 respectively. The shaded areas in Figures E.1a and E.1b graphically represent E_T of both tests. Moreover, a definition to several of the used variable names of Figures E.1a and E.1b, is provided by Table E.1. However, since the computation of E_T requires the use of measured quantities, it is impossible to fully match the transferred energy between two tests beforehand.

Knowing the energy carried by the ram mass at an infinitesimal instant before impact E_H, it is possible to compute the efficiency of the driver system η_{ds} through Equation 4.26:

$$\eta_{ds} = \frac{E_T}{E_H}$$

Where E_H can be computed in accordance with Equation 4.28:

$$E_{H,\text{centrifuge}} = (m_H \cdot \overline{a} \cdot h) \cdot \eta_h$$

Where m_H is the mass of the hammer, $\overline{a}$ is the acceleration (averaged over the h due to the gravity curve in the centrifuge), h is the stroke and η_h is the hammer efficiency as defined in Table 2.3. It is apparent that fixing $m_H \cdot a \cdot h$ between tests is inadequate to synchronize E_T. Full comparison also requires the establishment of test specific values for η_{ds} and η_h, as it is imaginable that aforementioned efficiencies varies with h (v_0). For this reason, the set-up has been equipped with sensory equipment which enables the capture of F_P, v_P and v_0, respectively through the use of strain gages, an accelerometer and light sensors (or alternatively hall sensors). For more information on the sensory equipment, the reader is referred to 5.2.3. Due to the use of the aforementioned equipment, it is possible to determine η_h and η_{ds} through Equations E.11 and E.12.

$$\eta_h = \frac{1/2 \cdot v_{0,\text{measured}}^2}{\overline{a} \cdot h} \tag{E.11}$$

For an idealized frictionless scenario Equation E.11 equals one as all potential energy is converted into kinetic energy. It is the expectation that in reality, the latter will not hold. The latter also stresses the importance of impact velocity measurement in the centrifuge. Hence, the instead of using v_0^2 (a theoretical value based on energy balance calculations), the impact velocity is denoted as $v_{0,measured}^2$ as it is, in fact, a measured quantity. Similar to Equation E.11, the efficiency of the driver system η_{ds} can be computed as:

$$\eta_{ds} = \frac{E_T}{1/2 \cdot m_H \cdot v_{0,\text{measured}}^2} \tag{E.12}$$

Where E_T is computed in accordance with Equation 4.25. After rearrangement of terms and substitution of Equation E.12 into Equation E.9, and equivalent expression for Equation E.10 is found:

$$(1/2 \cdot m_{H,\text{light}} \cdot v_{0,\text{light}}^2) \cdot \eta_{\text{ds, light}} = (1/2 \cdot m_{H,\text{heavy}} \cdot v_{0,\text{heavy}}^2) \cdot \eta_{\text{ds, heavy}} \tag{E.13}$$

Please observe that expression E.13 has also been used in Figures E.1a and E.1b to quantify the shaded area.

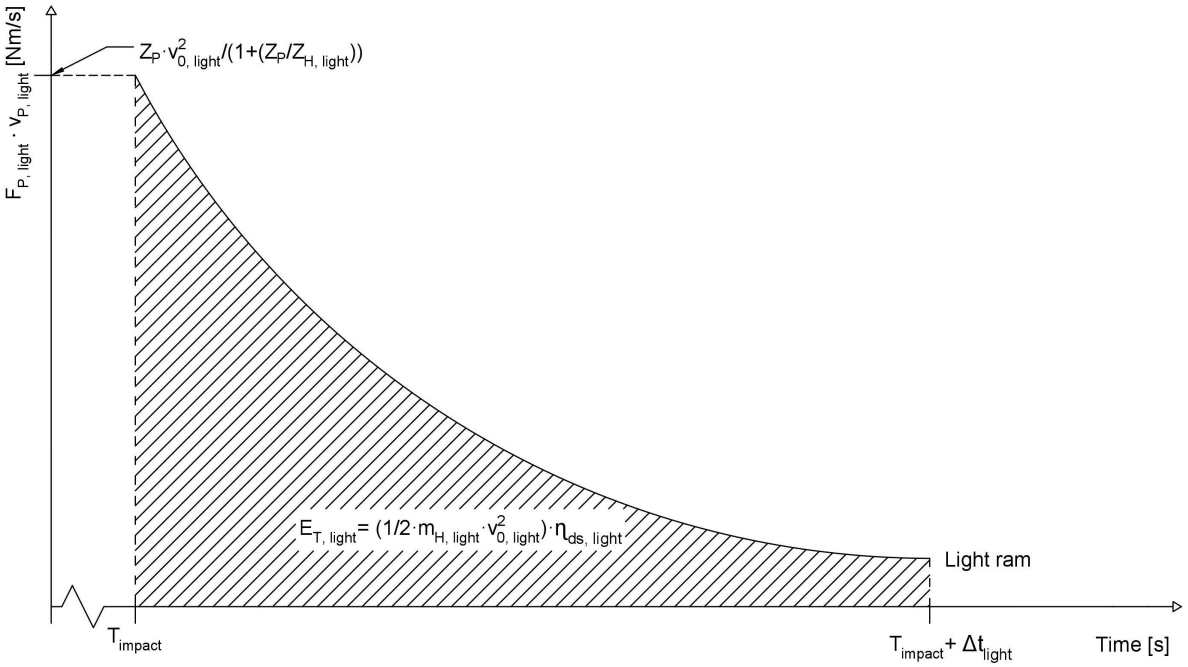

(a) Energy flux versus time, idealized for the use of a light ram mass

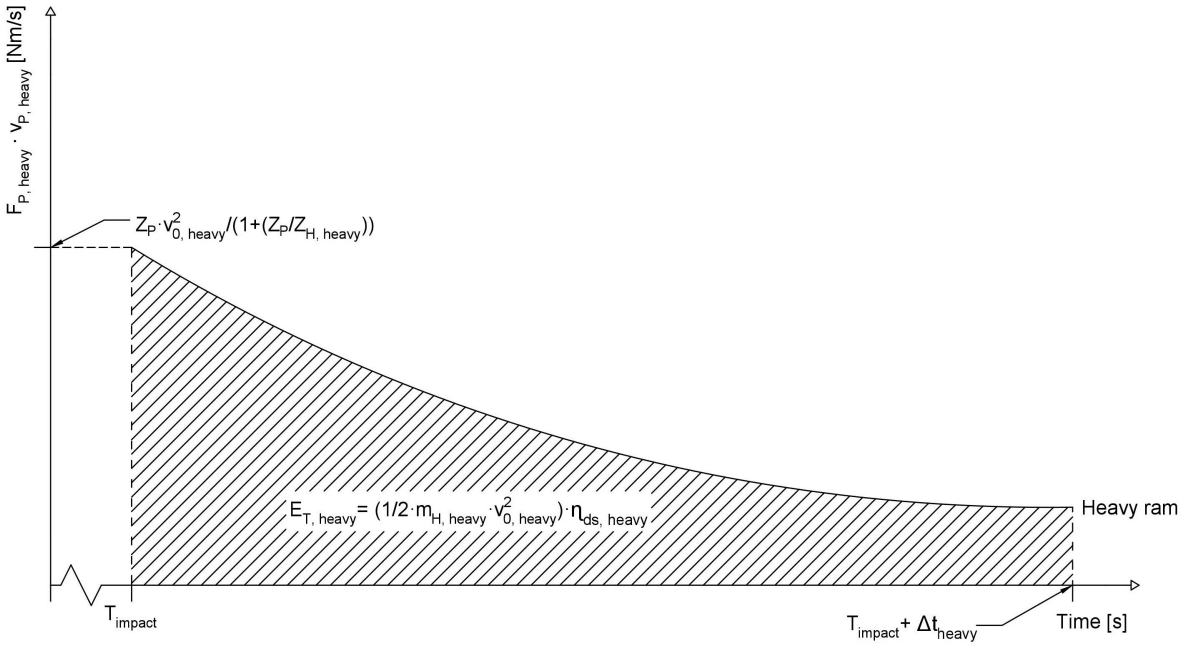

(b) Energy flux versus time, idealized for the use of a heavy ram mass

Despite of the previously presented derivation, Table A.1 is drafted under the assumption that η_{ds} and η_h are constant. The author recognizes the possibility that the latter assumption is invalidated upon evaluation of the test results, presumably due to the extensive forces associated with the contact of the ram mass and the guiding rod. A problem which is likely to aggravate under the influence of abrasion. However, through reevaluation of stroke h it is possible proper synchronize E_T between tests.

———————

———————